



5-2019

Electrochemical Engineering of All-Vanadium Redox Flow Batteries for Reduced Ionic and Water Crossover via Experimental Diagnostics and Multiscale Modeling

Yasser Ashraf Gandomi
University of Tennessee, yashrafg@vols.utk.edu

Follow this and additional works at: https://trace.tennessee.edu/utk_graddiss

Recommended Citation

Ashraf Gandomi, Yasser, "Electrochemical Engineering of All-Vanadium Redox Flow Batteries for Reduced Ionic and Water Crossover via Experimental Diagnostics and Multiscale Modeling." PhD diss., University of Tennessee, 2019.
https://trace.tennessee.edu/utk_graddiss/5441

This Dissertation is brought to you for free and open access by the Graduate School at TRACE: Tennessee Research and Creative Exchange. It has been accepted for inclusion in Doctoral Dissertations by an authorized administrator of TRACE: Tennessee Research and Creative Exchange. For more information, please contact trace@utk.edu.

To the Graduate Council:

I am submitting herewith a dissertation written by Yasser Ashraf Gandomi entitled "Electrochemical Engineering of All-Vanadium Redox Flow Batteries for Reduced Ionic and Water Crossover via Experimental Diagnostics and Multiscale Modeling." I have examined the final electronic copy of this dissertation for form and content and recommend that it be accepted in partial fulfillment of the requirements for the degree of Doctor of Philosophy, with a major in Mechanical Engineering.

Matthew Mench, Major Professor

We have read this dissertation and recommend its acceptance:

David Keffer, Kenneth Kihm, Feng-Yuan Zhang, Doug Aaron

Accepted for the Council:

Dixie L. Thompson

Vice Provost and Dean of the Graduate School

(Original signatures are on file with official student records.)

**Electrochemical Engineering of All-Vanadium Redox
Flow Batteries for Reduced Ionic and Water Crossover
via Experimental Diagnostics and Multiscale Modeling**

A Dissertation Presented for the
Doctor of Philosophy
Degree
The University of Tennessee, Knoxville

Yasser Ashraf Gandomi
May 2019

Copyright © 2019 by Yasser Ashraf Gandomi
All rights reserved.

DEDICATION

To my father, mother, and brother.

ACKNOWLEDGEMENTS

First and for most, I would like to thank Prof. Matthew Mench, my mentor and PhD advisor. When I first came to University of Tennessee, I did not have prior experience in this field (electrochemical energy storage and conversion devices), however, Prof. Mench believed in me, continued to support and encourage me during this path. I am very grateful for him for providing me with the opportunity to learn and grow, personally and professionally. No word can express my appreciation for Prof. Mench and his support.

I would like to thank my lab mates (past and present) at University of Tennessee. Ms. Kathy Williams, our administrator, for her tremendous help and support; Dr. Doug Aaron, our internal lab manager, for his leadership, support and encouragement.

I also thank my committee members, Dr. Kenneth Kihm, Dr. David Keffer, Dr. Feng-Yuan Zhang, and Dr. Doug Aaron for their support and invaluable recommendations and feedback throughout this thesis. We have had several collaborations with Dr. Kihm's group in addition to this PhD work. I have learned from his vast knowledge during a redox flow battery project funded by Volkswagen USA Corp. (Grant R011370023). Dr. David Keffer introduced me to molecular dynamic (MD) simulations of polymeric membranes and guided me through completion of the MD model developed in this work. His patience, encouragements, and support were beyond words. Dr. Feng-Yuan Zhang was our lab internal manager when I joined Prof. Matthew Mench's group. Dr. Zhang taught me on the principles of polymer electrolyte fuel cells. Later on, we had collaboration with Dr.

Zhang's group on a project related to high-performance polymer electrolyte membrane fuel cell stack funded by W.L. GORE and Associates. I really appreciate the support I received from Dr. Zhang during that time. Dr. Doug Aaron was a fantastic lab manager and I frequently received support from him not only on my PhD research; but also, I learned from him during the completion of microbial fuel cell project.

During my studies at University of Tennessee, I worked on multiple side projects where I had the honor to work and collaborate with several professors and group leaders including Dr. Chien-Te Hsieh, Dr. Thomas Zawodzinski, Dr. Kivanc Ekici, Dr. Anming Hu, Dr. Seungha Shin, and Dr. Subhadeep Chakraborty. I sincerely thank them for their help and support.

At the Department of Mechanical, Aerospace, and Biomedical Engineering at University of Tennessee, I was elected as the president of American Society of Mechanical Engineers (ASME) for three consecutive years. Therefore, I had the honor to work with Dr. Eric Wade, ASME student chapter advisor; I learned a lot from his experience and leadership. Dr. Wade was extremely supportive and supported me along with Prof. Mench and Dr. Doug Aaron to land my next job.

I thank University of Tennessee for providing me the Chancellor Fellowship. I also appreciate W. L. GORE and Associate for providing the membranes used in some sections of this work, and I appreciate useful discussions I had with the W. L. GORE and Associate

staff including Dr. Alexander Agapov, Dr. Erin Redmond, Dr. M. D. Edmundson, and Dr. F. Colin Busby.

Finally, I want to thank my fabulous family, my mother (Shamsi), my father (Naser), and my brother (Amin) for tremendous help and support during this adventure. Without their help and sacrifices throughout these years, I would not be able to go after my goals.

ABSTRACT

Scalable and open architecture of redox flow batteries (RFBs) is a promising solution for large-scale energy storage. Among many chemistries developed for RFBs, all-vanadium redox flow batteries (VRFBs) currently show great potential for widespread commercialization. VRFBs utilize vanadium ions with different oxidation states in the negative and positive electrolytes; this characteristic frees them from irreversible capacity decay as a function of electroactive species transport through the membrane (i.e. crossover). However, crossover of vanadium ions and water during the charge/discharge cycling not only results in a lost discharge capacity, but also has real-time influence on the cell performance.

Several parameters affect solute and solvent crossover during cycling. In this dissertation, experimental data along with multiscale computational modeling tailored to quantify the contributions to capacity decay stemming from ion-exchange membrane properties (e.g. equivalent weight and degree of reinforcement), flow field design, electrolyte properties, and operating conditions. A major focus has been to understand the effect of the electrode/membrane interface on the capacity decay and contact resistance. Novel ex-situ conductivity cells have been devised to assess ionic conductivity of the ion-exchange membranes along with electrolytes leading to details on the impact of interfacial phenomena on ionic conductivity and crossover.

To quantify the long-term influence of crossover, a unique set-up (we call it IonCrG: Ionic Crossover Gauge) was built and fabricated enabling real-time measurement of the ionic transport across the polymeric membrane using ultraviolet-visible (UV/Vis) spectroscopy. The IonCrG enables separation of contributions to crossover emerging from concentration and electrostatic potential gradients. To investigate the instantaneous impact of crossover on the performance, a real-time current density distribution diagnostic has been implemented for measuring the in-plane current density distribution.

The insights gained from this suite of experimental diagnostics and multiscale modeling have inspired design of systems with enhanced performance and greatly decreased crossover losses. Novel cell topologies along with asymmetric electrolyte compositions were designed and engineered for mitigating the ionic crossover during the operation of VRFBs. The cell architecture as well as the electrolyte configuration proposed in this dissertation provides an inexpensive and passive solution for retaining capacity during extended cycling of aqueous RFBs.

TABLE OF CONTENTS

Chapter One : Introduction to Redox Flow Batteries	1
Scholarly contributions	2
Abstract	2
1.1. Introduction.....	2
1.2. Redox Flow Battery Architectures.....	8
1.3. Performance Metrics for Redox Flow Batteries	15
1.3.1. Voltage efficiency	16
1.3.2. Coulombic efficiency.....	17
1.3.3. System level energy efficiency	17
1.3.4. Theoretical Capacity Utilization	18
1.3.5. Discharge capacity fade over long-term cycling	18
Chapter Two : Literature Review on Solute and Solvent Crossover Assessment in Redox Flow Batteries	20
Scholarly contributions	21
Abstract	21
2.1. Introduction.....	21
2.2. Previous efforts on crossover measurement	23
Chapter Three : Mathematical Modeling of RedOx Flow Batteries and In-Situ Potential Distribution Diagnostics	31
Scholarly contributions	32
Abstract	32
3.1. Introduction.....	33
3.2. Experiment.....	34
3.2.1. In-situ potential distribution set-up.....	34
3.2.2. VRFB architecture	35
3.2.3. Electrolytes	36
3.3. Mathematical Model	38
3.3.1. Model formulation	40
3.3.2. Porous carbon electrodes	40
3.3.3. Membrane	51
3.3.4. Boundary conditions for multi-domain modeling approach.....	53
3.3.5. Boundary conditions for the conservation of charge	53
3.3.6. Boundary conditions for the conservation of momentum.....	54
3.3.7. Boundary conditions for the conservation of mass.....	55
3.3.8. Numerical Modeling Approach	56
3.4. Results and Discussion	56
3.4.1. The effect of convective mass transport on the species distribution	57
3.4.2. Analysis of overpotential on the species distribution	73
3.4.3. Experimental validation of the potential-distribution simulation data	75
3.5. Conclusions.....	78
3.6. Acknowledgments.....	80

Chapter Four : Coupled Membrane Transport Parameters for Ionic Species in All-Vanadium Redox Flow Batteries	81
Scholarly contributions	82
Abstract	82
4.1. Introduction	83
4.2. Experimental	85
4.2.1. Schematic of the set-up	85
4.2.2. Different components	87
4.2.3. Electrolyte	88
4.2.4. Testing protocol	90
4.2.5. UV/Vis spectroscopy	91
4.3. Mathematical Model	92
4.4. Results and Discussion	98
4.4.1. Concentration-induced crossover	98
4.4.2. Electric-field-induced crossover	106
4.5. Summary and Conclusions	128
4.6. Acknowledgments	129
4.7. Nomenclature	130
Chapter Five : Influence of Membrane Equivalent Weight and Reinforcement on Ionic Species Crossover in All-Vanadium Redox Flow Batteries	131
Scholarly contributions	132
Abstract	132
5.1. Introduction	133
5.2. Experimental	137
5.2.1. Membrane selection and pretreatment	137
5.2.2. Method of approach	138
5.2.3. Testing protocol	141
5.2.4. UV/Vis spectroscopy	142
5.2.5. Vanadium Ion Permeability Assessment	144
5.3. Results and Discussion	145
5.3.1. Capacity decay during long-term cycling	145
5.3.2. Crossover of vanadium ions	155
5.4. Summary and Conclusions	165
5.5. Acknowledgments	168
5.6. Nomenclature	168
Chapter Six : Realtime Influence of Ionic Crossover on the Performance of Redox Flow Batteries	169
Scholarly contributions	170
Abstract	170
6.1. Introduction	172
6.2. Experimental	175
6.2.1. Ultra-thin high-performance membranes for all-vanadium redox flow batteries	175

6.2.2. Distributed Current Diagnostics for real-time assessment of ionic crossover	178
6.3. Results and Discussion	181
6.3.1. The influence of convection flux on the distributed current measurement ..	182
6.3.2. The influence of membrane morphology on the real-time distributed current	187
6.3.2. The influence of flow field design on the distributed current measurement	195
6.4. Conclusions.....	199
6.5. Acknowledgments.....	201
Chapter Seven : Influence of Flow Field Design on Crossover of Ionic Species in Redox	
Flow Batteries	202
Scholarly contributions	203
Abstract	203
7.1. Introduction.....	204
7.2. Experimental	206
7.2.1. Flow field geometries	207
7.2.2. UV-Vis spectroscopy	211
7.2.3. Long-duration cycling.....	213
7.3. Results and Discussion	214
7.3.1. Capacity decay for extended cycling	214
7.3.2. Influence of flow field design on ionic crossover in VRFBs	220
7.3.3. Influence of convective-enhanced flow on ionic crossover and long-term	
capacity decay in VRFBs.....	230
7.4. Conclusions.....	238
7.5. Acknowledgments.....	239
Chapter Eight : Techniques for Capacity Retention in RFBs	240
Scholarly contributions	241
Abstract	241
8.1. Introduction.....	242
8.2. Design Strategies for Mitigating Crossover.....	244
8.2.1. Impermeable membranes for redox active species and solvent.....	247
8.2.2. Recovering capacity via remixing external electrolytes	247
8.2.3. Filtering the electroactive species out from opposite electrolytes	248
8.2.4. Engineering the direction of crossover flux	248
Chapter Nine : Asymmetric Cell and Electrolyte Topologies for Passive Mitigation of	
Capacity in Aqueous RFBs	250
Scholarly contributions	251
Abstract	251
9.1. Introduction.....	253
9.2. Theoretical Background.....	254
9.3. Experimental	256
9.3.1. Asymmetric cell configuration for reduced crossover.....	256
9.3.2. Engineering Electrolyte composition for reduced crossover	263
9.4. Results and Discussion	264

9.4.1. Asymmetric cell configuration for capacity retention during extended cycling	264
9.4.2. Asymmetric electrolyte composition for capacity retention during cycling.	270
9.5. Conclusions.....	274
9.6. Acknowledgments.....	276
Chapter Ten : Interplay Between Diffusivity and Surface Barriers on IonIC Transport in Polymeric Membranes for All-Vanadium Redox Flow Batteries.....	277
Scholarly contributions	278
Abstract	278
10.1. Introduction.....	279
10.2. Experimental	281
10.2.1. Experimental set-up for crossover measurement.....	281
10.2.2. UV/Vis spectroscopy	281
10.2.3. Membrane selection and pretreatment	283
10.2.4. Electrochemical impedance spectroscopy (EIS).....	283
10.2.5. Ionic conductivity assessment for ion-exchange membranes and electrolytes	284
10.3. Results and Discussion	288
10.3.1. Assessing membrane-electrode interface resistance for VRFBs	289
10.3.2. Determining MacMullin number for Nafion® membranes within VRFBs architecture.....	291
10.3.3. Membrane stacking: An inexpensive approach for capacity retention	295
10.3.4. Multilayer IEM membranes for reduced crossover	302
10.3.5. IEM selection chart for reducing ionic crossover in VRFBs	309
10.4. Conclusions.....	311
10.5. Acknowledgments.....	311
Chapter Eleven : Concentrated Solution Model of Transport in Ion-Exchange Membranes	312
Scholarly contributions	313
Abstract	313
11.1. Introduction.....	313
11.2. Mathematical Membrane Transport Model	317
11.3. Results and Discussion	321
11.4. Conclusions.....	326
Chapter Twelve : Molecular Dynamic Model of Nafion Swelled in Nonaqueous Solvents	327
Scholarly contributions	328
Abstract	328
12.1. Introduction.....	329
12.2. Mathematical Model	332
12.2.1. Structural Models.....	332
12.2.2. Force field formulation	335
12.2.3. Force-field parameters	338
12.2.4. Modeling details.....	340

12.3. Results and Discussion	347
12.3.1. Structural analysis of the PFSA ionomer swelled in non-aqueous solvents	347
12.3.2. Assessing diffusivities for the PFSA ionomer swollen with ACN and DMSO	355
12.4. Conclusions.....	359
12.5. Acknowledgments.....	360
Chapter Thirteen : Water Management in Polymer Electrolyte Membrane Fuel Cells ...	361
Scholarly contributions	362
Abstract	362
13.1. Introduction.....	363
13.2. Experimental	367
13.2.1. Experimental Approach	370
13.2.2. Operating conditions.....	372
13.2.3. PEFC Configurations	373
13.2.4. Net Water Drag Calculations	377
13.3. Mathematical Model	380
13.3.1. Mathematical Model Development.....	383
13.3.2. Boundary conditions	385
13.4. Results and Discussion	385
13.4.1. Numerical Results.....	385
13.4.2. Experimental Results	386
13.5. Conclusions.....	401
13.6. Acknowledgments.....	402
13.7. Nomenclature	403
Chapter Fourteen : Summary and Conclusions	404
14.1. Summary and Motivations	405
14.2. Objectives and Contributions to the Field	407
14.2.1. Design and fabrication of a novel setup for real-time measurement of ionic crossover and in-situ potential distribution assessment within VRFB architecture	407
14.2.2. Assessing the influence of electric-field and electrolyte composition on the ionic crossover	409
14.2.3. Investigating the influence of ion-exchange membrane's equivalent weight and reinforcement on ionic crossover	411
14.2.4. Probing real-time influence of ionic crossover on the redox flow battery performance using distributed, in-plane current distribution diagnostic	412
14.2.5. Exploring the influence of convective flux distribution on the ionic crossover	414
14.2.6. Developing a macroscale, continuum mathematical model for simulating the performance of VRFBs	415
14.2.7. Multiscale modeling of the ion-exchange membranes	417
14.2.8. Ion-exchange membrane stacking: an inexpensive approach for reducing the ionic crossover in RFBs	419
14.2.9. Developing a novel, inexpensive, and passive approach for capacity retention during long-term cycling for aqueous RFBs.....	420

14.3. Recommendations for Future Work.....	422
References.....	425
Appendices.....	440
Appendix A.....	441
Appendix B.....	452
Vita.....	480

LIST OF TABLES

Table 1.1. Different Varieties of RFBs.....	6
Table 2.1. Summary of membrane crossover research in the literature.....	28
Table 3.1. Geometric, material and kinetic properties.....	42
Table 3.2. Electrolyte properties.....	43
Table 3.3. Reaction source term	45
Table 3.4. Initial species concentration.....	57
Table 4.1. Reaction source term	84
Table 4.2. Wavelength for spectroscopy measurement	91
Table 4.3. The permeability values for vanadium species ($m_2.s - 1 \times 10 - 12$)	103
Table 4.4. Deduced interaction coefficients for cocentration gradient-induced crossover	106
Table 4.5.: Electric-field-induced transport coefficient.....	118
Table 5.1. Initial and increase in ASR and ohmic overpotential (at 100 mA.cm^{-2}) as function of cycling for different membranes	153
Table 5.2. The details of the cation exchange membranes utilized in this work	158
Table 5.3. The vanadium V(IV) ion transport parameters through various ion-exchange	161
Table 6.1. Details of ultra-thin ion-exchange membranes tested in this work (Ref. ¹⁰²)	175
Table 6.2. The details regarding membranes swelling, ionic permeability, and long-term discharge capacity decay for the ion-exchange membranes (Data adopted from our previous publication, Ref. ¹⁰²).....	176
Table 6.3. Geometrical details regarding fully segmented flow fields	180
Table 7.1. Flow fields and channel geometries.....	210
Table 7.2. Ionic V(IV) permeability measured for different cell configurations.....	226
Table 9.1. Flow fields and channel geometries for serpentine and flow-through flow field designs.....	259
Table 9.2. Electrolyte compositions used for asymmetric acid tests	265
Table 10.1. Area-specific resistance (ASR) for series of Nafion® 115 membranes	290
Table 10.2. MacMullin number for IEMs within VRFBs configuration	294
Table 10.3. Comparison of ohmic overpotential for series of NR211 versus single-layer N115.....	306
Table 12.1. Van der Waals parameters for Nafion ionomer with equivalent weight of 1100 g.mol^{-1} (Data adopted from Ref. ²⁵⁷).....	339
Table 12.2. Van der Waals parameters for acetonitrile (Data adopted from Ref. ²⁵⁶)....	339
Table 12.3. Van der Waals parameters for dimethyl sulfoxide (Data adopted from Ref. ²⁵⁶)	341
Table 12.4. Van der Waals parameters for lithium (Data adopted from Ref. ²⁵⁶)	341
Table 12.5. Bond stretching coefficients for Nafion ionomer with $\text{EW}1100 \text{ g.mol}^{-1}$ (Data adopted from Ref. ²⁵⁷).....	341
Table 12.6. Bond stretching coefficients for acetonitrile (Data adopted from Ref. ²⁵⁶) .	342
Table 12.7. Bond stretching coefficients for dimethyl sulfoxide (Data adopted from Ref. ²⁵⁶)	342

Table 12.8. Bond angle coefficients for Nafion with EW1100 g.mol ⁻¹ (Data adopted from Ref. ²⁵⁷)	343
Table 12.9. Bond angle coefficients for acetonitrile (Data adopted from Ref. ²⁵⁶)	344
Table 12.10. Bond angle coefficients for dimethyl sulfoxide (Data adopted from Ref. ²⁵⁶)	344
Table 12.11. Dihedral coefficients for Nafion ionomer (Ref. ²⁵⁷).....	345
Table 12.12. Dihedral coefficients for dimethyl sulfoxide (Data adopted from Ref. ²⁵⁶).....	346
Table 12.13. Initial configuration of the system	347
Table 12.14. Diffusion coefficients calculated for PFSA ionomer swollen with various non-aqueous solvents, (cm ² /s × 10 ⁻⁷)	358
Table 13.1. Micro-Porous Layer (MPL) Properties.....	372
Table 13.2. Baseline operating conditions.....	376
Table 13.3. Operating conditions for net water drag tests	376
Table 13.4. PEFC configurations tested	376
Table 13.5. Mass transport resistance and thermal resistance ratio.....	378
Table 13.6. Modeling parameters (Ref. ²¹⁸).....	382
Table 13.7. Material properties expressions (Ref. ²¹⁸).....	383
Table 13.8. Model parameters.	384
Table A.1. Micro-Porous Layer (MPL) Properties.....	443
Table A.2. Baseline operating conditions	445
Table A.3. Operating conditions for net water drag calculations	446
Table A.4. PEFC configurations	446
Table B.1. Micro-Porous Comparison of the increase in output current from the 2 nd cycle to 7 th cycle in a carbon sensor at 60°C.....	464
Table B.2. Comparison of the increase in output current from the 2 nd cycle to 7 th cycle in a copper-coated sensor at 60°C.....	469

LIST OF FIGURES

Figure 1-1: Schematic representation of a single-cell RFB	9
Figure 1-2: Schematic representation of single-cell and stacked RFBs (a) Exploded view of a single cell, (b) Exploded view of stack of multiple cells, (c) schematic of the assembled stack of multiple cells)	10
Figure 1-3: Flow plate configurations (a) flow-frame architecture, (b) flow-channel architecture)	13
Figure 1-4: Schematic of membrane-less RFB (figure is taken from Ref. ⁸¹)	14
Figure 1-5: Schematic of HBr membrane-less RFB (figure is taken from Ref. ⁹²)	16
Figure 3-1: Schematic of the construction and placement of the DHE and Pt probes in the VRFB	37
Figure 3-2: 2-D Schematic of the computational domain.....	41
Figure 3-3: Sample cut-planes for computational analysis.....	58
Figure 3-4: Species distribution at 20 mL.min ⁻¹ and 200 mA.cm ⁻² discharge; (a) Vanadium species, (b) Protons and bisulphate	61
Figure 3-5: Species flux densities at 20 mL.min ⁻¹ and 200 mA.cm ⁻² discharge; (a) V(II)/V(V), (b) V(III)/V(IV), (c) Hanode + / Hcathode +, (d) HSO ₄ anode – / HSO ₄ cathode –	63
Figure 3-6: Species distribution at 20 mL.min ⁻¹ and 800 mA.cm ⁻² discharge; (a) Vanadium species, (b) Protons and bisulphate	65
Figure 3-7: Species flux densities at 20 mL.min ⁻¹ and 800 mA.cm ⁻² discharge; (a) V(II)/V(V), (b) V(III)/V(IV), (c) Hanode + / Hcathode +, (d) HSO ₄ anode – / HSO ₄ cathode –	66
Figure 3-8: Species distribution at 90 mL.min ⁻¹ and 200 mA.cm ⁻² discharge; discharge; (a) Vanadium species, (b) Protons and bisulphate.....	68
Figure 3-9: Species flux densities at 90 mL.min ⁻¹ and 200 mA.cm ⁻² discharge; (a) V(II)/V(V), (b) V(III)/V(IV), (c) Hanode + / Hcathode +, (d) HSO ₄ anode – / HSO ₄ cathode –	69
Figure 3-10: Species distribution at 90 mL.min ⁻¹ and 800 mA.cm ⁻² discharge; discharge; (a) Vanadium species, (b) Protons and bisulphate.....	71
Figure 3-11: Species flux densities at 90 mL.min ⁻¹ and 800 mA.cm ⁻² discharge; (a) V(II)/V(V), (b) V(III)/V(IV), (c) Hanode + / Hcathode +, (d) HSO ₄ anode – / HSO ₄ cathode –	72
Figure 3-12: Potential distribution in the through-plane direction of an operando VRFB; (a) 200 mA.cm ⁻² discharge, (b) 800 mA.cm ⁻² discharge.....	74
Figure 3-13: The potential of probes in through-plane direction of an operando VRFB during discharge; (a) 800 mA.cm ⁻² , (b) 600 mA.cm ⁻² , (c) 400 mA.cm ⁻² , (d) 200 mA.cm ⁻²	77
Figure 3-14: Potential distribution at the beginning of discharge.....	78
Figure 4-1: Schematic of the experimental setup (Blue lines (color on-line) represent Nafion® 117 membranes).....	86
Figure 4-2: The volume of deficient and enriched soluton at the end of 12-hour experiment.....	89

Figure 4-3: Drivers of crossover in an operating cell (“Cell 4”)	99
Figure 4-4: Concentration of diffused vanadium species to the interior chamber within the twelve-hour time range	100
Figure 4-5: Semi-natural log plot used to determine permeability based on diffused concentration.....	101
Figure 4-6: Measured permeability values for the vanadium species.....	102
Figure 4-7: Interaction coefficients for cocentration gradient-induced crossover.....	104
Figure 4-8: Schematic of the V(II)/V(III) symmetric test system at SoC: 50%	108
Figure 4-9: Schematic of the V(IV)/V(V) symmetric test system at SoC: 50%	110
Figure 4-10: Concentration of vanadium species within the interior chamber during discharge at SoC=50%	112
Figure 4-11: Fluxes of vanadium species during discharge at SoC=50%	114
Figure 4-12: Concentration of vanadium species within the interior chamber during charge at SoC=50%	116
Figure 4-13: Fluxes of vanadium species during charge at SoC=50%	117
Figure 4-14: The ratio of electrostatic potential gradient-induced crossover over concentration gradient-induced crossover at SoC = 50%. (a: V(II), b: V(III), c: V(IV) and d: V(V)).	122
Figure 4-15: The crossover current density (iV) at different potentials	127
Figure 5-1: Schematic of the experimental setup	140
Figure 5-2: (a) Capacity decay as a function of cycle number, (b) Theoretical capacity utilization as a function of cycle number.....	147
Figure 5-3: Capacity decay for different ion-exchange membranes as a function of (a) cycle number, (b) Time.....	149
Figure 5-4: Characteristic plots for the experimental membranes, (a) Coulombic efficiency, (b) voltage efficiency, (c) Polarization curves, (d) Power density	152
Figure 5-5: Concentration of diffused vanadium V(IV) ion to vanadium-deficient chamber within twenty-four-time period.....	156
Figure 5-6: Thickness of the membranes after soaking in the solution of 1.5 mol/L V(III)/V(IV) and 3.3 mol/L sulfuric acid.....	157
Figure 5-7: Measured permeability values for different membranes.....	159
Figure 5-8: Correlation between equivalent weight with V(IV) permeability and ASR	162
Figure 5-9: The discharge capacity decay at the end of cycling as function of vanadium V(IV) permeability.....	163
Figure 5-10: Correlation between V(IV) permeability and through-plane membrane swelling.....	164
Figure 6-1: Schematic of the distributed current diagnostic setup	179
Figure 6-2: Distributed current measurement for square flow-through flow field topology at high convective flow regime. (a) GORE-SELECT® EW1100 / 50 mL.min ⁻¹ , (b) Pure Cast Film EW800 / 50 mL.min ⁻¹ , (c) GORE-SELECT® EW1100 / 30 mL.min ⁻¹ , (d) Pure Cast Film EW800 / 30 mL.min ⁻¹	183
Figure 6-3: Distributed current measurement for serpentine flow field topology at high convective flow regime. (a) GORE-SELECT® EW1100 / 50 mL.min ⁻¹ , (b) Pure	

Cast Film EW800 / 50 mL.min ⁻¹ , (c) GORE-SELECT® EW1100 / 30 mL.min ⁻¹ , (d) Pure Cast Film EW800 / 30 mL.min ⁻¹	186
Figure 6-4: Distributed current measurement for square flow-through flow field topology at low convective flow regime. (a) GORE-SELECT® EW1100 / 10 mL.min ⁻¹ , (b) Pure Cast Film EW800 / 5 mL.min ⁻¹ , (c) GORE-SELECT® EW1100 / 10 mL.min ⁻¹ , (d) Pure Cast Film EW800 / 5 mL.min ⁻¹	188
Figure 6-5: Comparison of model simulation with experimentally measured distributed current for flow-through flow fields. (a) Schematic of the computational model domain (Ref. ¹²⁷) (b) Schematic of the flow direction in distributed current measurement setup (c) Predicted concentration depletion along flow direction at low convective flux (Ref. ¹²⁷) (d) Experimentally measured distributed current at high convective flux (e) Predicted concentration depletion along flow direction at low convective flux (Ref. ¹²⁷) (f) Experimentally measured distributed current at low convective flux	189
Figure 6-6: Distributed current measurement for serpentine flow field topology at low convective flow regime. (a) GORE-SELECT® EW1100 / 10 mL.min ⁻¹ , (b) Pure Cast Film EW800 / 10 mL.min ⁻¹ , (c) GORE-SELECT® EW1100 / 5 mL.min ⁻¹ , (d) Pure Cast Film EW800 / 5 mL.min ⁻¹	193
Figure 6-7: Schematic illustration along with experimentally measured distributed current for serpentine flow plates (a) Schematic illustration of the transport mechanism associated with serpentine flow plates, (b) Experimentally measured distributed current for serpentine flow filed at mass transport limited condition	195
Figure 6-8: Comparison of distributed current between various flow fields at 50 mL.min ⁻¹ , (a) square flow-through, GORE-SELECT® EW1100 (b) serpentine, GORE-SELECT® EW1100 (c) square flow-through, Pure Cast Film EW800 (d) serpentine, Pure Cast Film EW800	196
Figure 6-9: Comparison of distributed current between various flow fields at 10 mL.min ⁻¹ , (a) square flow-through, GORE-SELECT® EW1100 (b) serpentine, GORE-SELECT® EW1100 (c) square flow-through, Pure Cast Film EW800 (d) serpentine, Pure Cast Film EW800	198
Figure 7-1: Schematic of illustration of transport of active species from flow fields across the electrode	207
Figure 7-2: Schematic illustration of various flow field geometries used in this work. (a) Serpentine, (b) Interdigitated, (c) Square Flow-Through, (d) Rectangular Flow-Through	208
Figure 7-3: Schematic of ionic crossover setup	211
Figure 7-4: Variations in (a) discharge capacity and (b) theoretical capacity utilization for different flow plates design during extended cycling	215
Figure 7-5: The variation in coulombic efficiency during extended cycling for different configurations of flow plates	217
Figure 7-6: Capacity decay for different flow plate designs as a function of (a) cycle number, (b) Time	218

Figure 7-7: The variations of UV/Vis spectra during concentration-gradient induced crossover for (a) serpentine, (b) interdigitated, (c) square flow-through, and (d) rectangular flow-through	221
Figure 7-8: The concentration of vanadium ions (V(IV)) measured within vanadium-deficient electrolyte during crossover experiment for different flow field designs	223
Figure 7-9: Semi-natural log plot used to determine permeability of vanadium ions through the membrane for various configurations of flow fields	225
(b) Figure 7-10: Schematic illustration of macroscopic transport mechanism within the electrodes. (a) Serpentine, (b) Interdigitated, (c) Square Flow-Through, (d) Rectangular Flow-Through.....	227
(b) Figure 7-11: The variations in discharge capacity and capacity decay during cycling at 100 mA.cm ⁻² for different flow rates. (a) discharge capacity, (b) capacity decay as a function of cycle number, (c) capacity decay as a function of time	231
Figure 7-12: Comparison of the permeability values measured at 10 and 40 mL.min ⁻¹ for various flow plates	234
(b) Figure 7-13: Trend of capacity decay during extended cycling for different flow plates design at two various flow rates. (a) Serpentine, (b) Interdigitated, (c) Square Flow-Through, (d) Rectangular Flow-Through	236
Figure 8-1: Schematic of various membranes and species crossover (Inspired by Ref. ²³⁴)	243
Figure 8-2: Strategies for mitigating the crossover and/or recovering the capacity; (a) Impermeable membranes, (b) Connecting reservoirs externally, (c) Filtering the species out from opposite electrolytes, (d) Engineering the direction of crossover flux	245
Figure 9-1: Pressure drop data associated with three different flow plate design including flow-through, serpentine, and interdigitated (Data have been adopted from Ref. ²²⁵)	258
Figure 9-2: Schematic illustration of the flow fields used for asymmetric cell configuration (a) Serpentine, (b) Flow-through.....	260
Figure 9-3: IonCrG: A novel setup for measuring real-time ionic crossover and long-term capacity decay during cycling.....	261
Figure 9-4: Schematic of various flow fields (a) Serpentine, (b) Interdigitated, (c) Flow-through	266
Figure 9-5: Capacity decay during long-term cycling for symmetric and asymmetric flow field configurations. (a) as a function of cycle number. (b) as a function of time..	267
Figure 9-6: Coulombic efficiency as a function of cycle number for symmetric and asymmetric flow field configurations.	268
Figure 9-7: Concentration of a diffused vanadium V(IV) ion into vanadium-deficient chamber during crossover measurement for symmetric and asymmetric cell configurations.	269
Figure 9-8: Cell characterization for symmetric and asymmetric acid configurations. (a) Polarization curve, (b) Voltaic efficiency	271
Figure 9-9: Comparison of capacity decay during cycling for symmetric versus asymmetric acid configuration.....	273

Figure 10-1: Set-up for measuring concentration-gradient induced crossover.....	282
Figure 10-2: Set-up for measuring: (a) in-plane ionic conductivity of IEMs, (b) ionic conductivity of electrolytes.....	286
Figure 10-3: The ASR values for series of IEMs soaked in various bathing solutions ..	289
Figure 10-4: Add conductivity set-up image here	293
Figure 10-5: The ionic conductivity measured for various electrolytes	295
Figure 10-6: The ASR value for single-layer N115 and predicted ASR variation as a function of membrane thickness	297
Figure 10-7: Concentration of the vanadium in the vanadium-deficient electrolyte at the end of experiment. Predicted vanadium crossover based on Fickian dissusion behavior.....	300
Figure 10-8: UV/Vis spectrum of vanadium-deficient electrolyte during crossover test for series of IEMs	303
Figure 10-9: Electrochemical impedance spectroscopy for series of IEMs, (a) The spectra prior, during, and after crossover measurement, (b) Spectra at high-frequency region	304
Figure 10-10: Comparison of ASR for multilayers of NR211 with N115 Nafion membranes during crossover measurement.	305
Figure 10-11: comparison of concentration-gradient induced crossover between 5 layers of NR211 with 1 layer of N115	307
Figure 10-12: Schematic illustration of reduced ionic crossover for multilayer of IEMs, (a) 1 layer of N115, (b) 5 layers of NR211	308
Figure 10-13: IEM selection chart for reducing ionic crossover in VRFBs	309
Figure 11-1: Schematic of the VRFB including reservoirs for positive and negative electrolytes and peristaltic pumps.....	315
Figure 11-2: Species existing within the negative/positive electrodes and ion-exchange membrane.....	318
Figure 11-3: 1-D computational domain including flux of ionic species at the interface of control volumes.....	319
Figure 11-4: The species distribution within the membrane for various concentration of sulfuric acid of catholyte.....	323
Figure 11-5: Potential drop across the membrane for different sulfuric acid concentration of the catholyte.....	324
Figure 11-6: The contribution of the current being induced due to concentration gradient versus gradient in electrostatic potential.....	325
Figure 11-7: The ionic transference numbers and the water electro-osmotic drag coefficient for different sulfuric acid concentration of the catholyte.	325
Figure 12-1: The molecular structure of the PFSA ionomer (Nafion® ionomer with equivalent weight of 1100 g.mol ⁻¹); (a) Atomic type, number and connectivity (Adopted from Ref. ²⁵⁷) (b) 3D structure of the polymer chain (Decamer).....	333
Figure 12-2: The molecular structure of the acetonitrile (ACN), (a) Atomic type, number and connectivity, (b) 3D structure of the molecule (Adopted from NIST WebBook)	334

Figure 12-3: The molecular structure of the dimethyl sulfoxide (DMSO), (a) Atomic type, number and connectivity, (b) 3D structure of the molecule (Adopted from NIST WebBook)	336
Figure 12-4: Snapshots of the system at early stages without imposing the periodic boundary conditions within illustrations, (a) Acetonitrile system, (b) DMSO system	348
Figure 12-5: Snapshots of the ACN system at the end of simulation with periodic boundary conditions, (a) Perspective view, (b) Side view.....	350
Figure 12-6: Snapshots of the DMSO system at the end of simulation with periodic boundary conditions, (a) Perspective view, (b) Side view.....	351
Figure 12-7: Snapshots of the PFSA ionomer chain at the end of simulations for (a) ACN system, (b) DMSO system	352
Figure 12-8: Variations in radial distribution function between lithium ions and sulfonic group for ACN system versus DMSO system	354
Figure 12-9: The mean square displacement for (a) ACN system, (b) DMSO system .	356
Figure 13-1: Schematic of various modes of water transport in through-plane direction of a PEFC.	368
Figure 13-2: Schematic of the PEFC with in-line dew point temperature sensors for real time net water drag measurement.	373
Figure 13-3: Schematic of the: (a) configuration 1 (b) configuration 2 (c) configuration 3 (Not to scale).....	375
Figure 13-4: Schematic of the resistance-in-series analog for diffusion.	377
Figure 13-5: Computational Domain.	381
Figure 13-6: Predicted temperature distribution in through plane direction for the computational domain; (a) configuration 1 (b) configuration 2 (c) configuration 3.	388
Figure 13-7: Material configuration 1 operating at different operating conditions (a) Performance curve (b) Net water drag coefficient.....	389
Figure 13-8: Material configuration 2 operating at different operating conditions (a) Performance curve (b) Net water drag coefficient.....	391
Figure 13-9: Material configuration 3 operating at different operating conditions (a) Performance curve (b) Net water drag coefficient.....	393
Figure 13-10: Comparison of various material configuration at baseline conditions (a) Performance curve (b) Net water drag coefficient.....	395
Figure 13-11: Comparison of various material configuration at dry operating conditions. (a) Performance curve (b) Net water drag coefficient	398
Figure 13-12: Comparison of various material configuration at super dry operating conditions (a) Performance curve (b) Net water drag coefficient.....	400
Figure 14-1: IonCrG: A novel set-up for real-time measurement of ionic crossover (The figure is adopted from Yasser Ashraf Gandomi et al. ²⁰²)	408
Figure A-1: Different modes of water transport in through-plane direction of a PEFC.	444
Figure A-2: Schematic representation of PEFC with in-line dew point temperature sensors.....	445

Figure A-3: Polarization curves for different operating conditions and MPL configuration	448
Figure A-4: Polarization curves for “PEFC configuration 3” versus “PEFC configuration 4” for different operating conditions and MPL configurations	448
Figure A-5: Net water drag coefficients for “PEFC configuration 1” versus “PEFC configuration 2” for different operating conditions	450
Figure A-6: Net water drag coefficients for “PEFC configuration 3” versus “PEFC configuration 4” for different operating conditions	450
Figure B-1: Electrical conduction in carbon nanofiber exposed to DMMP vapor ²⁹⁹	454
Figure B-2: Schematic of test setup.	456
Figure B-3: Polarization curves (a) Schematic of the fs laser direct writing of sensor on a PI sheet, (b) a typical image of LIS, (c) Copper plating setup with two electrodes; (d) SEM images of the morphology of LIS before and (e) after copper coating.	458
Figure B-4: A current response of the interdigitated sensor exposed to DMMP and excited by a DC voltage over multiple cycles and equivalent circuit model used to fit the data.	459
Figure B-5: Pulsed voltage excitation protocol.	460
Figure B-6: DMMP detection using carbon sensor at two different temperatures (a) 25°C, (b) 60°C.	462
Figure B-7: Current-voltage response for DMMP detection using carbon sensor at two different temperatures, (a) 25°C, (b) 60°C.	465
Figure B-8: DMMP detection using copper-coated sensor at two different temperatures.	468
Figure B-9: Current-voltage response for DMMP detection using copper-coated sensor at two different temperatures (a) 25°C, (b) 60°C.	470
Figure B-10: DMMP detection using carbon and copper-coated sensors at two different temperatures for the voltage excitation of 9 V, (a) 25°C, (b) 60°C.	472
Figure B-11: DMMP detection for post-mode degradation using carbon and copper-coated sensors at 25°C for the voltage excitation of 9 V, (a) carbon, (b) copper-coated.	474
Figure B-12: DMMP detection for post-mode degradation using carbon and copper-coated sensors at 60°C for the voltage excitation of 9 V, (a) carbon, (b) copper-coated.	475

CHAPTER ONE :
INTRODUCTION TO REDOX FLOW BATTERIES

Scholarly contributions

This chapter is revised based on the published paper with permission from Journal of Electrochemical Society (JES) ¹.

Yasser Ashraf Gandomi, D. S. Aaron, J. Houser, M. Daugherty, J. Clement, A. Pezeshki, T. Ertugrul, D. Moseley, M. M. Mench. “Critical Review—Experimental Diagnostics and Material Characterization Techniques Used on Redox Flow Batteries” *Journal of Electrochemical Society*, 165 (5) A970-A1010 (2018) [DOI: 10.1149/2.0601805jes]

Abstract

Full integration of renewable energy sources into electric grid requires robust, high performance, and scalable energy storage devices. Several technologies developed for energy storage that among them, redox flow batteries (RFBs) are very promising. RFBs are scalable and the output power or available capacity can be engineered independently. In this chapter, an overview has been provided regarding various types of RFBs along with further details about the architecture and topology of these devices.

1.1. Introduction

The successful implementation of renewable energy sources to the electric grid requires robust energy storage systems. Grid scale energy storage systems are being developed at a higher rate than ever before and are available in multiple technological formats. There, is of yet, no superior energy storage option for all types of applications since technologies vary in terms of performance characteristics, capital requirements, maturity level, lifetime, safety, reliability and the level of environmental and human risks. A comprehensive

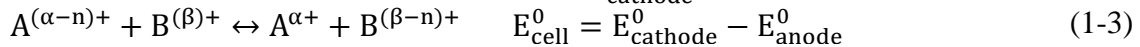
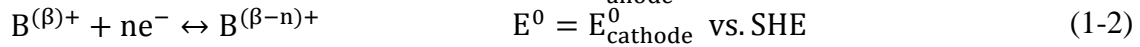
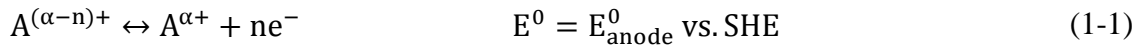
analysis of different storage technologies is available in a recent report from Sandia National Laboratory ². There are several electrochemical-energy-based storage technologies including redox flow batteries (RFBs), non-flowing secondary batteries, regenerative fuel cells (RFCs), rechargeable metal-air batteries, supercapacitors and many others. Several review papers have discussed these technologies in greater detail (e.g. ³⁻⁶).

Among the available storage technologies, RFBs have been a recent focus of interest. RFBs belong to the family of secondary batteries and have two broad categories: all-liquid and hybrid phase batteries. The hybrid phase RFBs has three main categories including gas/liquid, solid/liquid and semi-solid phases. For semi-solid hybrid RFBs, energy-dense solid particles are suspended within the liquid electrolyte. In terms of operation, all-liquid RFBs differ from conventional batteries since the electrodes themselves typically do not undergo any Faradaic reaction. In hybrid RFBs, Faradaic reactions can occur at solid electrodes which are typically paired with liquid- or gas-phase electrodes.

All-liquid RFBs boast the advantage of decoupling energy storage capacity from power capacity, because the electroactive redox couples are stored in external reservoirs and brought together in the reactor during operation. The storage of solutions in reservoirs separated from the reactor provides RFBs with unique benefits compared to other secondary batteries: safety is improved by minimizing the potential to short circuit; state of charge (SoC) monitoring can be done directly on the solution reservoirs, improving system control; and transport of electroactive materials and solvent through the membrane

(crossover) can be significantly curtailed. Some other properties of RFBs include relatively long cycle life and the possibility of rapid mechanical charging ^{4, 7, 8}. RFBs do have relatively low energy density, largely preventing their use in mobile applications.

Like some other secondary batteries, RFBs utilize reversible anodic and cathodic redox reactions of soluble species within the electrolyte. The negative and positive electrolytes are pumped inside the reactor where the half-cell electrochemical reactions occur. The generic half-cell reactions can be formulated as follows, assuming an n electron transfer process for the redox reactions.



Equation (1-1) is the negative half-cell reaction and Eq. (1-2) demonstrates the positive half-cell reaction; together they compose the overall cell reaction (Eq. (1-3)) with the maximum theoretical cell potential of E_{cell}^0 at standard conditions.

Myriad chemistries have been proposed and investigated for RFBs, with the primary differences being which compounds, organic or inorganic, carry charge in aqueous or non-aqueous solutions. Table 1.1 includes many of the predominant types of RFBs under development. The choice of electro-active redox couple depends on the particular application but ultimately is determined based on many factors, overall cost of the redox flow battery system being one of the strongest. The Department of Energy (DOE) has set a target cost of \$250/kWh for short-term grid storage system capital cost; \$150/kWh is the

long-term goal ⁹. Moreover, the Advanced Research Projects Agency-Energy (ARPA-E) Grid-Scale Rampable Intermittent Dispatchable Storage (GRIDS) program has proposed the more aggressive cost target of \$100/kWh ¹⁰.

One methodology for determining the total energy storage cost in the system level has been discussed using a performance-based cost model developed at Pacific National Laboratory (PNNL) ^{11,12}. It has been shown via model prediction that the overall system level cost is not only a function of the electroactive material selection, but also the stack design, performance, and operating conditions.

In order to achieve the aggressive cost targets determined by DOE for widespread commercialization of RFBs, decreasing the system material costs and increasing the cell performance are the logical pathways ^{8,13}.

Recently, a hybrid aqueous sulfur/sodium/air RFB has been demonstrated in the laboratory scale with the *chemical cost* of only \$1/kWh opening a door towards achieving the cost target assigned by DOE ¹⁴. In addition, a zinc-iron (Zn-Fe) RFB with double-membrane triple-electrolyte design has been demonstrated with an estimated system capital cost of under \$100/kWh ¹⁵. The all-liquid RFBs are types in which the electroactive species are dissolved in a solvent to constitute the anolyte and catholyte solutions. The most common solvent is water; usually, some supporting electrolyte is added to adjust pH and increase conductivity and solubility.

Table 1.1. Different Varieties of RFBs

			Negative electrolyte	Positive electrolyte	OCV (V)	Ref.	
All-liquid RFB	Aqueous solvent	Inorganic solutes	All-Vanadium	V(II)/V(III)	V(IV)/V(V)	1.26	16-19
			Iron-Chromium	Cr(II)/Cr(III)	Fe(II)/Fe(III)	1.18	20-23
			Polysulfide-Bromine	Sodium Polysulfide	Sodium Bromide	1.36	4, 20
			Vanadium-Bromine	V(II)/V(III)	Br ₂ /Br ⁻	1.3	24, 25
		Organic solutes	Quinone-Bromide	Quinone/Hydroquinone	Br ₂ /Br ⁻	0.92 (at SoC=90%)	26
			Anthraquinone - Benzoquinone	AQS/H ₂ AQS	BQDS/H ₂ BQDS	1.0	27
	Non-aqueous solvent	Inorganic solutes	Zinc-Cerium	Zn	Ce(III)/Ce(IV)	2.5	28
			Ruthenium Complexes	[Ru(bpy) ₃] ²⁺ /[Ru(bpy) ₃] ³⁺	[Ru(bpy) ₃] ⁺ /[Ru(bpy) ₃] ²⁺	2.6	29
			Chromium - Acetylacetonate	Cr(I)/Cr(II) Cr(II)/Cr(III)	Cr(III)/Cr(IV) Cr(IV)/Cr(V)	3.4	30-32
		Organic solutes	Anthraquinone	Li metal	Anthraquinone	2.6	33
			Lithium-based	Li-PAH _A	PAH _B	3.0	34
			Quinoxalines	N/A	N/A	N/A	35, 36
Hybrid RFB	Solid-Liquid		Zinc-Bromine	Zn/Zn ²⁺	Br ₂ /Br ⁻ /Br ₃ ⁻	1.67	18
			Zinc-Cerium	Zn/Zn ²⁺	Ce ³⁺ / Ce ⁴⁺	2.4	37, 38
			All-Iron	Fe/Fe(II)	Fe(II)/Fe(III)	1.2	39, 40
			All-Lead	Pb(II)/Pb	Pb(II)/PbO ₂	1.78	41, 42
			All-Copper	CuCl ₃ ²⁻ /Cu(s)	CuCl ₄ ²⁻ / CuCl ₃ ²⁻	0.773	43
	Semi-solid		Lithium-based	Li ₄ Ti ₅ O ₁₂	LiCoO ₂	4.5	44
	Gas-Liquid		Hydrogen-Bromine	H ₂ /H ⁺	Br ₂ /Br ⁻	1.09	45, 46
			Vanadium-Oxygen	V(II)/V(III)	H ₂ O/O ₂	1.49	47-49
			Hydrogen-Vanadium	H ₂ /H ⁺	V(IV)/V(V)	0.99	50, 51
			Sulfur-Sodium-Air	Polysulfide	Air	1.5	14

Aqueous solvents are typically limited by the water electrolysis potential window (The recorded onset potential for water splitting is 1.26V and 1.48V, depending on the presence of liquid and/or vapor water phase at the electrocatalyst-electrolyte interface ⁵²) and the low solubility and stability of the electroactive species within the electrolyte.

Non-aqueous solvents are also available for all-liquid RFBs. In general, non-aqueous electrolytes enable a wider operational potential window but at the cost of increased solvent cost, viscosity and ionic resistivity. More details regarding non-aqueous solvents are available through a relatively recent review paper in which comparisons are provided with reference to aqueous solvents ⁵³.

The electroactive species in all-liquid RFBs can be inorganic (mostly metals) or organic materials. The application of organic electroactive species is favorable because of generally lower cost and increased solubility ^{26, 54-61}.

Recent developments in organic redox flow batteries have been reviewed in Ref. ⁶² focusing on the chemistry, redox potentials, solubility, stability and materials perspectives. Hybrid batteries can be split into three main categories: solid/liquid, semisolid, and gas/liquid forms.

For solid/liquid hybrid batteries, the solid species deposits on an electrode. Dendrite formation at high current and surface passivation are usually limiting factors, especially

for system lifetime. In order to overcome this issue, semisolid RFBs show promise. The semisolid RFBs, demonstrated by Chiang et. al. ⁴⁴, utilize conductive materials that are suspended in solution and pumped inside the reactor ^{44, 63, 64}. Gas/liquid hybrid batteries utilize a half-cell reaction involving gaseous species.

As summarized in Table 1.1, there are many types of RFBs under development, with new chemistries frequently introduced and a rising interest in organic and/or non-aqueous solvents. Table 1.1 only includes the most-investigated types of RFBs; the readers are encouraged to refer to other review papers that discuss the different types summarized in Table 1.1 in greater detail (e.g. ^{4, 7, 8, 53, 65-71}).

Performance improvements have been demonstrated recently for all-vanadium ⁷²⁻⁷⁴ and hydrogen-bromine cells ⁷⁵⁻⁸⁰ with these chemistries still requiring optimization in order to approach the DOE cost target goal. RFB optimization is usually performed at the component level for any established chemistry.

1.2. Redox Flow Battery Architectures

Figure 1-1 is a schematic of a generic RFB. In general, a redox flow battery system includes the storage reservoirs (gas and/or liquid), electrochemical reactor, pumping system, temperature control system, and power control unit.

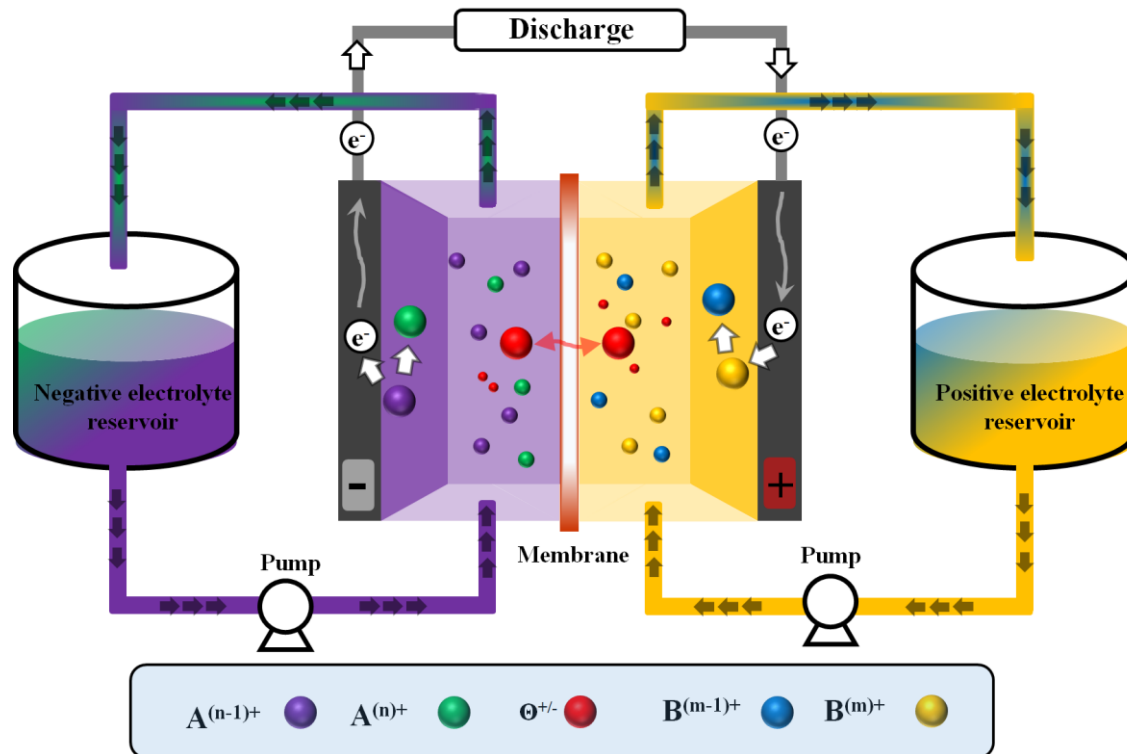
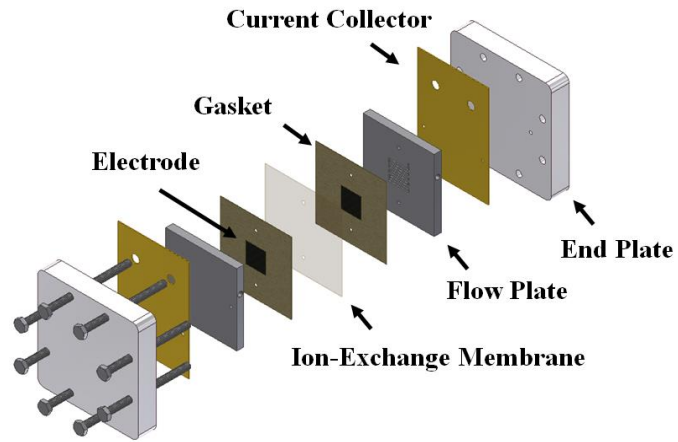


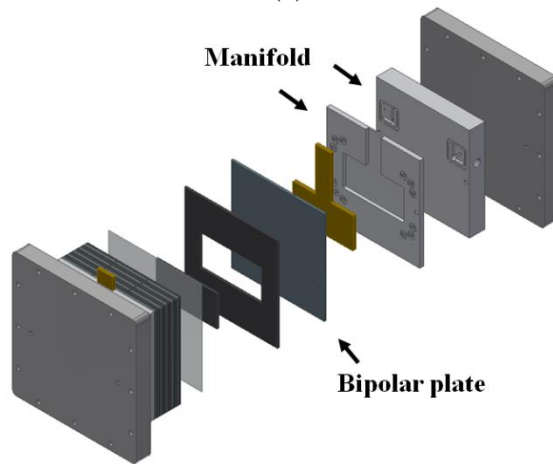
Figure 1-1: Schematic representation of a single-cell RFB

The reactor depicted in Fig. 1-1 is the most important part of the RFB system where energy conversion (between chemical and electrical) occurs. In general, the reactor includes the separator (with the exception of membrane-less RFBs⁸¹), porous electrodes, gaskets, flow plates, current collectors and endplates. In practical applications, an arrangement of parallel stacks of multiple reactors is used to achieve the desired power/voltage of the system.

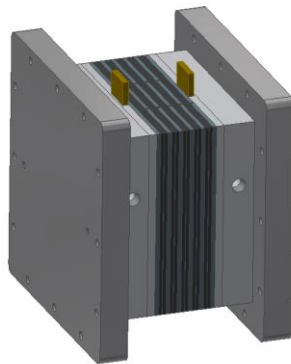
Figure 1-2 includes exploded views of a single cell as well as of a stack⁸². The major components used within the stack architecture includes manifolds, bipolar plates, separators (or membranes), electrodes, and gaskets.



(a)



(b)



(c)

Figure 1-2: Schematic representation of single-cell and stacked RFBs
 (a) Exploded view of a single cell, (b) Exploded view of stack of multiple cells,
 (c) schematic of the assembled stack of multiple cells)

The ion-exchange membrane (separator) in the reactor separates the anode and cathode sides; an ideal separator must have high ionic conductivity, very low permeability for the electroactive species, chemical and thermo-mechanical stability, and low cost. For many RFB systems, the separator is the most expensive single component, comprising 30-40% of the reactor's cost ¹¹.

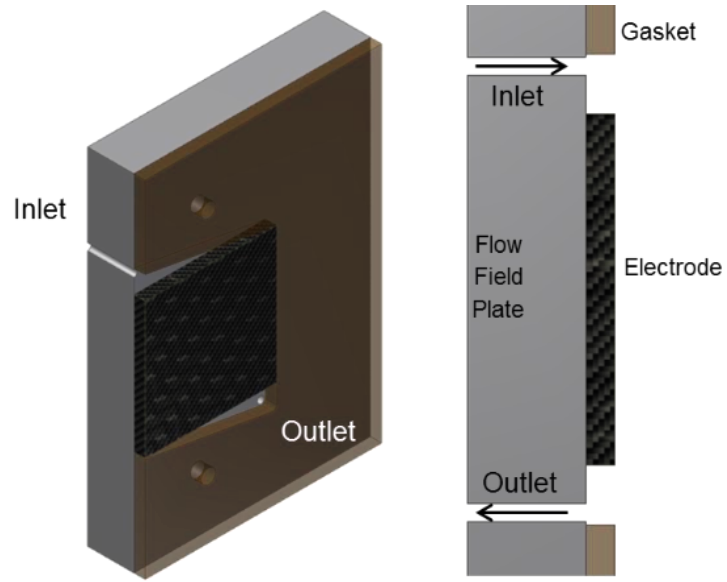
Nafion ® is a widely-used separator for aqueous RFBs and polymer electrolyte fuel cell systems (PEFC). More detailed information about Nafion ® membranes is available elsewhere (e.g. ⁸³). Recent progress on separator development for vanadium RFBs has been summarized ^{84, 85}. Although Nafion ® has successfully been used for aqueous RFBs, its application for non-aqueous RFBs faces considerable challenges. Shin et al. has recently reviewed the application of different separators for non-aqueous RFBs ⁸⁶.

Porous electrodes are used to provide high surface area for electroactive species redox reactions. The electrodes must also have high electrical conductivity and electrochemical stability. Electrode morphology directly affects transport of electroactive species and the surface chemistry of the electrodes can provide catalytic support for redox reactions on one or both sides of a RFB. The application of disparate electrode materials for each half of a particular RFB has been discussed in multiple review papers ^{65, 87}. The most common electrode materials are partially or fully-graphitized carbon in the form of paper or felt.

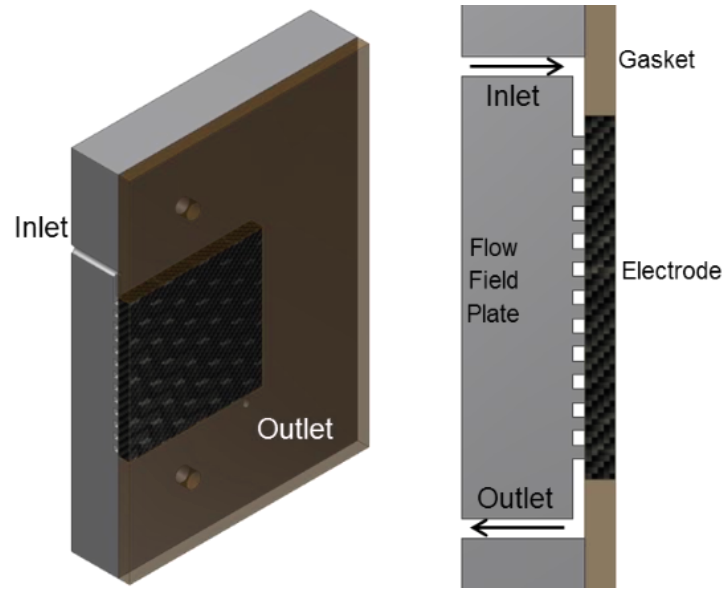
Flow plates in RFBs serve to distribute the electrolyte across the electrodes in each single cell while also functioning as bipolar plates in stacks. The flow plates should have high electrical conductivity and electrochemical stability and, at the same time, effectively-zero fluid permeability. Flow plates are often modified forms of graphite; many forms of graphite are porous; thus, some sealing treatment is typically done to prevent electrolyte leakage through the flow plates.

In general, there are two types of common configurations adopted for the flow plates (Fig. 1-3 (Ref. ⁸²)). In the first configuration (flow-frame architecture), the flow plates include electrolyte inlet and outlet ports with an optional gap in the top and bottom sections leading into and out of the electrode ⁸⁸. In the second configuration (flow-channel architecture), porous electrodes are pressed against flow plates that have a channel pattern and geometry. A review of different flow plate architectures is available in the review paper of X. Li et al. ⁸⁹.

The selection of gasket materials for any specific RFB is based on compressibility and material compatibility with regard to electrolytes. Teflon ® PTFE (DuPont™ Corporation) and Viton ® (DuPont™ Corporation) are among the common choices for gasket materials. The current collectors are only at the end of a stack of cells; they are typically manufactured from very conductive materials (Au or Cu), plated onto aluminum (usually for lab-scale cells), and are electronically isolated from the endplates.



(a)



(b)

Figure 1-3: Flow plate configurations
 (a) flow-frame architecture, (b) flow-channel architecture)

Figures 1-2 and 1-3 are only the most common reactor configurations for RFB systems. Membrane-less RFBs have attracted attention and are the focus of some research ^{81, 90-92}. Membrane-less RFBs avoid the high cost of a separator but have only been demonstrated at low Reynolds numbers ($Re < 10$) which reduces mixing of electrolytes. In membrane-less RFBs, two laminar electrolyte streams flow in a co-flow configuration, side-by-side (Fig. 1-4), through the reactor. The membrane-less RFB variant is reviewed here ⁸¹. The most popular chemistries for membrane-less flow batteries are all-vanadium ⁹³, hydrogen-bromine ⁹², zinc-bromine ⁹⁴, and Au based systems ⁹⁵. The concept of membrane-less RFBs is similar to the membrane-less microfluidic fuel cells introduced years earlier ^{96, 97}.

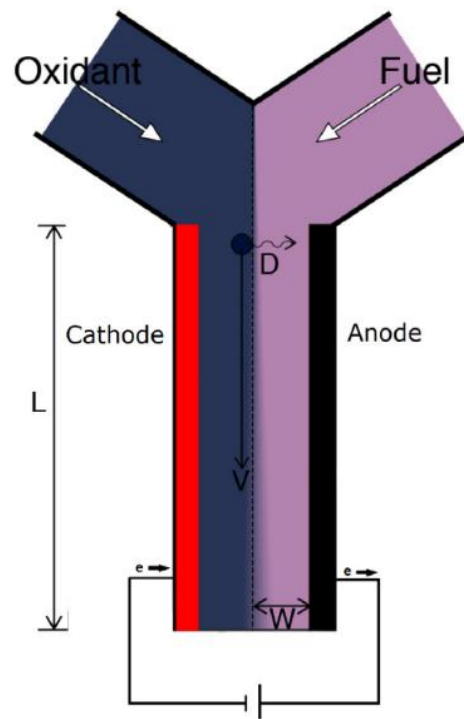


Figure 1-4: Schematic of membrane-less RFB (figure is taken from Ref. ⁸¹)

Although membrane-less RFBs can significantly decrease the cost of RFBs by eliminating the ion-exchange membranes, their application is mostly limited to low-power. Scale-up issues need to be solved before a transition to medium- or high-power can occur. Recently, Braff et al. demonstrated a promising hydrogen-bromine membrane-less flow battery that maintained voltage efficiency above 80% as high as $\sim 350 \text{ mW/cm}^2$ (Fig. 1-5)⁹². As the variety of chemistries continues to grow, the process of designing a high-performance RFB system becomes increasingly complex. Recently, online material databases and computational screening techniques have been the focus of attention for electrolyte material discovery and selection^{98, 99}. One of the successful implementations of these techniques is the Electrolyte Genome project¹⁰⁰. The Electrolyte Genome project has been designed to aid in the selection of battery electrolyte materials based on calculations of molecular properties¹⁰⁰. It is also important to note that the investigation of appropriate materials for optimum electrolyte must be followed by a further analysis for improved electroactive ions solubility and stability (chemical and thermal) for long-term cycling. An example of such an analysis is provided recently in a review paper focused for the various types of electrolytes to be used for VRFBs¹⁰¹.

1.3. Performance Metrics for Redox Flow Batteries

Performance metrics or figures of merit provide quantitative values to judge RFB performance from multiple perspectives. The most frequently-used figures of merit include voltage efficiency, coulombic efficiency, system level energy efficiency, theoretical capacity utilization and discharge capacity fade over long-term cycling.

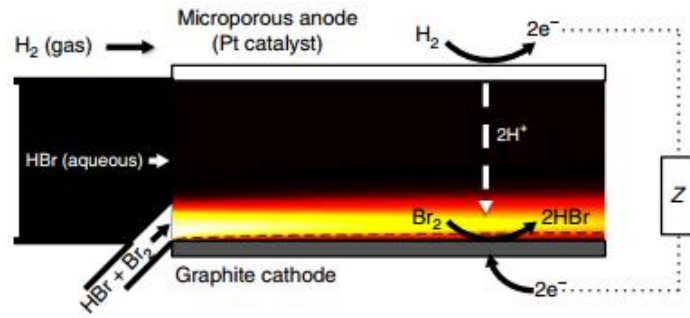


Figure 1-5: Schematic of HBr membrane-less RFB (figure is taken from Ref. ⁹²)

1.3.1. Voltage efficiency

The ratio of cell voltage during discharge and charge processes is defined as the voltage efficiency, shown in Equation (1-4) ⁴.

$$\eta_V = \frac{V_{Dchg}^{cell}}{V_{Chg}^{cell}} \quad (1-4)$$

Where the V_{Dchg}^{cell} and V_{Chg}^{cell} represent the average cell voltage during discharging and charging, respectively, at a certain time or desired SoC. For these measurements, current density is typically held constant.

At any particular current density, there are multiple sources of overvoltage including kinetic, ohmic, and mass transport losses which result in decreased voltage efficiency. All three sources of loss increase with current density, though not with the same dependence.

1.3.2. Coulombic efficiency

The ratio of total electrical charge withdrawn during discharge versus the charge stored after charging is defined as coulombic efficiency, as shown in Equation (1-5) ⁴.

$$\eta_c = \frac{Q_{Dchg}^{total}}{Q_{Chg}^{total}} = \frac{\int I_{Dchg} dt}{\int I_{Chg} dt} \quad (1-5)$$

where the Q_{Dchg}^{total} and Q_{Chg}^{total} represent the total electrical charge (in C or A-hr) during discharge and charge processes, respectively, and I_{Dchg} and I_{Chg} represent the discharge and charge currents (A). There are multiple contributors to coulombic losses including crossover of electroactive species and side reactions. The coulombic losses can be reversible or irreversible depending on the reaction and nature of the electroactive species.

1.3.3. System level energy efficiency

The voltage and coulombic efficiencies represent composite losses at the single cell level and include kinetic, ohmic, mass transport, crossover, and side reaction losses. However, there are other sources of losses when considering the overall RFB system shown in Fig. 1.

Parasitic losses (temperature control, pumping losses, and other auxiliary equipment) are generally the most important in terms of loss magnitude and added expense. In addition to single cell losses, stacks of multiple cells introduce new losses including shunt currents, uneven voltage distribution, and uneven electrolyte distribution among cells. System level

energy efficiency is defined to account for these sources of losses that are beyond a single cell level.

1.3.4. Theoretical Capacity Utilization

The maximum theoretical capacity of a RFB system is based on the amount of total electroactive material within the electrolyte. In aqueous systems, this capacity is determined by electroactive species solubility limits. Ideally, a RFB system would be capable of using all the available capacity. However, voltage limits and the various losses (especially mass transport losses at the system SoC limits) cause the practical utilization to be well below 100%. Capacity utilization strongly influences system cost, especially in the case of RFBs that depend on expensive charge carriers.

1.3.5. Discharge capacity fade over long-term cycling

One of the major drawbacks about different types of RFBs is the relatively rapid discharge capacity fade during long-term cycling. The major reasons for discharge capacity fade during long-term cycling include the undesired crossover of solvent and electroactive species through the ion-exchange membrane, degradation of various cell components, undesired side reactions and precipitation of electroactive species. Discharge capacity fade is an important metric in evaluating the stability and robustness of a particular RFB system in delivering the desired output current density ¹⁰².

As summarized in Table 1.1, several chemistries have been developed for RFBs. The performance metrics developed in Section 1.3 provide quantitative tools to assess the operation of RFBs. In addition, during the operation of RFBs, crossover of electroactive species and the solvent through the separator (i.e. crossover) is usually inevitable. Therefore, understanding the driving forces influencing the crossover and subsequently engineering cells and electrolyte compositions for reduced crossover is essential for retaining capacity during cycling. In this dissertation, series of experimental diagnostics along with multiscale mathematical models have been developed for investigating the ionic crossover in all-vanadium redox flow batteries. The insights gained from the experimental and modeling approaches have inspired design of novel all-vanadium redox flow batteries with unique cell topology and electrolyte configuration for passively retaining the discharge capacity during charge/discharge cycles.

CHAPTER TWO :
LITERATURE REVIEW ON SOLTUE AND SOLVENT CROSSOVER
ASSESSMENT IN REDOX FLOW BATTERIES

Scholarly contributions

This chapter is revised based on the published paper with permission from Journal of Electrochemical Society (JES) ¹.

Yasser Ashraf Gandomi, D. S. Aaron, J. Houser, M. Daugherty, J. Clement, A. Pezeshki, T. Ertugrul, D. Moseley, M. M. Mench. “Critical Review—Experimental Diagnostics and Material Characterization Techniques Used on Redox Flow Batteries” *Journal of Electrochemical Society*, 165 (5) A970-A1010 (2018) [DOI: 10.1149/2.0601805jes]

Abstract

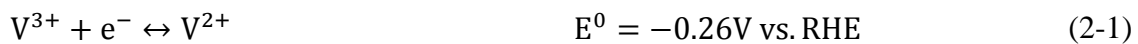
During cycling of redox flow batteries (RFBs), transport of electroactive redox materials through the membrane (crossover) is usually inevitable. The resulting capacity decay is one of the major issues yet to be addressed. Several experimental and numerical efforts have been dedicated to understanding the mechanism of crossover and subsequently measure the rate of species crossover. In this chapter, a summary of these efforts has been provided and areas of future work and development has been detailed.

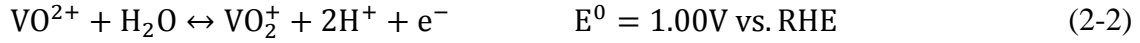
2.1. Introduction

As discussed in Chapter 1, redox flow batteries (RFBs) have many benefits including energy efficiency, capital cost, and life cycle costs compared with other grid-scale energy storage technologies ¹⁰³. RFBs are fundamentally different from traditional solid-state rechargeable batteries since energy is stored in the anolyte and catholyte and maintained within external reservoirs. As a result, the energy storage capacity is decoupled from power

capacity. This unique capability of redox flow batteries enables the design to be tuned based on the specific application for optimum power (function of stack size and design) and energy storage (function of electrolyte volume and solubility limit of active species). Multiple chemistries have been developed for redox flow batteries such as iron-chromium²⁰, all-vanadium¹⁸, bromine-polysulfide¹⁰⁴ and zinc-bromine¹⁰⁵. Among these many chemistries, the all-vanadium redox flow battery (VRFB) has been studied in great detail and is relatively mature with several full-size systems in operation around the world. Skyllas-Kazacos and co-workers proposed the all-vanadium redox flow battery (VRFBs) in 1985^{17, 18}. VRFBs are unique among other redox flow batteries since they utilize the same ion with different oxidation states at both anode and cathode; they do not suffer from cross contamination, although crossover does result in self-discharge⁷. Some of the other advantages of VRFBs are room temperature operation, and long cycle life. VRFBs are primarily intended to be utilized for grid-scale energy storage (load-leveling and peak shaving), and power backup units⁷³ with energy density of 25-30 Wh.kg⁻¹ and round-trip efficiency of 70-80%, depending on operating current^{106, 107}.

The VRFB employs the V(II)/V(III) redox couple at the negative side and the V(IV)/V(V) redox couple at the positive side, in the form of VO²⁺ and VO₂⁺. The kinetics associated with reduction and oxidation of vanadium species are known to be very complex^{108, 109}. Here, the following simplified set of global half-reactions are adopted for the negative and positive electrodes.





VRFBs have a wide operating temperature range from -5°C to 50°C ⁷³ and fast response (around 350 μs) for start-up and switching between charging and discharging processes, using a sulfuric and hydrochloric acid mixture¹⁰⁷. Cost is still the major barrier to VRFB commercialization. Zhang et al.¹¹⁰ estimated that the cell stack is one of the highest cost components with 31% of capital cost from a base case VRFB. One way to decrease the stack cost is to increase the power density of the VRFB during charge-discharge cycles, allowing for smaller stacks for the same power¹¹¹. In order to achieve high power density, the cells should operate at high current density with decreased polarization losses (activation, ohmic and concentration)¹¹². Among the components of the VRFB, electrode materials significantly contribute to activation and concentration overpotentials¹¹³. Many prior efforts have focused on electrode material development and modification to improve performance¹¹⁴⁻¹¹⁶. Along with better materials, there is also a need to develop an *in-situ* diagnostic of the physicochemical phenomena happening within the electrodes during cell operation.

2.2. Previous efforts on crossover measurement

For VRFB systems, there exist some possible additional reactions that directly affect the voltage and coulombic efficiencies of the battery¹¹⁷. The most important undesirable additional reactions include gas evolution side reactions (hydrogen, carbon dioxide, and oxygen evolution), V(II) oxidation by air, and different rates of vanadium ion crossover

through the membrane which lead to imbalance between the positive and negative electrolytes and subsequent loss of capacity ¹¹⁸.

Hydrogen evolution at the negative electrode occurs at very negative electrode potential ¹¹⁹. Conversely, carbon dioxide and oxygen evolution occur at the positive electrode at very positive electrode potential ¹²⁰. Therefore, parasitic gas evolution reactions are not overly problematic unless the battery is undergoing overcharge conditions or if the SoC window approaches 100%. Also, if the VRFB is sealed appropriately and the reservoirs containing V(II) are under an inert gas environment, oxidation of V(II) can be mitigated. However, vanadium crossover and the attendant capacity loss are inevitable during cell operation ¹²¹⁻¹²³. The following reactions are reported to occur when the active vanadium species cross through membrane according to Ref. ¹²⁴.



Reactions (2-3) and (2-4) correspond to the case where V(II) crosses the ion-exchange membrane and reacts immediately at the positive electrode. However, as long as V(V) is present in the positive side, reaction (2-4) does not occur. Reactions (2-5) and (2-4) correspond to V(III) and V(IV) transport and reactions (2-6) and (2-5) for V(V). Similar to the crossover of V(II), when V(V) crosses to the negative side of the cell, reaction (2-6) is

more likely; reaction (2-5) is for the case where V(II) starvation is occurring in the negative side which is an abnormal operating condition.

Crossover of vanadium species leads to self-discharge of the battery ¹²⁵. Since the permeabilities of the four vanadium states through the ion-exchange membrane are known to be dissimilar and might be a function of other ion concentrations and electrostatic potential among other parameters, accumulation of vanadium occurs at one side and this is a function of state of charge (SoC). At high vanadium concentration, asymmetric crossover can result in the vanadium solubility limit being reached, causing precipitation of species ¹²⁶. The loss of VRFB capacity can be mostly restored by rebalancing the electrolytes. However, a practical SoC monitoring method is required to determine the level of the imbalance to allow operation near the solubility limit. Different methods have been proposed to measure SoC, including monitoring open-circuit voltage and half-cell potentials ^{118, 127}, potentiometric titration, chromatography ^{128, 129}, electrolyte conductivity measurement ¹¹⁸ and spectrophotometric studies of the electrolyte ¹³⁰⁻¹³⁷.

Ionic selectivity is a key parameter for selecting the ion-exchange membranes in VRFB applications. In general, ionic selectivity is a strong function of the type of the polymer and strongly affects battery voltage and coulombic efficiencies. High protonic conductivity is desirable for the membranes, which favors the utilization of thin membranes in order to increase voltage efficiency. However, thinner membranes increase the crossover rate of vanadium species, decreasing coulombic efficiency. Therefore, selection of an appropriate

membrane for VRFBs faces a tradeoff between high protonic conductivity and minimal vanadium crossover rate; this tradeoff can depend on the intended operation. For high current density regime applications, maintaining superior protonic conductivity is more important than minimizing crossover; for low current density regime applications, decreased crossover is of greater importance^{84, 86}.

Different parameters affect species transport (both neutral and active) through the ion-exchange membrane. The ion-exchange membrane type (cation exchange membranes (CEM) or anion exchange membranes (AEM)), thickness, swelling state (specifically for hybrid redox flow batteries), equivalent weight, and membrane reinforcement are among the important membrane properties affecting species transport. Pretreatment protocol also affects the transport properties; for Nafion® membranes, this is a short term effect as it has been shown that different pretreatments result in convergent transport properties after cycling¹³⁸.

Overall, the membranes that have the potential to be utilized for VRFBs must meet several operational requirements, in addition to being economically viable¹³⁹. Operating conditions also strongly affect species transport. Concentration gradient (diffusion) is not the only driving force for species transport; the electric field (via migration and electro-osmosis) significantly influences species transport. It is desirable to increase the operating temperature of VRFBs for improved kinetics, but vanadium solubility at elevated temperatures imposes a limit on the operating temperature⁷³. It has been shown that the

application of mixed acid electrolytes along with other additives increase the solubility limit of vanadium species [34] and, accordingly, higher operating temperature regimes are possible. With higher possible temperature, species transport mechanisms at elevated temperatures must also be investigated if mixed acid electrolytes will be used. In addition, electrode properties, flow-field design, and cell compression are among other reactor parameters that can affect transport. Table 2.1. summarizes the major previous experimental work that has been published to quantify the species transport through the ion-exchange membranes for VRFB systems.

As shown in Table 2.1. there are two general approaches for measuring vanadium species permeability across the membranes in VRFB systems. The first approach targets concentration gradient-induced crossover via a permeability cell. In a permeability cell, the solution containing vanadium (enriched side) is circulated/resting on one side of a membrane while the other side (deficient side) has either aqueous sulfuric acid ¹⁴⁰ or sulfuric acid with another cation (e.g. magnesium) to equalize the ionic strength between two solutions, minimizing the cross-membrane difference in osmotic pressure of the water ^{141, 142}. The permeability cell has been used to determine the diffusion coefficients of vanadium ions across several cation exchange membranes (CMS, CMV, and CMX) ¹²³ and also to measure the diffusion coefficient across the Nafion® membranes ^{140, 143}. In the dialysis cell used by Sun et al. ¹⁴⁰, the solution containing vanadium species was the enriched side while the deficient side had only aqueous sulfuric acid solution.

Table 2.1. Summary of membrane crossover research in the literature

	Membrane properties		Operation parameters			Species Flux Equation	
	Type	Pretreatment protocol effect	Species type	Concentration gradient (diffusion)	Electric field (migration and electro-osmosis)	Nernst-Planck equation	Species interaction
E. Wiedemann et al. ¹²³	CEM CMS/CMV/C MX	×	V(II) V(III) V(IV) V(V)	✓	×	✓	×
X. Luo et al. ¹⁴¹	CEM PVDF-g- PSSA	×	V(III) V(IV) V(V)	✓	×	✓	×
C. Sun et al. ¹⁴⁰	CEM	×	V(II) V(III) V(IV) V(V)	✓	×	✓	×
Q. Luo et al. ¹⁴⁴	CEM	×	V(II) V(III) V(IV) V(V)	✓	✓	✓	×
D. C. Sing ¹⁴⁵	CEM Fumatech FX-7050	×	V(II) V(III) V(IV) V(V)	✓	✓	✓	×
J. S. Lawton et al. ¹⁴⁶	CEM	×	V(IV)	✓	×	✓	×
W. Xie et al. ¹³⁸	CEM	✓	V(IV)	✓	×	✓	×
J. G. Austing et al. ¹⁴⁷	CEM	×	V(II) V(III)	✓	×	✓	×

Utilizing aqueous sulfuric acid in the deficient side is beneficial since crossover is not affected by the possibility of counter-ion absorption coming from the deficient side of the battery. However, sulfuric acid concentration on the deficient side must be maintained with care in order to minimize any osmotic pressure gradient across the membrane. According to the data provided by Sun et al. ¹⁴⁰, the permeability of vanadium species across a CEM is in the following descending order: $V(II) > V(IV) > V(V) > V(III)$. Also, some recent work has focused on the permeability of $V(IV)$ for different cases. Lawton et al. ¹⁴⁶ investigated the permeability of $V(IV)$ through Nafion® membranes as a function of sulfuric acid concentration via electron paramagnetic resonance (EPR) spectroscopy. They found that the permeability of $V(IV)$ is strongly affected by the concentration of sulfuric acid and decreases with increasing sulfuric acid concentration ¹⁴⁶. Xie et al. utilized the permeability cell to investigate the permeability of $V(IV)$ as a function of different pretreatments of the Nafion® membrane ¹³⁸. They found that pretreatment protocol has a significant effect on the initial permeability of $V(IV)$, but these effects diminish after charge-discharge cycling. Permeability cells for crossover measurements have also been utilized for other systems like the vanadium/air redox flow battery ¹⁴⁷, and flow batteries with different types of non-aqueous electrolytes (propylene carbonate, ethylene carbonate, and dimethyl sulfoxide) ¹⁴⁸.

The permeability cell can also be used to investigate the water transfer across the separator. Water transport across the ion-exchange membrane is due to multiple driving forces including the concentration gradient, electro-osmotic drag, thermo-osmosis and hydraulic

pressure gradient ^{112, 149}. Water transfer behavior across Nafion® 112, GORE L-01009, and GORE L-570 during self-discharge at varying initial SoC have been studied with a permeability cell ¹²⁵. It was shown that water transport across the ion-exchange membrane is a function of the SoC of the battery. It was experimentally shown that when the SoC is higher than 50%, the net water transfer is from the negative side (V(II)/V(III)) towards the positive side (V(IV)/V(V)) for the discharge case and flips when the SoC is less than 50% ¹²⁵. This finding opens an interesting area to investigate how water transfer affects the permeability of vanadium species at different SoCs.

The second approach targets the effect of electric field on crossover behavior. Luo et al. ¹⁴⁴ utilized a mixture of iron and vanadium to distinguish between concentration gradient-induced crossover and electric-field-induced crossover. While this setup was useful for differentiating the concentration gradient-induced crossover from electric-field-induced crossover, the absorption of iron cations ($\text{Fe}^{2+}/\text{Fe}^{3+}$) in the membrane likely affected the transport behavior of the vanadium species. D. C. Sing investigated the effect of electric field on crossover using a triple-membrane setup. The concept introduced in this work was promising for studying the crossover, but the results were prone to uncertainty since the cell design suffered from leakage ¹⁴⁵.

CHAPTER THREE :
MATHEMATICAL MODELING OF REDOX FLOW BATTERIES AND IN-SITU
POTENTIAL DISTRIBUTION DIAGNOSTICS

Scholarly contributions

This chapter is revised based on the published paper with permission from Journal of Electrochemical Society (JES): ¹²⁷

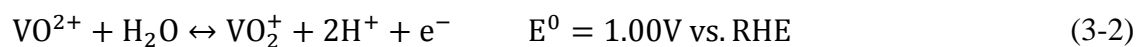
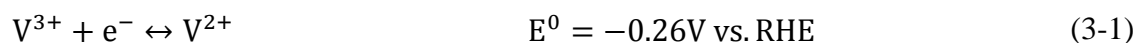
Yasser Ashraf Gandomi, D. S. Aaron, T. A. Zawodzinski, M. M. Mench. “In Situ Potential Distribution Measurement and Validated Model for All-Vanadium Redox Flow Battery” *Journal of Electrochemical Society*, 163 (1), A5188-A5201 (2016) [doi: 10.1149/2.0211601jes]

Abstract

An in-situ, local potential measurement technique was developed and applied to all-vanadium redox flow batteries to determine the potential distribution within multilayer electrodes of the battery. Micro-scale potential probes enabled in-situ measurement of local potential in electrode layers between the cell flow field and membrane. The local redox potentials were recorded for different operating conditions and states of charges. To further analyze the behavior of potential distribution in the through-plane direction, a mathematical model was developed and the species distribution as well as the flux density of any individual component was modeled in terms of contributions from convective, diffusive and electrophoretic fluxes at each operating condition. Good agreement was achieved between the mathematical model prediction and experimental data with maximum error of 9%. Both mathematical simulation and experimental data confirmed the distribution of potential in the through plane direction as a function of discharge current density, predicting the lowest potential in a region close to the flow plate.

3.1. Introduction

As discussed in Chapter 2, The VRFB employs the V(II)/V(III) redox couple at the negative side and the V(IV)/V(V) redox couple at the positive side, in the form of VO^{2+} and VO_2^+ . following simplified set of global half-reactions are adopted for the negative and positive electrodes.



Many prior efforts have focused on electrode material development and modification to improve the performance of VRFBs¹¹⁴⁻¹¹⁶. Along with better materials, there is also a need to develop an *in-situ* diagnostic of the physicochemical phenomena happening within the electrodes during cell operation. Therefore, in this chapter, a diagnostic technique is established based on the implementation of a dynamic hydrogen electrode (DHE) for *in-situ* measurement of the local potential distribution within the multilayer electrodes of the VRFB. Additionally, a mathematical model is presented that simulates the concentration distribution and local potential distribution within the VRFB electrode layers at different operating conditions. Finally, a comparison of experimental data and mathematical simulation has been provided.

3.2. Experiment

3.2.1. *In-situ potential distribution set-up*

Potential distribution measurements have been described in polymer electrolyte membrane fuel cell literature that include a reference electrode in the cell design^{150, 151}. Kjeang et al.¹⁵² placed reference electrodes in the reservoirs of an operating microfluidic flow battery where the reference electrodes' positions in the reservoirs resulted in large separation between the working electrode and the reference electrodes. Generally, sandwich-type and edge-type reference electrodes are commonly used for the study of thin layer cells. In the sandwich-type configuration, a fine wire reference electrode is inserted between two membranes^{153, 154}. For this configuration, since two membranes are used, the membrane resistance increases by a factor of two or more. In the edge-type configuration, the reference electrode is attached to a region of the ion-exchange membrane that is well outside the active area between the two electrodes^{155, 156}. For this configuration, membrane dehydration outside the active region is possible¹⁵⁵, thus the cell should be designed appropriately to prevent this¹⁵⁶.

In this work, a dynamic hydrogen electrode (DHE) has been used as the reference electrode. Usually, platinum (Pt) or palladium (Pd) are served as the working electrode for the DHE architecture where a small cathodic current produces hydrogen gas at the reference electrode location. Constant coverage of hydrogen on the electrode is required for the DHE to be operational at stable potential. Due to the simplicity within the DHE set-up, not only it does not contaminant the measured system but also does not need any salt bridge¹⁵⁵. For

the cell structure in this study, the DHE utilizes two platinum wires sandwiched between two membranes; one wire serves as the working electrode (WE) and forms a thin layer of hydrogen bubbles on its surface and the other probe functions as the counter electrode (CE). The equilibrium potential between the Pt wire and water between the membranes can then serve as in-situ reference electrode ¹⁵⁷. Equation (3-3) includes the forward and reverse reactions associated with the DHE for the WE and CE respectively ¹⁵⁸.



It is critical to place the DHE in a uniform potential region in order to ensure uniform current density at the working electrode ¹⁵⁷. Also, the distance between the reference electrode and the cell electrodes should be carefully selected so that the measurements be independent of the reference electrode location ¹⁵⁹. Finally, uneven current distribution should be avoided via precise alignment of the anode and cathode electrodes ^{159, 160}. To accomplish all the requirements mentioned earlier, the distance between the tips of the electrode wires was selected to be ~1 mm; and this was also the distance from the tips of the electrode wires to the active electrode area. Furthermore, the DHE was connected to its 9V battery at least 30 minutes before any measurement to give time for its potential to stabilize.

3.2.2. VRFB architecture

In this work, the VRFB architecture was based on the acid-proof, modified fuel cell architecture (Fuel Cell Technologies, Inc.) with 5cm² active area, which includes no-gap construction ^{72, 161}. The 10AA carbon paper electrodes (SGL Group) were sandwiched

between a flow plate and the membrane. On both sides, three layers of carbon paper were stacked to provide suitable surface area for electrode reactions. All measurements were performed on the positive half-cell. At the positive side, potential probes were placed between each layer of carbon paper. The tip of each probe was fixed to the center point on the surface of the carbon paper. The probes (125 μm diameter) were made of platinum wire covered by a layer of polytetrafluoroethylene (PTFE). Only the tip of Pt probe was exposed to electrolyte. At the negative side, the same number of carbon papers as the positive side was used, but no potential probes were installed. Two pieces of Nafion® 117 proton-exchange membrane (Ion Power, Inc) were used, between which was the reference electrode ¹⁶². PTFE gaskets were used to seal the cell and ensure even compression across the carbon paper electrode surface; gasket thickness resulted in ~25% compression of the carbon paper electrodes. A schematic of the construction and placement of the DHE and Pt probes within the layers of the VRFB electrodes is shown in Fig. 3-1.

3.2.3. Electrolytes

The electrolyte for all the experiments was 1M $\text{VOSO}_4 \cdot x\text{H}_2\text{O}$ (20.87 wt% vanadium, 99.9% purity, Alfa Aesar, U.S.) dissolved in 5M sulfuric acid (H_2SO_4) The initial volume of electrolyte was 50 and 100 ml at the negative and positive sides, respectively. Fully charging was assumed when the cell current was less than 20 mA ($4\text{mA}/\text{cm}^2$) at an imposed voltage of 1.8V. A two-channel peristaltic pump (Cole Parmer, U.S.) was used to circulate the electrolyte within the cell during testing. Nitrogen gas constantly purged the negative electrolyte to prevent oxidation of V(II).

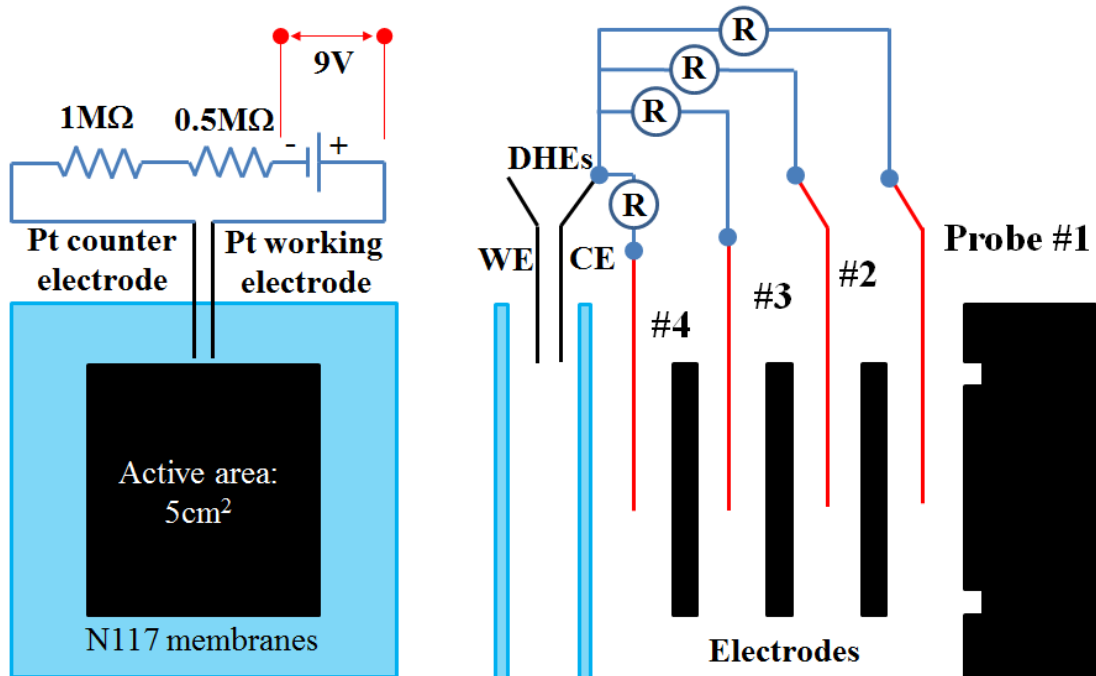


Figure 3-1: Schematic of the construction and placement of the DHE and Pt probes in the VRFB

In order to obtain the potential distribution experimental data, each potential probe was connected with the DHE through a multichannel potentiostat (Arbin Instruments, U.S.), and the potential differences between each probe and DHE were simultaneously recorded during single-cell operation for different operating conditions according to the procedure explained elsewhere ^{163, 164}. In order to conduct the experiments, replicate cells were assembled and the fully charged solution discharged at different current densities until the cell potential reached the cut-off voltage. The potentials referenced to the DHE from the 4 probes were simultaneously recorded at each SoC value.

3.3. Mathematical Model

Mathematical modeling aids in analyzing the VRFB system behavior since the presence of four different vanadium cations ($V(II)/V(III)$ on the negative side and $V(IV)/V(V)$ on the positive side) complicate interpretation of the experimental data. Several mathematical models have been developed for VRFBs, with varying levels of complexity. Li and Hikihara ¹⁶⁵ developed the first 0-D model for a VRFB to predict the dynamic performance of the battery. Shah et al. ¹⁶⁶ developed a 2-D transient model and simulated the distribution of current density, over-potential and reactant concentration during operation. The same group later expanded the model and simulated the effect of parasitic reactions including hydrogen and oxygen evolution ^{119, 120}. The model developed by Vynnycky ¹⁶⁷ was based on the asymptotic analysis that offered a significant simplification of the model already developed by Shah et al. The first 3-D model was developed by Ma et al. ¹⁶⁸ and further analyzed in greater depth by Xu et al. ^{169, 170}, Oh et al. ¹⁷¹ and Wang et al. ¹⁷². The modeling

of species crossover through the ion-exchange membrane originated with the work of Skyllas-Kazacos and co-workers^{124, 173} in which they modeled the species crossover considering diffusion as the only mechanism for crossover. Knehr et al. simulated the crossover rate of active species through the membrane using a model based on dilute solution approximation¹⁷⁴. Further analyses of crossover based on the dilute solution approximation have been recently performed^{175, 176}. Models based on the resistor-and pore-network methodology¹⁷⁷ and concentrated solution theory¹⁷⁸⁻¹⁸¹ have also been developed to simulate the transport of species through the ion-exchange membranes.

In this work, a mathematical model has been developed consisting of the porous electrodes, electrolytes and the membrane as shown in Fig. 2. In the negative electrolyte, V(II), V(III), H^+ , HSO_4^- , SO_4^{2-} ions and in the positive electrolyte V(IV), V(V), H^+ , HSO_4^- , SO_4^{2-} ions have been considered. The goal of this model is not to develop a sophisticated comprehensive mathematical simulation, rather it is to develop a tool to analyze the experimental data obtained via the potential distribution apparatus. The following assumptions have been adopted within the model:

- I. The geometry is two-dimensional
- II. The cell is isothermal
- III. The membrane is fully hydrated
- IV. H^+ ions can cross the membrane, but other ions cannot
- V. The dilute solution approximation is been used for species transport within the porous media
- VI. Side reactions are negligible

3.3.1. Model formulation

The model geometry is sketched in Fig. 3-2, which consists of three domains: negative electrode, ion-exchange membrane, and positive electrode. As illustrated in Fig. 3-2, the flow fields have not been plotted in this schematic since the flow-through flow fields have been considered here. The geometric, material, and kinetic properties are summarized in Table 3.1 and the properties of the electrolyte are given in Table 3.2.

3.3.2. Porous carbon electrodes

Adopting the transport equations in dilute solution¹⁸², the molar flux, N_j , of ionic species j in the porous medium of porosity ε can be expressed via the Nernst-Planck equation. The Nernst-Planck equation represents ionic transport due to diffusive, electrophoretic and convective fluxes.

$$N_j = -D_j^{eff} \nabla c_j - z_j u_j c_j F \nabla \phi_e + v_{a/c} c_j \quad (3-4)$$

where c_j denotes the concentration of species j , ϕ_e is the electric potential in the electrolyte, $v_{a/c}$ is the superficial molar-averaged velocity of the electrolyte in the anode or cathode electrode, z_j is the charge number for species j , and D_j^{eff} is the effective diffusion coefficient in porous media for species j , which can be related to the bulk diffusion coefficient, D_j , by the Bruggeman relation.

$$D_j^{eff} = \varepsilon^{3/2} D_j \quad (3-5)$$

The application of the Nernst-Planck equation in the form of Eq. (3-4) allows for the elimination of the ion mobility u_j as an independent parameter.

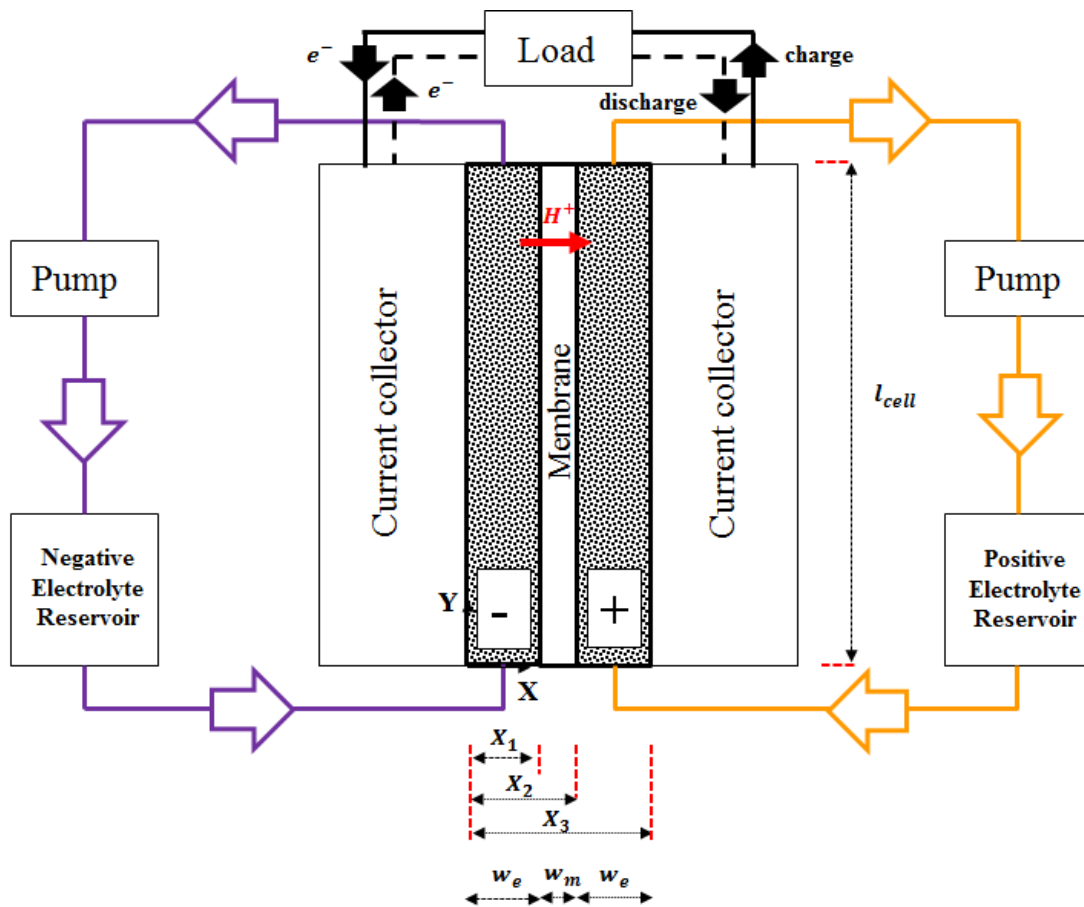


Figure 3-2: 2-D Schematic of the computational domain

Table 3.1. Geometric, material and kinetic properties

Parameter	Value
Length of cell, l_{cell} , [m]	0.0224
Thickness of electrode, w_e , [m]	0.0012
Thickness of membrane, w_m , [μm]	356
Porosity of electrode, ε , [-]	0.93 ¹⁷⁴
Width of electrode, t_e , [m]	0.03
Specific surface area of the electrode, a , [$\frac{m^2}{m^3}$]	3×10^4 ¹⁷⁴
Electronic conductivity of electrode, σ_s , [$\frac{S}{m}$]	66.7 ¹⁷⁴
Mean fiber diameter, d_f , [μm]	1.76×10^{-5}
Kozeny-Karman constant, K , [-]	180 ¹⁸³
Concentration of fixed-charge in the membrane, c_f , [$\frac{mol}{m^3}$]	1200 ¹⁸⁴
Valence of fixed-charge in the membrane, z_f , [-]	-1
Hydraulic permeability of membrane, k_m , [m^2]	1.58×10^{-18} ¹⁸⁵
Electrokinetic permeability of membrane, k_ϕ , [m^2]	1.13×10^{-19} ¹⁸⁶
Negative electrode reaction rate constant, k_a , [$\frac{m}{s}$]	3×10^{-9} ¹⁸⁷
Positive electrode reaction rate constant, k_c , [$\frac{m}{s}$]	1.75×10^{-7} ¹⁸⁸
Negative charge transfer coefficient, α_- , [-]	0.45 ¹⁷⁴
Positive charge transfer coefficient, α_+ , [-]	0.55 ¹⁷⁴

Table 3.2. Electrolyte properties

Parameter	Value
V(II) diffusion coefficient in the electrode, $[\frac{m^2}{s}]$	2.4×10^{-10} ¹⁸⁹
V(III) diffusion coefficient in the electrode, $[\frac{m^2}{s}]$	2.4×10^{-10} ¹⁸⁹
V(IV) diffusion coefficient in the electrode, $[\frac{m^2}{s}]$	3.9×10^{-10} ¹⁸⁹
V(V) diffusion coefficient in the electrode, $[\frac{m^2}{s}]$	3.9×10^{-10} ¹⁸⁹
H ⁺ diffusion coefficient in the electrode, $[\frac{m^2}{s}]$	9.3×10^{-9} ¹⁸²
HSO ₄ ⁻ diffusion coefficient in the electrode, $[\frac{m^2}{s}]$	1.3×10^{-9} ¹⁸²
SO ₄ ²⁻ diffusion coefficient in the electrode, $[\frac{m^2}{s}]$	1.1×10^{-9} ¹⁸²
Density of negative electrolyte, $[\frac{kg}{m^3}]$	1300 ¹⁹⁰
Density of positive electrolyte, $[\frac{kg}{m^3}]$	1350 ¹⁹¹
Dynamic viscosity of negative electrolyte, $[Pa \cdot s]$	0.0025 ¹⁹⁰
Dynamic viscosity of positive electrolyte, $[Pa \cdot s]$	0.005 ¹⁹⁰
Dissociation reaction rate constant, k_d , $[s^{-1}]$	10^4 ¹⁷⁴
HSO ₄ ⁻ degree of dissociation, β , $[-]$	0.25 ¹⁹²

$$u_j = \frac{D_j}{RT} \quad (3-6)$$

If a is the specific interfacial area (surface area of the pore walls per unit volume of the total electrode (m^2/m^3)), then the conservation of mass for the homogeneous reactions can be adopted for the heterogeneous reaction taking place at the electrode/electrolyte interface and formulated as:

$$\frac{\partial}{\partial t}(\varepsilon c_j) + \nabla \cdot \mathbf{N}_j = a\zeta_j \quad (3-7)$$

Where c_j is the bulk concentration and ζ_j is the pore-wall flux density of species j averaged over the interfacial area (Table 3.3). Three different averages within Eq. (3-7) are used: c_j is an average over the volume of the solution in the pores, ζ_j is an average over the interfacial area between the matrix and the pore solution, and \mathbf{N}_j is an average over a cross section through the electrode, dividing the matrix and pore.

Equation (3-7) states that the concentration at a point within the porous electrode can change due to divergence of the flux density \mathbf{N}_j , which forces the species to move away from a point, or because the species undergoes an electrode process (faradaic electrochemical reactions or double-layer charging) or simple dissolution of a solid material. Equation (3-7) applies to all charged species except SO_4^{2-} which is calculated from the condition of electroneutrality within the electrolyte.

$$\sum_j z_j c_j = 0 \quad (3-8)$$

Table 3.3. Reaction source term

Term	Negative electrode	Positive electrode
$\zeta_{V^{2+}}$	$\frac{j_n}{aF}$	-
$\zeta_{V^{3+}}$	$\frac{-j_n}{aF}$	-
$\zeta_{VO^{2+}}$	-	$\frac{-j_n}{aF}$
$\zeta_{VO_2^+}$	-	$\frac{j_n}{aF}$
ζ_{H^+}	$-\frac{S_d}{a}$	$\frac{2j_n}{aF} - \frac{S_d}{a}$
$\zeta_{HSO_4^-}$	$\frac{S_d}{a}$	$\frac{S_d}{a}$

It is a consequence of the assumption of electroneutrality that the divergence of the total current density is zero. Therefore, the charge leaving the matrix phases must enter the pore solution. For the macroscopic model,

$$\nabla \cdot \mathbf{i}_e + \nabla \cdot \mathbf{i}_s = 0 \quad (3-9)$$

where \mathbf{i}_e and \mathbf{i}_s are the ionic and electronic current densities that can be calculated using the following equations:

$$\mathbf{i}_e = F \sum_j z_j \mathbf{N}_j \quad (3-10)$$

$$\mathbf{i}_s = -\sigma_s^{eff} \nabla \phi_s \quad (3-11)$$

Where σ_s^{eff} is the effective electronic conductivity of the porous electrodes, which is related to the electronic conductivity of solid material, σ_s , through Eq. (3-12).

$$\sigma_s^{eff} = (1 - \varepsilon)^{3/2} \sigma_s \quad (3-12)$$

Eq. (3-10) can now be used to solve for the divergence of the ionic current.

$$\nabla \cdot \mathbf{i}_e = \nabla \cdot F \sum_j z_j \mathbf{N}_j = F \sum_j z_j \nabla \cdot \mathbf{N}_j \quad (3-13)$$

From the continuity equation substitution yields:

$$\nabla \cdot \mathbf{i}_e = F \sum_j z_j \left\{ a \zeta_j - \frac{\partial}{\partial t} (\varepsilon c_j) \right\} = aF \sum_j z_j \zeta_j - \varepsilon F \frac{\partial}{\partial t} \sum_j z_j c_j \quad (3-14)$$

The last term within Eq. (3-14) vanishes due to electroneutrality within the solution. Let j_n be the transfer current per unit volume of the electrode (A/m^3):

$$j_n = \nabla \cdot \mathbf{i}_e = aF \sum_j z_j \zeta_j = a i_n \quad (3-15)$$

Here i_n is the average transfer current density (A/m^2). The Butler-Volmer expressions are used to formulate the transfer current densities as a function of overpotentials¹⁹³. For the set of equations below, it is assumed that $f = \frac{F}{RT}$.

$$j_{na} = aFk_a (c_{V^{3+}})^{\alpha_-} (c_{V^{2+}})^{(1-\alpha_-)} \left[\left(\frac{c_{V^{2+}}^s}{c_{V^{2+}}} \right) \exp((1-\alpha_-)f\eta_a) - \left(\frac{c_{V^{3+}}^s}{c_{V^{3+}}} \right) \exp((- \alpha_-)f\eta_a) \right] \quad (3-16)$$

$$j_{nc} = aFk_c (c_{VO_2^+})^{\alpha_+} (c_{VO_2^{2+}})^{(1-\alpha_+)} \left[\left(\frac{c_{VO_2^{2+}}^s}{c_{VO_2^{2+}}} \right) \exp((1-\alpha_+)f\eta_c) - \left(\frac{c_{VO_2^+}^s}{c_{VO_2^+}} \right) \exp((- \alpha_+)f\eta_c) \right] \quad (3-17)$$

Here, j_{na} and j_{nc} are the transfer current per unit volume of the electrode of anode and cathode side respectively, k_c and k_a are reaction rate constants for heterogeneous reaction,

α_- and α_+ are the anodic and cathodic transfer coefficients for reactions (3-1) and (3-2), respectively, and η_c and η_a are the overpotentials, given by:

$$\eta_a = \phi_s - \phi_e - E_a \quad (3-18)$$

$$\eta_c = \phi_s - \phi_e - E_c \quad (3-19)$$

where E_a and E_c are the equilibrium potentials that can be calculated using the Nernst equation in which the proton activity in the positive half-cell due to participation of the protons in reaction has been taken into account ¹⁹⁴.

$$E_a = E_{0,a} + \frac{RT}{F} \ln\left(\frac{c_{V^{3+}}}{c_{V^{2+}}}\right) \quad (3-20)$$

$$E_c = E_{0,c} + \frac{RT}{F} \ln\left(\frac{c_{VO_2^+} c_{H_{pos}^+}^2}{c_{VO^{2+}}}\right) \quad (3-21)$$

where $E_{0,a}$ and $E_{0,c}$ denote the equilibrium potentials for negative and positive electrodes' reactions at standard conditions. Furthermore, there is a Donnan potential across the membrane due to the difference in proton activities across both half-cells ¹⁹⁴.

$$E_m = \frac{RT}{F} \ln\left(\frac{c_{H_{pos}^+}}{c_{H_{neg}^+}}\right) \quad (3-22)$$

Therefore, the full description of the open-circuit potential (OCP) for the VRFB can be formulated as the following:

$$E_{cell} = E_c - E_a + E_m = E_{0,c} - E_{0,a} + \frac{RT}{F} \ln\left(\frac{c_{V^{2+}} c_{VO_2^+} c_{H_{pos}^+}^3}{c_{V^{3+}} c_{VO^{2+}} c_{H_{neg}^+}}\right) \quad (3-23)$$

The modified Butler-Volmer relations expressed in Eq. (3-16) and (3-17) include the mass transfer effects from bulk solution to the solid-matrix/electrolyte interface. It is commonly assumed that there exists a linear concentration gradient within the Nernst diffuse layer ¹⁹⁵.

Therefore, the mass transfer flux ($Q_{mt}, [\frac{mol}{m^2s}]$) to the solid-matrix/electrolyte interface is obtained through the following:

$$Q_{mt} = \frac{D_0}{\delta_0} (c^* - c^s) \quad (3-24)$$

In Eq. (3-24), c^* is the bulk concentration and c^s is the concentration in the solid-matrix/electrolyte interface. Since the Nernst diffuse layer thickness (δ_0) is often unknown, it is convenient to combine it with the diffusion coefficient to produce the mass-transfer coefficient ($\beta_0, [\frac{m}{s}]$) and re-write the Eq. (3-24) in the form of following equation ¹⁹⁵.

$$Q_{mt} = \beta_0 (c^* - c^s) \quad (3-25)$$

Equation (3-25) needs to be written for the anode and cathode sides and for the species undergoing faradaic reaction; the mass transport flux is balanced by the flux of species consumption/production according to Butler-Volmer equation ¹⁹⁶.

$$Q_{V^{2+}} = \beta_{V^{2+}} (c_{V^{2+}} - c_{V^{2+}}^s) \quad (3-26)$$

$$= k_a (c_{V^{3+}})^{\alpha_-} (c_{V^{2+}})^{(1-\alpha_-)} \left[\left(\frac{c_{V^{2+}}^s}{c_{V^{2+}}} \right) \exp((1-\alpha_-)f\eta_a) - \left(\frac{c_{V^{3+}}^s}{c_{V^{3+}}} \right) \exp((- \alpha_-)f\eta_a) \right]$$

$$Q_{V^{3+}} = \beta_{V^{3+}} (c_{V^{3+}} - c_{V^{3+}}^s) \quad (3-27)$$

$$= k_a (c_{V^{3+}})^{\alpha_-} (c_{V^{2+}})^{(1-\alpha_-)} \left[\left(\frac{c_{V^{3+}}^s}{c_{V^{3+}}} \right) \exp((- \alpha_-)f\eta_a) - \left(\frac{c_{V^{2+}}^s}{c_{V^{2+}}} \right) \exp((1-\alpha_-)f\eta_a) \right]$$

$$Q_{VO^{2+}} = \theta_{VO^{2+}}(c_{VO^{2+}} - c_{VO^{2+}}^s) \quad (3-28)$$

$$= k_c(c_{VO_2^+})^{\alpha_+}(c_{VO^{2+}})^{(1-\alpha_+)} \left[\left(\frac{c_{VO^{2+}}^s}{c_{VO^{2+}}} \right) \exp((1-\alpha_+)f\eta_c) \right. \\ \left. - \left(\frac{c_{VO_2^+}^s}{c_{VO_2^+}} \right) \exp((-\alpha_+)f\eta_c) \right]$$

$$Q_{VO_2^+} = \theta_{VO_2^+}(c_{VO_2^+} - c_{VO_2^+}^s) \quad (3-29)$$

$$= k_c(c_{VO_2^+})^{\alpha_+}(c_{VO^{2+}})^{(1-\alpha_+)} \left[\left(\frac{c_{VO_2^+}^s}{c_{VO_2^+}} \right) \exp((-\alpha_+)f\eta_c) \right. \\ \left. - \left(\frac{c_{VO^{2+}}^s}{c_{VO^{2+}}} \right) \exp((1-\alpha_+)f\eta_c) \right]$$

Now, Eqs (3-26) through (3-29) can be solved to correlate the bulk concentration of species to surface concentration ¹⁹⁶.

$$c_{V^{2+}}^s = \frac{\Pi_2 c_{V^{3+}} + (1 + \Pi_2) c_{V^{2+}}}{1 + \Pi_1 + \Pi_2} \quad (3-30)$$

$$c_{V^{3+}}^s = \frac{\Pi_1 c_{V^{2+}} + (1 + \Pi_1) c_{V^{3+}}}{1 + \Pi_1 + \Pi_2} \quad (3-31)$$

$$c_{VO^{2+}}^s = \frac{\Pi_4 c_{VO_2^+} + (1 + \Pi_4) c_{VO^{2+}}}{1 + \Pi_3 + \Pi_4} \quad (3-32)$$

$$c_{VO_2^+}^s = \frac{\Pi_3 c_{VO^{2+}} + (1 + \Pi_3) c_{VO_2^+}}{1 + \Pi_3 + \Pi_4} \quad (3-33)$$

where Π_1 , Π_2 , Π_3 and Π_4 are calculated using the following equations.

$$\Pi_1 = \left(\frac{k_a}{\beta_{V^{2+}}} \right) \left(\frac{(c_{V^{2+}})^{(1-\alpha_-)}}{(c_{V^{3+}})^{\alpha_-}} \right) \exp((1-\alpha_-)f\eta_a) \quad (3-34)$$

$$\Pi_2 = \left(\frac{k_a}{\beta_{V^{3+}}} \right) \left(\frac{(c_{V^{3+}})^{\alpha_-}}{(c_{V^{2+}})^{(1-\alpha_-)}} \right) \exp((- \alpha_-) f \eta_a) \quad (3-35)$$

$$\Pi_3 = \left(\frac{k_c}{\beta_{VO_2^+}} \right) \left(\frac{(c_{VO_2^+})^{\alpha_+}}{(c_{VO_2^+})^{(1-\alpha_+)}} \right) \exp((1 - \alpha_+) f \eta_c) \quad (3-36)$$

$$\Pi_4 = \left(\frac{k_c}{\beta_{VO_2^+}} \right) \left(\frac{(c_{VO_2^+})^{(1-\alpha_+)}}{(c_{VO_2^+})^{\alpha_+}} \right) \exp((- \alpha_+) f \eta_c) \quad (3-37)$$

For the set of equations formulated above, the key parameter to determine is the mass-transfer coefficients ($\beta_{V^{2+}}$, $\beta_{V^{3+}}$, $\beta_{VO_2^+}$ and $\beta_{VO_2^+}$). This parameter has been determined as a function of electrolyte velocity in the work of Schmal et al. ¹⁹⁷; the results of that work are adopted here in the form of following equation.

$$\beta_0 = 1.6 \times 10^{-4} \mathbf{v}_{a/c}^{0.4} \quad (3-38)$$

Equation (3-38) as well as Eq. (3-4) requires the velocity field to be determined. To solve for the velocity field, Darcy's law is used:

$$\mathbf{v}_{a/c} = - \frac{d_f^2}{K\mu} \frac{\varepsilon^3}{(1 - \varepsilon)^2} \nabla p_{a/c} \quad (3-39)$$

where p_a and p_c are the liquid pressures in the anode and cathode electrodes respectively, μ is the dynamic viscosity of the liquid, d_f is the mean fiber diameter and K is the Kozeny-Karman constant. The application of Darcy's law for the transport through the porous electrodes is justified because the Reynolds number is less than unity. Reynolds number for porous carbon papers is defined based on the pore-size length scale, d , according to the following equation.

$$Re = \frac{\rho U d}{\mu} \quad (3-40)$$

where ρ is the density of the solution, U is the velocity, d is the characteristic length and μ is the dynamic viscosity of the solutions discussed earlier.

The negative and positive electrolytes are incompressible solutions; therefore, the continuity equation simplifies to the following equation:

$$\nabla \cdot \mathbf{v}_{a/c} = 0 \quad (3-41)$$

Inserting Eq. (3-39) into Eq. (3-41), we derive:

$$\nabla \cdot \nabla p_{a/c} = 0 \quad (3-42)$$

It is worth mentioning that $\mathbf{v}_{a/c}$ is the mass-averaged velocity, rather than the molar-averaged velocity that was shown in Eq. (3-4). However, within the limit of infinite dilution, these values are equal.

3.3.3. Membrane

The electroneutrality condition must hold within the membrane. This condition dictates that:

$$z_m c_m + z_f c_f = 0 \quad (3-43)$$

where z_f is the charge of the fixed sites and c_f is their concentration. The velocity of the liquid water in the membrane is obtained using Schlögl's equation.

$$\mathbf{v}_m = -\frac{k_\phi F c_{H^+}}{\mu} \nabla \phi_m - \frac{k_m}{\mu} \nabla p_m \quad (3-44)$$

Where p_m is the liquid pressure, ϕ_m is the ionic potential, k_ϕ is the electrokinetic permeability and k_m is the hydraulic permeability. The continuity equation within the membrane for water (incompressible) results in the following equation.

$$\nabla \cdot \mathbf{v}_m = 0 \quad (3-45)$$

Within the membrane, the conservation of current holds. Therefore,

$$\nabla \cdot \mathbf{i}_m = 0 \quad (3-46)$$

Since it is assumed that the protons are the only charge carriers within the membrane; the current density is formulated as:

$$\mathbf{i}_m = z_{H^+} F \mathbf{N}_{H^+} \quad (3-47)$$

The flux of the protons within the membrane can be calculated using the following equation.

$$\mathbf{N}_{H^+} = c_{H^+} \mathbf{v}_m - \frac{z_{H^+} F}{RT} D_{H^+,m} c_{H^+} \nabla \phi_m \quad (3-48)$$

where the $D_{H^+,m}$ is the proton diffusion coefficient in the membrane. Substituting Eqs. (3-47) and (3-48) into Eq. (3-46) we derive:

$$\nabla \cdot [z_{H^+} F \left(c_{H^+} \mathbf{v}_m - \frac{z_{H^+} F}{RT} D_{H^+,m} c_{H^+} \nabla \phi_m \right)] = 0 \quad (3-49)$$

Equation (3-49) can be simplified to:

$$\nabla \cdot (z_{H^+} F c_{H^+} \mathbf{v}_m) - \nabla \cdot \left(\frac{z_{H^+}^2 F^2}{RT} D_{H^+,m} c_{H^+} \nabla \phi_m \right) = 0 \quad (3-50)$$

According to Eq. (3-43), the proton concentration within the membrane is constant and therefore the first term in Eq. (3-51) vanishes due to conservation of mass and we derive:

$$\nabla \cdot (\sigma_m \nabla \phi_m) = 0 \quad (3-51)$$

where σ_m is the ionic conductivity of the membrane and is described below.

$$\sigma_m = \frac{z_{H^+}^2 F^2}{RT} D_{H^+,m} c_{H^+} \quad (3-52)$$

According to Eq. (3-52), constant ionic conductivity for the membrane is assumed and therefore:

$$\nabla \cdot \nabla \phi_m = 0 \quad (3-53)$$

Now, if Eq. (44) is inserted into Eq. (3-45) and Eq. (3-53) is adopted as well, we obtain:

$$\nabla \cdot \nabla p_m = 0 \quad (3-54)$$

3.3.4. Boundary conditions for multi-domain modeling approach

Definition of the boundary conditions at the outer surfaces is required in order to adopt the single-domain modeling approach¹⁷⁵. However, in this work, a multi-domain approach is used, requiring boundary conditions at all the boundaries of the computational domain, as well as internal interfaces.

3.3.5. Boundary conditions for the conservation of charge

The battery is operated in potentiostatic mode; thus, the electronic potentials have been incorporated as boundary conditions.

$$\phi_e = 0 \quad (X = 0) \quad (3-55)$$

$$\phi_e = \varphi_s \quad (X = X_3) \quad (3-56)$$

where φ_s is the applied electronic potential at the positive electrode/current collector interface. The membrane is not electronically conductive and the current (electronic and ionic) does not spread outside the computational domain.

$$\mathbf{i}_s \cdot \mathbf{n} = 0 \quad (X = X_1, X_2) \quad (3-57)$$

$$\mathbf{i}_s \cdot \mathbf{n} = 0 \quad (Y = 0, l_{cell}) \quad (3-58)$$

$$\mathbf{i}_e \cdot \mathbf{n} = 0 \quad (X = 0, X_3) \quad (3-59)$$

$$\mathbf{i}_e \cdot \mathbf{n} = 0 \quad (Y = 0, l_{cell}) \quad (3-60)$$

3.3.6. Boundary conditions for the conservation of momentum

At the inlets, the inlet velocity (v_{inlet}) is determined using the volumetric flow rate and used as the boundary condition. At the outlets the exit pressure is applied as the boundary condition. Also, no-slip boundary conditions are used at the interfaces of electrodes with current collectors and the membrane.

$$v_y = v_{in} \quad (Y = 0) \quad (3-61)$$

$$p = p_{out} \quad (Y = l_{cell}) \quad (3-62)$$

$$\nabla p \cdot \mathbf{n} = 0 \quad (X = 0, X_1, X_2, X_3) \quad (3-63)$$

The inlet velocity is determined using the following equation:

$$v_{inlet} = \frac{Q}{\varepsilon A_{in}} \quad (3-64)$$

where Q is the volumetric flow rate and A_{in} is the cross-sectional area.

3.3.7. Boundary conditions for the conservation of mass

Circulation of the electrolytes through their respective reservoirs alters the concentrations of all species entering the electrodes. To model this circulation, the inlet concentration for each species is simulated using the conservation of mass as follows:

$$\frac{\partial c_i^{in}}{\partial t} = \frac{\varepsilon t_e}{V_{res}} \left(\int v^{out} c_i^{out} dl - \int v^{in} c_i^{in} dl \right) \quad (3-65)$$

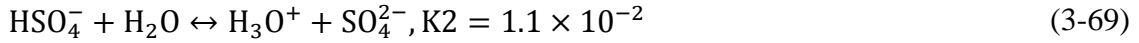
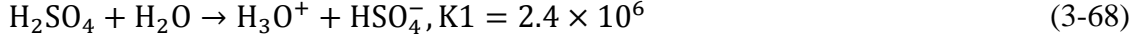
Here, V_{res} refers to the volume of the reservoir and t_e is the width of the electrode as shown in Table 3.1. The superscripts *in* and *out* are used for the value at the inlet and outlet of the electrodes. In a similar fashion, the changes in electrolyte volume can be calculated as follows:

$$\frac{\partial V_{res}}{\partial t} = \varepsilon A_{in} (v^{out} - v^{in}) = \varepsilon w_e t_e (v^{out} - v^{in}) \quad (3-66)$$

The initial concentrations for the simulations are given in 3.4. The initial concentrations in the electrolytes represent the concentration of the species at 95% state of charge (SoC). SoC is defined using the following equation:

$$SoC = \frac{c_{V(II)}}{c_{V(II)} + c_{V(III)}} = \frac{c_{V(V)}}{c_{V(V)} + c_{V(IV)}} \quad (3-67)$$

It is worth mentioning that it is critical to maintain electroneutrality within the negative and positive electrolytes while calculating the initial concentrations of the species as the input for the model. In some earlier modeling works¹⁷⁴, this fact was neglected, resulting in unrealistic initial concentrations to keep the solutions electrically neutral. In this work, a subroutine was developed to calculate the initial concentrations for the species to ensure electroneutrality within the solutions, taking into account the fact that the second step of sulfuric acid dissociation is incomplete according to Eq. (3-69).



According to Eq. (3-68), complete dissociation for the first step of sulfuric acid dissociation occurs and, for the second step, the dissociation happens according to the following manner¹⁷⁴.

$$S_d = k_d \left(\frac{c_{\text{H}^+} - c_{\text{HSO}_4^-}}{c_{\text{H}^+} + c_{\text{HSO}_4^-}} - \beta \right) \quad (3-70)$$

where S_d is the dissociation source term, k_d is the dissociation reaction coefficient, and β is the degree of dissociation for bisulphate ion and assumed to be constant¹⁹². Table 3.4 summarizes the initial concentration for the species at SoC of 95%.

3.3.8. Numerical Modeling Approach

The governing equations formulated above, subjected to specific boundary conditions for the battery geometries, operating parameters, and electrolyte properties presented in Table 3.1 and 3.2 are solved numerically using the finite-element software COMSOL Multiphysics.

3.4. Results and Discussion

For the model simulations, mesh sensitivity analysis was performed to ensure that the results were independent of the mesh size. In order to capture steep gradients within the model, the mesh size was refined for the intersections where different domains meet ($X =$

X_1, X_2). The final model consisted of 15202 elements after which increasing the number of elements did not change the accuracy of the numerical data. Figure 3-3 includes the schematic of the cross-sectional areas used for comparison between the model and experiment. $Y = Y_1$ simulates the data at the cell height of $l_{cell}/4$, $Y = Y_2$ simulates the data at the cell height of $l_{cell}/2$ and finally $Y = Y_3$ simulates the data at the cell height of $(31/32) \times l_{cell}$.

3.4.1. The effect of convective mass transport on the species distribution

During operation of the VRFB, the species concentration constantly changes within the electrodes, resulting in concentration gradients for both in-plane and through-plane directions. As a result, engineering mass transport to target the active sites undergoing faradaic reactions is of great importance. As indicated in Eq. (3-4), engineering mass

Table 3.4. Initial species concentration

Symbol	Description	Value (mol/m ³)
c_{II}^0	Initial concentration of $V(II)$	950
c_{III}^0	Initial concentration of $V(III)$	50
c_{IV}^0	Initial concentration of $V(IV)$	50
c_V^0	Initial concentration of $V(V)$	950
$c_{H^+,neg}^0$	Initial concentration of H^+ in negative electrolyte	3967
$c_{H^+,pos}^0$	Initial concentration of H^+ in positive electrolyte	4963
$c_{HSO_4^-,neg}^0$	Initial concentration of HSO_4^- in negative electrolyte	5989
$c_{HSO_4^-,pos}^0$	Initial concentration of HSO_4^- in positive electrolyte	5987
$c_{SO_4^{2-},neg}^0$	Initial concentration of SO_4^{2-} in negative electrolyte	16.6
$c_{SO_4^{2-},pos}^0$	Initial concentration of SO_4^{2-} in positive electrolyte	13.3

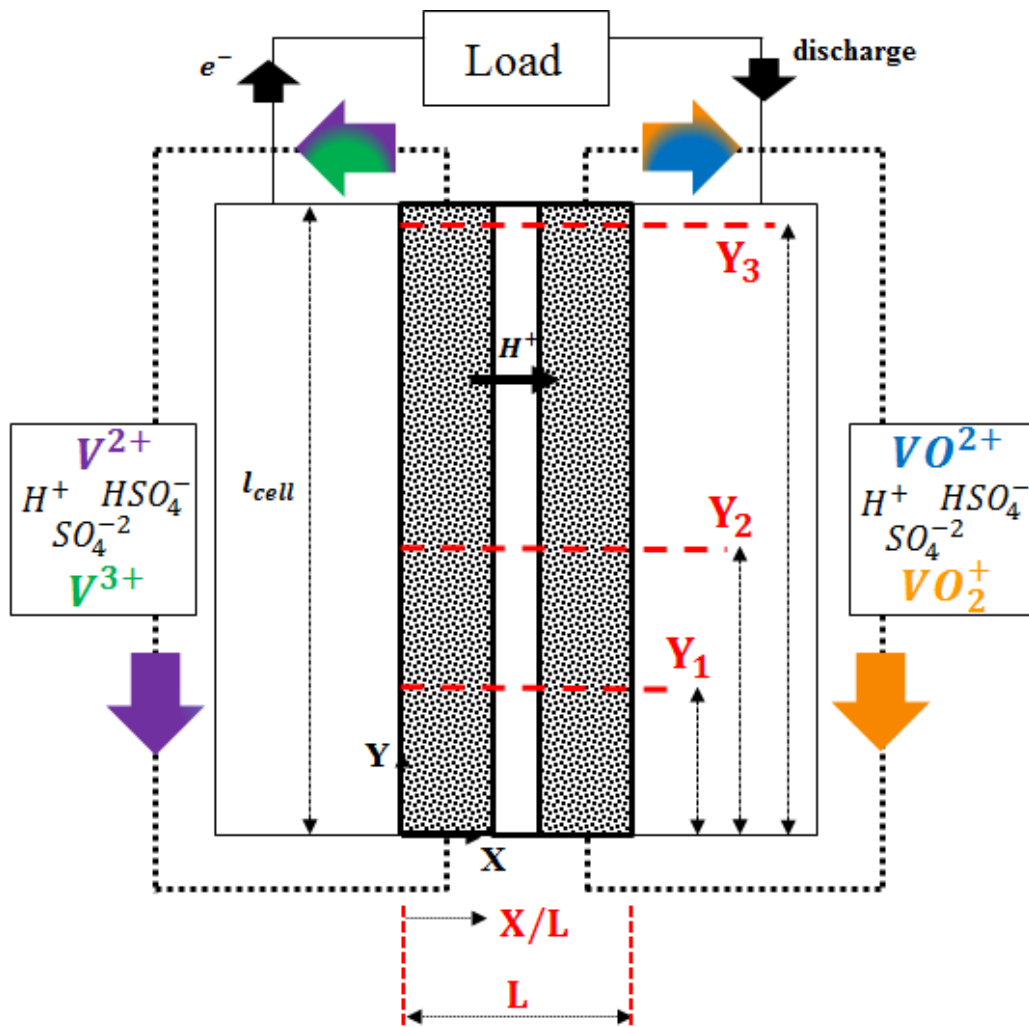


Figure 3-3: Sample cut-planes for computational analysis

transport within the porous media depends on understanding the dominant factors affecting the species flux densities. In essence, the flux density is a vector quantity indicating the direction in which the species are moving. First of all, this movement is due to the motion of the fluid with the bulk velocity $\mathbf{v}_{a/c}$ in the anode and cathode compartments. However, if there is a concentration gradient or electric field that the system is exposed to, the movement of the species can deviate from the average velocity. Of interest is how these fluxes affect mass transport and the relative portions of convective, diffusive and electrophoretic fluxes at different operational conditions of the battery.

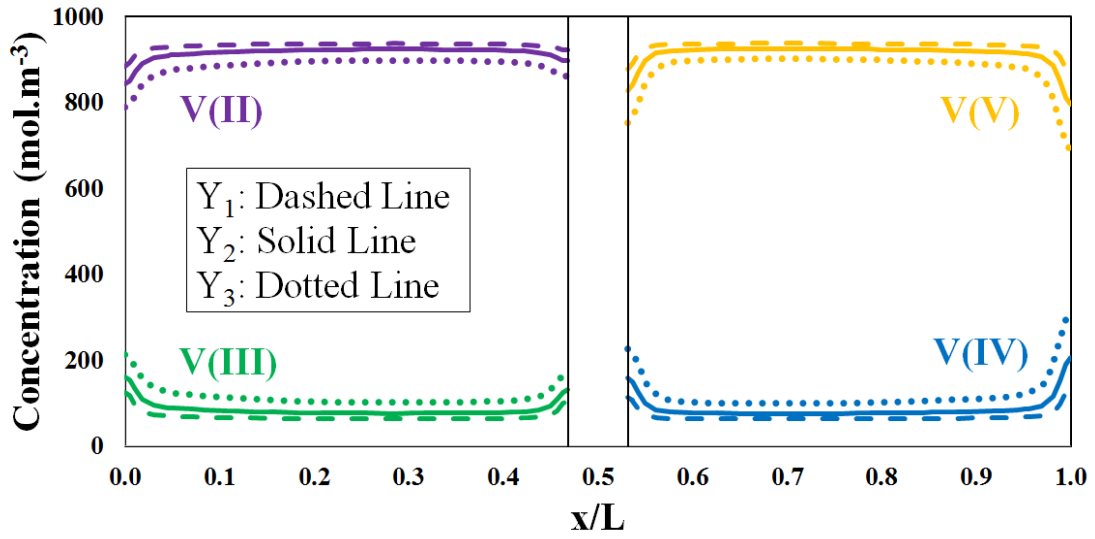
Initially, the model was utilized to predict the species concentration distribution at different operating conditions. At lab scale, peristaltic pumps are commonly employed to pump the solutions to the cells at different volumetric flow rates. Flow rates of 20 and 90 mL/min are common; these flow rates correspond to an inlet velocity range of approximately 0.1 cm/s to 0.45 cm/s for the cell geometry described in Table 3.1. The VRFB simulations here have been performed at 200 mA.cm⁻² and 800mA.cm⁻² in order to investigate the mass transport limitations on cell performance.

Figure 3-4 includes the simulation result for 20 mL.min⁻¹ electrolyte flow rate and the cell discharging at 200 mA.cm⁻². Comparing the concentration along the through-plane direction as shown in Fig. 3-4(a), depletion of charged species occurs along the flow direction and the concentration of V(II) and V(V) decreases while the concentration of V(III) and V(IV) increases. Fig. 3-4(b) shows that the concentration of H⁺ and HSO₄⁻ does

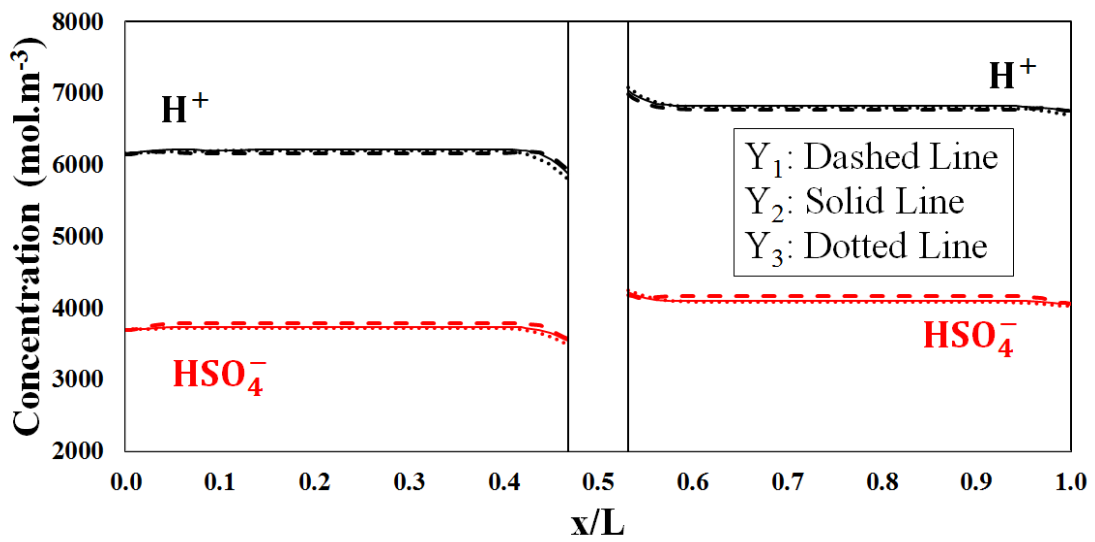
not significantly change along the flow direction. Charged species consumption is somewhat localized near the current collector and membrane sides of the electrodes (Fig. 3-4(a)) while the concentration gradient is higher near the current collector side. The same observation is the case for protons and bisulphate ions where, for the latter, the concentration gradient is greater adjacent to the membrane due to higher flux of protons at the membrane boundaries in combination with the acid dissociation reaction.

The other important observation in Fig. 3-4b is the difference in the concentration of protons and bisulphate ions between the anode and cathode side of the VRFB; the concentration of both ions is higher at the cathode side. Both experimental and theoretical work has been performed to measure the partitioning factor of the membrane exposed to different concentrations of sulfuric acid solutions. An early theoretical and experimental work by Verbrugge et al. observed severe de-swelling for the Nafion exposed to sulfuric acid; due to ionic cluster channel compression which led to decreased membrane porosity^{186, 198, 199}. Acid uptake by membranes can also result in significant water loss after equilibration with concentrated sulfuric acid solution²⁰⁰.

According to Fig. 3-4(b) when the membrane was exposed to solutions with varying concentration of protons at the anode and cathode sides, proton uptake will vary according to Eq. (3-23) and the Donnan potential across the membrane¹⁷⁹. It is important to quantify the convective, diffusive, and electrophoretic fluxes at different operating conditions in order to evaluate the portion of each flux density.



(a)

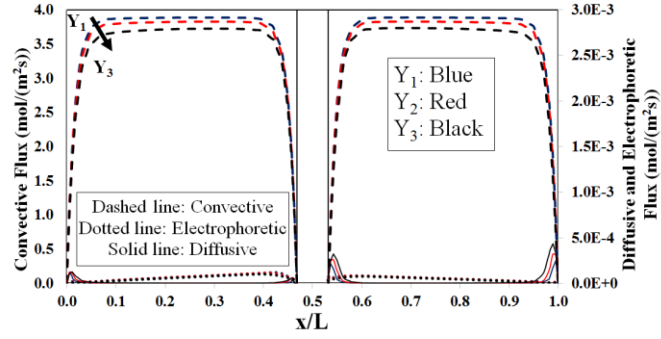


(b)

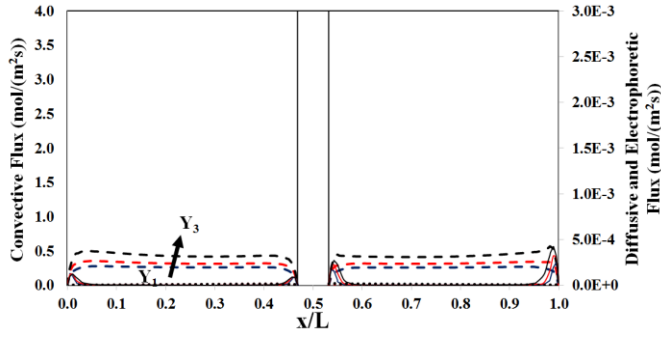
Figure 3-4: Species distribution at 20 mL.min⁻¹ and 200 mA.cm⁻² discharge; (a) Vanadium species, (b) Protons and bisulphate

It is important to quantify the convective, diffusive, and electrophoretic fluxes at different operating conditions in order to evaluate the portion of each flux density. Figure 3-5 includes the different sources of mass transport flux at a volumetric flow rate of $20 \text{ mL}\cdot\text{min}^{-1}$ and cell discharge current density of $200 \text{ mA}\cdot\text{cm}^{-2}$. As shown in Fig. 3-5(a) and 5(b), the diffusive flux density is relatively pronounced at the interface between the electrode/current collector and slightly pronounced at the electrode/membrane interface. This is clearly supported by the results shown in Fig. 3-4. Also, the electrophoretic and diffusive fluxes are on the same order and almost four orders of magnitude lower than the convective flux. Comparing the fluxes for protons, the convective flux is three orders of magnitude higher than the diffusive and electrophoretic fluxes, primarily due to greater diffusivity of protons versus vanadium ions. Also, the dissimilar proton convective fluxes in the anode and cathode are due to the difference in proton concentration at each cell location along the flow stream.

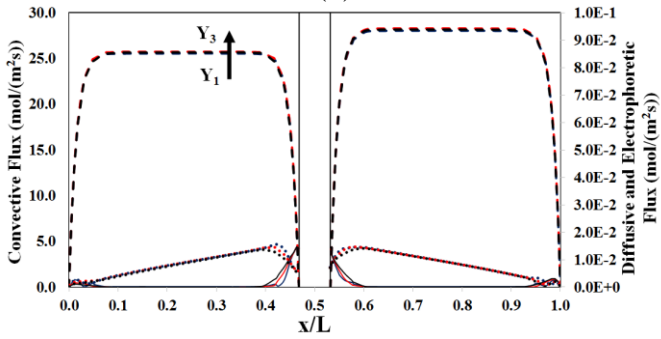
Figure 3-6 includes the simulation results for $20 \text{ mL}\cdot\text{min}^{-1}$ flow rate and discharge at $800 \text{ mA}\cdot\text{cm}^{-2}$. Along the flow direction, charged species consumption occurs resulting in a severe concentration gradient adjacent to the current collectors, suggesting that the reaction location is toward the flow-plate side. The species distribution profile clearly shows that along the flow path, species starvation occurs toward the current collectors at the cell exit port; as a result, mass transport limitations are the primary source of the cell starvation at high current density. Figure 3-6(b) illustrates that the Donnan potential is more pronounced at high current density.



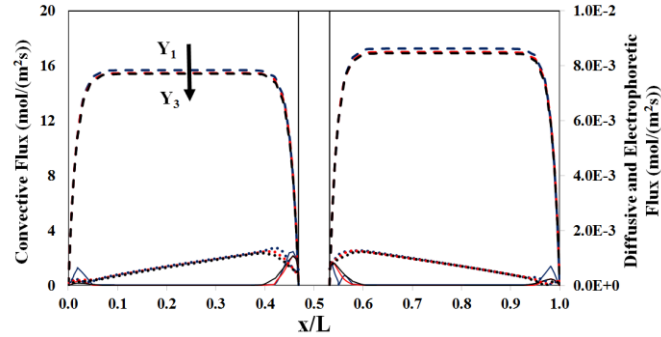
(a)



(b)



(c)



(d)

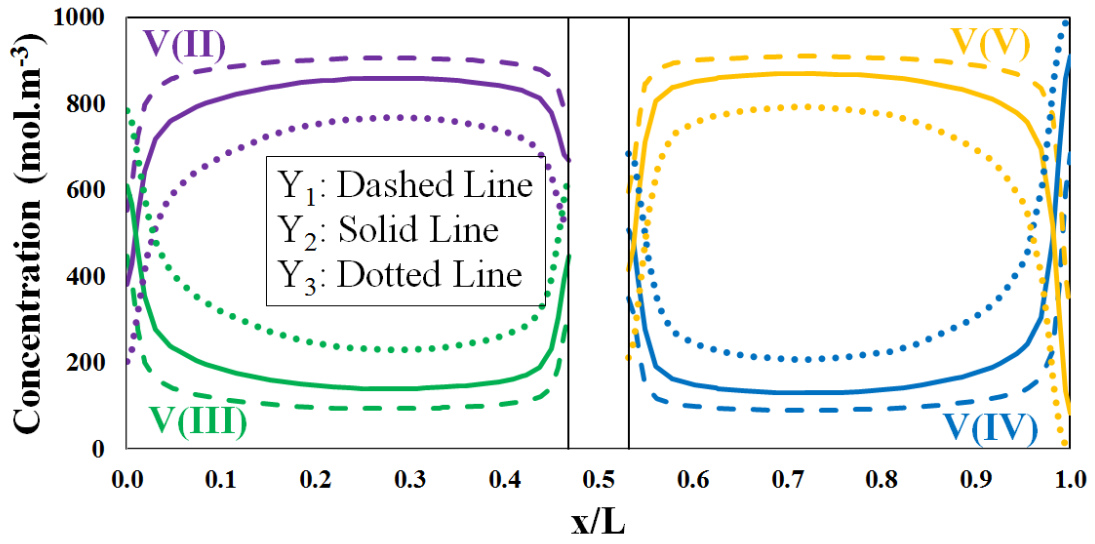
Figure 3-5: Species flux densities at $20 \text{ mL}\cdot\text{min}^{-1}$ and $200 \text{ mA}\cdot\text{cm}^{-2}$ discharge; (a) V(II)/V(V) , (b) V(III)/V(IV) , (c) $\text{H}^+_{\text{anode}} / \text{H}^+_{\text{cathode}}$, (d) $\text{HSO}_4^-_{\text{anode}} / \text{HSO}_4^-_{\text{cathode}}$

Also, comparing the concentration distribution of protons and bisulphate ions from Fig. 3-6(b) and 3-5(b) indicates that a large concentration gradient occurs adjacent to the membrane during high current discharge, resulting in the high rate of proton flux. However, even at high discharge current density, the concentrations of protons and bisulphate ions do not change to a great extent along the flow direction.

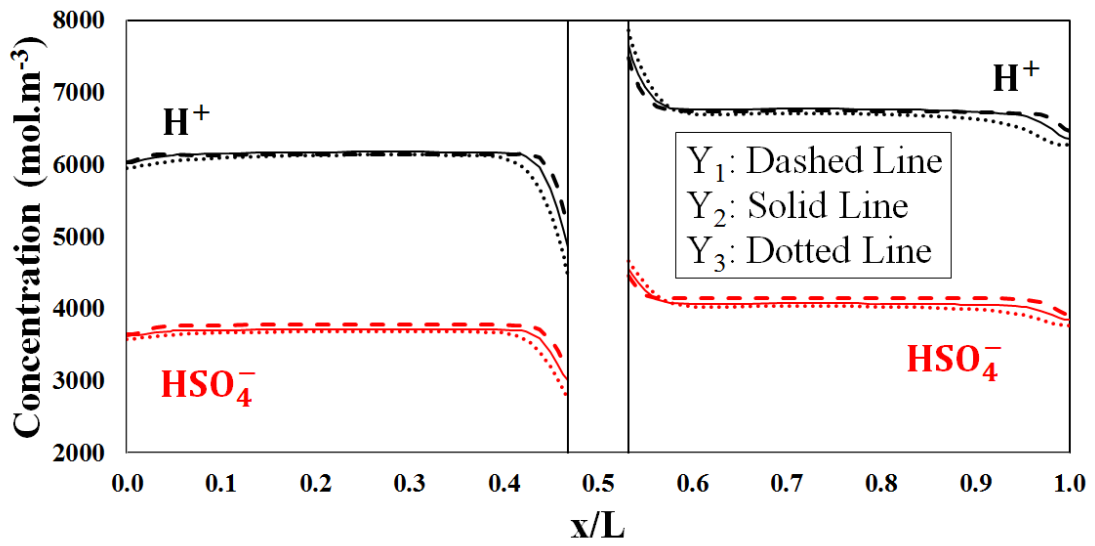
To further understand the concentration gradients in Fig. 3-6, it is important to quantify the mass flux for the vanadium species the same way as shown in Fig. 3-5. Figure 3-7 shows the different flux components for the vanadium species. The convective flux decreased greatly compared to Fig. 3-5 for V(II)/V(V) due to high rate of consumption along the flow direction. The same pattern is observed for V(III)/V(IV) where the increase in convective flux density is significant.

Of particular importance is the difference in diffusive flux in the electrode/current collector interface for V(II) and V(III) versus V(V) and V(IV). This difference is primarily due to the difference in diffusion coefficients tabulated in Table 3.2. The increased discharge current for this case is apparent in its impact on the electrophoretic flux.

Clearly, increased overpotential has resulted in greater electrophoretic flux for the species. Also, the difference for electrophoretic flux of the species for anode versus cathode is due to the difference in the mobility values for V(II) versus V(V) and V(III) versus V(IV).

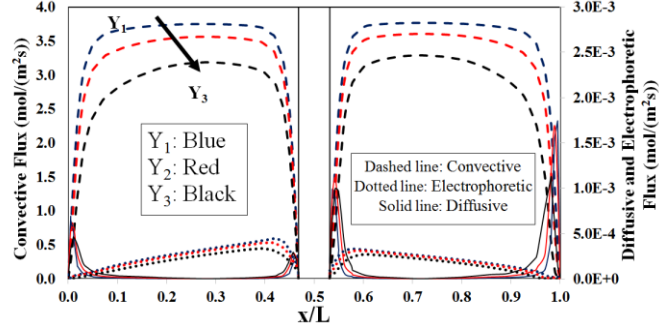


(a)

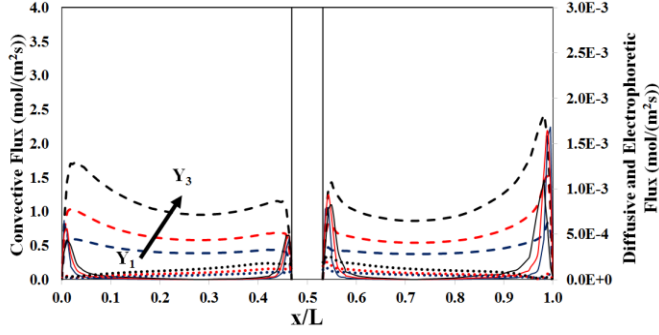


(b)

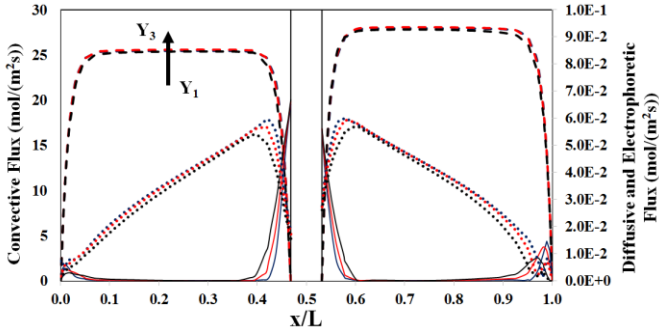
Figure 3-6: Species distribution at 20 mL.min^{-1} and 800 mA.cm^{-2} discharge; (a) Vanadium species, (b) Protons and bisulphate



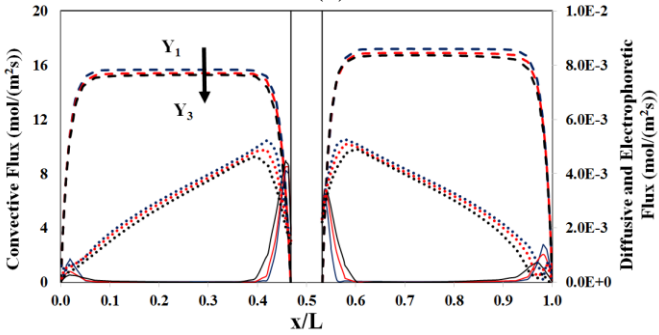
(a)



(b)



(c)



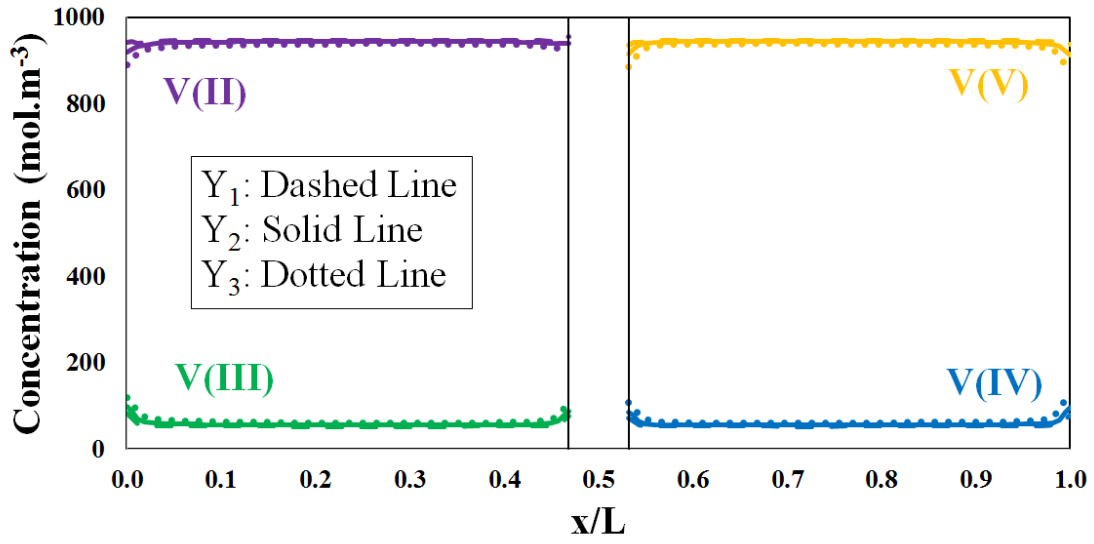
(d)

Figure 3-7: Species flux densities at 20 mL.min⁻¹ and 800 mA.cm⁻² discharge;
 (a) V(II)/V(V), (b) V(III)/V(IV),
 (c) H_{anode}⁺ / H_{cathode}⁺, (d) HSO_{4anode}⁻ / HSO_{4cathode}⁻

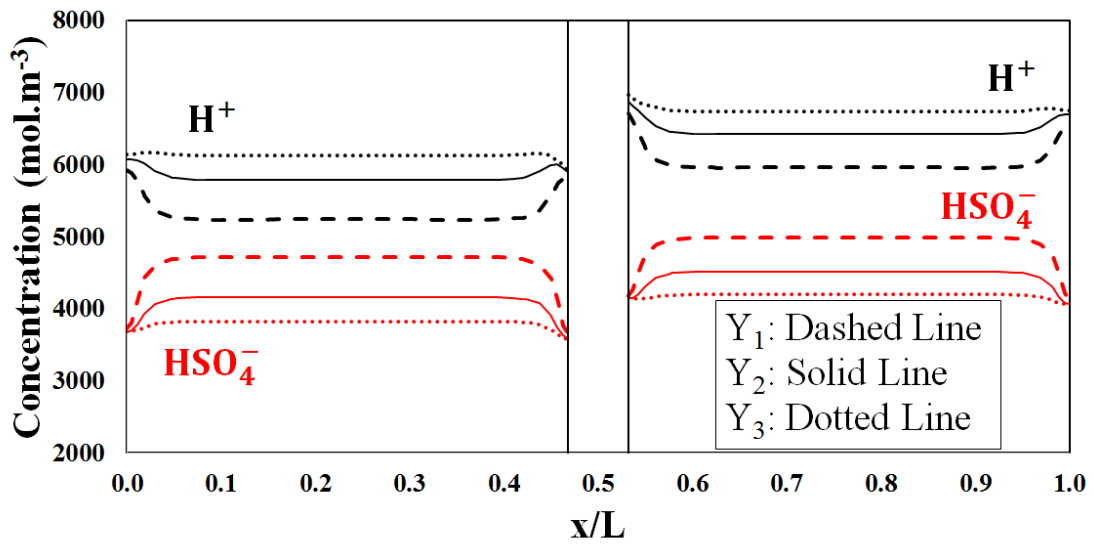
Figure 3-8 includes the simulation result for $90 \text{ mL}\cdot\text{min}^{-1}$ flow rate and discharge at $200 \text{ mA}\cdot\text{cm}^{-2}$. In this case, the concentration gradients adjacent to the current collectors are decreased considerably due to increased convective flow within the porous media. However, the concentration of species undergoing faradaic reactions has not changed to a great degree along the flow direction.

Finally, the concentrations of the bisulphate ions and protons change to a greater degree along the flow direction compared to Fig. 3-4 and Fig. 3-6. Along the flow path, the concentration of protons increased; conversely, the concentration of the bisulphate ions decreased due to higher rate of dissociation and convective flux.

Figure 3-9 shows the different components of the mass flux for the conditions in Figure 3-8 ($90 \text{ mL}\cdot\text{min}^{-1}$ flow rate and $200 \text{ mA}\cdot\text{cm}^{-2}$ discharge current). In this case, the diffusive and electrophoretic fluxes are six orders of magnitude lower than the convective flux for V(II) and V(V). Also, as expected, the increased convective mass flux decreased the rate of charged species (V(II) and V(V)) utilization along the flow direction. The difference in the concentration of protons and bisulphate ions observed along the flow direction in Fig. 8(b) can further be explained through Fig. 3-9(c) and 3-9(d). In this case the convective mass transport is different at varying cell location along the flow stream, causing the significant change in the concentration of the protons and bisulphate ions along the flow direction. This behavior was not observed at lower volumetric flow rate (Fig. 3-5).



(a)



(b)

Figure 3-8: Species distribution at 90 mL.min^{-1} and 200 mA.cm^{-2} discharge; discharge;
 (a) Vanadium species, (b) Protons and bisulphate

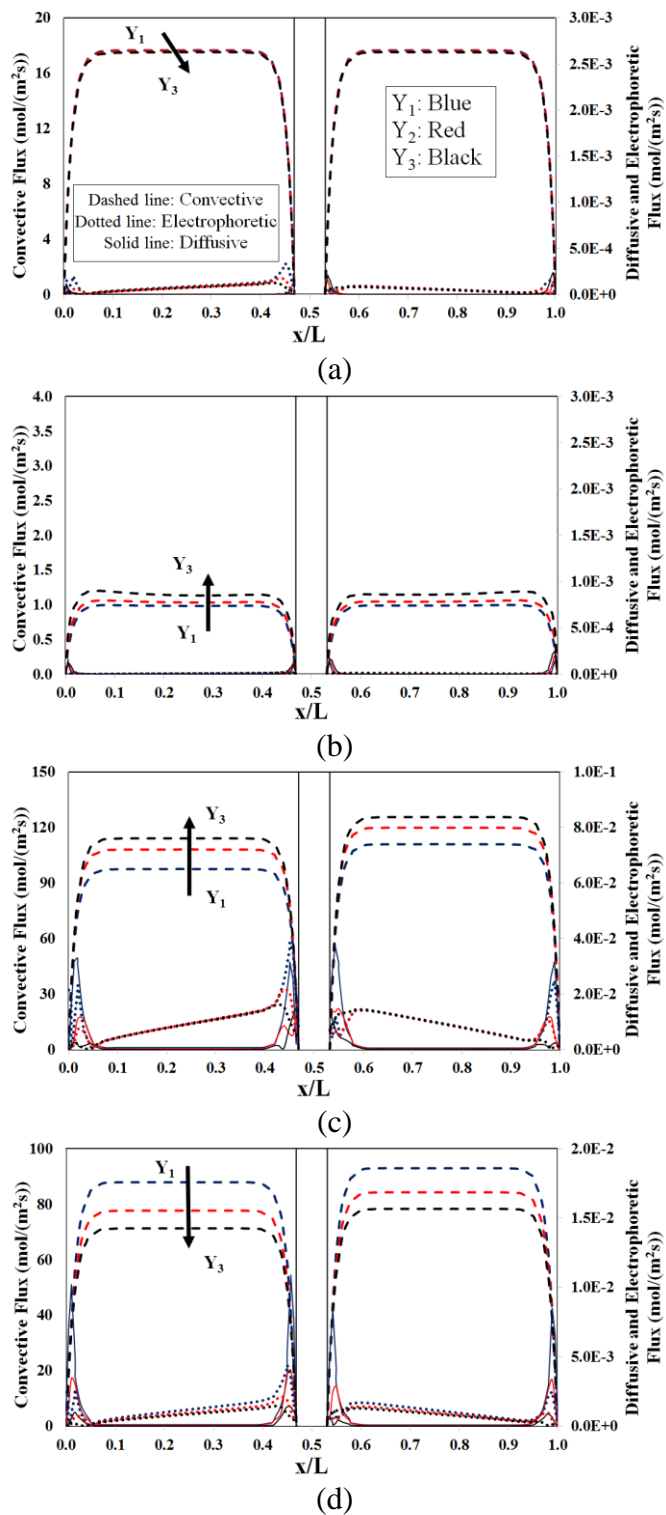
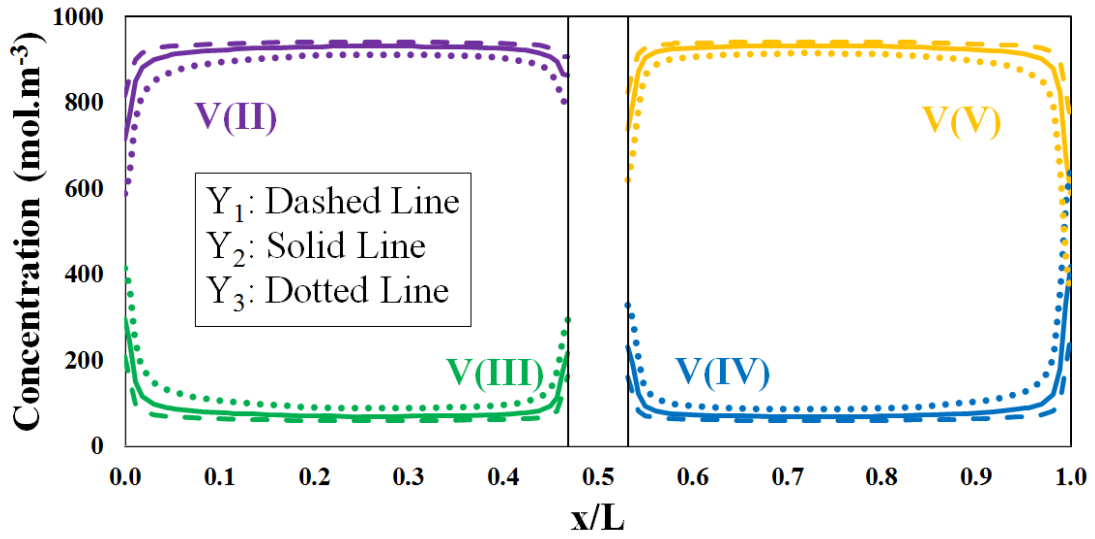


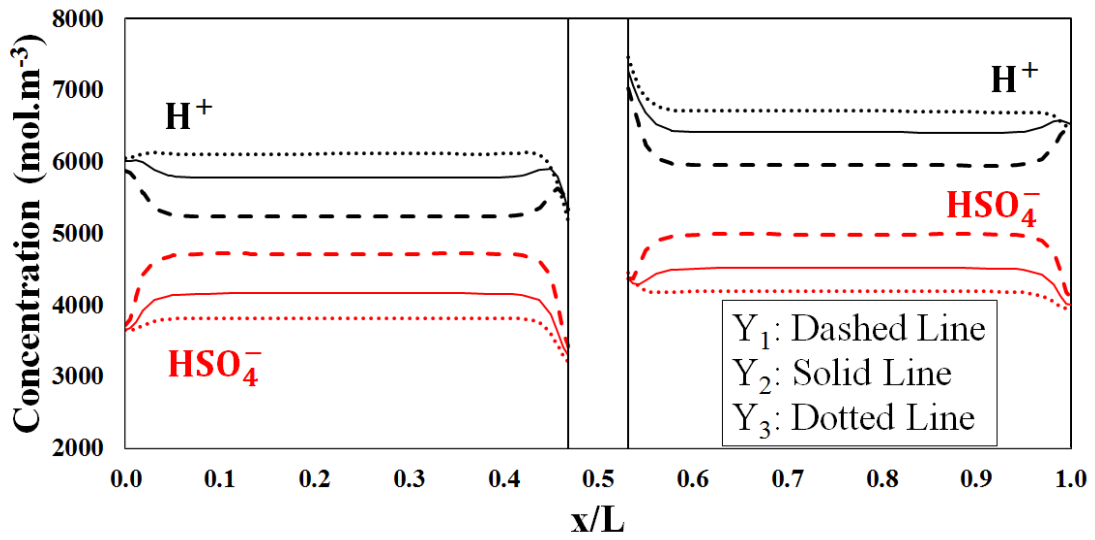
Figure 3-9: Species flux densities at $90 \text{ mL}\cdot\text{min}^{-1}$ and $200 \text{ mA}\cdot\text{cm}^{-2}$ discharge;
 (a) V(II)/V(V) , (b) V(III)/V(IV) ,
 (c) $\text{H}^+_{\text{anode}} / \text{H}^+_{\text{cathode}}$, (d) $\text{HSO}_4^-_{\text{anode}} / \text{HSO}_4^-_{\text{cathode}}$

Figure 3-10 includes the simulation results for operation at $90\text{mL}\cdot\text{min}^{-1}$ and $800\text{ mA}\cdot\text{cm}^{-2}$ discharge. Among the observations is the cell's ability to operate without starving at the exit port. Contrary to operations with high discharge rate and lower volumetric flow rate (Fig. 6), increased convective mass flux prevents the depletion of V(II) and V(V) at the exit port. As expected from previous results, the concentration gradient is higher toward the electrode/current-collector interface. Due to different diffusivity values for V(II) and V(V), somewhat different concentration gradients are observed. Therefore, increased convective flux of the species improves mass transport and therefore enables the cell to operate at high current density without starvation at the exit ports of the electrodes. Similar to the previous case, the concentration of protons increased along the flow direction while the bisulphate ion concentration decreased concurrently.

Figure 3-11 compares the different components of the mass flux. It is clear that the electrophoretic flux has increased compared to Fig. 3-9 due to increased overpotential for the vanadium species. The asymmetry observed for the electrophoretic fluxes of V(II) versus V(V) and V(III) versus V(IV) is due to differences in ion mobility in the solution. Compared to Fig. 3-9, the convective mass transport for V(II) and V(V) has decreased along the flow direction due to high discharge rate. Also, due to high current discharge, the diffusive mass flux increased compared to Fig. 3-9 but is still five orders of magnitude lower than the convective flux. The difference in concentration of protons and bisulphate ions for anode and cathode has imposed asymmetry for the electrophoretic flux.



(a)



(b)

Figure 3-10: Species distribution at 90 mL.min^{-1} and 800 mA.cm^{-2} discharge; discharge; (a) Vanadium species, (b) Protons and bisulphate

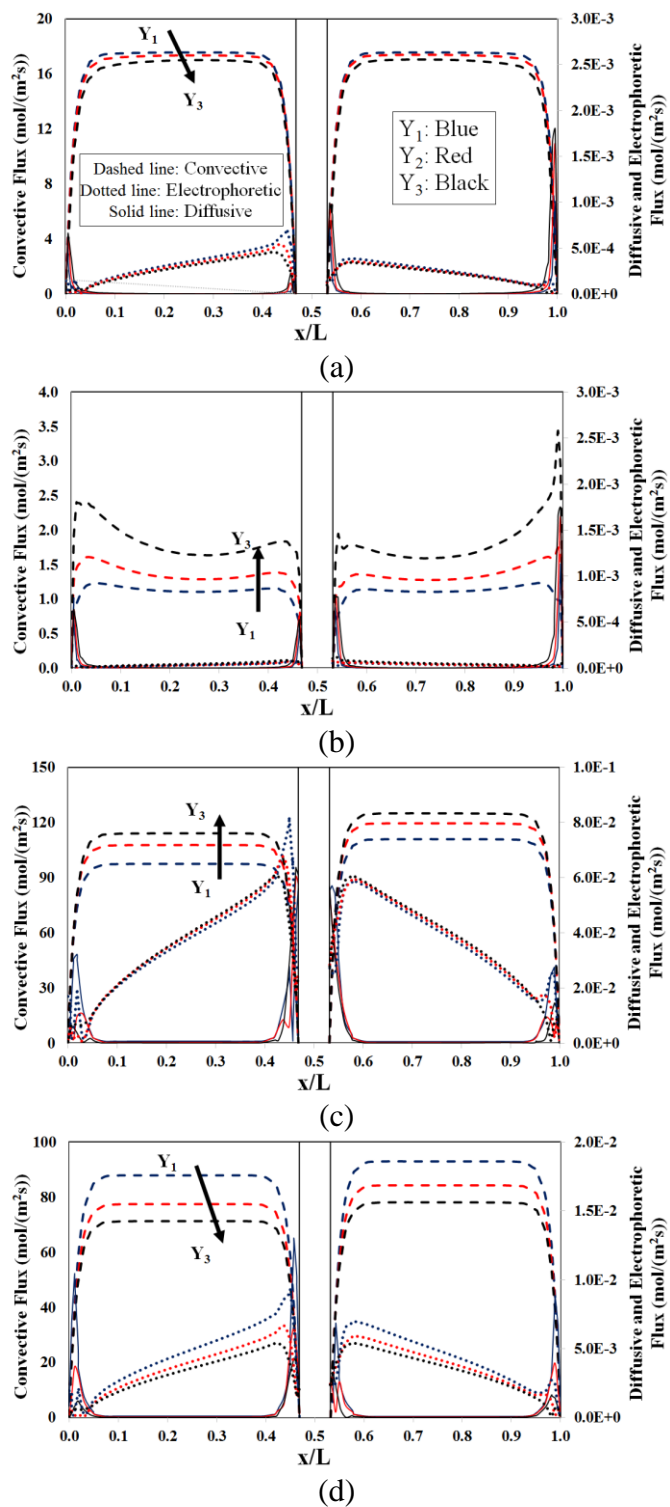


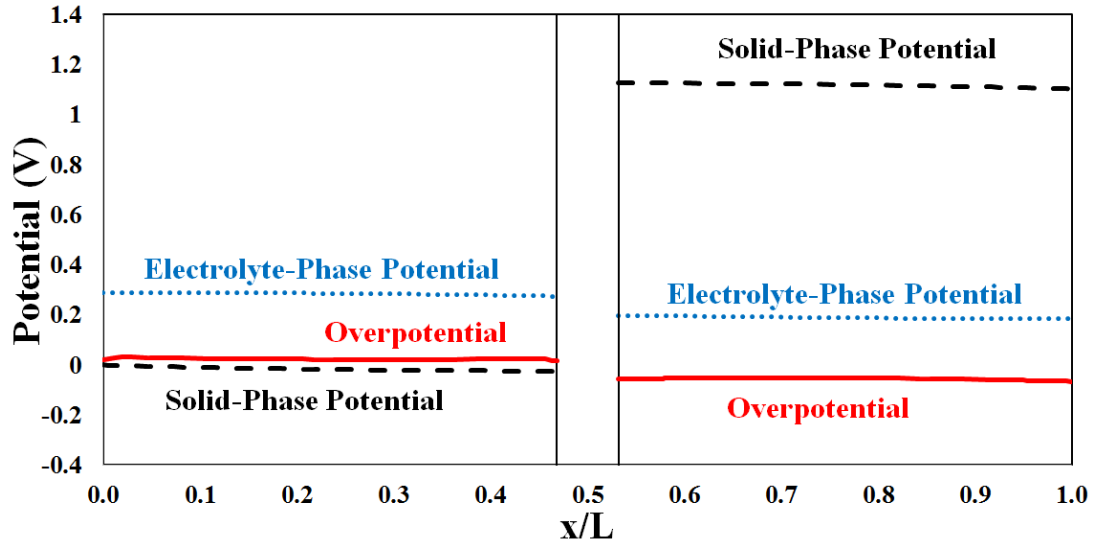
Figure 3-11: Species flux densities at $90 \text{ mL}\cdot\text{min}^{-1}$ and $800 \text{ mA}\cdot\text{cm}^{-2}$ discharge;
 (a) V(II)/V(V), (b) V(III)/V(IV),
 (c) $\text{H}^+_{\text{anode}} / \text{H}^+_{\text{cathode}}$, (d) $\text{HSO}_4^-_{\text{anode}} / \text{HSO}_4^-_{\text{cathode}}$

3.4.2. Analysis of overpotential on the species distribution

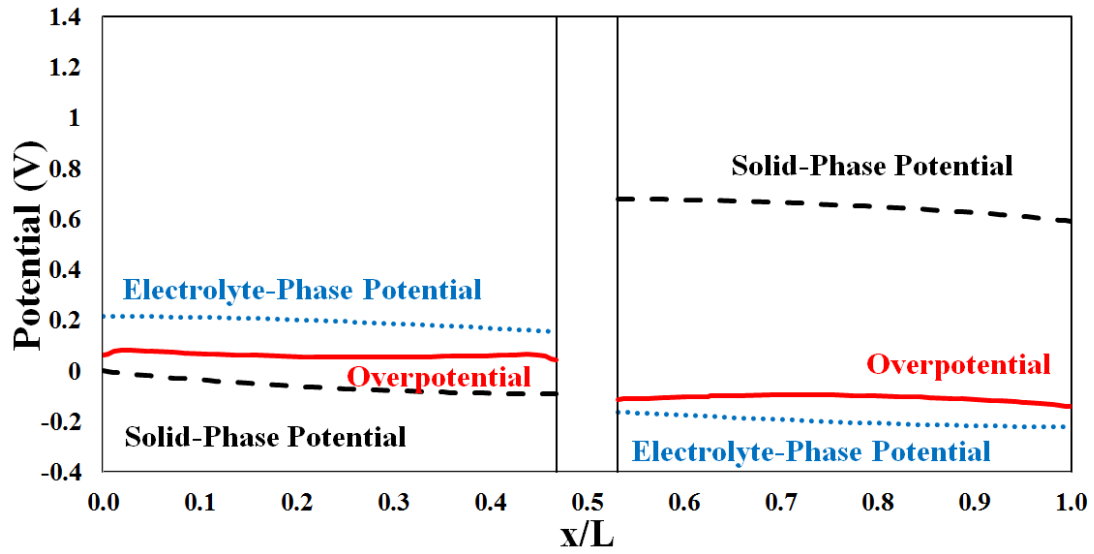
It was shown earlier that there exists a concentration difference for protons and bisulphate ions between the anode and cathode compartments. As a result, it is important to analyze the change in electrolyte potential as well as solid phase potential at different operating conditions. Figure 3-12 compares the electrolyte and solid phase potentials for the cases analyzed earlier: discharge at $200 \text{ mA}\cdot\text{cm}^{-2}$ and $800 \text{ mA}\cdot\text{cm}^{-2}$ at a flow rate of $90 \text{ mL}\cdot\text{min}^{-1}$.

The solid-phase and electrolyte potentials, as well as overpotentials, have been compared for both anode and cathode side at different discharge current densities in the through-plane direction of the VRFB in Fig. 3-12. The model predicts much higher overpotential in the anode than in the cathode, confirming more sluggish kinetic behavior for the anode side, agreeing with in-situ kinetics measurements²⁰¹. However, this is contrary to the experimental data of some who have found slower electrochemical reactions at the cathode side^{129, 191}. As shown in Fig. 3-12, the model simulates the lower solid-phase and electrolyte-phase potential for the cathode side for higher discharge current density (Fig. 3-12(b) versus Fig. 3-12(a)).

The solid-phase and electrolyte potentials, as well as overpotentials, have been compared for both anode and cathode side at different discharge current densities in the through-plane direction of the VRFB in Fig. 3-12.



(a)



(b)

Figure 3-12: Potential distribution in the through-plane direction of an operando VRFB; (a) 200 mA.cm⁻² discharge, (b) 800 mA.cm⁻² discharge

The model predicts much higher overpotential in the anode than in the cathode, confirming more sluggish kinetic behavior for the anode side, agreeing with in-situ kinetics measurements²⁰¹. However, this is contrary to the experimental data of some who have found slower electrochemical reactions at the cathode side^{129, 191}. As shown in Fig. 3-12, the model simulates the lower solid-phase and electrolyte-phase potential for the cathode side for higher discharge current density (Fig. 3-12(b) versus Fig. 3-12(a)).

3.4.3. Experimental validation of the potential-distribution simulation data

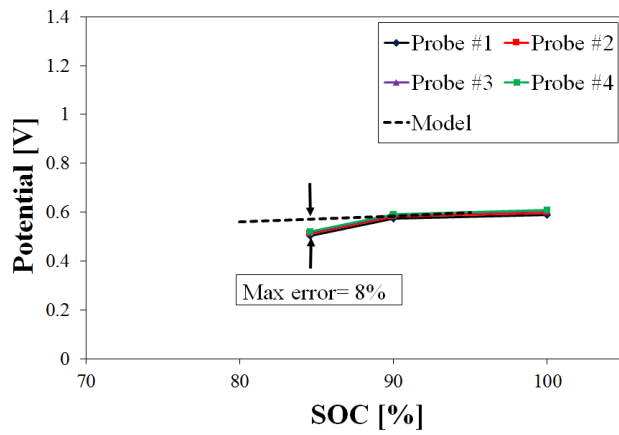
The micro-probes installed at the location of $Y = Y_2$ (according to Fig. 3-3) of the cathode side enable direct measurement of potential for comparison with simulated results at the center of the cell model.

Figure 3-13 summarizes the measured potentials at different operating conditions. Figure 3-13(a), (b), (c) and (d) include the potential data for discharge current densities at 800, 600, 400 and 200 mA.cm⁻², respectively. According to the experimental data, at a given SoC, the potentials from all the probes behaved in a similar manner as a function of SoC and exhibited lower potential (corresponding to greater overpotential) at decreased SoC. Also, for all measurements, measured potentials decreased with increasing discharge currents. As shown in Fig. 3-13, the experimental data are in good agreement with the numerical results. The discrepancy between the model prediction and experimental results is greatest at lower SoC and higher discharge rate where the maximum error is 9% for the discharge rate of 800 mA.cm⁻².

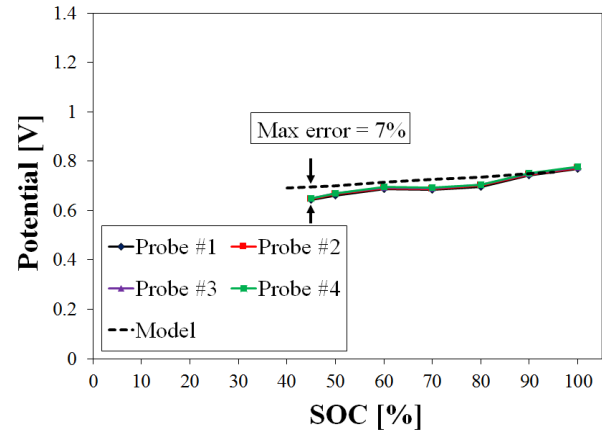
Figure 3-14 compares data from different probes at the beginning of discharge for 95% SoC and different discharge currents as well as open-circuit voltage (OCV). To obtain the experimental data, three different cells were built and tested. The experimental data shown here for each probe is the average of different builds and the error bars were calculated based on the divergence from the average data.

Fig. 3-14 shows measured potentials for all probes at OCV and during the constant current discharge at $200 \text{ mA}\cdot\text{cm}^{-2}$, $400 \text{ mA}\cdot\text{cm}^{-2}$, $600 \text{ mA}\cdot\text{cm}^{-2}$, and $800 \text{ mA}\cdot\text{cm}^{-2}$. When current was drawn from the cell, the probe potentials decreased relative to OCV with the lowest potential measured at probe #1 (current-collector side) and the maximum value at probe #4 (membrane side).

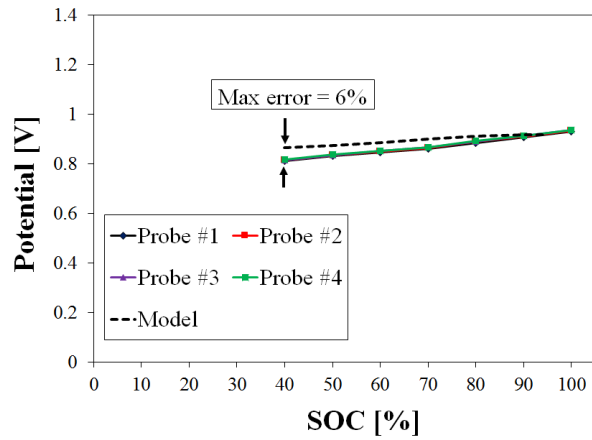
Greater discharge current increased the potential difference between probe #1 and probe #4, indicating that the reaction is more uniform across the electrode layers at low current density; and as the current density increased, the reaction shifted toward the flow plate side. The observed behavior among the potential probes have been compared with the model simulation for the solid-phase potential shown within Fig. 3-12 and this comparison has been provided in Fig. 3-14. As shown Fig. 3-14, good agreement was achieved between the model prediction and experimental results.



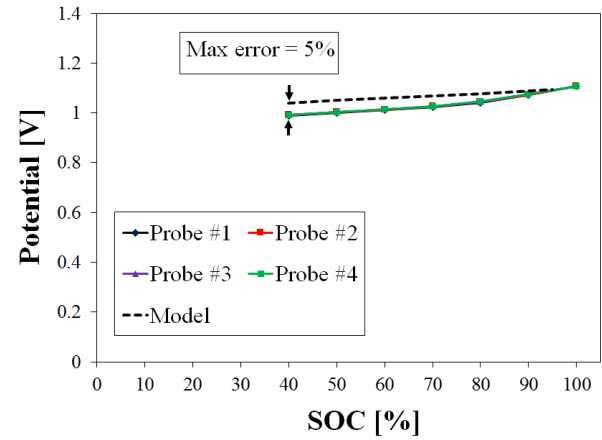
(a)



(b)



(c)



(d)

Figure 3-13: The potential of probes in through-plane direction of an operando VRFB during discharge; (a) $800 \text{ mA}\cdot\text{cm}^{-2}$, (b) $600 \text{ mA}\cdot\text{cm}^{-2}$, (c) $400 \text{ mA}\cdot\text{cm}^{-2}$, (d) $200 \text{ mA}\cdot\text{cm}^{-2}$

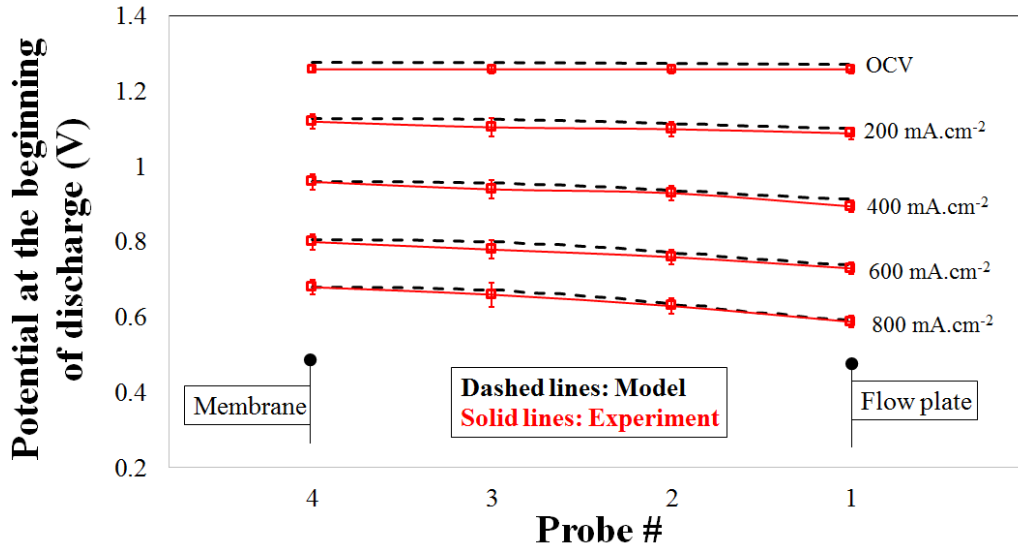


Figure 3-14: Potential distribution at the beginning of discharge

3.5. Conclusions

During operation of all-vanadium redox flow batteries (VRFB), several gradients form in the in-plane and through-plane directions of the cell. In order to quantify these gradients, an *in situ* potential distribution technique was developed. Micro potential probes were installed within the layered porous carbon electrode at the positive side of the VRFB.

The experimental results revealed that the reaction locations within the porous electrode shifted toward the flow plate side with increasing current density during discharge, indicating a mass transfer limited system. To describe the experimental results, a mathematical model was developed that quantified the species concentration distribution, multiple mass flux components, and solid-phase and electrolyte-phase potentials. The mathematical model agreed with the experimental data, with a maximum error of 9%. The

lowest predicted and measured potential occurred close to the electrode/current-collector interface, indicating the dominant reaction location in the through plane direction.

In addition, the model simulated the diffusive, convective and electrophoretic mass fluxes at different operating conditions. The model simulation showed that the convective mass transport flux is at least four orders of magnitude higher than the diffusive and electrophoretic fluxes at the corresponding cell location along the flow stream.

The concentration gradient not only occurs along the flow direction, but also in the through-plane direction with the highest concentration gradient at the electrode/current-collector interface. If the cell is to be operated at high current density ($800 \text{ mA}\cdot\text{cm}^{-2}$ and higher), starvation of active species (V(II)/V(V)) needs to be prevented at the electrode/current-collector interface. This goal is achieved partially by increased convective mass flux (which was shown in this work). Mass transport can further be increased by improved electrode design such that the mass transport resistance in the in-plane direction decreases along the flow direction. This would enable increased diffusion flux from the main stream of the flow towards the electrode/current-collector interface. Also, it was shown that when the cell is operating at high volumetric flow rate, a large concentration gradient of protons and bisulphate ions forms along the flow direction, resulting in varying conductivity values for the membrane along the flow direction. An improved design can eliminate this by providing more uniform distribution of the protons and bisulphate ions within the electrodes.

3.6. Acknowledgments

Partial Funding for this project was provided by the Office of Naval Research work under Long Range Broad Agency Announcement (BAA) #N00014-12-1-0887. A portion of this work (GMV-XPS) was supported by U.S. Department of Energy's Office of Basic Energy Science (DOE-BES), Division of Materials Sciences and Engineering, under contract with UT-Battelle, LLC. The authors thank Dr. Kivanc Ekici and Dr. E.L. Redmond for fruitful discussion.

CHAPTER FOUR :
COUPLED MEMBRANE TRANSPORT PARAMETERS FOR IONIC SPECIES
IN ALL-VANADIUM REDOX FLOW BATTERIES

Scholarly contributions

This chapter is revised based on the published paper with permission from Elsevier: ²⁰²

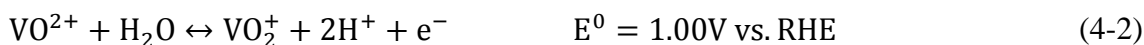
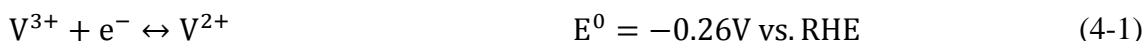
Yasser Ashraf Gandomi, D. S. Aaron, M. M. Mench. “Coupled Membrane Transport Parameters for Ionic Species in All-Vanadium Redox Flow Batteries” *Electrochimica Acta*, 218, 174-190 (2016) [<https://doi.org/10.1016/j.electacta.2016.09.087>]

Abstract

One of the major sources of capacity loss in all-vanadium redox flow batteries (VRFBs) is the undesired transport of active vanadium species across the ion-exchange membrane, generically termed crossover. In this work, a novel system has been designed and built to investigate the concentration- and electrostatic potential gradient-driven crossover for all vanadium species through the membrane in real-time. For this study, a perfluorosulphonic acid membrane separator (Nafion® 117) was used. The test system utilizes ultraviolet/visible (UV/Vis) spectroscopy to differentiate vanadium ion species and separates contributions to crossover stemming from concentration and electrostatic potential gradients. It is shown that the rate of species transport through the ion-exchange membrane is state of charge dependent and, as a result, interaction coefficients have been deduced which can be used to better estimate expected crossover over a range of operating conditions. The electric field was shown to increase the negative-to-positive transport of V(II)/V(III) and suppress the positive-to-negative transport of V(IV)/V(V) during discharge, with an inverse trend during charging conditions. Electric-field-induced transport coefficients were deduced directly from experimental data.

4.1. Introduction

As discussed in Chapter 3, for VRFBs, the electrochemical energy is stored in the oxidation states of the vanadium ions: V(II), V(III), V(IV) and V(V). The kinetics associated with reduction and oxidation of vanadium species are known to be complex^{108, 109}. In this work, the following simplified set of global half-reactions is adopted for the negative and positive electrodes, respectively.



Also, as covered in Chapter 3, during the operation of VRFBs, vanadium crossover and the attendant capacity loss are inevitable during cell operation¹²¹⁻¹²³. The following self-discharge reactions are assumed to happen as a function of vanadium ion crossover¹²⁴.



Reactions (4-3) and (4-4) correspond to the case where V(II) crosses the ion-exchange membrane and reacts immediately at the positive electrode. However, as long as V(V) is present in the positive side, reaction (4-4) does not occur. Reactions (4-5) and (4-4) correspond to V(III) and V(IV) transport and reactions (4-6) and (4-5) for V(V). Similar to the crossover of V(II), when V(V) crosses to the negative side of the cell, reaction (4-6) is more likely; reaction (4-5) is for the case where V(II) starvation is occurring in the negative side which is an abnormal operating condition.

It was mentioned in Chapter 3 that the prior efforts devoted to investigation of vanadium ion crossover in VRFBs have largely focused on concentration gradient-induced crossover and lacks in-depth analysis of the effect of electric field on crossover. As shown in some previous work (e.g. Ref. ¹⁴⁶), the permeability of V(IV) is significantly influenced by the concentration of sulfuric acid in the solution. Accordingly, the coupled nature of species transport across the membrane must be included in analysis and predictions. In this paper, the effect of electric field on crossover has been experimentally analyzed via differentiating concentration gradient-induced crossover from electrostatic potential gradient-induced crossover. In addition, the SoC dependence of vanadium permeability has been investigated via the introduction of interaction coefficients. The results of this study should be useful to modelers and system designers by clarifying and predicting expected transport under a wide range of operating conditions in an operating VRFB. Table 4.1, includes further details about the various aspects of the crossover study covered in this chapter.

Table 4.1. Reaction source term

	Membrane properties		Operation parameters			Species Flux Equation	
	Type	Pretreatment protocol effect	Species type	Concentration gradient (diffusion)	Electric field (migration and osmosis)	Dilute solution theory	Concentrated solution theory
This work	CEM	×	V(II) V(III) V(IV) V(V)	✓	✓	✓	Hybrid model

4.2. Experimental

4.2.1. Schematic of the set-up

A schematic of the experimental setup used in this work is shown in Fig. 4-1. The setup includes four in-house designed single cells, two-channel peristaltic pumps (Cole Parmer, Masterflex L/S), and external reservoirs as well as an ultraviolet/visible (UV/Vis) spectroscopy setup including light sources (Ocean-Optics) and spectrometers (THORLABS). Also, a central temperature control unit was designed and implemented in order to maintain a constant temperature of 30°C for all cells and reservoirs. The initial electrolyte of interest was prepared using “Cell 1” which was a 25cm² active area cell. The 10AA carbon paper electrodes (SGL Group, Germany) were sandwiched between a flow plate and the membranes. Two membranes were utilized in “Cell 1” in order to reduce the rate of crossover during the preparation of solution of interest and to enable the application of reference electrodes within “Cell 1” (the data corresponding to reference electrodes have not been reported in this paper).

Two electrolyte reservoirs were used in conjunction with “Cell 1” for negative (V(II)/V(III)) and positive (V(IV)/V(V)) sides as shown in the figure. In order to investigate real-time crossover behavior, “Cell 4” was designed to have two extra flow chambers in the cell. For “Cell 4”, the vanadium-enriched solutions flowed from the main reservoirs through the exterior chambers. One layer of 10AA carbon paper electrodes was used in exterior chambers in between the flow plates and membrane.

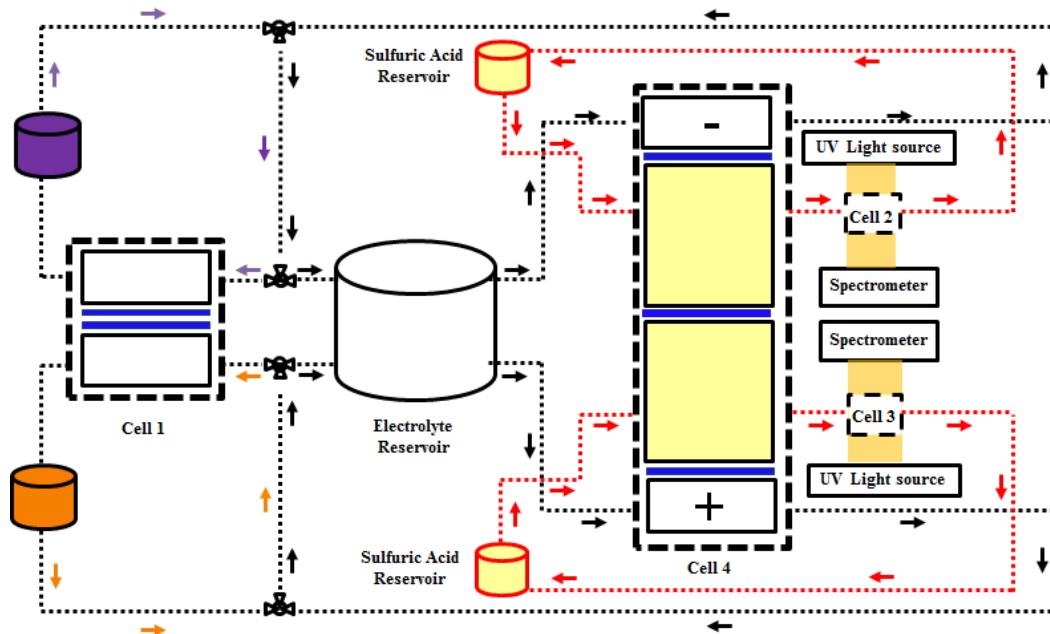


Figure 4-1: Schematic of the experimental setup
(Blue lines (color on-line) represent Nafion® 117 membranes)

It is important to note that the anode and cathode electrolytes shared the same reservoir since symmetric operation was used for the experiments described here. In the following section, further discussion of the benefits of symmetric cell operation is presented. In “Cell 4” the vanadium-deficient solutions of sulfuric acid were circulated from separate reservoirs through the interior chambers. The volumes of the interior chamber solutions were 80 mL each with the sulfuric acid concentration selected to balance osmotic pressure across the membrane. All reservoirs were sealed and under nitrogen gas protection and stir bars were employed to guarantee uniform composition of the reservoir solutions. The solutions of the interior chambers were circulated through “Cell 2” and “Cell 3” which were single-chamber flow-through cells designed and implemented to allow for real-time monitoring of species crossover using UV/Vis spectroscopy. Also, the spectra of

standardized vanadium species with known concentrations were taken using the same parameters as the experiment in order to calculate the concentrations from the spectroscopic data. The real-time spectroscopic data were integrated and analyzed with scripts written in-house. The application of UV/Vis absorption spectroscopy for the VRFB has been demonstrated primarily for the determination of SoC of the electrolyte^{103, 131, 134, 135}.

Incorporating two extra fluid chambers in “Cell 4” enables differentiating the concentration gradient-induced crossover from electric-field induced crossover. The electrolyte of interest from the reservoir is circulated through the exterior chambers in “Cell 4” where the transport of active species takes place from the exterior chambers to the interior chambers with/without operation of the cell. Operation of “Cell 4” in a symmetric mode minimizes transport between the interior chambers by minimizing differences between the two internal solutions.

4.2.2. Different components

Perfluorosulphonic acid-based Nafion® (E. I. DuPont Company, USA) is a commonly used membrane for VRFB applications. Other types of membranes have also been utilized for VRFBs to reduce the crossover rate and the overall cost^{140, 142, 203}. In this work, commercially-available N117 with equivalent weight of 1100 g.mol⁻¹ was investigated to provide benchmark data for modelers and operators using common components. A common pretreatment protocol was applied in which as-received N117 membranes were

treated in 3 different stages including immersion in deionized water at ambient temperature, followed by immersion in 0.5 M sulfuric acid and then immersion in deionized water. As shown in Fig. 1, “Cell 4” has N117 membranes between the exterior chambers and interior chambers, as well as between the two interior chambers.

4.2.3. Electrolyte

All tests were based on two sets of electrolytes; one set for exterior chambers and one set for interior chambers. For exterior chambers, the electrolyte was 1.7M $\text{VOSO}_4 \cdot x\text{H}_2\text{O}$ (Alfa Aesar, U.S.) dissolved in 3.3M sulfuric acid (H_2SO_4). In order to conduct the crossover measurements, it is necessary to minimize the solvent (water) transport across the membrane due to the combined effects of osmotic and hydraulic pressure gradient.

In order to balance osmotic pressure, multiple approaches have been described in the literature; matching sulfate concentration on both sides¹⁴⁰ or providing a counter cation on the vanadium deficient side¹⁴⁴ are common. The approaches described in the literature have successfully decreased the osmotic pressure gradient across the ion-exchange membrane, but they introduce new complications to the system. It should be noted that typical VRFB conditions can result in incomplete dissociation of sulfuric acid^{121, 192}; this behavior has not been fully considered in previous work. Here, a different approach was used in an effort to alleviate this complication: the concentration of sulfuric acid in the interior chambers was selected to minimize the volume change of interior and exterior chambers' solutions. In order to distinguish the transport of solvent (water) due to osmotic and hydraulic pressure gradients, two different sets of experiments were conducted. First,

“cell 1,” which was a regular two-chamber cell, was utilized. In one side of “cell 1” the vanadium enriched solution (1.7M $\text{VO}_2\text{SO}_4 \cdot x\text{H}_2\text{O}$ dissolved in 3.3M sulfuric acid (H_2SO_4)) was circulated and in the other side, the vanadium deficient side, an aqueous sulfuric acid solution (with varying concentrations of the sulfuric acid) was circulated. The initial volume of enriched and deficient side was 100 mL and 80 mL, respectively, and the volume of the solutions were recorded at the end of a 12-hour experiment. The final volume as a function of deficient-side acid concentration has been plotted in Fig. 4-2. According to Fig. 4-2, increased acid concentration in the vanadium deficient side results in reduced electrolyte volume loss in the deficient side. Thus, adopting 5 M acid concentration on the deficient side, when there is no hydraulic pressure gradient, minimizes the volume change of electrolyte for the time range of a 12-hour experiment.

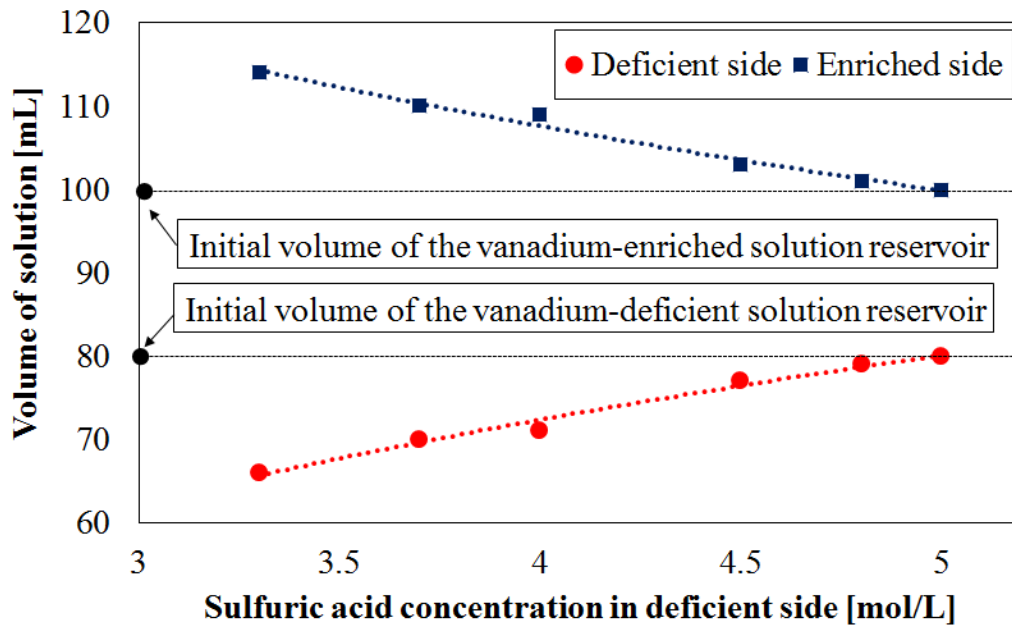


Figure 4-2: The volume of deficient and enriched solution at the end of 12-hour experiment

However, water transfer is a function of both osmotic pressure and hydraulic pressure differences. If there is any hydraulic pressure gradient across the ion-exchange membrane, the osmotic pressure can be deliberately imbalanced in order to balance the overall pressure. To test this approach, “Cell 4” was used for water transport experiments. A hydraulic pressure gradient across the ion-exchange membrane (between the exterior and interior chambers within “cell 4”) was inevitable; in order to balance the combined effect of osmotic and hydraulic pressure gradients across the membrane, the sulfuric acid concentration could not be 5 M. In order to maintain the volumes of the interior, vanadium-deficient, chamber solutions at a constant value of 80 mL during a 12-hour experiment, the concentration of sulfuric acid of the vanadium deficient side was chosen to be 3.7 M instead of the 5 M that was applicable when hydraulic pressure was balanced. The experimental tests operating the multi-chamber cell (“Cell 4”) with the interior solutions of 3.7 M sulfuric acid and exterior chambers with enriched vanadium solution (1.7M $\text{VOSO}_4 \cdot x\text{H}_2\text{O}$ dissolved in 3.3M sulfuric acid (H_2SO_4)) maintained the volume of interior and exterior chamber solutions at 80 and 100 mL over the range of 12-hour tests, indicating that both hydraulic and osmotic pressure gradients were net balanced.

4.2.4. Testing protocol

A multichannel potentiostat/galvanostat (Arbin Instruments, College Station, TX) was employed to conduct the charge-discharge processes and apply the desired overpotential or current to the cells in the symmetric mode. Operating cells in symmetric mode resulted

in a constant SoC for the duration of the experiments. It is assumed that any overpotential applied to the symmetric VRFB was distributed evenly to the two half-cells.

4.2.5. UV/Vis spectroscopy

The electrolytes used for VRFBs are vividly colored because of the strong absorbance spectra of vanadium species. It has been shown in previous work that the absorbance spectra of the mixture of V(II)/V(III) is a linear combination of the individual V(II) and V(III) spectra^{133, 137}. However the spectra of a concentrated solution of V(IV)/V(V) electrolyte is not a linear combination of individual spectra of V(IV) and V(V)¹³¹, necessitating electrolyte dilution in order to obtain the concentration of V(IV) and V(V) from the spectra of the mixture.

In this work, spectrophotometric measurements were made using spectrometers in a transmission configuration with a spectral range from 400 to 900 nm. The individual vanadium species have different spectral responses, requiring absorption to be measured at two different wavelengths for each mixture of V(II)/V(III) and V(IV)/V(V). Such measurement allowed application of the Beer-Lambert law¹⁴⁷. Absorbance at the following wavelengths (Table 4.2) was used for in-situ spectrometry and the spectra were recorded in intervals of three hours.

Table 4.2. Wavelength for spectroscopy measurement

	V(II) and V(III)	V(IV) and V(V)
λ_1 (nm)	605	440
λ_2 (nm)	854	760

It is important to note that, since the concentration of vanadium species in the interior chambers is low (ca. 0.05 M), the spectra of vanadium mixtures were reproducible by linear combination of the individual species. In order to obtain the spectra for the interior chambers, spectrophotometry of an operating VRFB was performed using secondary pumps circulating the vanadium-deficient sulfuric acid solution from the reservoirs through “Cell 2” and “Cell 3,” as shown in Figure 4-1.

4.3. Mathematical Model

To model species transport through the membrane, conservation of mass must hold for each species across the membrane. The following continuity equation is applied in the membrane phase for the species.

$$\frac{\partial c_i^m}{\partial t} = -\nabla \cdot \mathbf{N}_i^m \quad (4-7)$$

In Eq. (4-7), \mathbf{N}_i^m is the flux of species through the membrane, essentially vanadium crossover. Crossover during VRFB operation is due to the concentration gradient and migration induced by the electric field. The choice for modeling the flux equation (\mathbf{N}_i^m) determines the framework of the model. In general, two different approaches are common for modeling the flux. The first approach is the assumption of infinitely dilute solutions, thus accounting only for the interaction of solutes with the solvent. The second approach assumes concentrated solution theory, accounting for the interactions of each solute with all the other solutes as well as the solvent¹⁷⁹.

Due to the repulsive nature of the membrane towards strong anions, sulfate is not present in the membrane in large concentration; still, there are 8 different species present in the membrane (V(II), V(III), V(IV), V(V), H⁺, HSO₄⁻, SO₃⁻, and H₂O). Because of this, using dilute solution theory provides diffusion data of limited utility unless a broad range of operation conditions are investigated. The application of concentrated solution theory, although more accurate, is cumbersome since it requires 28 binary diffusion coefficients to be determined. Here, a hybrid approach is proposed. The permeability of individual species has been measured, taking into account interactions with the solution when there are no other vanadium species present, and the flux equation has been corrected for co-existence of the other significant species in the solution. This approach enables application of the SoC dependence relationship for permeability through the membrane with reasonable accuracy and reduced complexity compared to concentrated solution theory.

The vanadium species transfer through the ion-exchange membrane has two driving forces in the experiments here: concentration gradient and electrostatic potential gradient. It is important to note that the existence of an electrostatic potential gradient not only results in solute migration, but also results in solvent transport (convection). The Nernst-Planck equation includes diffusion, migration and convection terms and is utilized to model the flux of the species in the membrane phase, as shown in Eq. (4-8)¹⁸².

$$N_i^m = -D_i^m \nabla c_i^m - z_i u_i^m F c_i^m \nabla \Phi^m + c_i^m v_0 \quad (4-8)$$

The Nernst-Einstein relation is used to correlate the mobility to diffusivity in Eq. (4-9)¹⁸².

$$u_i^m = \frac{D_i^m}{RT} \quad (4-9)$$

Substituting Eq. (4-9) into Eq. (4-8) results in the flux described in Eq. (4-10):

$$N_i^m = -D_i^m \nabla c_i^m - \frac{z_i D_i^m F c_i^m}{RT} \nabla \Phi^m + c_i^m v_0 \quad (4-10)$$

Components of the flux equation include diffusion (first term), migration (second term), and convection (third term). A careful consideration of Eq. (4-10) reveals that solvent transport affects the solute transport via the convective term. In Eq. (10), D_i^m is the diffusion coefficient for species i in the membrane, c_i^m is the concentration of species i in the membrane, and Φ^m is the electrostatic potential in the membrane phase. According to Eq. (4-10), in order to model the flux of vanadium species, the diffusivity, concentration, electrostatic potential for the solute and the velocity field for the solvent in the membrane phase are required. The measurement of these values in the membrane phase of an operating cell as a function of different operating conditions is required to utilize Eq. (4-10). Alternatively, one can substitute the parameters of the membrane phase with different parameters that are measurable at the cell scale and then correlate them back to the membrane scale.

Ohm's law correlates the potential gradient across the membrane to the current density via conductivity (κ), shown in Eq. (4-11). The conductivity of the ion-exchange membrane might change as a function of different operating conditions and composition of the electrolyte; however, the current density can be measured at the cell scale.

$$i^m = -\kappa \nabla \Phi^m \quad (4-11)$$

This equation can be substituted into Eq. (10), resulting in Eq. (12):

$$N_i^m = -D_i^m \nabla c_i^m + \frac{z_i D_i^m F c_i^m}{\kappa R T} i^m + c_i^m v_0 \quad (4-12)$$

It is important to note that solvent transport (water, in this case) must be minimized during solute crossover measurements. To this end, the driving force at equilibrium and no-current conditions should be minimized. Furthermore, the Gibbs-Duhem equation, shown in Eqn. (4-13) must be satisfied¹⁷⁸.

$$\sum_i c_i \nabla \mu_i = \nabla p - \frac{S}{V_0} \nabla T \quad (4-13)$$

In Eq. (4-13), μ_i is the chemical potential of species i in the electrolyte, c_i is the concentration of species i in the electrolyte, and S is the entropy of the solution. The testing was conducted under precise temperature control and the combined effect of osmosis and hydraulic pressure gradients was minimized. Weber and Newman¹⁸⁰ derived Eq. (4-14) for the flux of water through the ion-exchange membrane, neglecting an additional thermos-osmosis and hydraulic pressure gradient term.

$$N_0^m = \frac{\xi i^m}{F} - \alpha \nabla \mu_0 \quad (4-14)$$

In Eq. (4-14), ξ is the water electro-osmosis coefficient, α is the transport coefficient. As formulated in Eq. (4-13) and described, the combined effect of osmotic and hydraulic pressure gradient in experiments was minimized under precise temperature control; as a result, the only driving force for the solvent flux according to Eq. (4-14) is the electro-osmotic drag which can be used to determine the solvent velocity.

$$|v_0| = \frac{|N_0|}{c_0} = \frac{\xi |i^m|}{c_0 F} \quad (4-15)$$

Darling et al.¹⁷⁶ derived an equation similar to Eq. (4-15) for the velocity of solvent across the ion-exchange membrane in which they assumed a constant number of 3 for the electro-osmotic drag coefficient of water. Substituting Eq. (4-15) into Eq. (4-12), results in Eq. (4-16):

$$N_i^m = -D_i^m \nabla c_i^m + \frac{z_i D_i^m F c_i^m}{\kappa R T} i^m + \frac{\xi c_i^m}{F c_0} i^m \quad (4-16)$$

The concentration gradient in the membrane can be re-written in the form of Eq. (4-17) with the assumption that no reaction happens inside the membrane and the concentration of the species becomes zero on the other side due to rapid reaction.

$$|\nabla c_i^m| \approx \frac{\Delta c_i^m}{t_m} = \frac{c_i^m}{t_m} = \frac{K c_i^{bulk}}{t_m} \quad (4-17)$$

In Eq. (4-17), t_m is the thickness of the membrane, K is the partitioning coefficient, a dimensionless parameter determining how much vanadium is allowed to enter the membrane with respect to the concentration of the adjacent enriched vanadium solution.

Substituting Eq. (4-17) into Eq. (4-16) yields Eq. (4-18):

$$N_i^m = -\frac{D_i^m c_i^m}{t_m} + \frac{z_i D_i^m F c_i^m}{\kappa R T} i^m + \frac{\xi c_i^m}{F c_0} i^m \quad (4-18)$$

Further simplification results in the following:

$$N_i^m = \left[-\frac{K D_i^m}{t_m} + \left(\frac{z_i K D_i^m F}{\kappa R T} + \frac{K \xi}{F c_0} \right) i^m \right] c_i^{bulk} \quad (4-19)$$

The experimental approach usually focuses on the measurement of permeability values which is based on the concentrations in the bulk solution adjacent to the membrane and not concentrations in the membrane. As a result, it is necessary to write the first term of Eq.

(4-19) in terms of permeability values of individual species (P_i^m). The second and third terms in Eq. (4-19) do not need to be formulated based on the permeability values since they deal with the concentrations inside the membrane.

$$N_i^m = \left[-\frac{P_i^m}{t_m} + \left(\frac{z_i K D_i^m F}{\kappa R T} + \frac{K \xi}{F c_0} \right) i^m \right] c_i^{bulk} \quad (4-20)$$

Building on Eq. (4-20) for the flux equation, the following transport parameters have been introduced in order to be determined via fitting the experimental data.

$$N_i^m = [A_i^{m,diff} + (\Omega_i^{m,mig} + \Omega_i^{m,conv}) i^m] c_i^{bulk} \quad (4-21)$$

Also, using the condition of negligible combined hydraulic and osmotic pressure gradient across the membrane from the experiments conducted here, the flux equation can be further simplified via introducing the electric-field-induced transport coefficient. The electric-field-induced transport coefficient ($\Omega_i^{m,mig|conv}$) includes the combined effect of the migration and convection terms and was determined based on the experimental data.

$$N_i^m = [A_i^{m,diff} + (\Omega_i^{m,mig|conv}) i^m] c_i^{bulk} = N_i^{m,diff} + N_i^{m,mig|conv} \quad (4-22)$$

In order to obtain transport parameters for N117, permeability values for different species need to first be determined under concentration gradient-only conditions; based on that, diffusive transport parameters for a membrane can be determined under purely concentration gradient-driven conditions for each vanadium species ($A_i^{m,diff}$). It is important to note that, based on the work conducted by J. S. Lawton et al.²⁰⁴, the permeability of V(IV) through the ion-exchange membrane is strongly affected by the concentration of sulfuric acid in the solution. This effect causes up to a 7-fold change in

permeability, thus it cannot be neglected. Accordingly, it is critical to consider that the permeability values determined in this manner need to be corrected when other significant co-solutes exist in the solution; this consideration is modeled here via introduction of a dimensionless interaction coefficient (θ_i). The interaction coefficient accounts for the interaction of the species of interest with the solution as a function of state of charge. Finally, the electric-field-induced transport coefficient due to the applied overpotential can be determined from the crossover measurements after determining the interaction coefficients. This formulation is shown in Eq. (4-23), and based on Eq. (4-22), the magnitude of fluxes can be used since the direction of the flux is already known for the charge and discharge processes.

$$N_i^m = \left\{ \theta_i A_i^{m,diff} \pm \Omega_i^{m,mig|conv} i^m \right\} c_i^{bulk} = N_i^{m,diff} \pm N_i^{m,mig|conv} \quad (4-23)$$

In order to determine the electric-field-induced transport coefficient, the slope of a plot of $N_i^{m,mig|conv}$ versus i^m is used. In Eq. (4-23), the interaction coefficient accounts for the codependent behavior of the solutes in solution. This parameter is particularly useful for determining the dependence of crossover rate on SoC.

4.4. Results and Discussion

4.4.1. Concentration-induced crossover

In order to better illustrate the effect of different driving forces on crossover behavior, a schematic representation of the relevant forces is shown in Figure 4-3 for the discharge

process of an operating VRFB. In any case, concentration gradient-driven crossover occurs from the exterior, vanadium-rich electrolytes to the interior, sulfuric acid solution across N117. However, during discharge, protons migrate from the negative half of the cell to the positive half; this direction flips during the charging process. As discussed, the experimental procedure started with investigating the concentration gradient-induced crossover for individual vanadium species. Figure 4-4 shows the concentration of vanadium species on the vanadium-deficient side over a twelve-hour time; the crossover behavior observed here corresponds to conditions at 0% SoC and 100% SoC.

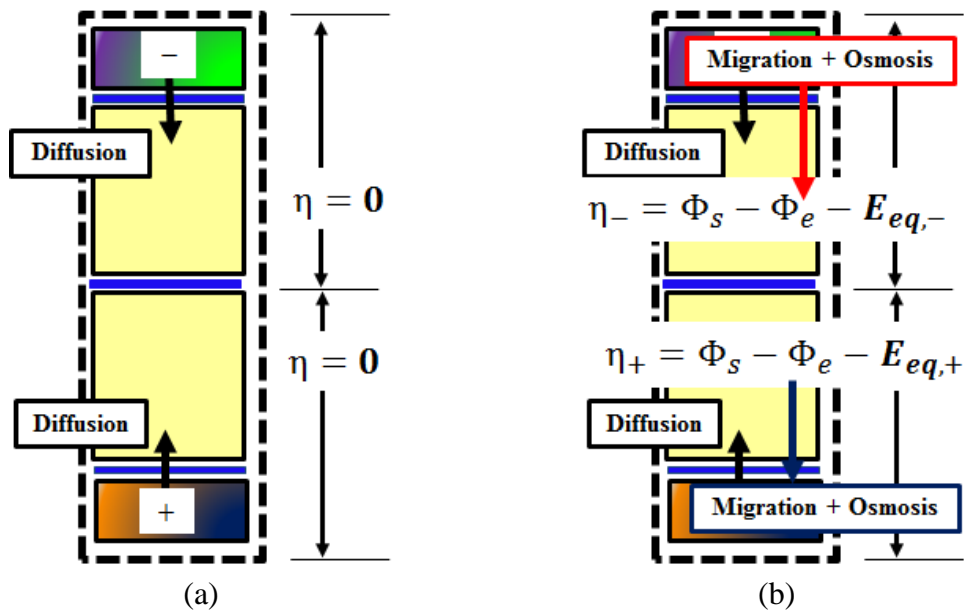


Figure 4-3: Drivers of crossover in an operating cell (“Cell 4”)

(a: concentration gradient-induced crossover, b: electric-field-induced crossover plus concentration gradient-induced crossover)

(Note: η_- and η_+ correspond to the V(II)/V(III) and V(IV)/V(V) couples, respectively)

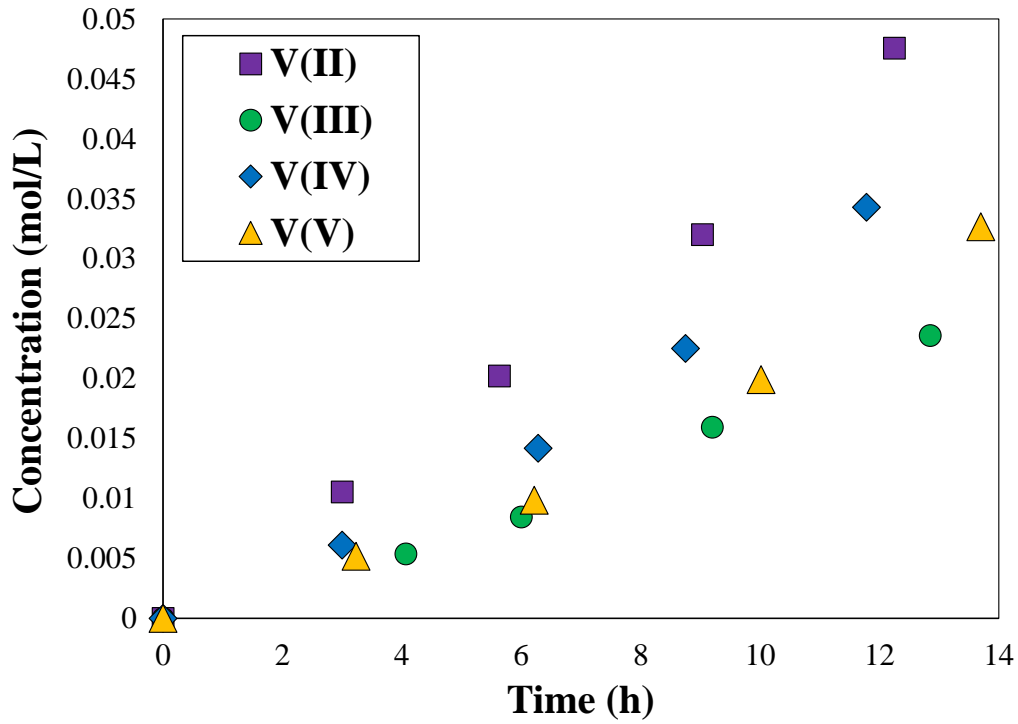


Figure 4-4: Concentration of diffused vanadium species to the interior chamber within the twelve-hour time range

The concentration of diffused species shown in Fig. 4-4 can be used to obtain the permeability values of individual vanadium species ¹⁴⁰. The concentration change in the interior chamber is described by the following ordinary differential equation:

$$V_{int} \frac{dC_i(t)}{dt} = P_i^m \frac{A}{t_m} [C_e - C_i(t)] \quad (4-24)$$

In Eq. (4-24), the concentration of vanadium species in the exterior chambers (C_e) is assumed to be constant, since the external electrolyte reservoirs are relatively large compared to the internal reservoirs (2.5 times). Equation (4-24) can be integrated in order to obtain the permeability values.

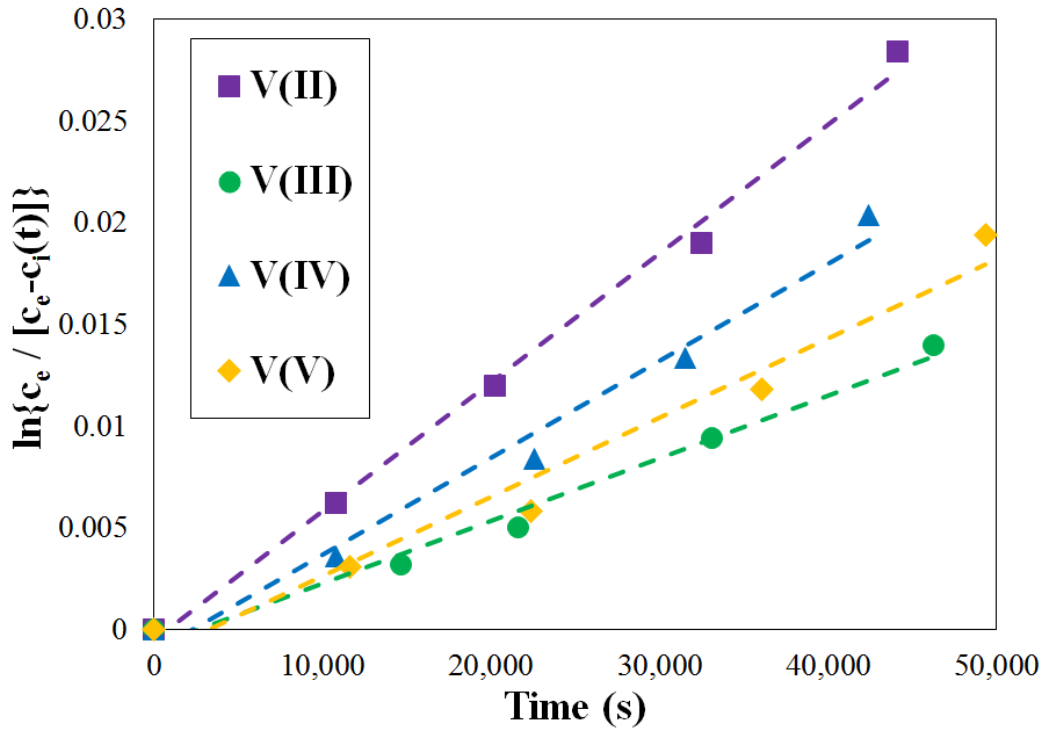


Figure 4-5: Semi-natural log plot used to determine permeability based on diffused concentration.

$$\int_0^{c_i} \frac{d(C_e - C_i(t))}{(C_e - C_i(t))} = - \int_0^t \frac{P_i^m A}{V_{int} t_m} dt \quad (4-25)$$

Integrating Eq. (4-25) yields Eq. (4-26):

$$\ln\left(\frac{C_e}{C_e - C_i(t)}\right) = \frac{P_i^m A}{V_i t_m} t \quad (4-26)$$

According to Eq. (4-26), plotting the left side of the equation versus time can be used to obtain the permeability values. This relationship is illustrated in Figure 5. The resultant permeability values, based on the linear fits in Figure 4-5, are compared for each vanadium species in Figure 4-6 and Table 4.3.

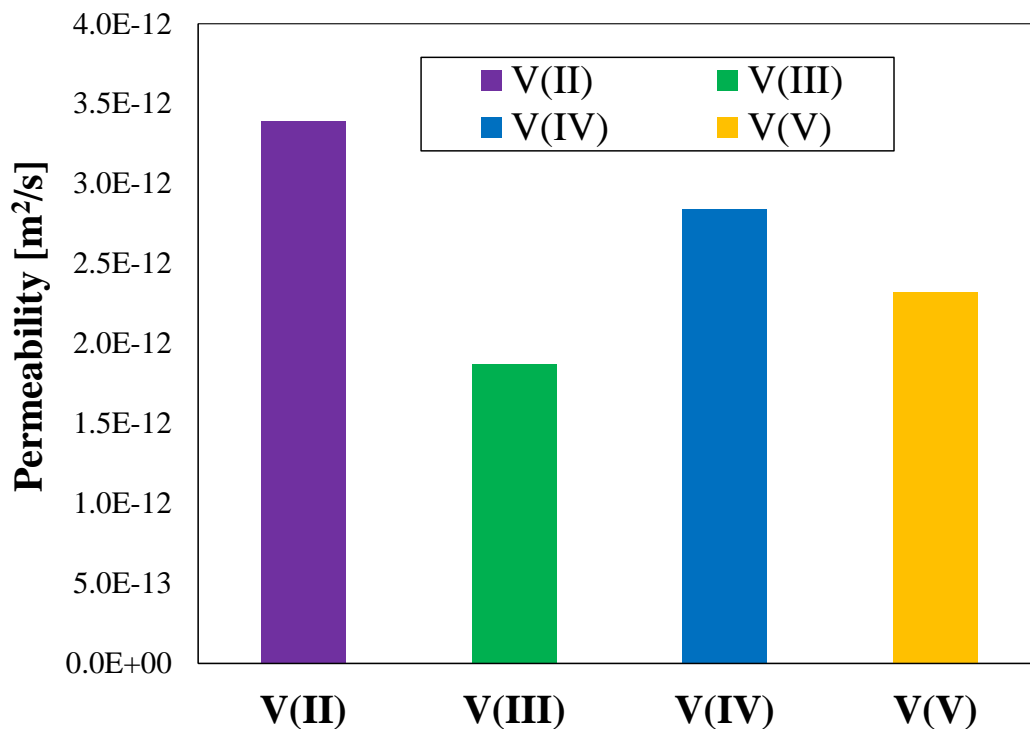


Figure 4-6: Measured permeability values for the vanadium species

The permeability values are in the descending order of $V(II) > V(IV) > V(V) > V(III)$; this finding is consistent with results reported by C. Sun et al.¹⁴⁰. Table 4 compares the permeability values that have been reported earlier (for N115 membrane) with the values measured in this work. Some of the possible reasons for the discrepancy in reported values for permeability (Table 4) are discussed in the following section. The higher permeability of V(II) versus V(III) has been also reported for vanadium/air batteries¹⁴⁷. The two important factors affecting the permeability of vanadium species are the affinity of the ion to the functional groups of the membrane and the mobility of the ion²⁰⁵. Greater affinity is due to higher valence; however, higher valence also results in lower mobility.

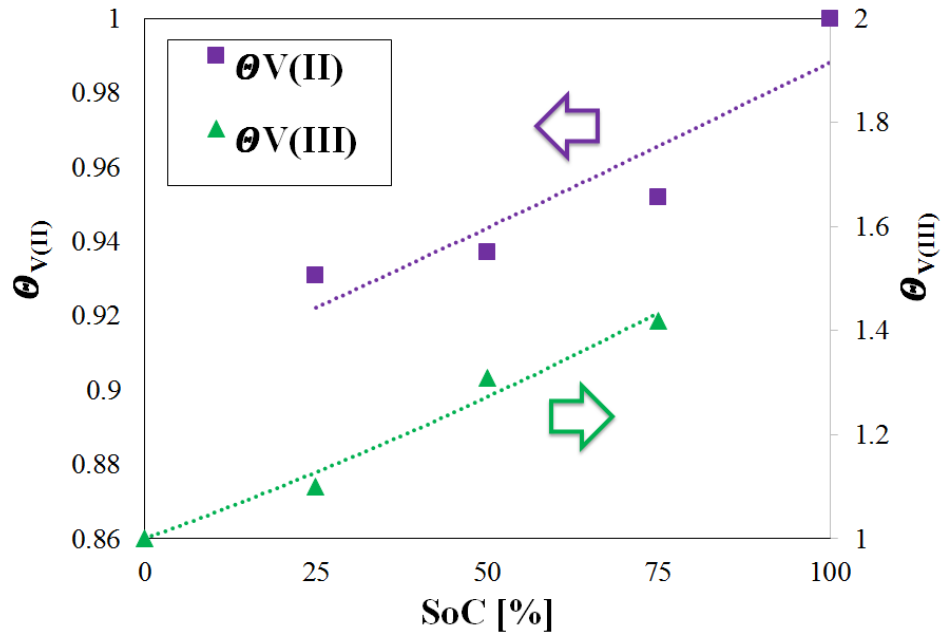
Table 4.3. The permeability values for vanadium species
($m^2 \cdot s^{-1} \times 10^{-12}$)

	C. Sun et al. [36]	Q. Luo et al. [37]	This publication
$P_{V(II)}^m$	8.77	9.44	3.39
$P_{V(III)}^m$	3.22	14.45	1.87
$P_{V(IV)}^m$	6.83	4.45	2.84
$P_{V(V)}^m$	5.90	2.40	2.32

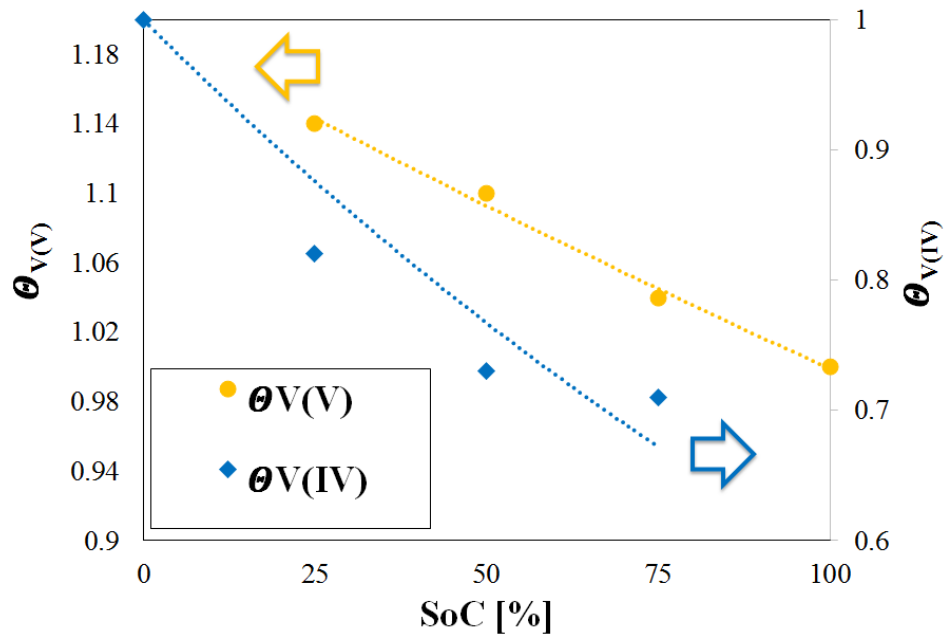
Thus, for any specific vanadium ion, permeability is dependent on which of these opposing factors dominates. In earlier works, diffusion through the swollen channels and hopping across the fixed acid sites have been accepted as likely pathways for cation transport mechanisms which link the ionic permeability to water content as well as the free water content²⁰⁶; it is currently unclear which mechanism dominates for a particular species.

Following assessment for individual species, interactions occurring when multiple species are present were analyzed. Solutions of 25%, 50% and 75% SoC were prepared and the coupled permeability values were determined under the concentration gradient-only condition. The procedure for determining the permeability values from vanadium mixtures was similar to the procedure described for obtaining single-species permeabilities. Figure 4-7 shows interaction coefficient results for varying SoC mixtures on both halves of the VRFB.

Figure 4-7 includes the fitting curves for the interaction coefficients. Because interaction coefficients are multipliers for single species permeabilities (see Eq. (23)), the interaction coefficients shown in Fig. 4-7 exhibit the same responses as permeability for each species with SoC.



(a)



(b)

Figure 4-7: Interaction coefficients for concentration gradient-induced crossover (a: V(II)/V(III), b: V(IV)/V(V))

In Fig. 4-7, the x-axis is SoC; therefore, results at SoC=0% and 100% correspond to the permeability values that have been measured for the single species cases. Also shown in Fig. 4-7, the permeability of the vanadium species is sensitive to the SoC. According to Fig. 4-7(a), the highest value for V(II) permeability occurs at SoC=100% and decreases as SoC decreases. Conversely, V(III) permeability was lowest at SoC=0% and increases with increasing SoC. This observed behavior demonstrates the coupled nature of diffusion for V(II)/V(III). According to Fig. 4-7(b), the permeability of V(IV) decreases with increased concentration of V(V), corresponding to increased SoC. However, an opposite trend is observed for V(V) where the permeability increases with increased V(IV) concentration. This finding is consistent with observations reported by Luo et al. in which the transport rate of V(IV)/V(V) decreased with increasing SoC¹⁴⁴. The authors concluded that the change in transport rate of V(IV)/V(V) originates primarily from disparate properties of V(IV) and V(V)¹⁴⁴.

Vijayakumar et al. investigated fouling mechanisms of Nafion® membranes exposed to vanadium cations²⁰⁷. The XPS spectra revealed that V(III) and V(V) are deposited on both sides of the Nafion® membrane during VRFB operation²⁰⁷. It is important to note that according to the permeability data reported earlier in Table 4, V(III) and V(V) have the lowest permeability values. However, V(II) and V(IV), with higher permeability as summarized in Table 4-4, were assumed to enter and accumulate inside the Nafion® channels²⁰⁷. It has also been shown that the presence of vanadium ions in the membrane results in lower mobility of the species²⁰⁸.

Table 4.4. Deduced interaction coefficients for cocentration gradient-induced crossover

SoC	$\theta_{V(II)}$	$\theta_{V(III)}$	$\theta_{V(IV)}$	$\theta_{V(V)}$
0%	-	1.0	1.0	-
25%	0.931	1.1	0.82	1.14
50%	0.937	1.31	0.73	1.11
75%	0.952	1.42	0.71	1.04
100%	1.0	-	-	1.0

As a result, the coupled diffusive behavior is the result of multiple mechanisms simultaneously occurring. The interactions between vanadium species are believed to occur through their hydration shells; thus, the affinity of the ions to the fixed sites and their mobility through the swollen pathways are factors that determine the interactive behavior of different species where there exists other significant cation(s). Table 4-4 includes the calculated numerical values for vanadium interaction coefficients.

4.4.2. Electric-field-induced crossover

To investigate the effect of electric field on crossover, solutions were prepared at 50% SoC for the V(II)/V(III) and V(IV)/V(V) couples. These solutions were circulated through “Cell 4” as shown in Fig. 4-1 in symmetric mode, maintaining constant SoC during cell operation. It has been shown that the 400 mV overpotential range across the whole cell applied in this work avoids hydrogen evolution for the negative couple since it results in 200 mV overpotential on each half-cell^{209, 210}. The first set of measurements consisted of applying varying overpotentials for the symmetric V(II)/V(III) couple. Figure 4-8 shows the solutions for the interior chambers at the end of each twelve-hour experiment. Figure 4-8(a) shows that the internal solutions are initially free of vanadium. Fig. 4-8(b)

corresponds to the case where the only driving force for transport is the concentration gradient. This case corresponds to the scenario shown in Fig. 3-3(a). As was expected, crossover was symmetric from the exterior chambers to the interior chambers.

Figures 4-7(c) to 4-7(e) demonstrate the cases where overpotential was applied to the battery from 0.05V to 0.4V, resulting in asymmetric crossover behavior. Application of overpotential across the symmetric cell has driving forces summarized in Fig. 4-3(b). In this case, both the concentration gradient and electrostatic potential gradient are driving forces for species crossover.

The direction of proton flux during symmetric operation is expected to enhance or suppress vanadium crossover based on migration and convection terms being driven by the ionic flux. This suspicion is supported by the observation that increasing overpotential results in a higher concentration of vanadium in the solution of the interior chamber that has concentration-driven flux in the same direction to proton flux (labeled “-“ in the figures).

The opposite happens for the other solution (labeled “+“ in the figures) in which it is qualitatively apparent that diffused species concentration is relatively lower. The electric field affects the crossover to a great degree since the migration and convection fluxes oppose the diffusive flux in this condition.

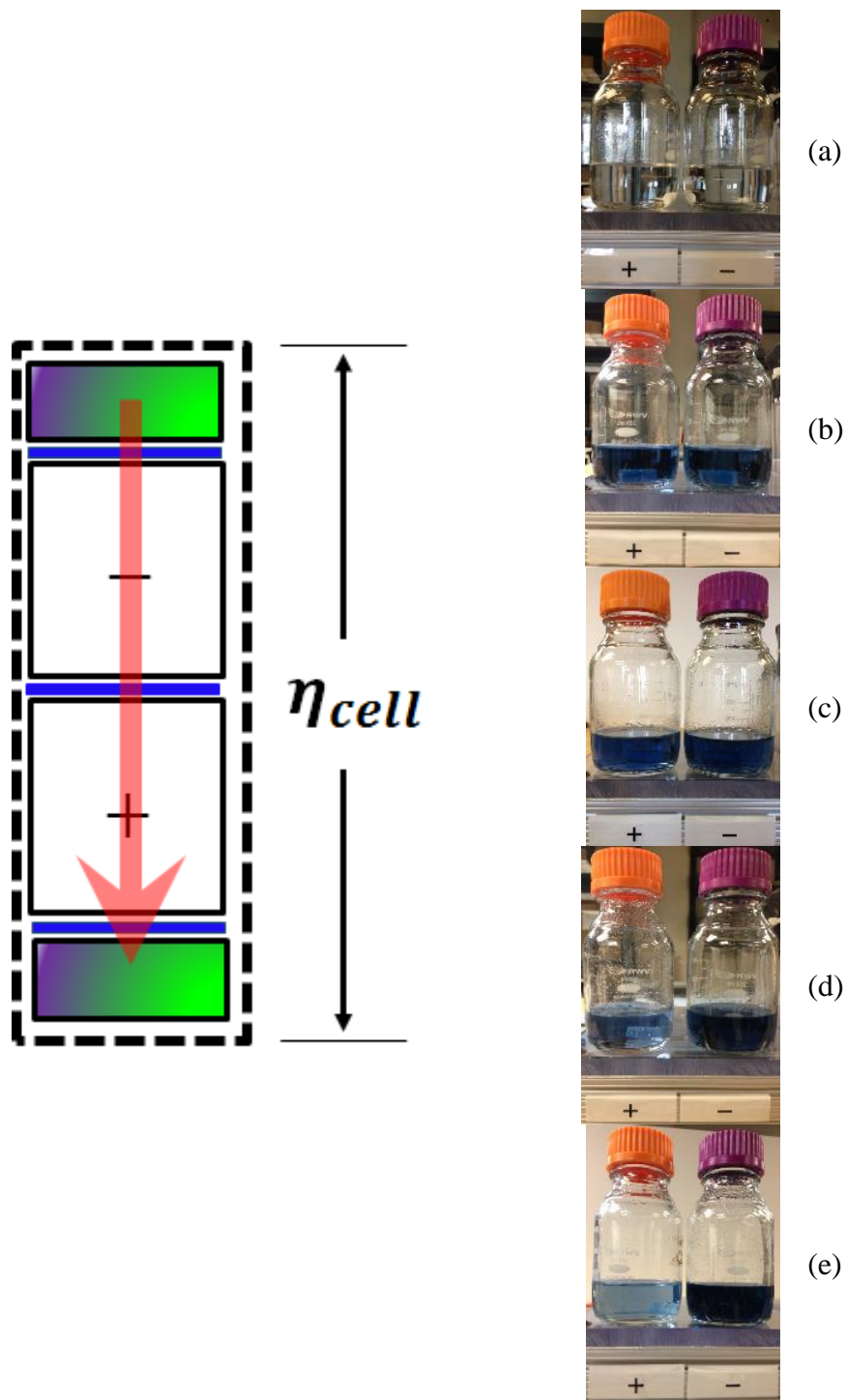


Figure 4-8: Schematic of the V(II)/V(III) symmetric test system at SoC: 50%
(a: Initial solution, b: $\eta_{cell} = 0V$, c: $\eta_{cell} = 0.05V$, d: $\eta_{cell} = 0.2V$, e: $\eta_{cell} = 0.4V$)

It has been demonstrated numerically and experimentally elsewhere^{127,201} that the sluggish kinetics of the V(II)/V(III) couple versus V(IV)/V(V) couple results in relatively higher required overpotentials for the negative side. Accordingly, applying the same overpotential for the V(IV)/V(V) couple would result in quite high current and would not be a realistic representative of an operating cell. Considering that the formulation of Eq. (23) is based on current, matching the current density between two symmetric cell cases (V(II)/V(III) versus V(IV)/V(V)) is more appropriate than matching overpotentials. Consequently, the V(IV)/V(V) couple measurements were conducted at cell currents identical to those that resulted in the V(II)/V(III) couple measurements (9, 34, and 62 mA/cm² for 0.05, 0.2 and 0.4V overpotentials, respectively). Figure 4-9 shows the schematic of the setup and the solutions for interior chambers for V(IV)/V(V) couple.

As shown in Fig. 4-9(b), symmetric crossover occurred when no current was passed, identical to no applied overpotential for the negative symmetric cell. However, any current passage resulted in asymmetric behavior, similar to that observed for the V(II)/V(III) couple. Increased current through the cell resulted in accumulation in the negative interior chamber and relative depletion in the positive interior chamber. Comparing the crossover behavior of Figures 4-7 and 4-8, increased overpotential increases the negative to positive and decreases the positive to negative vanadium crossover when the battery is discharging; the opposite happens in the charging mode. This finding is consistent with the findings of Luo et al.¹⁴⁴, confirming that net crossover responds strongly to the existence of an electric field.

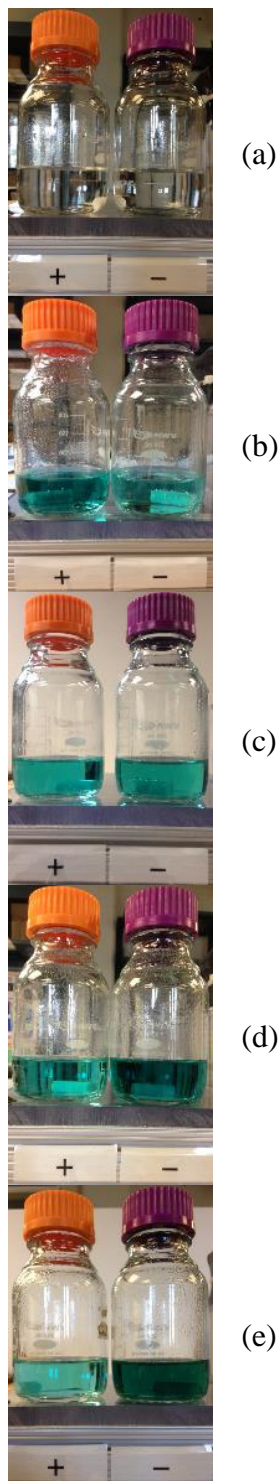
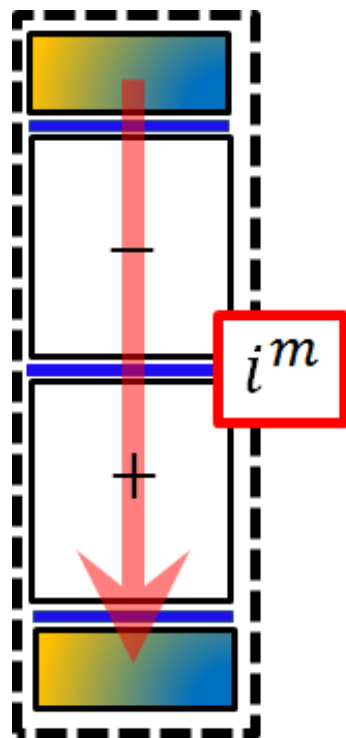
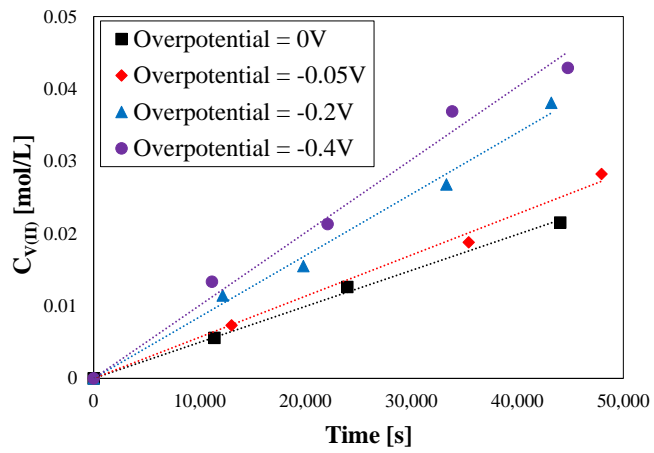


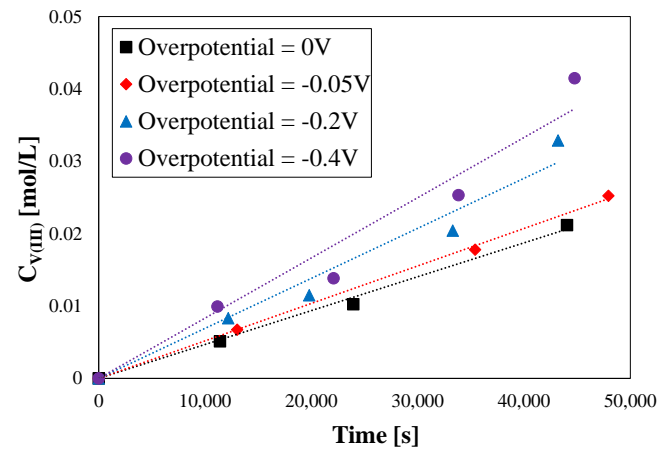
Figure 4-9: Schematic of the V(IV)/V(V) symmetric test system at SoC: 50%
 (a: Initial solution, b: $i^m = 0 \text{ mA/cm}^2$, c: $i^m = 9 \text{ mA/cm}^2$,
 d: $i^m = 34 \text{ mA/cm}^2$, e: $i^m = 62 \text{ mA/cm}^2$)

In order to quantify the effect of the electric field on crossover, the spectra of diffused species were analyzed in the same manner as for the single species crossover measurements. Figure 4-10 includes the concentration of diffused species over time during discharge for a range of applied overpotentials (for V(II)/V(III) symmetric cell) and current density (for V(IV)/V(V) symmetric cell) at SoC=50%. Figures 9(a), (b), (c) and (d) show the internal chamber vanadium concentrations for V(II), V(III), V(IV) and V(V) respectively. It is apparent that the concentration of vanadium species increases over-time for any applied overpotential. The concentration of V(II) and V(III) increases with increased overpotential, indicating more rapid crossover; the concentration of V(IV) and V(V) decreases with increasing overpotential under discharge conditions, indicating suppressed crossover.

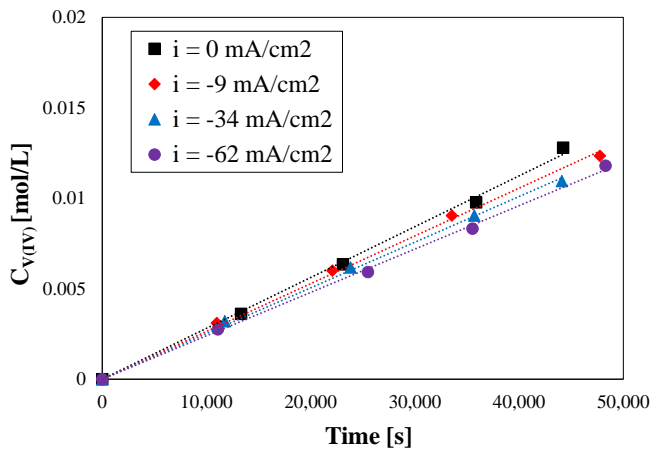
It is important to note that the rate of concentration change for increased overpotential is more pronounced for the V(II)/V(III) solution than for V(IV)/V(V) solution. This behavior is discussed in more detail in the following section. With these measurements completed, it is possible to numerically investigate the contributions of concentration gradient- and electrostatic potential gradient-induced fluxes to the total flux during discharging conditions at 50% SoC. Figure 4-11(a), (b), (c) and (d) includes the magnitude of fluxes for V(II), V(III), V(IV) and V(V) during discharge. In this case, the electrostatic potential-induced flux includes the migration and convection modes.



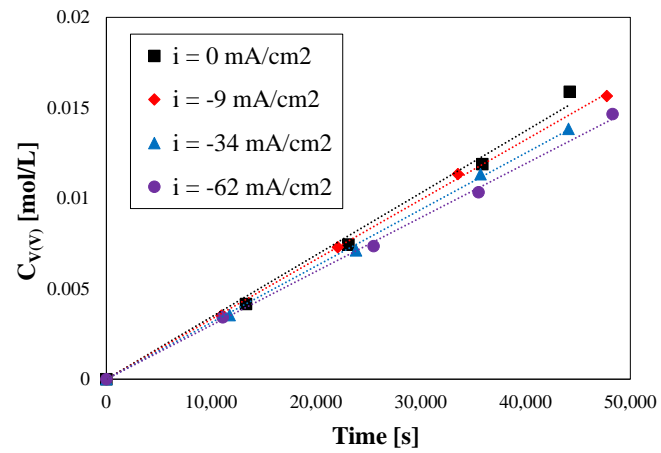
(a)



(b)



(c)



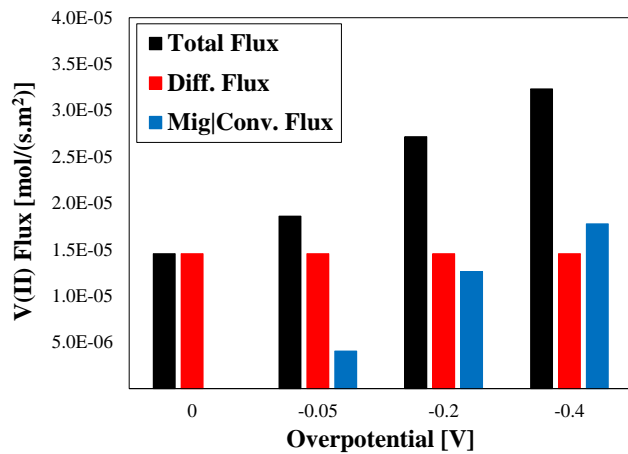
(d)

Figure 4-10: Concentration of vanadium species within the interior chamber during discharge at SoC=50% (a: V(II), b: V(III), c: V(IV) and d: V(V))

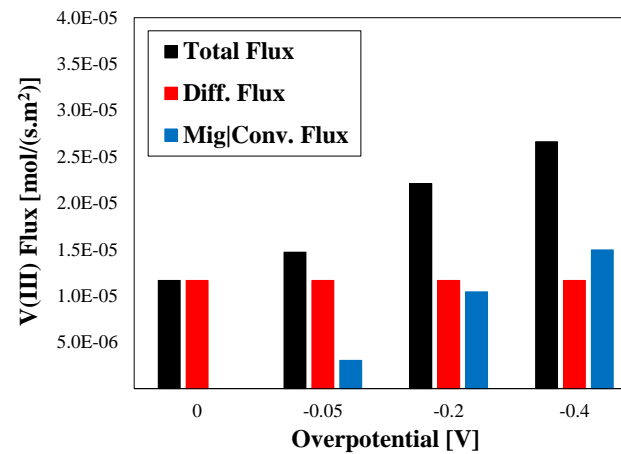
As shown in Fig. 4-11(a) and (b), the contribution of electrostatic potential gradient-induced flux increases with increased overpotential. Also, the electrostatic potential gradient-induced flux is in the same direction as concentration gradient-induced flux for the V(II)/V(III) side.

When there is no overpotential applied, diffusive flux is the only transport mechanism and comprises the total flux. By accounting for inter-ion interaction, a higher rate of diffusion for V(II) versus V(III) was observed. For the V(IV)/V(V) couple during discharge, it is shown in Fig. 4-11(c) and (d) that the electrostatic potential gradient-induced flux is in the opposite direction of the diffusive flux; this results in decreased total flux relative to solely concentration gradient-driven flux. The electric-field induced crossover portion again increases with increased overpotential for the V(IV)/V(V) couple. The behavior observed for the varying-SoC measurements is thus an extension of that observed for the single-species (i.e. 0% or 100% SoC) cases.

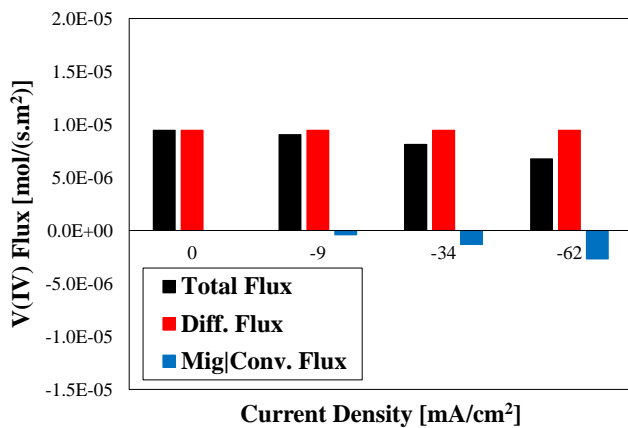
Crossover behavior during charging conditions at SoC=50% was also considered. Fig. 4-12 shows the measured concentration of vanadium species in corresponding interior chambers (positive chamber for V(II)/V(III) and negative one for V(IV)/V(V)) when the battery was charging. Figures 4-11(a), (b), (c) and (d) include vanadium ion transport concentrations for V(II), V(III), V(IV) and V(V) respectively for charging conditions.



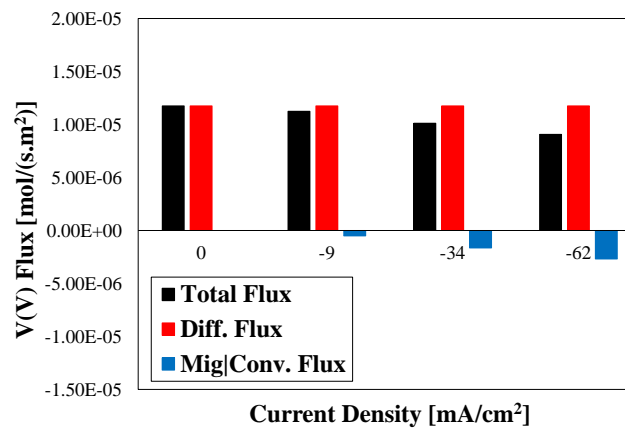
(a)



(b)



(c)



(d)

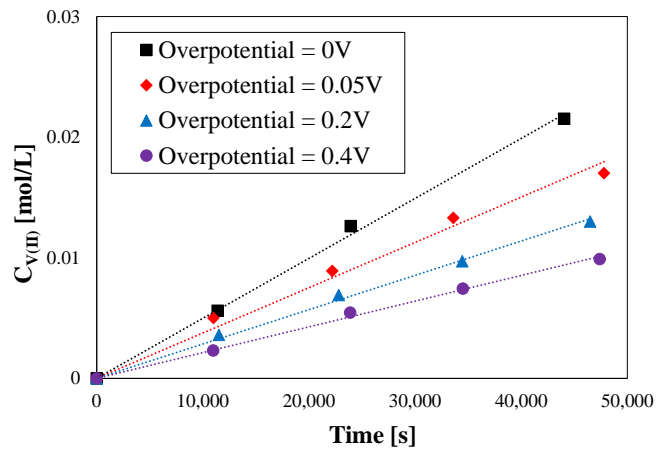
Figure 4-11: Fluxes of vanadium species during discharge at SoC=50%
 (a: V(II), b: V(III), c: V(IV) and d: V(V))

It is apparent that the interior concentrations increased over time for all vanadium species. The concentrations of V(II) and V(III) decreased with increased overpotential while the concentration of V(IV) and V(V) increased with increasing the overpotential at charging conditions. As expected, when the cell is charging, the crossover of the V(IV)/V(V) couple increased while the V(II)/V(III) couple decreased relative to the pure diffusion case.

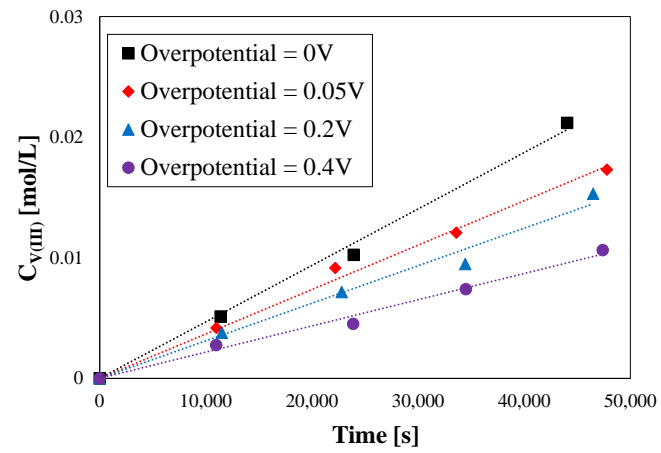
Knowing these concentrations under charging conditions, it is possible to compare diffusive flux with the electrostatic potential gradient-driven flux. These comparisons are shown in Figure 4-13 for all four vanadium species during charging.

As shown in Fig. 4-13(a) and (b), the electrostatic potential gradient-induced flux is in the opposite direction of diffusive flux for V(II) and V(III). However, the directions of these two types of fluxes coincide for V(IV) and V(V), as shown in Fig. 4-13(c) and (d). As observed in the single species measurements, the net transfer of vanadium ions was from the positive to negative side during charging.

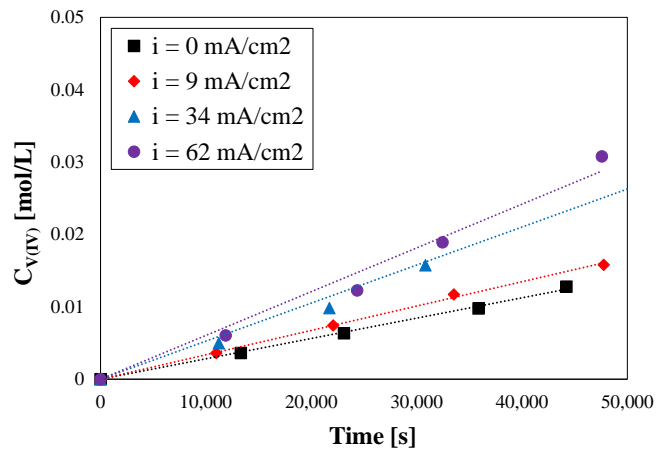
According to Eq. (4-23), the magnitude of the fluxes illustrated in Figs. 4-10 and 4-12 can be utilized to obtain the electric-field-induced transport coefficients. In Table 4.5, the coefficient values for the charge and discharge cases have been calculated and are compared for the different vanadium species.



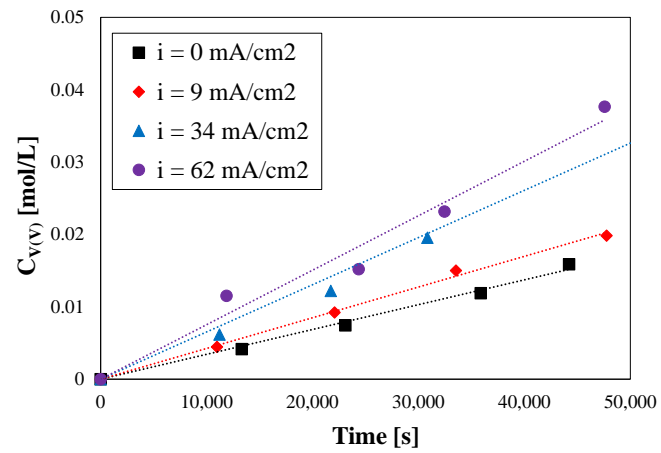
(a)



(b)

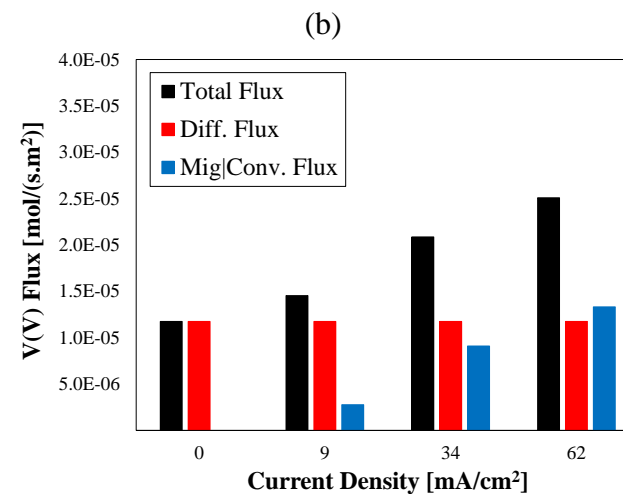
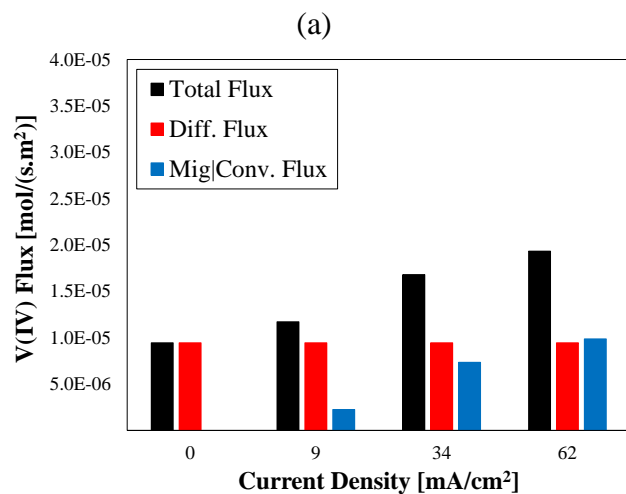
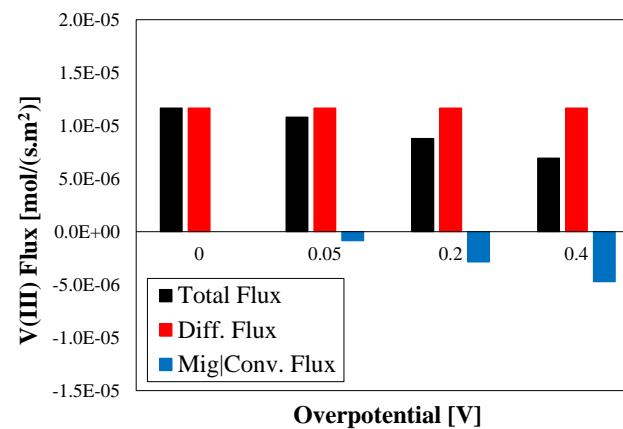
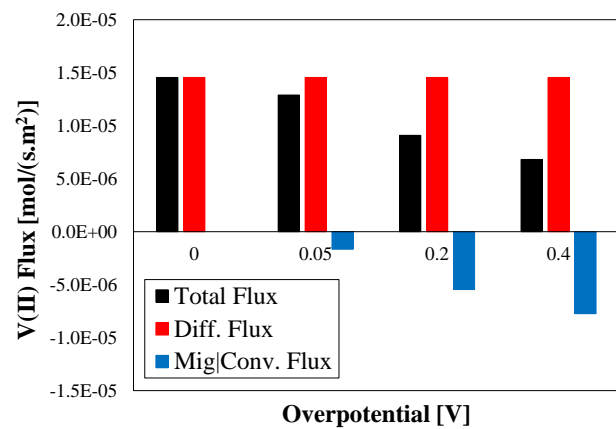


(c)



(d)

Figure 4-12: Concentration of vanadium species within the interior chamber during charge at SoC=50% (a: V(II), b: V(III), c: V(IV) and d: V(V))



(a) (b)
 (c) (d)
 Figure 4-13: Fluxes of vanadium species during charge at SoC=50%
 (a: V(II), b: V(III), c: V(IV) and d: V(V))

The electric-field-induced transport coefficients can be used to describe the relative contribution of electric field on each species. As shown in Table 4.5, for the negative couple, the electric field has more impact on V(II) and the effect is more pronounced for V(V) out of the positive couple. Also, it should be noted that the electric-field-induced transport coefficient is higher for any individual vanadium species when the direction of proton flux is in the same direction as the concentration gradient: during discharge for V(II)/V(III) and during charge for V(IV)/V(V), confirming the asymmetric impact of electric-field on crossover for different vanadium species (these regions are colored gray in Table 4.5).

Also evident in Table 4.5, the effect of electric field on the vanadium species is more pronounced for V(II) and V(III) in comparison with V(IV) and V(V), especially during discharge. This finding is consistent with Luo et al. ¹⁴⁴ where they reported higher permeation rate for V(II)/V(III) versus V(IV)/V(V) under the influence of an electric field; they explained this behavior based on the higher charge number and smaller size of V(II) and V(III).

Table 4.5.: Electric-field-induced transport coefficient

$\Omega_i^{m,mig conv} [\frac{m^3}{A.s}]$	Discharge	Charge
V(II)	3.63e-11	1.58e-11
V(III)	3.04e-11	9.24e-12
V(IV)	5.00e-12	2.05e-11
V(V)	5.28e-12	2.69e-11

The experimental data in this paper are consistent with modeling efforts that have been described elsewhere^{174, 175, 211-213}. These models have utilized the Nernst-Planck equation along with the Nernst-Einstein relation (formulated in Eq. (4-10)). The modeling simulations are particularly useful to simulate the responses of crossover to changes in particular parameters and, accordingly, simulating trends.

The numerical values that are provided by models not only are a function of the formulae chosen for simulating the flux of species, but also a strong function of the diffusivity values. Since the Nernst-Planck equation is used in these models, the models are not able to predict SoC impacts on permeability. Also, as shown in Eq. (4-10), diffusivity values are used not only in the diffusive flux but also in the migration flux component. As a result, prediction of the flux values for different species is a function of the diffusivity values. The diffusivity values for these models have been adopted from various experimental works. A careful comparison of the permeability values reported in the literature (Table 4.3) reveals that there is not an overall agreement on such widely-used values^{140, 144}. Some possible reasons for the discrepancy of the reported permeability values in the literature are related to the procedures adopted for balancing osmotic pressure, the membrane treatment history, and manufacturing process^{138, 214-216}. The values reported in this work are consistent with the values of Sun et al.¹⁴⁰. Also, in this work, since electrode materials have been used while measuring the permeability values, the reported values are lower than the values reported by Sun et al.¹⁴⁰.

This work also allows investigation of the self-discharge process under concentration gradient only conditions at 50% SoC. The comparison of concentration gradient-induced fluxes (Fig. 4-11 and 4-12) reveals that there exists a very small net flux towards the positive side (about $0.6e-5$ [mol/(s. m²)]). This behavior indicates that, if the battery only undergoes concentration gradient-driven crossover with no overpotential, the capacity of the negative side gradually decreases while the SoC range (window) of the positive side gradually increases and the cell will be limited by the capacity of the negative side.

This observation is consistent with experimental data found by Luo et al.²¹⁷ and numerical simulation performed by Darling et al.¹⁷⁶. VRFB self-discharge due solely to a concentration gradient does not happen very often since there is usually a load (overpotential) and the existence of overpotential greatly affects the overall crossover trend of the cell. Therefore, it is important to compare the relative importance of the electrostatic potential gradient-induced crossover flux and concentration gradient-induced flux via the dimensionless gamma parameter (γ_i^m).

$$\gamma_i^m = \frac{|N_i^{m,mig|conv}|}{|N_i^{m,diff}|} \quad (27)$$

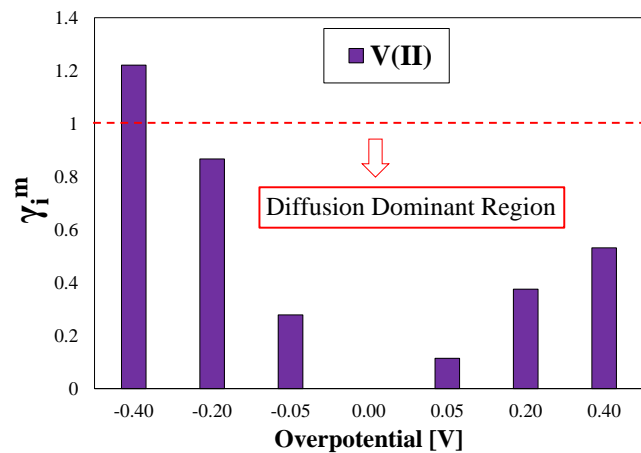
The gamma parameter (γ_i^m) quantifies the relative importance of electrostatic potential gradient-induced flux over the concentration gradient-induced flux. The gamma parameter is zero when the cell is at open circuit; when the magnitude of gamma is less than 1, the dominant flux is due to the concentration gradient. However, for magnitudes larger than 1, the electrostatic potential gradient flux is dominant.

Figure 4-14 shows the behavior of this gamma parameter for vanadium species at charging and discharging conditions for SoC=50%.

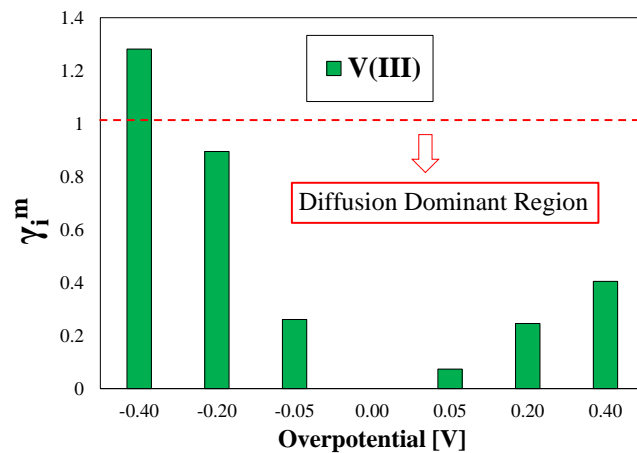
Since these experiments were conducted in symmetric mode (SoC = 50%), positive overpotential corresponds to charging mode while negative overpotential corresponds to discharging mode for Fig. 4-14 (a) and (b); positive current corresponds to charging while negative current corresponds to discharging for Fig. 4-14 (c) and (d).

It is important to note that the diffusive flux (the denominator of gamma) for each vanadium species is different due to the difference in permeability values, but it remains constant for charge and discharge cases for any individual species. Since the diffusive fluxes vary between species, the gamma values for each vanadium species should not be compared with the other vanadium species.

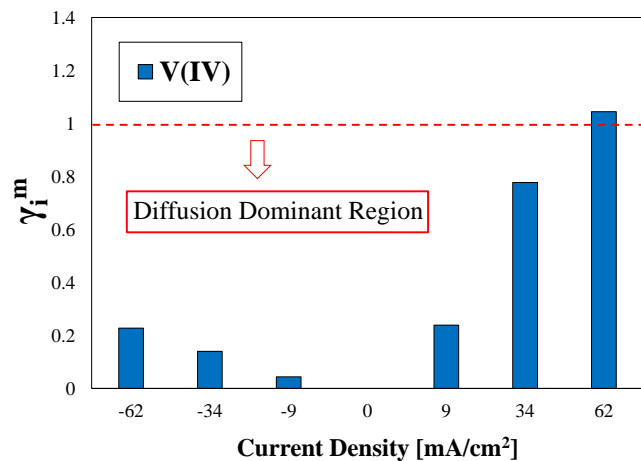
As apparent in Fig. 4-14, the relative importance of electrostatic potential gradient-induced crossover over concentration gradient-induced crossover increases with increasing overpotential, regardless of direction (i.e. charging or discharging). This experimental observation is consistent with the formulation of Eq. (4-23).



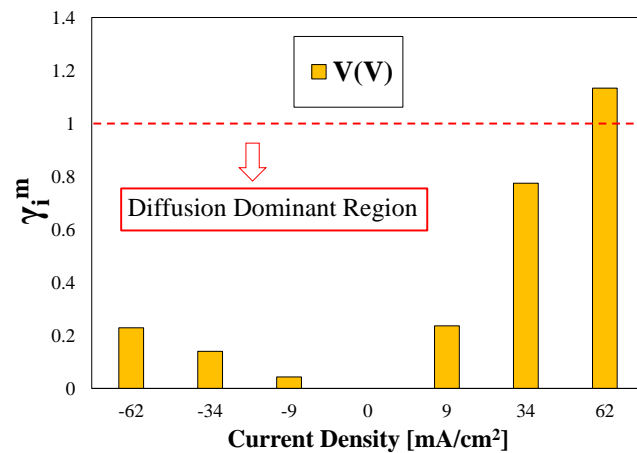
(a)



(b)



(c)



(d)

Figure 4-14: The ratio of electrostatic potential gradient-induced crossover over concentration gradient-induced crossover at SoC = 50%. (a: V(II), b: V(III), c: V(IV) and d: V(V)).

It is apparent from Eq. (4-23) that the diffusive flux ($\theta_i \Lambda_i^{m,diff} c_i^{bulk}$) is independent of current density and is a function of interaction coefficients (θ_i), concentration of vanadium on the enriched side (c_i^{bulk}), and the diffusive transport parameter ($\Lambda_i^{m,diff}$) which is directly proportional to permeability and inversely related to the membrane thickness. As a result, increased overpotential has no effect on the magnitude of diffusive flux and the diffusive flux remains constant for charge and discharge conditions. The electrostatic potential gradient-induced flux ($\Omega_i^{m,mig|conv} i^m c_i^{bulk}$) is a function of the electric-field-induced transport coefficient ($\Omega_i^{m,mig|conv}$), concentration of vanadium in the enriched side, and current density. As a result, the magnitude of electrostatic potential gradient-induced flux increases with increasing current density, but asymmetrically for charge and discharge modes. As apparent in Fig. 4-14, when the electrostatic potential gradient-induced crossover is in the opposite direction of concentration gradient-induced crossover, as is the case for V(II)/V(III) at positive overpotentials and V(IV)/V(V) at negative currents, the gamma parameter is reduced compared to the case when the electrostatic potential gradient-induced current is in the same direction as the concentration gradient-induced current. A careful consideration of the rate of change in the magnitude of the electrostatic potential gradient-induced flux with increased overpotential reveals that the rate of increase is much smaller when the electrostatic potential gradient-induced current is in the opposite direction of concentration gradient induced current and gamma would approach 1 at high enough current densities. This behavior indicates that the gamma value is always smaller than 1 when the electrostatic potential gradient-induced current is in the opposite direction of concentration gradient-induced current; thus, the system is always

diffusion-controlled. However, if the current density is high enough, the diffusive crossover will be greatly suppressed. Conversely, when the electrostatic potential gradient-induced crossover is in the same direction of concentration gradient-induced crossover, the rate of increase in the gamma value is greater.

As demonstrated via the trend of gamma values, for all the vanadium species, the ratio of electrostatic potential gradient-induced flux over concentration gradient-induced crossover has asymmetric behavior for charge and discharge cases. For instance, considering discharge conditions, the magnitude of electric-field-induced crossover increases with increasing overpotential for all the species; however, the rate of change in the flux is more pronounced for the V(II)/V(III) couple than for the V(IV)/V(V) couple. The same observation holds for the V(IV)/V(V) couple versus the V(II)/V(III) couple in the charging case. It is important to consider the qualitative comparison from the images shown in Fig. 4-8 and 4-9 with the results shown in Fig. 4-14. The asymmetric behavior shown is confirmed by the numerical results of Fig. 14. When the direction of proton flux coincides with the concentration gradient, the magnitude of electric-field-induced crossover increases with increasing overpotential with a higher rate for all the species (V(II)/V(III) for discharge case and V(IV)/V(V) for charge case). However, when the direction of proton flux is in the opposite direction, the rate of increase in the electric-field-induced crossover is slower. According to the trend observed at high current density, electric-field-induced migration approaches the magnitude of concentration gradient-induced flux (V(II)/V(III) at charge and V(IV)/V(V) for discharge); this is the case when the gamma value approaches

1. When gamma approaches 1, and the concentration gradient-induced crossover flux is in the opposite direction of electric-field-induced flux, the total net crossover approaches zero, resulting in interior chamber concentrations approaching zero. Additionally, when the electric field is in the opposite direction of the concentration gradient, the effect is more pronounced for the V(II)/V(III) couple versus the V(IV)/V(V) couple. This behavior is illustrated by the observation that the electric-field-induced flux component is smaller for the V(IV)/V(V) couple compared to the overall flux. Supporting this conclusion is the relative insensitivity of interior chamber concentration to changes in overpotential as shown in Fig. 4-10(c) and (d). The asymmetric behavior that is observed for the charge and discharge conditions originates from the fact that the direction for the concentration gradient-induced crossover is always down the concentration gradient, regardless of ionic current. The electrostatic potential gradient across the membrane results in migration and convection down the electrostatic potential gradient, but this direction changes when charging or discharging. When these two directions oppose, the net flux of crossover decreases since the direction of the solvent transport is in the opposite direction of the concentration gradient. This behavior can be considered through the lens of Eq. (4-23). The electrostatic potential gradient-induced flux magnitude is a function of the concentration of vanadium and therefore, when the concentration gradient is in the opposite direction of electrostatic potential gradient, the electrostatic potential gradient-induced crossover can only suppress the magnitude of the concentration gradient-induced flux. The effect of electrostatic potential gradient flux is independent of the thickness of the membrane, and as a result, the conclusion is applicable for other, thinner membranes, especially at high

current density where the electrostatic potential gradient flux is dominant. It is expected that the application of thinner membranes would result in higher crossover flux at low current density where the system is diffusion controlled (gamma value less than 1) since the magnitude of the diffusive flux (Eq. (4-23)) is inversely related to the thickness of the membrane and the effect of diffusion flux is dominant at low current density regimes.

One can also quantify the portion of current that is passed via transport of vanadium species across the membrane. The ionic current across the membrane can be calculated as described in Eq. (4-28):

$$i_e = F \sum_j z_j N_j \quad (4-28)$$

According to Eq. (4-28), all the charged species within the membrane (protons, bisulphate ions, and vanadium species) contribute to the ionic current. It is possible to isolate the portion of the current being passed by the vanadium species via reformulating Eq. (4-28).

$$i_e = FN_{H^+} - FN_{HSO_4^-} + F \sum_{j \neq H^+, HSO_4^-} z_j N_j = i_{H^+} - i_{HSO_4^-} + i_V \quad (4-29)$$

According to Eq. (4-29), the current density associated with the net crossover of vanadium species (i_V) can be obtained at different overpotentials. Figure 4-15 shows the value of i_V at different overpotentials where positive current density value corresponds to net current towards the cathode side and negative current towards the anode side.

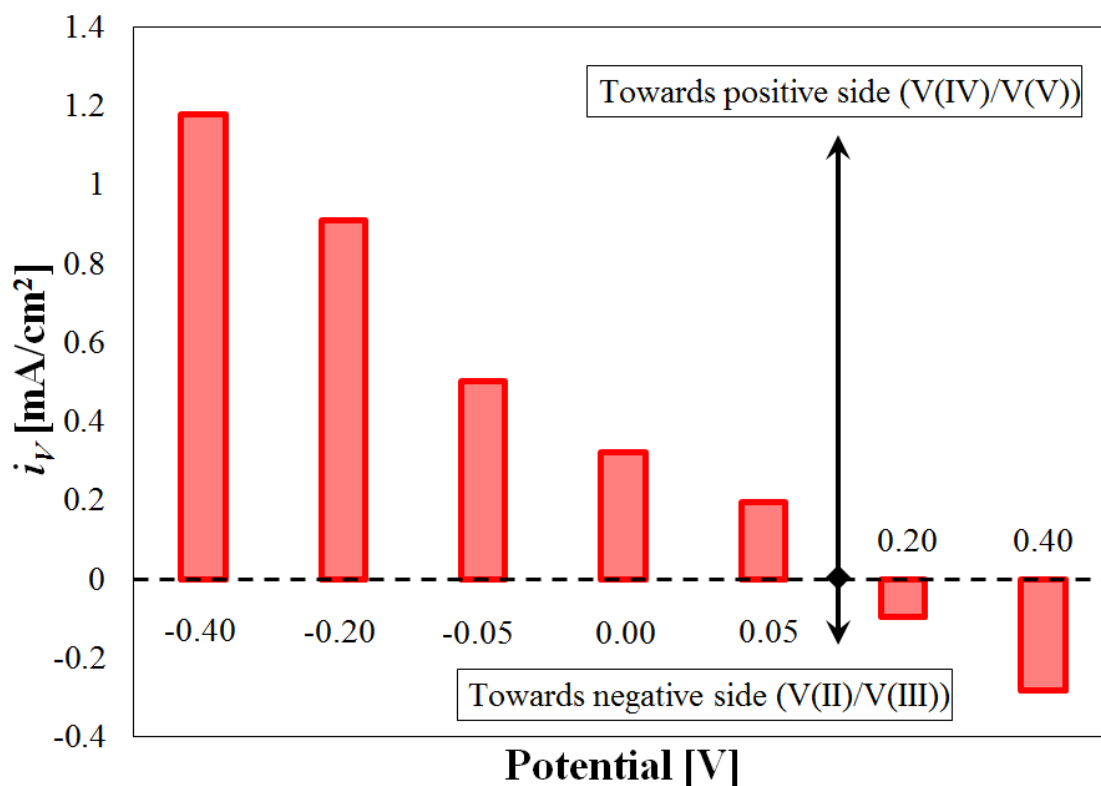


Figure 4-15: The crossover current density (i_V) at different potentials

The magnitude of crossover current density increases with increasing overpotential; but, as expected, with an asymmetric trend. Within the range of current density tested here, the maximum net crossover current density is 1.2 mA/cm² in discharge mode with 0.4V overpotential applied across the cell. This magnitude is similar to the net crossover current density range (1.7mA/cm²) that has been predicted via simulation ¹³⁹; deviation between the results here and the simulation is likely due to the fact that the referenced simulation used dilute solution theory. Finally, as shown in Fig. 4-15, there is a small diffusive current towards the cathode side when there is no overpotential; this current flips towards the anode side with increased charging overpotential.

4.5. Summary and Conclusions

In this work, a novel in-house test configuration including four cells was utilized to experimentally investigate the transport of vanadium species through a perfluorosulphonic type (Nafion® 117) ion-exchange membrane of an operating all-vanadium redox flow battery. Differentiating the concentration gradient-induced crossover and electrostatic potential gradient-induced crossover for a wide range of operating conditions was the focus of the experimental investigation. It was shown that the permeability of vanadium species through the ion-exchange membrane is SoC dependent and, therefore, simplified interaction coefficients were introduced in order to account for this behavior. It was also shown that the electric field has a significant effect on crossover and increases the rate of crossover for V(II)/V(III) and decreases the rate of crossover for V(IV)/V(V) during discharge; the opposite happens during charging conditions. The electric-field-induced transport coefficients were defined via fitting the experimental data to account for two additional modes of crossover, as an addition to concentration gradient-induced crossover. The electric-field-induced transport coefficients account for migration and convection transport modes due to the electric field. Also, it was experimentally shown that the effect of the electric field on crossover is asymmetric for charge and discharge processes for any vanadium species; this asymmetric trend was formulated via defining the dimensionless number γ to account for the relative importance of electric-field-induced crossover versus concentration gradient-induced crossover. Also, it was shown that the electric field effect is more significant on V(II)/V(III) than V(IV)/V(V) when the electric field is in the opposite direction of the concentration gradient-induced crossover.

4.6. Acknowledgments

Yasser Ashraf Gandomi would like to acknowledge University of Tennessee for providing Chancellors Graduate Fellowship support.

4.7. Nomenclature

N_i	Flux of species i [mol/(m ² .s)]
D_i	Diffusion coefficient i [m ² /s]
c_i	Concentration of species i [mol/ m ³]
z_i	Charge number of species i [-]
u_i	Mobility of species i [(mol.m ²)/(J.s)]
F	Faraday's constant, 96,485 [C/equiv]
Φ	Electric potential [V]
v_0	Solvent (water) velocity within membrane [m/s]
κ	Conductivity [S/m]
i	Current density [A/ m ²]
ξ	Water electro-osmosis coefficient [-]
α	Transport coefficient [mol ² /(J.m.s)]
μ_0	Chemical potential of solvent (water) [J/mol]
K	Partitioning coefficient [-]
t_m	Thickness of ion-exchange membrane [m]
P_i	Permeability of species i [m ² /s]
Λ_i	Diffusive transport parameter of species i [m/s]
Ω_i	Electric-field-induced transport coefficient of species i [m ³ /(A.s)]
Θ_i	Interaction coefficient of species i [-]
V	Volume of the electrolyte [m ³]
A	Area of the ion-exchange membrane [m ²]
i_v	Current density due to net vanadium crossover [A/ m ²]
<i>Subscripts</i>	
i	Species i
int	Interior chamber
<i>Superscript</i>	
m	Inside ion-exchange membrane
$diff$	Diffusive
$mig conv$	Migration-convective

CHAPTER FIVE :
INFLUENCE OF MEMBRANE EQUIVALENT WEIGHT AND
REINFORCEMENT ON IONIC SPECIES CROSSOVER IN ALL-VANADIUM
REDOX FLOW BATTERIES

Scholarly contributions

This chapter is revised based on the published paper with permission from Membranes: ¹⁰²

Yasser Ashraf Gandomi, D. S. Aaron, M. M. Mench. “Influence of Membrane Equivalent Weight and Reinforcement on Ionic Species Crossover in All-Vanadium Redox Flow Batteries” *Membranes*, 7, 29 (2017) [doi:10.3390/membranes7020029]

Abstract

One of the major sources of lost capacity in all-vanadium redox flow batteries (VRFBs) is the undesired transport (usually called crossover) of water and vanadium ions through the ion-exchange membrane. In this work, an experimental assessment of the impact of ion-exchange membrane properties on vanadium ion crossover and capacity decay of VRFBs has been performed. Two types of cationic membranes (non-reinforced and reinforced) with three equivalent weights of 800, 950 and 1100 g.mol⁻¹ were investigated via a series of in-situ performance and capacity decay tests along with ex-situ vanadium crossover measurement and membrane characterization. For non-reinforced membranes, increasing the equivalent weight (EW) from 950 to 1100 g.mol⁻¹ decreases the V(IV) permeability by ~30% but increases the area-specific resistance (ASR) by ~16%. This increase in ASR and decrease in V(IV) permeability was accompanied by increased through-plane membrane swelling. Comparing the non-reinforced with reinforced membranes, membrane reinforcement increases ASR but V(IV) permeability decreases. It was also shown that there exists a monotonic correlation between the discharge capacity decay over long-term cycling and V(IV) permeability values. Thus, V(IV) permeability

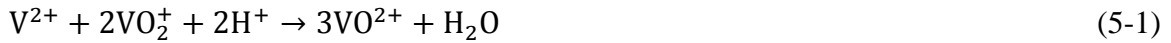
is considered a representative diagnostic for assessing the overall performance of a particular ion-exchange membrane with respect to capacity fade in a VRFB.

5.1. Introduction

Incorporating non-hydroelectric renewable energy sources (e.g. solar and wind power) into the electric grid requires robust and large-scale energy storage systems. Redox flow batteries (RFBs) are promising candidates for efficient, large-scale energy storage. Among many chemistries developed for RFBs, all-vanadium redox flow batteries (VRFBs) are the focus of this study. VRFBs are unique among all major chemistries developed for RFBs since they utilize the same ion (vanadium) in multiple oxidation states for negative and positive electrolytes; as a result, they do not suffer from irreversible capacity decay due to vanadium ion transport through the ion-exchange membrane ¹. VRFB systems were initially proposed by Skyllas-Kazacos and co-workers and significant improvements have been made in increasing the power density and the performance via different research groups [2-6]. Typical VRFB systems have energy density of 25-30 Wh.kg⁻¹ and round-trip efficiency of 70-80%, depending on operating current. Recently, a high performance VRFB cell with up to 88% energy efficiency at current density of 400 mA.cm⁻² has been demonstrated successfully ^{1, 127, 202}.

Although significant progress has been made in improving the performance of VRFBs, there are many issues yet to be addressed. One of the major remaining issues is relatively rapid capacity decay during cycling compared to expected component lifetime. The primary contributions to capacity loss are undesired vanadium and water transport through

the ion-exchange membrane, degradation of cell components (predominantly electrodes and membrane), and gas-generating side reactions. Appropriate material selection, pretreatment protocol, and operating voltage range can largely avoid material degradation and side reactions. However, capacity decay due to vanadium and water transport across the membrane is inevitable. For VRFB systems, the following reactions are reported to occur when vanadium ions cross through the membrane ^{102, 127, 202}.



Reactions (5-1) and (5-2) correspond to the case where vanadium ions of the positive electrolyte (V(IV) and V(V)) cross through the ion-exchange membrane and react with V(II) in the negative electrode. A similar case occurs when the vanadium ions of the negative electrolyte (V(II) and V(III)) travel through the membrane and react with V(V) in the positive electrode according to reactions (5-3) and (5-4).

Several parameters contribute to capacity decay due to solute (vanadium ion) and solvent (water) transport through the membrane. The properties of the cell components (ion-exchange membrane, electrodes, and flow-fields) and operating conditions (flow rate, temperature, vanadium and acid concentration, state of charge (SoC) and cell overpotential) are significant contributors to net transport.

Concentration gradient (diffusion) and electric field (via migration and electro-osmosis) significantly contribute to vanadium and water transport across the ion-exchange membranes. Water transport can also be affected by gradients in osmotic and hydraulic pressure^{112, 218}. The most common experimental approach for assessing the concentration-gradient induced crossover is via permeability cells, which has been used by several research groups^{102, 202}. The effect of various pretreatments of the membrane on the vanadium crossover has been investigated using a permeability cell^{102, 202}. Experimental approaches targeting the effect of electric field on vanadium and water crossover are rare and usually require sophisticated experimental set-ups²⁰². Therefore, assessing the effect of electric field on crossover is more frequently studied via numerical modeling approaches^{174, 176}.

It is also important to note that the transport of vanadium species through the ion-exchange membrane is influenced by electrolyte composition, thus it is SoC dependent²⁰². Recently, the effect of the electric field on vanadium crossover has been investigated and interaction coefficients for quantifying vanadium crossover as a function of SoC for Nafion® membranes has been introduced²⁰². As a result, the transport parameters for vanadium ions and water, with and without the effect of electric field and as a function of SoC, are now known for Nafion®²⁰². It has been shown that the permeability values of vanadium ions with different oxidation states through the ion-exchange membrane are dissimilar and accordingly, as a function of cycling, vanadium ion accumulation is asymmetric between the negative and positive sides. This asymmetry results in imbalanced vanadium concentration in the negative and positive electrolytes over long-term cycling, causing

capacity fade ²⁰². To understand this behavior, several modeling studies have been developed to simulate vanadium ion and water crossover through Nafion ® membranes ^{127, 202, 218}. Ultimately, however, more direct experimental tests are needed to confirm and validate any modeling study for these complex solutions and different membranes.

The ideal membrane should have low ohmic loss, high chemical, mechanical and thermal stability, and superior ionic selectivity. Maintaining high ionic conductivity favors the utilization of thin membranes in order to reduce ohmic overpotential, but necessarily increases diffusive crossover of vanadium ions and water, resulting in increased capacity fade as a function of time and concentration gradient. As a result, selection of an appropriate membrane for VRFB applications is a tradeoff between high ionic conductivity and decreased vanadium ion and water crossover.

Controllable properties of ion-exchange membranes include polymer type (anionic versus cationic), equivalent weight, and membrane reinforcement; the effects of these properties on vanadium ion crossover and capacity decay are of great importance. In addition, the membranes to be used for VRFB applications must meet several transport requirements to ensure economic and technical viability ¹³⁹. The incorporation of hydrophobic ionic liquids as membrane dopants has shown promising results for reduced vanadium ion and water crossover ²¹⁹.

Perfluorosulphonic acid-based Nafion ® (E. I. DuPont Company, USA) is a commonly-used membrane for VRFB applications. Although Nafion ® membranes have high mechanical and chemical stability, they have relatively high material cost and poor ionic selectivity. Considering the overall cost of a VRFB system, the ion-exchange membrane

contributes to 25%-45% of the total cost depending on energy capacity. Also, the overall cost of an ion-exchange membrane is correlated with equivalent weight (EW); thus, lower EWs are preferable from a material cost perspective. However, lower EW decreases the mechanical stability of the membrane among other changes.

The main motivation of the present work is to better understand the effect of equivalent weight and reinforcement on overall cell performance, ionic species crossover and capacity decay. In this work, we report the results based on VRFB cells that used GORE-SELECT® or pure cast film membranes over a range of equivalent weight. Throughout this paper, “GORE-SELECT®” is conventionally used to indicate reinforced membranes, except in figures and tables where “GORE-SELECT®” has been used for labeling these types of ion-exchange membranes.

The test matrix includes in-situ capacity decay experiments for different cell configurations under constant current density subjected to long-term cycling, polarization curves (obtained to demonstrate the cell voltage as a function of current density), AC impedance tests, ex-situ membrane characterization and vanadium crossover tests.

5.2. Experimental

5.2.1. Membrane selection and pretreatment

The first set of membranes included non-reinforced cationic exchange membranes with equivalent weights of 800, 950 and 1100 g.mol⁻¹. The second set of membranes was

reinforced cationic exchange membranes with the same three equivalent weights as the non-reinforced membranes (800, 950 and 1100 g.mol⁻¹). It is important to note that when the ion-exchange membranes are exposed to a solution containing vanadium, sulfuric acid and water, they physically expand; it is necessary to measure this expansion to calculate accurate diffusive crossover rate constants. The details of such measurements have been provided in the results section.

5.2.2. Method of approach

A schematic of the experimental test system used in this work is in Figure 5-1. The test rig includes four single cells, two-channel peristaltic pumps (Cole Parmer, Masterflex L/S), and external reservoirs as well as ultraviolet/visible (UV/Vis) spectrometers (THORLABS) with light sources (Ocean-Optics).

Also, a central temperature control unit maintains a constant temperature of 30°C for all the cells and reservoirs. The initial electrolyte of interest was prepared using Cell 1 which was a 25 cm² active area cell. Pristine 39AA carbon paper electrodes (SGL Group, Germany) were sandwiched between a flow plate and the membranes.

Two membranes (Nafion ® 117, E. I. DuPont Company, USA) were utilized in Cell 1 in order to reduce the rate of crossover during electrolyte preparation. Two electrolyte reservoirs were utilized in conjunction with Cell 1 for V(II)/V(III) and V(IV)/V(V)

couples. All reservoirs were sealed and under constant nitrogen purge while stir bars were utilized to ensure uniform composition of the reservoir solutions.

Cell 2 was used to record polarization curves and capacity decay data for the pure cast film and GORE-SELECT® membranes. This cell utilized a 9 cm² active area with single-path serpentine flow fields and 39AA (pristine, 1 layer, SGL Group, Germany) carbon papers as electrodes. Prior to conducting cycling experiments, pristine membranes (pure cast film or GORE-SELECT® membranes) were immersed in a solution of 3.3M sulfuric acid at room temperature for more than a week. A flow rate of 70 mL/min was supplied using a two-channel peristaltic pump. Cycling experiments were conducted at a current density of 100 mA/cm² with cut-off voltage limits of 0.2 V and 1.9 V for discharge and charge modes, respectively.

In order to assess vanadium transport behavior, we have focused solely on the concentration-gradient induced crossover due the number of ion-exchange membranes considered in this work. Utilizing concentration-gradient induced crossover to represent actual crossover is common when many membranes are investigated and/or the current density is low¹⁰².

Cell 3 was designed to investigate the concentration-gradient induced V(IV) permeability for a series of different membranes. Cell 3 was a two-chamber 9 cm² active area cell with flow-through flow fields and no electrodes.

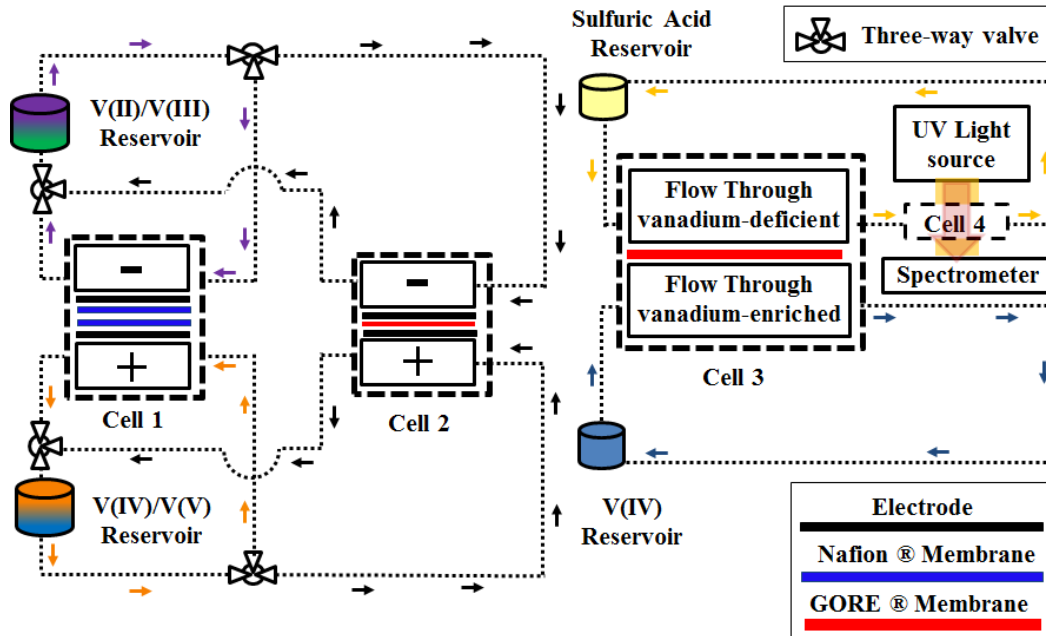


Figure 5-1: Schematic of the experimental setup

For Cell 3, the vanadium-enriched solution flowed from the V(IV) reservoir and vanadium-deficient solution was circulated from the sulfuric acid reservoir and passed through a flow-through UV-Vis measurement unit cell (labeled as Cell 4 in Figure 5-1) to monitor the vanadium-deficient side's solution in real-time. The total time of electrolyte circulation was 24 hours. During the circulation of vanadium-enriched and vanadium-deficient electrolytes, concentration gradient-driven crossover occurred from the vanadium-rich electrolyte to the aqueous sulfuric acid solution across the ion-exchange membrane of interest. The vanadium-deficient solution was directed to Cell 4 for real-time monitoring of V(IV) crossover using UV/Vis spectroscopy. To calculate the concentration of V(IV) on the vanadium-deficient side from the spectroscopic data, the spectra of standardized V(IV) with known concentration were recorded using the same parameters as the experiment. The real-time spectroscopic data were integrated and analyzed with scripts

written in-house. This experimental procedure was repeated for different configurations of Cell 3 assembled using various pure cast film and GORE-SELECT® membranes.

5.2.3. Testing protocol

A multichannel potentiostat/galvanostat (Arbin Instruments, College Station, TX) was employed to prepare electrolyte. The initial electrolyte was 1.5 mol/L $\text{VOSO}_4 \cdot x\text{H}_2\text{O}$ (Alfa Aesar, USA) dissolved in 3.3 mol/L sulfuric acid (H_2SO_4). The initial volume of negative electrolyte was 50 mL and the positive electrolyte was 100 mL; after initial charging at 1.8 V until reaching a cut-off current of 4 mA, 50 mL of positive electrolyte was removed to prepare equal volumes of negative and positive electrolyte at near-100% SoC. The electrolyte was discharged to 50% SoC at a constant 100 mA/cm² to obtain the condition for polarization curves. A single-channel Bio-Logic SP240 potentiostat (BioLogic Science Instruments, France) was used to conduct the charge-discharge processes and apply the desired overpotential or current. Cell 2 as shown in Figure 5-1 was utilized to conduct the polarization and cycling experiments. The cycling experiments were conducted at a constant current of 100 mA/cm² for both discharging and charging until reaching cut-off voltages of 0.2 V and 1.9 V, respectively. AC impedance (at open circuit voltage) data were also obtained using the Bio-Logic SP240 potentiostat.

To assess membrane conductivity, Cell 2 was utilized at open-circuit and 50% SoC conditions using AC impedance. AC impedance experiments were conducted with the positive electrode serving as working electrode and a 5-mV perturbation amplitude; ohmic

impedance was taken as the high frequency impedance with no imaginary components (high frequency x-axis intercept on a Nyquist plot). To estimate the contact resistance of the other cell components, a cell was assembled without any membrane and the resistance was found to be $\sim 0.03 \text{ Ohm-cm}^2$ and this magnitude was subtracted from the total high-frequency impedance to assess the ohmic impedance associated with the membrane.

5.2.4. UV/Vis spectroscopy

To conduct the vanadium ion permeability tests, Cell 3 and Cell 4 were utilized. Vanadium-enriched solution was circulated in one side of Cell 3 while vanadium-deficient solution was circulated in the other side; the vanadium-deficient solution was directed to Cell 4 after leaving Cell 3 (refer to Figure 5-1). Therefore, two sets of electrolytes were prepared: one set for vanadium-enriched side and one set for vanadium-deficient side. For the vanadium-enriched side, the electrolyte was 1.5 mol/L $\text{VOSO}_4 \cdot x\text{H}_2\text{O}$ (Alfa Aesar, USA) dissolved in 3.3 mol/L sulfuric acid (H_2SO_4).

To conduct the V(IV) permeability measurements, it is necessary to minimize water transport across the membrane so that V(IV) permeability is only a function of its concentration gradient. To this end, the undesired driving forces of water transport (combined effects of osmotic and hydraulic pressure gradients) need to be balanced.

Utilizing the symmetric configuration for Cell 3 (vanadium-deficient side versus vanadium-enriched side) prevents any hydraulic pressure gradient across the membrane.

However, the osmotic pressure gradient must also be minimized. To balance osmotic pressure, multiple approaches have been described in the literature including matching sulfate concentration on both sides or providing a counter cation on the vanadium-deficient side ^{102, 140, 144}. The use of a counter ion in the vanadium-deficient side introduces new complications to transport measurement and is not used in this work.

Only sulfuric acid solution can be used in the vanadium-deficient side if the concentration of the sulfuric acid is chosen based on the procedure explained in our previous work ²⁰². Therefore, for the vanadium-deficient side, the sulfuric acid concentration was 4.8 M, resulting in zero osmotic pressure gradient for the solvent across the membrane. The volumes of the vanadium-enriched and vanadium-deficient reservoirs were selected to be 200 and 80 mL, respectively.

The electrolytes used for VRFBs exhibit strong visible light absorbance. Therefore, UV/Vis spectroscopy can be utilized to assess the composition of the solution. In this work, the spectrophotometric measurements were made using spectrometers in a transmission configuration with a spectral range from 400 to 900 nm.

Since the focus of this work is to assess the permeability of V(IV), electrolyte absorbance was measured at 760 nm wavelength ²⁰². Such measurements allowed the application of the Beer-Lambert law to determine the relative concentration of V(IV) ²⁰². To obtain the spectra associated with the vanadium-deficient solution, real-time spectrophotometry was

performed while the solution of the vanadium-deficient side was circulating through Cell 4, as shown in Figure 5-1.

5.2.5. Vanadium Ion Permeability Assessment

To obtain the transport parameters for the different types of membranes, permeability values for V(IV) must be determined under a concentration gradient; based on that value, diffusive transport parameters for the particular membrane are formulated according to the procedure explained elsewhere ²⁰². Concentration gradient-driven crossover occurs from the vanadium-enriched side to the vanadium-deficient side across the membrane. The concentration of diffused vanadium ions is used to obtain the permeability values for a particular membrane ²⁰². The concentration of diffused V(IV) ions in the vanadium-deficient side can be described using the following equation.

$$V_{v_d} \frac{dC_{v_d}(t)}{dt} = P_{V(IV)}^m \frac{A}{t_m} [C_{v_e} - C_{v_d}(t)] \quad (5-5)$$

In Equation (5-5), V_{v_d} represents the volume of the vanadium-deficient electrolyte reservoir, C_{v_d} is the concentration of the vanadium ion in vanadium-deficient electrolyte, C_{v_e} is the concentration of vanadium ion of vanadium-enriched solution, A is the active area of the membrane in contact with solution, t_m represent the thickness of the membrane (after equilibration with electrolyte) and $P_{V(IV)}^m$ is the permeability of the V(IV) through the membrane of interest. In Equation (5-5), the concentration of vanadium in the vanadium-enriched solution is assumed to be constant over the course of each vanadium permeability experiment (24 hours), since the vanadium-enriched reservoir is relatively large compared

to the vanadium-deficient reservoir. To calculate permeability values, Equation (5-6) can be integrated.

$$\int_0^{C_{v,d}} \frac{d(C_{v,e} - C_{v,d}(t))}{(C_{v,e} - C_{v,d}(t))} = - \int_0^t \frac{P_{V(IV)}^m A}{V_{v,d} t_m} dt \quad (5-6)$$

$$\ln\left(\frac{C_{v,e}}{C_{v,e} - C_{v,d}(t)}\right) = \frac{P_{V(IV)}^m A}{V_{v,d} t_m} t \quad (5-7)$$

According to Equation (5-7), the trend of the left side of the equation versus time can be used to obtain the permeability. After obtaining the permeability values, diffusive transport parameters can be calculated based on Equation (5-8).

$$\Lambda_{V(IV)}^m = \frac{P_{V(IV)}^m}{t_m} \quad (5-8)$$

In Equation (5-8), $\Lambda_{V(IV)}^m$ represents the V(IV) diffusive transport parameter.

5.3. Results and Discussion

5.3.1. Capacity decay during long-term cycling

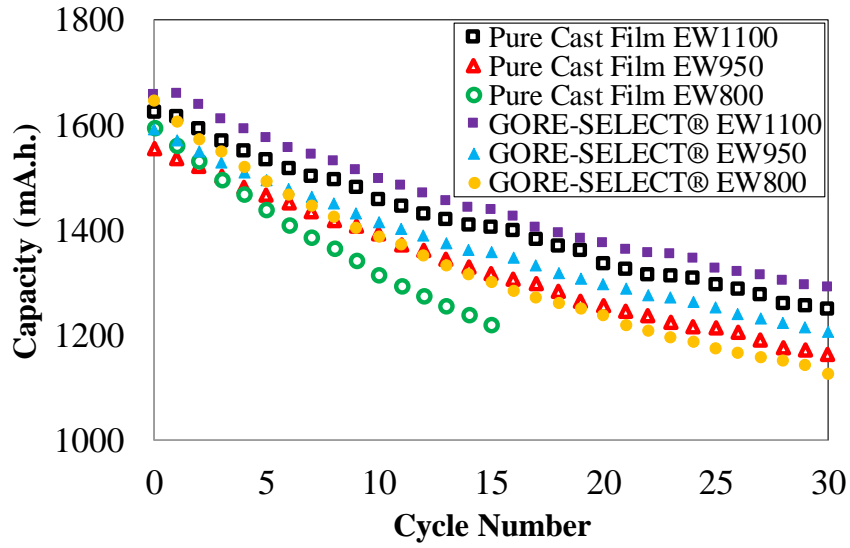
Figure 5-2(a) includes the discharge capacity as a function of cycle number for the first 30 cycles for different pure cast film and GORE-SELECT® membranes. In Figure 5-2(a), the capacity decay data for the pure cast membrane with EW800 has only been reported for the first 15 cycles since the cell capacity became unstable due to membrane's degradation. Figure 5-2(b) shows the theoretical capacity utilization for different membranes over the same duration. It is important to note that the theoretical capacity is determined using Cell 1 (from Fig. 5-1) while charging the initial electrolyte; half of the total charge transferred

to the electrolyte during the initial charge is evaluated as the theoretical capacity. Since both electrolytes were similar (1.5 mol/L V(IV) as $\text{VOSO}_4 \cdot x\text{H}_2\text{O}$ (Alfa Aesar, USA) dissolved in 3.3 mol/L H_2SO_4), half of the total initial charge corresponds to the full capacity window for an operating VRFB.

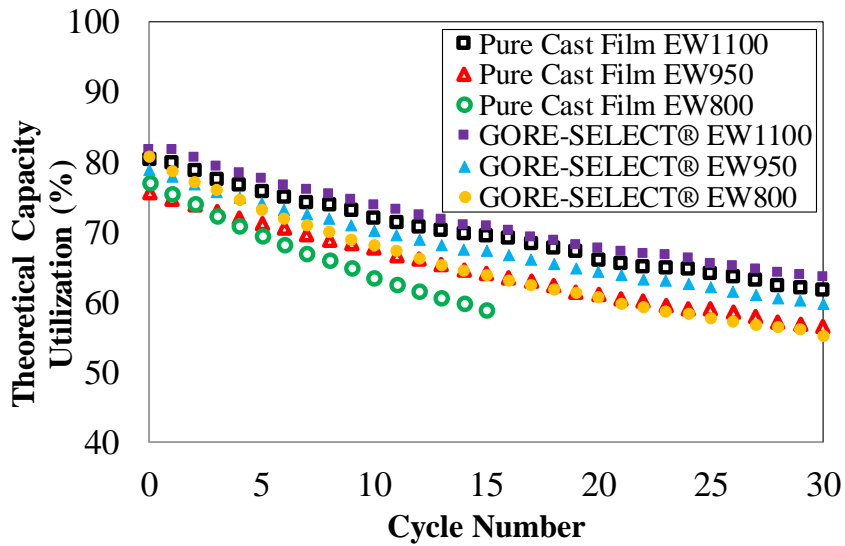
As shown in Figure 5-2(a) and 5-2(b), the capacity and theoretical capacity utilization both decrease during cycling. The theoretical capacity utilization is an important metric for assessing overall vanadium ion utilization within a VRFB cell. Due to imposing voltage limits while maintaining the cycling current (in this work, 0.2 V and 1.9 V) the theoretical capacity utilization is always lower than 100% since the total content of all dissolved vanadium ions cannot be utilized.

The properties of the ion-exchange membrane directly affect the theoretical capacity utilization through the crossover rate. A higher rate of crossover decreases the open-circuit voltage (OCV) of the cell and consequently results in reaching the voltage limits sooner during a cycle, all other contributing parameters being equal.

According to Fig. 5-2(b), at the end of 30 cycles, the reinforced/EW1100 exhibits the highest magnitude of theoretical capacity utilization of ~64% and the non-reinforced/EW800 shows the lowest theoretical capacity utilization (~59%, at the end of just 15 cycles).



(a)



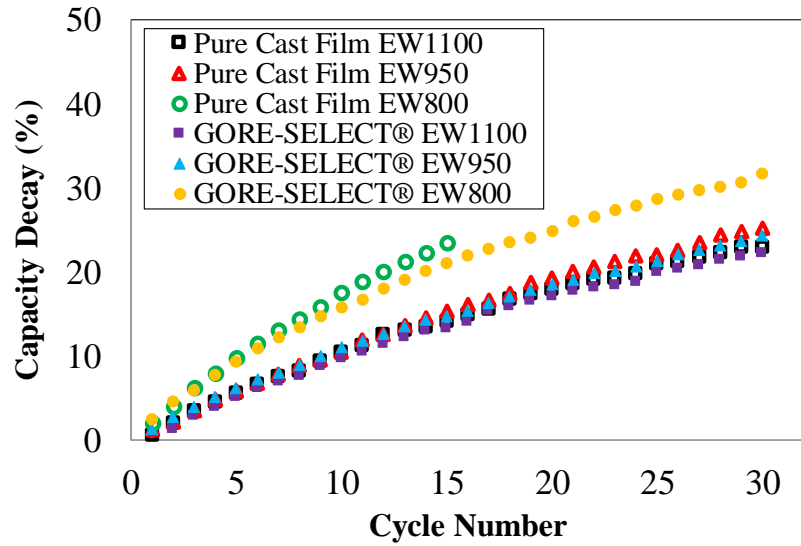
(b)

Figure 5-2: (a) Capacity decay as a function of cycle number, (b) Theoretical capacity utilization as a function of cycle number

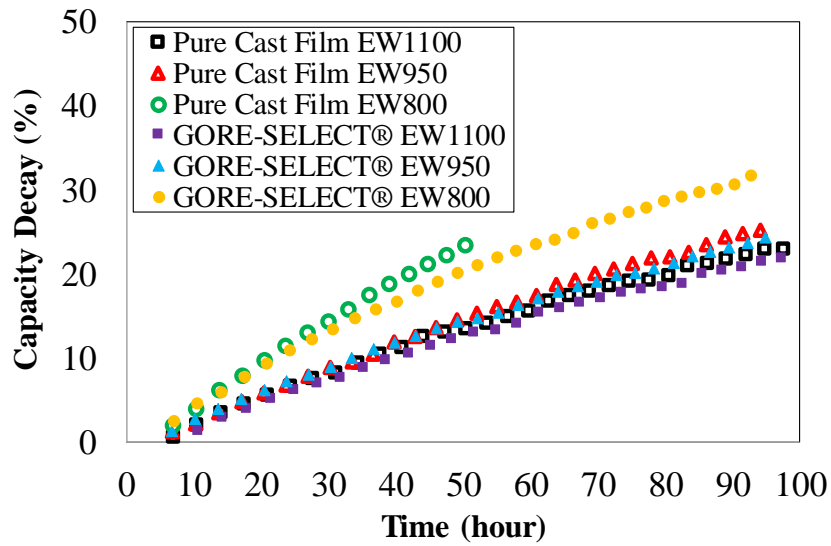
Also, as seen in Figure 5-2(b), increased equivalent weight results in increased theoretical capacity utilization for both reinforced and non-reinforced membranes. Comparing similar equivalent weights of non-reinforced and reinforced membranes, reinforcement increases the theoretical capacity utilization. For example, the EW1100 membrane showed 2% greater capacity utilization resulting from reinforcement; for the EW950 membrane, reinforcement increases the theoretical capacity utilization by 3% at the end of 30 cycles compared to non-reinforced.

Figure 5-3 includes the discharge capacity decay for different membranes as a function of cycle number and as a function of time. Here, the capacity decay is defined as the ratio of the decrease in discharge capacity to the initial discharge capacity of the battery. According to Figure 5-3(a), the reinforced EW1100 membrane exhibits the lowest rate of capacity decay (~22% at the end of 30 cycles) and non-reinforced EW800 shows the highest rate of capacity decay (~24% at the end of just 15 cycles).

It is important to note that, although the number of cycles for all the experimental membranes was 30 (except non-reinforced EW800), the total cycling time for the different configurations varied due to different ohmic overpotentials imposed as a function of membrane conductivity. However, in general, cycling experiments were conducted over the course of approximately 100 hours.



(a)



(b)

Figure 5-3: Capacity decay for different ion-exchange membranes as a function of (a) cycle number, (b) Time

Similar to Figure 3(a), the reinforced membrane with EW1100 exhibits the lowest rate of capacity decay (~22% at the end of ~100 hours) and non-reinforced EW800 results in the highest rate of capacity decay (~24% at the end of ~59 hours) as a function of time.

According to Figure 5-3, increased equivalent weight mitigates capacity decay for both non-reinforced and reinforced membranes. As shown in Figure 5-3, increasing the equivalent weight from 950 to 1100 g.mol⁻¹ decreases the capacity decay by ~3% at the end of 30 cycles. The effect on capacity decay is more pronounced when increasing equivalent weight from 800 to 950 g.mol⁻¹ for reinforced membranes in which the capacity decay decreased by 7% at the end of 30 cycles. Also, it can be observed from Figure 5-3 that reinforcement decreases the capacity decay for identical-EW membranes. Comparing the non-reinforced and reinforced membranes, for the case of EW1100 and EW950, reinforcement decreased the capacity decay by ~1.5% at the end of 30 cycles. The observed differences in capacity decay are primarily due to vanadium crossover since the other components (electrodes, flow fields and electrolyte) were kept consistent.

Figure 5-4(a) includes coulombic efficiency for the membranes in this work. The coulombic efficiency was calculated here as the ratio of discharge capacity over charge capacity at 100 mA/cm². The coulombic efficiency for all membranes tested in this work exceeded 95%. Figure 5-4(b) shows the voltage efficiency for the membranes over a range of current density. Voltage efficiency is defined here as the ratio of average discharging voltage over the average charging voltage up to 150 mA/cm².

As shown in Figure 5-4(b), increasing the current density decreases the voltage efficiency for all experiments; voltage efficiencies exceeded 75% at 150 mA/cm². Figure 5-4(c) shows polarization curve results at 50% SoC for cells based on each membrane. Figure 5-4(d) includes power density data for membranes as a function of current density for discharging conditions. As shown, a power density of 181-190 mW/cm² was achieved at a discharge current density of 150 mA/cm². Also, it is important to note that for clarity, the polarization curves and power density curves are shown just for discharge conditions since the charge and discharge cases were nearly symmetric.

It is important to note that, according to Figure 5-4(a), coulombic efficiency for different membranes does not exhibit a direct correlation to increased equivalent weight or the addition of membrane reinforcement. The primary reason for such a trend lies in the definition of coulombic efficiency for VRFB systems.

Coulombic efficiency is defined as the ratio of the discharge capacity over charge capacity¹; therefore, for a membrane, both of these quantities can be small compared to the theoretical capacity while the cell still achieves high coulombic efficiency. Therefore, comparing Figure 5-4(a) with Figure 5-3, capacity fade as a function of cycle number or/and capacity decay as a function of time is a better metric to assess the viability of a particular membrane. Such a metric better represents superior ionic selectivity and the reduction of vanadium crossover rate.

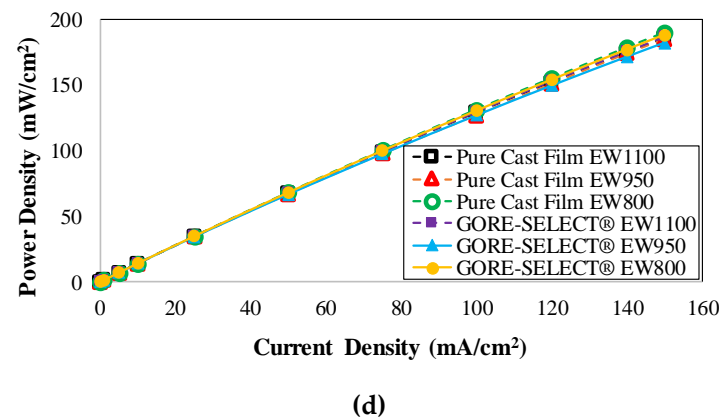
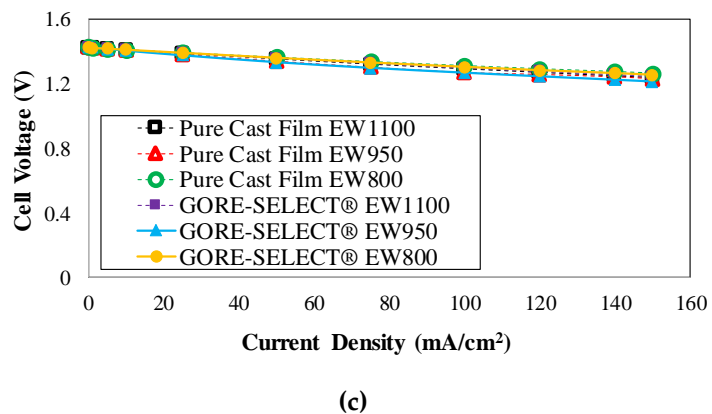
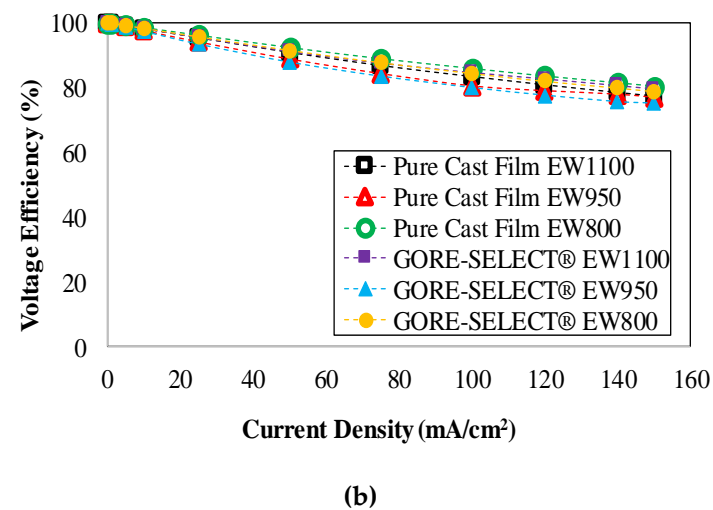
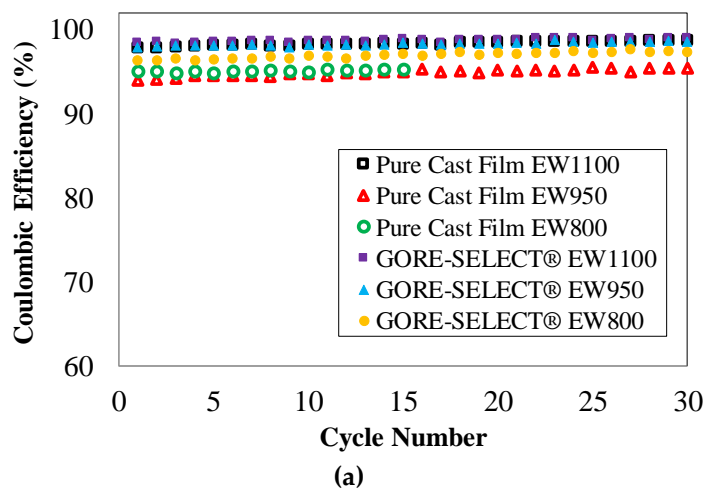


Figure 5-4: Characteristic plots for the experimental membranes, (a) Coulombic efficiency, (b) voltage efficiency, (c) Polarization curves, (d) Power density

According to Figure 5-4, voltage efficiency and polarization curves do not show a linear correlation to either increased equivalent weight and/or membrane reinforcement. An ideal ion-exchange membrane would decrease vanadium ion crossover and ohmic overpotential simultaneously. However, if the reduction of vanadium ion crossover via use of a particular membrane is obtained at the cost of increased ohmic overpotential, the polarization curves and voltage efficiency (consequently the power density) show a negative impact, as evidenced by Figure 5-4(b), (c) and (d). This observation has been further clarified through measuring area-specific resistance (ASR) associated with each membrane. Table 5-1 includes pre- and post-cycling ASR values for each pair of membranes at 100 mA/cm². For all experimental membranes, the ASR value increased during cycling (~ 9% - 18%).

Table 5.1. Initial and increase in ASR and ohmic overpotential (at 100 mA.cm⁻²) as function of cycling for different membranes

	Initial ASR (ohm.cm ²)	Relative increase in ASR (%)	Initial ohmic overpotential at 100 mA.cm ⁻² (mV)	Increase in ohmic overpotential at 100 mA.cm ⁻² during 30 cycle (mV)
Pure Cast Film EW1100	0.240	14.17	24.0	3.41
Pure Cast Film EW950	0.206	14.08	20.6	2.94
Pure Cast Film EW800	0.151	17.88	15.1	2.74
GORE-SELECT® EW1100	0.282	16.67	28.2	4.66
GORE-SELECT® EW950	0.244	12.70	24.4	3.11
GORE-SELECT® EW800	0.171	16.96	17.1	2.93

For non-reinforced and reinforced membranes, increasing the equivalent weight yielded increased ASR: increasing equivalent weight from 800 to 950 g.mol⁻¹ increased the ASR by ~36% and increasing the equivalent weight from 950 to 1100 g.mol⁻¹ increased the ASR by another ~ 16%. Considering the reinforced membranes, increasing the equivalent weight from 800 to 950 g.mol⁻¹ increased the ASR by ~43% while increasing the equivalent weight from 950 to 1100 g.mol⁻¹ increased the ASR by a similar ~ 16%. According to Table 5.1, across all equivalent weights, reinforcement increased the ASR.

Comparing the non-reinforced with reinforced membranes, for the EW1100 and EW950 sets, the ASR increases by ~18% due to membrane reinforcement and for the EW800 pair, the increase in ASR is ~13%. In summary, the non-reinforced EW800 exhibits the lowest (0.15 ohm.cm²) and the reinforced EW1100 results in the highest value (0.28 ohm.cm²) of ASR. A comparison of results in Table 5-1 and Figure 5-3 reveals that both of these membrane modification techniques (reinforcement and increased equivalent weight) resulted in decreased capacity decay; therefore, this simultaneous mixed effect is the primary reason for the trend observed for polarization curves, coulombic and voltage efficiencies, and power density graphs shown in Figure 5-4.

This mixed effect has been further clarified in the next section. The increase in ASR during cycling results in an increase in ohmic overpotential as tabulated in the following table (Table 1) for the case of constant discharge at 100 mA.cm⁻².

5.3.2. Crossover of vanadium ions

The major source for discharge capacity decay during cycling (as shown in Figure 5-3) is the undesired transport of vanadium ions through the ion-exchange membrane. In general, concentration gradient and electric field are the main driving forces for vanadium ion crossover. In this work, we have investigated the crossover of vanadium ions as a function of concentration gradient only. Among vanadium ions, concentration gradient-driven crossover has been assessed via focusing on the transport of V(IV) since the electrolyte preparation does not require any additional charge/discharge processes, ensuring uniform electrolyte composition. Figure 5-5 shows the concentration of vanadium V(IV) ion on the vanadium-deficient side over a twenty-four-hour time period; the crossover behavior observed here corresponds to conditions at SoC=0% on the positive side. The UV/Vis spectra were recorded at 6-hour intervals (5 sampling spectra) for each membrane and the recorded spectra were utilized to calculate the concentrations shown in Figure 5-5. As shown in Figure 5-5, the concentrations of diffused V(IV) to the vanadium-deficient side differ as a function of membrane composition. The maximum concentration of diffused V(IV) at the end of a 24-hour crossover test was measured for the non-reinforced membrane with EW800 ($\sim 0.114 \text{ mol.L}^{-1}$), and the minimum concentration was achieved by reinforced membrane with EW1100 ($\sim 0.023 \text{ mol.L}^{-1}$). The concentration of diffused vanadium V(IV) ions shown in Figure 5-5 can be used to obtain the permeability values for different membrane morphologies using the slope of a semi-natural log plot, formulated in Equation (5-7). As indicated by Equation (5-7), the slope of semi-natural log plots can be used to calculate permeability values; here, it is necessary to incorporate the expanded

thickness of the membranes in the modeling framework. To this end, a solution of aqueous sulfuric acid and vanadium (3.3 mol/L acid, 1.5 mol/L vanadium (V(III)/V(IV) mix) was prepared and the membranes were soaked in this solution for more than a week at room temperature. This composition was chosen to reflect the only stable vanadium species that can coexist in the membrane; V(II) and V(V) are expected to react with V(III) and V(IV). While the external solution is known to influence membrane properties, it is the internal environment that defines membrane properties. Figure 5-6 shows the thickness of the membranes measured after soaking in electrolyte. To measure the thickness, three sets of measurements were conducted using a digital micrometer (Mitutoyo, Japan) and each reported thickness value was the average of all measurements; error bars were calculated based on the deviation of maximum and minimum thickness measurements from the average value.

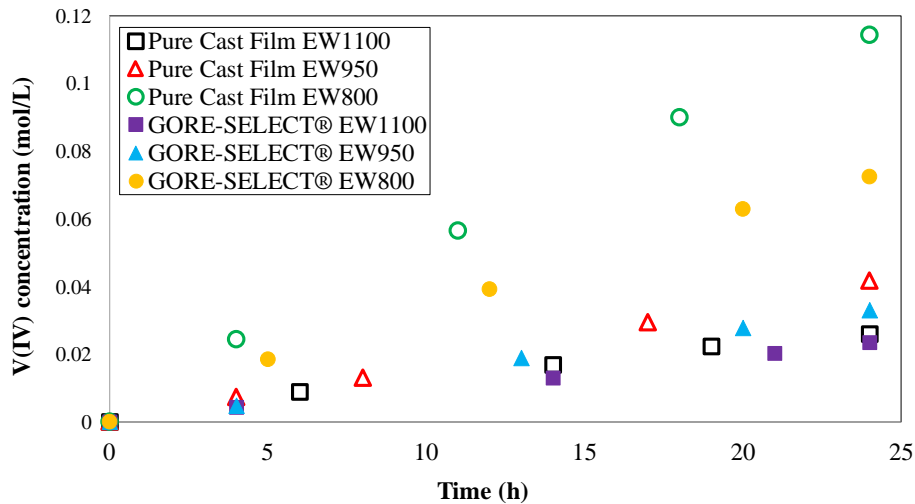


Figure 5-5: Concentration of diffused vanadium V(IV) ion to vanadium-deficient chamber within twenty-four-time period

As shown in Figure 5-6, the nominal thickness for all membranes tested was 30 μm . However, expansion (degree of swelling) differed significantly as a function of membrane properties. As a general trend, for both non-reinforced and reinforced membranes, the expansion was greater for higher equivalent weights. For example, among the non-reinforced membranes, EW1100 exhibits $\sim 62\%$ expansion in the through-plane direction and EW800 shows $\sim 35\%$. However, the reinforced EW1100 membrane expanded by $\sim 29\%$ and reinforced EW800 expanded by $\sim 16.5\%$. As expected, the addition of reinforcement significantly decreases through-plane expansion. The quantitative details of the cation exchange membranes tested in this work are shown in Table 5-2. Figure 5-7 includes the resultant permeability values, based on the linear fits formulated in Equation (5-7).

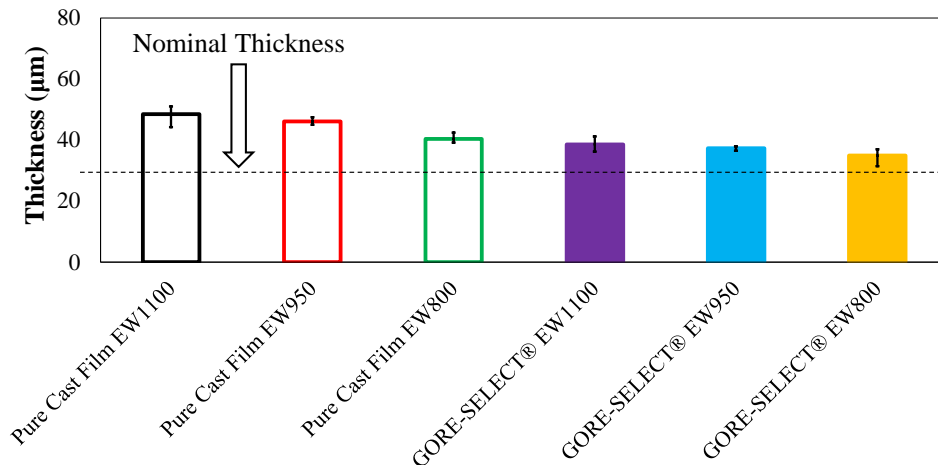


Figure 5-6: Thickness of the membranes after soaking in the solution of 1.5 mol/L V(III)/V(IV) and 3.3 mol/L sulfuric acid

It is important to note that, for calculating the permeability values of V(IV) ions for each membrane, the thickness of the membranes equilibrated with the aqueous vanadium and sulfuric acid (as tabulated in Table 5-2) was utilized.

According to Figure 5-7, it is clear that, for both non-reinforced and reinforced membranes, increasing the equivalent weight decreases the V(IV) ion permeability.

For non-reinforced membranes, decreasing the equivalent weight from 1100 to 950 g.mol⁻¹ increases the V(IV) permeability by 42% and further decreasing the equivalent weight to 800 g.mol⁻¹ results in 155% greater V(IV) permeability.

Table 5.2. The details of the cation exchange membranes utilized in this work

	Manufacturing Details	Nominal Thickness (μm)	Average Thickness after soak (μm)	Through-plane swelling (%)
Pure Cast Film EW1100	Cast film	30	49	62
Pure Cast Film EW950	Cast film	30	46	54
Pure Cast Film EW800	Cast film	30	40	35
GORE-SELECT® EW1100	Reinforced	30	39	29
GORE-SELECT® EW950	Reinforced	30	37	24
GORE-SELECT® EW800	Reinforced	30	35	16

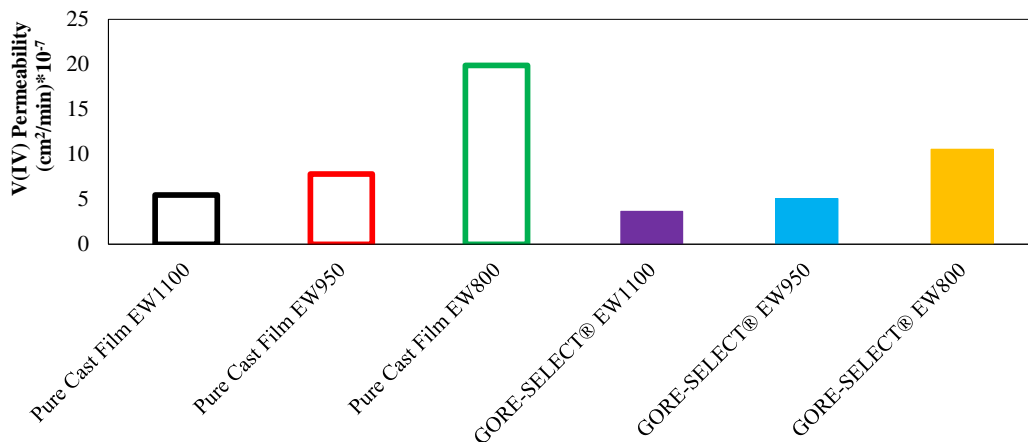


Figure 5-7: Measured permeability values for different membranes

In comparison, for reinforced membranes, decreasing the equivalent weight from 1100 to 950 g.mol⁻¹ increases the V(IV) permeability by 39% and further decreasing the equivalent weight to 800 g.mol⁻¹ further increases the V(IV) permeability by 109%. Table 5-3 includes the numerical values of V(IV) permeability for each ion-exchange membrane as well as the diffusive transport parameter which has been formulated based on Equation (5-8). The diffusive transport parameter is utilized to calculate the concentration-gradient-induced crossover flux according to the mathematical formulation provided in our previous publication²⁰². It is also important to quantify the effect of reinforcement on the reduction of V(IV) permeability. Figure 5-8 is a plot of V(IV) ion permeability and ASR as a function of equivalent weight. When comparing similar equivalent weights, reinforcement decreases the V(IV) permeability for all three compositions considered in this work. However, the effect is not linear. As shown in Figure 5-8, the observed trend for the ASR is the opposite of V(IV) permeability and exhibits an increase as a function of increased equivalent weight and reinforcement. For the EW800 membranes, reinforcement decreased

the V(IV) permeability by ~47%; for EW950, reinforcement decreased the V(IV) permeability by ~35%; and, for EW1100, the reduction of V(IV) permeability as a function of membrane reinforcement was ~33%.

As discussed earlier, the primary reason for capacity fade as a function of cycling was assumed to be the crossover of vanadium ions. Therefore, to validate this assumption, it is critical to investigate any correlation between the discharge capacity decay and the V(IV) ion permeability values. As shown in Figure 5-3, discharge capacity of cells with different configurations decreased as a result of cycling regardless of the type of the membrane, but with different rates.

No contribution is expected from side reactions since the voltage limits avoided their onset and also due to lack of observed gas generation. In addition, component degradation should be negligible or consistent since all tests were conducted under identical conditions. Thus, crossover of vanadium ions should be the primary driver of capacity fade.

Figure 5-9 includes the discharge capacity decay at the end of 30 cycles (or approximately 90 hours) for non-reinforced and reinforced membranes as a function of vanadium V(IV) permeability. In Figure 5-9, the discharge capacity decay data associated with non-reinforced EW800 have been extrapolated since the cycling test for this membrane was only conducted for the first 15 cycles.

Table 5.3. The vanadium V(IV) ion transport parameters through various ion-exchange

	$P_{V(IV)}^m$ ($cm^2 \cdot min^{-1} \times 10^{-7}$)	$A_{V(IV)}^m$ ($cm \cdot min^{-1} \times 10^{-7}$)
Pure Cast Film EW1100	5.49	1131
Pure Cast Film EW950	7.80	1689
Pure Cast Film EW800	19.87	4919
GORE-SELECT® EW1100	3.66	948
GORE-SELECT® EW950	5.08	1361
GORE-SELECT® EW800	10.59	3029

As evident in Figure 5-9, there exists a strong correlation between the discharge capacity decay at the end of cycling with V(IV) permeability values. According to Figure 5-9, for non-reinforced membranes, increasing the equivalent weight from 800 to 950 g.mol⁻¹, decreases the discharge capacity decay (after 90h) from 53% to 25% while decreasing the V(IV) permeability by 61% and further increasing the equivalent weight to 1100 g.mol⁻¹, decreases the discharge capacity decay to 22% while the V(IV) permeability decreases by 30%.

A similar trend was observed for reinforced membranes: increasing the equivalent weight from 800 to 950 g.mol⁻¹ decreases the discharge capacity decay from 31% to 24% while decreasing the V(IV) permeability by 52%; further increasing the equivalent weight from 950 to 1100 g.mol⁻¹ decreases the discharge capacity decay to 21% while decreasing the V(IV) permeability by 28%.

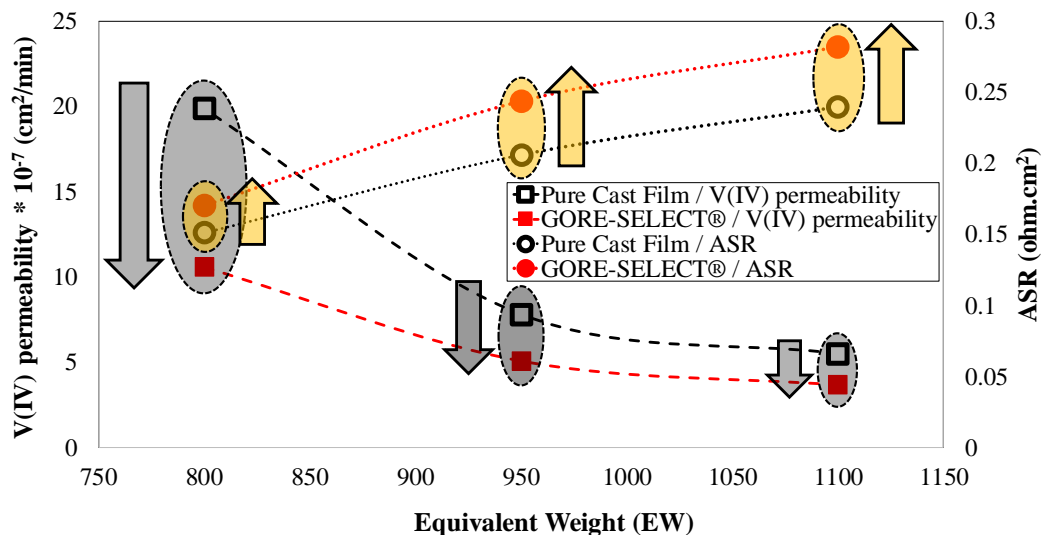


Figure 5-8: Correlation between equivalent weight with V(IV) permeability and ASR

Finally, it is important to quantify vanadium crossover as a function of membrane thickness. As shown in Figure 5-6, the ion-exchange membranes selected for this work all had a nominal thickness of 30 μm ; however, when soaked in a solution of aqueous sulfuric acid and vanadium, they swelled as a function of membrane reinforcement and equivalent weight.

Given the permeability and swelling responses to EW, the following figure (Fig. 5-10) compares vanadium ion permeability (V(IV)) as a function of through-plane membrane swelling. As shown in Figure 5-10, V(IV) permeability decreases for both the pure cast film and GORE-SELECT® membranes as a function of increased through-plane membrane swelling. As tabulated in Table 5.2, increased equivalent weight increases through-plane swelling and this results in reduced permeability for V(IV) ion.

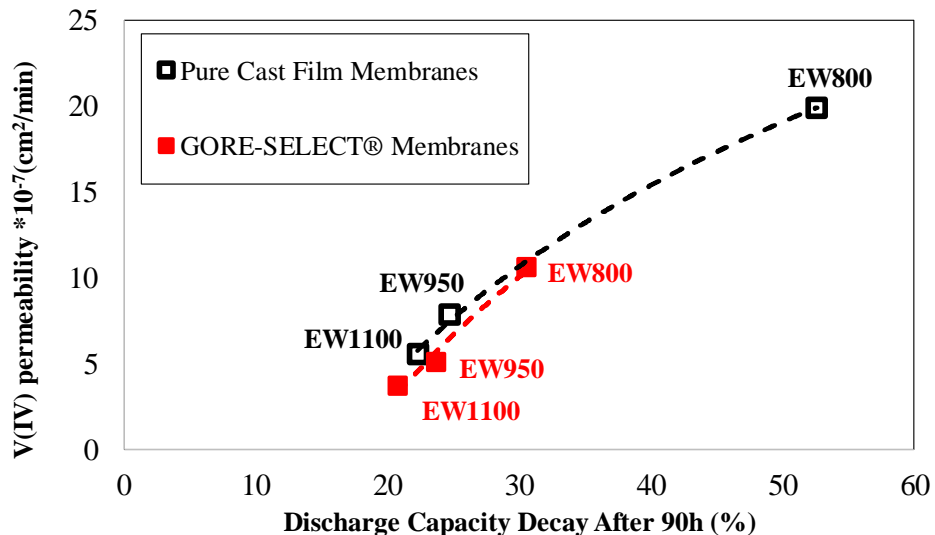


Figure 5-9: The discharge capacity decay at the end of cycling as function of vanadium V(IV) permeability

Therefore, an inverse correlation exists between swelling and permeability for pure cast film and GORE-SELECT® membranes. The likely cause of this relationship is greater membrane thickness impeding V(IV) crossover. A physicochemical description of the two distinct trends observed in Figure 5-8 is also of interest. First, as shown in Figure 5-8, increased equivalent weight results in decreased V(IV) permeability for both pure cast film and reinforced membranes. A macroscopic mathematical model based on conservation of mass, charge, momentum, and energy along with a meso-scale model based on dissipative particle dynamics (DPD) has previously been used to assess vanadium ion crossover behavior due to a concentration gradient²⁰². Based on the macroscopic model of vanadium ion transport through polymeric membranes, vanadium crossover under concentration gradient can be best described by the diffusive transport parameter.

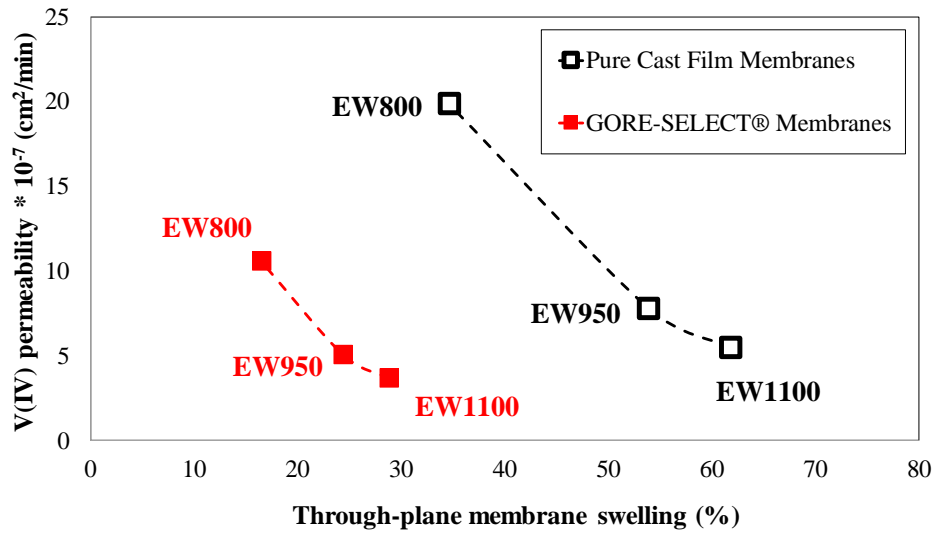


Figure 5-10: Correlation between V(IV) permeability and through-plane membrane swelling

As included in Table 5-3, the diffusive transport parameter decreases with increased equivalent weight. With a concentration-gradient induced driving force for vanadium ion crossover, increased equivalent weight results in greater membrane swelling (as shown in Figure 5-6), resulting in higher diffusion resistance via increased path-length for the transport of vanadium ions; accordingly, the diffusive transport parameter is decreased. A meso-scale model description of vanadium ion transport has also been formulated by others based on DPD simulations and it shows that increasing equivalent weight results in a stronger vanadium-sulfonate bond and accordingly more structured configuration¹⁰². The stronger anion-cation interaction (V(IV) and sulfonate) as a function of increased equivalent weight thus results in decreased diffusivity of vanadium ions¹⁰².

As shown in Figure 5-8, membrane reinforcement results in decreased vanadium ion permeability for all equivalent weights. This observation is likely due to water transport behavior through the membranes; advection of vanadium ions through the membrane is influenced by water transport. It is well-established that water permeability through the membranes is both in equilibrium (solubility) and non-equilibrium (diffusivity) and is a strong function of the porous structure of the membrane^{102, 218}. Water transport has two distinct steps including surface adsorption (permeation through the surface) and internal absorption and transport across the membrane (diffusion); accordingly, the water transport rate is governed by water uptake and release rates. The implementation of reinforcement decreases vanadium ion permeability by acting as a molecular sieve in the porous structure of the membrane. The porous structure of the reinforced layer allows for the transport of water molecules while decreasing the transport of vanadium ions (V(IV)) by size exclusion. Accordingly, the contribution of vanadium ion transport via advection increases with decreased equivalent weight. Therefore, as shown in Figure 5-8, the inclusion of reinforcement results in a sharper decrease in vanadium permeability for lower equivalent weight membranes.

5.4. Summary and Conclusions

In this work, the effects of equivalent weight and membrane reinforcement on capacity fade and crossover in a VRFB system have been experimentally investigated. Three

equivalent weights (800, 950 and 1100 g.mol⁻¹) were considered for non-reinforced and reinforced membranes.

It is shown that vanadium crossover in VRFB systems can be mitigated either by increasing the ion-exchange membrane's equivalent weight or implementing reinforcement. However, there is a tradeoff between decreasing capacity decay and increasing area-specific resistance (ASR), though this tradeoff is strongly dependent on equivalent weight. For non-reinforced membranes, increasing the equivalent weight (EW) from 950 to 1100 g.mol⁻¹ decreases the V(IV) permeability by ~30% but increases the area-specific resistance (ASR) by ~16%. Furthermore, increasing the equivalent weight from 800 to 950 g.mol⁻¹ decreases the V(IV) permeability by ~61% but increases the ASR by ~36%. Comparing the non-reinforced with reinforced membranes, for the EW1100 and EW950 membrane, the ASR increases by ~18% due to membrane reinforcement; but, reinforcement decreases the V(IV) permeability by ~35% for EW950 membranes and by ~33% for EW1100 membranes. However, for the EW800 membranes, reinforcement decreases the V(IV) permeability by ~47% but increases the ASR by ~13%.

Also, it was shown that there exists a direct correlation between the discharge capacity decay over long-term cycling with V(IV) permeability values, confirming that the main contributor to capacity fade during cycling is due to vanadium crossover. As an example, for non-reinforced membranes, increasing the equivalent weight from 800 to 950 g.mol⁻¹, decreases the discharge capacity decay at the end of cycling by ~53% and V(IV)

permeability by ~61%. For reinforced membranes, increasing the equivalent weight from 800 to 950 g.mol⁻¹ decreases the discharge capacity decay at the end of cycling by ~23% and V(IV) permeability by ~52%. This implies that V(IV) crossover tests can be utilized to assess the viability of a particular membrane of interest for long-term VRFB applications.

Finally, increased equivalent weight of the ion-exchange membrane decreases vanadium permeability, resulting in decreased the capacity fade over cycling. When the membranes (pure cast film and GORE-SELECT® membranes) are exposed to aqueous sulfuric acid and vanadium, they swell, but with different magnitudes. Increased equivalent weight increases the extent of swelling in both non-reinforced and reinforced membranes. As a result, the higher equivalent weight membranes impose extra resistance to vanadium crossover via increased diffusion path-length, ultimately reducing capacity fade. Comparing the pure cast and GORE-SELECT® membranes, reinforcement decreases the degree of membrane swelling. However, the degree of vanadium crossover mitigation significantly increases as a function of reinforcement, as well. Since the impact of reinforcement on permeability is greater than that of through-plane swelling, reinforced ion-exchange membranes with higher equivalent weight best mitigate vanadium crossover. The results of this study should provide deeper insight for ion-exchange membrane developers seeking optimized membrane structures for reduced vanadium ion and water crossover.

5.5. Acknowledgments

Yasser Ashraf Gandomi would like to acknowledge University of Tennessee for providing a Chancellors Graduate Fellowship. The authors also thank W. L. Gore for providing the ion-exchange membranes and fruitful discussions.

5.6. Nomenclature

$V_{v,d}$	Volume of the vanadium-deficient electrolyte [m ³]
$C_{v,d}$	Concentration of V(IV) ion in vanadium-deficient electrolyte [mol/ m ³]
$C_{v,e}$	Concentration of V(IV) ion in vanadium-enriched electrolyte [mol/ m ³]
$P_{V(IV)}^m$	Permeability of V(IV) ion through membrane m [m ² /s]
t_m	Thickness of ion-exchange membrane [m]
A	Area of the ion-exchange membrane [m ²]
$\Lambda_{V(IV)}^m$	Diffusive transport parameter of V(IV) ion through membrane m [m/s]

CHAPTER SIX :
REALTIME INFLUENCE OF IONIC CROSSOVER ON THE PERFORMANCE
OF REDOX FLOW BATTERIES

Scholarly contributions

The Abstract is revised based on the talk presented in 232th Electrochemical Society (ECS) Meeting & Electrochemical Energy Summit, National Harbor, MD (Oct. 1-5, 2017).

- Abstract ID: MA2017-02 3
- Title: Direct Observation of Crossover and Current Distribution in All-Vanadium Redox Flow Batteries

This chapter is revised based on the manuscript prepared for submission to the Journal of Power Sources.

Yasser Ashraf Gandomi, T. Y. Ertugrul, D. S. Aaron, M. M. Mench. “Probing real-time influence of ionic crossover on the performance of redox flow batteries using in-plane current distribution diagnostics” *in preparation*, (2018).

Abstract

One of the critical ways to improve the performance of all-vanadium redox flow batteries (VRFBs) is through improved cell design and material selection. However, there are certain issues yet to be addressed, including overcoming rapid capacity decay over long-term cycling, and deeper understanding of the contributions to this decay. The primary reason for capacity loss during cycling is undesired vanadium ion and water transport through the ion-exchange membrane (usually labeled crossover).

One common technique for mitigating the capacity loss is utilization of thicker membranes along with periodic electrolyte rebalancing (further details are available in Chapters 8 and 11). However, these techniques are only partially effective, and each introduces additional performance losses in the system. Accordingly, the focus of active research is to develop new ion exchange membranes with reduced crossover and improved ionic conductivity.

Usually, long term cycling experiments are conducted to assess the influence of ionic crossover on discharge capacity decay. However, the crossover of ionic species, for high permeable membranes, can indeed has real-time influence on the cell performance. To the best of our knowledge, no previous work has reported the real-time and instantaneous effect of crossover on the cell performance.

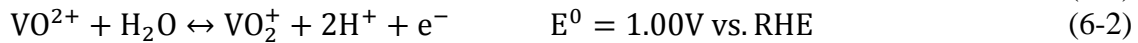
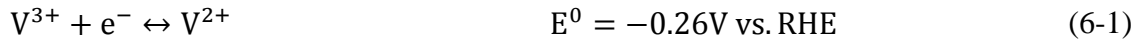
Therefore, in this chapter, we have implemented two diagnostics techniques to probe the real-time influence of ionic crossover on the long-term and short-term cell metrics. First, we have designed and built the IonCrG (Ionic Crossover Gauge: Unique experimental setup equipped with UV/Vis spectroscopy capable of measuring rate of ionic crossover in real-time) to analyze the rate of ionic crossover for series of ultra-thin and high-performance ion-exchange membranes. Subsequently, passive, real-time, in-plane distributed current measurement has been conducted to explore the instantaneous influence of ionic crossover on the cell performance. The in-plane current distribution setup utilized printed circuit board along with fully segmented flow plates to prevent lateral current spread. Utilizing current density distribution diagnostics, in-plane distribution of vanadium ions has been assessed. To the best of our knowledge, there is no published work focused on the investigation of in-plane distribution of vanadium ion crossover. Therefore, here, for the first time, we have demonstrated that the localized current distribution for an operando redox flow battery is not solely a function of electrolyte transport in the electrode due to the combined effects of diffusion, advection, and migration; it is also affected by the vanadium ion crossover.

6.1. Introduction

Energy storage systems have grown substantially during last years in various technological formats including thermal storage, flywheels, pumped-hydro, secondary batteries and supercapacitors. Redox flow batteries, as secondary batteries, utilize an open structure. Utilizing an open configuration, RFBs can be tailored for delivering desired output power without a need for altering the storage capacity. From the other side, time of service, or storage capacity, can be engineered independently without affecting the size and configuration of the reactor. Therefore, such a scalable architecture enables RFBs with vast engineering opportunities for the cell stack, electrolytes, operating conditions, auxiliary units, and infrastructure.

The major impediment preventing wide-spread adoption of RFBs as a major energy storage medium is the cost. Several parameters contribute to the overall cost of an RFB cell that among them, the size of the reactor is a significant contributor. One possible pathway for reducing the overall cost of RFBs is decreasing the size of the reactor while maintaining the desired output power. Therefore, designing high-performance cells capable of operation at high-current densities is of a great interest ¹². Various chemistries developed for negative and positive electrolytes of RFBs with the objective of enabling robust, stable, and high-performance operation while reducing the capital cost of the battery ¹⁴. However, during the operation of a RFB cell, the transport of electroactive species from one electrolyte through the ion-exchange membrane to the other electrolyte (generically called crossover) is usually unavoidable (Please see Chapter 8 for further analysis). This

undesired ionic transport usually results in an irreversible capacity loss of the battery due to initiating parasitic side-reactions. However, for all-vanadium redox flow batteries (VRFBs) the unwanted crossover of vanadium ions through the membrane does not result in a permanent discharge capacity loss since the negative and positive electrolytes share the same metallic element (but with different oxidation states; V(II), V(III), V(IV), and V(V)). The following simplified half-reactions are usually considered to occur on the negative and positive electrodes of a typical VRFB ²⁰².



Nonetheless, the transport of vanadium ions and water for VRFBs is undesirable since it adversely affects the capacity (long-term influence of crossover) and performance (instantaneous influence of crossover).

First, when vanadium ions transport through the ion-exchange membrane, they discharge the charged ions (V(II) in the negative electrolyte, and V(V) in the positive electrolyte); decrease the state of charge (SoC) and consequently reduces the discharge capacity. This undesired ionic transport is commonly known as self-discharge process ¹⁰².

Second, the parasitic side-reaction being initiated due to the crossover of vanadium ions (as formulated above) along with the transport of water across the membrane, disturbs the state of charge (SoC) balance of negative and positive electrolytes, and consequently reduces the discharge capacity ²⁰².

Therefore, the long-term influence of vanadium and water crossover is limiting the discharge capacity of the battery via shrinking the SoC window in either negative or positive electrolytes. This unfavorable long-term influence on the capacity has been the subject of several modeling and experimental studies^{102, 174, 179, 202, 213}.

The crossover of vanadium ions, however, can also impact the performance of the battery in real-time (we refer to it as instantaneous influence of crossover) and this phenomenon, based on our best knowledge, has not been explored in the literature yet. Therefore, in this chapter, we have explored the instantaneous impact of vanadium crossover on the cell performance using real-time, in-plane current distribution diagnostics.

In-plane distributed current measurement has already been demonstrated for VRFBs along with other electrochemical devices. Previous efforts on utilizing distributed current measurement have only explored the variations in current density distribution across the electrode as a function of electrolyte transport in the electrode due to the combined effects of diffusion, advection, and migration.

Therefore, in this chapter, for the first time, the dependency of distributed current measurement on the vanadium ion crossover has been reported.

6.2. Experimental

6.2.1. Ultra-thin high-performance membranes for all-vanadium redox flow batteries

A series of ultra-thin high-performance ion-exchange membranes with various equivalent weight (EW) and degree of reinforcement were provided by W. L. Gore and Associates (Newark, DE).

The membranes were labeled as “GORE-SELECT®” or “pure cast film” based on the degree of reinforcement. Three different configurations of the ion-exchange membranes with equivalent weights of 800, 950 and 1100 g.mol⁻¹ were tested. Table 6.1 includes further details regarding the membranes tested in this work.

Table 6.1. Details of ultra-thin ion-exchange membranes tested in this work (Ref. ¹⁰²)

	Nominal thickness (µm)	Manufacturing details
Pure Cast Film EW1100	30	Cast Film
Pure Cast Film EW950	30	Cast Film
Pure Cast Film EW800	30	Cast Film
GORE-SELECT® EW1100	30	Reinforced
GORE-SELECT® EW950	30	Reinforced
GORE-SELECT® EW800	30	Reinforced

The membrane characterization included long-term cycling within aggressive state of charge and state of discharge window, AC impedance tests, ex-situ membrane characterization, and ionic crossover experiments. Summary of the results related to characterization of the membrane series is listed in Table 6.2. The readers are encouraged to refer to a relevant publication for further details ¹⁰². Table 6.2 includes the average thickness of the membranes swelled in the electrolyte (1.5 mol/L VOSO₄.xH₂O (Alfa Aesar, USA) dissolved in 3.3 mol/L sulfuric acid (H₂SO₄)), ionic permeability to V(IV), and discharge capacity decay for cycling at current density of 100 mA/cm² with an aggressive cut-off voltage window (0.2 V - 1.9 V). As listed in Table 6.2, the long-term discharge capacity decay drastically changes for different membranes. ion.

Table 6.2. The details regarding membranes swelling, ionic permeability, and long-term discharge capacity decay for the ion-exchange membranes (Data adopted from our previous publication, Ref. ¹⁰²)

	Average thickness after swelled in the electrolyte (μm)	$P_{V(IV)}^m$ (cm ² .min ⁻¹ × 10 ⁻⁷)	Discharge capacity decay after 90 hours (%)
Pure Cast Film EW1100	49	5.49	22.3
Pure Cast Film EW950	46	7.80	24.7
Pure Cast Film EW800	40	19.87	52.6
GORE-SELECT® EW1100	39	3.66	20.8
GORE-SELECT® EW950	37	5.08	23.7
GORE-SELECT® EW800	35	10.59	30.6

Here, our objective is to explore real-time influence of ionic crossover in the cell performance. Therefore, among the membranes listed in Table 6.2, GORE-SELECT® EW1100 and Pure Cast Film EW800 were selected since they demonstrated the highest ($3.66 \times 10^{-7} \text{ cm}^2 \cdot \text{min}^{-1}$) and lowest ($19.87 \times 10^{-7} \text{ cm}^2 \cdot \text{min}^{-1}$) permeability to V(IV). It is also important to note that the long-term capacity decay (cycling $100 \text{ mA} \cdot \text{cm}^{-2}$ for 90 hours) associated with GORE-SELECT® EW1100 and Pure Cast Film EW800 was 20.8% and 52.6% respectively. Therefore, the application of GORE-SELECT® EW1100 as the separator resulted in lowest ionic crossover along with reduced long-term capacity decay. However, utilization of Pure Cast Film EW800 as the membrane within VRFB structure resulted in a very high ionic crossover and subsequent substantial capacity decay (52.6%) during cycling. Characterizing the long-term influence of ionic crossover on capacity decay is very informative, however, it is not enough. It is crucial to probe the influence of ionic crossover on the real-time performance of the cell since according to the following equations, crossover of ionic species results in self-discharge²⁰².



The self-discharge reactions listed above subsequently decreases state of charge for an operating cell if the membrane is very permeable to vanadium ions. Therefore, here, we have probed the influence of real-time ionic crossover on the cell performance and self-discharge reactions via utilizing distributed current diagnostics for GORE-SELECT® EW1100 and Pure Cast Film EW800 membranes.

6.2.2. Distributed Current Diagnostics for real-time assessment of ionic crossover

The implementation of distributed current diagnostics has already been demonstrated for VRFBs²²⁰. Similar setup has been used in this work for assessing the real-time influence of ionic crossover on the cell performance. Schematic of the setup has been shown in Fig. 6-1.

As shown in Fig. 6-1, the distributed current diagnostics utilizes segmented printed circuit board (PCB). As shown in Fig. 6-1, the segmented PCB is a passive approach to assess 2D, Realtime, and in-plane current distribution for an operating cell. The segmented PCB utilized segments in square shape (4.5 mm × 4.5 mm) with segment spacing of 0.5 mm. Further details regarding the schematic of segmented PCB board is available elsewhere²²¹. As shown in Fig. 6-1, fully segmented flow fields were used along with segmented PCB. The application of fully segmented flow plates enabled recording the distributed current without any lateral current spread¹. Two different configurations of fully segmented flow plates were used (serpentine and square flow-through). Further details regarding the geometrical properties of the flow plates are listed in the following table.

The electrodes shown in Fig. 6-1, were pristine 39AA carbon paper electrodes (SGL Group, Germany) without any prior treatment. As discussed in Section 6.2.1, two various configurations of ion-exchange membranes (i.e. GORE-SELECT® EW1100 and Pure Cast Film EW800) were used within distributed current diagnostics shown in Fig. 6-1.

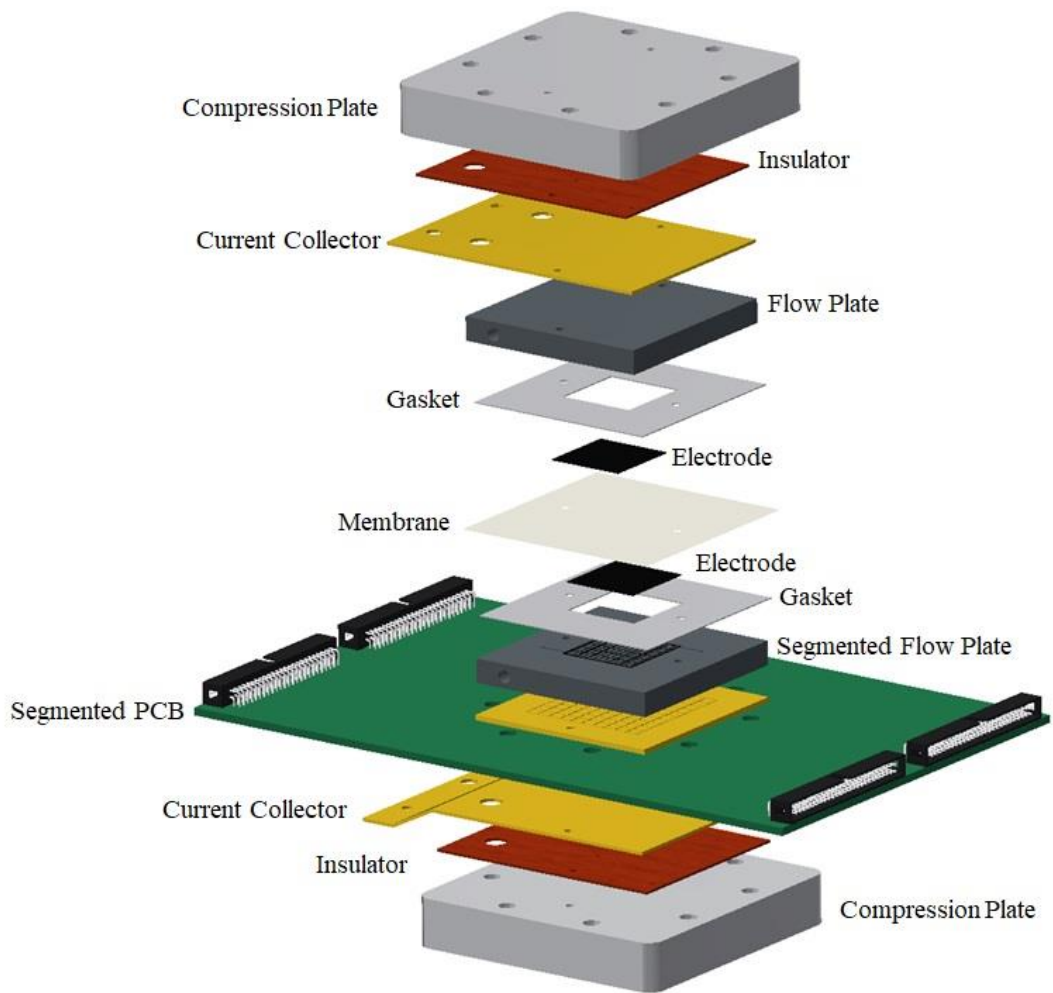
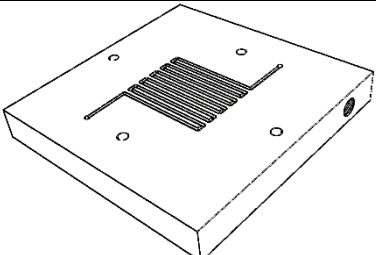
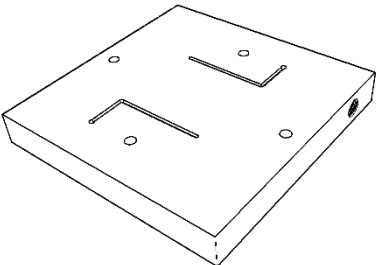


Figure 6-1: Schematic of the distributed current diagnostic setup

Table 6.3. Geometrical details regarding fully segmented flow fields

	Flow field geometry (cm ²)	Channel geometry (mm ²)
 Serpentine	3 × 3	1 × 1
 Square flow-through	3 × 3	1 × 1

To control the cell in the desired load (potentiostatic or galvanostatic mode), a multichannel potentiostat (Arbin Instrument, College Station, TX) was utilized. To obtain distributed current data, ribbon cables were attached to the segmented PCB board and the LabVIEW™ (with scripts written in-house) was used to record the data in real-time. The data acquisition was conducted for 6 seconds with 1 second intervals. The final data were averaged over 6 seconds. To better illustrate the deviations in distributed current data, a percent deviation from the average current across the entire distribution was used. It is worth mentioning that the placement of segmented PCB board (being in negative (V(II)/V(III)) or positive (V(IV)/V(V) sides) has very minor influence on the distributed current²²¹, therefore, here, the influence of the PCB board placement on the results has been neglected.

6.3. Results and Discussion

The details regarding membrane characterization and polarization curve assessments for the series of membrane listed in Table 6.2 are available in Chapter 5 and are also available in a relevant publication ¹⁰². In this section, we have only focused on the localized distributed current analysis for different membranes.

The distributed current for all-vanadium redox flow battery has already been explored for various operating conditions. The previous works, however, have not reported the influence of variations in membrane properties on the distribution. Therefore, here, we have investigated the variations in the distributed current for different membranes along with different flow plate designs. The initial electrolytes were prepared using a protocol described in Chapter 4 and in a recent publication ²⁰². The electrolytes contained 1 mol.L⁻¹ vanadyl sulfate (Alfa Aesar, USA) with 3.3 mol.L⁻¹ sulfuric acid as supporting electrolyte with the water as the solvent. After initial preparation, the electrolytes were charged to 100% state of charge and single-path electrolyte circulation was implemented to confirm the uniformity in the state of charge. Further details regarding the implementation of single-path electrolyte circulation technique is available in a recent publication from our group ¹.

The operating conditions, electrode morphology (porosity, tortuosity, and wettability), flow field designs, state of charge and compression has all been shown to affect the distributed current. As mentioned earlier, this work, for the first time, reports the influence of variations in the membrane morphology on the distributed current. To this end, it was

necessary to make sure the other contributing parameters remain unchanged among various cell assemblies.

The protocol used for assembling the cells was similar for various membranes. However, the membrane morphology directly influences the degree of expansion and swelling. In this work, GORE-SELECT® EW1100 and Pure Cast Film EW800 membranes were. According to Table 6.2, the swelling state for these membranes is similar after being soaked within the vanadium electrolyte. Therefore, it is safe to assume that the compression state between different cell assemblies remained unchanged.

To conduct the distributed current experiments, different operating points within the polarization curves can be chosen. However, to illustrate the influence of membrane morphology on the distributed current, we have operated the cells at ultra-high current density regime.

6.3.1. The influence of convection flux on the distributed current measurement

To illustrate the influence of convective flux on the distributed current measurements, two different cell configurations along with two different flow rates (30 and 50 mL.min⁻¹) were considered. The first configuration utilized flow-through flow fields with GORE-SELECT® EW1100 and Pure Cast Film EW800 membranes as shown in Fig. 6-2.

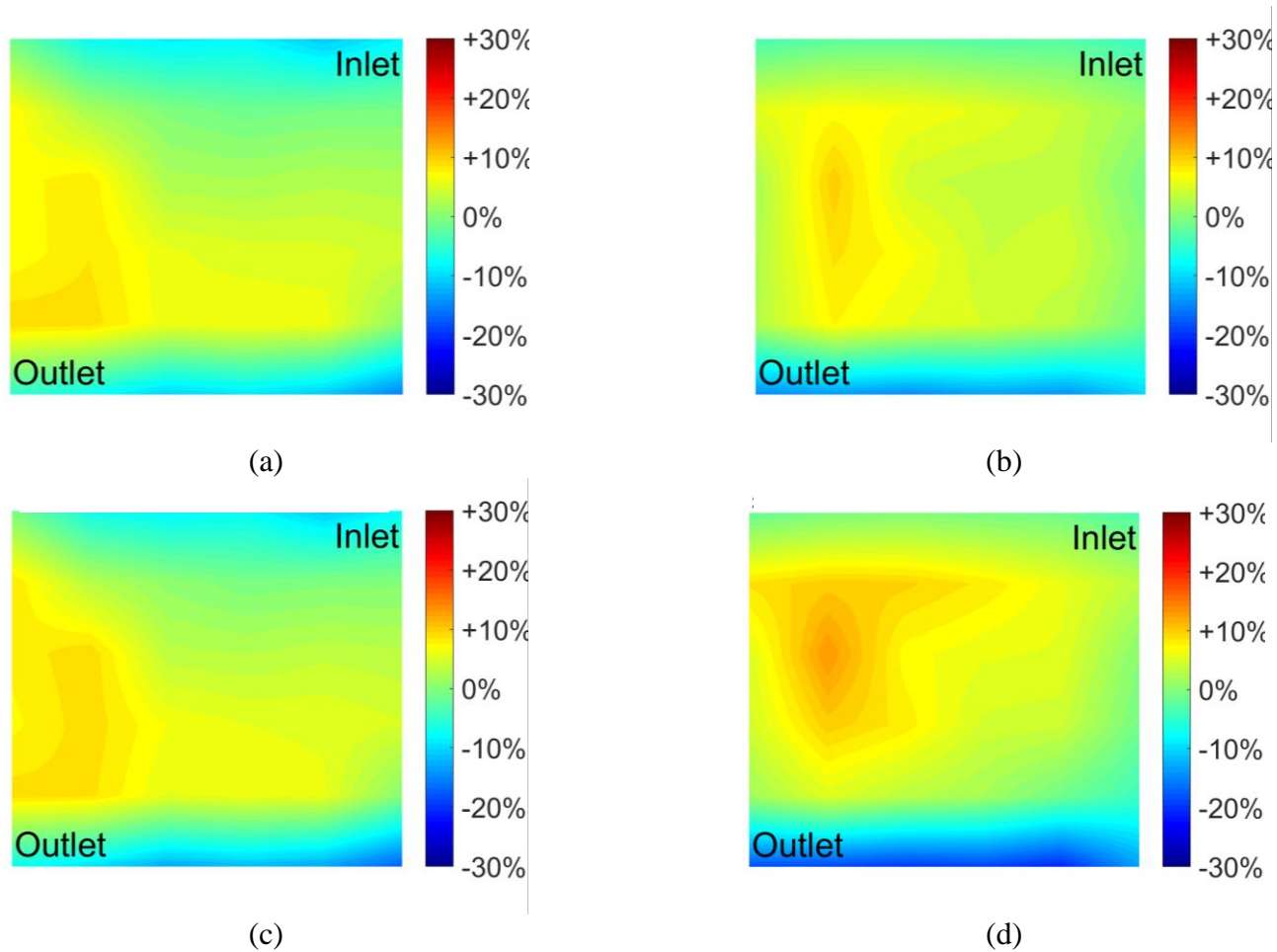


Figure 6-2: Distributed current measurement for square flow-through flow field topology at high convective flow regime. (a) GORE-SELECT® EW1100 / 50 mL.min⁻¹, (b) Pure Cast Film EW800 / 50 mL.min⁻¹, (c) GORE-SELECT® EW1100 / 30 mL.min⁻¹, (d) Pure Cast Film EW800 / 30 mL.min⁻¹

As shown in Fig. 6-2, the distributed current value has been shown as percentage deviation from the average current. In Chapter 5, comprehensive analysis provided comparing the polarization behavior of cells with GORE-SELECT® EW1100 and Pure Cast Film EW800 membranes. Very similar performance was demonstrated at medium and low operating conditions. Following similar approach, here, the main focus was to explore ultra-high current density regimes. Therefore, all the cells were operated at the maximum current density via holding the potential at 0.2 V.

The electrochemical impedance spectroscopy analysis at high frequency was conducted and the area specific resistance for GORE-SELECT® EW1100 and Pure Cast Film EW800 membranes were 0.282 and 0.151 ohm.cm² (Details are available in Chapter 5 and in Ref. 102).

Therefore, the ohmic overpotential associated with GORE-SELECT® EW1100 membrane is significantly higher. Operating at 0.2 V for the cell with GORE-SELECT® EW1100 membrane resulted in a discharge current of 21 and 19 A at 50 and 30 mL.min⁻¹. However, due to reduced ohmic losses, the cell with Pure Cast Film EW800 membrane was discharged at 35 and 33 A at 50 and 30 mL.min⁻¹.

Despite having significantly different current values, the current distribution was similar for these two configurations. In addition, as demonstrated in Fig. 6-2, the cells are not limited by mass transport limitations since the current is evenly distributed across the entire

electrode. Therefore, it can be concluded that the influence of membrane permeability on the real-time performance of the cell for high convective flow conditions is minor. Figure 6.3 includes cell configurations with GORE-SELECT® EW1100 or Pure Cast Film EW800 membrane and serpentine flow fields at two different flow rates (at 50 and 30 mL.min⁻¹).

As shown in Fig. 6-3, for high flow rate operation (30 and 50 mL.min⁻¹), no significant difference is detectable in the distributed current pattern for the cells using serpentine flow plate along with GORE-SELECT® EW1100 or Pure Cast Film EW800 membranes. This observation is consistent with the results obtained for flow-through flow field configuration (Fig. 6-2).

Comparing the variations observed within the current distribution patterns for the cells with either GORE-SELECT® EW1100 or Pure Cast Film EW800 at volumetric flow rate of 30 and 50 mL.min⁻¹ confirms that the cells are not limited by mass transport limitations; thus, relatively similar current distribution was achieved.

In addition, from Fig. 6-3, it can be inferred that the influence of membrane permeability on the real-time performance of the cells with serpentine flow plates operating at high convective flow regimes is miniscule.

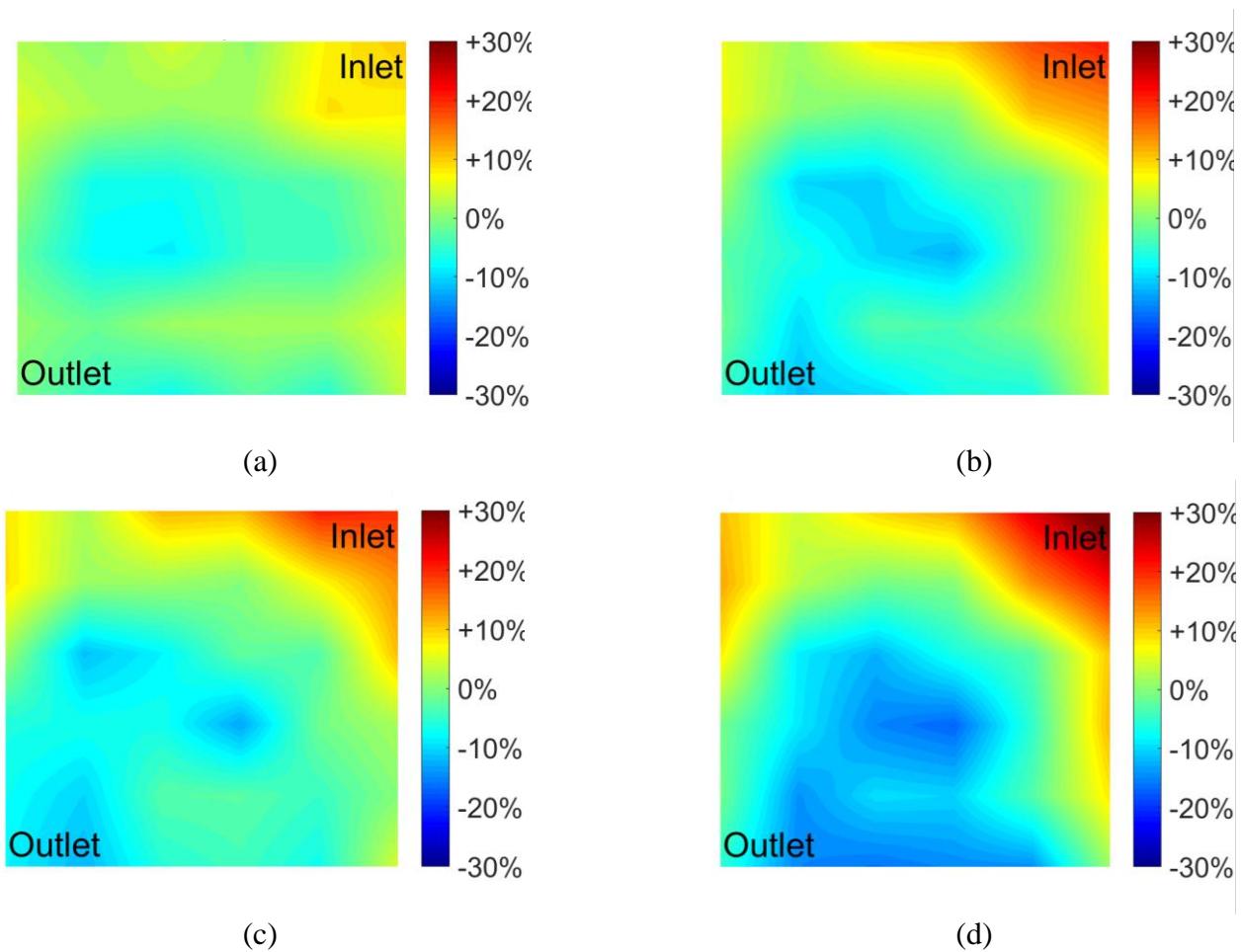


Figure 6-3: Distributed current measurement for serpentine flow field topology at high convective flow regime. (a) GORE-SELECT® EW1100 / 50 mL.min⁻¹, (b) Pure Cast Film EW800 / 50 mL.min⁻¹, (c) GORE-SELECT® EW1100 / 30 mL.min⁻¹, (d) Pure Cast Film EW800 / 30 mL.min⁻¹

6.3.2. The influence of membrane morphology on the real-time distributed current

In previous section (Section 6.3.1) the influence of convective flux on the distributed current across the electrodes were discussed. Two configurations for flow fields (square flow-through and serpentine) along with two different membrane structures (GORE-SELECT® EW1100 or Pure Cast Film EW800) was considered. It was shown that the influence of membrane permeability on the real-time performance of the cell is minor if the stoichiometry of the redox active species is high within the cell (i.e. the cells are not operating under mass transport limitations). However, increased convective flux increases the pressure drop across the cell and subsequently reduces the energy efficiency of the system. Therefore, it is important to explore the performance limitations at relatively lower stoichiometries. In this section, the distributed current data have been provided for cells operating at reduced convective flux. Figure 6-4 demonstrates the distributed current data for cell configurations utilizing flow-through flow fields with various membranes.

Figure 6-4, includes the distributed current data for flow-through flow field configurations with GORE-SELECT® EW1100 or Pure Cast Film EW800 membranes at 5 and 10 mL.min⁻¹. Comparing the distributed current data provided in Fig. 6-2 and Fig. 6-4, it is apparent that reducing convective flux (reducing the volumetric flow rate by one order of magnitude) results in severe mass transport limitations. It is also important to compare the distributed data obtained from current distribution diagnostics with the mathematical model predictions provided in Chapter 3. Figure 6-5 includes such a comparison for square flow-through flow plates.

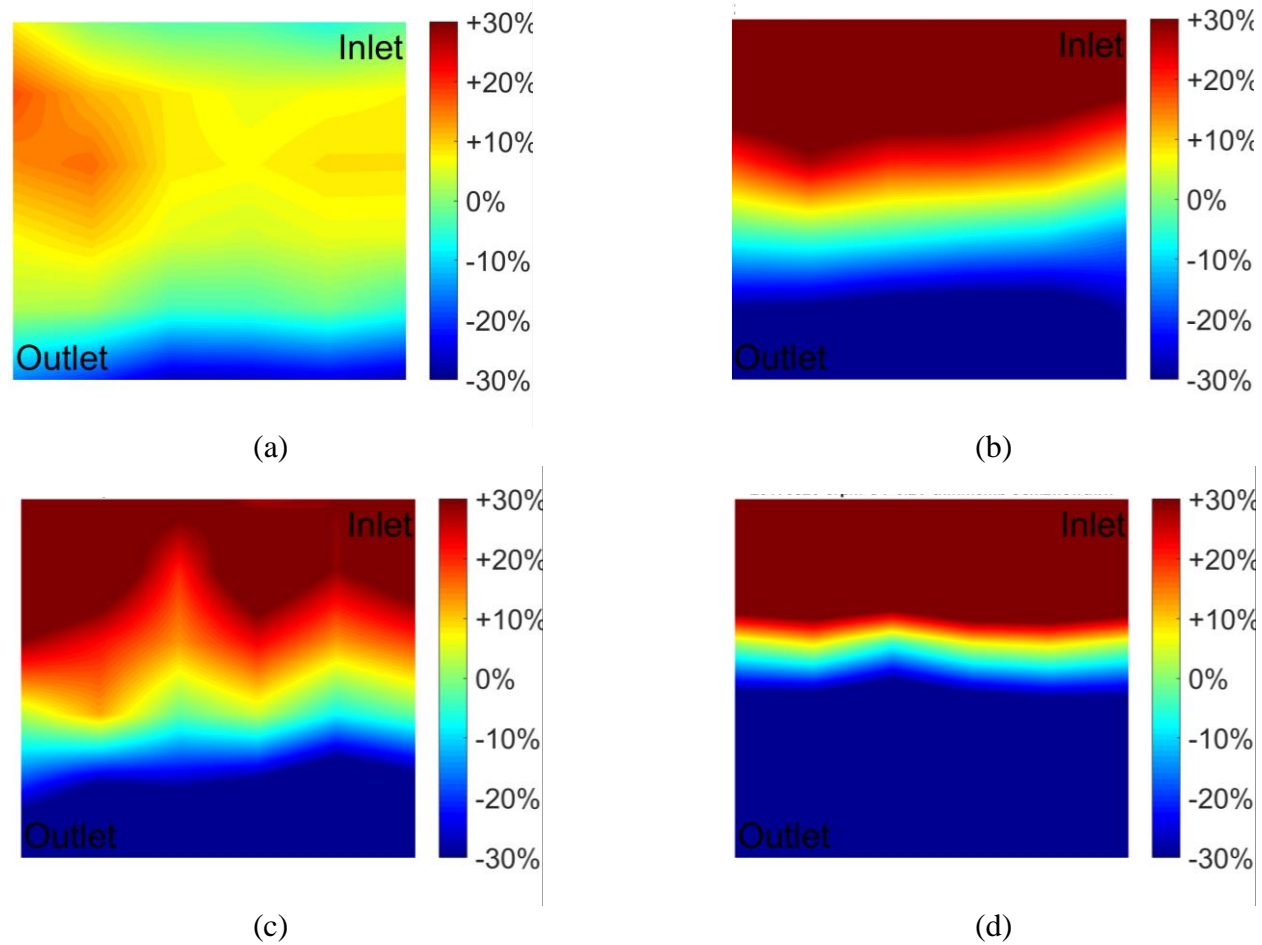


Figure 6-4: Distributed current measurement for square flow-through flow field topology at low convective flow regime. (a) GORE-SELECT® EW1100 / 10 mL.min⁻¹, (b) Pure Cast Film EW800 / 5 mL.min⁻¹, (c) GORE-SELECT® EW1100 / 10 mL.min⁻¹, (d) Pure Cast Film EW800 / 5 mL.min⁻¹

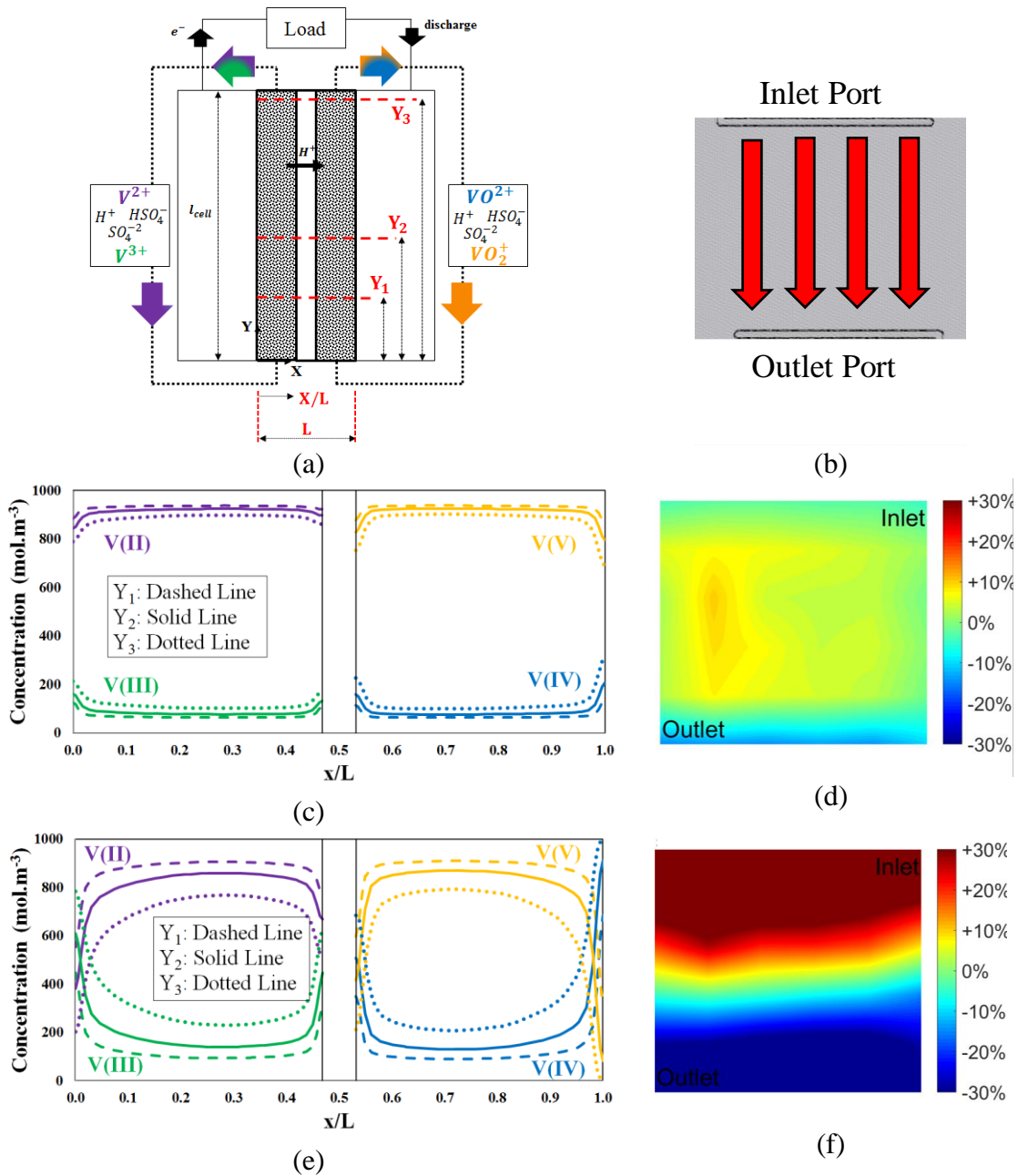


Figure 6-5: Comparison of model simulation with experimentally measured distributed current for flow-through flow fields. (a) Schematic of the computational model domain (Ref. ¹²⁷) (b) Schematic of the flow direction in distributed current measurement setup (c) Predicted concentration depletion along flow direction at low convective flux (Ref. ¹²⁷) (d) Experimentally measured distributed current at high convective flux (e) Predicted concentration depletion along flow direction at low convective flux (Ref. ¹²⁷) (f) Experimentally measured distributed current at low convective flux

Figure 6-5 compares the mathematical model predictions for the electroactive species (V^{2+} , VO_2^+) concentration depletion through the electrode with experimentally measured distributed current for various flow regimes. The schematic of the computational setup has been shown in Fig. 6-5(A) where the electrolytes at high state of charge (100%) is supplied to the cell (The schematic shown in Fig. 6-5(a) is adopted from Yasser Ashraf Gandomi et al. ¹²⁷). Fig. 6-5(b) demonstrates the direction of the flow within fully segmented flow-through flow plates used to obtain the distributed current data shown in Figs. 6-5(d) and 6-5(f).

Along the flow and through the electrodes, when the electrochemical load is applied, the concentration of electroactive species in the negative ($V^{2+} \rightarrow V^{3+} + e^-$) and positive ($VO_2^+ + 2H^+ + e^- \rightarrow VO^{2+} + H_2O$) sides deplete and subsequently state of charge decreases. As shown in Fig. 6-5(c) for high convective flow regimes (here, $50 \text{ mL}\cdot\text{min}^{-1}$ equivalent to $5.56 \text{ mL}\cdot\text{min}^{-1}\text{cm}^{-2}$) the model predicts negligible change in the concentrations of charged species (V^{2+} , VO_2^+) along the flow direction within the electrodes (Fig. 6-5(c) is adopted form Yasser Ashraf Gandomi et al. ¹²⁷). Figure 6-5(d) demonstrates the distributed current measured for an operating cell at $50 \text{ mL}\cdot\text{min}^{-1}$. As shown in Fig. 6-5(d) the distribution of the current across the entire electrode is relatively uniform confirming the model predictions shown in Fig. 6-5(c).

The model prediction of electroactive species depletion along the flow direction within the electrode has been shown in Fig. 6-5(e) for a low stoichiometric operating condition (i.e. 5

mL.min⁻¹ equivalent to 0.556 mL.min⁻¹cm⁻²). Therefore, a significant reduction in the concentration of charged species along the flow is predicted that subsequently results in mass transport limitations (Fig. 6-5(c) is adopted from Yasser Ashraf Gandomi et al. ¹²⁷). The experimentally measured distributed current (Fig. 6-5(f)) for low flow rate operation further confirms the predictions made by the model.

As illustrated in Fig. 6-5(f), the concentration of charged vanadium ions (V(II)) decreases along the flow direction and subsequently full depletion happens towards the outlet port. It is important to note that although the distributed current data have been recorded for the negative side (V(II)/V(III)), similar distributed current is expected for the positive side (V(IV)/V(V)) since the placement of fully segmented plate along with segmented printed circuit board has no influence on the distributed current analysis. Comparing Figs. 6-5(e) and 6-5(f), very good agreement was achieved between model predictions and experimentally measured distributed current.

Establishing a good correlation between the model predictions and experimentally measured distributed current, the influence of membrane permeability on the distributed current can be investigated with higher level of certainty. Figure 6-4(a) and 6-4(b) illustrates the influence of the membrane permeability on the distributed current. Comparing the distributed current provided in Fig. 6-4(a) for the cell utilizing square flow-through flow plates and GORE-SELECT® EW1100 membrane with a cell with similar configuration and Pure Cast Film EW800 membrane reveals that the increased ionic

permeability associated with Pure Cast Film EW800 membrane has resulted in significant self-discharge reaction according to the set of equations formulated in Eq. (6-3) through Eq. (6-6).

Similar trend was observed where the volumetric flow rate decreased to $5 \text{ mL}\cdot\text{min}^{-1}$ (equivalent to $0.556 \text{ mL}\cdot\text{min}^{-1}\text{cm}^{-2}$) where the cell configuration with Pure Cast Film EW800 membrane demonstrates a developed mass transport limited region within ~50% depth (measured from the inlet port) into the electrode (Fig. 6-4(d)). However, a fully mass transport limited condition was not observed for the cell configuration with the Pure Cast Film EW800 membrane until ~75% depth within the electrode. Therefore, the self-discharge reactions due to ionic crossover noticeably increased when the Pure Cast Film EW800 membrane was used; thus, at lower stoichiometric flows, the real-time distributed current through the electrode was significantly altered.

It is also important to explore the influence real-time ionic crossover on the distributed current for cell configurations utilizing different flow field designs. Therefore, here, serpentine flow plates (as schematically shown in Fig. 6.3) with two different membrane structures and the relevant distributed currents were recorded at lower flow rates. Figure 6-6 includes the variations in distributed current for cell configurations with serpentine flow fields and GORE-SELECT® EW1100 or Pure Cast Film EW800 membrane at relatively low stoichiometric flow (10 and $5 \text{ mL}\cdot\text{min}^{-1}$).

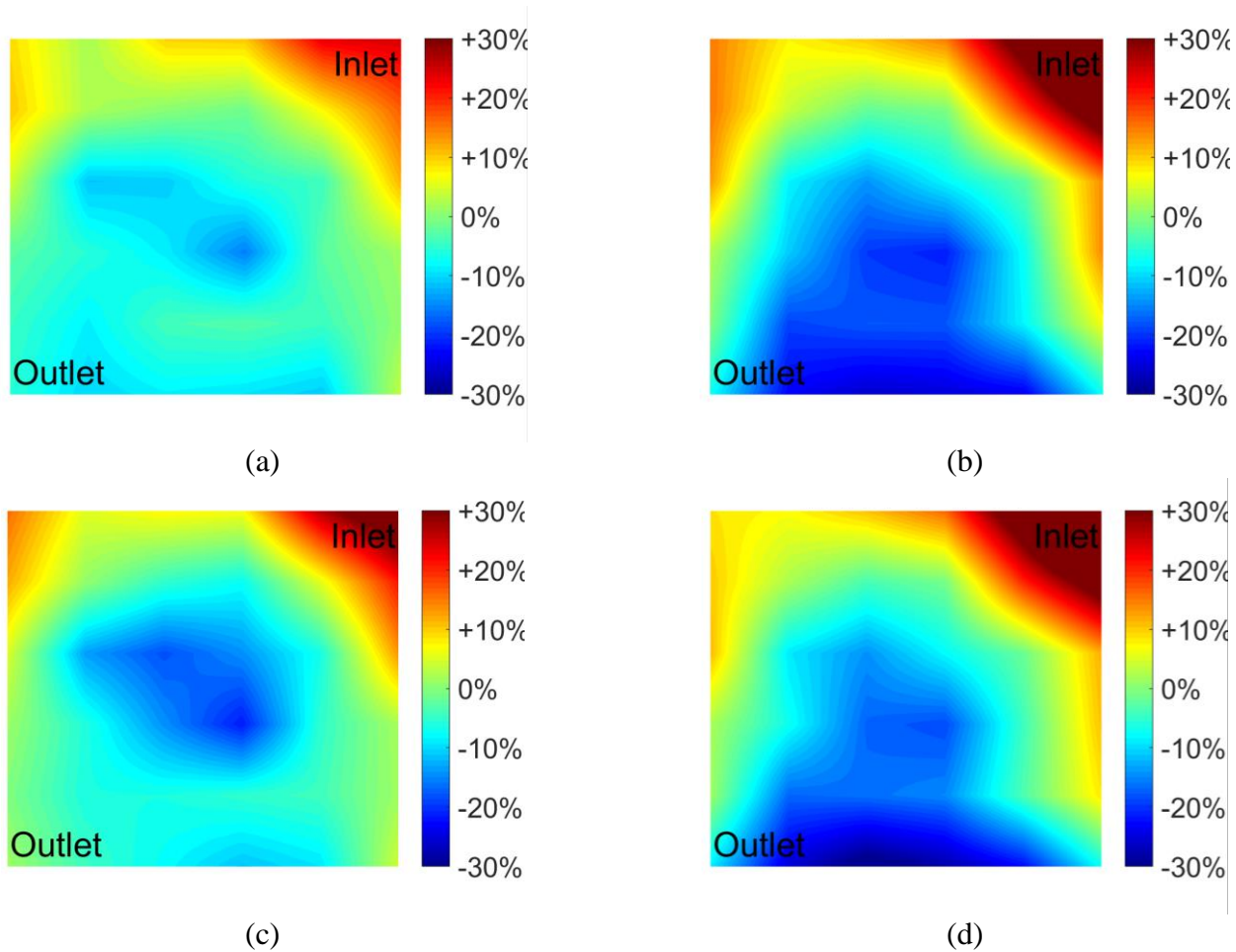
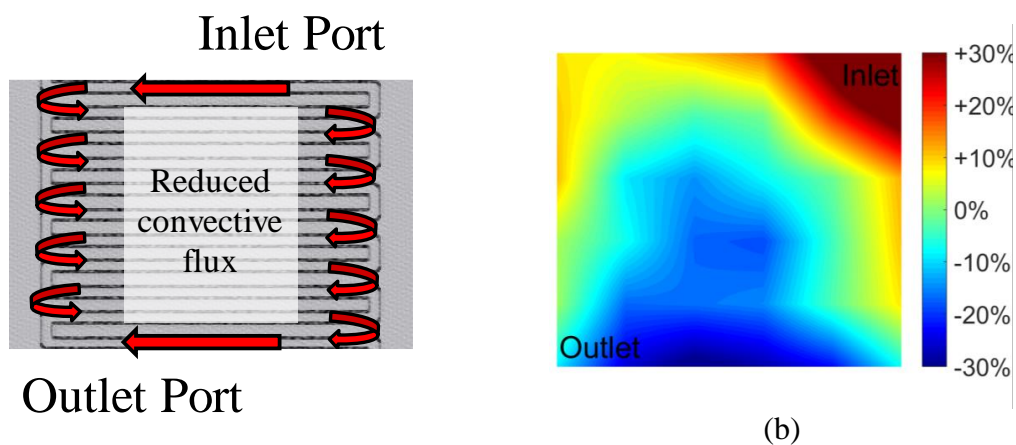


Figure 6-6: Distributed current measurement for serpentine flow field topology at low convective flow regime. (a) GORE-SELECT® EW1100 / 10 mL.min⁻¹, (b) Pure Cast Film EW800 / 10 mL.min⁻¹, (c) GORE-SELECT® EW1100 / 5 mL.min⁻¹, (d) Pure Cast Film EW800 / 5 mL.min⁻¹

Comparing Fig. 6-6 with Fig. 6-4, the most noticeable difference is the current distribution pattern associated with the serpentine flow plate design compared to square flow-through flow plates. Several modeling efforts have confirmed the concave shape of the distributed current shown in Figs. 6-6(b) and 6-6(d) for the cell configurations utilizing serpentine flow plates under mass transport limited conditions^{222, 223}. A schematic illustration of the transport mechanism for the cells utilizing serpentine flow fields has been shown in Fig. 6-7. As illustrated in Fig. 6-7(a), the transport mechanism within the electrode for serpentine flow plates is mostly dominated by the transport along the edges where the hydraulic pass way is shorter. Therefore, reduced pressure drop through the electrodes at the meanders of the flow field pushes the electrolyte to bypass the interior channels at those locally high-pressure regions. Therefore, the transport mechanism shown in Fig. 6-7(b) is expected based on previous modeling reports as schematically illustrated in Fig. 6-7(a).

Revisiting Fig. 6-6 reveals that the influence of membrane permeability on the distributed current is also pronounced for the cells with serpentine flow plate design. At $10 \text{ mL}\cdot\text{min}^{-1}$, the local mass transport limited condition was reached (Fig. 6.6(b)) where the cell with GORE-SELECT® EW1100 membrane exhibited relatively uniform distributed current throughout the electrode (Fig. 6.6(a)). Similar trend was observed for reduced flow rate ($5 \text{ mL}\cdot\text{min}^{-1}$) where an increased membrane permeability significantly affected the distributed current across the electrode (Fig. 6-6(c) and 6-6(d)). Therefore, the influence of ionic crossover on the real-time performance of the cell was probed via several cell configurations.



(a)
 Figure 6-7: Schematic illustration along with experimentally measured distributed current for serpentine flow plates
 (a) Schematic illustration of the transport mechanism associated with serpentine flow plates,
 (b) Experimentally measured distributed current for serpentine flow field at mass transport limited condition

6.3.2. The influence of flow field design on the distributed current measurement

In previous sections, the influence of membrane permeability on the real-time performance of the cell was explored. In this section, a comparison is provided among the cells with different cell configurations. In particular, the influence of flow field design on the distribution is provided. Figure 6-8 demonstrated the influence of flow field design on the distributed current for two different cell configurations at high stoichiometric flow condition ($50 \text{ mL}\cdot\text{min}^{-1}$).

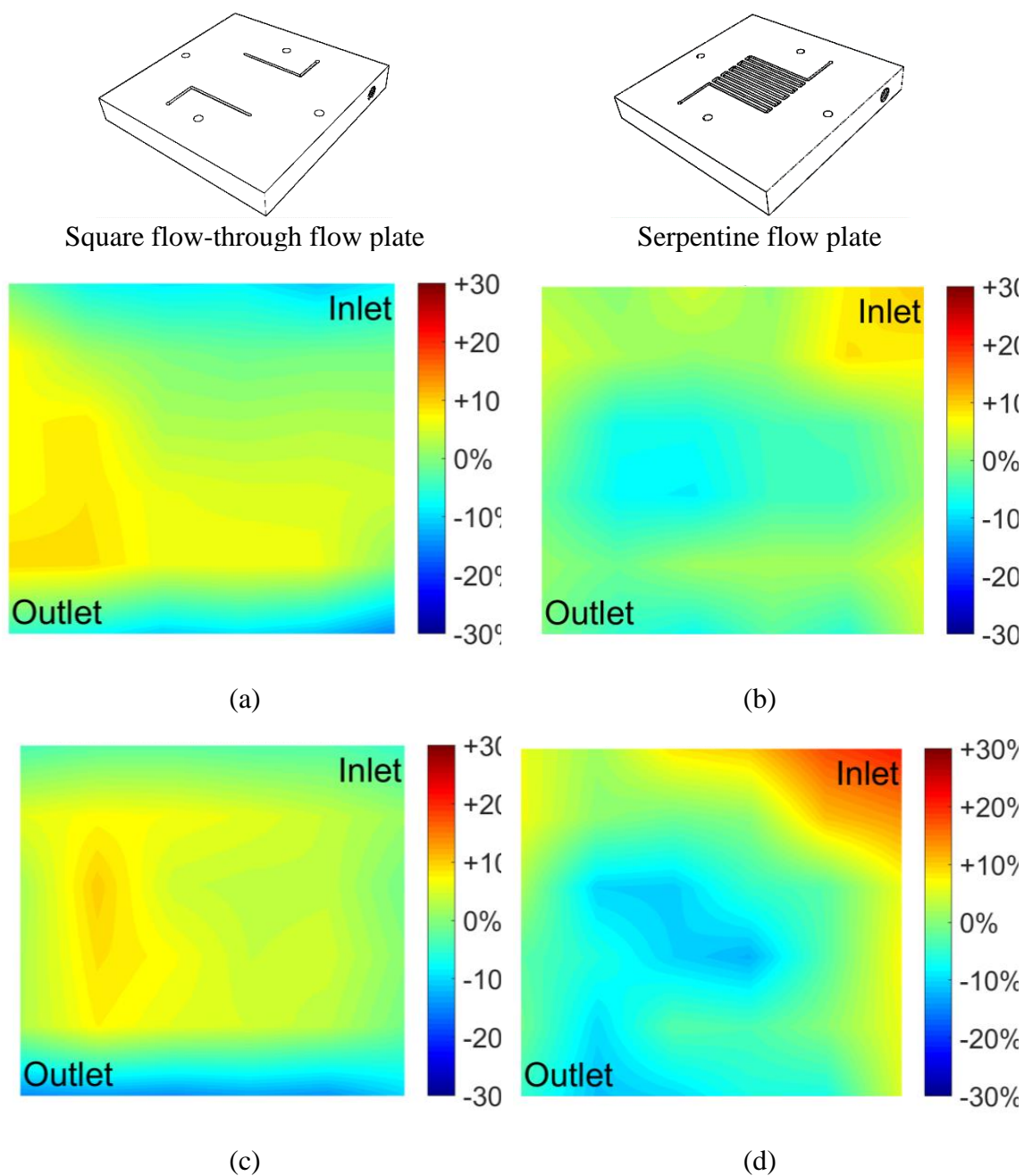
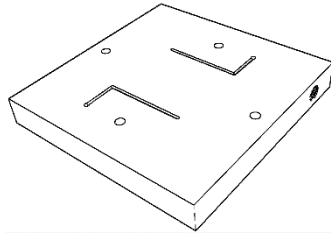


Figure 6-8: Comparison of distributed current between various flow fields at $50 \text{ mL}\cdot\text{min}^{-1}$, (a) square flow-through, GORE-SELECT® EW1100 (b) serpentine, GORE-SELECT® EW1100 (c) square flow-through, Pure Cast Film EW800 (d) serpentine, Pure Cast Film EW800

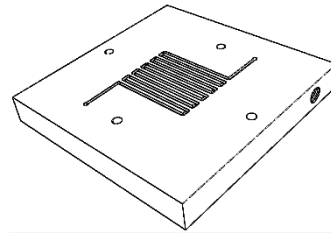
In chapter 3, a comprehensive mathematical formwork was developed to assess the influence of different mass transport fluxes (diffusion, convection, and migration) on the cell performance. It was shown that the convective flux through the electrodes is substantially higher (at least two orders of magnitude) compared to other flux component (diffusion and migration) ¹²⁷. Therefore, increasing convective flux within the electrodes was identified as a detrimental and key parameter for improving the performance ¹²⁷. This point can be further explored via analyzing the distributed current patterns provided in Fig. 6-8.

Comparing Figs. 6-8(a) 6-8(c) clearly shows that the permeability of the membrane at high stoichiometric flows (here 50 mL.min⁻¹) has negligible influence on the distribution for the cells utilizing square flow-through flow plates. Similar conclusion can be made if we compare Figs. 6-8(b) and 6-8(d) where serpentine flow plates have been replaced.

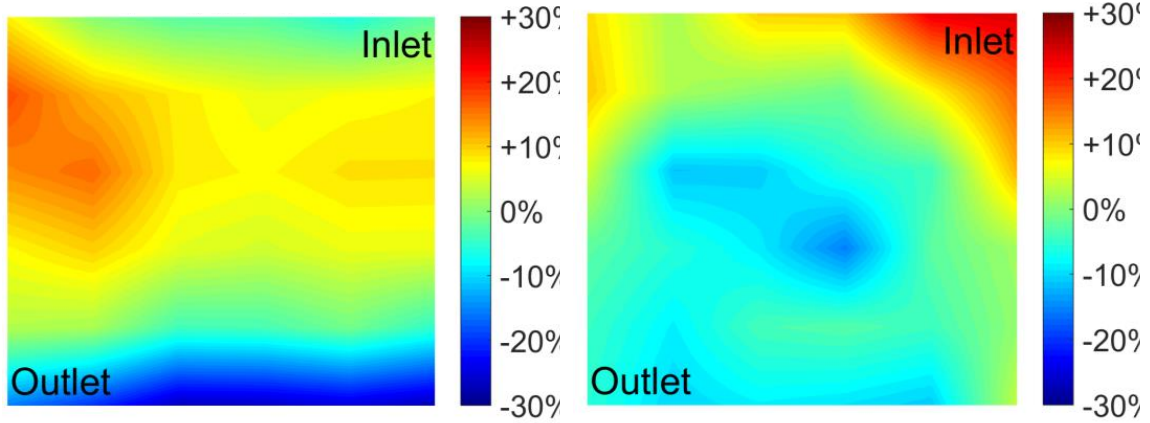
Therefore, at high stoichiometric flows, the distributed current pattern is mostly dominated by the convective transport mechanism across the electrodes (compare Figs. 6-8(a) and 6-8(b) or Figs. 6-8(c) and 6-8(d)); thus, the ionic crossover has negligible influence on the real-time distributed current. However, at low stoichiometric condition, the influence of ionic current through the ion-exchange membrane on the real-time performance can be significant as shown in Fig. 6-9.



Square flow-through flow plate

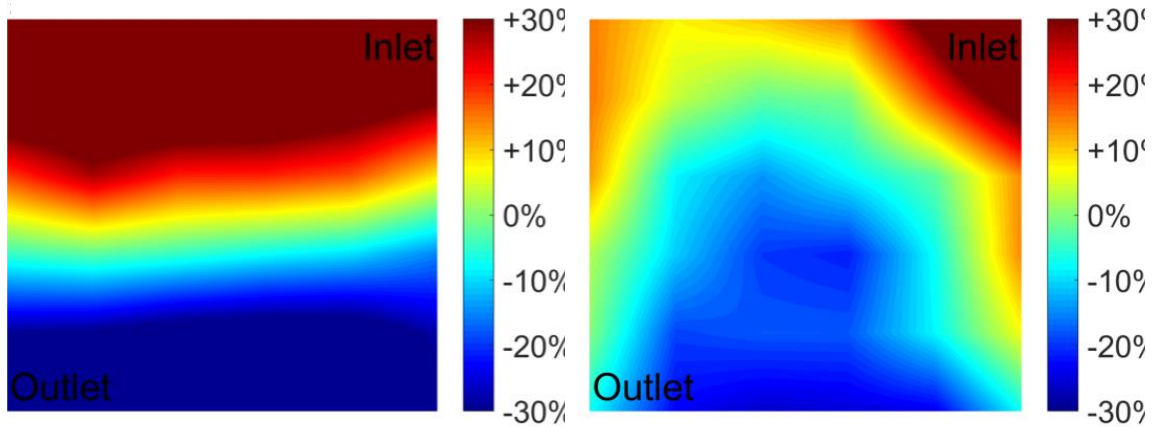


Serpentine flow plate



(a)

(b)



(c)

(d)

Figure 6-9: Comparison of distributed current between various flow fields at $10 \text{ mL}\cdot\text{min}^{-1}$, (a) square flow-through, GORE-SELECT® EW1100 (b) serpentine, GORE-SELECT® EW1100 (c) square flow-through, Pure Cast Film EW800 (d) serpentine, Pure Cast Film EW800

The distributed current patterns have been illustrated for cell configurations with serpentine or square flow-through flow plates at lower flow rate ($10 \text{ mL}\cdot\text{min}^{-1}$, lower stoichiometry) in Fig. 6-9. For reduced stoichiometric flow conditions, the influence of ionic crossover on the real-time performance of the cells is significant if the membrane selectivity is low. Comparing the current distribution across the electrode for cells with serpentine flow field and GORE-SELECT® EW1100 membrane (Fig. 6-9(b)) versus serpentine flow field and similar membrane (Fig. 6-9(a)) reveals that the distributed current is largely being altered by the transport mechanism induced by the flow plate design. However, for the cells with high-permeable membrane (Pure Cast Film EW800), as illustrated in Figs. 6-9(c) and 6-9(d), the distributed current patterns not only are influenced by the electrolyte transport mechanism within the electrodes, but also being significantly affected by the self-discharge reactions initiated via ionic crossover through the membrane.

6.4. Conclusions

During cycling of all-vanadium redox flow batteries (VRFBs), the transport of ionic species through the membrane is inevitable (considering the ion-exchange membranes available off-the-shelf at the time of writing this dissertation). Therefore, the capacity of the battery decreases during cycling due to undesired ionic and water crossover through the membrane. This long-term influence of ionic and water crossover has been the subject of several studies in the field. In this dissertation, several chapters have been dedicated for exploring this long-term influence of crossover from various perspectives.

For VRFBs utilizing permeable membranes, the influence of ionic crossover on the real-time performance of the cell is expected. However, to the best of our knowledge, no previous works have reported on this subject. Therefore, in this chapter, for the first time, the real-time influence of ionic crossover on the cell performance was explored.

The distributed current diagnostics has already been developed for VRFBs. This diagnostic provides in-plane resolution for the current distribution across the electrodes. In this work, the distributed current diagnostics, for the first time, was employed to investigate the real-time influence of ionic crossover on the cell performance. A series of membrane with varied equivalent weight and degree of reinforcement was characterized. Among them, two configurations with the highest and lowest ionic permeabilities (labeled as “Pure Cast Film EW800” and “GORE-SELECT® EW1100” respectively) selected and the real-time distributed current was implemented at various stoichiometric flows and with different flow plate designs.

The current distribution patterns measured for various flow plates configuration were confirmed by the mathematical model predictions developed by the same authors and others. It was shown that for the cells utilizing selective ion-exchange membrane, the distributed current across the electrode is dominated by the mass transport mechanism imposed by flow field design regardless of the flow condition. However, for the cell configurations with very permeable membrane, the distributed current is significantly altered by the ionic crossover through the membrane at low stoichiometric flow conditions.

Increased flow stoichiometry, diminishes the dependency of distributed current on the ionic current even for highly permeable ion-exchange membranes.

6.5. Acknowledgments

Yasser Ashraf Gandomi thanks University of Tennessee for providing Chancellor Fellowship.

CHAPTER SEVEN :
INFLUENCE OF FLOW FIELD DESIGN ON CROSSOVER OF IONIC SPECIES
IN REDOX FLOW BATTERIES

Scholarly contributions

The Abstract is revised based on the talk presented in 230th Electrochemical Society (ECS) Meeting & Electrochemical Energy Summit, Honolulu, Hawaii (October 2 - 7, 2016).

- Abstract ID: MA2016-02 40
- Title: The Influence of Flow Field and Electrode Design on Crossover of Ions in All-Vanadium Redox Flow Batteries

This chapter is revised based on the manuscript prepared for submission to the Journal of Power Sources.

Yasser Ashraf Gandomi, J. R. Houser, D. S. Aaron, M. M. Mench. “Influence of Flow Field Design on the Ionic Crossover in Redox Flow Batteries” to be submitted to *Journal of Power Sources* (2018).

Abstract

One of the key factors obstructing the commercialization process of the all-vanadium redox flow battery (VRFB) is the high cost of these systems, resulting from relatively poor performance. Flow field design is considered to be key optimization factors in VRFBs that can enable high battery performance and resultant market competitiveness. The flow field and electrode designs are known to directly affect the mass transport, performance, capacity utilization, and parasitic pressure losses. Much experimental and modeling work has been done to understand the combined effect of flow field design and electrodes on mass transport behavior and performance of VRFBs. However, neither modeling nor experimental approaches targeting the direct effect of flow fields on vanadium crossover has been reported.

In this chapter, experimental data have been provided in which different flow fields have been tested from multiple perspectives related to capacity decay in VRFBs including ionic

vanadium crossover and long-term cycling. A UV-Vis spectroscopy setup has been implemented to quantify vanadium crossover under different operating conditions.

7.1. Introduction

Flow fields within redox flow battery (RFB) topology plays crucial role influencing the real-time performance and characterization metrics (voltaic, coulombic, and energy efficiencies) of RFBs ¹. Engineering flow fields for RFBs include designing flow field geometry along with channel architecture. The material used for flow fields is also of great importance since it must be compatible with the electrolyte and must have superb conductivity and corrosion resistivity ¹. The porosity of these plates must also be assessed while selecting the fabrication method since some materials (mostly graphite composites) have intrinsic higher porosity within the structure.

Traditionally, the flow field geometries used for RFBs have been adopted from fuel cell community. Commonly used flow field geometries for fuel cells include serpentine, interdigitated, flow-through, parallel, and parallel-serpentine designs ¹. Although these designs are frequently used within RFB community, going forward, electrolyte specific flow field design must be replaced where the design of flow fields is tailored to the chemistry or performance metrics of interest. In particular, the contribution of flow plates to the faradic current being generated during cycling (charge or discharge) can be engineered via understanding the kinetics associated with these plates. Indeed, flow plates

can be considered as additional active sites providing pathways for occurrence of redox reactions.

As fully discussed in a recent publication from our lab ¹, the flow field geometry directly influences the pressure drop and subsequently alters the energy efficiency since the pressure drop can be correlated to the overall pumping energy needed for cycling the battery ¹ (Eq. (7-1)).

$$E_{pump} = \frac{\Delta p_s \cdot Q_s}{\eta_{pump}} \cdot t \quad (7-1)$$

Here, Δp_s is the pressure drop (for the entire system), Q_s is the volumetric flow rate, η_{pump} is the pump efficiency, t and is the total time of the experiment. Therefore, as formulated in Eq. (7-1), flow field geometry directly influences the pressure drop associated with the system and subsequently affects the system-level energy efficiency (η_{system}) according to the following equation:

$$\eta_{system} = \frac{E_{discharge} - E_{ancillary, discharge}}{E_{charge} + E_{ancillary, charge}} \quad (7-2)$$

Here, $E_{discharge}$ is the total energy during discharge, E_{charge} is the total energy during charge, and $E_{ancillary}$ is the energy required for all other ancillary operations during charge or discharge cycles.

Therefore, many efforts in the field have been devoted to analyzing the overall energy efficiency and pressure drop associated with various flow field designs ²²³⁻²²⁸. The

influence of flow field design on the mass transport limitations during RFB operation has also been explored ^{224, 225}. Some recent works have been focused on identifying the key mass transport limitations imposed by various flow field design via non-dimensional and limiting current analysis ^{222, 229}. As briefly described in this section, significant amount of work has been dedicated to researching the influence of flow field design on the performance, mass transport, and system-level analysis for various types of RFBs. However, to the best of our knowledge, no prior work has reported the influence of flow field design on the crossover and subsequent capacity decay in RFBs. This is particularly important since the assessment of flow field design on long-term cycling provides an additional engineering aspect for optimizing the flow field designs. Therefore, in this chapter, we have experimentally explored the impact of commonly used flow field designs on the ionic crossover and capacity decay in VRFBs. We believe, the materials provided in this chapter are very useful for engineering VRFBs for extended capacity retention.

7.2. Experimental

As described in previous section, the influence of flow field design on the ionic crossover is of a great importance and has not been explored in the literature. The primary purpose of flow fields is uniform distribution of electroactive species across the electrode with minimum pressure drop. A schematic illustration has been provided in Fig. 7-1 describing the mechanism of species transport across the electrodes. As schematically illustrated in Fig. 7-1, the flow fields affect electrolyte distribution within the electrodes. As a result, the vanadium ion concentration in the electrode-membrane interface is being altered

depending on the flow field design and electrolyte flow pattern across the electrodes. Since flow field geometry and volumetric flow rates are of special interest for optimizing the VRFB performance for extended cycling; here, we have focused on these two key parameters.

7.2.1. Flow field geometries

In this work, 4 different flow field geometries have been explored. Schematic illustration of these plates has been provided in Fig. 10-2.

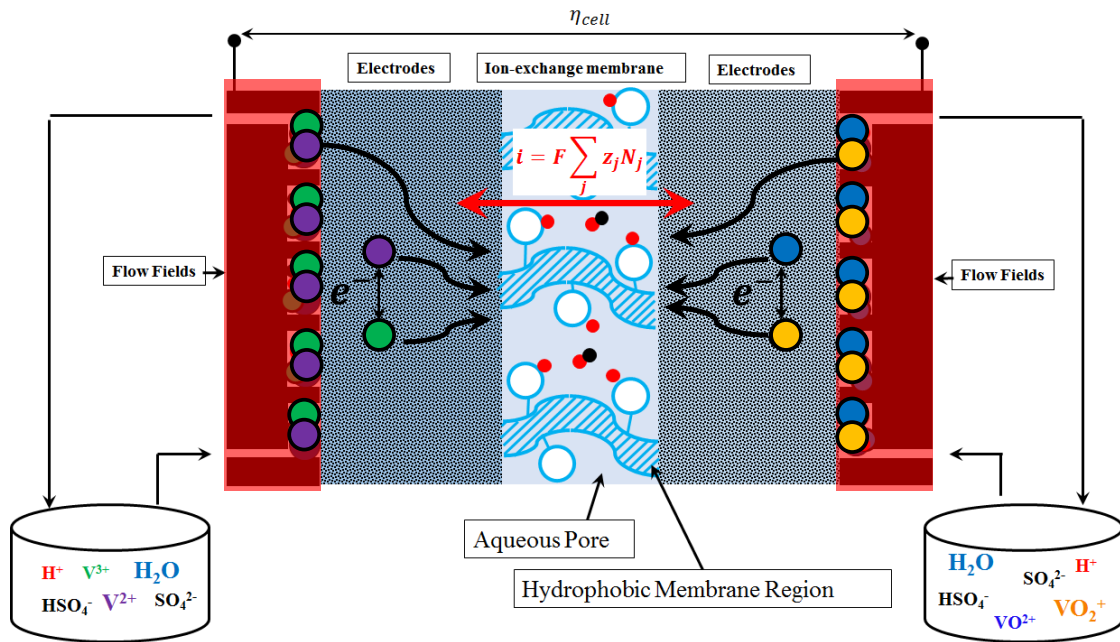
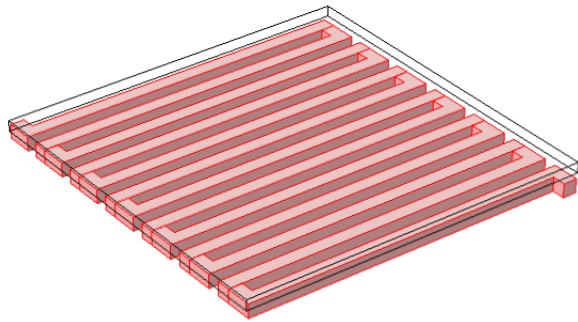
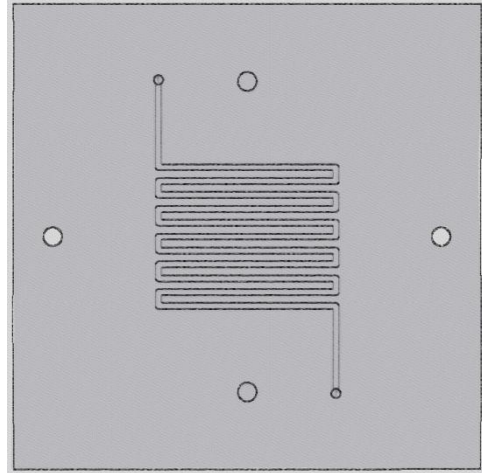


Figure 7-1: Schematic of illustration of transport of active species from flow fields across the electrode

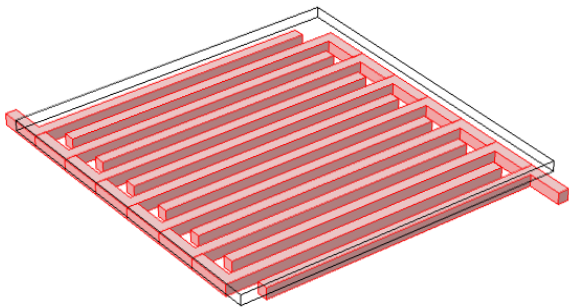


3D view of square serpentine flow fields

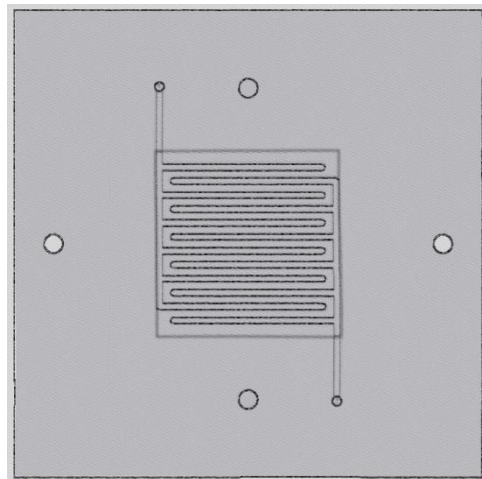


Front view of square serpentine flow fields

(a)



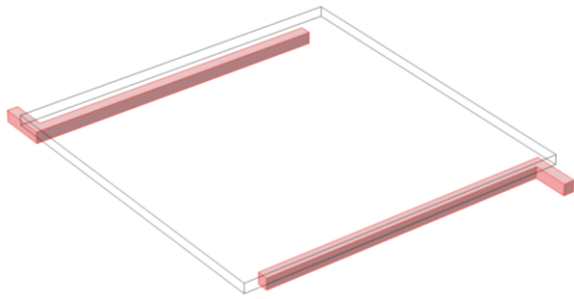
3D view of square interdigitated flow fields



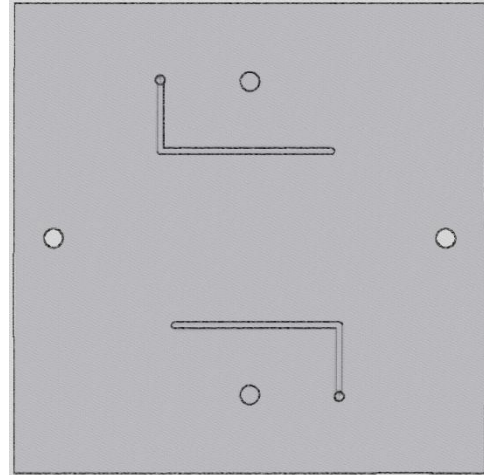
Front view of square interdigitated flow fields

(b)

Figure 7-2: Schematic illustration of various flow field geometries used in this work. (a) Serpentine, (b) Interdigitated, (c) Square Flow-Through, (d) Rectangular Flow-Through

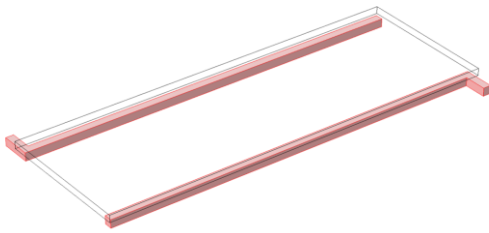


3D view of square flow-through flow fields

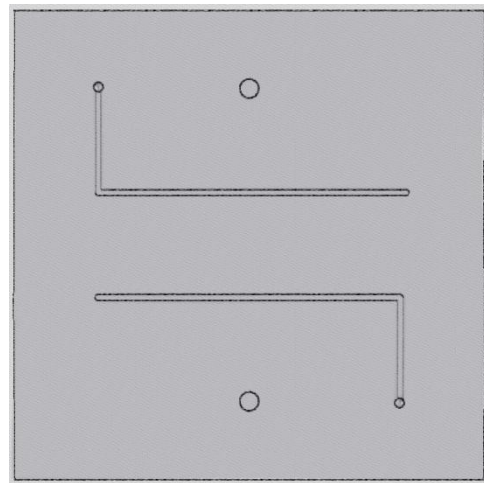


Front view of square flow-through flow fields

(c)



3D view of rectangular flow-through flow fields



Front view of rectangular flow-through flow fields

(d)

Figure 7-2 continued

Four different flow plate geometries including square serpentine, square interdigitated, square flow-through and rectangular flow-field designs considered in this work. Further details regarding geometry of the flow plates have been summarized in Table 7.1.

As tabulated in Table 7.1, the active area for all the flow fields design was 9 cm^2 . The serpentine, interdigitated, and square flow-through designs had identical length and width ($3 \text{ cm} \times 3 \text{ cm}$) as schematically illustrated in Fig. 7.2(a), (b), and (c). However, the rectangular flow-through plates (Fig. 7.2(d)) had dissimilar length and width ($4.5 \text{ cm} \times 2 \text{ cm}$). The channel geometry was similar among all the plates where the width and depth of the channels were both 1 mm.

The channel geometries shown in Fig. 7-2 were built in-house. Densified and resin-filled molded graphite plates (Grade: FC-GR347B) were purchased from Graphtek LLC (Northbrook, IL, USA) and subsequently were machined. These molded graphite plates have good chemical resistivity and are almost impermeable to the electrolytes within the flow conditions tested in this work.

Table 7.1. Flow fields and channel geometries

	Flow field geometry (cm^2)	Channel geometry (mm^2)
Serpentine	3×3	1×1
Interdigitated	3×3	1×1
Square flow-through	3×3	1×1
Rectangular flow-through	4.5×2	1×1

Along with flow plates, 1 layer as-received SIGRACET® 39AA carbon paper electrode (SGL, Germany) was utilized at each side. The nominal thickness of the carbon paper electrode is 280 micron with uncompressed porosity of 89% and mean pore diameter of 42-44 μm . Nafion® 117 was utilized within VRFB architecture. The membranes were soaked in the aqueous sulfuric acid solution (3.3M) for more than a week at room temperature prior to cell assembly. To make sure the variations in the crossover is not caused by the membrane, same membrane was used within various tests.

7.2.2. UV-Vis spectroscopy

To assess the influence of various flow field designs on the ionic crossover, concentration-gradient induced crossover was investigated for array of flow plates schematically shown in Fig. 7-2.

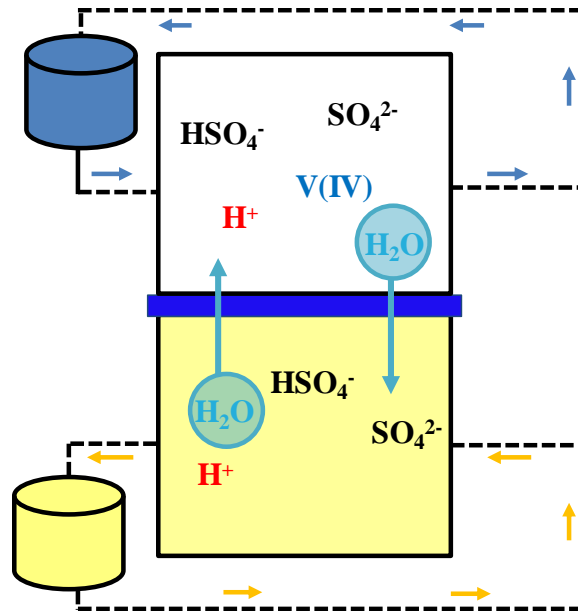


Figure 7-3: Schematic of ionic crossover setup

Figure 7-3 includes the schematic of the setup used to assess the influence of flow field design on the ionic crossover. Vanadium-enriched electrolyte (1.5M V(IV), 3.3M sulfuric acid aqueous solution) was circulated in one side of the battery. Vanadium-deficient solution (4.8M aqueous sulfuric acid) was circulated in the other side. Two-channel peristaltic pumps (Cole Parmer, Masterflex L/S, Vernon Hills, IL, USA) was utilized to circulate the electrolytes through the cell.

The UV/Vis spectroscopy setup included the light sources (Ocean-Optics, Dunedin, FL, USA) as well as ultraviolet/visible (UV-Vis) spectrometers (THORLABS, Newton, NJ, USA). The vanadium-enriched and vanadium deficient electrolytes were directed to flow-through flow cells enabling real-time measurement of electrolyte composition using UV/Vis spectroscopy. Full description of the set-up has been provided in Chapter 4 and also has been discussed in our recent publications ^{1, 102, 202}.

For a redox flow battery during cycling, the concentration gradient along with electric field induced crossover are the major driving forces for the transport of electroactive ions through the membrane. The quantitative analysis of electric-field induced crossover flux and concentration-gradient induced crossover for Nafion® membranes is already available in a recent publication from our lab ²⁰². Therefore, here, we have only focused on the concentration-gradient induced crossover to assess the variations of crossover flux with the flow-field design.

7.2.3. Long-duration cycling

To conduct the long-duration cycling experiments, a multichannel potentiostat/galvanostat (Arbin Instruments, College Station, TX) was used to prepare the initial negative (V(II)/V(III) couple) and positive (V(IV)/V(V)) electrolytes. The initial electrolyte was 1.5 mol/L $\text{VO}_2\text{SO}_4 \cdot x\text{H}_2\text{O}$ (Alfa Aesar, USA) dissolved in 3.3 mol/L sulfuric acid (H_2SO_4). The initial volume of negative and positive electrolytes were 50 and 100 mL respectively. The charging was conducted potentiostatically at 1.8 V a cut-off current (4 mA) was reached. Subsequently, 50 mL of positive electrolyte was removed. The electrolyte then discharged to 50% state of charge prior to conducting long-duration cycling experiments.

The charge-discharge cycling experiments were conducted using a single-channel BioLogic SP240 potentiostat (BioLogic Science Instruments, France). A constant current of 100 mA/cm² was applied until reaching cut-off voltages during discharging and charging cycles. The cut-off voltages were 0.2 V and 1.9 V for discharging and charging states, respectively.

To explore the influence of convective flow on the cycling and ionic crossover characteristics, two different volumetric flow rates, 10 and 40 mL.min⁻¹, was used. The upper limit for volumetric flow rate (i.e. 40 mL.min⁻¹) was chosen considering the maximum hydraulic pressure tolerable by the experimental setup.

7.3. Results and Discussion

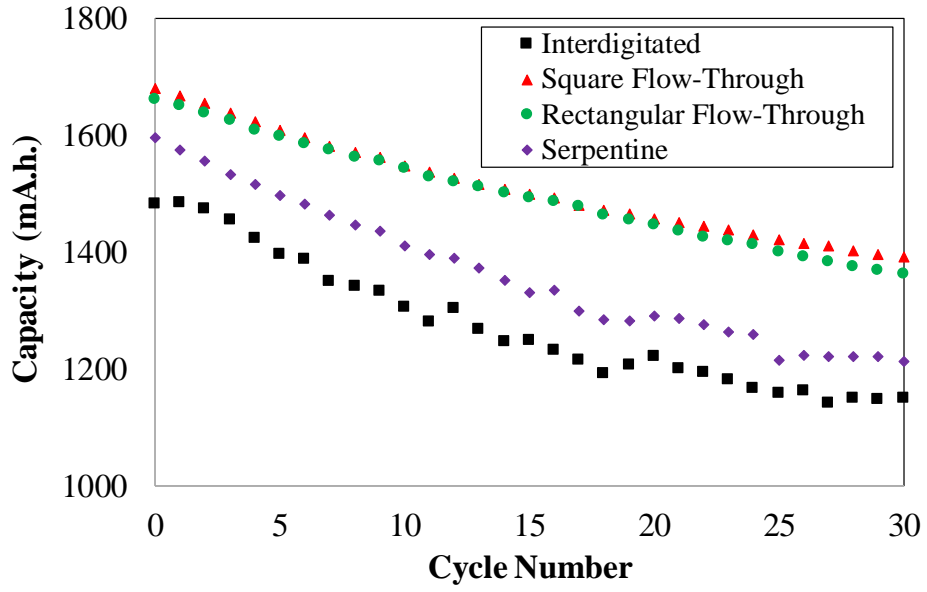
7.3.1. Capacity decay for extended cycling

Figure 7-4(a) shows the variations in discharge capacity during cycling for different configurations of flow fields used in this work. Figure 7-4(b) demonstrates the theoretical capacity utilization for various cell topologies duration the charge-discharge experiment. It is important to note that the theoretical capacity utilization has been assessed based on maximum dischargeable capacity determined based on the initial concentration of vanadium ions within the solution. (1.5M V(IV)).

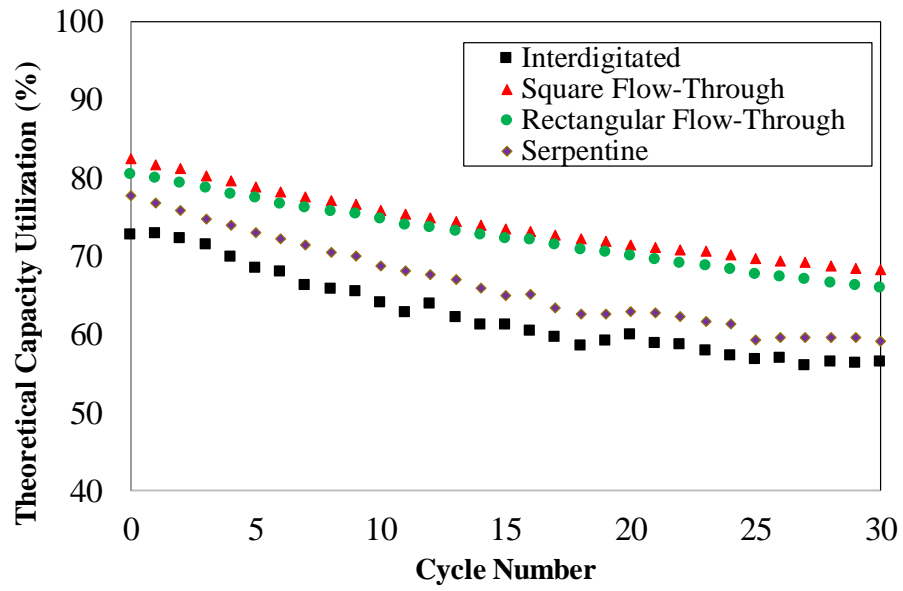
The variations of capacity decay and theoretical capacity utilizations during cycling shown in Fig. 7-4 has been obtained for symmetrical charge-discharge profile at 100 mA.cm^{-2} with volumetric flow rate of 40 mL.min^{-1} .

As demonstrated in Fig. 7-4, the discharge capacity along with theoretical capacity utilization decreases during cycling. Among various contributors, ionic vanadium crossover through the ion-exchange membrane is the major contributor to decreased capacity as discussed in Chapters 4 and 5 (related publications are available in Refs. ^{102, 202}).

According to Fig. 7-4(a), the trend of capacity decline follows the trend observed for the variations in theoretical capacity utilization during cycling (Fig. 7-4(b)).



(a)



(b)

Figure 7-4: Variations in (a) discharge capacity and (b) theoretical capacity utilization for different flow plates design during extended cycling

It is important to note that the starting points (discharge capacity at cycle 0) is different among various flow plates. As discussed in previous section, the initial solutions used for cycling different configurations of the flow fields were identical. Therefore, the difference in available initial practical capacity observed in Fig. 7-4(a) is to variations in mass transport overpotentials imposed by different flow plates. Figure 7-5 demonstrates the variations in coulombic efficiency during extended cycling for different configurations of flow plates.

Figure 7-5 demonstrates the variations in coulombic efficiency during extended cycling for different configurations of flow plates. As shown in Fig. 7-5, the coulombic efficiency for all different flow plate designs remains higher than 96%. Commonly, the coulombic efficiency is used as a metrics for assessing the lost in capacity due to electroactive species crossover through the membrane. However, in this case, when comparing various flow plates design, it is not rigorous to directly correlate higher rate of crossover to decreased coulombic efficiency since the initial available practical capacity is different among various flow plates configuration. Also, as discussed in a recent publication, according to the protocol used for evaluating the coulombic efficiency (the ratio of the discharge capacity over charge capacity ¹); if both of these quantities are small compared to the theoretical capacity, the coulombic efficiency would still be high despite higher rate of crossover ¹⁰². Therefore, more detailed analysis is needed. We have utilized UV/Vis spectroscopy to measure the rate of crossover for various flow plate architectures in the following sections.

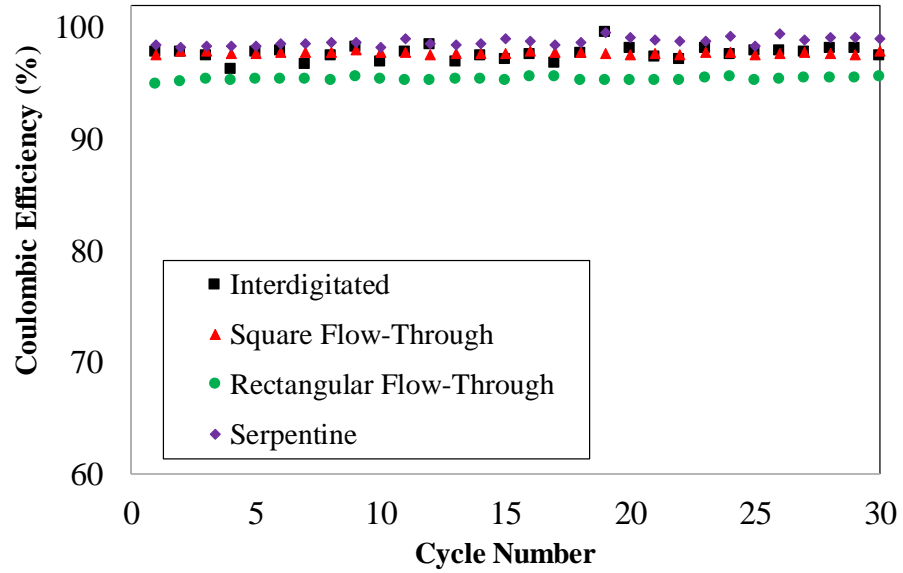
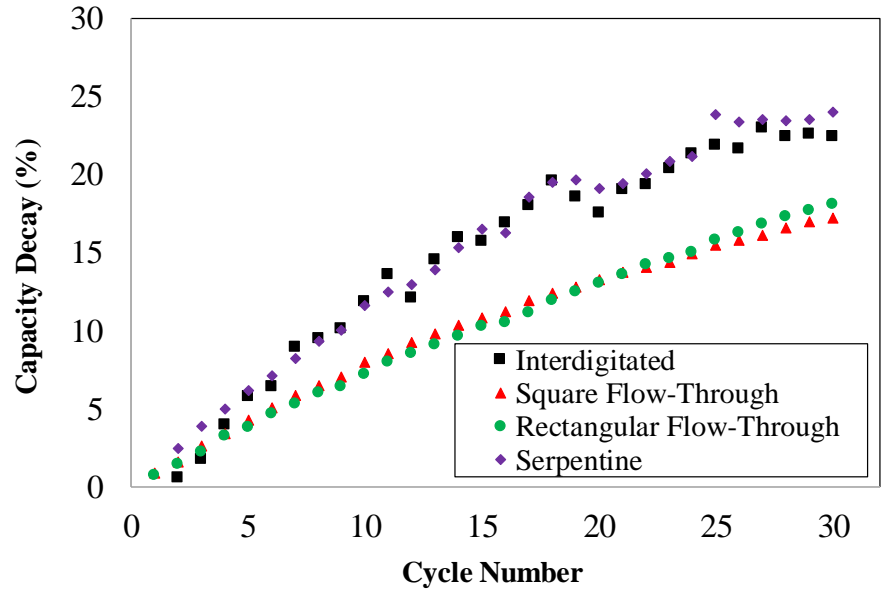


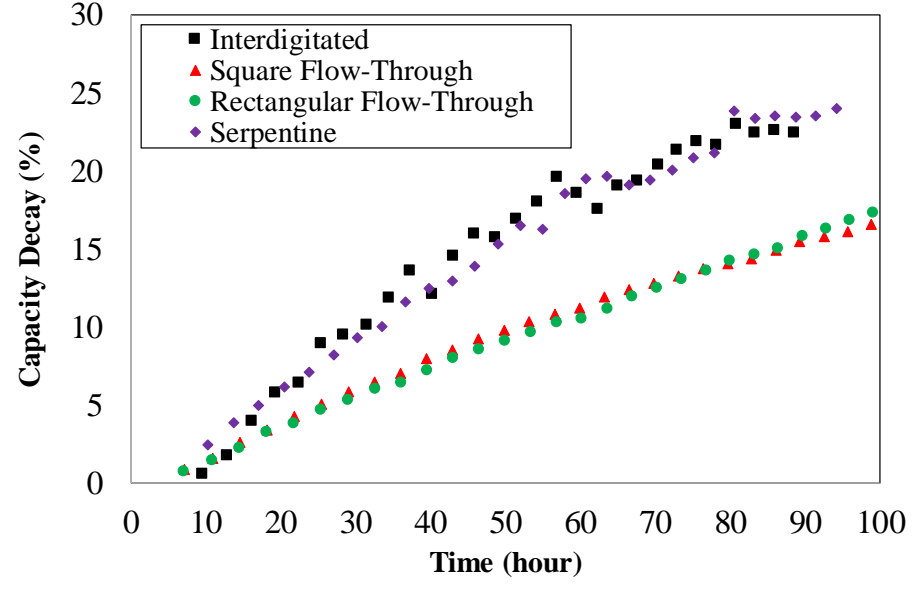
Figure 7-5: The variation in coulombic efficiency during extended cycling for different configurations of flow plates

Based on the initial practical capacity measured for each flow field configuration (Fig. 7-4(a)), it is feasible to calculate the capacity decay over extended cycling as plotted in Fig. 7-6. The capacity decay used in Fig. 7-6 is defined as the ratio of the decrease in discharge capacity to the initial practical discharge capacity of the battery ¹⁰².

Figure 7-6 includes the capacity decay for different flow plate designs as a function of cycle number (Fig. 7-6(a)) and as a function of Time (Fig. 7-6(b)). According to Figure 7-6(a), the application of the square flow-through flow field results in the lowest capacity decay (~17% at the end of 30 cycles) among various designs. The serpentine flow field design however, demonstrated the highest capacity decay (~24%) for the similar cycle number (30 cycles).



(a)



(b)

Figure 7-6: Capacity decay for different flow plate designs as a function of (a) cycle number, (b) Time

As shown in Fig. 7-6(a), the discharge capacity decay (for charge-discharge cycling at 100 mA.cm⁻²) at the end of 30 cycles for the interdigitated and rectangular flow-through flow fields is 22% and 18% respectively.

According to Fig. 7-6(b), since a wider state of charge and discharge window has been selected; the cycling experiments have been finalized at an extended time frame. However, despite being cycled for the same number of charge/discharge cycles, the total time of the experiment was different among various flow fields designs. As shown in Fig. 7.6(b), the total time of the experiment for flow-through (square and rectangular), serpentine, and interdigitated flow fields were ~100, ~95, and ~90 hours respectively.

Decreased total time of cycling (for 30 cycles) implies that the voltage limits (upper or lower) are being reached faster during the cycling. Hitting the voltage limits faster is an indication that either state of charge window in one of the electrolytes (negative or positive) has shrunk or the overpotentials are high that a deep charge/discharge state is not attainable.

A decreased state of charge window is the direct result of ionic crossover which has been discussed in Chapter 4 and in a recent publication ²⁰². Not being able to achieve a deep discharge state, despite having relatively aggressive voltage windows, indicates that one or series of overpotentials are high for the cell topology. Since the flow field designs are the only variable component among various cell architectures; it is clear that the interdigitated flow fields have higher mass transport overpotentials (Fig. 7-4(b) and Fig. 7-6(b)).

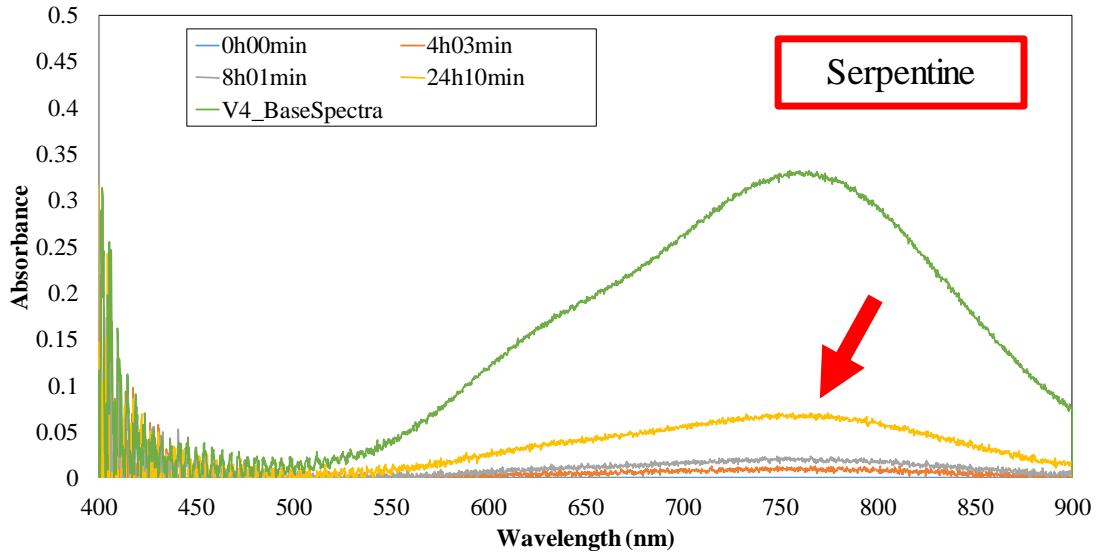
Although, it must be mentioned that the conclusion of higher mass transport overpotential for interdigitated flow fields is caused due to combination of cell components (electrode and membrane) and redox active materials stoichiometry (concentration of active species along with volumetric flow rate) adopted in this work.

7.3.2. Influence of flow field design on ionic crossover in VRFBs

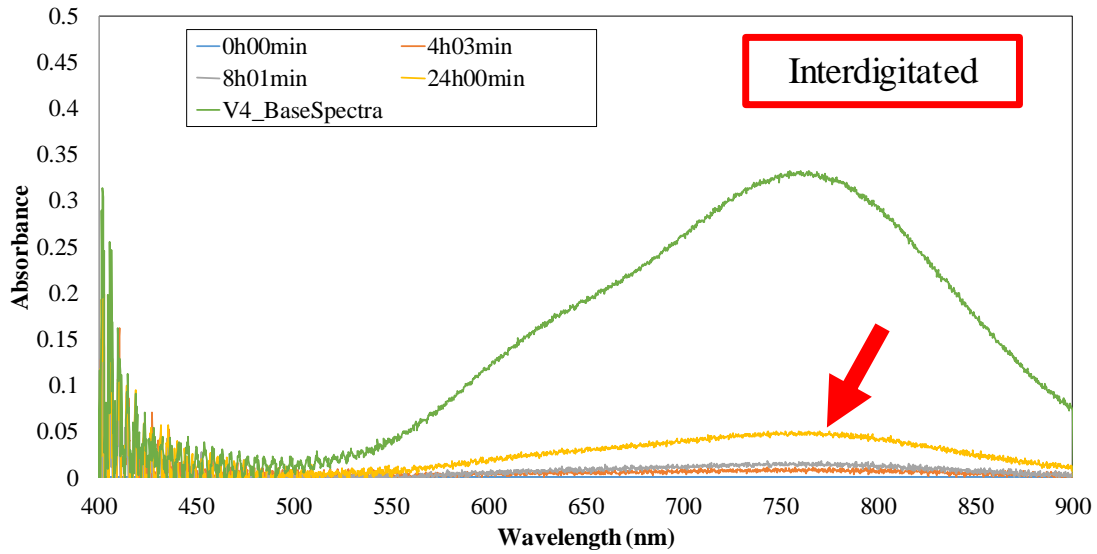
As briefly discussed in previous section, it is important to assess the crossover of ionic species for various configurations of flow fields. The experimental setup for conducting the concentration-gradient induced crossover was already detailed in Section 7.2.2. Here, the major results of crossover analysis are discussed.

The UV/Vis spectroscopy was conducted using spectrometers in a transmission configuration with a spectral range from 400 to 900 nm. As discussed in a recent publication ²⁰², the UV/Vis spectra demonstrate highest sensitivity for V(IV) ion at wavelength of 760 nm. Therefore, here, the UV/Vis spectra were recorded after 4, 8 and 24 hours into the crossover experiment. Figure 7-7 includes the variations of UV/Vis spectra during concentration-gradient induced crossover experiment for different flow fields design.

In Fig. 7-7, the red arrows are used to identify the UV/Vis spectrum recorded at the end of 24-hour experiment.

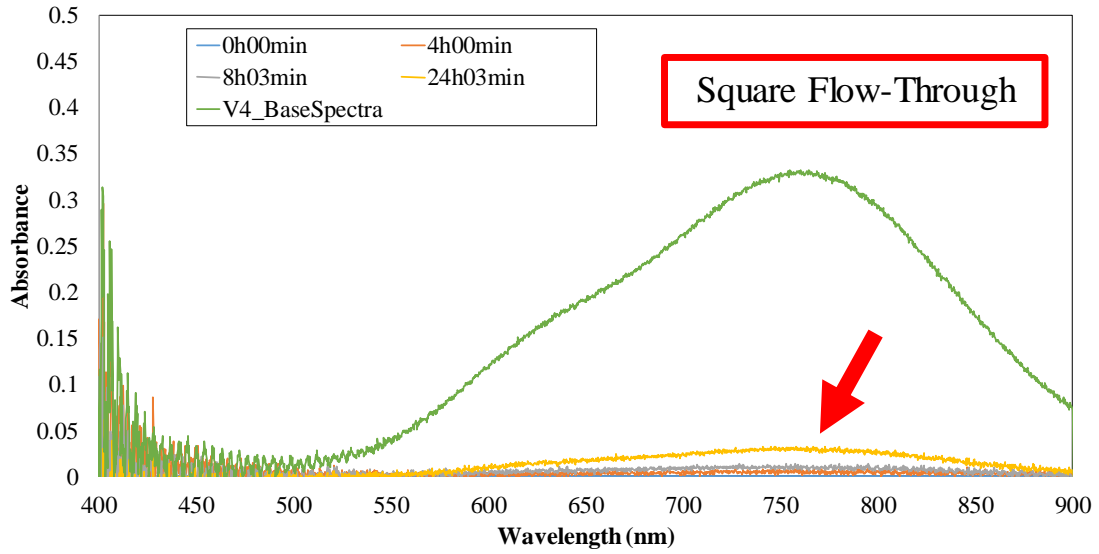


(a)

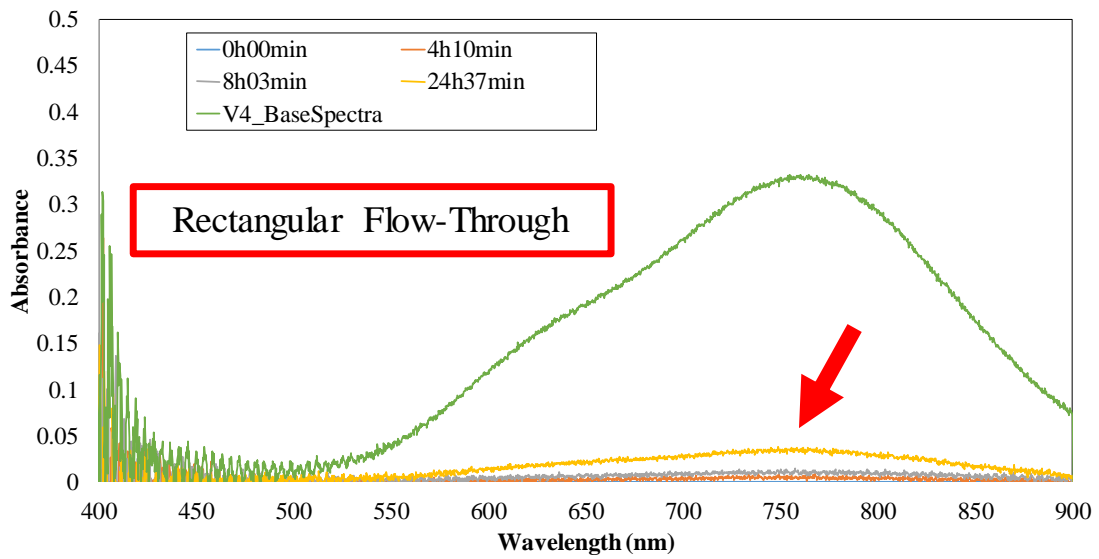


(b)

Figure 7-7: The variations of UV/Vis spectra during concentration-gradient induced crossover for (a) serpentine, (b) interdigitated, (c) square flow-through, and (d) rectangular flow-through



(c)



(d)

Figure 7-7 continued

As shown in Fig. 7-7, the UV/Vis absorbance spectra have been recorded at various times for different configurations of flow fields. To determine the concentration of vanadium ions in the vanadium-deficient electrolyte, it is necessary to calibrate the setup. To this end, an absorbance spectrum with precisely controlled concentration (labeled as “V4_BaseSpectra” within Fig. 7-7) has been used. Figure 7-8 includes the concentration of vanadium ions diffused through the membrane to the vanadium-deficient electrolyte for different flow field designs.

As shown in Fig. 7-8, the concentration of vanadium ions has been determined at the end of experiment (~25 hours) for various cell configurations. Based on the data shown in Fig. 7-8, the concentration of vanadium ions in the vanadium-deficient solution at the end of experiment was ~0.02, ~0.0144, ~0.009, and ~0.009 mol.L⁻¹ for serpentine, interdigitated, rectangular, and square flow plate designs respectively.

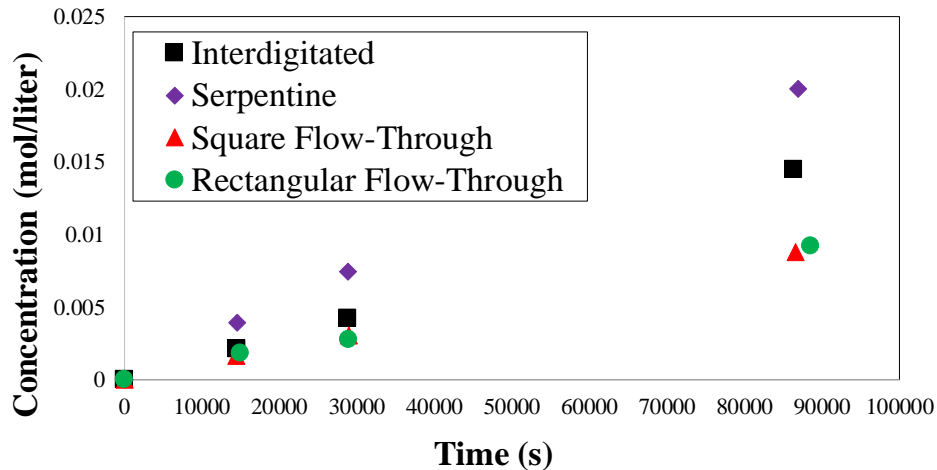


Figure 7-8: The concentration of vanadium ions (V(IV)) measured within vanadium-deficient electrolyte during crossover experiment for different flow field designs

During the operation of VRFBs, if similar flow plates are used in both sides, no hydraulic pressure gradient is expected across the membrane. Therefore, here, the analysis of permeability is only conducted for concentration-gradient induced crossover flux. The readers are encouraged to refer to Chapter 9 of this PhD dissertation for the influence of asymmetric flow fields design on the ionic crossover in all-vanadium redox flow batteries.

Chapter 10 includes a comprehensive discussion regarding the correlation of membrane permeability to the solubility of ionic species and corresponding diffusivities in the membrane phase. Therefore, here, we have limited our analysis to the assessment of permeability for various cell configurations. Based on the concentration of vanadium ions measured within the vanadium-deficient electrolyte at different timesteps, the following equation can be used to determine the permeability^{102, 202}.

$$V_d \frac{dC_d(t)}{dt} = P_{V(IV)}^m \frac{A}{t_m} [C_e - C_d(t)] \quad (7-1)$$

In Equation (7-1), V_d is the volume of the vanadium-deficient electrolyte (80 mL), C_d and C_e represent the concentration of the vanadium ion in vanadium-deficient and vanadium-enriched electrolytes, respectively (mol.L^{-1}). A is the cross-sectional area of the membrane (9 cm^2), t_m is the thickness of the membrane swelled in the vanadium electrolyte, and $P_{V(IV)}^m$ symbolizes the permeability the vanadium ions through the membrane.

It is also assumed that the changes in concentration of vanadium ions in the vanadium-enriched electrolyte is negligible^{102, 202}. To calculate the permeability, it is necessary to

integrated Eq. (7-1) during the entire time of the experiment. In the set of experiments conducted in this work, the integration has been conducted using Eq. (7-2) and (7-3).

$$\int_0^{C_d} \frac{d(C_e - C_d(t))}{(C_e - C_d(t))} = - \int_0^t \frac{P_{V(IV)}^m \cdot A}{V_d t_m} dt \quad (7-2)$$

$$\ln\left(\frac{C_e}{C_e - C_d(t)}\right) = \frac{P_{V(IV)}^m \cdot A}{V_d t_m} t \quad (7-3)$$

Based on Eq. (7-3), plotting left side of the equation ($\ln(\frac{C_e}{C_e - C_d(t)})$) versus time (t), can be used to determine the permeability as shown in Fig. 7-9. According to Fig. 7-9, the slope of the trendlines plotted for each cell configuration can be used to determine the permeability for each topology since the rest of the parameters contributing to the slope ($\frac{A}{V_d t_m}$) have remained unchanged among cases. Table 7.2 includes the permeability values determined based on the slope of trendlines shown in Fig. 7-9.

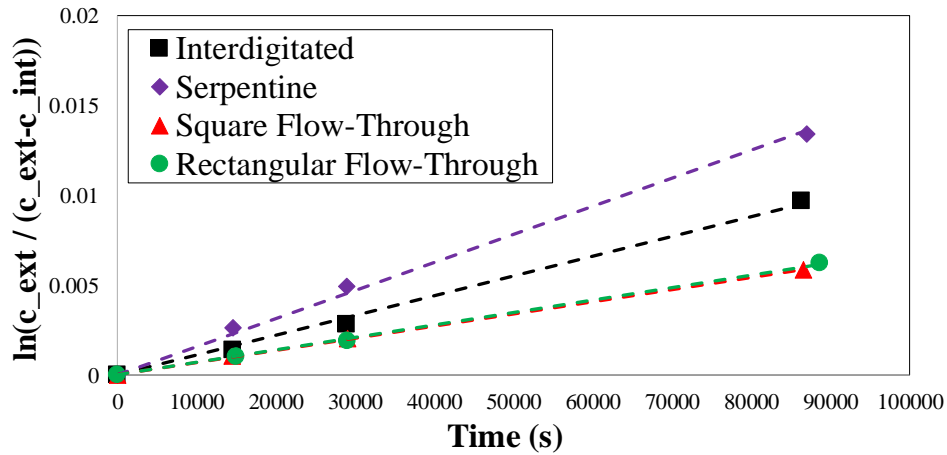


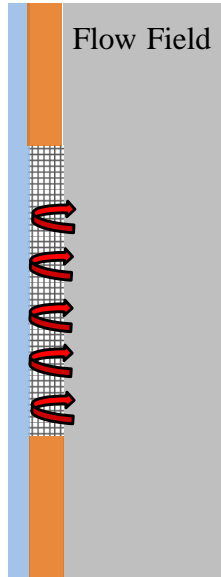
Figure 7-9: Semi-natural log plot used to determine permeability of vanadium ions through the membrane for various configurations of flow fields

Table 7.2. Ionic V(IV) permeability measured for different cell configurations

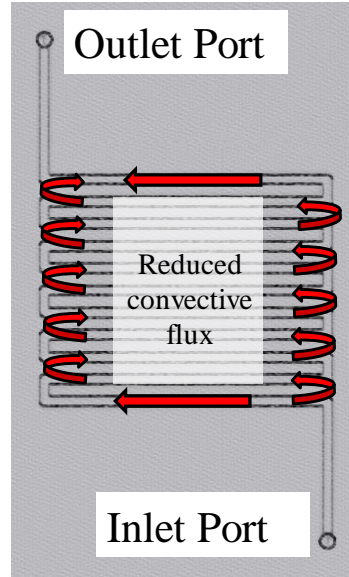
	V(IV) permeability ($\text{cm}^2 \cdot \text{s}^{-1}$) $\times 10^{-8}$
Serpentine	3.02
Interdigitated	2.37
Square flow-through	1.62
Rectangular flow-through	1.62

As tabulated in Table 7.2. the application of serpentine flow field design results in highest permeability ($3.02 \times 10^{-8} \text{ cm}^2 \cdot \text{s}^{-1}$) for V(IV) ion among other designs. The utilization of flow-through designs, however, causes a significant reduction (46%) in the permeability of V(IV) ions compared to serpentine design. To better clarify this point, it is important to consider the transport mechanism from the flow fields to the electrodes for various flow field designs.

Several computational efforts have been devoted elaborating the influence of flow field designs on the transport of electroactive species across the electrode ^{222, 223}. However, to the best of our knowledge, no previous work has reported the influence of flow field designs on the ionic crossover through the membrane. Therefore, using the knowledge gained from previous computational efforts, we have identified the key parameter influencing the crossover of vanadium ions across the membrane as tabulated in Table 7.2. Figure 7-10 schematically demonstrates the transport mechanism across the electrodes for various flow field designs.

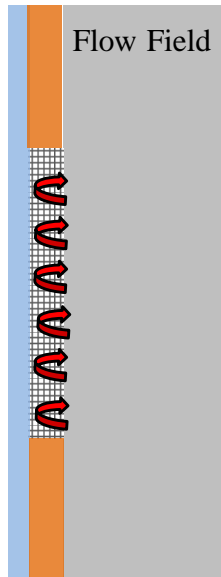


Side view, serpentine flow field

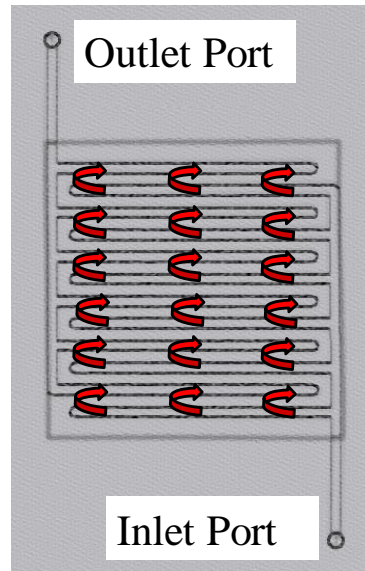


Front view, serpentine flow field

(a)



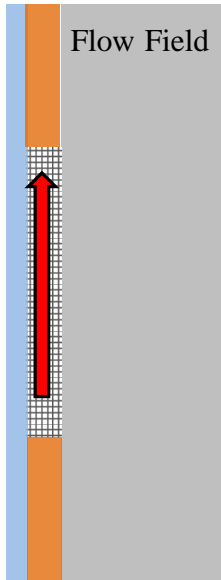
Side view, interdigitated flow field



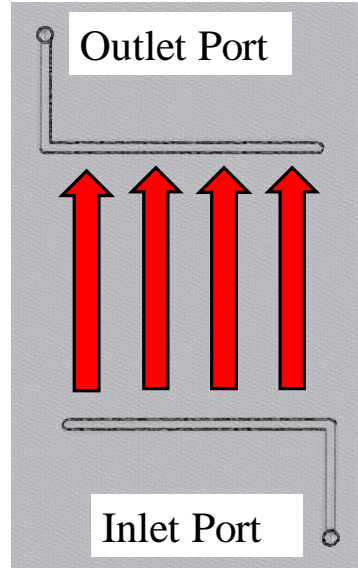
Front view, interdigitated flow field

(b)

Figure 7-10: Schematic illustration of macroscopic transport mechanism within the electrodes. (a) Serpentine, (b) Interdigitated, (c) Square Flow-Through, (d) Rectangular Flow-Through

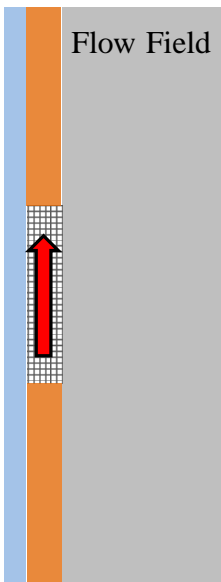


Side view, square flow-through flow field

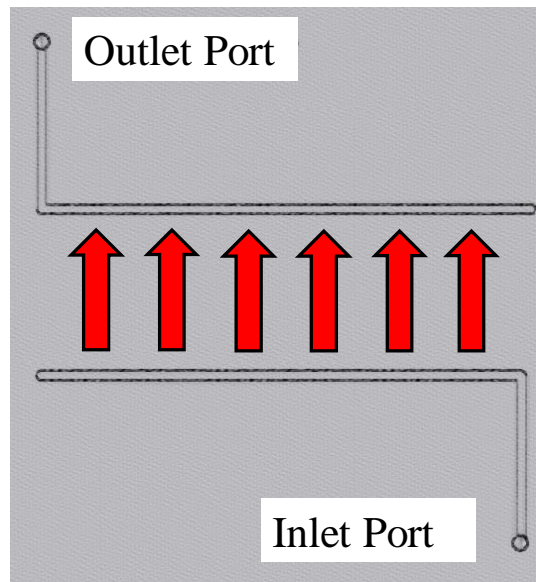


Front view, square flow-through flow field

(c)



Side view, rectangular flow-through flow field



Front view, rectangular flow-through flow field

(d)

Figure 7-10 continued

Figure 7-10 includes a simplified schematic of macroscopic transport mechanism within the electrodes for various flow field designs. Several experimental and modeling works have confirmed the validity of schematics shown in Fig. 7-10^{220, 222-225, 228, 229}. It is important to note that no previous work has reported the influence of transport mechanism across the electrode on the crossover of ionic species. Therefore, here, using an experimental approach, our objective is to describe such a dependency.

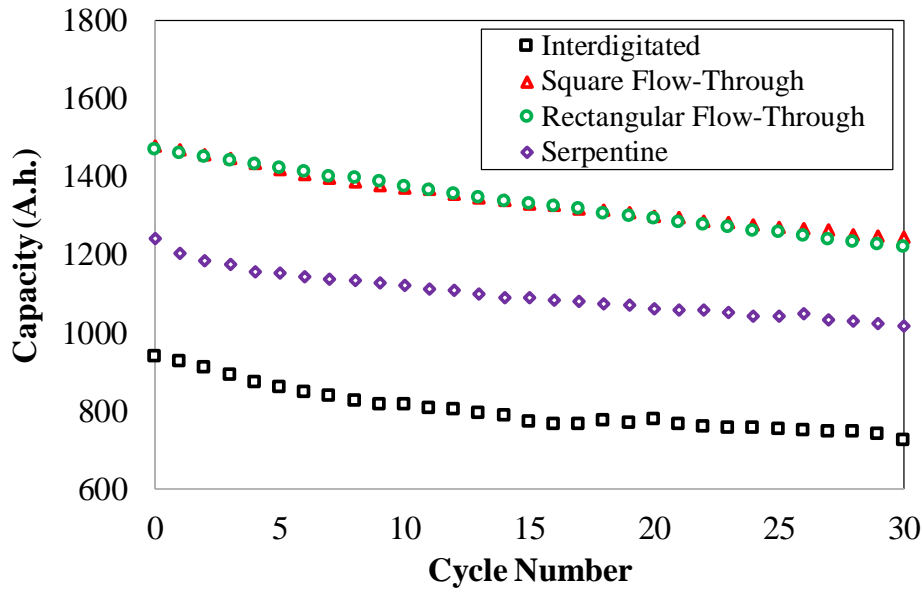
Considering the various transport mechanisms described in Chapter 4, here, no hydraulic pressure gradient exists across the membrane since similar flow plates have been used in both sides for each configuration. However, the transport mechanism from the flow field to the electrodes is vastly different among various flow plates shown in Fig. 7-10. For the flow-through designs, the velocity vector is dominated by the in-plane component. For the serpentine flow plate however, the electrolyte is being pushed into the electrodes at the far-end turning points. Therefore, at these locally high-pressure regions, substantial increase in the in-plane velocity vector is expected where the middle portion of the electrode experiences almost zero convective flow. The transport mechanism associates with the interdigitated flow plates exhibit similar behavior to serpentine flow plate but with significantly lower in-plane velocity component. It should also mention that such observations are only valid for the cell geometry considered in this work. For example, switching the carbon paper electrodes to carbon felt electrodes (with high porosity and lower pressure drop) or reducing the flow rate can substantially change the trends observed here. The influence of altering volumetric flow rate has been discussed in the next section.

7.3.3. Influence of convective-enhanced flow on ionic crossover and long-term capacity decay in VRFBs

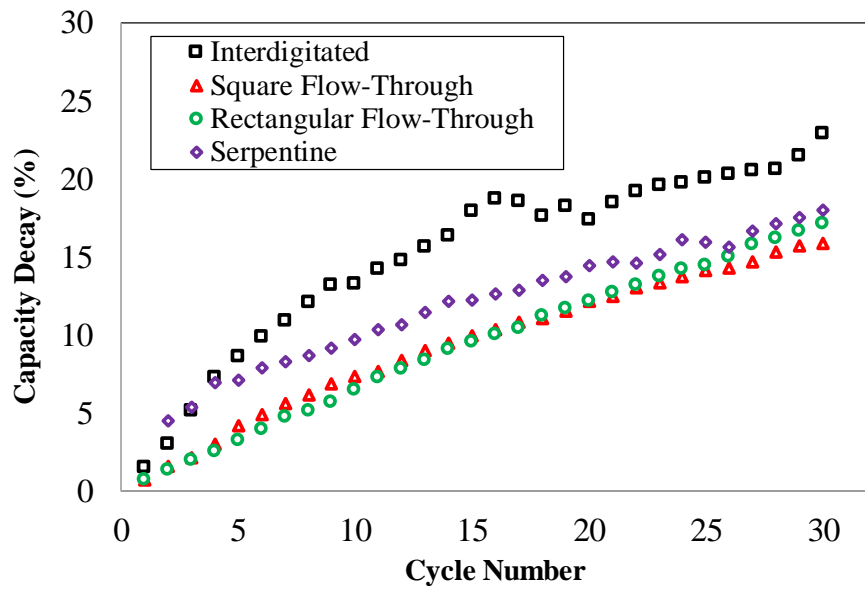
As briefly described in the previous section, here, we have explored the influence of variations in the volumetric flow rate on the ionic crossover and subsequent long-term capacity decay. To this end, identical cell architectures have been considered here where as-received carbon paper electrodes (39AA) along with Nafion®117 were used.

The composition of the electrolytes for cycling experiment as well as ionic crossover tests were remained unchanged. The readers are encouraged to refer to Sections 7.2.2 and 7.2.3 for further details. For the set of experiments considered in this section, the volumetric flow rate was $10 \text{ mL}\cdot\text{min}^{-1}$. Figure 7-11 includes the variations in discharge capacity and capacity decay during long-term cycling at $100 \text{ mA}\cdot\text{cm}^{-2}$.

Figure 7-11 includes variations in discharge capacity during cycling (Fig. 7-11(a)), capacity decay as a function of cycle number (Fig. 7-11(b)), and capacity decay as a function of time (Fig. 7-11(c)) for different flow plate designs. According to Fig. 7-11(b), the application of interdigitated flow fields design results in highest discharge capacity decay at the end of cycling (~23%). The utilization of serpentine, rectangular flow-through, and square flow-through designs result in ~18%, ~17%, and ~16% respectively.

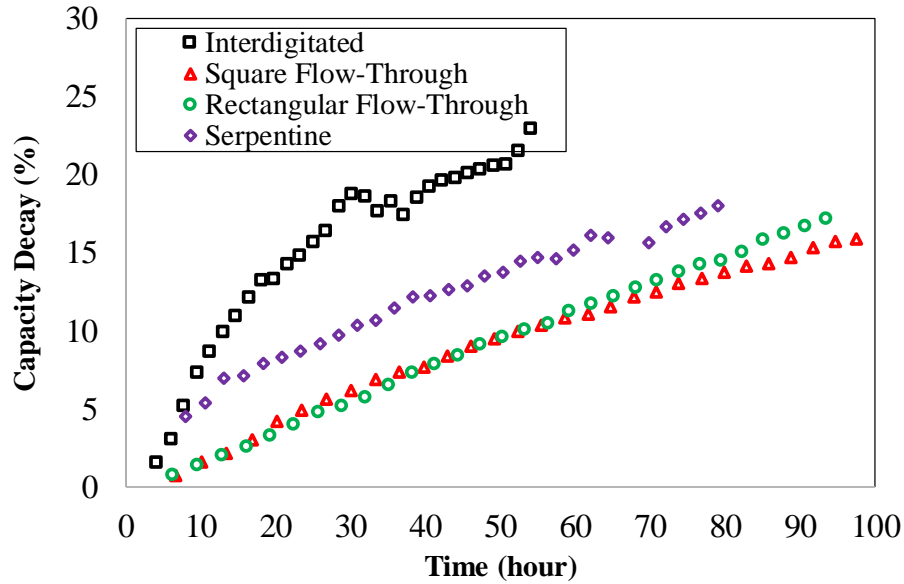


(a)



(b)

Figure 7-11: The variations in discharge capacity and capacity decay during cycling at $100 \text{ mA}\cdot\text{cm}^{-2}$ for different flow rates. (a) discharge capacity, (b) capacity decay as a function of cycle number, (c) capacity decay as a function of time



(c)

Figure 7-11 continued

The analysis of capacity decay as a function of cycle number can be misleading if the analysis does not include the variations in time. In particular, in this case, we have considered a very aggressive voltage windows (0.2 V – 1.8 V) where the cyclin spans a very wide state of charge and state of discharge window.

According to Fig. 7-11(c), the variations of capacity decay by time is significantly different from the trend observed for higher convective flows within the electrodes (see Section 7.3.1). The total time of cycling has shrunk to ~50, and ~80 hours for the interdigitated and serpentine flow plates. Here, it is evident that mass transport limitations hugely affect the accessible state of discharge for the interdigitated plates and thus, contributes to substantial decrease in total time of cycling.

To further analyze the variations in ionic crossover among different flow plates at relatively low convective flow rates (i.e. 10 mL.min⁻¹), UV/Vis spectroscopy has been performed for a similar set of cell architectures. The details of the setup along with electrolyte composition for conducting crossover experiments were already discussed in Sections 7.2.2 and 7.3.2.

The methodology for determining the permeability was also covered in Section 7.3.2. Therefore, here, a comparison is provided regarding the permeability values between low and high convective flow regimes. Figure 7-12 includes the permeability values measured at 10 and 40 mL.min⁻¹ for various flow plates.

As shown in Fig. 7-12, the variations in convective flow within the electrodes have substantial influence on serpentine flow plate design where the ionic permeability decreases to $1.7 \times 10^{-8} \text{ cm}^2.\text{s}^{-1}$ (~44% reduction) as a function of reduced flow rate.

The interdigitated design exhibits ~11% reduction in ionic permeability as a function of reduced flow rate. However, the flow-through plates demonstrate a miniscule sensitivity to decreased flow rate. The variations observed for ionic permeability for reduced convective flow is consistent with the rationale provided in previous section along with schematic demonstrations (Fig. 7-10).

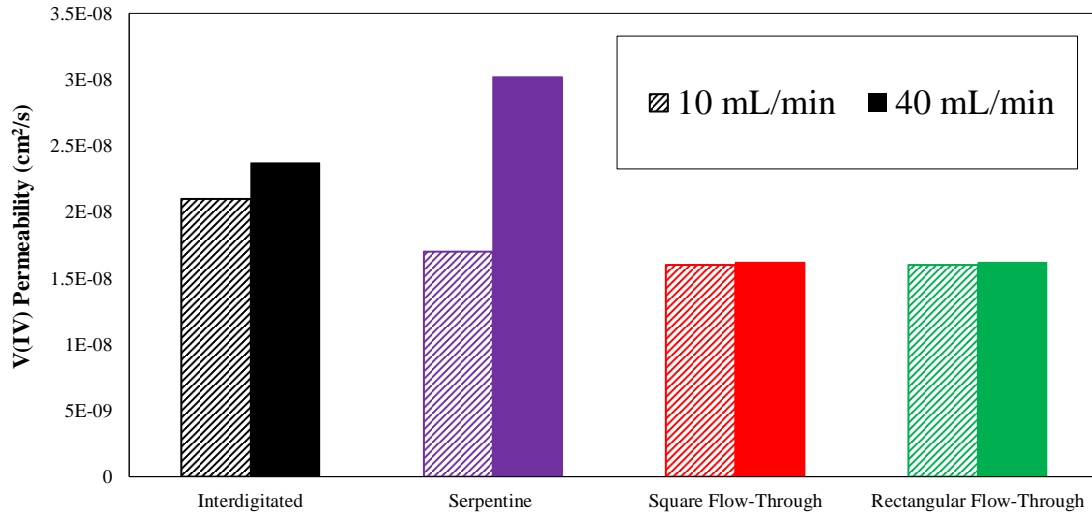


Figure 7-12: Comparison of the permeability values measured at 10 and 40 mL.min⁻¹ for various flow plates

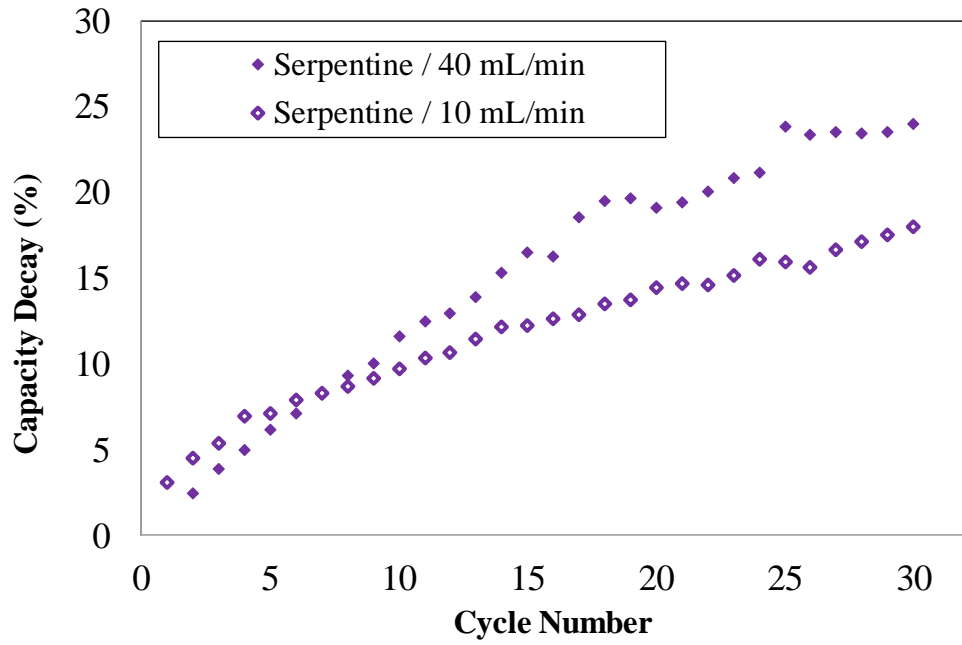
As noted in Section 7.3.2, the in-plane velocity component of the pattern of the convective flux within the electrode plays a significant role influencing the rate of crossover. The serpentine flow rate demonstrated highest capacity decay among other samples when the flow rate was 40 mL.min⁻¹. As shown in Fig. 7-10, in-plane component of the velocity vector is greatly enhanced towards the edges reducing the convective flow in the interior portion of the electrodes (Fig. 7-10(a)). However, the flow-through designs are dominated by in-plane component of the convective flux.

Therefore, as predicted, the sensitivity of flow-through designs to the changes in convective flow for homogeneous electrolytes (here, by homogenous we refer to electrolyte with no variations in state of charge) is minor. This prediction is confirmed with the permeability values provided in Fig. 7-12. For the interdigitated flow plates, decreased

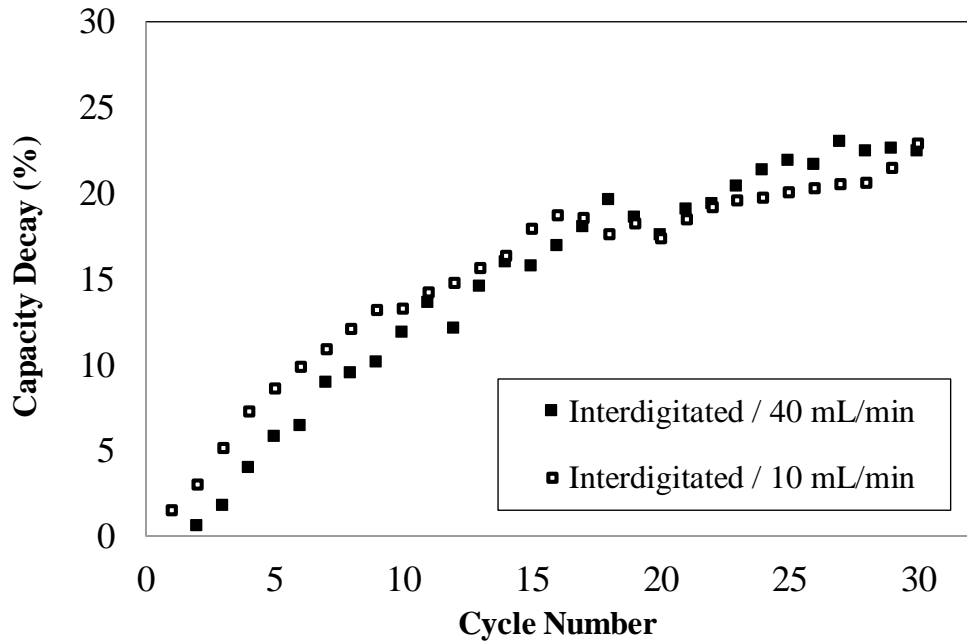
flow rate decrease the in-plane component of velocity vector and subsequently decreases the ionic crossover shown in Fig. 7-12. It is also important to compare the long-term capacity decay for various flow rates. Fig. 7-13 includes the variations in capacity decay for different flow plate designs at two different flow rates.

As shown in Fig. 7-13, the capacity decay corresponding to the serpentine flow field design demonstrates highest sensitivity to the changes in volumetric flow rate. As illustrated in Fig. 7-13(a), the capacity decay at the end of cycling for serpentine flow field architecture is ~18% for $10 \text{ mL}\cdot\text{min}^{-1}$ as compared to ~24% for $40 \text{ mL}\cdot\text{min}^{-1}$. This is consistent with the permeability values shown in Fig. 7-12.

The predictions made based on the permeability assessment for flow-through designs (Fig. 7-12) is also confirmed by the capacity decay analysis provided in Fig. 7-13 where the variations of capacity decay at the end of cycling is minor for flow-through flow field designs (Fig. 7-13(c) and 7-13(d)). However, according to Fig. 7-13(b), the variations in capacity decay as a function of flow rate for interdigitated plate set is not following the predictions made based on crossover analysis (Fig. 7-12). We believe the major reason for such inconsistent behavior is increased mass transport limitations for interdigitated plates at reduced volumetric flow rate that extremely shrinks the depth of charge and discharge for this configuration. This analysis is further confirmed when we consider the results provided in Fig. 7-11(c) where the total cycling time for the interdigitated plates has reduced to about 50 hours at lower flow rate ($10 \text{ mL}\cdot\text{min}^{-1}$).

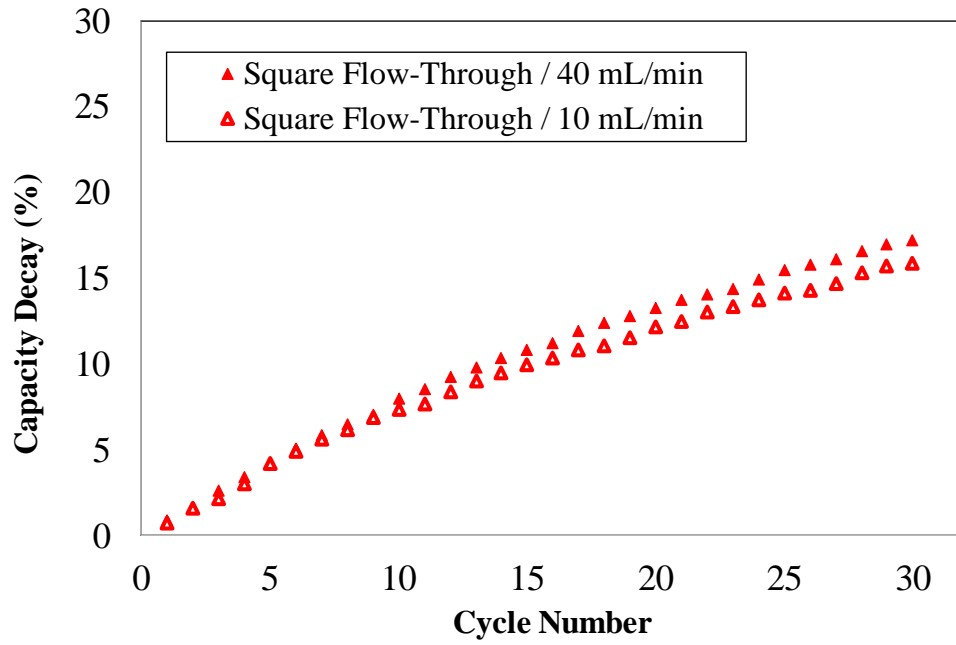


(a)

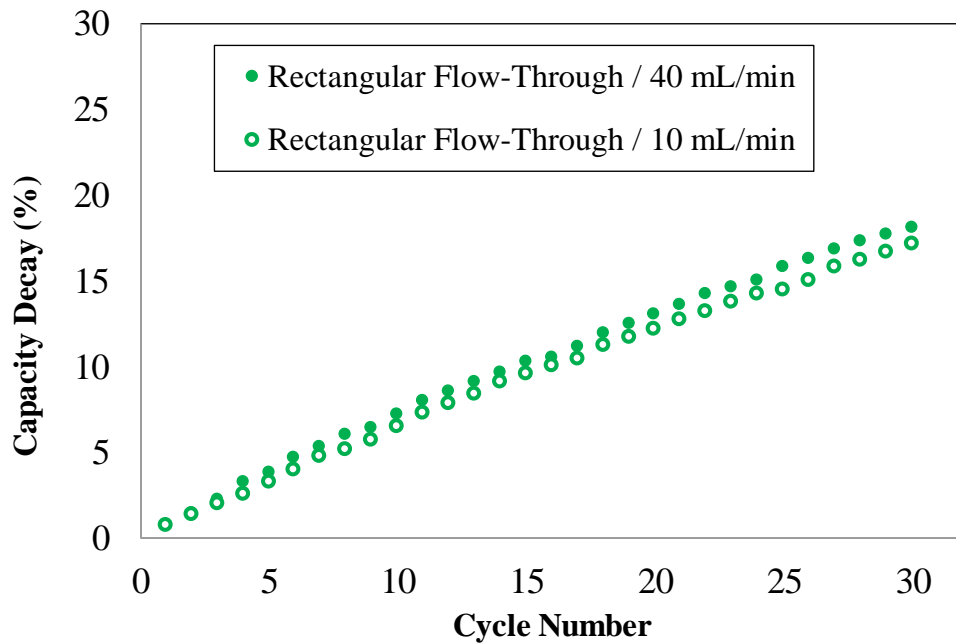


(b)

Figure 7-13: Trend of capacity decay during extended cycling for different flow plates design at two various flow rates. (a) Serpentine, (b) Interdigitated, (c) Square Flow-Through, (d) Rectangular Flow-Through



(c)



(d)

Figure 7-13 continued

7.4. Conclusions

Among mass transport mechanisms through the electrodes (bulk diffusion, migration and convection), the convective flux can be engineered to substantially improve the performance of the cells. However, increased convection through the electrodes commonly increases the pressure drop for the system and subsequently decreases the system-level energy efficiency. The tradeoff between improved performance and increased pressure drop via increasing the convective flux within the electrodes is well-established in the field. In this work, we introduce another important criterion in engineering flow plate designs that substantially influences the capacity retention over long-term cycling for VRFBs. Based on the analysis provided in this work, it was shown that the distribution of the convective flux is the detrimental factor influencing the crossover and resulting capacity decay in an operating cell.

Several parameters can be tuned to alter the convective flux within the electrodes. Flow plates design is one of the major components that can be engineered for promoting the convection flux. Four different flow plates including serpentine, interdigitated, square flow-through, and rectangular flow-through designs were investigated. Long term cycling experiments with aggressive voltage limits were considered to span a large state of charge and state of discharge window. In addition, UV/Vis spectroscopy was used to explore the concentration-gradient induced crossover for various flow plates.

It was shown that the serpentine flow plates exhibit higher sensitivity for the variations in convective flux. Increasing the convective flux within the electrodes substantially increases the rate of crossover for this design. However, the flow-through designs exhibit miniscule sensitivity to increased convective mass flux. Considering the mass transport mechanism within the electrodes, the through-plane component of the convective flux (through-plane average velocity component) was determined to be the key parameter directly affecting the rate of crossover. Therefore, future flow field designs must focus on optimizing the performance, reducing the pressure drop, and decreasing the ionic crossover via engineering the through-plane component of the convective flux.

To the best of our knowledge, no previous work has reported the influence of flow field design (i.e. convective flux) on the ionic crossover and subsequent capacity decay. Therefore, in this work, for the first time, we explored the effect of flow field design on the crossover.

7.5. Acknowledgments

Yasser Ashraf Gandomi thanks University of Tennessee for providing Chancellor Fellowship.

CHAPTER EIGHT :
TECHNIQUES FOR CAPACITY RETENTION IN RFBS

Scholarly contributions

The contents of this chapter have been presented during an invited talk (entitled “Passive mitigation of ionic crossover in all-vanadium redox flow batteries via novel asymmetric cell topologies”) at Massachusetts Institute of Technology in August 28, 2018.

This chapter is revised based on a manuscript prepared for submission to the Journal of Electrochemical Society.

Yasser Ashraf Gandomi, D. S. Aaron, M. M. Mench. “Passive Techniques for Capacity Retention in Redox Flow Batteries” *in preparation*, (2018)

Abstract

Maintaining initial capacity during cycling of a redox flow battery (RFBs) is a major design criterion. Various redox active species with aqueous or non-aqueous solvents are being introduced for RFBs and designing cells capable of retaining initial capacity via mitigating crossover of the active species and solvent is of great importance. In this chapter, an overall overview of different class of redox active species used for RFBs is provided. In addition, various techniques have been suggested for maintaining/recovering initial capacity for extended cycling. In particular, the methods of capacity retention have been summarized for the major electroactive species used within RFBs including redox-active colloids (RACs), redox-active polymers (RAPs), redox-active oligomers (RAOs), redox-active organic molecules (ROMs), and redox-active transition metal salts (RAMs).

8.1. Introduction

As discussed in Chapter 1, various redox active species have been used for redox flow batteries. Inorganic redox materials, in particular, transition metal salts are hugely employed for RFBs and long-term structural stability have been demonstrated for this class of RFBs. However, the transition metal salts are expensive. Therefore, alternative redox active species are explored in the field. Organic redox materials are relatively cheap compared to inorganic ones, and their properties can be tuned molecularly to achieve desired storage/stability characteristics. The inorganic redox molecules are often used with non-aqueous solvents and such a combination allows achieving wider electrochemical potential operating windows compared to aqueous solvents.

Figure 8-1 categorizes various types of redox active species that have been used for redox flow batteries based on the size of the redox active core unit. Redox active colloids (RACs) are polymer-based spherical particles with modular design capabilities. Recently, RACs with an average spherical diameter in the range of 80–800 nm with reversible redox activity have been reported as promising energy storage carriers²³⁰. Redox active polymers (RAPs) are also explored as nanoscale energy storage medium for RFBs in some recent applications^{231, 232}. Various types of smaller redox active materials including redox active oligomers (RAOs), redox active organic molecules (ROMs), and redox active transition metal salts (RAMs) are also being employed for different applications²³³.

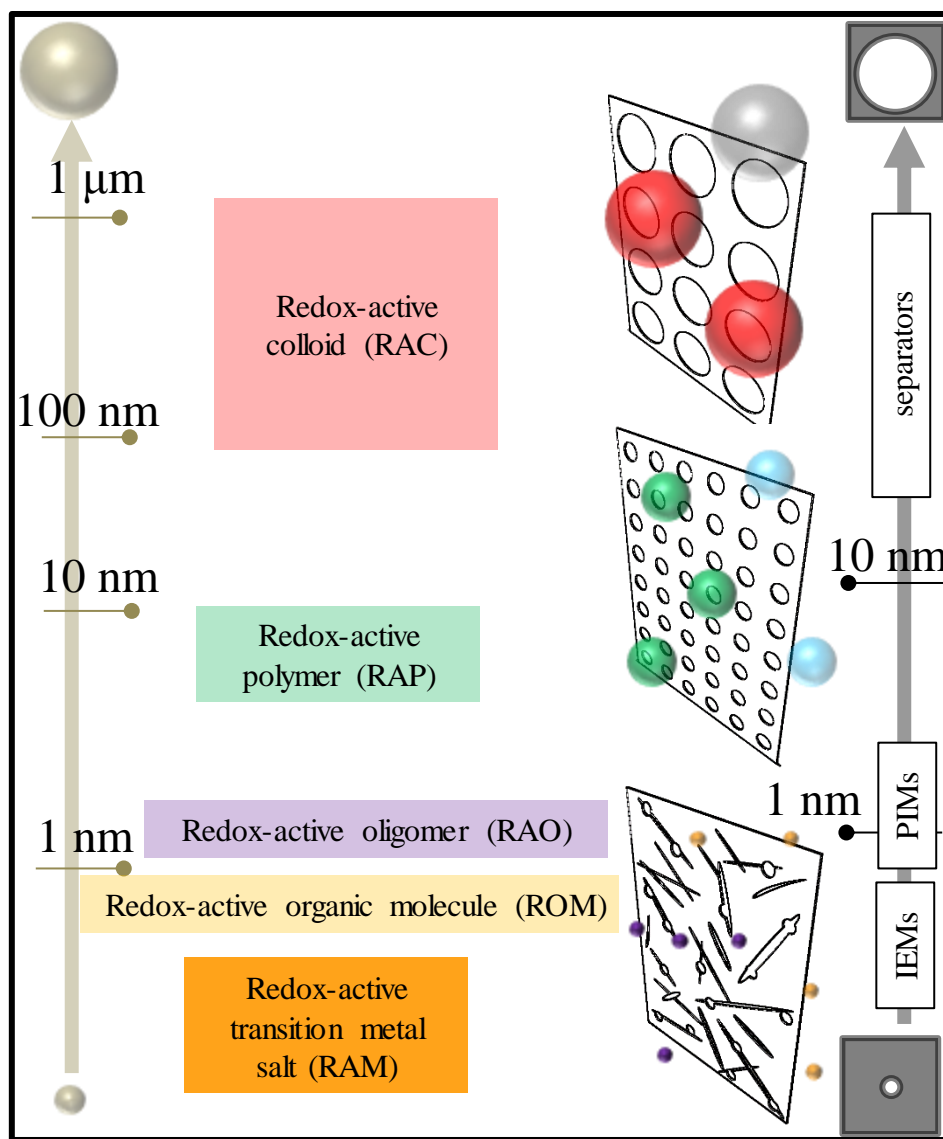


Figure 8-1: Schematic of various membranes and species crossover (Inspired by Ref. ²³⁴)

As detailed in Chapter 1, commonly used topologies for RFBs include separators (membranes) within their structure. An ideal separator must be selective towards major charge balancing ions and must blockade the crossover of redox active materials and the solvent. In addition, it must be electrically insulating to prevent internal short-circuiting.

Mechanical, chemical, and electrochemical stability is also a major design criterion for the separators. In principle, tuning the pore size of the separator can be a logical pathway towards mitigating the crossover of active redox molecules and the solvent. As shown in Fig. 8-1, based on the size of the redox active materials, various separators with different pore size have been explored. Separators with pore size larger than 10 nm (e.g. Celgard, Daramic), polymers with intrinsic microporosity (PIMs, pore size ~1 nm), and ion-exchange membranes (IEMs, pore size < 1 nm) are some available options^{56, 102, 233}.

8.2. Design Strategies for Mitigating Crossover

In practical applications, four different pathways are available for mitigating the crossover of redox active species and the solvent through the membrane as schematically illustrated in Fig. 8-2.

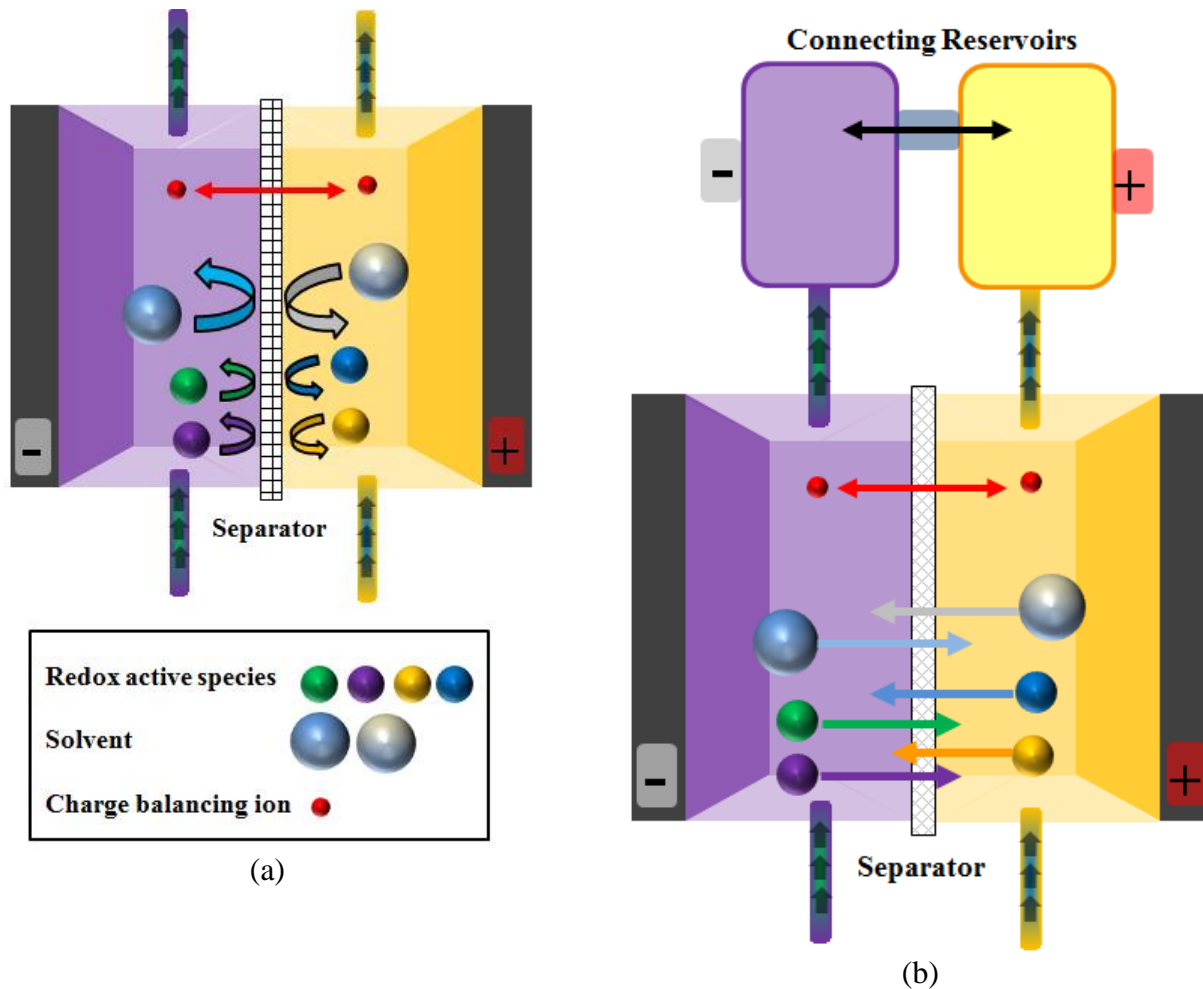
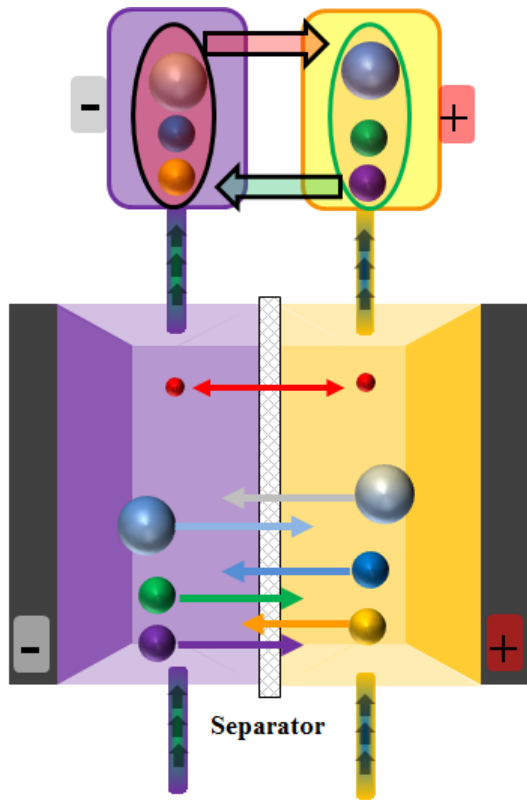
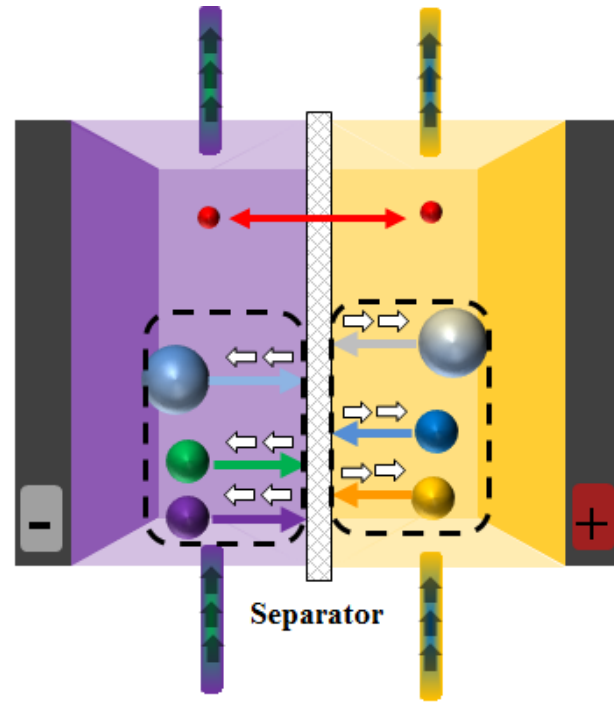


Figure 8-2: Strategies for mitigating the crossover and/or recovering the capacity; (a) Impermeable membranes, (b) Connecting reservoirs externally, (c) Filtering the species out from opposite electrolytes, (d) Engineering the direction of crossover flux



(c)



(d)

Figure 8-2 continued

8.2.1. Impermeable membranes for redox active species and solvent

One of the major thrusts in RFB research is developing membranes that are impermeable for redox active species as well as the solvent. As schematically illustrated in Fig. 8-2(a), developing highly selective membranes can ultimately result in zero-crossover RFB systems. To this end, size selectivity along with charge selectivity can be implemented. As illustrated in Fig. 8-1, there is an increasing interest for the application of PIMs to prevent the crossover for non-aqueous RFBs that utilize organic redox active species²³³. For RFBs utilizing aqueous solvents and transition metal salts (e.g. all-vanadium redox flow batteries), various polymeric membranes along with implementation of different treatments have been explored to effectively reduce the crossover^{85, 102, 138, 235-237}.

8.2.2. Recovering capacity via remixing external electrolytes

For some class of RFBs that the crossover of electroactive species and solvent through the separator is inevitable during the cycling; under certain conditions, the lost capacity due to species and solvent crossover can be recovered via periodic remix and rebalancing the external electrolytes (see Fig. 8-2(b))¹. It is important to note that this technique is feasible if the side reactions initiated due to the crossover of redox active species and solvent is reversible. Successful implementations of this technique have been demonstrated for the all-vanadium and all-iron redox chemistries. This technique requires precise assessment of the state of charge within electrolytes since without an exact measurement, the electrolytes will be out of charge-balance after remixing.

Real-time implementation of this technique has also been demonstrated recently via electrolyte-reflow method where the external reservoirs are connected providing a pathway for hydraulically balancing the electrolytes that have become off-balance due to crossover

238

8.2.3. Filtering the electroactive species out from opposite electrolytes

As schematically illustrated in Fig. 8-2(c), if the crossover of electroactive materials and the solvent through the separator is unstoppable during cycling, to recover the capacity, it is possible to filter out the electroactive species along with the solvent from opposing electrolytes. Of course, the major requirement for utilization of this technique is stability of the diffused species in the opposing electrolytes. If the diffused species remain stable in the opposing electrolytes, various filtration techniques based on the electric charge, size, and electromagnetic properties can be implemented. Phase separation techniques are also possible in this case.

8.2.4. Engineering the direction of crossover flux

Although remix and subsequent rebalancing of the external electrolytes has been widely used for RFBs utilizing transition metal salts (e.g. all-vanadium redox flow batteries), this technique has major drawbacks. The periodic nature of this technique along with a need for precise assessment of state of charge for each electrolyte is cumbersome and for large-scale applications is very inefficient. Therefore, an alternative method is needed.

As illustrated in Fig. 8.2(d), engineering the direction of crossover flux for electroactive species and the solvent is a promising way to mitigate the crossover. As discussed in Chapter 4, we have successfully been able to assess the magnitude and directionality of the net crossover current for an operando all-vanadium redox flow battery under symmetric loading conditions. Knowing the directionality of net crossover flux, Jong Ho Park et al. have implemented asymmetric concentration of vanadium ions in negative and positive electrolytes for passively mitigating the crossover²³⁹. Asymmetric electrolyte volume has also been implemented for passive mitigation of crossover during long term cycling²⁴⁰. The implementation of asymmetric vanadium concentration is a promising technique; however, it results in reduced initial available capacity. It also suffers from capacity decline after initial increase of capacity. Although the magnitude of such a decline is lower compared to symmetric vanadium concentration. The implementation of asymmetric electrolyte volumes is also promising; however, it requires precise control of the electrolyte compositions and is relatively expensive due to increased size of the reservoirs (specifically for large-scale applications).

We have built based on the knowledge gained from the influence of electric field on the crossover (Chapter 4), to redesign the cell architecture along with engineering the electrolytes composition to passively mitigate the crossover of vanadium ions as well as the solvent (water). Further details are presented in the following chapters.

CHAPTER NINE :
ASYMMETRIC CELL AND ELECTROLYTE TOPOLOGIES FOR PASSIVE
MITIGATION OF CAPACITY IN AQUEOUS RFBS

Scholarly contributions

* The Abstract is revised based on an award-winning talk presented in 233th Electrochemical Society (ECS) Meeting & Electrochemical Energy Summit, Honolulu, Hawaii (May 13 - 17, 2018).

- Abstract ID: MA2018-01 13
- Title: (Industrial Electrochemistry and Electrochemical Engineering Division Student Achievement Award Address) Mitigating Ionic and Water Transport through Polymeric Membranes in All-Vanadium Redox Flow Batteries Via Design, Engineering, and Prototyping Novel Asymmetric Cell Topologies

** The contents of this chapter have been presented during an invited talk (entitled “Passive mitigation of ionic crossover in all-vanadium redox flow batteries via novel asymmetric cell topologies”) at Massachusetts Institute of Technology in August 28, 2018.

*** This chapter is revised based on a manuscript prepared for submission to the Journal of Electrochemical Society.

Yasser Ashraf Gandomi, D. S. Aaron, M. M. Mench. “Passive Techniques for Capacity Retention in Redox Flow Batteries” *in preparation*, (2018)

**** The contents of this chapter are under invention disclosures at the University of Tennessee

Yasser Ashraf Gandomi, M. M. Mench, “Novel all-vanadium redox flow battery cell for passive mitigation of capacity decay using asymmetric configuration of flow fields”, *University of Tennessee Research Foundation’s Reference ID: 17156-03*, filed May 25, 2017, Patent pending.

Abstract

Numerous parameters affect solute (vanadium ions) and solvent (water) transport through the membrane during cycling of all-vanadium redox flow batteries (VRFBs); these include: membrane properties (polymer type, thickness, equivalent weight, and reinforcement), battery configuration (electrode morphology, flow field design), electrolyte composition and operating conditions (flow rate, temperature, and charge/discharge current). The

concentration gradient and the electric field (via migration and electro-osmosis, respectively) are dominant driving forces for vanadium ion transport across the membrane. Water transport is due to multiple driving forces including electro-osmotic drag, thermo-osmosis, and osmotic and hydraulic pressure gradients. Therefore, it is necessary to understand these coincident forces affecting the transport of vanadium ions and water through the membrane.

In previous chapters, various parameters (cell components, operating conditions, electrolyte composition) influencing the transport of vanadium ions and the solvent (water) were thoroughly discussed. Based on the insights gained, in this chapter, we have proposed novel VRFB topologies with asymmetric configuration of the negative and positive sides. Such asymmetry in the reactor and external electrolytes passively mitigates vanadium ion and water crossover during long-term cycling, improving the energy storage efficiency of VRFBs.

The novel cell configurations designed and engineered for this work are under invention disclosures at the University of Tennessee and provide an inexpensive and passive solution for further adopting the VRFBs as a safe and robust technology for grid-scale storage.

9.1. Introduction

The transport of vanadium ions and water across the ion-exchange membranes is inevitable during cycling of all-vanadium redox flow batteries (VRFBs). The undesired transport of water and vanadium ions through the ion-exchange membrane (usually called crossover) significantly limits the applications of VRFBs. Decreasing the radical capacity decay is an active area of research for startup companies and research centers all over the world involved in commercializing the technology. A quick survey of the companies involved in VRFB business reveals that there is a significant commercialization potential for any technology that mitigates the capacity decay in VRFBs.

In Chapter 8, a comprehensive summary of the techniques developed for tackling crossover issue in redox flow batteries (RFBs) was provided. As discussed, developing impermeable membranes to redox active species, remixing external electrolytes (real-time or offline), filtering the electroactive species out from the opposite electrolytes, and engineering the direction of crossover flux are the major thrusts towards mitigating crossover in RFBs.

For all-vanadium redox flow batteries, developing impermeable membranes to vanadium ions is an active area of research. However, in most cases, commercially available ion-exchange membranes (e.g. Nafion® family) are used where the crossover of vanadium ions and the solvent (water) is unavoidable. Therefore, remixing and subsequent rebalancing the negative and positive electrolytes is commonly used for recovering the capacity. However, as explained in Chapter 8, this technique requires additional procedures and

often results in off-the-balance state of charge for negative and positive electrolytes. Therefore, engineering the direction of crossover flux is a promising technique to tackle the crossover issue in an operating VRFB. In Chapter 4 and in a related publication ²⁰², we demonstrated a novel experimental and modeling approach and measured the direction and magnitude of crossover current for an operando VRFB. Therefore, based on the insight gained from our previous work; here, we have proposed novel techniques to passively mitigate the crossover in operating VRFBs. Engineering the cell architecture along with electrolyte composition have been explored in this section for developing passive strategies capable of retaining the discharge capacity for extended cycling.

9.2. Theoretical Background

The mathematical modeling framework for the transport of vanadium ions and the solvent was established in Chapter 4 and is accessible in a recent publication ²⁰². As discussed, the conservation of mass must hold within the membrane phase for different ionic species as described in Eq. (9-1) ²⁰².

$$\frac{\partial c_i^m}{\partial t} = -\nabla \cdot \mathbf{N}_i^m \quad (9-1)$$

In Eq. (9-1), \mathbf{N}_i^m is the flux of species i within the membrane ($\text{mol}\cdot\text{m}^{-2}\text{s}^{-1}$). Three major driving forces including concentration gradient, electrostatic potential gradient, and the advection contribute to the flux as formulated in the following ²⁰²:

$$\mathbf{N}_i^m = -D_i^m \nabla c_i^m - z_i u_i^m F c_i^m \nabla \Phi^m + c_i^m \mathbf{v}_0 \quad (9-2)$$

Full description of the terms used in Eq. (9-2) is available in Chapter 4 (also in a recent publication ²⁰²). Among the flux components shown in Eq. (9-2) the advection term is of great importance since it is directly linked to the solvent transport (Eq. (9-3)) as formulated in Chapter 4 and is also shown in other publications ^{176, 202}.

$$v_0 = \frac{\xi i^m}{c_0 F} \quad (9-3)$$

Therefore, as shown in Eq. (9-3), the solvent (water) velocity is directly correlated to electro-osmosis drag coefficient (ξ) as well as the current density (i^m). However, Eq. (9-3) was derived from Eq. (9-4) assuming negligible gradient in chemical potential of the water.

$$N_0^m = \frac{\xi i^m}{F} - \alpha \nabla \mu_0 \quad (9-4)$$

Therefore, in all the previous efforts to measure the crossover rate for vanadium ions, we designed the experimental setup along with external electrolyte composition to minimize the gradient in chemical potential of the water and subsequently minimize undesired transport of the water through the membrane.

Being able to measure the net direction of vanadium ion crossover for an operando VRFB as demonstrated in Chapter 4 and in a related publication ²⁰²; we can indeed revisit Eq. (9-4) with the idea of engineering the water flux via altering the gradient in chemical potential of the water. The major goal is to tune the direction of the water transport through engineering the cell components or electrolyte composition.

In general, the chemical potential of the water in the functional form can be written in the form of Eq. (9-5).

$$\mu_0 = F(P, T, X_p) \quad (9-5)$$

Therefore, to alter the chemical potential, we can write:

$$d\mu_0 = \left(\frac{\partial\mu_0}{\partial P}\right)_{T, X_p} dP + \left(\frac{\partial\mu_0}{\partial X_p}\right)_{T, P} dX_p + \left(\frac{\partial\mu_0}{\partial T}\right)_{X_p, P} dT \quad (9-6)$$

The VRFBs commonly operate at room temperature, therefore, to impose any gradient in chemical potential via implementing temperature gradient, a substantial increase in the operating temperature is needed. Such an increase in operating temperature of the solvent results in vanadium ion precipitation. Therefore, for VRFBs, isothermal operating condition is preferred, and such a requirement further simplifies Eq. (9-6).

$$d\mu_0 = \left(\frac{\partial\mu_0}{\partial P}\right)_{T, X_p} dP + \left(\frac{\partial\mu_0}{\partial X_p}\right)_{T, P} dX_p \quad (9-7)$$

In the following sections, we have implemented Eq. (9-7) to engineer the water flux across the ion-exchange membranes via designing novel cell topologies along with engineering electrolyte composition.

9.3. Experimental

9.3.1. Asymmetric cell configuration for reduced crossover

As formulated in Section 9.2, engineering direction of water flux during cycling of VRFBs is of great importance. According to Eq. (9-7), the main objective is engineering cell

architecture along with electrolyte composition for tuning the solvent transport through the ion-exchange membrane. As discussed in Chapter 7, flow field designs are usually tailored for reduced pressure drop and/or mass transport overpotentials. Figure 9-1 includes the pressure drop associated with three commonly used flow field design (i.e. flow-through, serpentine, interdigitated). The pressure drop data shown in Fig. 9-1 has been adopted from a recent publication from our lab ²²⁵.

According to Fig. 9-1, flow-through flow field design imposes the highest pressure drop, followed by serpentine and interdigitated designs. According to Eq. (9-7), implementing hydraulic pressure gradient can be used to alter the gradient in chemical potential of the solvent. Therefore, maintaining similar composition for the negative and positive electrolytes, Eq. (9-7) can be simplified to Eq. (9-8).

$$d\mu_0 = \left(\frac{\partial \mu_0}{\partial P} \right)_{T, X_p} dP \quad (9-8)$$

Based on Eq. (9-8) and the data provided in Fig. 9-1, hydraulic pressure gradient can be applied via utilizing asymmetric flow field configuration. To demonstrate this concept and novelty, various flow field pairs can be selected. However, as shown in Chapter 7, the interdigitated flow field designs demonstrated reduced theoretical capacity utilization along with increased mass transport overpotentials within the experimental conditions considered in this work. Therefore, here, since our objective is to explore the influence of asymmetric flow field design on the crossover and capacity retention without adversely being affected from reduced mass transport within the electrodes, serpentine/flow-through pair was selected.

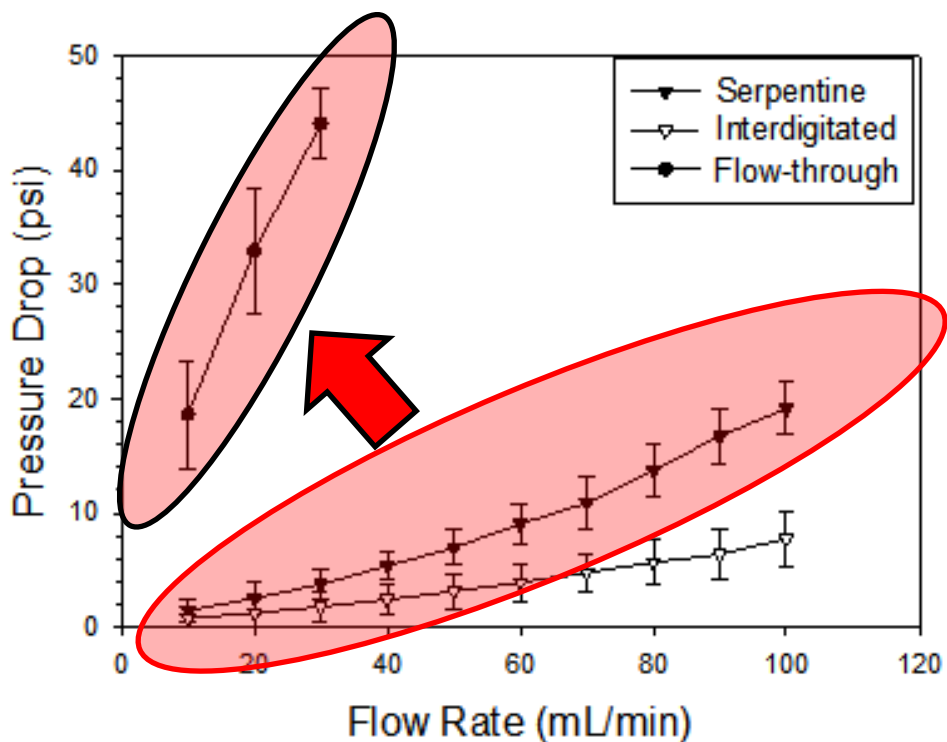


Figure 9-1: Pressure drop data associated with three different flow plate design including flow-through, serpentine, and interdigitated (Data have been adopted from Ref. ²²⁵)

Considering the pressure limitations associated with our experimental setup, increasing the flow rate beyond $40 \text{ mL}\cdot\text{min}^{-1}$ for flow-through flow field configuration was not possible. Therefore, we decided to conduct the experiments at $40 \text{ mL}\cdot\text{min}^{-1}$ using flow-through/serpentine pair. The flow fields were designed and built in-house. The schematic of the flow fields has been shown in Fig. 9-2. The geometrical details associated with the flow fields are provided in Table 9.1.

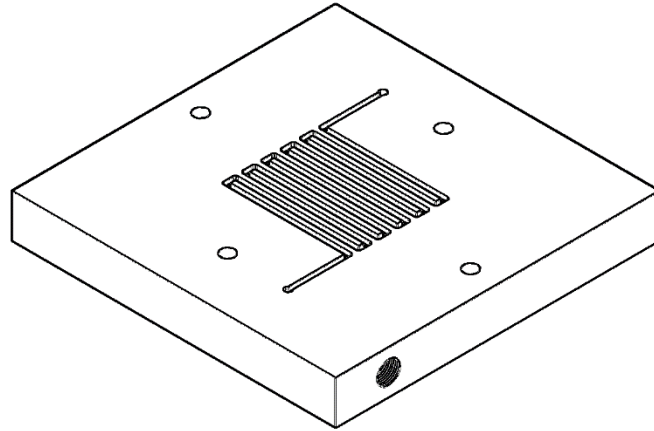
To conduct the experiments associated with long-term cycling along with UV/Vis spectroscopy, a novel setup (we call it **IonCrG: Ionic Crossover Gauge**) was designed

and built as shown in Fig. 9-3. Further details regarding IonCrG is shown in Fig. 9-3. The IonCrG includes four single cells (including novel cell design), two-channel peristaltic pumps (Cole Parmer, Masterflex L/S), and external reservoirs as well as ultraviolet/visible (UV/Vis) spectrometers (THORLABS) with light sources (Ocean-Optics). Also, a central temperature control unit maintains a constant temperature of 30° C for all the cells and reservoirs. Maintaining constant temperature throughout the experiment among various cells and electrolytes is crucial since a substantial temperature gradient across the membranes can initiate undesired solvent transport. In addition, significant increase/decrease in operating conditions can result in vanadium precipitation.

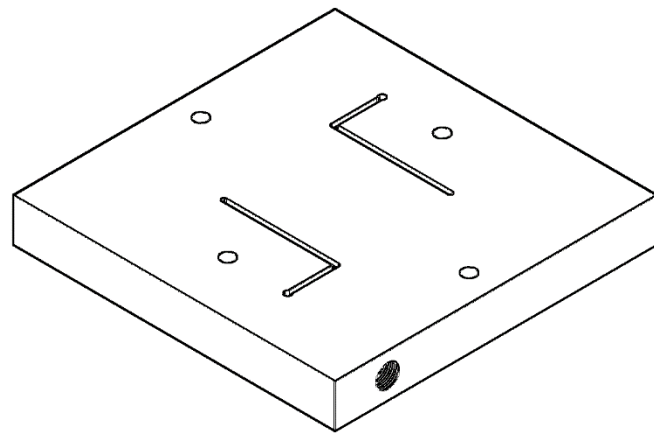
The initial electrolyte of interest was prepared using Cell 1 which was a 25 cm² active area cell. Pristine 39AA carbon paper electrodes (SGL Group, Germany) were sandwiched between a flow plate and the membranes.

Table 9.1. Flow fields and channel geometries for serpentine and flow-through flow field designs

	Flow field geometry (cm ²)	Channel geometry (mm ²)
Serpentine	3 × 3	1 × 1
Square flow-through	3 × 3	1 × 1



(a)



(b)

Figure 9-2: Schematic illustration of the flow fields used for asymmetric cell configuration (a) Serpentine, (b) Flow-through

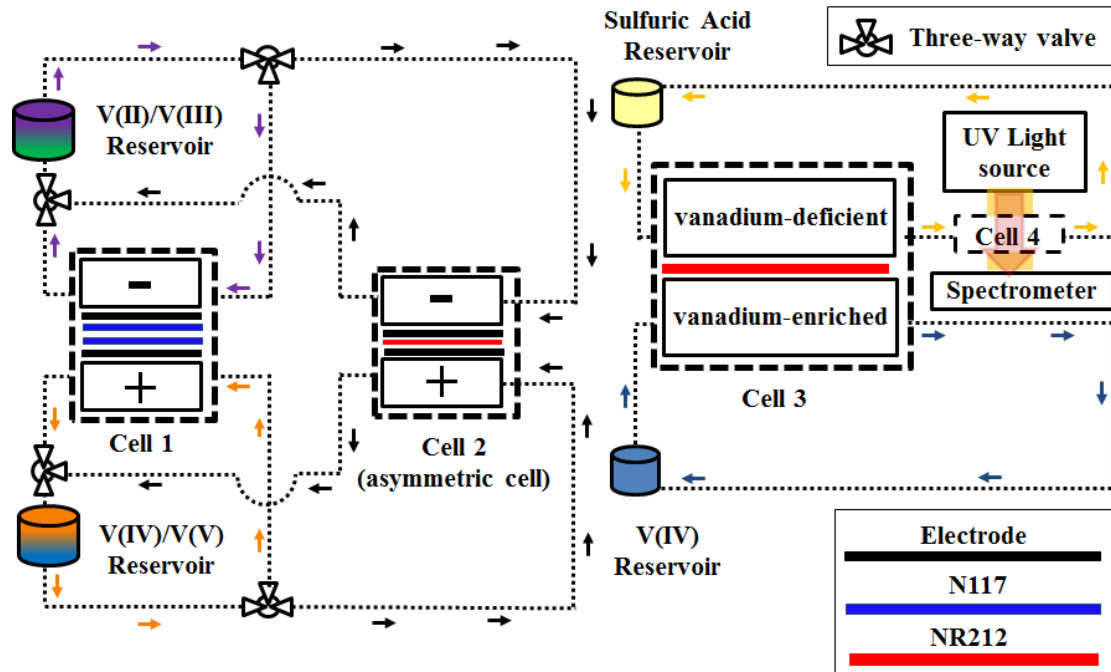


Figure 9-3: IonCrG: A novel setup for measuring real-time ionic crossover and long-term capacity decay during cycling

Two membranes (Nafion[®] 117, E. I. DuPont Company, USA) were utilized in Cell 1 in order to reduce the rate of crossover during electrolyte preparation. Two electrolyte reservoirs were utilized in conjunction with Cell 1 for V(II)/V(III) and V(IV)/V(V) couples. All reservoirs were sealed and under constant nitrogen purge while stir bars were utilized to assure uniform composition of the reservoir solutions.

Cell 2 was designed in order to mitigate the capacity decay for an operating VRFB. The novel cell had an asymmetric flow field configuration of negative and positive sides and utilized a 9 cm² active area with a single-path serpentine flow field at the anode side and a 9 cm² active area with a square flow through flow field at the cathode side. This asymmetric

cell topology was engineered based on the direction of net crossover current measured in Chapter 4 (further details are available in Ref. ²⁰²).

Both the negative and positive sides of cell 2 had 39AA (pristine, 1 layer, SGL Group, Germany) carbon papers as electrodes. A flow rate of 40 mL/min was supplied using a two-channel peristaltic pump. Cycling experiments were conducted at a current density of 100 mA/cm² with cut-off voltage limits of 0.2 and 1.9V for discharge and charge modes, respectively.

Cell 3 was designed to investigate the concentration-gradient induced V(IV) permeability for a series of different membranes. Cell 3 was a two-chamber 9 cm² active area cell. For Cell 3, the vanadium-enriched solution flowed from the V(IV) reservoir and vanadium-deficient solution was circulated from the sulfuric acid reservoir and passed through a flow through UV-Vis measurement unit cell (labeled as Cell 4 in Fig. 9-3) to monitor the vanadium-deficient side's solution in real-time. The total time of electrolyte circulation was 24 hours. During the circulation of vanadium-enriched and vanadium-deficient electrolytes, concentration gradient-driven crossover occurred from the vanadium-rich electrolyte to the aqueous sulfuric acid solution across the ion-exchange membrane of interest. The vanadium-deficient solution was directed to Cell 4 for real-time monitoring of V(IV) crossover using UV/Vis spectroscopy. To calculate the concentration of V(IV) on the vanadium-deficient side from the spectroscopic data, the spectra of standardized V(IV) with known concentration were recorded using the same parameters as the

experiment. The real-time spectroscopic data were integrated and analyzed with scripts written in-house. Further details regarding the experimental procedure is available in Chapters 4, 5, and 7 and is also available in our recent publications ^{1, 102, 202}.

9.3.2. Engineering Electrolyte composition for reduced crossover

As discussed in Section 9.2, the second approach for imposing chemical potential gradient across the membrane for the solvent is through engineering the electrolyte composition of the negative and positive electrolytes while maintaining similar pressure and temperature in both sides as formulated in Eq. (9-9).

$$d\mu_0 = \left(\frac{\partial \mu_0}{\partial X_p} \right)_{T,P} dX_p \quad (9-9)$$

To alter the composition of the electrolytes (labeled as X_p) two feasible approaches are altering the concentration of electroactive species or supporting salt (electrolyte). Utilizing different concentration of electroactive species have already been demonstrated by Park et al ²³⁹. The utilization of asymmetric concentration of vanadium in both sides results in significantly reduced capacity decay within initial cycles. Here, we are interested to explore another pathway. Altering the composition of supporting slats (for VRFBs, sulfuric acid concentration) based on Eq. (9-9) can be used to engineer the direction of the solvent transport flux. Therefore, here, we have used asymmetric sulfuric acid concentrations for both sides.

High performance VRFBs usually utilize the supporting electrolyte of sulfuric acid with symmetric concentrations in the negative and positive electrolytes. The concentration of supporting electrolyte (sulfuric acid) is commonly in the range of 2-4 M.

Therefore, to demonstrate the validity of our approach, the performance characterization along with extended cycling experiments were conducted for symmetric and asymmetric acid concentrations of negative and positive electrolytes. The readers are encouraged to refer to one of our recent publications for further details regarding the influence of differential concentrations of solute on the solvent transport ²⁰².

The schematic of the setup was already shown in Fig. 9-3. The initial electrolytes of interest were prepared using Cell 1 according to the procedure explained in Section 9.2.1. To demonstrate the validity of our approach, three different electrolytes compositions were considered as summarized in Table 9.2. The cell characterization along with cycling experiments have been provided in the Results section (Section 9.3).

9.4. Results and Discussion

9.4.1. Asymmetric cell configuration for capacity retention during extended cycling

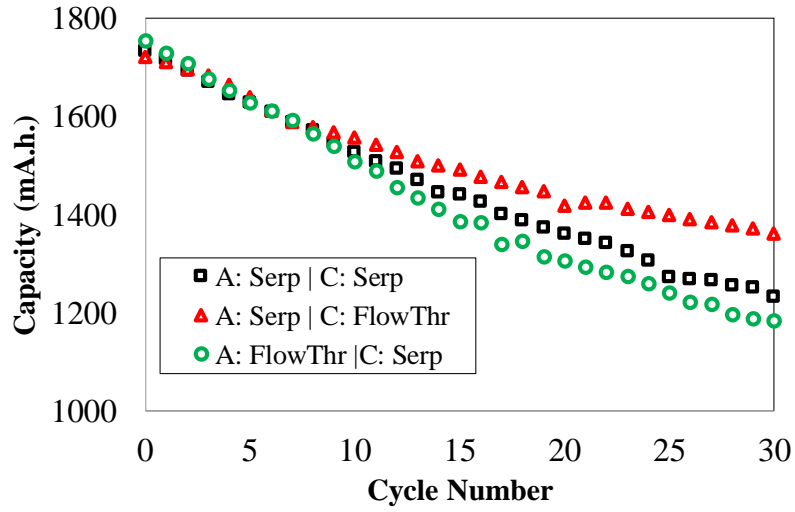
Figure 9-4 includes the variations in discharge capacity and theoretical capacity utilization for symmetric and asymmetric cell configurations. Figure 9-4 includes three different configurations including serpentine/serpentine, serpentine/flow-through, and flow-

through/serpentine pairs. Here, flow-through/flow-through pair has not been included since the theoretical capacity utilization was vastly different for this set as elaborated in Chapter 7.

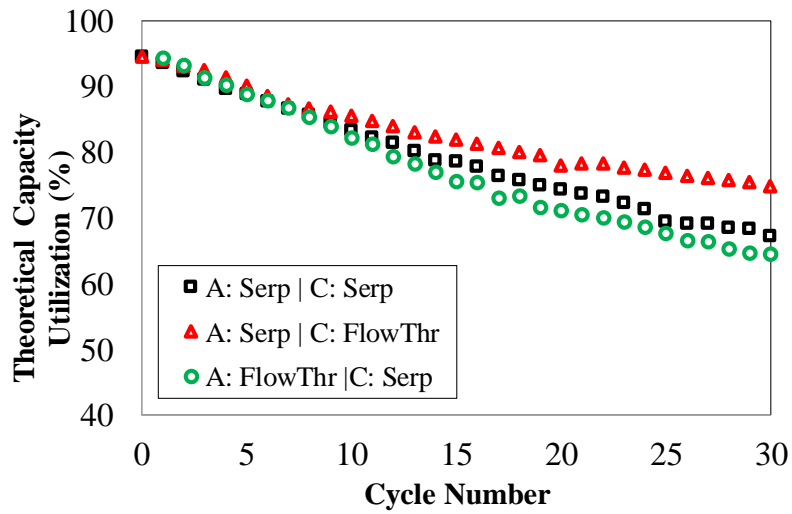
According to Fig. 9-4, the implementation of asymmetric cell configuration significantly alters the trend of the capacity decay (Fig. 9-4(a)) and theoretical capacity utilization (Fig. 9-4(b)). As shown in Fig. 9-4(a), when the flow-through flow field is used in the cathode side, the decline in discharge capacity along with theoretical capacity utilization is lower compared to symmetric configuration. Here, we have implemented very aggressive voltage limits (0.2 V – 1.9 V) to cover wider state of charge/discharge window. Based on the variations in capacity shown in Fig. 9-4(a), it is important to assess the capacity decay as a function of cycle number and as a function of total time of cycling. This analysis is shown in Fig. 9-5. It is important to note that within figures used in this section, we have referred to negative side (V(II)/V(III)) with symbol “A” and for positive side (V(IV)/V(V)), we have used “C”.

Table 9.2. Electrolyte compositions used for asymmetric acid tests

	Vanadium ion concentration in negative electrolyte (mol.L ⁻¹)	Sulfuric acid concentration in negative electrolyte (mol.L ⁻¹)	Vanadium ion concentration in positive electrolyte (mol.L ⁻¹)	Sulfuric acid concentration in positive electrolyte (mol.L ⁻¹)
Case I	1.5	2	1.5	2
Case II	1.5	4	1.5	4
Case III	1.5	4	1.5	2

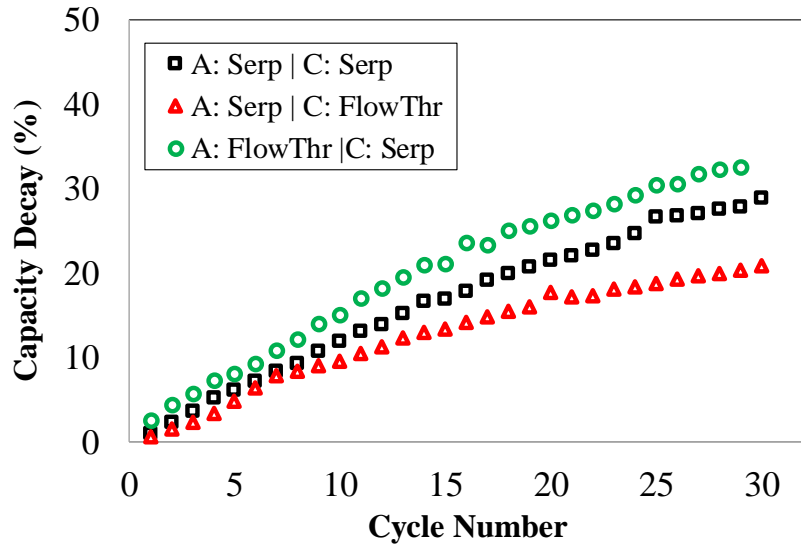


(a)

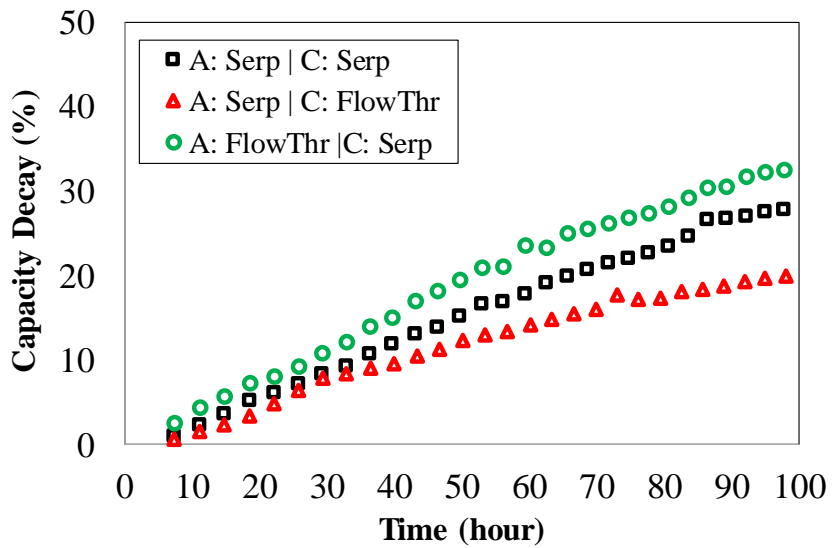


(b)

Figure 9-4: Schematic of various flow fields (a) Serpentine, (b) Interdigitated, (c) Flow-through



(a)



(b)

Figure 9-5: Capacity decay during long-term cycling for symmetric and asymmetric flow field configurations. (a) as a function of cycle number. (b) as a function of time

Figure 9-5 compares capacity decay during long-term cycling for symmetric versus asymmetric flow field configuration. As demonstrated in Figs. 9-5(a), 9-5(b), and 9-5(c), total time of the experiment for conducting 30 cycles at $100 \text{ mA}\cdot\text{cm}^{-2}$ (charge and discharge) was ~ 100 hours confirming covering an aggressive state of charge and discharge window. As shown in Fig. 9-5(a), implementing flow-through flow field in the positive side (V(IV)/V(V)) along with serpentine flow field in the negative side (V(II)/V(III)) increases the capacity retention by 33% compared to symmetric configuration. However, flipping the flow fields orientation and utilizing the flow-through flow-fields in the negative side, increases the capacity decay from 29% (symmetric configuration) to $\sim 33\%$ at the end of cycling. It is also important to make sure that asymmetric configuration does not adversely influence the coulombic efficiency. Figure 9-6 includes the coulombic efficiency for symmetric and asymmetric flow configurations.

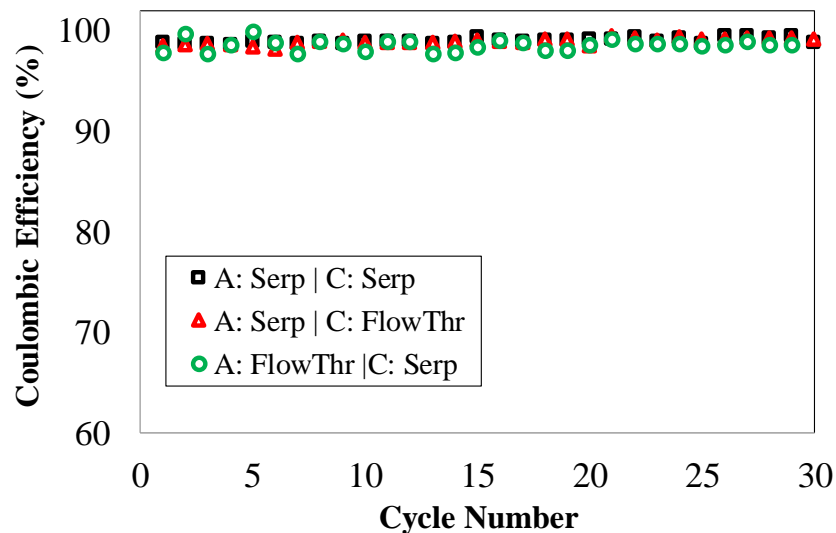


Figure 9-6: Coulombic efficiency as a function of cycle number for symmetric and asymmetric flow field configurations.

As shown in Fig. 9-6, the coulombic efficiencies associated with various configurations do not differ significantly. Therefore, superior coulombic efficiency (>98%) is achieved for asymmetric configurations during cycling of VRFB cell.

Although superb capacity retention is achieved with asymmetric flow field configuration, it is also necessary to further confirm this conclusion via conducting vanadium crossover experiment. The IonCrG as schematically illustrated in Fig. 9-3, was utilized to assess the concentration-gradient induced crossover for various configurations of the flow fields. A detailed description of the procedure has already been explained in Section 9.3 and is also available in recent related publications^{102, 202}. Figure 9-7 includes the concentration of vanadium ions (V(IV)) within the electrolyte-deficient electrolyte (please see Fig. 9-3) diffused from the vanadium-enriched electrolyte during the crossover experiment.

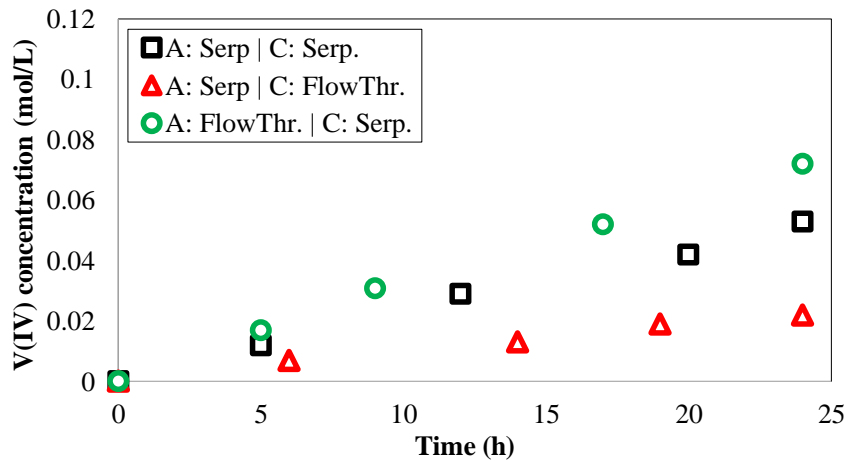
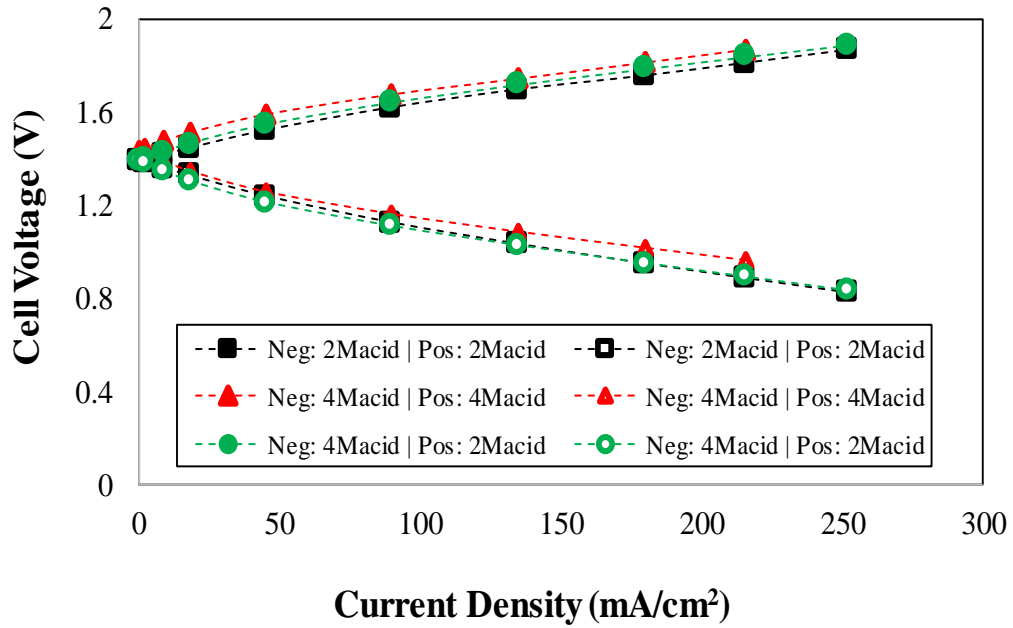


Figure 9-7: Concentration of a diffused vanadium V(IV) ion into vanadium-deficient chamber during crossover measurement for symmetric and asymmetric cell configurations.

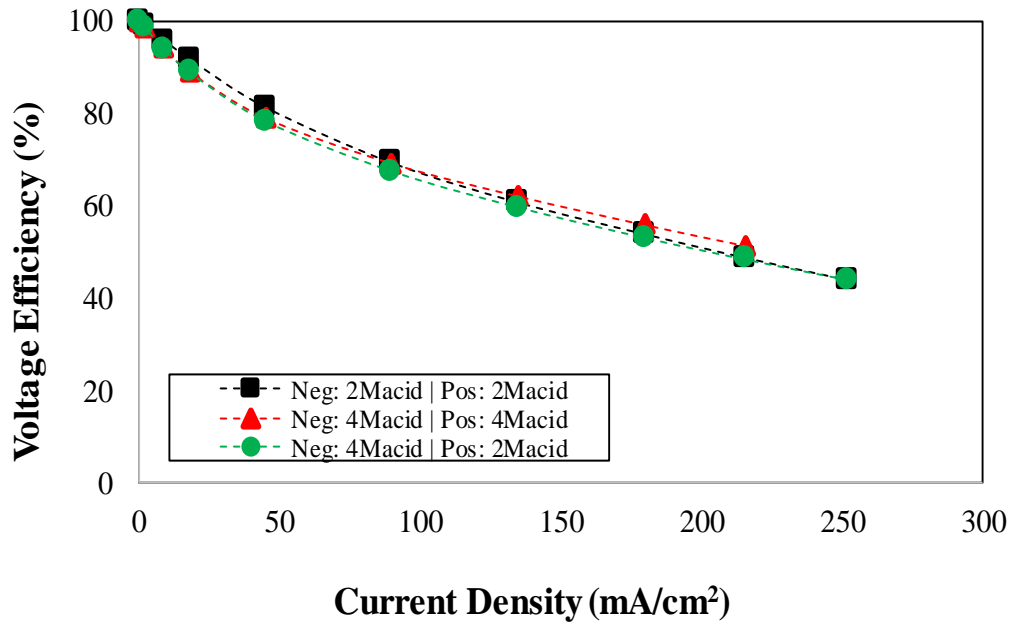
As shown in Fig. 9-6, the concentration of vanadium ions in the vanadium deficient electrolyte at the end of 24-hour experiment was ~ 0.072 , ~ 0.053 , and ~ 0.022 mol.L⁻¹. Therefore, the trend observed from the analysis of concentration-gradient-induced crossover is consistent with the capacity decay evaluation depicted in Fig. 9-5.

9.4.2. Asymmetric electrolyte composition for capacity retention during cycling

As discussed in Section 9.2.2, another approach for initiating the solvent transport across the ion-exchange membranes is utilizing asymmetric configurations of the electrolytes. We are interested to explore such an effect via imposing asymmetric acid configurations across the ion-exchange membrane. Therefore, three different compositions for the external electrolytes were considered in this work as tabulated in Table 9.2. It is important to note that the concentration of the supporting salt (for VRFBs, sulfuric acid) must be tuned with ultimate care. Excessive acid concentration commonly results in membrane dry-out and therefore, adversely influences the performance of the cell. Therefore, it was critical to confirm that the performance metrics for the cell does not being significantly influenced via imposing asymmetric acid concentration. To this end, first, cell characterization was conducted using IonCrG. Figure 9-8 includes the polarization curves along with voltage efficiency measured for the cells with symmetric and asymmetric acid concentration. As shown in Fig. 9-8(a), the implementation of the asymmetric acid configuration does not significantly influence the cell performance. It must be mentioned that a minor discrepancy observed in Fig. 9-8(a) among various configurations is due to variations in the protons concentration within the electrolytes.



(a)



(b)

Figure 9-8: Cell characterization for symmetric and asymmetric acid configurations. (a) Polarization curve, (b) Voltaic efficiency

A comprehensive modeling framework was developed in Chapter 3 where the influence of acid concentration in the open-circuit voltage was simulated. The readers are encouraged to refer to a related publication for further details ¹²⁷. Figure 9-6(b) includes the voltaic efficiency for symmetric and asymmetric acid configurations. As vividly depicted in Fig. 9-6(b), the asymmetric acid concentration has miniscule influence on the voltaic efficiency over the entire discharge current density (up to 250 mA.cm⁻²) considered in this work. Therefore, it is safe to conclude that utilizing asymmetric acid concentrations within negative and positive electrolytes does not adversely influence real-time cell metrics. We have to also mention that due to severe vanadium precipitation, we could not conduct asymmetric sulfuric acid concentration with lower acidity level in the negative electrolytes (i.e. Neg. 2Macid | Pos. 4Macid). Although the influence of asymmetric acid configuration on the cell metrics was minor; it is critical to explore the influence of asymmetric acid configuration on the long-term cycling.

As formulated in Eq. (9-9), the major rationale behind selecting higher acid concentration (4M) for the negative side versus positive side (2M) is to impose the solvent transport towards negative side to ultimately reduce the net crossover flux which was measured from the negative to positive electrolyte (please see Chapter 4 or refer to Ref. ²⁰² or further details).

Figure 9-9 provides a comparison of capacity decay during cycling for symmetric versus asymmetric acid configuration. As shown in Fig. 9-9, the capacity decay at the end of 30

cycle (at $100 \text{ mA}\cdot\text{cm}^{-2}$) is $\sim 38\%$ for symmetric acid configurations. However, the implementation of asymmetric acid configuration with increased acidity in the negative electrolyte reduces the overall capacity decay by 47% at the end of 30 cycles. Total cycling experiments shown in Fig. 9-9 was conducted within ~ 100 hours covering a wide state of charge window. As depicted in Fig. 9-9, implementation of an asymmetric acid configuration across the membrane imposes osmotic pressure gradient. The solvent (water) transport through the semi-permeable membrane towards the electrolyte with higher solute concentration. The direction of the flux associated with the solvent is from positive to negative side. Therefore, imposing such an asymmetry in the acid concentration is a promising solution for reducing the ionic crossover in VRFBs.

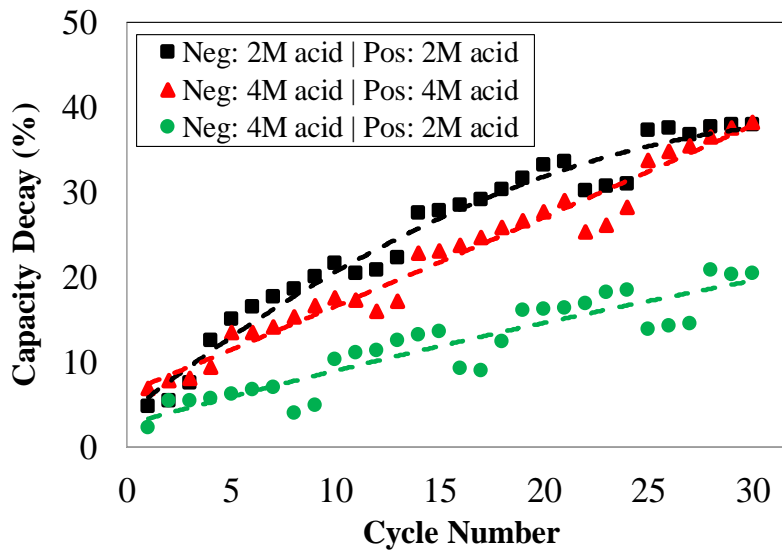


Figure 9-9: Comparison of capacity decay during cycling for symmetric versus asymmetric acid configuration

9.5. Conclusions

In this chapter, a theoretical framework was developed for altering the chemical potential of the solvent across the ion-exchange membrane to reducing the ionic crossover. Three feasible strategies including imposing temperature gradient, hydraulic pressure gradient, and osmosis pressure gradient across the semi-permeable membrane were discussed. Considering the room-temperature operation of VRFBs and the vanadium precipitations issues associated with relatively high and low temperature operation, implementing temperature gradient across the semi-permeable membrane is not practical. Therefore, engineering hydraulic and osmotic pressure gradients across the membrane is of interest.

Two cases were explored to demonstrate the applicability of this approach in reducing the radical capacity decay during long-term cycling of VRFBs; imposing an asymmetric configuration of the cell architecture along with electrolyte composition. First, an asymmetric flow field configuration of the negative and positive sides was implemented for a 9 cm² cell with serpentine flow field in the negative side (V(II)/V(III)) and flow-through flow field for the positive side (V(IV)/V(V)). It was shown that the asymmetric configuration of the flow field reduces the capacity decay by 33% (within 30 cycles) compared to symmetric flow field configuration. It was also demonstrated that the coulombic efficiency for the asymmetric flow field configuration remains unchanged compared to symmetric one (> 98%). The validity of asymmetric flow field configuring in reducing ionic crossover was further confirmed via conducting real-time concentration-

gradient induced crossover experiments using UV/Vis spectroscopy apparatus within IonCrG.

Second, asymmetric acid configuration of the negative and positive electrolytes was implemented to impose osmotic pressure gradient across the ion-exchange membrane. Negative electrolyte with higher acidity (4M) compared to positive electrolyte (2M) was prepared. It was shown that implementing asymmetric acid configuration does not adversely alter the cell performance and performance metrics (i.e. voltaic efficiency). However, during long-term cycling (30 cycles at $100 \text{ mA}\cdot\text{cm}^{-2}$, ~ 100 hours, wide state of charge and state of discharge window), asymmetric acid configuration reduces the capacity decay by 47% compared to symmetric acid configurations (for both 2M/2M and 4M/4M setups) at the end of cycling.

Although carbon paper electrodes were utilized for proof of concept in this chapter, the choice of carbon paper or carbon felt should make minor difference. The basic concept concerns the use of an asymmetric cell (in which each side has a different flow field design) to inhibit the ionic crossover through the ion-exchange membrane. This novel approach can be optimized for any particular system (e.g., redox active chemistries, flow rates, electrolytes, etc.).

Imposition of asymmetric supporting electrolyte salt was demonstrated for VRFBs as a promising technique for reducing ionic crossover during cycling. This approach is easily

applicable for other RFBs utilizing aqueous electrolytes along with semi-permeable membranes in their structure.

9.6. Acknowledgments

Yasser Ashraf Gandomi thanks University of Tennessee for providing Chancellor Fellowship.

CHAPTER TEN :
INTERPLAY BETWEEN DIFFUSIVITY AND SURFACE BARRIERS ON IONIC
TRANSPORT IN POLYMERIC MEMBRANES FOR ALL-VANADIUM REDOX
FLOW BATTERIES

Scholarly contributions

The Abstract is revised based on an Abstract and talk presented in 2018 Materials Research Society (MRS) Spring Meeting & Exhibit, Phoenix, Arizona. Talk ID: EN09.04.06. (April 2 - 6, 2018).

This chapter is revised based on manuscripts prepared for submission to the Journal of Electrochemical Society.

Yasser Ashraf Gandomi, D. J. Keffer, D. S. Aaron, M. M. Mench. “Interplay Between Diffusivity and Surface Barriers on Vanadium-Ion Transport in Polymeric Membranes for All-Vanadium Redox Flow Batteries” *Submitted to Journal of Electrochemical Society*, (2018).

Yasser Ashraf Gandomi, Z. Nolan, A. Ahmadi, D. S. Aaron, M. M. Mench. “Probing Multilayer Stacking of Ion-exchange Membrane for Reducing Crossover in Redox Flow Batteries” *to be submitted to Journal of Electrochemical Society*, (2018).

Some portions of this chapter (Experimental section) is revised based on the published paper with permission from Journal of Electrochemical Society (JES) ¹.

Yasser Ashraf Gandomi, D. S. Aaron, J. Houser, M. Daugherty, J. Clement, A. Pezeshki, T. Ertugrul, D. Moseley, M. M. Mench. “Critical Review—Experimental Diagnostics and Material Characterization Techniques Used on Redox Flow Batteries” *Journal of Electrochemical Society*, 165 (5) A970-A1010 (2018) [DOI: 10.1149/2.0601805jes]

Abstract

Among various components being used in redox flow batteries (RFBs), the ion-exchange membrane plays a significant role, influencing the rate of ionic crossover as well as the performance of the battery. It is well-known that the ohmic overpotential is dominated by the membrane in most aqueous RFBs. Therefore, engineering ion exchange membranes must improve ionic conductivity while reducing crossover. One of the major issues to be addressed is the contribution from interfacial phenomena (contact resistance between

electrodes and membrane) to the ionic conductivity along with ionic and water transport through the ion-exchange membrane. In this chapter, we have utilized a novel experimental set-up (capable of measuring the ionic crossover in real-time) to quantify the permeability of ionic species.

In addition, we have designed, engineered and prototyped several conductivity cells for measuring the ionic conductivity of the ion-exchange membranes and electrolytes ex-situ. Such a comprehensive experimental diagnostic has enabled us to provide further details regarding the impacts of interfacial phenomena on ionic conductivity and crossover. The results of this study provide deeper insight into the optimization of VRFBs for high-performance and robust applications.

10.1. Introduction

Redox flow batteries (RFBs) commonly includes a separator (membrane) within their architecture. As discussed in Chapter 8, for RFBs utilizing transition metal salts as the electroactive redox materials (e.g. all-vanadium redox flow batteries (VRFBs)), ion-exchange membranes (IEMs) are the primary choices for separating the negative and positive electrolytes. IEMs must provide a conductive ionic pathway for the charge balancing ions (i.e. protons within VRFB architecture) and prevent electronic internal short-circuiting.

One of our recent publications has been dedicated for assessing the influence of membrane equivalent weight (EW) and reinforcement on the conductivity and selectivity of polymeric

membranes ¹⁰². This recent work along with several other works suggest that the ionic conductivity of IEMs generally increases with increased dielectric constant of the membrane, solubility of charge balancing ion, and solvent concentration within membrane phase ^{102, 241-243}. The ionic conductivity commonly decreases with increased EW and implementation of reinforcement. It is also been shown that the vanadium crossover decreases by increased EW and degree of reinforcement ¹⁰². Therefore, there exist a competing pattern between increased conductivity and electroactive ionic crossover.

The contributions from the surface barriers (electrode-membrane and membrane-membrane interface) to the conductivity and crossover of ionic species is expected to play a significant role in this regard. The contributions from the surface barriers on the water transport across zeolite membranes has been already reported ²⁴⁴. However, the influence of surface barriers on the ionic transport for the polymeric membranes have not been explored in the field.

Therefore, in this chapter, a comprehensive experimental data has been provided to assess the influence of surface barriers on the ionic conductivity and crossover for all-vanadium redox flow batteries. The contact impedance has been measured for a stack of IEMs and a novel strategy has been introduced for mitigating the vanadium crossover without adversely influencing the protonic conductivity.

10.2. Experimental

10.2.1. Experimental set-up for crossover measurement

Figure 10-1 demonstrates the experimental set-up used for measuring the ionic crossover through a stack of IEMs. A series of vanadium crossover experiments with commercially available ion-membrane membranes were conducted to assess the influence of surface barriers on the ionic crossover. To conduct crossover experiments, an in-house experimental test system (Fig. 10-1) including flow cells, peristaltic pumps (Cole Parmer, Masterflex L/S, Vernon Hills, IL, USA), external reservoirs, light sources (Ocean-Optics, Dunedin, FL, USA) as well as ultraviolet/visible (UV-Vis) spectrometers (THORLABS, Newton, NJ, USA) was utilized. Full description of the set-up has been provided in Chapter 4. For an operating cell, the concentration gradient along with electric field are the major driving forces for vanadium crossover. The relative importance of electric-field induced crossover over concentration gradient induced crossover flux has been already quantified for Nafion® membranes in a recent publication from our lab ²⁰². Therefore, here, we have only focused on the concentration-gradient induced crossover to assess the variations of crossover flux with the ion-exchange configuration.

10.2.2. UV/Vis spectroscopy

The cell architecture shown in Fig. 10-1 was used to explore the concentration-gradient-induced crossover for various configurations of the strip cell. As shown in Fig 10-1, the

cell includes flow through flow plates (9 cm²), as-received carbon paper electrodes (39AA, 1 layer) along with stack of various IEMs.

Two different electrolyte solutions (i.e. vanadium-enriched and vanadium-deficient electrolytes) were used to assess the rate of crossover for different configurations. Vanadium-enriched electrolyte was 1.5 mol/L VOSO₄·xH₂O (Alfa Aesar, USA) and 3.3 mol/L sulfuric acid (Alfa Aesar, USA); whereas the vanadium-deficient side was 4.8 mol/L aqueous sulfuric acid. The readers are encouraged to refer to previous publications from our lab (or Chapters 4 and 5 of this dissertation) for further details regarding the rationale behind the choice of electrolytes' composition^{102, 202}. The vanadium-enriched and vanadium-deficient solutions were circulated through the cell using a two-channel peristaltic pump at volumetric flow rate of 20 mL/min.

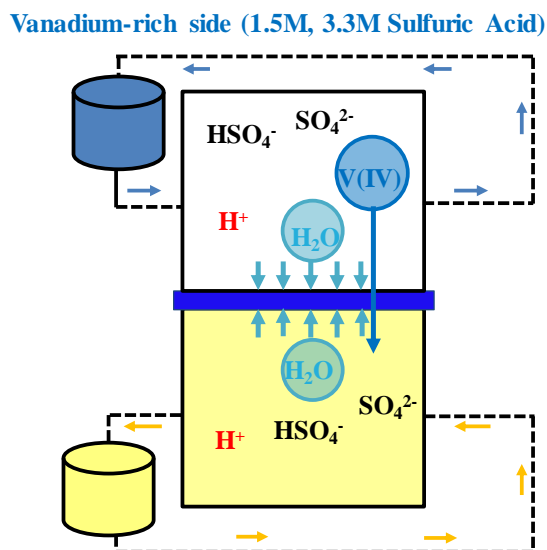


Figure 10-1: Set-up for measuring concentration-gradient induced crossover

The solutions were subsequently directed to UV-Vis flow-cells to quantify the composition of the vanadium-deficient side's electrolyte in real time. The total time of experiment was ~24 hours.

The real-time spectroscopic data were recorded (with the intervals of ~6 hours) and subsequently analyzed with scripts written in-house^{102, 202}. The spectroscopic data were used to quantify the concentration of vanadium ions within the vanadium-deficient electrolyte according to a procedure explained in some previous publications^{102, 202}. Similar experimental procedure was repeated for various configurations of the membranes.

10.2.3. Membrane selection and pretreatment

The commercially available perfluorinated Nafion® membranes with various configurations (i.e. N117, N115, NR212, and NR211) were investigated. These cationic exchange membranes have the equivalent weight of 1100 g.mol⁻¹ with nominal thickness of 7, 5, 2, and 1 mils for N117, N115, NR212, and NR211 respectively. The as-received membranes were soaked in a solution containing aqueous sulfuric acid (3.3 M) for more than a week at ambient temperature before being used in the cell.

10.2.4. Electrochemical impedance spectroscopy (EIS)

A single-channel Bio-Logic SP240 potentiostat (BioLogic Science Instruments, France) was used to conduct the electrochemical impedance spectroscopy analysis. AC impedance

(at open circuit voltage) data were obtained within the frequency range of 300 kHz to 100 MHz. To assess the area specific resistance for various membrane combinations, the AC impedance experiments were conducted with the positive electrode serving as working electrode and a 5-mV perturbation amplitude; ohmic impedance was taken as the high frequency impedance with no imaginary components (high frequency x-axis intercept on a Nyquist plot).

10.2.5. Ionic conductivity assessment for ion-exchange membranes and electrolytes

To measure the in-plane ionic conductivity of the ion-exchange membranes, an in-house ionic conductivity cell was designed and fabricated (Fig. 10-2(a)). Similar cell as shown in Fig. 10-2(b) was designed and built to assess the ionic conductivity of the electrolytes with varying composition.

Usually, in-situ conductivity measurements include combined effects of both ionic and electronic conductivity of the series-connected components in the cell. As a result, ex-situ conductivity measurements are of great importance because they enable the study of conductivity at the individual component level ¹.

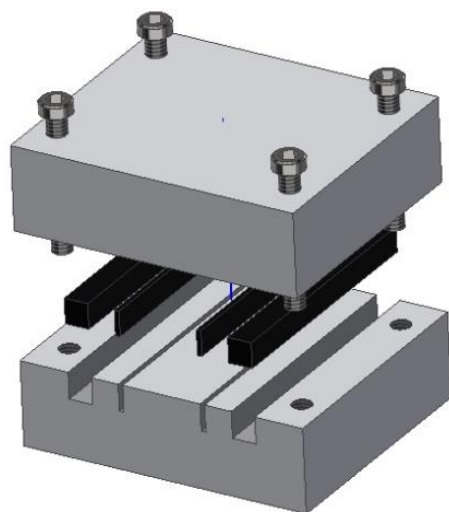
Additionally, ex-situ conductivity measurement can be done on relatively small samples and with greater rapidity than those done in-situ. Conductivity measurements can be done to assess electronic, thermal, and ionic conductivity.

Electronic conductivity measurement is usually straight forward and operates on the principle of Ohm's law for a conductor. The ionic conductivity is usually measured to assess the conductivity of the electrolyte as well as the conductivity of the ion-exchange membrane (Fig. 10-2).

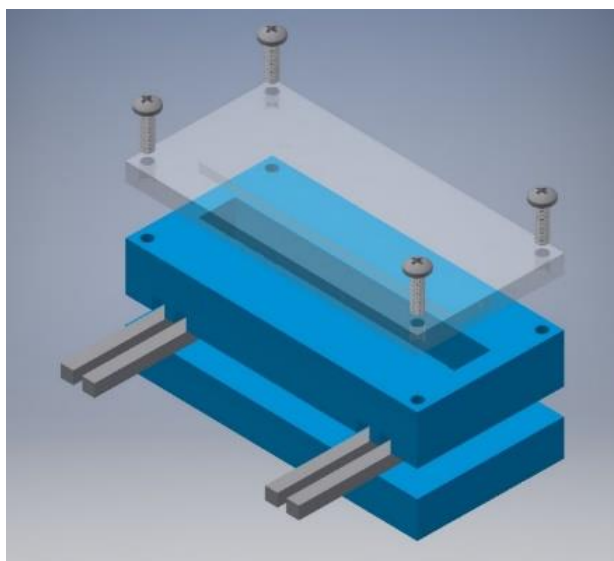
In order to measure the conductivity of a liquid electrolyte, an external conductivity meter is usually used. Skyllas-Kazacos et al. measured the conductivity of vanadium electrolyte as a function of state of charge (SoC) and of supersaturated vanadium solutions^{103, 245}.

The ionic conductivity of these solutions is of interest since it comprises a significant share of the total internal resistance in most RFBs. However, little optimization of solution conductivity has been done to date.

The ionic conductivity of separators is usually measured using the four-electrode (Fig. 10-2(a)) AC impedance technique. T. A. Zawodzinski et al.²⁴⁶ measured the conductivity of partially-hydrated Nafion membranes using such a conductivity cell, as shown in Fig 10-2(a). M. Doyle et al.²⁴⁷ measured the conductivity of perfluorinated ionomers as a function of non-aqueous solvent properties using the conductivity cell shown in Fig. 10-2(a). Y. Sone et al.²⁴⁸ measured the proton conductivity of Nafion 117 using a four-electrode cell (Fig. 10-2(a)).



(a)



(b)

Figure 10-2: Set-up for measuring: (a) in-plane ionic conductivity of IEMs, (b) ionic conductivity of electrolytes

As shown in Fig. 10-2(a), two platinum foil electrodes (3 cm apart) were used to conduct current and two platinum needles (1 cm apart) were used to measure the potential drop ¹. To calculate the ionic in-plane conductivity of the membrane and electrolytes, the following equation has been used ¹.

$$\sigma = \frac{L_s}{R_s S_s} \quad (10-1)$$

Where L_s is the distance between voltage probes (in both conductivity cells (Fig. 10-2)), R_s is the resistance of the medium (e.g. a membrane, electrolyte), and S_s is the cross-sectional area of the medium. In our experiments, the resistance, R_s , was evaluated by measuring the high frequency resistance between the voltage probes.

The ionic conductivity measurement using a four-electrode cell, although facile and rapid, requires care since this test is conducted ex-situ under conditions likely very dissimilar from those experienced in the cell. It is critical to guarantee the species uptake states are similar to the in-situ operational conditions. Therefore, for the set of experiments conducted in this work, the ion-exchange membranes were soaked in various bathing solutions (i.e. DI water, aqueous sulfuric acid (3.3M sulfuric acid), and vanadium solutions (1.5M vanadium and 3.3M sulfuric acid)) for more than a week prior to conducting the experiments. It is important to note that the conductivity measured using a conductivity cell enables the measurement of in-plane conductivity for the membranes. Depending on the morphology of the membranes and the degree of reinforcement, the properties of the

membranes might exhibit inhomogeneity and therefore, the through-plane conductivity may differ from the in-plane conductivity.

The through-plane conductivity is usually measured using electrochemical impedance spectroscopy as described in Section 10.2.4. Also, it is important to note that in comparison of in-plane and through-plane conductivity assessment, the electrolyte in contact with the membrane is also critical. The in-plane conductivity measurement usually is performed in ambient environment; however, the through-plane measurement is conducted in real cell conditions in which the electrolyte-electrode-membrane boundary is the boundary conditions for the membrane for equilibrium and non-equilibrium conditions. In addition, it is important to mention that according to Eq. (10-1), it is critical to precisely measure the thickness and the width of the samples being used in conductivity cell. This measurement is cumbersome since the ionic uptake, elongation and stress-strain characteristics of the samples are strongly being affected by the soaking solution. Additionally, the applied pressure within the conductivity cells are not necessarily accurately controlled, which can also affect the measurement if not taken into account. These issues have been addressed in this work via repeating the experimental procedure for 3 different samples.

10.3. Results and Discussion

As described in previous section, stack of IEMs with various configurations were evaluated for ionic crossover as well as area specific resistance. The following section includes further details.

10.3.1. Assessing membrane-electrode interface resistance for VRFBs

To measure the resistance associated with the electrode-membrane interface, area specific resistance was assessed for a series of N115 membranes. Flow cells with 9 cm² flow-through plates and as-received 39AA electrodes were used with cell topology. Similar cell architectures were utilized for series of cells assembled with 1, 2, 3, and 4 layers of N115 ion-exchange membranes. Also, area specific resistance was assessed for similar cell architecture without any membrane to assess the impedance associated with electrodes, electrolytes, flow plates, current collectors and related contact resistances. Figure 10-2 includes the area-specific resistance associated with these cases. To assess the impedance associated with the electrode-membrane interface, first, flow cells with no membrane within the architecture assembled.

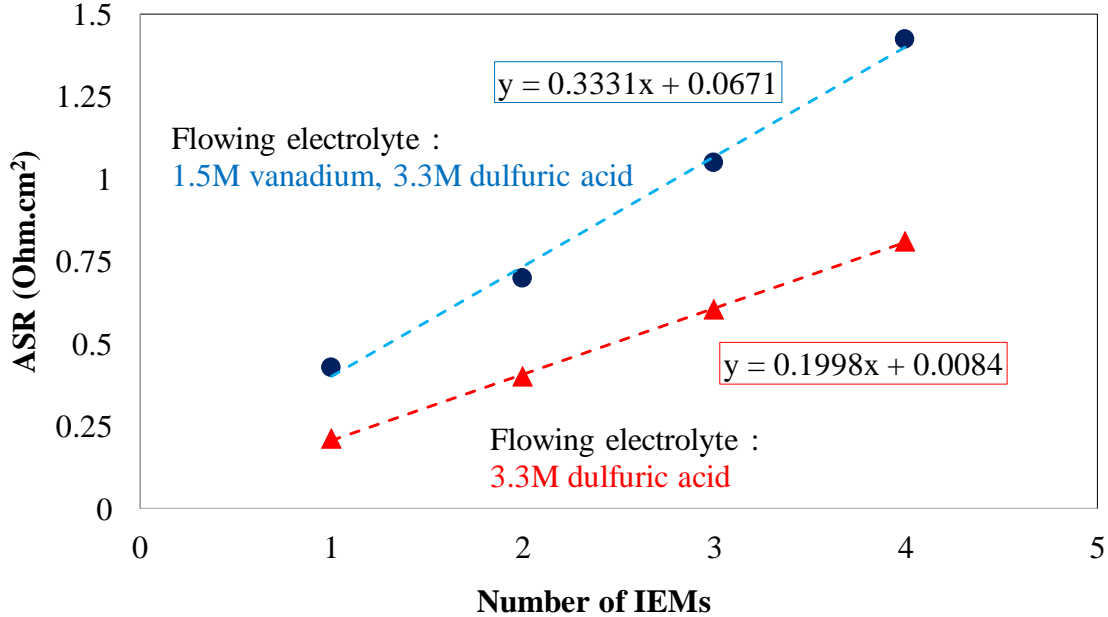


Figure 10-3: The ASR values for series of IEMs soaked in various bathing solutions

No-membrane architecture included as-received carbon paper electrodes (1 layer, 39AA) along with flow-through flow plates and current collectors. The solutions of aqueous sulfuric acid (3.3M) and enriched vanadium solutions (1.5M V(IV), 3.3M sulfuric acid) were circulated through the cell and the area specific resistance was assessed for this case. Similar experiments were repeated for cell architectures including 1, 2, 3, and 4 layers of N115. The area specific resistance associated with each case has been summarized in Table 10.1. It is important to note that the membranes initially soaked within 3.3M sulfuric acid solution for more than a week before being used in the cell.

It is important to note that the ASR values listed in Table 10.1 for cells including membranes have been assessed accounting for the ASR associated with no-membrane architecture.

Table 10.1. Area-specific resistance (ASR) for series of Nafion® 115 membranes

	ASR with flowing electrolyte aqueous sulfuric acid (3.3M) (ohm.cm ²)	ASR with flowing electrolyte enriched vanadium solution (1.5M V(IV), and 3.3M sulfuric acid) (ohm.cm ²)
No-membranes	0.0718	0.0806
1 layer of N115	0.2142	0.4294
2 layers of N115	0.4010	0.6979
3 layers of N115	0.6040	1.0512
4 layers of N115	0.8124	1.4224

To deduce the impedance associated with the electrode-membrane interface, as shown in Fig. 10-3, the ASR values have been plotted for different configuration of membranes with various flowing electrolytes. A linear trendline has been plotted for data series and the y-axis intersection has been evaluated for the impedance associated with electrode-membrane interface.

Therefore, for solution including aqueous sulfuric acid (3.3M), the electrode-membrane impedance is 0.0084 ohm.cm² and for the case with enriched-vanadium solution (1.5M V(IV) and 3.3M sulfuric acid), the interface impedance is 0.0671 ohm.cm². Therefore, the electrode-membrane interface resistance, based on the flowing electrolyte, varies in the range of 0.0084-0.0671 ohm.cm² for VRFBs.

10.3.2. Determining MacMullin number for Nafion® membranes within VRFBs architecture

As discussed in previous section (10.3.1), the ASR values corresponding to stack of IEMs were greatly influenced by the flowing electrolyte. Considering the porosity of the membranes, it is important to quantify the dependency of membrane conductivity to the conductivity of the flowing electrolyte. The MacMullin number (N_M) is a strong tool to explore such a dependency for porous separators. The MacMullin number for porous separators is calculated using the following equation ²⁴⁹:

$$N_M = \frac{\kappa_{\text{electrolyte}}}{\kappa_{\text{mem}_{\text{eff}}}} \quad (10-2)$$

As shown in Eq. (10-2), the MacMullin number correlates the conductivity of the electrolyte to effective conductivity of the porous separators (IEMs in this case). Therefore, to determine MacMullin number, it is necessary to measure the conductivity of the electrolytes and IEMs separately. In this work, the conductivity cells shown in Fig. 10-2 have been used to measure the conductivities. Several samples of Nafion® 115 were used to assess the in-plane ionic conductivity and to confirm the repeatability of the measurements. Various bathing solutions including DI water, aqueous sulfuric acid (3.3M), and enriched vanadium solution (1.5M V(IV) and 3.3M sulfuric acid) were prepared and the membranes were soaked in these bathing solutions for more than a week. Subsequently, the in-plane conductivities were evaluated using Eq. (10-1). Figure 10-4 includes the in-plane conductivity of the Nafion® 115 membranes soaked in various bathing solutions. As shown in Fig. 10-4, the in-plane conductivity of the Nafion® membranes is a strong function of the bathing solution. The highest value of conductivity achieved for the membranes soaked in DI water ($\sim 0.09 \text{ S.cm}^{-1}$) followed by aqueous sulfuric acid (3.3M; $\sim 0.076 \text{ S.cm}^{-1}$), and enriched vanadium solution (1.5M V(IV), and 3.3M sulfuric acid; $\sim 0.032 \text{ S.cm}^{-1}$) subsequently.

Therefore, the in-plane conductivity of the membranes soaked in aqueous sulfuric acid is significantly higher compared to enriched vanadium solution. The conductivity trend observed in this case is consistent with the ASR values shown in Fig. 10-3 and tabulated in Table 10.1.

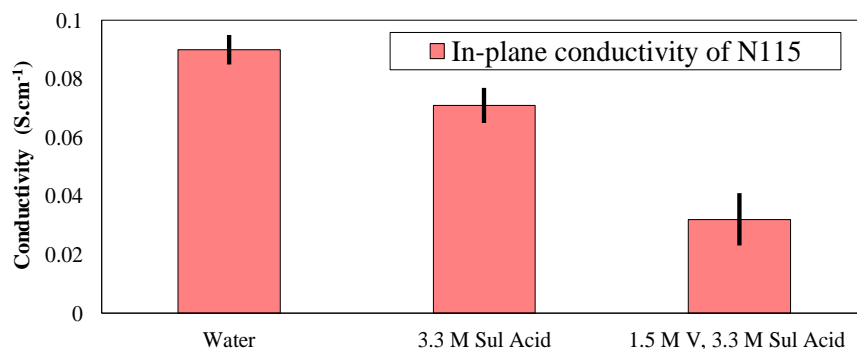


Figure 10-4: Add conductivity set-up image here

To further assess the influence of bathing solution on the in-plane conductivity of the membranes, the conductivity of the electrolytes was also measured ex-situ. To this end, electrolytes with various configurations were prepared; i.e. aqueous sulfuric acid with 3.3M acid concentration, aqueous sulfuric acid with 4.8M acid concentration, and enriched vanadium solution (1.5M V(IV), 3.3M sulfuric acid). The conductivity cell shown in Fig. 10-2(b) was used to measure the ionic conductivity of the solutions. To confirm that the conductivity values obtained using conductivity cells are cell-independent; multiple configurations of conductivity cells with various cell geometries were designed and fabricated in-house. Therefore, the ionic conductivities reported here are confirmed to be cell-independent. Figure 10-5 includes the ionic conductivities for various bathing solutions.

As illustrated in Fig. 10-5, the ionic conductivity of the electrolytes varies significantly with the composition. The macroscopic description of the ionic conductivity can be formulated using the following equation^{1, 127}.

$$\kappa = F^2 \sum_i z_i^2 u_i c_i \quad (10-3)$$

In Eq. (10-3), κ resembles the ionic conductivity ($\text{S}\cdot\text{cm}^{-1}$), F the Faraday constant (C), z_i charge of species i , u_i mobility of ion i ($\text{cm}^2\cdot\text{V}^{-1}\cdot\text{s}^{-1}$), and c_i concentration of species i ($\text{mol}\cdot\text{cm}^{-3}$). Therefore, as formulated in Eq. (10-3), the concentration of charge carrying ions along with corresponding mobility are the major contributors to the ionic conductivity. As shown in Fig. 10-5, increased acid concentration within the electrolytes increase the ionic conductivity. However, enriched vanadium solution demonstrates significantly lower ionic conductivity. This trend is contributed to the decreased ionic mobility of major charge carriers (protons) within concentrated electrolyte solutions. Measuring electronic conductivity of membranes along with electrolytes enables quantifying the MacMullin number (N_M) as tabulated in Table 10.2.

As tabulated in Table 10.2, the MacMullin number for IEMs used within VRFB architectures with vanadium enriched and aqueous sulfuric acid solutions is in the range of 7.29-7.33. The agreement between these two cases is an important factor confirming the dominant influence of electrolyte conductivity on the in-plane conductivity of the membranes.

Table 10.2. MacMullin number for IEMs within VRFBs configuration

	Electrolyte type: Aqueous sulfuric acid (3.3M)	Electrolyte type: Enriched vanadium solution (1.5M V(IV), and 3.3M sulfuric acid)
N_M	7.29	7.33

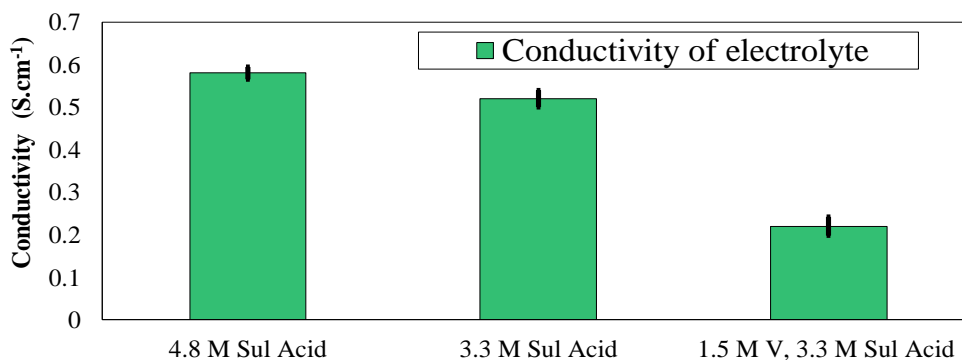


Figure 10-5: The ionic conductivity measured for various electrolytes

It is important to note that higher MacMullin number for enriched vanadium solution is expected since the mobility of the charge carrying ions are further constrained in the membrane phase ¹⁰². Detailed discussion in the conductivity of the ion-exchange membrane and micro-phase separation of hydrophobic and hydrophilic regions are discussed in Chapter 12.

10.3.3. Membrane stacking: An inexpensive approach for capacity retention

As described in Section 10.3.1, stacking multilayers of ion-exchange membranes results in an increased ASR. An increased ASR increases the ohmic overpotential associated with the cell according to the following equation ¹:

$$\eta_{ohmic} = ASR \cdot j \quad (10-4)$$

Where η_{ohmic} is the ohmic overpotential (V), ASR is the area specific resistance (ohm.cm²), and j is the current density (A.cm⁻²). As formulated in Eq. (10-4), increased ASR directly increases the ohmic overpotential and subsequently reduces the power generated by the

battery. Therefore, reducing ASR is an important design criterion for improving the performance of RFBs. Commonly, reducing the membrane thickness is recommended as a feasible approach for reducing the ASR. However, reduced membrane thickness usually results in higher rate of crossover. Although, as discussed in Chapter 5, via engineering membrane morphology an optimum configuration can be achieved for reduced ionic crossover or reduced ASR without significantly altering the competing aspect.

In many practical applications, it is common to use commercially available ion-exchange membranes. Therefore, usually a thicker off-the-shelf membrane is replaced with a thinner one (e.g. N115 with NR212) if the objective is to reduce ASR and consequently improve the performance. Therefore, increased crossover of electroactive species becomes a significant issue for long-term applications. Therefore, in this Chapter, we are introducing a technique based on stacking multiple layers of ion-exchange membranes to tackle this issue. We believe, this technique is a practical, inexpensive and easy-to-use approach for achieving reduced crossover in RFBs without adversely affecting the ASR.

To investigate the influence of multiple ion-exchange membranes on the ASR, initially, the area specific resistance for commercially available Nafion® 115 membrane (single layer soaked in 3.3M aqueous sulfuric acid for more than a week) was measured. Figure 10-6 includes the ASR value measured for a single layer N115 as a function of membrane nominal thickness (marked with red symbol on the figure).

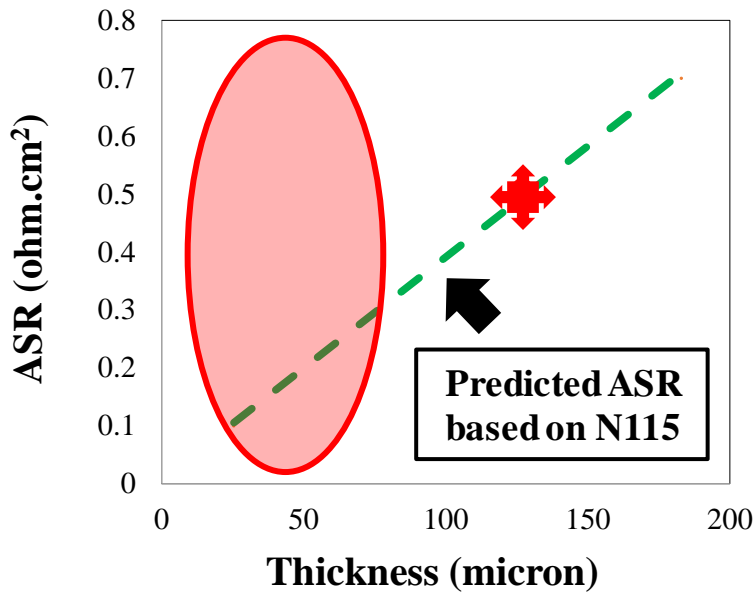


Figure 10-6: The ASR value for single-layer N115 and predicted ASR variation as a function of membrane thickness

All-vanadium redox flow batteries utilize aqueous solutions; thus, it is safe to assume that the membrane degree of wetting is complete. Under this assumption, the ohmic resistance imposed by the membrane can be formulated using the following equation ²⁴⁹.

$$R_{mem} = \frac{\tau_m l_m}{\epsilon_m \kappa_m} \quad (10-5)$$

Here, R_{mem} is the ohmic resistance associated with the membrane (ohm), τ_m tortuosity of the membrane, l_m thickness of the membrane swelled in the electrolyte (cm), ϵ_m porosity of the membrane, and κ_m conductivity of the membrane (S.cm⁻¹). Also, for aqueous electrolytes, the dominant contributor to the ohmic overpotential is the ionic transport

resistance imposed by the membrane; therefore, the area-specific resistance can be formulated as ¹:

$$\mathbf{ASR} = R_{mem}A_m \quad (10-6)$$

Here, A_m is the projected area of the membrane (cm²). Therefore, combining Eq. (10-5) and Eq. (10-6), we can write:

$$\mathbf{ASR} = \frac{A_m \tau_m l_m}{\epsilon_m \kappa_m} \quad (10-7)$$

Therefore, as formulated in Eq. (10-7), assuming the membrane morphological properties (i.e. tortuosity, porosity, and ionic conductivity) remains unchanged; the ASR values is linearly dependent to the thickness of the membrane (for similar cell active areas). Such a similar trend has been shown in Fig. 10.6 (green dashed line). Therefore, a linear trend is expected for ASR based on the ASR value measured for N115.

To explore the influence of membrane stacking in crossover, the concentration-gradient induced vanadium crossover was assessed for a single layer Nafion 115. The schematic of the setup was already shown in Fig. 10-1, where vanadium enriched side (1.5M V(IV), and 3.3M sulfuric acid) was circulated in one side and vanadium deficient side (4.8M sulfuric acid) was circulated in the other side of the battery. One layer as-received carbon paper electrode was used in each side along with flow-through flow plates. The flow-through flow plates were used to minimize the influence of transport mechanism within the electrodes on the observed behavior. The total concentration of vanadium ions (V(IV)) was measured at the end of experiments (~24 hours) based on the procedure explained in our

recent publication ¹⁰². Figure 10-7 includes the concentration of vanadium within vanadium-deficient electrolyte at the end of experiment (highlighted in red). Assuming a Fickian diffusion for concentration-gradient induced crossover, the diffusive flux can be formulated in the form of following equation ¹.

$$J(x, t) = -D \frac{\partial C(x, t)}{\partial x} \quad (10-8)$$

It is important to note that the diffusive model based on Fickian behavior is an overly simplified model and more rigorous modeling approach is needed; however, for an experimental assessment provided in this chapter, we believe this simplified model can be used since it does not significantly alter the major conclusions. Readers are encouraged to refer to Chapter 11 or a publication based on this chapter ¹⁷⁹ for more rigorous approaches using concentrated solution theory for modeling crossover in ion-exchange membranes.

According to Fig. 10-7, an exponential behavior for the concentration of diffused vanadium ions within vanadium deficient electrolyte as a function of membrane thickness is predicted based on Fickian diffusion (shown with green dashed line in Fig. 10-7). Consequently, the concentration-gradient induced flux can approach zero (mathematically) as the membrane thickness approaches infinity. Therefore, tackling the issue of lost capacity due to crossover of electroactive species via manipulating the thickness of the membrane is not a robust and stable strategy for long-term cycling of RFBs.

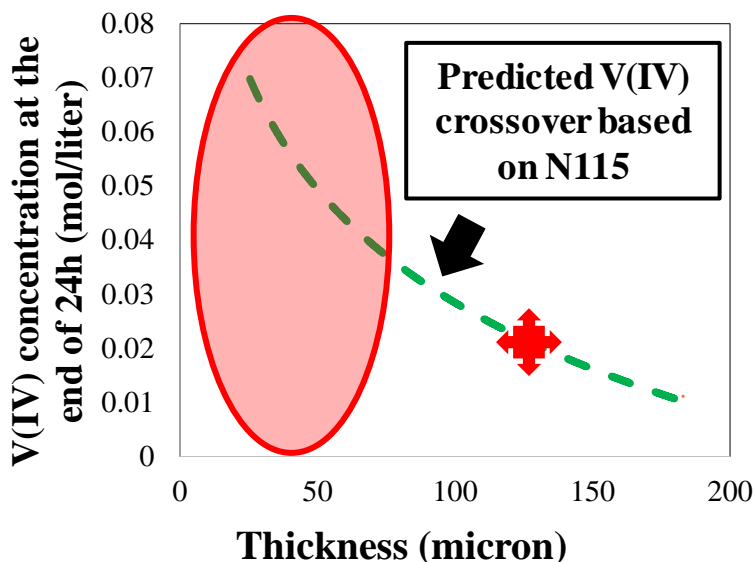


Figure 10-7: Concentration of the vanadium in the vanadium-deficient electrolyte at the end of experiment. Predicted vanadium crossover based on Fickian diffusion behavior.

From the other side, the application of ultra-thin membranes for reducing the ASR is not rigorous either since it hugely increases the concentration-gradient induced crossover (the regions highlighted in red ovals within Figures 10-6 and 10-7).

Therefore, single-phase manipulation of the membrane thickness for achieving desired transport properties is not a promising approach for long-term applications. Here, we have implemented multilayer membrane stacking to address this issue.

The ionic conductivity of the membrane formulated in Eq. (10-5), strictly applies for the membrane phase. However, the concentration of vanadium ions measured using the setup illustrated in Fig. 10-1 is measured in the external electrolyte phase. Therefore, permeability of the various IEMs towards a particular electroactive ionic species (e.g. ϖ) can be formulated as:

$$P_{\varpi} = S_{\varpi} D_{\varpi} \quad (10-9)$$

In Eq. (10-9), P_{ϖ} is the permeability ($\text{cm}^2 \cdot \text{min}^{-1}$), S_{ϖ} is the solubility, and D_{ϖ} is diffusivity of species ϖ within the membrane phase ($\text{cm}^2 \cdot \text{min}^{-1}$). Equation (10-3) formulates the correlation between ionic conductivity and mobility of ionic species within the electrolyte. The Nernst-Einstein equation correlates the diffusivity and mobility of ionic species ¹.

$$u_{\varpi} = \frac{q D_{\varpi}}{kT} \quad (10-10)$$

In Eq. (10-10), u_{ϖ} is the mobility, $q = 1.6 \times 10^{-19}$ C is the elementary charge, k is the Boltzmann constant, and is the temperature T ²⁴¹. Therefore, plugging Eq. (10-10) in Eq. (10-9), we have:

$$P_{\varpi} = \frac{S_{\varpi} u_{\varpi} kT}{q} \quad (10-11)$$

The membrane ionic uptake values for protons and vanadium ions (V(IV)) has already been measured as a function of the concentration of these ions in the bathing solution ²⁰⁰. The concentration of protons in the membrane phase decreases as a function of decreased concentration in the bathing solution. The same trend has also been observed for vanadium V(IV) ions. Therefore, according to Eq. (10-11), the solubility plays a key role controlling the permeability of ionic species through the membrane.

The solubility within the membrane phase, being a strong function of concentration of ionic species ϖ in the adjacent electrolyte phase, can be manipulated via stacking multiple IEMs

and this is the core reasoning for adopting this approach for reducing ionic crossover without significantly altering the ASR. In the following section, more details are provided.

10.3.4. Multilayer IEM membranes for reduced crossover

To explore the influence of stacking multiple IEMs on the crossover of vanadium ions, the setup shown in Fig. 10-1 was utilized. 5 layers of Nafion® 211 was used along with flow-through flow plates and single layer of as-received carbon paper electrodes (39AA, SGL, Germany).

The concentration-gradient induced crossover was explored based on the procedure explained in Section 10.2. The real-time UV/Vis spectra were recorded for vanadium-deficient electrolytes as shown in Fig. 10-8. The spectra were analyzed to obtain the concentration of vanadium ions in the vanadium deficient electrolyte in real-time based on the procedure outlined in our previous publications^{102, 202}.

Along with vanadium crossover measurement, electrochemical impedance spectroscopy was also utilized to assess the real-time influence of vanadium crossover on the area-specific resistance. The details regarding the implementation of EIS have already been discussed in Section 10.2. Figure 10-9 includes the real-time EIS spectra recorded during crossover experiment.

As shown in Fig. 10-9(a), the EIS spectra were obtained prior to crossover test where a similar aqueous sulfuric acid solution (3.3M) were circulated in both sides of the redox flow battery. Subsequently, vanadium deficient side was replaced with aqueous sulfuric acid with 4.8M acid concentration and the vanadium-enriched side was set to 1.5M vanadium V(IV) and 3.3M sulfuric acid. The EIS spectra, as shown in Fig. 10-9(b) were recorded at T=0, 9, 18, and 25 hours into the crossover measurement. Finally, both solutions were replaced with vanadium enriched solution and the EIS spectra were recorded.

As shown in Fig. 10-9, the area-specific resistance for series of IEMs increases as a function of increased vanadium concentration in the vanadium-deficient electrolyte. This trend is consistent with the trend observed for single layer Nafion®115 (Table 10.1).

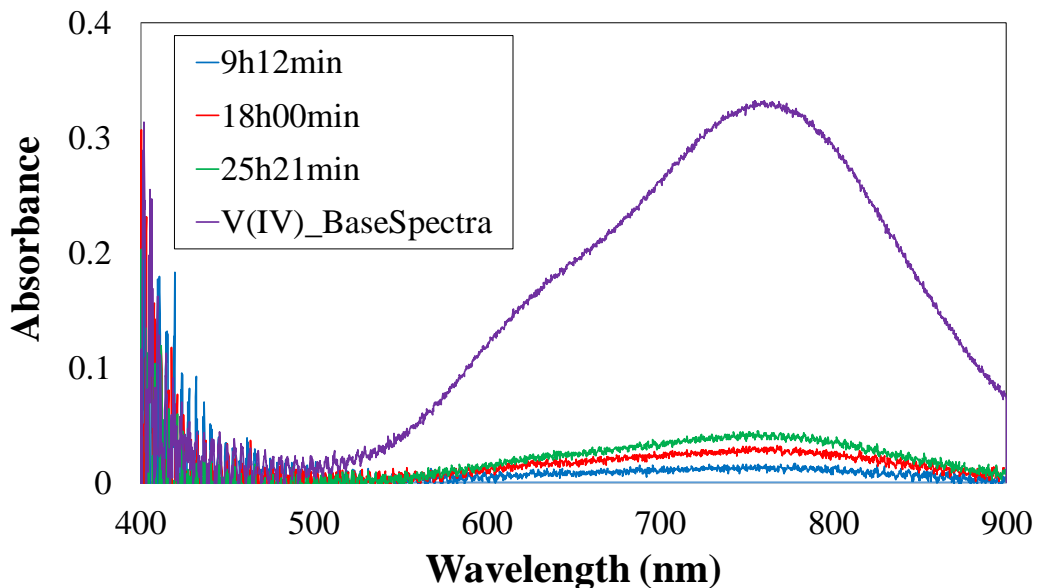
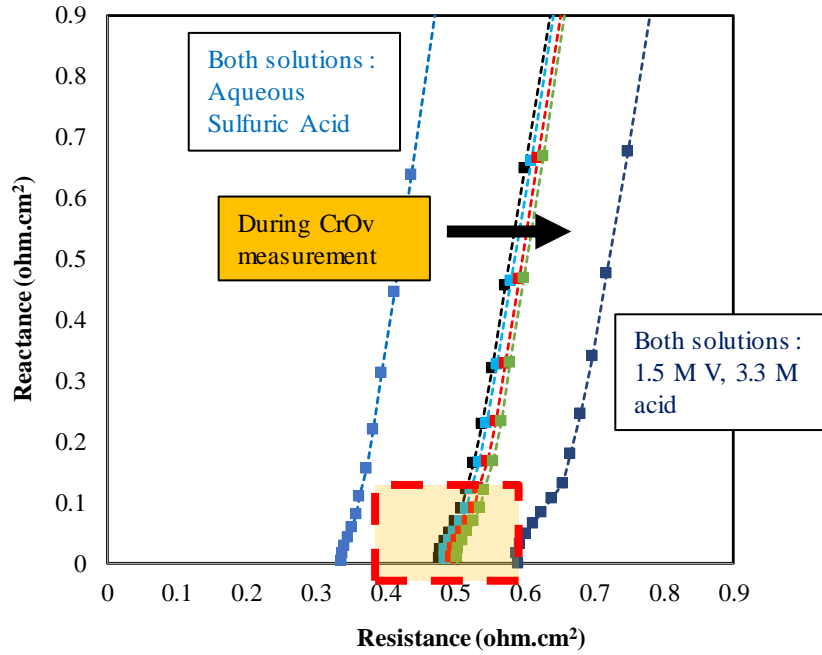
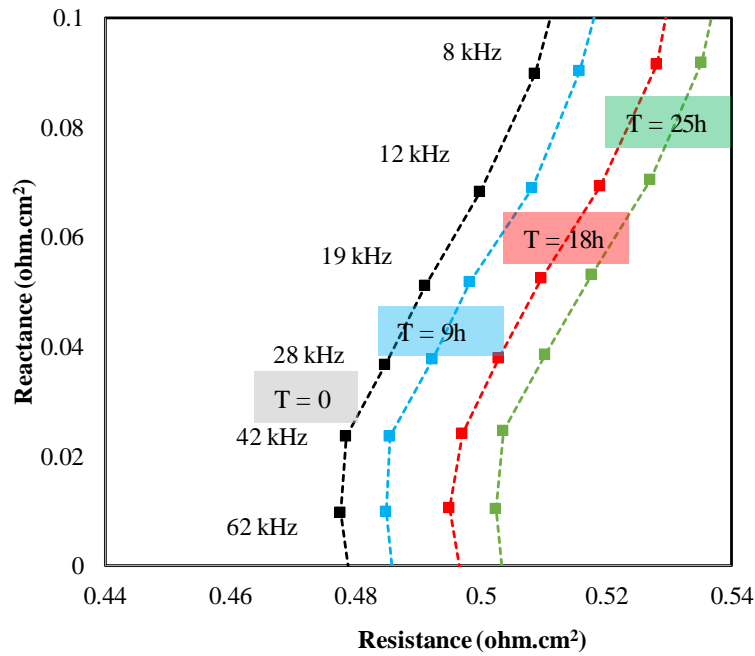


Figure 10-8: UV/Vis spectrum of vanadium-deficient electrolyte during crossover test for series of IEMs



(a)



(b)

Figure 10-9: Electrochemical impedance spectroscopy for series of IEMs, (a) The spectra prior, during, and after crossover measurement, (b) Spectra at high-frequency region

The increased ASR as a function of increased vanadium concentration in the vanadium deficient electrolyte can be explained via exploring the MacMullin number calculated for Nafion membranes (Table 10.2). MacMullin number correlates the ionic conductivity of the bathing electrolytes to the effective ionic conductivity of the membrane. Increased MacMullin number for vanadium-enriched electrolytes indicates that the conductivity of the membrane does not scale linearly with the changes in conductivity of electrolytes when the electrolytes include vanadium ions.

Also, as shown in Fig. 10-5, conductivity of electrolytes including vanadium ions (V(IV)) is significantly lower compared to aqueous vanadium solutions (3.3M acid concentration). Therefore, increased ASR as a function of increased vanadium concentration in the vanadium deficient electrolytes is reasonable and justified. To explore the influence of IEMs stacking on the ASR, a comparison has been provided between 5 layers of Nafion® 211 with a single layer N115 in Fig. 10-10.

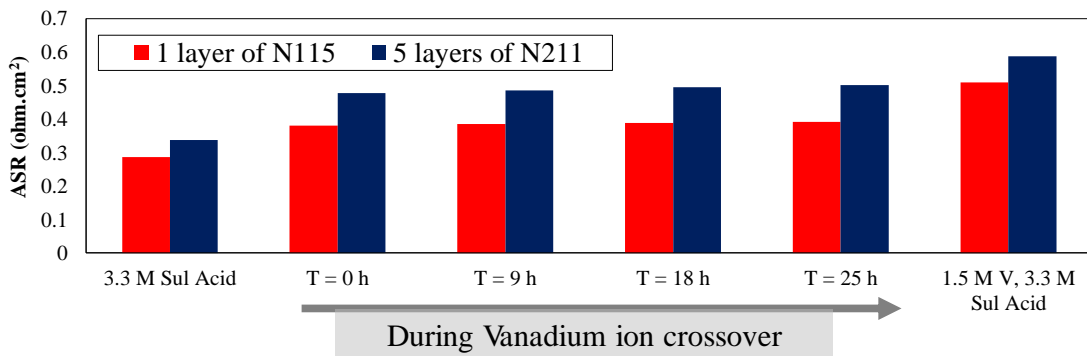


Figure 10-10: Comparison of ASR for multilayers of NR211 with N115 Nafion membranes during crossover measurement.

As shown in Fig. 10-10, the ASR associated with multilayers of NR211 is higher regardless of the bathing solution. As explained earlier, the influence bathing solution on the ASR for both cases is similar (increased ASR as a function of increased vanadium concentration in the vanadium-deficient electrolyte). However, to provide more tangible comparison in the cell level, the ohmic overpotential (Eq. 10-4) associated with each case has been calculated in Table 10.3. As tabulated in Table 10.3, the application of 5 layers of NR211 instead of 1 layer of N115 membrane, increases the ohmic overpotential from 51 mV to 59 mV at 100 mA.cm⁻². For high performance VRFBs (i.e. high current density operation (e.g. 500 mA.cm⁻²)) the ohmic overpotential increases from 255 mV to 294 mV when stack of NR211 membranes is replaced with a single-layer N115 within battery architecture. Therefore, implementation of multilayer NR211 membranes in comparison to 1 layer of N115, increases the ohmic overpotential by ~15%. To have a more comprehensive picture, it is also necessary to explore the influence of IEM stacking on the crossover. A comparison of concentration-gradient induced crossover between 5 layers of NR211 with 1 layer of N115 is provided in Fig. 10-11.

Table 10.3. Comparison of ohmic overpotential for series of NR211 versus single-layer N115

	Ohmic overpotential at 100 mA.cm ⁻² (mV)	Ohmic overpotential at 500 mA.cm ⁻² (mV)
5 layers of NR211	51	59
1 layer of N115	255	294

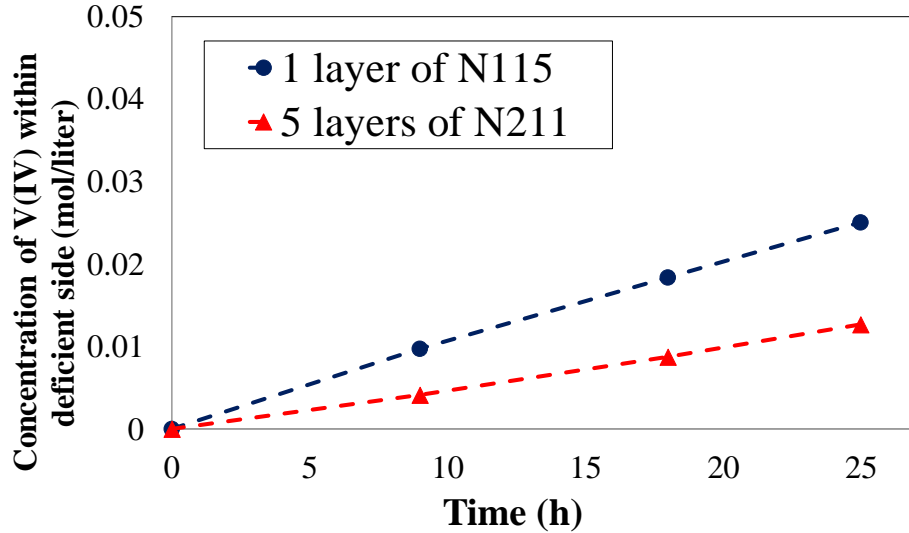


Figure 10-11: comparison of concentration-gradient induced crossover between 5 layers of NR211 with 1 layer of N115

As shown in Fig. 10-11, the concentration of vanadium ions in the vanadium deficient side has been compared for both cases at various time frames (9, 18, and 25 hours). As clearly illustrated in Fig. 10-11, the implementation of multiple membrane stacking (in this case, 5 layers of NR211 instead of N115) significantly reduces the crossover of ionic species. For instance, comparing the concentration of vanadium ions diffused through the membrane to the vanadium-deficient electrolyte at the end of experiment (after 25 hours of continuous operation under concentration-gradient), the vanadium crossover reduces by 37% when 5 layers of NR211 is replaced with 1 layer of N115. Therefore, the reduction in ionic crossover compared to increase in ASR is meaningfully higher when 5 layers of NR211 membranes is replaced with a single-layer N115 within the VRFB architecture. Figure 10-12 schematically illustrates the mechanism of reduced ionic crossover for multilayer of IEMs.

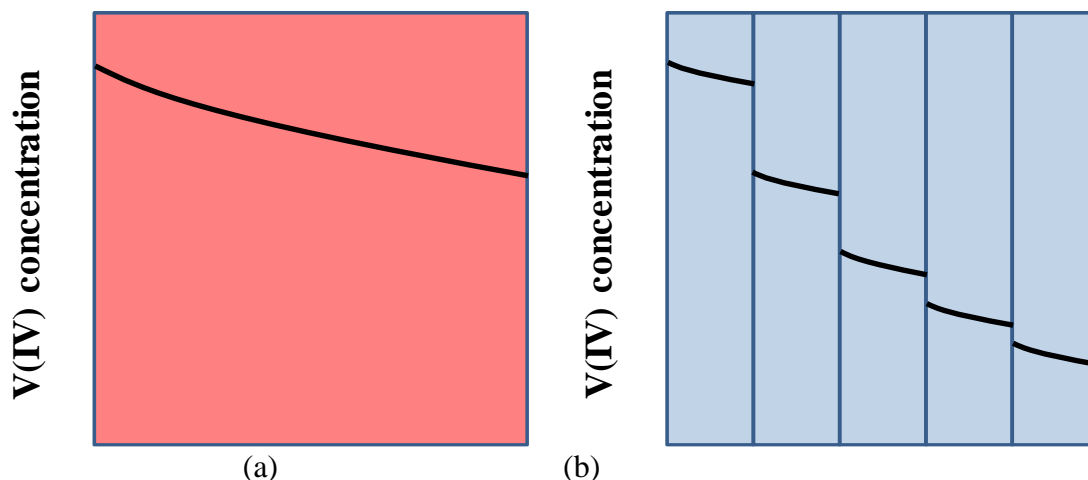


Figure 10-12: Schematic illustration of reduced ionic crossover for multilayer of IEMs, (a) 1 layer of N115, (b) 5 layers of NR211

As schematically illustrated in Fig. 10-12, imposing phase boundary within multilayers of IEMs results in reduced crossover since it results in ionic concentration discontinuity in the overall stack. It has already been shown that the ionic uptake from bathing solution reduces with reduced concentration of ions in the bathing solution ²⁰⁰. The ratio of vanadium concentration in the membrane phase to the adjacent electrolyte phase increases with decreased concentration of vanadium ions in bathing solution ²⁰⁰. Therefore, the concentration discontinuity in the membrane-membrane interface decreases as the concentration of vanadium ions in the adjacent membrane phase decreases. This is an overly simplified illustration (Fig. 10-12) since the uptake mechanism will be different from the adjacent membrane phase compared to bathing electrolyte. It is also important to note that increased ASR observed here is not only due to increased overall thickness, but also due to extra contact resistances imposed via stacking multiple IEMs. Under the compression and due to variations in the adjacent electrolyte composition, IEMs considerably deform (elastic or plastic deformation). The conductivity of ion-exchange

membranes also varies when the composition of bathing solutions is altered. Therefore, due these complications and uncertainties, it is not rigorous to extrapolate the impedance associated with a single-layer membrane to explore quantitative description for membrane-membrane interface impedance for stack of IEMs.

10.3.5. IEM selection chart for reducing ionic crossover in VRFBs

The comparison of multilayer NR211 with N115 in terms of ASR and concentration-gradient induced crossover provides a promising approach for tackling crossover issues in VRFBs. Therefore, similar analysis was further expanded to cover other IEMs commonly used in the field. In this section (Fig. 10-13), more comprehensive analysis has been provided including commercially available IEMs (N117, N115, NR212, and NR211).

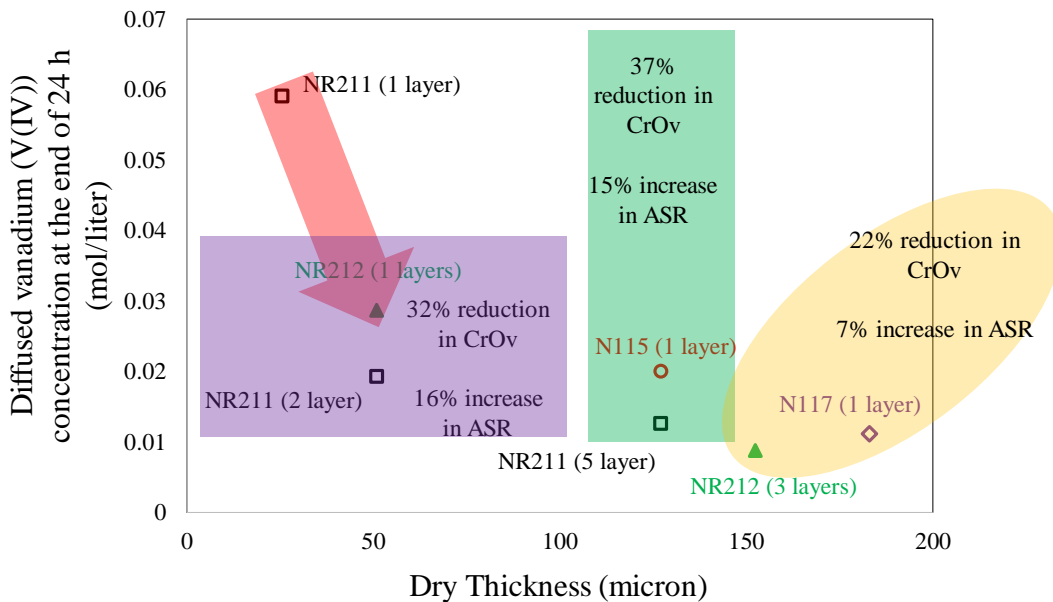


Figure 10-13: IEM selection chart for reducing ionic crossover in VRFBs

Figure 10-13 includes IEM selection chart for reducing ionic crossover in VRFBs. Three cases are included in Fig. 10-13 which provides selection guidelines for designing the battery for a particular target. For high-performance VRFBs (case I), it is necessary to minimize the ASR associated with the membrane. Therefore, among off-the-shelf IEMs, NR211 has the lowest ASR. However, the application of NR211 results in significant capacity decay due to crossover. Therefore, usually the second off-the-shelf choice is to utilize NR212. However, according to Fig. 10-13, we recommend utilizing 2 layers of NR211 instead of NR212 since it only increases the ASR by 16%, but the reduction in ionic crossover is 32% compared to a single-layer NR212. Case II is for designing VRFBs for relatively short-term capacity retention. Implementation of 5 layers of NR211 instead of a single layer N115 is recommended according to Fig. 10-13 since the reduction in crossover (37%) is more pronounced compared to an increase in ASR (15%) when multilayer NR211s are utilized.

Designing VRFBs for extended and long-term duration is of special interest (case III). Usually, Nafion 117 is the primary off-the-shelf choice. However, we recommend using 3 layers of NR212 instead of a single layer N117 since it results in 22% higher capacity retention and the increase in ASR is miniscule (only ~7%). It is also important to note that if the costs associated with the membrane within VRFB systems scales up linearly with the nominal thickness of the membrane, the implementation of multilayer IEM stacking does not significantly alter the overall cost. In some cases (case III), it even reduces the total cost since the thickness of the membrane is reduced.

10.4. Conclusions

In this chapter, implantation of multilayer stacking of ion-exchange membranes for reduced ionic crossover was investigated. Ex-situ conductivity cells were designed, built, and subsequently used to measure the in-plane conductivity of the membranes along with bathing solutions. The MacMullin number for Nafion membranes was determined to correlate the ionic conductivity of the bathing solutions to the in-plane conductivity of the membranes.

A unique setup was utilized to assess the ASR and real-time crossover of vanadium ions. The ASR associated with electrode-membrane interface was also deduced. Subsequently, a series of off-the-shelf ion-exchange membranes (i.e. NR211, NR212, N115, and N117) were investigated in terms of ASR and vanadium crossover. Stacking multiple off-the-shelf membranes was explored as a promising yet inexpensive technique for tackling the rapid capacity decay issue associated with the operation of all-vanadium redox flow batteries. Design criteria for VRFBs utilizing stack of off-the-shelf membrane were introduced for high-performance, short-term, and extended (long-duration) cycling experiments.

10.5. Acknowledgments

Yasser Ashraf Gandomi thanks University of Tennessee for providing Chancellor Fellowship.

CHAPTER ELEVEN :
CONCENTRATED SOLUTION MODEL OF TRANSPORT IN ION-EXCHANGE
MEMBRANES

Scholarly contributions

This chapter is revised based on the published paper with permission from Journal of Electrochemical Society ¹⁷⁹:

Yasser Ashraf Gandomi, Thomas A. Zawodzinski, Matthew M. Mench. “Concentrated solution model of transport in all vanadium redox flow battery membrane separator” *ECS Transactions*, 61 (13), 23-32 (2014) [doi: 10.1149/06113.0023ecst]

Abstract

A model of transport across the ion-exchange membrane in all-vanadium redox flow batteries has been proposed based on concentrated solution theory for species with high concentration. The model is based upon the Stefan-Maxwell multicomponent diffusion equation where the fluxes of the species including protons (H^+), bisulfate (HSO_4^-), water (H_2O) and the sulfonate functional groups ($-SO_3^-$) are fully coupled. The driving force for species transport has been modeled in terms of concentration and electrostatic potential gradients. The ionic transference numbers as well as water electro-osmosis drag coefficient has been calculated for different acid concentrations.

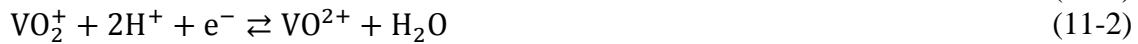
11.1. Introduction

Renewable energy sources such as wind, solar and tidal energy typically suffer from intermittency. One possible solution to overcome this issue is to use energy storage. Among different technologies, redox flow batteries (RFBs) are considered as an important potential candidate. There are currently several types of RFBs under development, each employing

different redox couples. One of the most promising types is the all-vanadium redox flow batteries (VRFB) as originally conceived by Skyllas-Kazacos and coworkers ¹.

In contrast to conventional batteries such as lead-acid storage cells, for VRFBs, the energy is stored externally in two reservoirs containing different redox couples for the anolyte (V(II)/V(III)) versus the catholyte (V(IV)/V(V)) where the reactants flowing across the electrodes enter from these reservoirs to the electrochemical cell with a porous carbon based electrode, and the electrolytes in the two compartments are separated by an ion-selective membrane or ceramic separator. A general schematic of the VRFB is shown in Fig. 11-1. The ion-exchange membrane separates the positive cell from the negative cell.

An external pumping system circulates the electrolyte solutions through the porous electrodes with V(II)/V(III) solution circulates through the negative cell and V(IV)/V(V) solution circulating through the positive cell. The governing electrochemical reactions for negative and positive cell reactions of an operating VRFB are given in Eq. (11-1) and (11-2) respectively ¹⁷⁹.



The forward arrows in Eq. (11-1) and (11-2) are the discharging (galvanic) direction, the reverse arrows are the charge direction. In reaction (11-1) the discharging process oxidizes the V(II) ion to the V(III) species, while in reaction (11-2) the V(V) ion is reduces to form the V(IV) species and accordingly reducing the state of the charge of the battery.

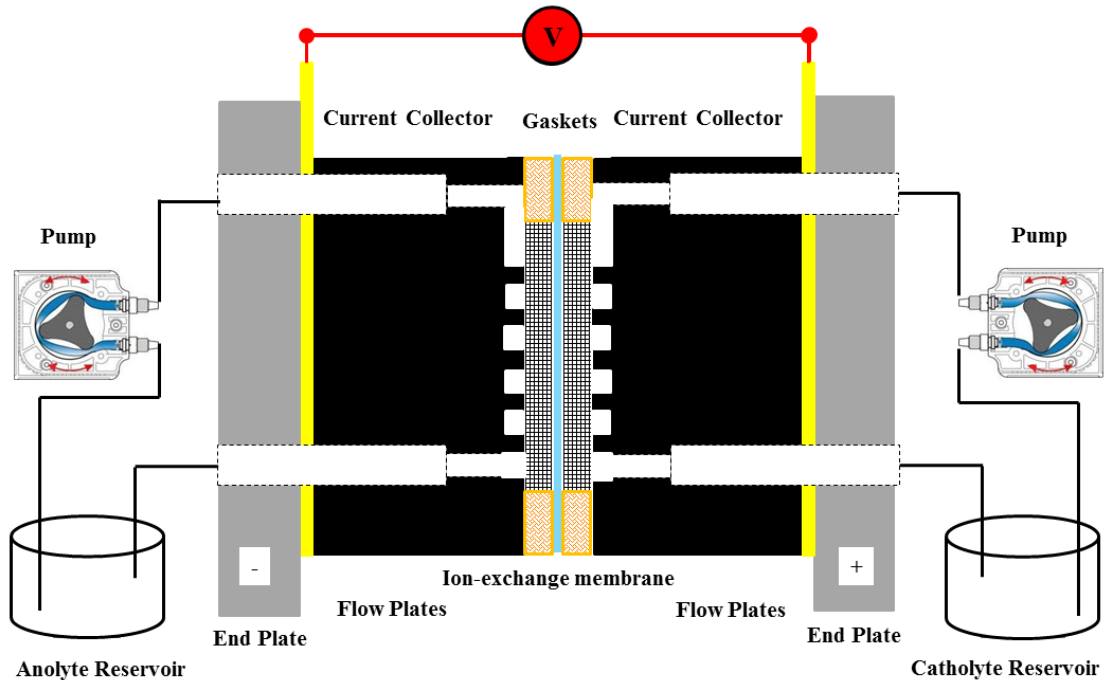


Figure 11-1: Schematic of the VRFB including reservoirs for positive and negative electrolytes and peristaltic pumps

In order to optimize and improve the VRFB performance; mathematical modeling can be utilized. In general, the models developed for RFBs are based on approaches adopted from polymer electrolyte fuel cell (PEFC) modeling and have common assumptions. In those models the dilute solution approximation has been utilized for species transport ¹. In the dilute solution theory approach, the driving forces for the transport of species has decoupled gradients of concentration and hydraulic pressure, as well as transport due to voltage or temperature gradients ¹⁷⁹.

Among different components of the VRFB, the ion-exchange membrane is a key component. The ion-exchange membrane directly affects the voltage and coulombic efficiencies of the VRFB.

Increased voltage efficiency is obtained through decreased ohmic losses associated with the membrane and increased coulombic efficiency is achieved via decreased cross-over of reactant species through the membrane. Therefore, there are tradeoffs that need to be considered for improved efficiency of the battery. Accordingly, the motivation for this work is to develop a transport model for the membrane of the VRFBs based on a comprehensive description of mass, charge energy and momentum transport including concentrated solution theory for species with coupled transport effects.

Concentrated solution theory has its basis in irreversible thermodynamics and Stefan-Maxwell diffusion. Solute-solute interactions are included and the theory account for transport by diffusion, migration and electroosmotic drag without the need for viscous- or pressure-driven terms.

For ion-exchange membranes, since the distinction between solute and solvent is unclear, it is sometimes necessary to apply the concentrated solution theory for modeling studies. Concentrated solution theory has been applied to multicomponent cation-exchange membranes at some previous works¹⁷⁹. The equations for material balance, current flow, and electroneutrality remain valid for concentrated solutions, but the flux equation requires modification. The Nafion® perfluorosulfonic acid (PFSA) membrane has been widely utilized as the ion-exchange membrane of choice in VRFB studies and in this work; the mathematical model has been adopted for Nafion 117 membrane.

11.2. Mathematical Membrane Transport Model

The relative transport of ions and solvent in membranes is affected by the physical and chemical properties of the ions and solvent in solution, the properties of the membrane, and the mutual interactions between solutes, solvent and membrane ¹⁷⁹.

Fig. 11-2 demonstrates the species within the negative and positive electrodes as well as the N117 membrane of the VRFB. The ion exchange properties of the membrane are the result of sulfonate functional groups ($-\text{SO}_3^-$) which act as fixed charge sites in the membrane ¹⁷⁹.

The fundamental equation describing isothermal mass transport in the membrane is given in the following equation ¹⁷⁹.

$$c_i \nabla \mu_i = \sum_j K_{ij} (\mathbf{v}_j - \mathbf{v}_i) \quad (11-3)$$

Where c_i , μ_i and \mathbf{v}_i are the concentration, electrochemical potential, and velocity of species i respectively and K_{ij} is the frictional coefficient between species i and j . The frictional coefficients can be replaced with binary interaction coefficients, D_{ij} by using the Eq. (11-4) ¹⁷⁹ where R and T are the gas constant and absolute temperature and c_T is the total concentration of all species present in the membrane

$$K_{ij} = \frac{RTc_i c_j}{c_T D_{ij}} \quad (11-4)$$

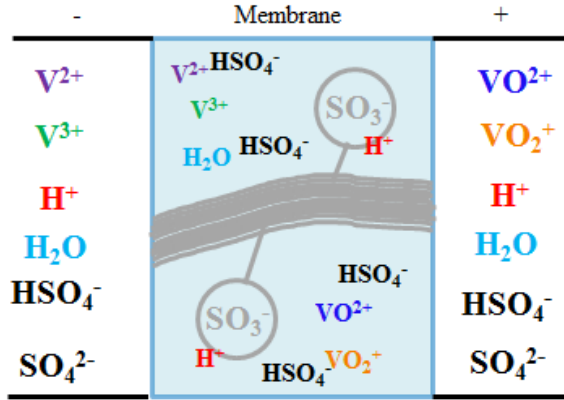


Figure 11-2: Species existing within the negative/positive electrodes and ion-exchange membrane

For this work, the species with the high concentration within the membrane has been considered in the modeling including protons (H^+), bisulfate (HSO_4^-), water (H_2O) and the sulfonate functional groups ($-SO_3^-$). The binary interaction coefficients among the species have been obtained from the work of P. H. Michael. Also, through the application of the Gibbs-Duhem equation there are only three independent transport equations ($i = +, -, 0$). This analysis assumes that the membrane is stationary and $\mathbf{v}_m = 0$. Therefore, Eq. (11-3) can be written in the form of following set of equations ¹⁷⁹.

$$c_+ \nabla \mu_+ = \frac{RTc_+c_-}{c_T D_{+-}} (v_- - v_+) + \frac{RTc_+c_0}{c_T D_{+0}} (v_0 - v_+) - \frac{RTc_+c_m}{c_T D_{+m}} (v_+) \quad (11-5)$$

$$c_- \nabla \mu_- = \frac{RTc_+c_-}{c_T D_{+-}} (v_+ - v_-) + \frac{RTc_-c_0}{c_T D_{-0}} (v_0 - v_-) - \frac{RTc_-c_m}{c_T D_{-m}} (v_+) \quad (11-6)$$

$$c_0 \nabla \mu_0 = \frac{RTc_+c_0}{c_T D_{+0}} (v_+ - v_0) + \frac{RTc_-c_0}{c_T D_{-0}} (v_- - v_0) - \frac{RTc_0c_m}{c_T D_{0m}} (v_0) \quad (11-7)$$

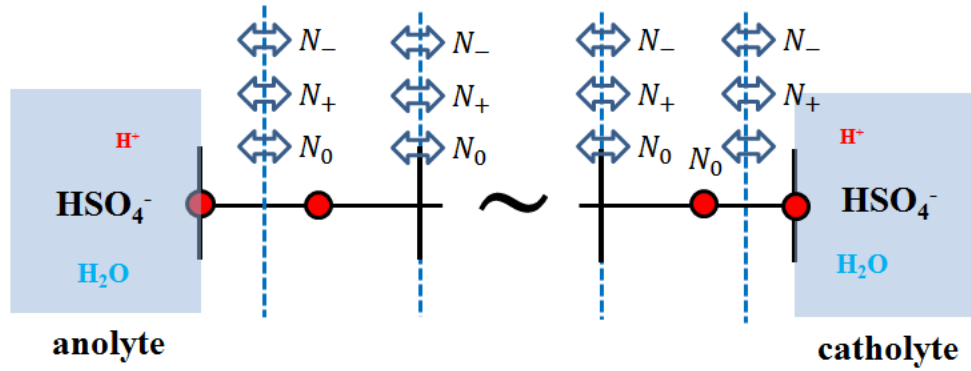


Figure 11-3: 1-D computational domain including flux of ionic species at the interface of control volumes

The in-house model is developed based on finite-volume discretization and the multicomponent ionic transport has been modeled in 1-D since the membrane is very thin. The computational domain is shown in Fig. 11-3.

At each control volume, the governing equations include differential material balance for each individual species (Eq. (11-8)) and electroneutrality condition (Eq. (11-9)).

$$\frac{\partial c_i^m}{\partial t} = -\nabla \cdot \mathbf{N}_i^m \quad (11-8)$$

$$z_m c_m + \sum_i z_i c_i^m = 0 \quad (11-9)$$

The parameter c_m is the concentration of the fixed charge sites within the membrane and z_m is the valence of the membrane's sulfonate functional groups.

In order to calculate the flux of the species within the membrane ($\mathbf{N}_i^m, i = +, -, 0$), it is assumed that the activity coefficients' variation within the membrane phase is negligible

¹⁷⁹ and therefore the gradient in electrochemical potential can be written in terms of gradient in concentration and gradient in electrostatic potential as it is shown in Eq. (11-10).

$$c_i \nabla \mu_i = RT \nabla C_i + z_i F c_i \nabla \phi \quad (11-10)$$

To calculate the velocity of the species within the membrane (\mathbf{v}_i) the M_{ij} matrix is constructed first based upon the frictional coefficients (K_{ij}) according to Eq. (11-11) through Eq. (11-13) ¹⁷⁹.

$$M_{ij} = \begin{pmatrix} M_{00} & M_{0+} & M_{0-} & M_{0m} \\ M_{+0} & M_{++} & M_{+-} & M_{+m} \\ M_{-0} & M_{-+} & M_{--} & M_{-m} \\ M_{m0} & M_{m+} & M_{m-} & M_{mm} \end{pmatrix} \quad (11-11)$$

Where:

$$M_{ij} = K_{ij} \text{ (if } i \neq j \text{)} \quad (11-12)$$

$$M_{ij} = K_{ij} - \sum_k K_{ik} \text{ (if } i = j \text{)} \quad (11-13)$$

Assuming the membrane at stationary condition, the row and column associated with the membrane can be eliminated from M_{ij} matrix and the remainder of M_{ij} matrix is called M_{ij}^0 and the L_{ij}^0 can be calculated based on Eq. (11-14).

$$L_{ij}^0 = -(M_{ij}^0)^{-1} \quad (11-14)$$

The flux of the species within the membrane ($\mathbf{N}_i^m, i = +, -, 0$) is calculated based upon Eq. (11-10) and (11-14).

$$\mathbf{N}_i = c_i \mathbf{v}_i = -c_i \sum_{j \neq m} L_{ij}^0 (RT \nabla c_j + z_j c_j F \nabla \phi) \quad (11-15)$$

The model can simulate potentiostatic and galvanostatic mode and the concentrations of the species within the membrane as well as the distribution of the electrostatic potential at each control volume. The boundary conditions for the concentration profiles are obtained from the uptake values ¹⁷⁹.

11.3. Results and Discussion

The distribution of species concentration including proton and bisulfate ions as well as water is shown in Fig. 11-4. In a typical VRFB the concentration of the vanadium species is in the range of 1000 mol.m⁻³ to 2000 mol.m⁻³ with the supporting electrolyte of sulfuric acid in the 3000 mol.m⁻³ to 6000 mol.m⁻³ range.

In this work, not only this range has been covered for sulfuric acid, but also higher ranges are also investigated to distinguish the diffusive transport from the transport induced by the gradient in electrostatic potential.

In Fig. 11-4, the horizontal axis is the dimensionless value for through-plane direction of the membrane and the vertical axis is the molar concentration with the unit in mol.m⁻³. It is also important to note that the commonly used units for the concentrations of active species as well as the supporting electrolyte is mol.L⁻¹. Here, we have plotted the concentrations using mol.m⁻³ to be consistent with the SI units. Fig. 11-4 demonstrates the case where the concentration of the sulfuric acid at anolyte has kept constant at 2000 mol.m⁻³

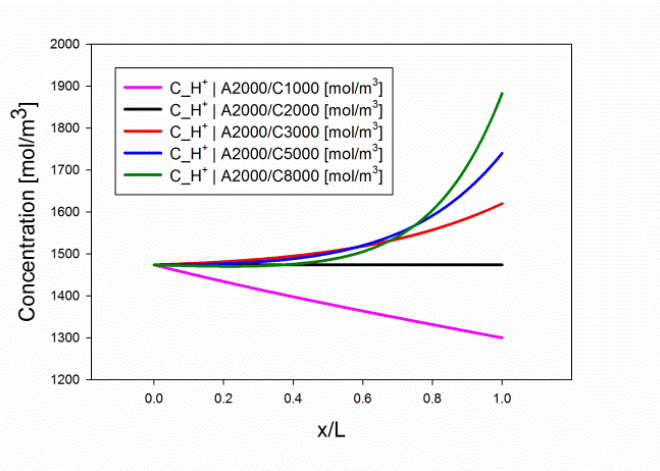
³ and the concentration of the sulfuric acid at catholyte varied and the VRFB operated at constant discharge current of $400 \text{ mA}\cdot\text{cm}^{-2}$ for all cases.

As it is shown in Fig. 11-4, increased acid concentration in the catholyte increases the proton and bisulfate ion uptake values within the membrane and accordingly decreases the concentration of the water (and ionic conductivity) in the membrane.

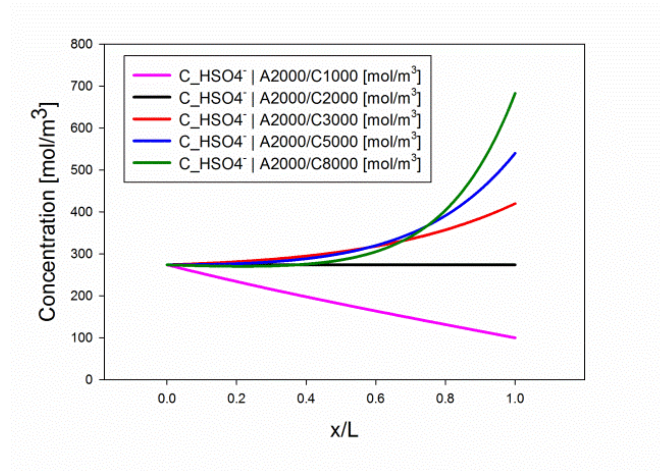
Also, the trend of the concentration profiles for protons and bisulfate ions distribution is similar, confirming the model's capability for maintaining the electroneutrality within the membrane.

The potential drop across the membrane has been shown in Fig. 11-5 for different sulfuric acid concentrations of the catholyte, and for a constant current discharge of $400 \text{ mA}\cdot\text{cm}^{-2}$. As shown in Fig. 11-5; the potential drop across the membrane increases with increased acid concentration of the catholyte.

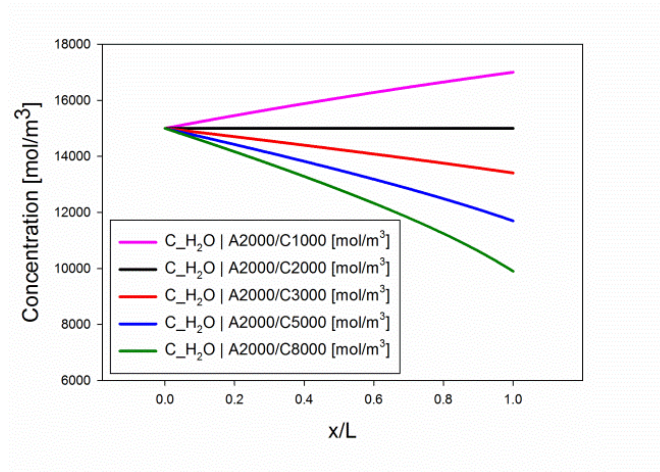
This is an important point since the concentration of the supporting electrolytes (here sulfuric acid) within the negative and positive electrolytes can be engineered for improved ionic conductivity within the ion-exchange membrane as well as improved stability of the electrolytes.



(a) H^+ concentration within the membrane



(b) HSO_4^- concentration within the membrane



(c) H_2O concentration within the membrane

Figure 11-4: The species distribution within the membrane for various concentration of sulfuric acid of catholyte

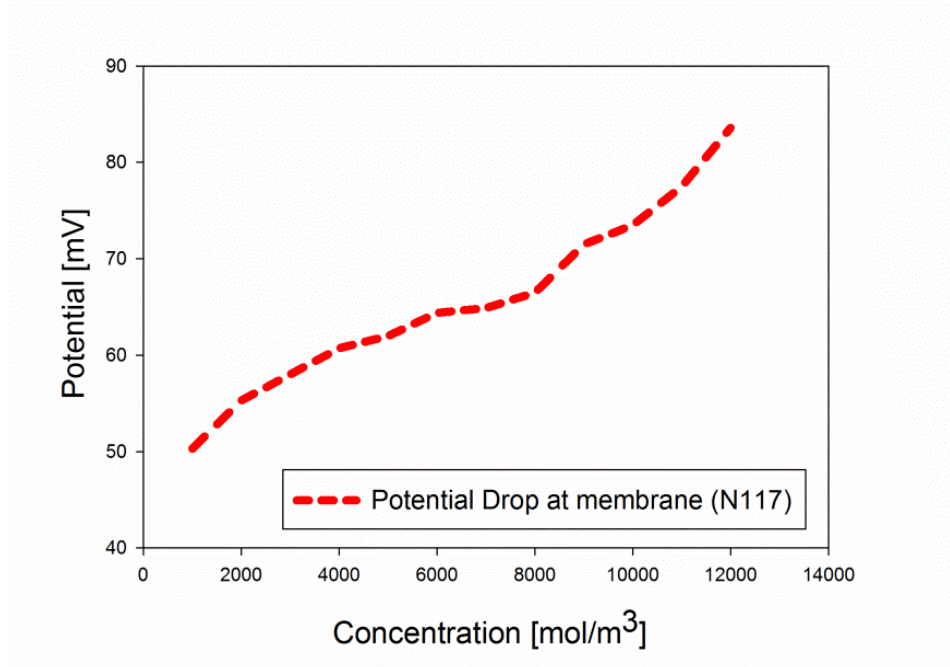


Figure 11-5: Potential drop across the membrane for different sulfuric acid concentration of the catholyte

The model is capable to decouple the current being induced due to gradient in concentration and the current due to gradient in electrostatic potential. The contribution of induced current through these two driving forces has been shown in Fig. 11-6. According to Fig. 11-6, the back diffusion induced via gradient in sulfuric acid concentration increases by increased acid concentration resulting in increased potential drop as shown in Fig. 11-5. The electro-osmotic water drag coefficient as well as the ionic transference numbers as a function of catholyte acid concentration is shown in Fig. 11-7. The electro-osmotic drag coefficient is simulated for different sulfuric acid concentration of the catholyte and the simulated value is in a good agreement with the literature ¹⁷⁹. Also, for different sulfuric acid concentration, the sum of ionic transference numbers is unity, suggesting that a fraction of the current is being carried via counter ions.

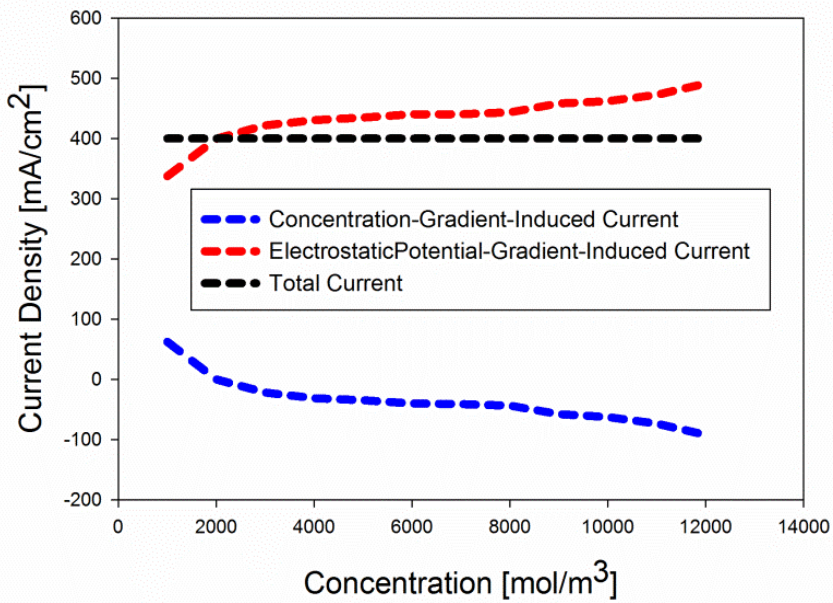


Figure 11-6: The contribution of the current being induced due to concentration gradient versus gradient in electrostatic potential

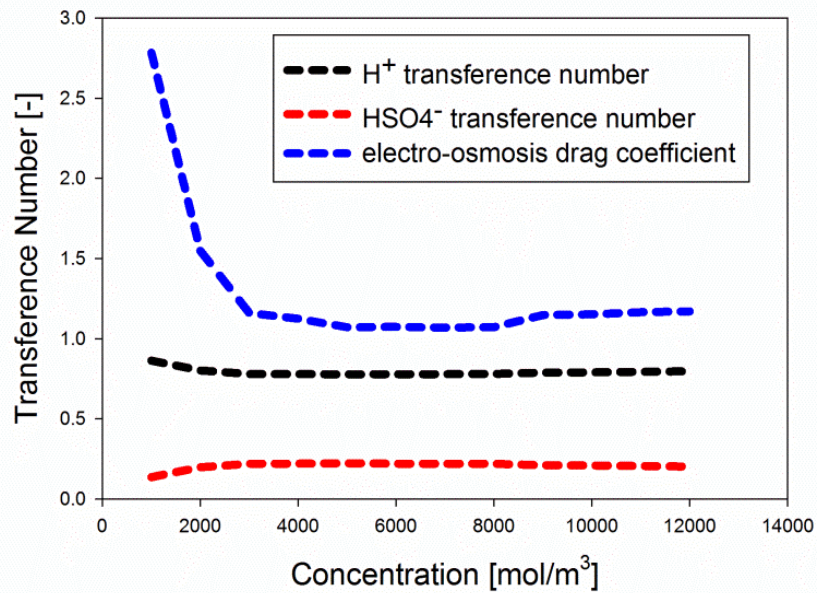


Figure 11-7: The ionic transference numbers and the water electro-osmotic drag coefficient for different sulfuric acid concentration of the catholyte.

11.4. Conclusions

A model is proposed for transport in the membrane of an all-vanadium redox flow battery based upon the Stefan-Maxwell multicomponent diffusion equation. The multicomponent diffusion equation results in the simulation of the species flux equations which are fully coupled. In this work, the transport of the species within the membrane with the high concentration (including protons (H^+), bisulfate (HSO_4^-), water (H_2O) and the sulfonate functional groups ($-\text{SO}_3^-$)) modeled and their interaction was simulated in a fully coupled framework. The driving force for species transport has been considered to be the gradient in electrochemical potential which can be decoupled in terms of the gradient of concentration and the gradient in electrostatic potential. The model successfully simulates the ionic transport numbers as well as water electro-osmosis drag coefficient for different acid concentrations. Experimental validation of these results is underway in our lab.

CHAPTER TWELVE :
MOLECULAR DYNAMIC MODEL OF NAFION SWELLED IN NONAQUEOUS
SOLVENTS

Scholarly contributions

This chapter is revised based on the manuscript prepared for the submission to the Journal of Electrochemical Society.

Yasser Ashraf Gandomi, David J. Keffer, Doug S. Aaron, Matthew M. Mench. “Modeling Conductivity of Ion-Exchange Membranes Swelled in Non-Aqueous Solvents: A Molecular Dynamics Approach” *in preparation*, (2018)

Abstract

One approach for reducing the overall cost of RFB systems is replacing the redox active transition metal salts (RAMs) with redox active organic molecules (ROMs). The ROMs are inexpensive with tunable structure. Therefore, redox couples with multiple electron transfer capabilities can be designed and fabricated. Using ROMs, the redox active couples with higher potential differences can be used to increase the open-circuit voltage of the battery. In this case, non-aqueous solvents must be used since the aqueous solvents are limited by the voltage stability limit of water (~1.23 V). Most frequently, sodium or lithium salts are used along with non-aqueous solvents to provide charge-balancing ions (i.e. Ni^+ or Li^+).

Usually, the conductivity of the membranes swelled in non-aqueous solvents is substantially lower compared to aqueous solvents. Therefore, the ohmic overpotential associated with the membrane is a major limiting factor for RFBs utilizing non-aqueous solvents. One approach for reducing the ohmic overpotential is to engineer the solvent structure for improved conductivity. The rapid progress in the membrane and non-aqueous

solvent developments necessitates developing rigorous mathematical models capable of predicting the conductivity of the membranes swelled in non-aqueous solvents. Therefore, in this work, a molecular dynamic approach has been adopted for modeling the diffusivity of lithium ions in Nafion® membranes swelled in various non-aqueous solvents.

12.1. Introduction

The redox active transition metal salts (RAMs) are commonly used within the structure of aqueous redox flow batteries (RFBs). The aqueous electrolytes containing RAMs are usually stable and durable during long-term cycling. However, RAMs are expensive, and the aqueous solvent used with RAMs is limited by the voltage stability limit of the water (~1.23 V). Therefore, there is an increasing interest to replace the RAMs with redox active organic molecules (ROMs) to decrease the cost. ROMs are usually inexpensive and have tunable molecular structures. Therefore, their molecular configuration can be engineered for improved stability, electrochemical durability, and charge storage capacity. Recently, significant progress has been made in developing two-electron organic donors/acceptors via engineering phenothiazine and naphthoquinone derivatives^{250, 251}.

Usually, non-aqueous solvents are used with ROMs and a supporting salt is also added to provide charge-balancing shuffling ions. Lithium and sodium salts are commonly used within the electrolytes of non-aqueous RFBs (NAqRFBs). Although ROMs are inexpensive, the supporting electrolyte (supporting salt and solvent) is costly. Therefore, NAqRFBs must utilize highly concentrated electrolytes and must be operated at high-

current densities to offset the increased cost of the electrolyte. To this end, the cell architectures must be optimized via reducing the major sources of overpotentials (i.e. ohmic or mass transport overpotentials). Usually, the kinetics associated with NAqRFBs is facile; thus, the kinetic overpotential is not a major concern for NAqRFBs.

An illustration was provided in Chapter 8 comparing the average pore size for various separators used in RFBs. As shown in Chapter 8, the ion-exchange membranes (IEMs) are used extensively for aqueous RFBs. Nafion® is a widely used membrane for aqueous redox flow battery architectures thanks to high durability, stability and conductivity. The ionic conductivity of the Nafion strongly depends on the bathing electrolyte. In Chapter 10, ex-situ measurements conducted for measuring the in-plane ionic conductivity of Nafion swelled in various aqueous electrolytes. It was shown that the in-plane ionic conductivity of the Nafion membrane swollen with water is the highest compared to other aqueous vanadium solutions with sulfuric acid as the supporting electrolyte ($\text{pH} < 7$). Therefore, the dependency of the ionic conductivity of the Nafion membranes on the composition of the aqueous solvents are relatively well understood. However, the ionic conductivity of the Nafion membranes swelled in non-aqueous solvents is not explored in detail.

Some pioneering experimental works on the influence of non-aqueous solvent properties on the conductivity of Nafion membranes have been reported by Doyle et al.^{247, 252} (2001), Sachan et al.²⁵³ (2002), Klein et al.²⁵⁴ (2007), and Escalante-Garcia et al.²⁵⁵ (2015).

The influence of non-aqueous solvent properties on the conductivity of perfluorinated ionomer membranes have also been investigated via molecular dynamic (MD) simulations. Burlatsky et al. developed a comprehensive MD framework to simulate the diffusivity of lithium ions within Nafion ionomer swollen with different non-aqueous solvents ²⁴¹. In particular, they compared the conductivity of the lithiated polymeric membranes swelled in dimethyl sulfoxide (DMSO) and acetonitrile (ACN) ²⁴¹. The MD simulation has also been used for predicting the lithium solvation in various non-aqueous electrolytes. Semino et al. ²⁵⁶ developed a MD model for predicting solvation of Li^+ in various binary mixtures including dimethyl sulfoxide and acetonitrile.

As briefly summarized, some excellent prior experimental and modeling works have been focused on the influence of non-aqueous solvent properties on the ionic conductivity either in the membrane phase or within the electrolyte. However, the reports are not consistent. Therefore, we decided to further explore the interaction of the polymeric membrane with the non-aqueous solvents via developing a molecular dynamic model. Our objective was to simulate the diffusivity of the lithium ions within the membrane phase swollen with different non-aqueous solvents. The dimethyl sulfoxide and acetonitrile are promising non-aqueous solvents being considered for various NAqRFBs. Therefore, in this work, we have focused on these non-aqueous solvents.

The MD model developed in this work provides molecular level understanding on the influence of the solvent molecular structure on the diffusivity of charge balancing ions

within the membrane. Therefore, the model can be used as a screening tool to identify potential and promising solvent structures to be used within NAqRFB systems.

In the following, the model development has been described in detail. The molecular dynamic simulations have been conducted using the LAMMPS software package (Large-scale Atomic/Molecular Massively Parallel Simulator; developed in Sandia National Laboratories) with thermostat and barostat configurations.

12.2. Mathematical Model

12.2.1. Structural Models

The first step for developing a model based on molecular dynamics is creating a stable molecular structure. For the polymer chain, schematic representation of the atomic connectivity was adopted from Ref. ²⁵⁷. The atomic number, atomic type, and atomic connectivity of the perfluorinated sulfonic-acid (PFSA) ionomer along with 3D model has been shown in Fig. 12-1.

Figure 12-1 includes schematic representation of the atomic type, atomic number and atomic connectivity (Fig. 12-1(a)) for the PFSA ionomer. Further details regarding the atomic number are provided in the following.

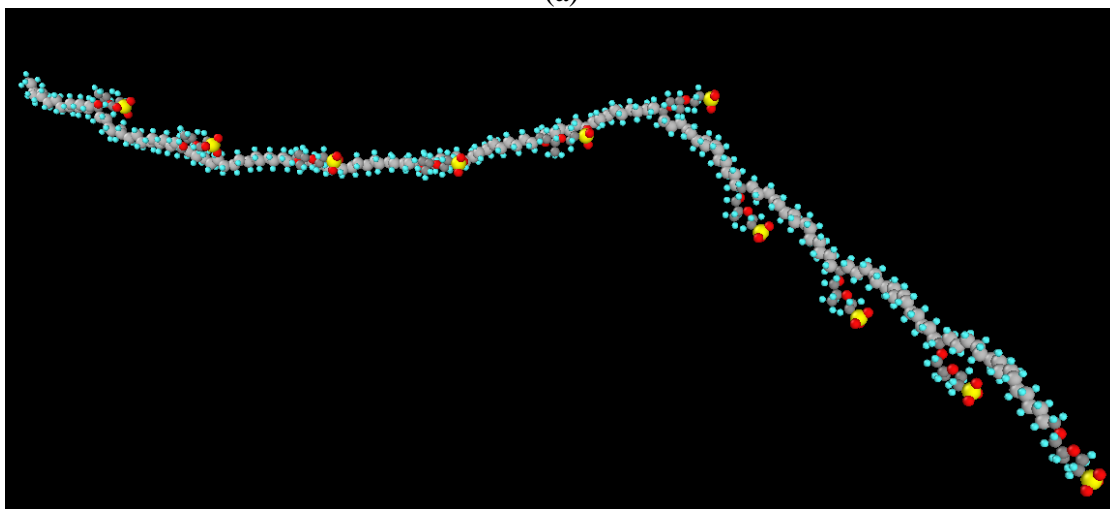
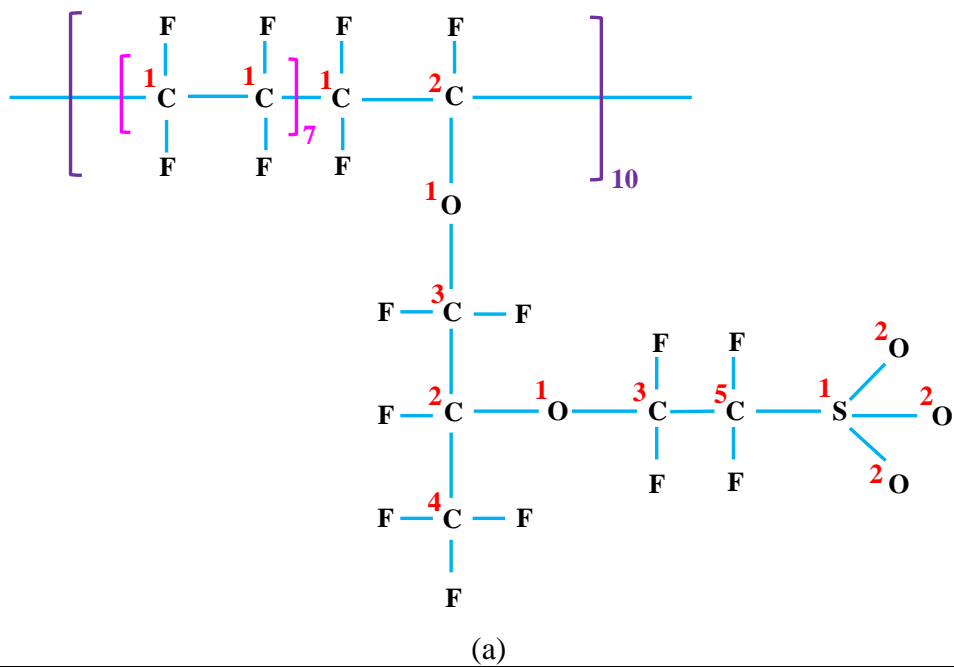


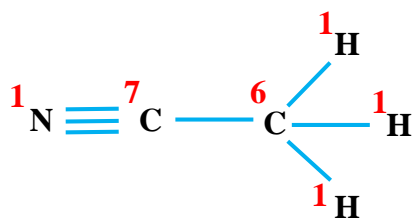
Figure 12-1: The molecular structure of the PFSA ionomer (Nafion® ionomer with equivalent weight of $1100 \text{ g}\cdot\text{mol}^{-1}$);

(a) Atomic type, number and connectivity (Adopted from Ref. ²⁵⁷)

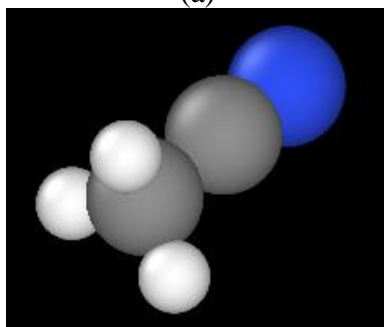
(b) 3D structure of the polymer chain (Decamer)

The 3D structure of the polymer chain is shown in Fig. 12-1(b). In Fig. 12-1(b), the carbon atoms have been shown in gray, the oxygen atoms are red, the fluorine atoms are cyan, and the sulfur atoms have been demonstrated in yellow. The polymer chain consisted of 10 monomers as shown in Fig. 12-1 (b). The equivalent weight associated with a single polymer chain was 1100 g.mol^{-1} .

To construct the structural models for the non-aqueous solvents, the atomic connectivity was adopted from the NIST (National Institute of Standards and Technology) WebBook. The schematic of the molecular structure along with 3D model has been shown in Fig. 12-1.



(a)



(b)

Figure 12-2: The molecular structure of the acetonitrile (ACN),
(a) Atomic type, number and connectivity,
(b) 3D structure of the molecule (Adopted from NIST WebBook)

The atomic type, atomic number and atomic connectivity for the acetonitrile has been shown in Fig. 12-2(a). The 3D structure has been adopted from NIST WebBook (Fig. 12-2(b)). In Fig. 12-2(b), the carbon atoms are gray, the nitrogen atom is dark blue, the hydrogen atoms have been shown in white. The atomic structure along with 3D model of dimethyl sulfoxide has been illustrated in Fig. 12-3.

Figure 12-3(a) illustrates the atomic type, atomic number and atomic connectivity for the dimethyl sulfoxide. The 3D molecular model shown for dimethyl sulfoxide in Fig. 12-3(b) has been adopted from NIST WebBook. In Fig. 12-3(b), the oxygen atom is red, the carbon atoms are shown in gray, the hydrogen atoms are illustrated in white, and the sulfur atom is visualized in yellow.

12.2.2. Force field formulation

The total potential fields used for extracting the force field parameters can be modeled as sum of contributions from bonded and non-bonded parts.

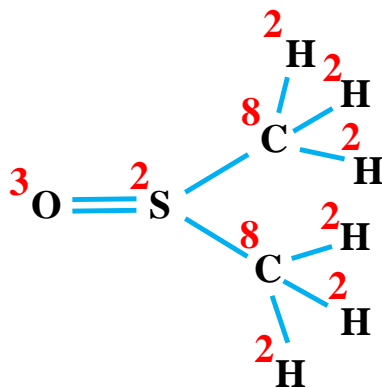
$$U = U_{bonded} + U_{non-bonded} \quad (12-1)$$

Using the total potential, the forces required for keeping the hydrated ions in pores can be calculated²⁵⁸.

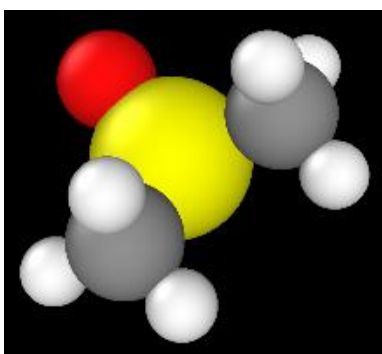
$$F = -\nabla U \quad (12-2)$$

The contributions from the bonded energy can be summarized as following²⁵⁹:

$$U_{bonded} = E_{stretching} + E_{bending} + E_{twisting} + E_{ImpTorsion} \quad (12-3)$$



(a)



(b)

Figure 12-3: The molecular structure of the dimethyl sulfoxide (DMSO),
 (a) Atomic type, number and connectivity,
 (b) 3D structure of the molecule (Adopted from NIST WebBook)

The stretching energy component is commonly modeled as:

$$E_{stretching} = \sum_{bond} K_b(b - b_0)^2 \quad (12-4)$$

Here, $E_{stretching}$, refers to the energy of chemical bonds stretching in harmonic vibration form. The bending energy contribution can be formulated as the following ²⁴¹:

$$E_{bending} = \sum_{angle} K_\theta(\theta - \theta_0)^2 \quad (12-5)$$

Here, $E_{bending}$ is the energy required for bending angles formed though two consecutive chemical bonds. The energy for twisting dihedral angles ($E_{twisting}$) can be modeled using the following set of equations (in LAMMPS referred to as *Class2*)

$$E = E_d + E_{mbt} + E_{ebt} + E_{at} + E_{aat} + E_{bb13} \quad (12-6)$$

$$E_d = \sum_{n=1}^3 K_n[1 - \cos(n\Phi - \Phi_n)] \quad (12-7)$$

As described in the LAMMPS documentation, here E_d is the dihedral term which can be formulated using Eq. (12-7) and the remaining terms including middle-bond-torsion (E_{mbt}), end-bond-torsion (E_{ebt}), angle-torsion (E_{at}), angle-angle-torsion (E_{aat}), and bond-bond-13 (E_{bb13}) have been assumed to be zero for the set of molecules and polymer chain modeled in this work.

It is important to note that the energy for improper torsion ($E_{ImpTorsion}$) can be assessed using the following model ²⁵⁷. Although, the contribution of this term is usually insignificant for the set of molecules being considered in this work.

$$E_{ImpTorsion} = \sum_{improper} \frac{K_{\chi}}{2} [(1 + \cos(n\chi - \chi_0))] \quad (12-8)$$

For non-bonded energy terms, the contributions from electrostatic (Coulombic) and van der Waals energies must be considered. The van der Waals forces are commonly modeled using Lennard-Jones (LJ) model.

$$U_{electrostatic} = \sum_{nonbond} \left[\frac{q_i q_j}{r_{ij}} \right] \quad (12-9)$$

$$U_{van\ der\ Waals} = \sum_{nonbond} \left\{ \varepsilon_{ij} \left[\left(\frac{\sigma_{ij}^0}{r_{ij}} \right)^{12} - 2 \left(\frac{\sigma_{ij}^0}{r_{ij}} \right)^6 \right] \right\} \quad (12-10)$$

Here, the subscriptions i and j refers to atom pairs and r_{ij} is the distance between those atom pairs. The pairwise constants for Lennard-Jones (LJ) model can be calculated using the following arithmetic approximation²⁵⁷.

$$\varepsilon_{ij} = \sqrt{\varepsilon_i \varepsilon_j} \quad (12-11)$$

$$\sigma_{ij}^0 = \frac{\sigma_i^0 + \sigma_j^0}{2} \quad (12-12)$$

12.2.3. Force-field parameters

The force field parameters for the set of equations described in Section 12.2.2 are summarized in this section. The van der Waals parameters for Nafion ionomer with equivalent weight of 1100 g.mol⁻¹, acetonitrile, dimethyl sulfoxide, and lithium are listed in Tables 12.1, 12.2, 12.3, and 12.4 respectively.

Table 12.1. Van der Waals parameters for Nafion ionomer with equivalent weight of 1100 g.mol⁻¹ (Data adopted from Ref. ²⁵⁷)

Site	σ (Å)	ϵ (kcal. mol ⁻¹)	z (e)
C1 (C1 is carbon with 2 C & 2 F neighbors)	3.9286	0.0660	0.2164
C2 (C2 is carbon with 2 C & 1 F & 1 O neighbors)	3.9286	0.0660	0.1983
C3 (C3 is carbon with 1 C & 2 F & 1 O neighbors)	3.9286	0.0660	0.3065
C4 (C4 is carbon with 1 C & 3 F neighbors)	3.9286	0.0660	0.3246
C5 (C5 is carbon with 1 C & 2 F & 1 S neighbors)	3.9286	0.0660	-0.0805
F	3.3113	0.0530	-0.1082
O1 (O1 is oxygen with 2 C neighbors)	3.2551	0.1400	-0.1802
O2 (O2 is carbon with 1 S neighbor)	3.3225	0.1700	-0.5863
S1 (S1 is sulfur with 1 C & 3 O neighbors)	3.9847	0.2500	1.0559

Table 12.2. Van der Waals parameters for acetonitrile (Data adopted from Ref. ²⁵⁶)

Site	σ (Å)	ϵ (kcal. mol ⁻¹)	z (e)
C6 (C6 is carbon with 3 H & 1 C neighbor)	3.40	0.1094	-0.479
C7 (C7 is carbon with 1 C & 1 N neighbor)	3.40	0.0860	0.481
H1 (H1 hydrogen with 1 C neighbor)	2.65	0.0157	0.177
N1 (N1 is nitrogen with 1 C neighbor)	3.25	0.1700	-0.532

The bond stretching coefficients for Nafion ionomer, acetonitrile, and dimethyl sulfoxide are listed in the following tables (Tables 12.5, 12.6, and 12.7). The bond angle coefficients for PFSA ionomer, acetonitrile, and dimethyl sulfoxide are listed in Tables 12.8, 12.9, and 12.10 respectively. The dihedral coefficients for Class2 functional form formulated in Eq. (12-7) for Nafion EW1100 $\text{g}\cdot\text{mol}^{-1}$ and dimethyl sulfoxide are tabulated in Tables 12.11 and 12.12. Considering the structural form of acetonitrile, no dihedral twisting angles exists within the structure.

12.2.4. Modeling details

The prior approaches for MD simulations of the Nafion ionomer mostly relies on thermalization process to achieve the equilibrium state. During the thermalization process, isothermal-isobaric (NPT) ensemble is performed at relatively low temperature and constant pressure; subsequently the system is heated up and then down allowing the system to achieve an equilibrium state. Therefore, the density of the system reaches a realistic density as a function of this annealing process. An excellent analysis has been performed by Burlastsky et al.²⁴¹ for achieving an optimum density for the Nafion ionomer swelled in dimethyl sulfoxide and acetonitrile.

Table 12.3. Van der Waals parameters for dimethyl sulfoxide
(Data adopted from Ref. ²⁵⁶)

Site	σ (Å)	ϵ (kcal. mol ⁻¹)	z (e)
C8 (C8 is carbon with 3 H & 1 S neighbor)	3.64	0.0780	-0.148
H2 (H2 hydrogen with 1 C neighbor)	2.39	0.0240	0.090
O3 (O3 is oxygen with 1 S neighbor)	3.03	0.1200	-0.556
S2 (S2 is sulfur 2 C & 1 O neighbor)	3.56	0.3500	0.312

Table 12.4. Van der Waals parameters for lithium (Data adopted from Ref. ²⁵⁶)

Site	σ (Å)	ϵ (kcal. mol ⁻¹)	z (e)
Li ⁺	1.39	0.165	1

Table 12.5. Bond stretching coefficients for Nafion ionomer with EW1100 g.mol⁻¹ (Data adopted from Ref. ²⁵⁷)

Bond	b_0 (Å)	K_b (kcal. mol ⁻¹ . Å ⁻²)
C1-C1	1.5356	276.0580
C1-C2	1.5356	276.0580
C1-C3	1.5356	276.0580
C1-C4	1.5356	276.0580
C1-F	1.3485	338.8046
C2-C3	1.5356	276.0580
C2-C4	1.5356	276.0580
C2-F	1.3485	338.8046
C2-O1	1.3622	297.7457
C3-C5	1.5356	276.0580
C3-F	1.3485	338.8046
C3-O1	1.3622	297.7457
C4-F	1.3485	338.8046
C5-F	1.3485	338.8046
C5-S	1.8545	176.4593
O2-S	1.4800	587.9230

Table 12.6. Bond stretching coefficients for acetonitrile (Data adopted from Ref. ²⁵⁶)

Bond	b_0 (Å)	K_b (kcal. mol ⁻¹ . Å ⁻²)
C6-C7	1.458	400.0000
C6-H1	1.090	340.0000
C7-N1	1.157	600.0000

Table 12.7. Bond stretching coefficients for dimethyl sulfoxide (Data adopted from Ref. ²⁵⁶)

Bond	b_0 (Å)	K_b (kcal. mol ⁻¹ . Å ⁻²)
C8-H2	1.110	322.0000
C8-S2	1.800	240.0000
O3-S2	1.530	540.0000

Table 12.8. Bond angle coefficients for Nafion with EW1100 g.mol⁻¹
(Data adopted from Ref. ²⁵⁷)

Angle	b_{θ} (deg)	K_{θ} (kcal. mol ⁻¹ . rad ⁻²)
C1-C1-C1	109.0639	44.4644
C1-C1-C2	109.0639	44.4644
C1-C1-C3	109.0639	44.4644
C1-C1-C4	109.0639	44.4644
C1-C1-F	106.7816	60.7610
C1-C2-C1	109.0639	44.4644
C1-C2-F	106.7816	60.7610
C1-C2-O1	110.7657	43.5794
C1-C3-F	106.7816	60.7610
C1-C3-O1	110.7657	43.5794
C1-C4-F	106.7816	60.7610
C2-C1-F	106.7816	60.7610
C2-C3-F	106.7816	60.7610
C2-C3-O1	110.7657	43.5794
C2-C4-F	106.7816	60.7610
C2-O1-C3	120.6078	117.1048
C3-C1-F	106.7816	60.7610
C3-C2-C4	109.0639	44.4644
C3-C2-F	106.7816	60.7610
C3-C2-O1	110.7657	43.5794
C3-C5-F	106.7816	60.7610
C3-C5-S	115.2954	18.3324
C3-O1-C3	120.6078	117.1048
C4-C1-F	106.7816	60.7610
C4-C2-F	106.7816	60.7610
C4-C2-O1	110.7657	43.5794
C5-C3-F	106.7816	60.7610
C5-C3-O1	110.7657	43.5794
C5-S-O2	112.0818	62.4607
F-C1-F	107.9771	85.7607
F-C2-O1	108.9077	63.9312
F-C3-F	107.9771	85.7607
F-C3-O1	108.9077	63.9312
F-C4-F	107.9771	85.7607
F-C5-F	107.9771	85.7607
F-C5-S	109.7797	33.5332
O2-S-O2	125.8476	98.8656

Table 12.9. Bond angle coefficients for acetonitrile (Data adopted from Ref. ²⁵⁶)

Angle	b_{θ} (deg)	K_{θ} (kcal. mol ⁻¹ . rad ⁻²)
C6-C7-N1	180	80.0000
C7-C6-H1	110	35.0000
H1-C6-H1	109.5	35.0000

Table 12.10. Bond angle coefficients for dimethyl sulfoxide (Data adopted from Ref. ²⁵⁶)

Angle	b_{θ} (deg)	K_{θ} (kcal. mol ⁻¹ . rad ⁻²)
C8-S2-C8	95.0	34.0000
C8-S2-O3	106.750	79.0000
H2-C8-H2	108.400	35.5000
H2-C8-S2	111.300	46.1000

Table 12.11. Dihedral coefficients for Nafion ionomer (Ref. ²⁵⁷)

Dihedral	K_1 (kcal. mol ⁻¹)	Φ_1 (rad)	K_2 (kcal. mol ⁻¹)	Φ_2 (rad)	K_3 (kcal. mol ⁻¹)	Φ_3 (rad)
C1-C1-C1-C1	-0.2	0.0	0.099	3.141592654	-0.0695	0.0
C1-C1-C1-C2	-0.2	0.0	0.099	3.141592654	-0.0695	0.0
C1-C1-C1-C3	-0.2	0.0	0.099	3.141592654	-0.0695	0.0
C1-C1-C1-C4	-0.2	0.0	0.099	3.141592654	-0.0695	0.0
C1-C1-C1-F	0.0	0.0	0.0	3.141592654	-0.0785	0.0
C1-C1-C2-C1	-0.2	0.0	0.099	3.141592654	-0.0695	0.0
C1-C1-C2-F	0.0	0.0	0.0	3.141592654	-0.0785	0.0
C1-C1-C2-O1	0.0	0.0	-1.92715	3.141592654	0.48995	0.0
C1-C1-C3-F	0.0	0.0	0.0	3.141592654	-0.0785	0.0
C1-C1-C3-O1	0.0	0.0	-1.92715	3.141592654	0.48995	0.0
C1-C1-C4-F	0.0	0.0	0.0	3.141592654	-0.0785	0.0
C1-C2-C1-F	0.0	0.0	0.0	3.141592654	-0.0785	0.0
C1-C2-O1-C3	0.0	0.0	-0.8853	3.141592654	-0.22025	0.0
C1-C3-O1-C3	0.0	0.0	-0.8853	3.141592654	-0.22025	0.0
C2-C1-C1-F	0.0	0.0	0.0	3.141592654	-0.0785	0.0
C2-C3-O1-C2	0.0	0.0	-0.8853	3.141592654	-0.22025	0.0
C2-C3-O1-C3	0.0	0.0	-0.8853	3.141592654	-0.22025	0.0
C2-O1-C3-C5	0.0	0.0	-0.8853	3.141592654	-0.22025	0.0
C2-O1-C3-F	0.0	0.0	-0.85995	3.141592654	-0.0412	0.0
C3-C1-C1-F	0.0	0.0	0.0	3.141592654	-0.0785	0.0
C3-C2-C4-F	0.0	0.0	0.0	3.141592654	-0.0785	0.0
C3-C2-O1-C3	0.0	0.0	-0.8853	3.141592654	-0.22025	0.0
C3-C5-S-O2	0.0	0.0	-1.2385	3.141592654	0.0739	0.0
C3-O1-C2-C4	0.0	0.0	-0.8853	3.141592654	-0.22025	0.0
C3-O1-C2-F	0.0	0.0	-0.85995	3.141592654	-0.0412	0.0
C3-O1-C3-F	0.0	0.0	-0.85995	3.141592654	-0.0412	0.0
C4-C1-C1-F	0.0	0.0	0.0	3.141592654	-0.0785	0.0
C4-C2-C3-F	0.0	0.0	0.0	3.141592654	-0.0785	0.0
C4-C2-C3-O1	0.0	0.0	-1.92715	3.141592654	0.48995	0.0
F-C1-C1-F	0.0	0.0	0.0	3.141592654	0.0245	0.0
F-C1-C2-F	0.0	0.0	0.0	3.141592654	0.0245	0.0
F-C1-C2-O1	100.0	75.0	100.0	70.0	80.0	60.0
F-C1-C3-F	0.0	0.0	0.0	3.141592654	0.0245	0.0
F-C1-C3-O1	100.0	75.0	100.0	70.0	80.0	60.0
F-C1-C4-F	0.0	0.0	0.0	3.141592654	0.0245	0.0
F-C2-C3-F	0.0	0.0	0.0	3.141592654	0.0245	0.0
F-C2-C3-O1	100.0	75.0	100.0	70.0	80.0	60.0
F-C2-C4-F	0.0	0.0	0.0	3.141592654	0.0245	0.0
F-C3-C2-O1	0.0	0.0	-2.2974	3.141592654	-0.0846	0.0
F-C3-C5-F	0.0	0.0	0.0	3.141592654	0.0245	0.0
F-C3-C5-S	0.0	0.0	1.6541	3.141592654	0.0306	0.0
F-C4-C2-O1	0.0	0.0	-2.2974	3.141592654	-0.0846	0.0
F-C5-C3-O1	0.0	0.0	-2.2974	3.141592654	-0.0846	0.0
F-C5-S-O2	0.0	0.0	-1.48795	3.141592654	-0.07725	0.0
O1-C2-C3-O1	0.0	0.0	-3.7986	3.141592654	-0.6465	0.0
O1-C3-C5-S	0.0	0.0	-0.25175	3.141592654	-0.3125	0.0

Here, we have implemented the density values reported by Burlastsky et al.²⁴¹ to construct the models. Table 12.13 includes further details regarding the initial configuration of the system.

As tabulated in Table 12.13, the number of lithium ions have been chosen similar to the total number of PFSA polymer chains to maintain electroneutrality within the membrane phase. The molecules reported in Table 12.13 were randomly distributed in a cube with $95.08 \times 95.08 \times 95.308 \text{ \AA}^3$ for the simulations with dimethyl sulfoxide and $69.04 \times 69.04 \times 69.04 \text{ \AA}^3$ for the simulations with acetonitrile. Periodic boundary conditions were applied and the LAMMPS minimization algorithm was used for achieving an optimum initial configuration.

The time step of 1 fs was chosen and NVT ensemble was used for the simulations. In addition, a multi-step time integration algorithm (r-ReSPA) was adopted. The total number of atoms for the simulations were 70384 and 26940 atoms for the simulations including DMSO and ACN respectively.

Table 12.12. Dihedral coefficients for dimethyl sulfoxide (Data adopted from Ref.²⁵⁶)

Dihedral	K_1 (kcal. mol ⁻¹)	Φ_1 (rad)	K_2 (kcal. mol ⁻¹)	Φ_2 (rad)	K_3 (kcal. mol ⁻¹)	Φ_3 (rad)
C8-S2-C8-H2	0.0	0.0	0.0	0.0	-0.2	0.0
H2-C8-S2-O3	0.0	0.0	0.0	0.0	-0.2	0.0

Table 12.13. Initial configuration of the system

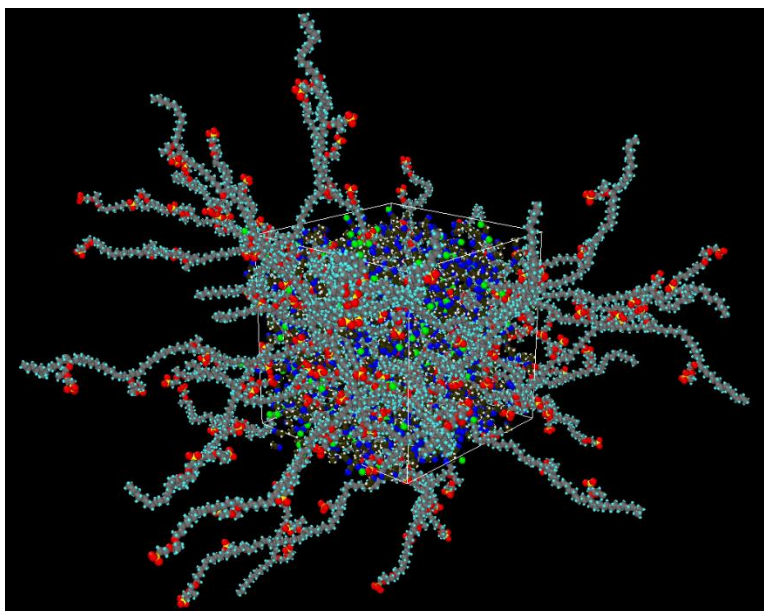
	ASR with flowing electrolyte aqueous sulfuric acid (3.3M) (ohm.cm ²)
Number of PFSA polymer chain (Decamer)	27
Number of lithium ions	270
Number of ACN molecules	1376
Number of DMSO molecules	5170

12.3. Results and Discussion

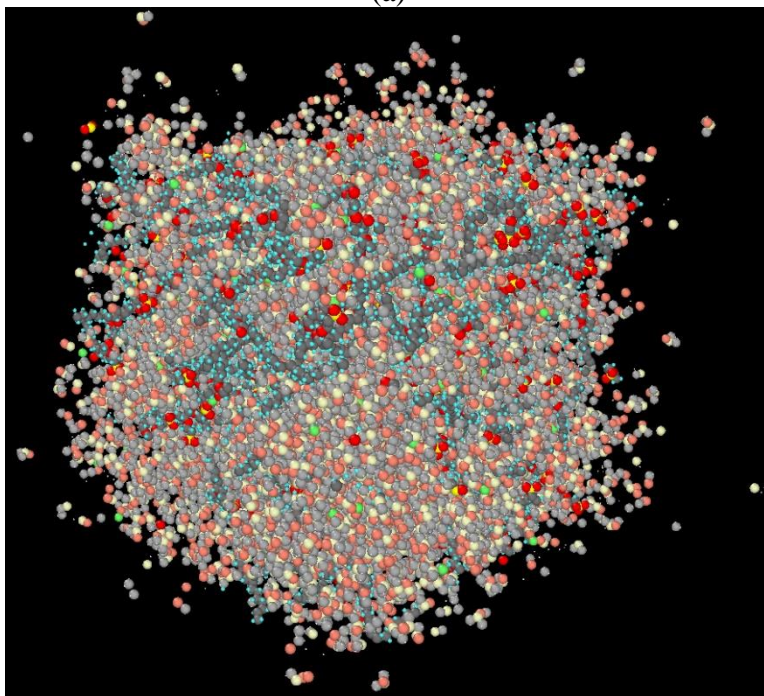
12.3.1. Structural analysis of the PFSA ionomer swelled in non-aqueous solvents

To illustrate the morphological changes imposed by the PFSA-solvent interactions, snapshots of the system at various configurations have been provided. As discussed in Section 12.2, periodic boundary conditions have been used for the simulations.

Here, the snapshots of the system have been illustrated for the DMSO and ACN systems. Before demonstrating the systems within periodic boundary conditions at the end of the simulation, two configurations at the initial stages (Fig. 12-4) of the simulations have been provided for better visualization of the systems without imposing periodic boundary conditions. Figure 12-5 shows the configurations of the ACN system at the end of the simulations with periodic boundary conditions.



(a)

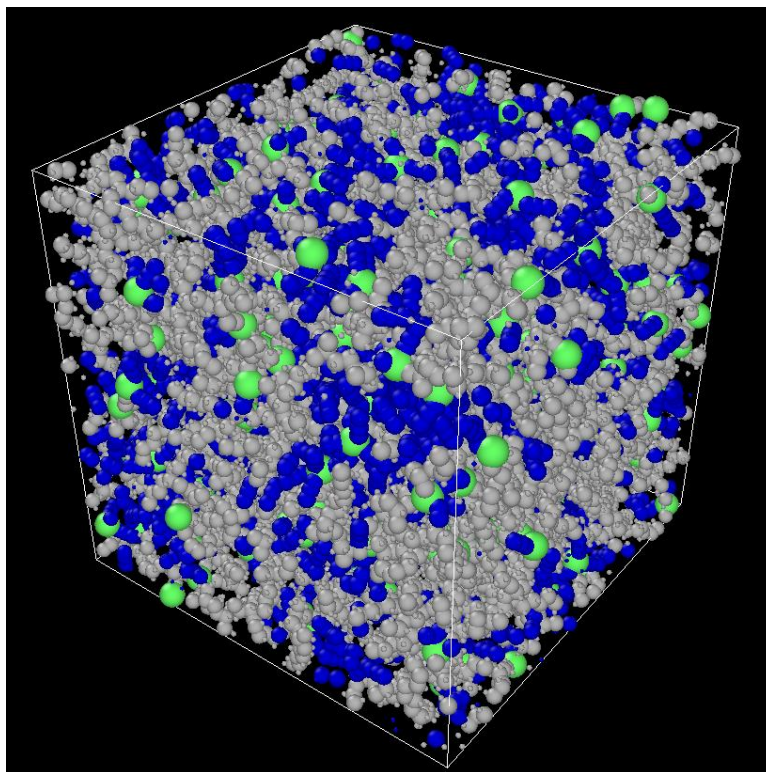


(b)

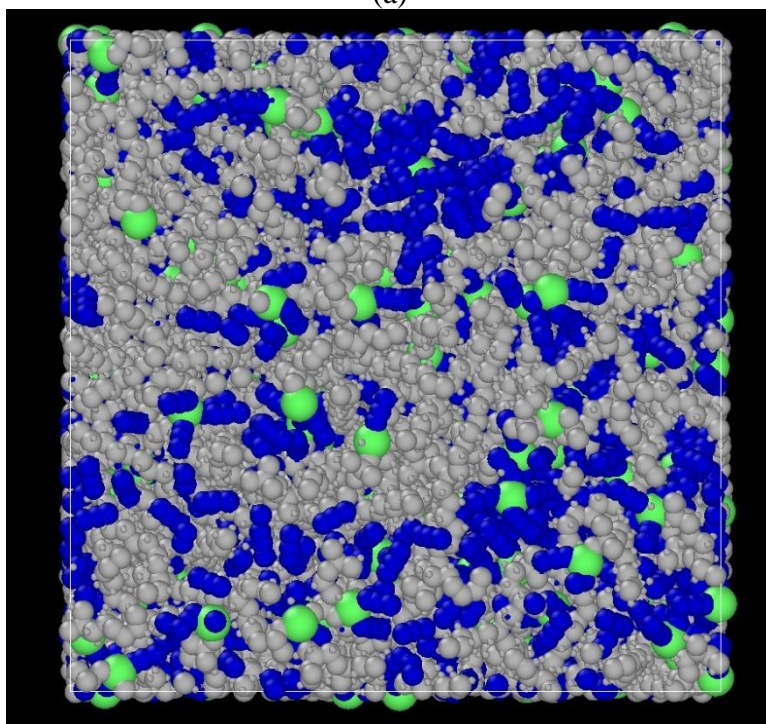
Figure 12-4: Snapshots of the system at early stages without imposing the periodic boundary conditions within illustrations,
(a) Acetonitrile system,
(b) DMSO system

The total time of the simulations for the ACN system was 8 ns. In Figures 12-5, for better illustration, uniform coloring scheme has been used for the PFSA ionomer chain (light gray), the solvent (dark blue), and the charge balancing ion (green, shown slightly larger for better demonstration). The configuration of the Nafion swelled in DMSO with lithium ion as the ion-balancing ion is shown in Figure 12-6 at the end of simulation with periodic boundary conditions. The total simulation time for the DMSO system was 10 ns. Similar to Fig. 12-5, to better illustrated the configurations and positioning the solvent, PFSA ionomer, and the charge shuffling ions, uniform coloring has been used in Fig. 12-6. In Figures 12-6 the polymer chain has been shown in light gray, the solvent (DMSO) is red, and the lithium ions are bright green. It is also important to demonstrate the polymer chain configuration at the end of simulations. Figure 12-7 includes the PFSA ionomer chain without showing other molecules for ACN system (Fig. 12-7(a)) as well as the DMSO system (Fig. 12-7(b)). A uniform color scheme has been used for better illustration.

The micro-phase separation is vividly illustrated in Fig. 12.7. As shown in the snapshots, non-polar phase is formed by the molecules constitute the ionomer's backbone structure. However, the polar phase is developed via the solvent molecules. This observation is consistent with the reports available elsewhere ²⁴¹. Although the Nafion ionomer swelled in both ACN and DMSO solvents exhibit micro-phase separation; the distinction between polar and non-polar phases is well pronounced when the PFSA ionomer chain swollen with the DMSO.

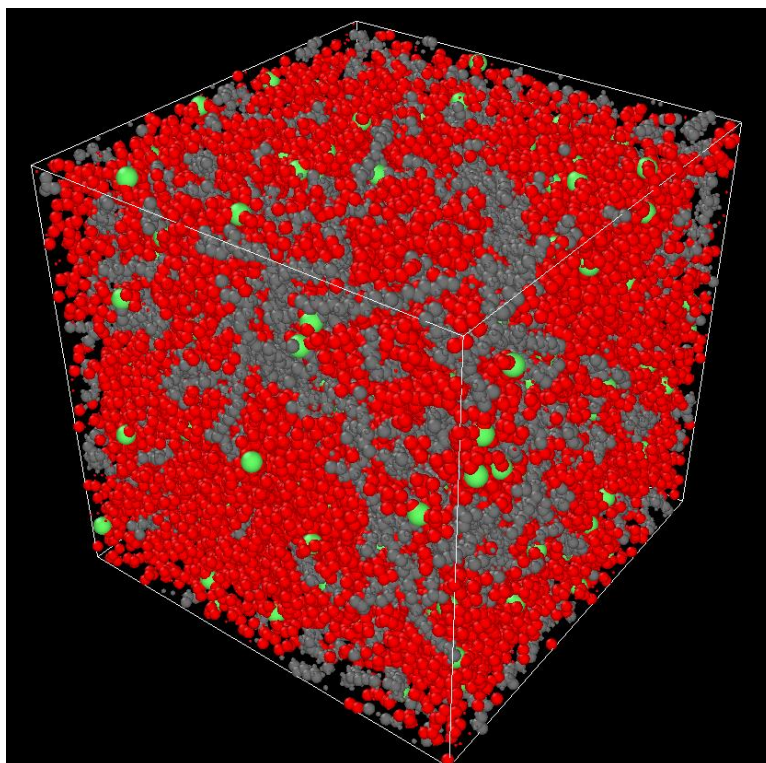


(a)

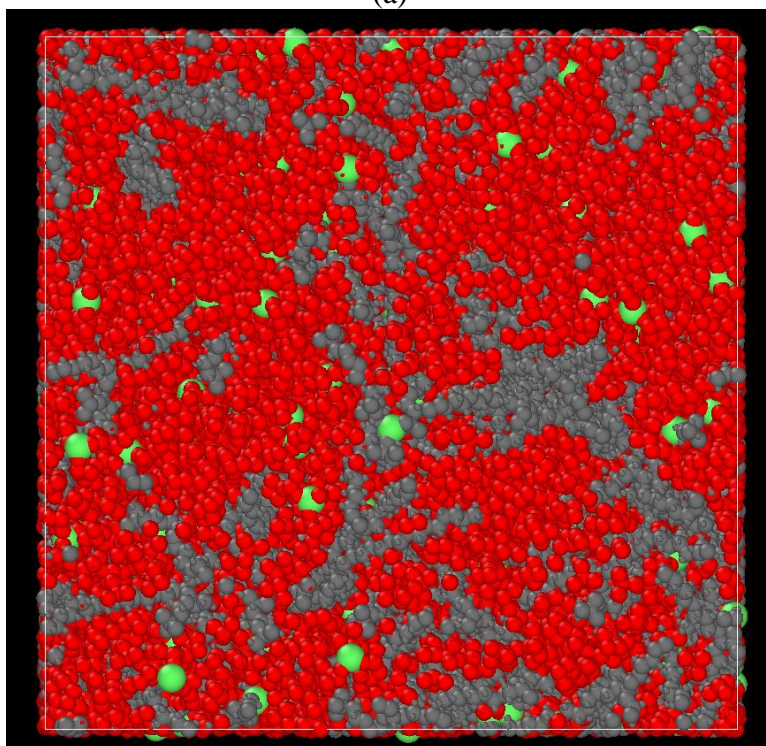


(b)

Figure 12-5: Snapshots of the ACN system at the end of simulation with periodic boundary conditions, (a) Perspective view, (b) Side view

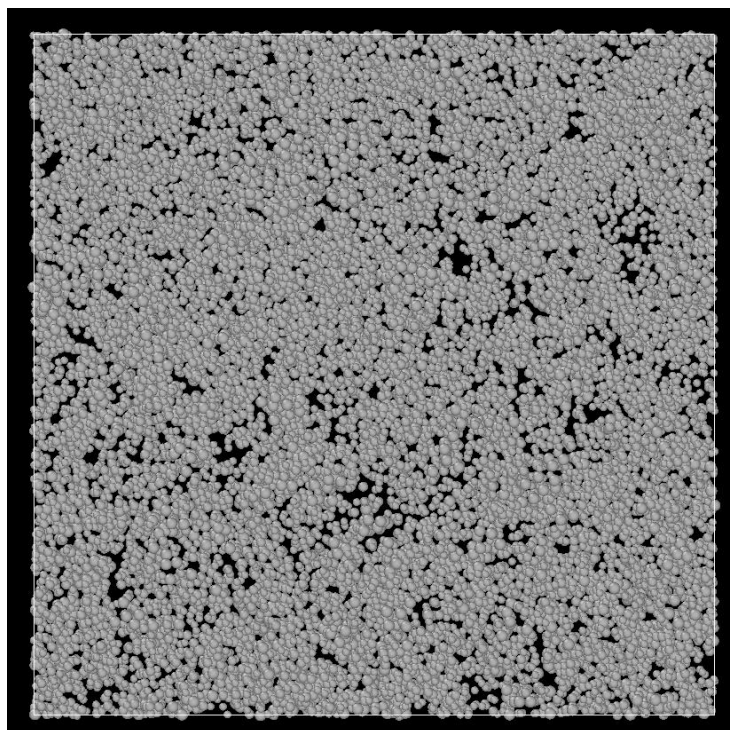


(a)

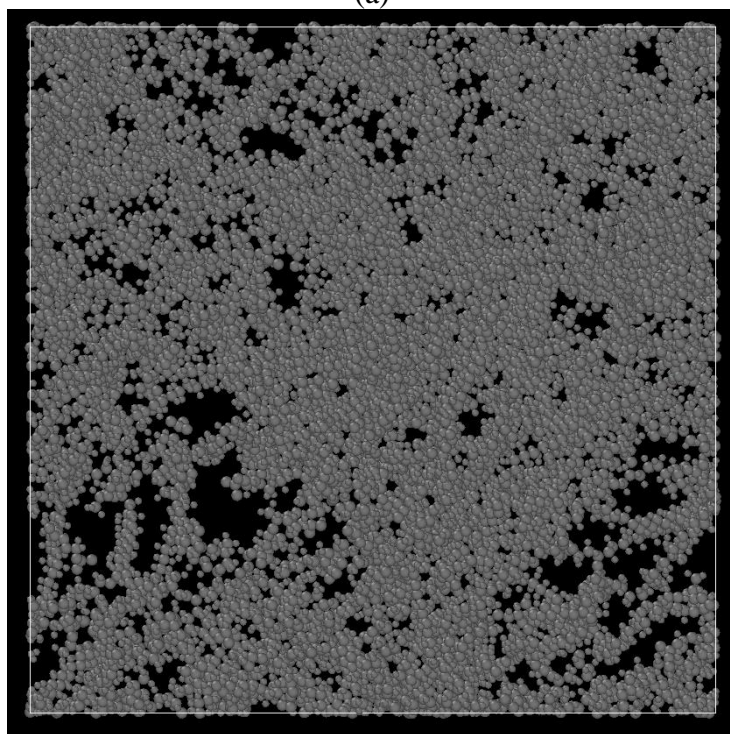


(b)

Figure 12-6: Snapshots of the DMSO system at the end of simulation with periodic boundary conditions, (a) Perspective view, (b) Side view



(a)



(b)

Figure 12-7: Snapshots of the PFSA ionomer chain at the end of simulations for (a) ACN system, (b) DMSO system

The mobility of the lithium ions within the membrane phase is directly influenced by the coupling mechanism between the sulfonic acid group (SO_3^-) of the ionomer and the lithium ions. Therefore, it is necessary to evaluate the degree of this coupling. The trajectories simulated via molecular dynamic modeling can be used to calculate the radial distribution function (or pair correlation function), $g(r)$. The radial distribution function is a strong tool to assess the interactions between any atoms in the configuration. Here, the radial distribution function has been used between lithium ions and the nearest SO_3^- groups within the membrane phase. Figure 12-8 compares the radial distribution function for DMSO and ACN systems.

Figure 12-8 demonstrates the radial distribution function between lithium ions and sulfonic acid group of the PFSA ionomer swelled in ACN versus DMSO non-aqueous solvent. As illustrated in Fig. 12-8, at $\sim 3 \text{ \AA}$, for both ACN and DMSO cases, there exist a sharp peak. This peak illustrates a strong interaction and coupling between lithium ions within the membrane with the sulfonic acid group (SO_3^-) of the PFSA ionomer.

Comparing these sharp peaks in Fig. 12-8 reveals that the significant percentage of lithium ions within the ACN system are strongly coupled with sulfonic acid group compared to the DMSO system. As a result of such a strong coupling, the mobility of lithium ions substantially decreases within the polymer chain swelled in ACN.

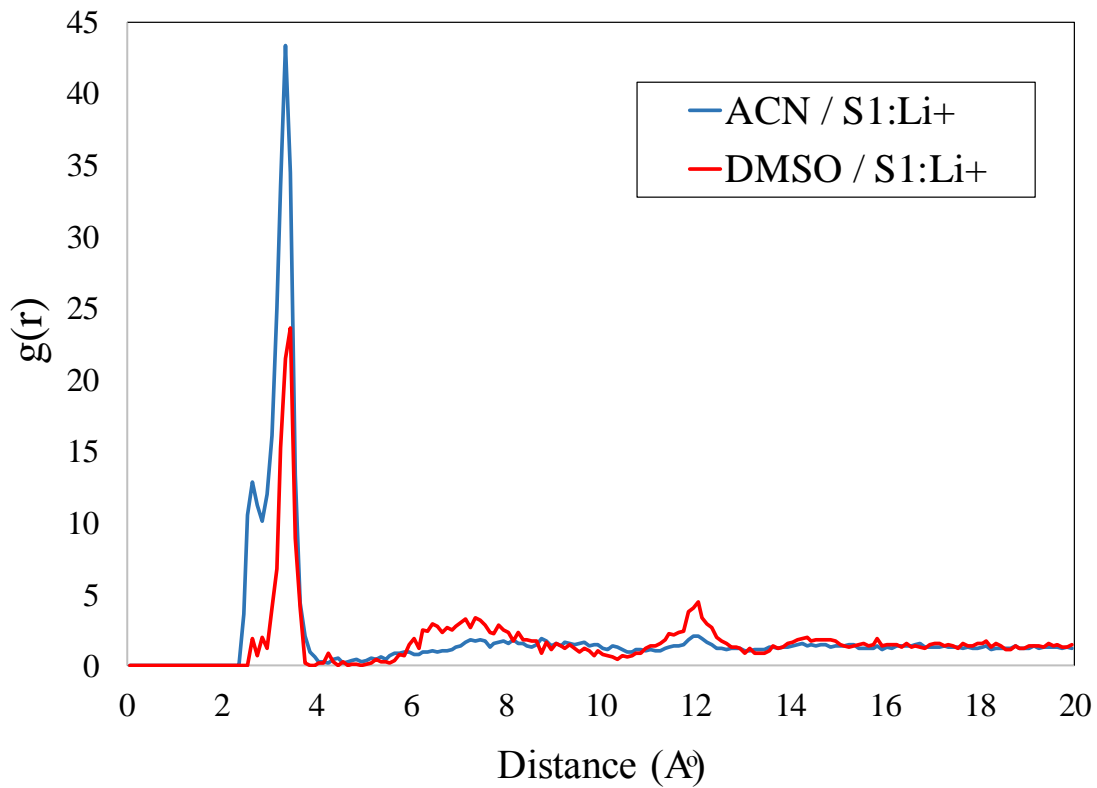


Figure 12-8: Variations in radial distribution function between lithium ions and sulfonic group for ACN system versus DMSO system

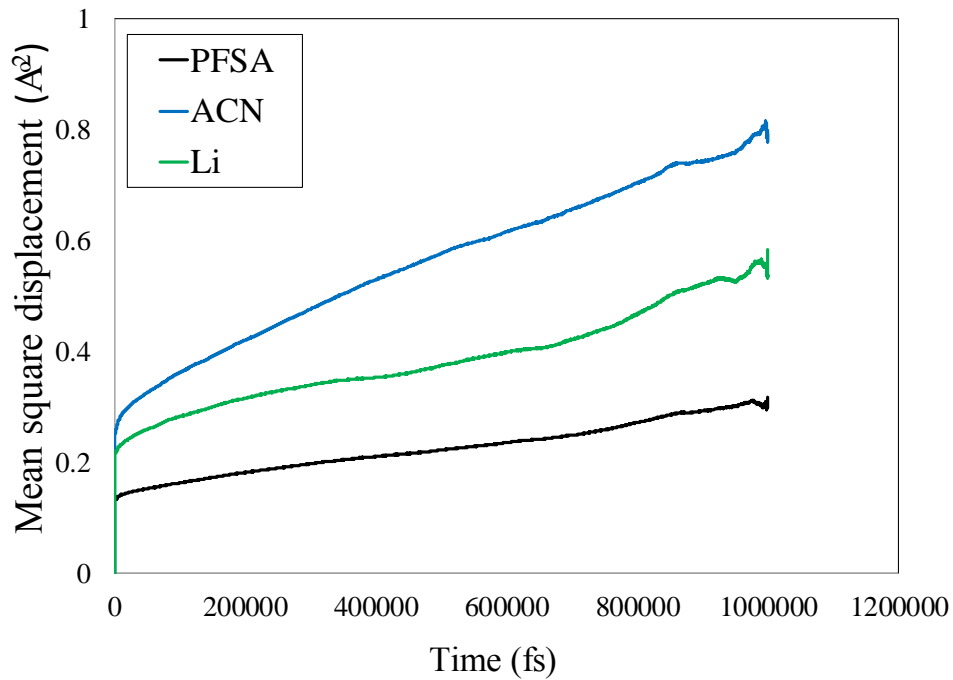
Figure 12-8 also demonstrates a wider peak at $\sim 7 \text{ \AA}$ for the DMSO system. This wider peak demonstrates the interaction of the lithium ions with the solvent. Therefore, according to Fig. 12-8, higher percentage of lithium ions in the DMSO system are indeed located in the polar (solvent) phase (please see Fig. 12-7(b)). This prediction is consistent with the reports elsewhere ²⁴¹. Therefore, it is expected that the mobility of the lithium ions within the DMSO system would be higher. Analysis of the diffusivities provided in the next section will further clarify this point.

12.3.2. Assessing diffusivities for the PFSA ionomer swollen with ACN and DMSO

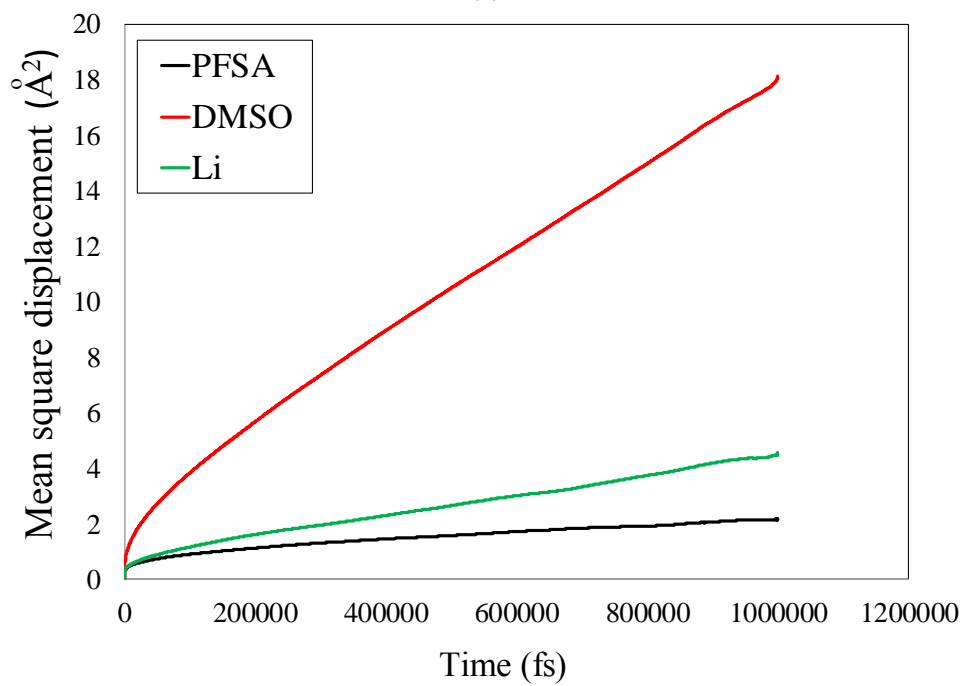
The trajectories simulated for various atoms/molecules within the system, can be used to calculate diffusivities for different components. To calculate the diffusivities, it is first necessary to evaluate the mean square displacement (MSD) for the components. Equation 12-13 is commonly used for calculating the mean square displacement ²⁴¹.

$$\Sigma_i^2(t) = \frac{1}{N} \sum_{i=1}^N [\vec{r}_i(t) - \vec{r}_i(0)]^2 \quad (12-13)$$

In Eq. 12-13, $\Sigma_i^2(t)$ is the mean square displacement for species i (\AA^2), N total number of atoms, $\vec{r}_i(t)$ is the position of species i at time t , and $\vec{r}_i(0)$ is the initial position of particle i . Figure 12-9 includes the MSD graphs calculated for ACN and DMSO systems.



(a)



(b)

Figure 12-9: The mean square displacement for
 (a) ACN system,
 (b) DMSO system

The mean square displacements have been shown for ACN and DMSO systems in Fig. 12-9. Fig. 12-9(a) includes the MSD graphs for PFSA ionomer, the solvent (ACN), and charge balancing ion (lithium). Fig. 12-9(b), demonstrates the MSD variations for the polymer ionomer chain (PFSA), the solvent (DMSO), and the lithium ions. Due to computational limitations, the graphs have only been shown for 1 ns (or 1000000 fs). The linear and non-linear trends shown in Fig. 12-9 have been thoroughly analyzed in the literature for other PFSA based systems.

The MSD being proportional to time, the transient and non-transient transport mechanism are detectable. Usually, the linear portion of the MSD graphs are used for evaluating the diffusivities. Further insights can be gained from transient behavior shown in Fig. 12-9 regarding the different time-scales associated with the interactions within polar and non-polar phases (please see 12-7).

Here, such a discussion is not our focus and therefore, we have only concentrated on evaluating the diffusivity values. The linear portions of the graphs shown in Fig. 12-9 are used for calculating the diffusivities via linear regression of the MSD plots according to the following equation.

$$D = \frac{1}{6t} \overline{\Delta r_i^2(t)} \quad (12-14)$$

Table 12-14 includes the diffusivities calculated for the different components.

Table 12.14. Diffusion coefficients calculated for PFSA ionomer swollen with various non-aqueous solvents, ($\text{cm}^2/\text{s} \times 10^{-7}$)

	PFSA	Li ⁺	Non-aqueous solvent
ACN system	0.02	0.02	0.09
DMSO system	0.23	0.58	2.64

Table 12.14 includes the diffusivity values calculated for different components of the system. As tabulated in Table 12.14, for the ACN system, the diffusivity of the lithium ions is similar to the PFSA ionomer indicating a strong interaction between the sulfonic acid groups of the polymer chain and the charge balancing ions. This also indicates that the transport of lithium ions within the polar phase is strictly limited. This observation is consistent with the previous reports in the field ²⁴¹.

Comparing the diffusivity values of the PFSA ionomer with the lithium ions in Table 12.14 for the DMSO system reveals that the diffusivity values of the lithium ions is noticeably higher (~2.5 times higher) than the polymer chain. This trend is most probably due to increased mobility of lithium ions within the solvent polar phase. Based on the data provided in Table 12.14, the diffusivity of the lithium ions in DMSO system is ~29 times higher than the diffusivity of the lithium ions in ACN system. As discussed earlier, the increased mobility of the lithium ions within the solvent phase (please see Fig. 12-7) is the major contributor to increased diffusivity of lithium ions for the PFSA ionomers swelled in DMSO. It is also important to note that our calculations are in good agreement with the reports in the literature. Burlatsky et al. reported 31.6 times higher diffusivity for the lithium ions within DMSO system compared to ACN systems ²⁴¹.

12.4. Conclusions

The application of non-aqueous solvents for redox flow batteries utilizing redox-active organic molecules (ROMs) is increasing in the field. Therefore, developing screening techniques for evaluating the performance of RFBs with different non-aqueous solvents is of a great importance. In this work, we have developed a molecular dynamic model capable of simulating the PFSA ionomers swelled in various non-aqueous solvents.

Here, two promising non-aqueous solvents were modeled; dimethyl sulfoxide (DMSO) and acetonitrile (ACN). The model included the Nafion ionomer (with equivalent weight of 1100 g.mol⁻¹), the solvent, and the lithium ions as the charge-balancing species. The morphological simulation of the system revealed a micro-phase separation for the DMSO as well as the ACN systems where the non-aqueous solvents constitute the polar phase and the sulfonic acid group of the membrane formed the non-polar phase. Although both systems demonstrated the micro-phase separation, the degree of separation was more pronounced for the DMSO system.

The diffusion coefficient for the lithium ions was calculated based on the mean square displacements. It was shown that the diffusion coefficient of the lithium ions within the PFSA ionomer swelled in DMSO is ~29 times higher than ACN system. The major contributor for an increased diffusivity for the DMSO system was increased mobility within the polar phase filled by the non-aqueous solvent. The analysis of radial distribution functions between the lithium ions and the sulfonic group of the membrane suggested a

strong coupling between the lithium ions and the PFSA ionomer for the ACN system; thus, decreased mobility for the lithium ions within the polymer chain swollen with the ACN solvent is expected.

Although this model was developed for Nafion membranes, it can easily be used for any other membrane type along with the solvent and charge balancing ions.

12.5. Acknowledgments

Yasser Ashraf Gandomi thanks University of Tennessee for providing Chancellor Fellowship.

CHAPTER THIRTEEN :
WATER MANAGMENT IN POLYMER ELECTROLYTE MEMBRANE FUEL
CELLS

Scholarly contributions

This chapter is revised based on two published papers with permission from the Journal of Electrochemical Society (JES) ^{112, 218}.

Yasser Ashraf Gandomi, M. D. Edmundson b, F. C. Busby, Matthew M. Mench. “Water Management in Polymer Electrolyte Fuel Cells through Asymmetric Thermal and Mass Transport Engineering of the Micro-Porous Layers” *Journal of Electrochemical Society*, 163 (8), F933-F944 (2016) [doi: 10.1149/2.1331608jes]

Yasser Ashraf Gandomi, Matthew M. Mench. “Concentrated solution model of transport in all vanadium redox flow battery membrane separator” *ECS Transactions*, 58 (1), 1375-1382 (2013) [doi: 10.1149/05801.1375ecst]

Abstract

For polymer electrolyte fuel cells (PEFCs) operating at very high current, prevention of anode dry-out through enhanced back flux of water and restriction of evaporation is required. In this work, back flux of water to the anode is engineered using an asymmetric anode and cathode micro-porous layer (MPL) configuration. Extensive experimental tests have been conducted to study the impact of thermal and mass transport resistances on the net water flux coefficient for extremes of wet and dry operating conditions. The net water drag coefficient was measured in the range of -0.17 to +0.18 depending on the operating conditions and material configurations. A simplified model has also been developed to investigate the effect of temperature gradient on the net water drag coefficient. It is shown that with an asymmetric configuration, the net flux of water can be reversed under certain conditions, greatly enhancing high current density performance. For wet operating conditions, the cell configuration with asymmetric mass transport resistance can be utilized

to tailor the back flux of water. For dry operating conditions, the thermal resistance is the key controlling parameter to affect the net water drag.

13.1. Introduction

Water management remains an important topic in polymer electrolyte fuel cell (PEFC) systems. Water is required to keep the membrane hydrated to maintain ionic conductivity. However, excessive liquid-water accumulation in the gas flow channels and in the porous media (gas diffusion layer (GDL), and catalyst layers) limits reactants' transport to the electrocatalyst (a phenomenon called flooding). The membrane's transport properties are known to be a strong function of water content within the membrane. Extensive dry-out at the anode side and subsequent conductivity loss results in poor overall performance. Several passive and active approaches have been utilized for water management within the PEFCs (e.g.^{112, 218, 260-264}). A good review of these techniques has been provided in Ref. ²⁶⁵ and a recent review of water transport within PEFCs is discussed in Ref. ²⁶⁶. The microporous layer (MPL) at the electrodes have been used to improve the performance of PEFC via water management. Pasaogullari et al. ²⁶⁷ modeled the two-phase transport in the porous layers of a PEFC cathode side. Their modeling results predicted that the existence of a MPL in the cathode side enhances liquid-water removal and reduces liquid saturation in the catalyst layer. Weber and Newman ²⁶⁸ explored the effects of MPL in terms of water management using a two-phase flow and membrane model. Their simulation predicted that the MPL acts as a valve that pushes water away from the GDL in the cathode side through the membrane and accordingly minimizes flooding. Yan et al. ²⁶⁹ measured the net water

flux transferred across the membrane under various operating conditions. They measured the net flux coefficients ranging from +0.93 to -0.2 depending on the current density and humidification of feed gases. R. Zaffou et al.²⁷⁰ quantified the temperature-gradient-driven water transport within the PEFC and they found that the magnitude of temperature-gradient-driven water flux is proportional to the temperature gradient and the average temperature. Atiyeh et al.²⁷¹ studied the role of a MPL on the water transport and performance of the PEFC. Their results indicated that the presence of MPL improves the cell performance, but it does not affect the net water drag coefficient. Spornjak et al.²⁷² conducted experiments to visualize the liquid water formation and transport in an operational single-serpentine PEFC. They observed no liquid water in the anode flow field unless cathode GDLs had an MPL. They concluded that the MPL on the cathode side creates a pressure barrier for water produced at the catalyst layer pushing the water across the membrane to the anode side, resulting in anode flow field flooding close to the H₂ exit. Husar et al.²⁷³ measured the water transfer through the membrane due to the three different mechanisms of water transfer, i.e., electro-osmotic drag, diffusion and hydraulic permeation. It is important to note that hydraulic pressure gradient across the MEA is the result of a gas phase pressure gradient or as a result of capillary pressure gradient across the MEA. Gostick et al.²⁷⁴ measured the capillary pressure and water saturation at the point of water breakthrough in GDL. Based on their observation, water percolation through the MPL results in limited access of water to the GDL inlet face and therefore dramatically reducing GDL saturation. The capillary pressure measurement in the catalyst layers within the PEFCs have also been conducted recently²⁷⁵. Kim and Mench²⁷⁶ investigated phase-

change-induced (PCI) water transport through porous fuel cell materials subjected to a temperature gradient. They observed a net flux of water to flow from the hot to the cold side of the catalyst layer (CL) and diffusion medium (DM). They developed Arrhenius functions to describe the net water drag where these functions were dependent on material set, temperature gradient, and average temperature across the materials. The same group studied the water transport in PEFC membranes subjected to a temperature gradient for different polymer membrane types (non-reinforced Nafion®, and reinforced Gore-Select® and Flemion® membranes)²⁷⁷. They observed thermo-osmosis flux in all membranes and measured the water flow direction in the membrane from the cold to hot side. Also, their results showed that the water flux was proportional to temperature gradient, increased with average membrane temperature and membrane type and reinforcement affected the net flux. Malevich et al.²⁷⁸ investigated the influence of the MPL on polarization and electrochemical impedance behavior of PEFC. Based on their data, PEFCs with an MPL showed higher performance and lower variability in the charge-transfer and mass-transfer regions of the polarization curve. They concluded that the presence of a MPL helps reducing the water saturation in the porous transport layer improving the oxygen transport to the cathode catalyst layer. Kim et al.²⁷⁹ utilized electrochemical impedance spectroscopy (EIS) to study the electrochemical losses as a function of the MPL arrangement in PEFC. They observed that the oxygen-mass-transport resistance of cells in the presence of an MPL on the cathode are lower than the values of the cells with MPL on both electrodes and cells without MPL indicating the molar concentration of oxygen at the reaction surface of the catalyst layer is higher. Therefore, they concluded that the MPL

forces the liquid water from the cathode side to the anode side and decreases the liquid saturation in GDL at high current densities. Owejan et al.²⁸⁰ studied the different water transport mechanisms in the gas diffusion layer of PEFCs. They showed that the cathode MPL improves PEFC performance by providing a thermal barrier that keeps the flow in PCI mode away from cathode and prevents back flux of water. More details regarding the current understanding of the water management within PEFC are available in Ref.²¹⁸.

For PEFC systems operating at high current densities such as those found in automotive applications, anode dry-out resulting from excessive electro-osmotic flux of water to the cathode has been shown to be a key limiting phenomenon^{112, 218}. One potential method to engineer the back flux of water to the anode is to utilize an asymmetric anode and cathode micro-porous layer configuration. We have investigated this idea in our previous work^{112, 218} and recently R. Schweiss²⁸¹ explored the advantages of utilizing the asymmetric gas diffusion media within the PEFC via comparing the polarization curves of different asymmetric cell assemblies. Although the previous studies have shown the promise of utilizing the asymmetric gas diffusion media on the performance of PEFCs, the effect of thermal and mass transport resistance specifically in the MPL on overall water balance within the cell is not completely understood, so that the impact of various thermal and mass transport resistance of MPL configurations is not straightforward. The motivation of this work is to understand the range of ability to engineer net water drag through MPL configurations with asymmetric mass and heat transport properties. Another objective is

to further decouple the interaction between thermal and mass transport resistance in water management and net water drag coefficient.

13.2. Experimental

Water transport across the PEFC occurs by several driving modes, including gradients in potential, concentration, temperature and pressure^{112, 218}. These driving modes are shown schematically in Fig. 13-1.

As depicted in Fig. 13-1, the pressure driven flow across the PEM is one of the driving forces for the water transport. The pressure gradient across the PEM occurs as a result of gas phase or capillary pressure differential. Previous studies on the pressure driven water transport across the PEM has shown that the effect of this mode of transport is at least one order of magnitude smaller than of the other transport mechanisms across the PEM for cells under standard conditions.

The other water transport mechanisms across the PEM are diffusion, electro-osmosis and thermos-osmosis. Weber and Newman¹⁸⁰ showed the following equation for the flux of water (N_0^m) through the ion-exchange membrane neglecting an additional thermo-osmosis term.

$$N_0^m = \frac{n_d i^m}{F} - \alpha \nabla \mu_0 \quad (13-1)$$

According to Eq. (13-1), the water flux is driven by electro-osmosis (first term) and gradient in the chemical potential (second term).

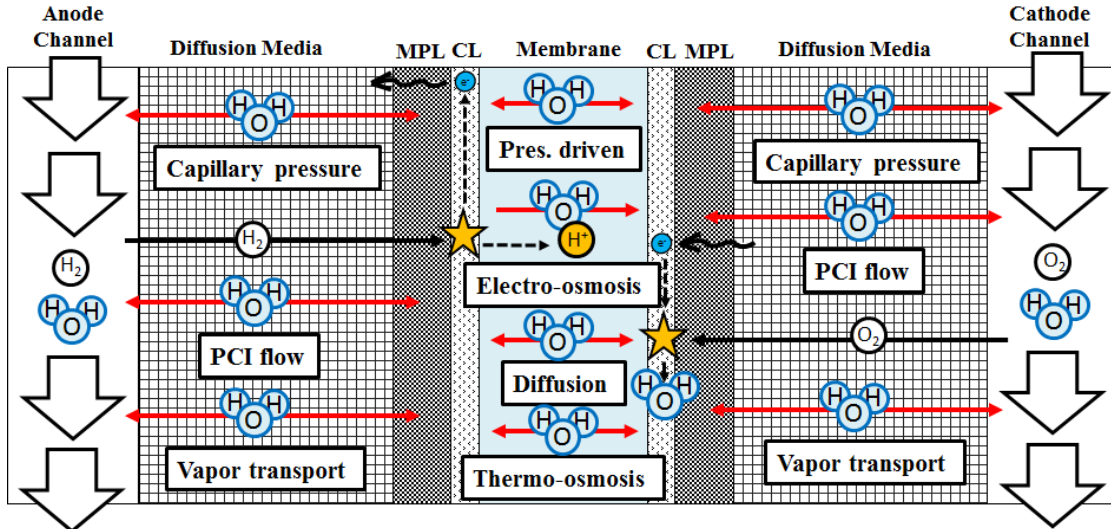


Figure 13-1: Schematic of various modes of water transport in through-plane direction of a PEFC.

Within Eq. (13-1), n_d is the water electro-osmotic drag coefficient, α is the transport coefficient and μ_0 is the chemical potential of water. It has been shown in some previous work that the electro-osmotic drag coefficient is a function of the water content with the ion-exchange membrane and is 1.0 for vapor-equilibrated Nafion® membranes and is 2.5 for liquid-equilibrated condition²⁸². According to Eq. (13-1), the diffusion of water across the PEM is due to the gradient in the activity of water across the membrane. A thorough analysis of water diffusion across Nafion® N115 has been conducted by Motupally et al.²⁸³ where they fit the experimental diffusion data in the form of Fickian diffusion transport. Electro-osmotic drag of water across the PEM has also been investigated in more detail with the purpose of measuring the electro-osmotic drag coefficient. Zawodzinski et al.²⁸² have reported the electro-osmotic drag coefficient of water across Nafion membranes as a function of water content of the membrane and they concluded that for the perfluorosulfonic acid membranes equilibrated with the water vapor, the electro-osmotic

drag coefficient is unity for the wide range of operating conditions. According to Eq. (13-1), the electro-osmosis of water is a function of current density and is always from anode to cathode side. Thermo-osmosis water flux ($N_0^{m|Th}$) across the PEM is expressed in a similar way to mass diffusion flux ²¹⁸.

$$N_0^{m|Th} = -D_T \nabla T \quad (13-2)$$

Within Eq. (13-2), D_T is the thermo-osmotic diffusivity and ∇T is the temperature gradient across the PEM. The direction of the electro-osmosis water transport depends on the membrane properties and is always in the direction of increased total entropy. For Nafion® membranes, it has been shown that the direction of electro-osmosis is from cold to hot side but altogether, the magnitude of electro-osmosis flux is generally smaller than of the diffusion within the normal operational current density range of the PEFC.

The water transport in the gas diffusion medium is due to the pressure gradient (capillary pressure and vapor transport) and PCI flow. In operation, the water near the CL in the gas phase diffuses through the gas diffusion media and condenses at the gas channel or on the land which is cooler ⁸. The resulting phase change induced flow is a particularly dominant transport mechanism at higher temperature regimes where temperature gradients are higher internally. The direction of PCI flow is from hot to cold region, and the magnitude of the PCI flow is non-linearly proportional to the temperature gradient ²¹⁸.

In summary, according to Fig. 13-1, the water distribution throughout the PEFC is a function of different driving forces and determined by the interplay amongst water uptake

(function of water concentration), the electro-osmotic drag (from anode to cathode), the diffusion of water down the activity gradient, and temperature gradient driven flow in the membrane and porous media. The PCI flow is particularly important here since the temperature gradient can be engineered via selection of the GDL thermal properties. The measurement of net water drag coefficient for different material configurations and operating conditions provides a quantitative tool to study the net effect of different water transport mechanism on the water balance within the PEFC.

13.2.1. Experimental Approach

The fuel cell used in this work has a single channel serpentine flow field, an active area of 5cm^2 , and was manufactured by Fuel Cell Technologies (Albuquerque, NM). The anode and cathode reactant flows are operated in a co-flow arrangement. All testing was conducted in galvanostatic mode. The membrane electrode assemblies (MEA) used were manufactured by Ion-Power (New Castle, DE). Membranes were $25.4\ \mu\text{m}$ (dry) thickness with a catalyst loading of $0.3\ \text{mg Pt}\cdot\text{cm}^{-2}$ on both the anode and cathode. The diffusion media (DM) plays an important role in water management within the PEFC and similar to DM, the microporous layer (MPL) also consists of carbon but in the form of black powder and an additional hydrophobic agent like PTFE.

One of the primary functions of the MPL is to protect the catalysts layer from damage by DM fibers, promote suitable contact resistance and it also plays a critical role in water management. In this work, the DM used on both electrodes was provided by W. L. Gore

and Associates (Newark, DE) and was the same in all tests, with a thickness of 165 μ m and uncompressed porosity of 0.705. The DM type in this work was non-woven carbon fiber paper. The free-standing MPLs used were PTFE-carbon black composite web with continuous, highly-uniform (crack-free), and conformable structure. The MPLs were specifically engineered to provide varied thermal and mass transport resistance as summarized in Table 13.1.

The thermal conductivities of the MPL samples were measured using a QTM-500 conductivity meter from Kyoto Electronics Manufacturing, Ltd (Kyoto, Japan). The nominal precision and reproducibility of the instrument were +/- 5% and +/- 3%, respectively.

MPL1 was comprised of approximately 70 w% Ketjenblack EC300J carbon black, 10w% graphite powder, and PTFE binder. MPLs 2 and 3 were each comprised of 70w% proprietary carbon black (the same raw material in both cases), and PTFE binder. The higher conductivity of MPL 2 was achieved by increasing the carbon packing density.

A Scribner Associates Inc. (Southern Pines, NC) fuel cell test station was used to control the gas flow rates and other operating parameters. The test station was subjected to an extensive calibration and characterization process similar to the procedure outlined in Ref. ²⁸⁴ in order to make sure that the humidification bottles and mass flow controllers deliver the targeted dew points and flow rates.

Table 13.1. Micro-Porous Layer (MPL) Properties.

MPL type	Thickness (μm)	Thermal Conductivity (MPL) (W/(m.K))	Thermal Conductivity (DM + MPL) (W/(m.K))	Porosity (-)
GORE MPL1	70	0.13	0.15	0.83
GORE MPL2	45	0.23	0.18	0.62
GORE MPL3	45	0.12	0.17	0.83

For real time net water drag measurement, four calibrated dew point temperature sensors (HMT336) by Vaisala Inc. (Helsinki, Finland) were used to measure the dew point temperatures of the gases entering and exiting the anode and cathode in real-time. The data acquisition system (NI 9207, National Instruments Corporation, Austin, TX) was implemented using LabView to calculate the real-time net water drag coefficient. Tape heaters with multi-zone PID controller (Omega Engineering Inc., Stamford, CT) were utilized to heat the lines entering and exiting the dew point temperature sensors as well as the sensors in order to avoid water condensation. A schematic of the test configuration is shown in Fig. 13-2.

13.2.2. Operating conditions

Baseline operating conditions are summarized in Table 13.2. The fuel cell flow field temperature for all testing was 80°C. Hydrogen (ultra-high purity) was used at the anode, and air (ultra-zero grade) utilized at the cathode. Constant anode and cathode stoichiometries of 4 were used for all the tests described here.

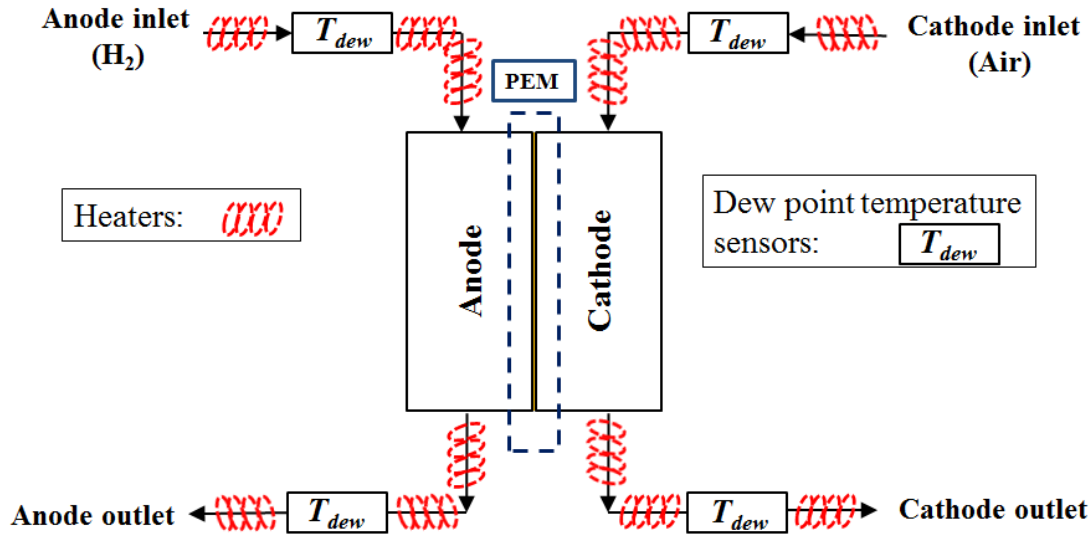


Figure 13-2: Schematic of the PEFC with in-line dew point temperature sensors for real time net water drag measurement.

The anode and cathode inlet relative humidities were both 100% at 80°C for the baseline operating conditions. A back pressure of 50 kPa (gauge pressure) was applied to both anode and cathode for all the tests.

The wide range of operating conditions used are listed in Table 13.3. All operational parameters in these tests are identical to the baseline, with the exception of the relative humidity conditions as shown.

13.2.3. PEFC Configurations

The different combinations of MPLs used listed in Table 13.4. A schematic illustration of the cross section of the symmetric and asymmetric material configurations is shown in Fig. 13-3. The fuel cell in all configurations, consists of a membrane sandwiched between two

gas diffusion electrodes with different MPL properties of anode and cathode side. These assemblies are pressed between two flow fields of serpentine design.

The transport of reactant species occurs by diffusion and convection within the PEFC. However, the local transport to the active catalyst site is normally dominated by diffusion. The diffusion phenomenon involves bulk diffusion in the gas phase, Knudsen diffusion within the small pores followed by the dissolution and diffusion through water and ionomer adjacent to the catalyst site. Adopting the single-phase transport model, the local diffusive flux can be linearized through defining the mass transfer coefficient, k , which is defined as the ratio of overall diffusion coefficient over the diffusion path.

The mass transfer coefficient is of a great interest since it can be obtained from the experimental data of flux and the concentration difference (ΔC) even if the exact geometry or diffusion distance, is not known. The inverse of the mass transfer coefficient is defined as the mass transport resistance, R_M .

$$J = -k\Delta C = -\frac{\Delta C}{R_M} \quad (13-3)$$

The resistance network analogy similar to the analogy has been defined in Ref. ²⁸⁵ can be used to account for the resistance in series, shown schematically in Fig. 13-4. Although the diffusion coefficient and diffusion path length vary from inlet to outlet of the fuel cell and gas channels, an average value for the transport resistance is considered.

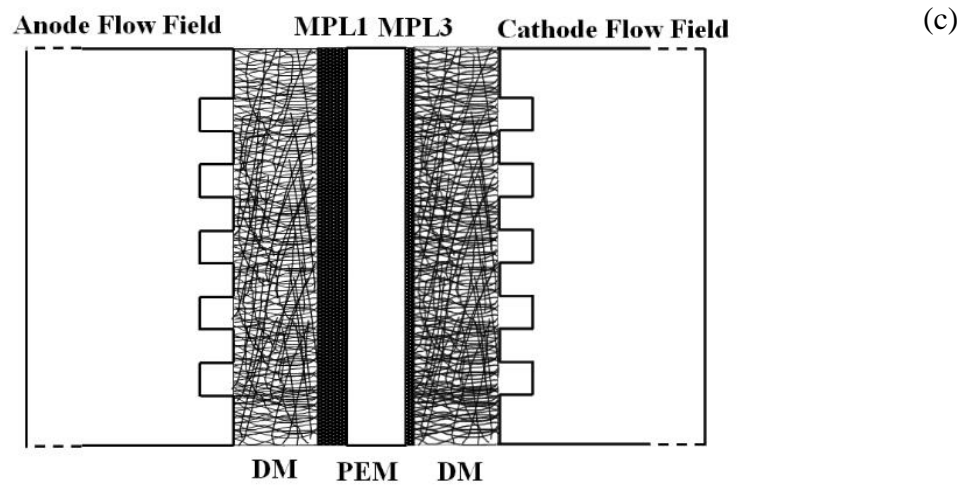
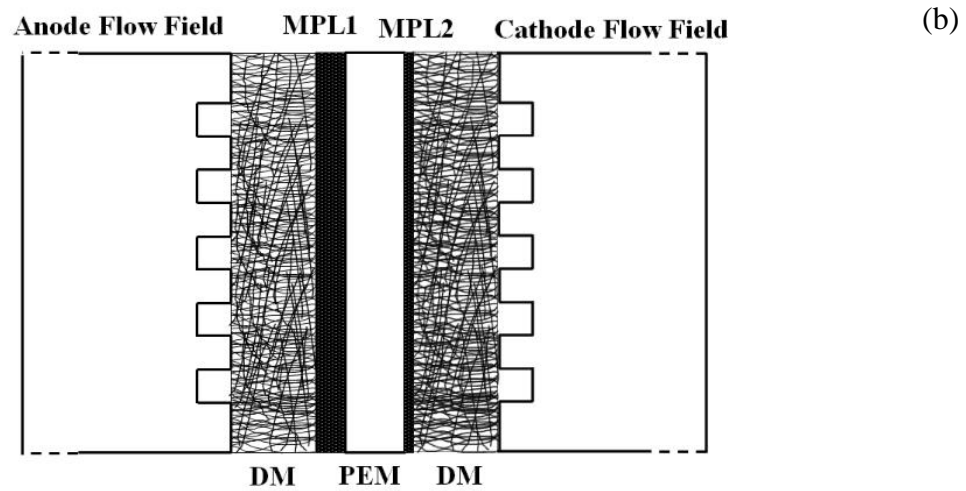
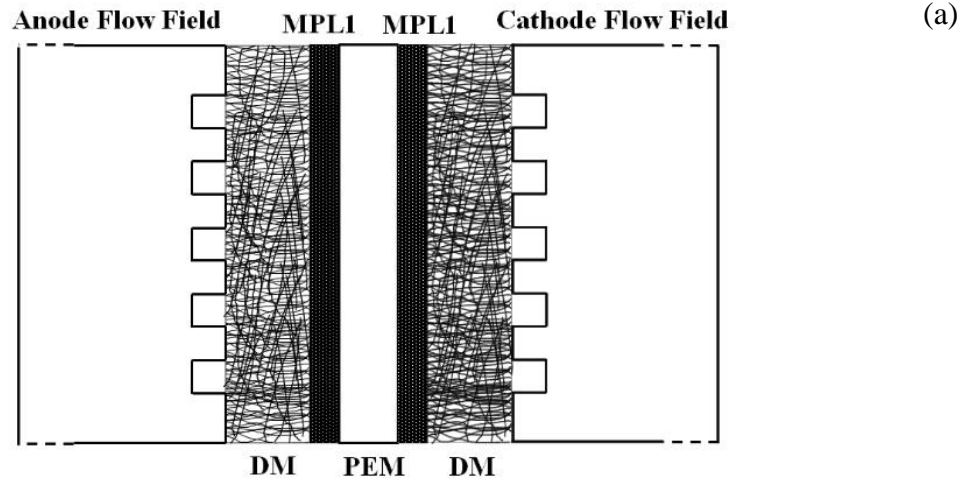


Figure 13-3: Schematic of the: (a) configuration 1 (b) configuration 2 (c) configuration 3 (Not to scale).

In this work, as depicted in Fig. 13-3, the difference among the various configurations is the change in microporous layer. Accordingly, the focus here is the diffusion dominant mode. Accounting for the tortuosity, the empirical Bruggeman formula is applied to approximate the effective diffusion coefficient^{112, 218}. The mass transport resistance ratio for the cathode sides of the different material configurations are calculated using Eq. (13-4). It is important to note that the MPL within the diffusion media is the only component of the resistance-in-series analog that is being changed among the different material configurations and as it was mentioned, we have considered the diffusion as the dominant transport mechanism.

Table 13.2. Baseline operating conditions.

	Anode	Cathode
Gas stoichiometry	4	4
Relative humidity (%)	100	100
Inlet pressure (kPa, absolute)	150	150

Table 13.3. Operating conditions for net water drag tests

	Relative Humidity (Anode/Cathode)
OC 1 (Baseline)	100% / 100%
OC 2 (Dry condition)	50% / 50%
OC 3 (Super Dry condition)	50% / Dry

Table 13.4. PEFC configurations tested

	Anode	Cathode
configuration 1 (symmetric)	MPL1	MPL1
configuration 2 (asymmetric)	MPL1	MPL2
configuration 3 (asymmetric)	MPL1	MPL3

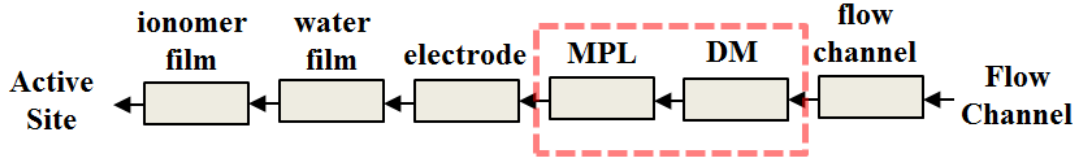


Figure 13-4: Schematic of the resistance-in-series analog for diffusion.

The diffusion media used here includes the macroscopic porous section (it will be referred as DM within the whole paper) and micro-porous layer (MPL).

$$\frac{(R_M)_{asym}}{(R_M)_{sym}} = \frac{(l_{DM} + l_{MPL})_{asym}}{(l_{DM} + l_{MPL})_{sym}} \times \left(\frac{\varepsilon_{sym}}{\varepsilon_{asym}}\right)^{3/2} \quad (13-4)$$

$$\varepsilon = \frac{\varepsilon_{DM}l_{DM} + \varepsilon_{MPL}l_{MPL}}{(l_{DM} + l_{MPL})} \quad (13-5)$$

The same approach is applied to derive the thermal resistance (R_T) ratios for the cathode sides of the different material configurations.

$$\frac{(R_T)_{asym}}{(R_T)_{sym}} = \frac{(l_{DM} + l_{MPL})_{asym}}{(l_{DM} + l_{MPL})_{sym}} \times \left(\frac{k_{sym}}{k_{asym}}\right) \quad (13-6)$$

The mass transport resistance and thermal resistance ratios for the set of materials tested are shown in Table 13-5. Mass and thermal resistance ratios of unity indicate that the transport properties are unchanged versus the symmetric baseline case (configuration 1).

13.2.4. Net Water Drag Calculations

The net water drag (NWD) is defined as the net water transferred across the membrane towards the cathode side, and includes the combined effects of all modes of transport in the membrane.

Table 13.5. Mass transport resistance and thermal resistance ratio.

	$\frac{(R_M)_{sym}}{(R_M)_{asym}}$	$\frac{(R_T)_{sym}}{(R_T)_{asym}}$
configuration 1	1.0	1.0
configuration 2	1.0	0.74
configuration 3	0.9	0.79

Accordingly, considering the conservation of mass on the water in the anode, the net water drag coefficient (C_{NWD}) is defined according to the following:

$$C_{NWD} = \frac{\dot{n}_{H_2O}^{in,an} - \dot{n}_{H_2O}^{out,an}}{\frac{iA}{F}} \quad (13-7)$$

According to Eq. (13-7), a positive net water drag coefficient implies an overall water transport from the anode to the cathode. A negative net water drag coefficient implies a net transport from cathode to the anode.

The dew point sensor at the anode inlet and outlet are used to determine the inlet and outlet water vapor flow rate, respectively, based on the following formulas.

$$\dot{n}_{H_2O}^{in,an} = \psi_{H_2} \frac{iA}{2F} \frac{P_{sat}(T_{dew}^{in,an})}{\left[P - P_{sat}(T_{dew}^{in,an}) \right]} \quad (13-8)$$

$$\dot{n}_{H_2O}^{out,an} = (\psi_{H_2} - 1) \frac{iA}{2F} \frac{P_{sat}(T_{dew}^{out,an})}{\left[P - P_{sat}(T_{dew}^{out,an}) \right]} \quad (13-9)$$

where ψ_{H_2} represents the stoichiometric coefficient of hydrogen. Dew point temperature sensors are also used in the reactant flow lines to calculate the water vapor flow rates in

the inlet and outlet of the cathode. A calculation at steady state was performed to verify that the total mass is conserved and the gauges were functioning properly.

$$\dot{n}_{H_2O}^{in,an} + \dot{n}_{H_2O}^{in,cat} + \dot{n}_{H_2O}^{gen} = \dot{n}_{H_2O}^{out,an} + \dot{n}_{H_2O}^{out,cat} \quad (13-10)$$

Where:

$$\dot{n}_{H_2O}^{in,cathode} = \psi_{O_2} \frac{iA}{4F} \frac{P_{sat}(T_{dew,cathode,in})}{\left[P - P_{sat}(T_{dew,cathode,in}) \right]} \quad (13-11)$$

$$\dot{n}_{H_2O}^{out,cathode} = (\psi_{O_2} - 1) \frac{iA}{4F} \frac{P_{sat}(T_{dew,cathode,out})}{\left[P - P_{sat}(T_{dew,cathode,out}) \right]} \quad (13-12)$$

$$\dot{n}_{H_2O}^{gen} = \frac{iA}{2F} \quad (13-13)$$

Within Eqs (13-11) and (13-12), ψ_{O_2} is the stoichiometric coefficient of the oxygen. The net water drag coefficient from the sensor readings is therefore computed through Eqs. (13-8), (13-9) and (13-7). The water amount at the cathode inlet and outlet, as well as water generation rate, was calculated using Eqs. (13-11), (13-12) and (13-13) respectively. The resulting outcome was then plugged into Eq. (10) in order to verify the mass conservation. For all the data discussed here, the experimental deviation from achieving conservation of mass with Eq. (13-10) was less than 5%, confirming a true steady state was achieved and any storage/depletion of water from measured data was negligible during measurement.

Three different configurations of the cell material assemblies were tested, as described in Table IV. Polarization curves and net water drag coefficients were obtained for different cell assemblies and operating conditions. The tests for each operation conditions and material configurations were repeated 4 times, recording continuous data for 3 minutes at each point and accordingly, the final average data were obtained as presented. The error

bars at each condition were calculated based on the maximum deviation from the average data points. It is important to note that the error bars have been shown for net water drag values only since the error bars associated with the polarization curves were small (maximum error was 4%).

13.3. Mathematical Model

A single-phase, non-isothermal mathematical model has been developed to analyze the computational domain which depicted in Fig. 13-5. The cell dimension and modeling parameters of the individual cell components are listed in Table 13.6, and material properties are summarized in Table 13.7. In general, the single-phase model is not sufficient and accurate enough to capture the mass transport limitations near the limiting current and under super-saturated operating conditions. As a result, the main goal of the simple model developed in this paper is to simulate the temperature distribution within the membrane and porous media of an operating cell for the ohmic dominated regions and under the dry operating conditions. The following assumptions have been adopted within the model:

Model is two-dimensional (in x and y) as shown in Fig. 13-5 and has reached steady state

1. The dominant mode of heat transfer in the fuel cell components is conduction. Convective heat transfer due to flow of reactant gas species in porous media and membrane phase is neglected since the Peclet number is small.
2. Thermal contact resistance is neglected.
3. Material properties are homogeneous but can be anisotropic

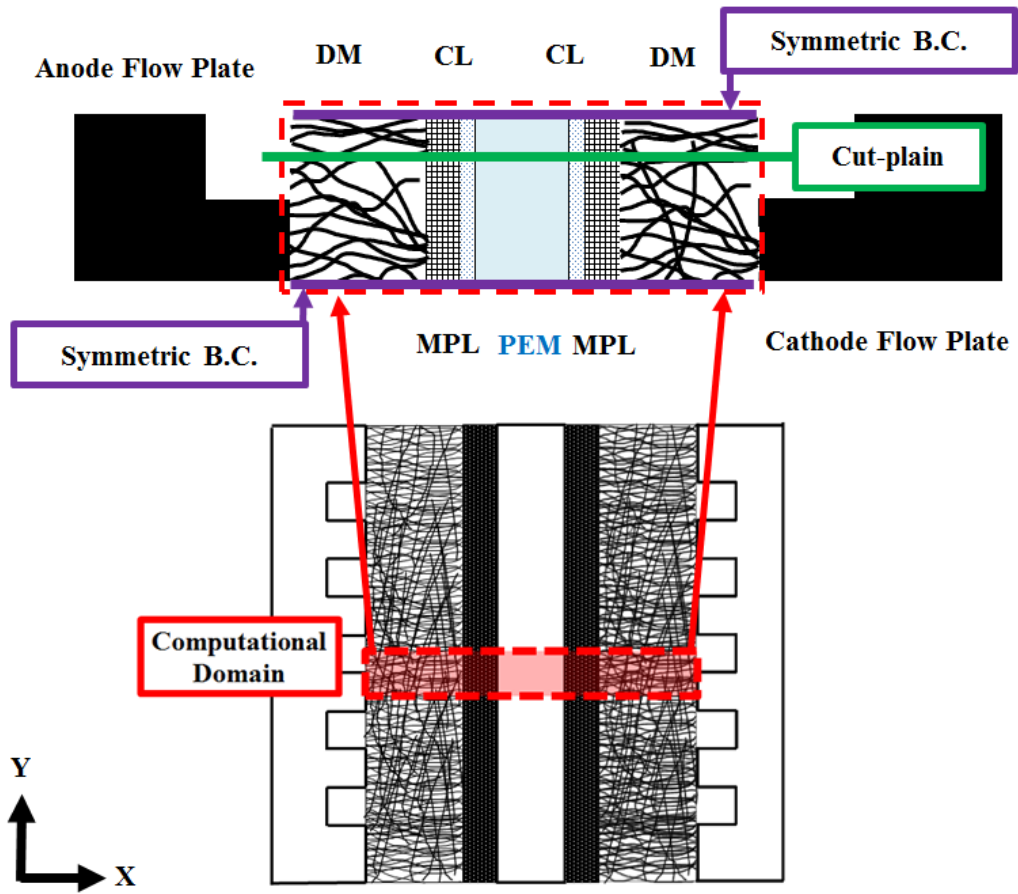


Figure 13-5: Computational Domain.

Table 13.6. Modeling parameters (Ref. ²¹⁸).

Symbol	Parameter	Value	Unit
$\alpha_{a,a}$	Anodic transfer coefficient for hydrogen oxidation reaction	1	-
$\alpha_{a,c}$	Cathodic transfer coefficient for hydrogen oxidation reaction	1	-
$\alpha_{c,c}$	Cathodic transfer coefficient for oxygen reduction reaction	1	-
ΔS_a	Change in entropy for anode	0.104	$J(mol.K)^{-1}$
ΔS_c	Change in entropy for cathode	-326.36	$J(mol.K)^{-1}$
t_{DM}	Anode and Cathode DM thickness	165	μm
t_{MPL}	Anode and Cathode MPL thickness	Table I	-
t_{CL}	Anode and Cathode CL thickness	10 (GORE series MEA)	μm
t_m	Membrane thickness	25.4	μm
ϵ_{DM}	DM uncompressed porosity (Provided by the Manufacturer)	0.705	-
ϵ_{MPL}	MPL porosity	Table I	-
ϵ_{CL}	CL porosity	0.6	-
ϵ_{mc}	Volume fraction of ionomer in CL	0.26	-
$ai_{0,a}$	Anode total exchange current density	1×10^9	Am^{-3}
$ai_{0,c}$	Cathode total exchange current density	1×10^4	Am^{-3}
$D_{H_2,a}$	Diffusivity of hydrogen in the anode gas channel	1.1028×10^{-4}	m^2s^{-1}
$D_{O_2,c}$	Diffusivity of oxygen in the cathode gas channel	3.2348×10^{-5}	m^2s^{-1}
$D_{w,c}$	Diffusivity of water vapor in the cathode gas channel	7.35×10^{-5}	m^2s^{-1}
F	Faraday constant	96485	$C(mol - eq)^{-1}$
R	Universal gas constant	8.314	$J(mol.K)^{-1}$
$C_{H_2,ref}$	Reference hydrogen molar concentration	40	$molm^{-3}$
$C_{O_2,ref}$	Reference oxygen molar concentration	40	$molm^{-3}$

Table 13.7. Material properties expressions (Ref. ²¹⁸).

Symbol	Property	Expression	Unit
λ	Water content	$[0.043 + 17.81a - 39.85a^2 + 36.0a^3, 0 < a \leq 1$ $14 + 1.4(a - 1), 1 < a \leq 3$	-
κ	Ionic conductivity	$(0.5139\lambda - 0.326)\exp[1268(\frac{1}{303} - \frac{1}{T})]$	$S m^{-1}$
n_d	Electro-osmotic drag coefficient	$\max\{1, \frac{2.55\lambda}{22} \exp[\frac{4000}{R}(\frac{1}{T_0} - \frac{1}{T})]\}$	-
a	Water activity	$\frac{y_w P}{P_{sat}(T)}$	-
$P_{sat}(T)$	Saturation pressure	$\log(P_{sat}(T)) = -2.18 + 0.029(T - 273.15)$ $- 9.18 \times 10^{-5}(T - 273.15)^2$ $+ 1.45 \times 10^{-7}(T - 273.15)^3$	atm
D_w	Diffusivity of water in membrane	$[3.1 \times 10^{-7}\lambda(e^{0.28\lambda} - 1)\exp[\frac{-2436}{T}], 0 < \lambda \leq 3$ $4.17 \times 10^{-8}\lambda(1 + 161e^{-\lambda})\exp[\frac{-2436}{T}], 3 \leq \lambda < 17$	$m^2 s^{-1}$
D_i	Diffusivity of species in gas phase	$D_0 (\frac{T}{T_0})^{\frac{3}{2}} (\frac{P_0}{P})$	$m^2 s^{-1}$

13.3.1. Mathematical Model Development

An in-house simple single-phase model has developed, and the coupled species, energy and charge transport equations have been solved. These equations can be cast in the more general form of Eq. (13-14) for the 2-D domain. Equation (13-14) has been used for modeling species transport, energy transport and charge transport and the description of various variables are provided in Table 13.8.

$$\Pi_i^x \frac{\partial^2 \theta_i}{\partial x^2} + \Pi_i^y \frac{\partial^2 \theta_i}{\partial y^2} = -\omega_i \quad (13-14)$$

Table VIII includes the modeling parameters for the conservation equations depicted in Eq. (13-14) where for the energy transport, the conduction is assumed to be the dominant heat transfer mode.

$$\eta = \varphi_s - \varphi_e - U_{OC} \quad (13-15)$$

Table 13.8. Model parameters.

	Π_i^x	Π_i^y	Θ_i	ω_i
Species transport	$D_i^{eff} = \varepsilon^{1.5} D_i$	$D_i^{eff} = \varepsilon^{1.5} D_i$	Anode: H_2, H_2O Cathode: $O_2, N_2,$	$C.L. (H_2, O_2): \omega_i = -\frac{J_{gen}}{nF}$ $C.L. (H_2O): \omega_i = -\frac{J_{gen}}{nF} - \nabla \cdot \left(\frac{n_d}{F} i_e\right)$
Energy transport	k_x	k_y	T	$C.L.: \omega_i = J_{gen} \left(\eta + \frac{T\Delta S}{nF}\right) + \frac{i_e^2}{\kappa} + \frac{i_s^2}{\sigma}$ $PEM: \omega_i = \frac{i_e^2}{\kappa}$ $Porous Media: \omega_i = \frac{i_s^2}{\sigma}$
Charge transport (Protons)	κ_x	κ_y	φ_e	Anode C.L.: $\omega_i = a_{i_{0,a}}^{ref} \left(\frac{C_{H_2}}{C_{H_2,ref}}\right)^{\frac{1}{2}} \left(\frac{\alpha_a + \alpha_c}{RT} F\eta\right)$ Cathode C.L.: $\omega_i = -a_{i_{0,c}}^{ref} \left(\frac{C_{O_2}}{C_{O_2,ref}}\right) \exp\left(\frac{-\alpha_c}{RT} F\eta\right)$
Charge transport (Electrons)	$-\sigma_x$	$-\sigma_y$	φ_s	Anode C.L.: $\omega_i = a_{i_{0,a}}^{ref} \left(\frac{C_{H_2}}{C_{H_2,ref}}\right)^{\frac{1}{2}} \left(\frac{\alpha_a + \alpha_c}{RT} F\eta\right)$ Cathode C.L.: $\omega_i = -a_{i_{0,c}}^{ref} \left(\frac{C_{O_2}}{C_{O_2,ref}}\right) \exp\left(\frac{-\alpha_c}{RT} F\eta\right)$

where η represents overpotential, φ_s represents solid phase potential, φ_e is the electrolyte phase potential and U_{OC} is the open circuit potential, which is zero on anode side. For the cathode side of a low temperature fuel cell, U_{OC} can be approximated as the following ²¹⁸.

$$U_{OC} = 1.23 - 9.0 \times 10^{-4}(T - 298.15) \quad (13-16)$$

The effective proton conductivity of the anode and the cathode catalyst layers is described using Bruggeman correlation:

$$\kappa^{eff} = \varepsilon_{mc}^{1.5} \kappa \quad (13-17)$$

Where ε_{mc} is the volume fraction of ionomer in the CL and κ is proton conductivity as a function of temperature and water content.

13.3.2. Boundary conditions

In this work we have adopted the single domain approach and as a result, the boundary conditions are only required at the external surfaces of the computational domain. According to the computational domain shown in Fig. 13-5, due to symmetry, the boundary conditions are only specified in the through-plane direction and the rest of the boundaries are treated as symmetric. At the anode/cathode channel inlet, the species concentrations are determined by the inlet pressure and humidity. For the thermal boundary conditions, a constant temperature is applied to the anode and cathode land boundary consistent with a liquid cooled system. At the anode/cathode channel inlet, convective boundary conditions are applied for energy equation with Nusselt number calculated from the internal laminar flow.

13.4. Results and Discussion

13.4.1. Numerical Results

The computational model was used to perform a parametric study of the effect of MPL properties of cathode side on the temperature distribution within the operando PEFC at dry operating conditions. For the simulations, conditions were chosen so that the material configurations were not subjected to extreme dry-out or flooding and therefore, the model assumptions mentioned earlier, will stay true for these conditions. Also, since the main objective is to compare the temperature distribution among the different configurations, neglecting the contact resistance in the modeling framework does not affect the validity of

such a comparison. The material configurations 1, 2 and 3 were modeled at two different cases of operation at 0.75V and 0.6V. In order to compare the through-plane temperature distributions among the different configurations, the predicted through-plane temperature distribution have been plotted in the following figure for the cut-plane shown within Fig. 13-6. The simulated through-plane temperature distribution profiles are shown in Fig. 13-6. The model simulation is generally in good agreement with the reported simulation data from other models ²⁸⁶.

13.4.2. Experimental Results

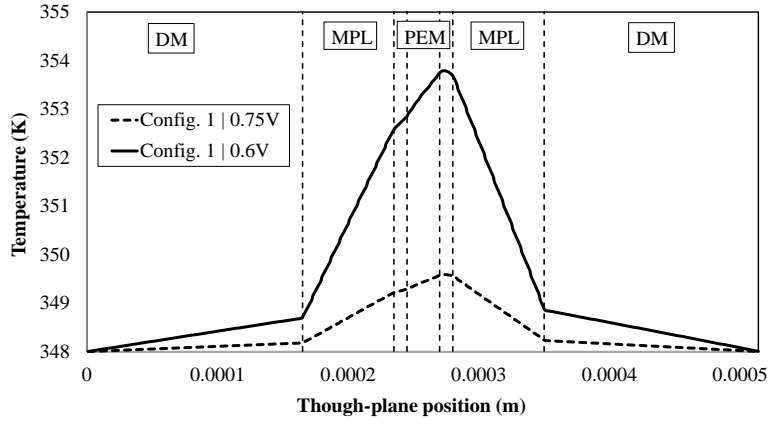
Figure 13-7 shows the performance curves and net water drag coefficients for material configuration 1. Comparing wet and dry operating condition (Fig. 7(a)), the inflection point shifts from current density of 0.8 A.cm⁻² for wet operating condition to 1.1 A.cm⁻² for dry operating condition, confirming significant mass transport improvement. The super dry operating condition exhibits the inflection point of 0.8 A.cm⁻² but with a considerable increase in ohmic losses due to the severe decrease in water content. Figure 13-7(b) shows the net water drag coefficient measured for material configuration 1 for different operating conditions. For wet operating conditions, the net water drag coefficient is +0.0242 (molH₂O/molH⁺) at current density of 0.2 A.cm⁻² and decreases to -0.1125 (molH₂O/molH⁺) at current density of 1.2 A.cm⁻².

Therefore, for the range of current densities tested, the net flux of water increases towards the anode side with increased current density. For dry operating conditions, the net water

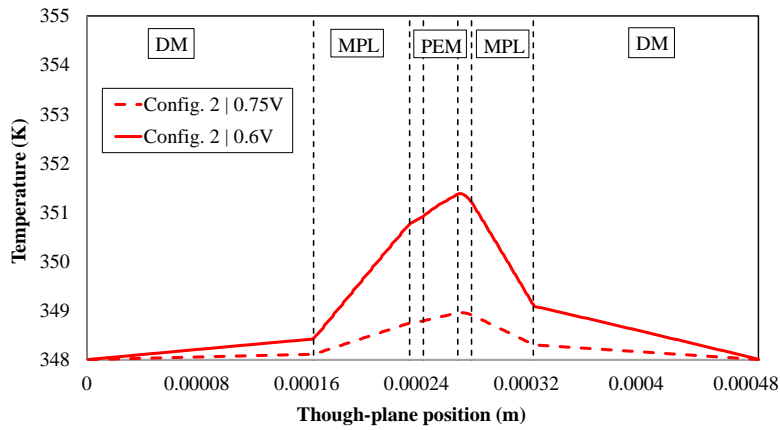
drag coefficient is -0.005 ($\text{molH}_2\text{O}/\text{molH}^+$) at a current density of 0.2 A.cm^{-2} and increases to $+0.0676$ ($\text{molH}_2\text{O}/\text{molH}^+$) at a current density of 1.2 A.cm^{-2} .

The trend of net water drag coefficients for this case confirms the higher net flux of water towards cathode with increased current. For super dry operating conditions, the net water drag coefficient is $+0.1679$ ($\text{molH}_2\text{O}/\text{molH}^+$) at current density of 0.2 A.cm^{-2} and increases to $+0.1840$ ($\text{molH}_2\text{O}/\text{molH}^+$) at current density of 0.9 A.cm^{-2} . Similar to dry operating conditions, the values of net water drag coefficients are all positive, confirming the net water drag from anode to cathode side with considerable increase in the amount of water flux compared to dry operating conditions towards the cathode side. Figure 13-8 shows the performance curves and net water drag coefficients for material configuration 2 in which the thermal resistance of the cathode side has been decreased. For this material configuration, the polarization curve (Fig. 13-8(a)) exhibit similar dependencies on the operating conditions as observed for symmetric configuration.

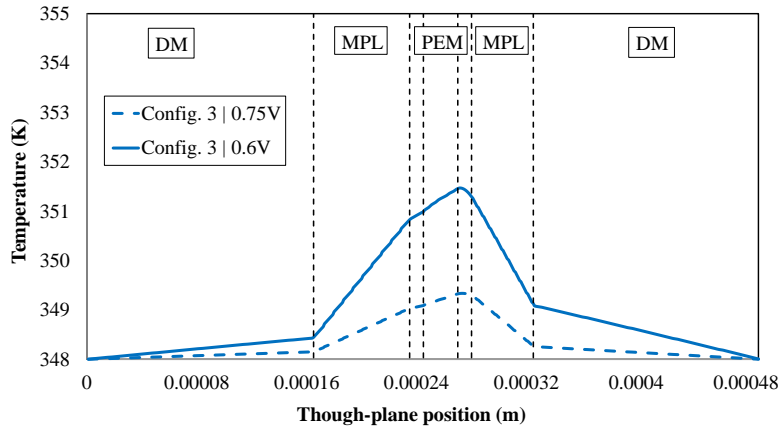
Fig. 13-8(b) demonstrates the net water drag coefficient. For wet operating conditions, increased current increases the water flux towards the cathode side, similarly to the symmetric material configuration 1. For dry operating conditions, the net water flux is towards cathode side at low current densities but at current density of $0.68 \text{ (A.cm}^{-2}\text{)}$ the direction of water flux changes and increases towards anode side with increased current. This behavior is different than the trend already shown for symmetric material configuration indicating the ability to manipulate the net water flux direction using engineered MPL asymmetric architecture.



(a)

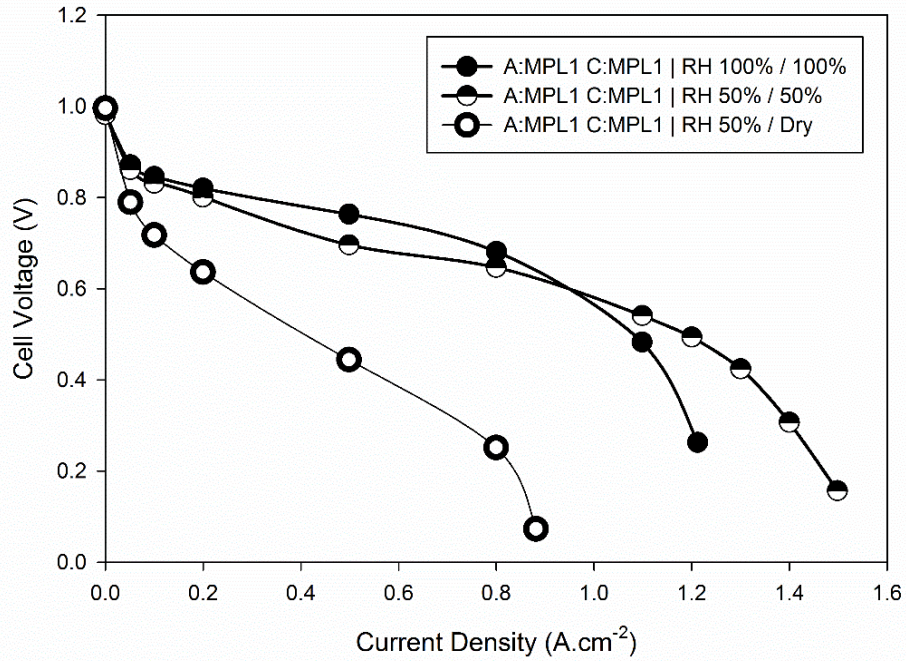


(b)

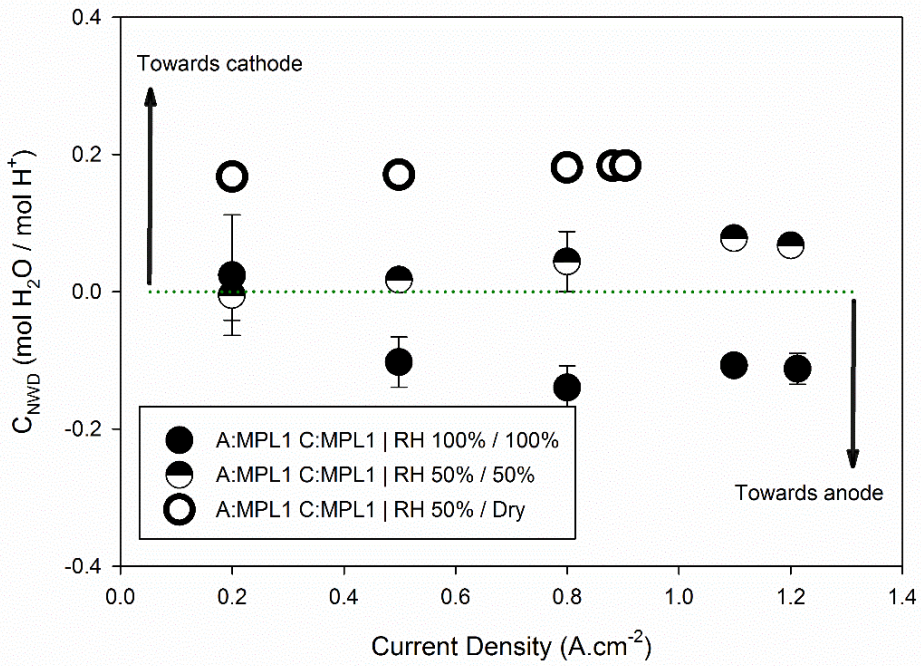


(c)

Figure 13-6: Predicted temperature distribution in through plane direction for the computational domain; (a) configuration 1 (b) configuration 2 (c) configuration 3.



(a)

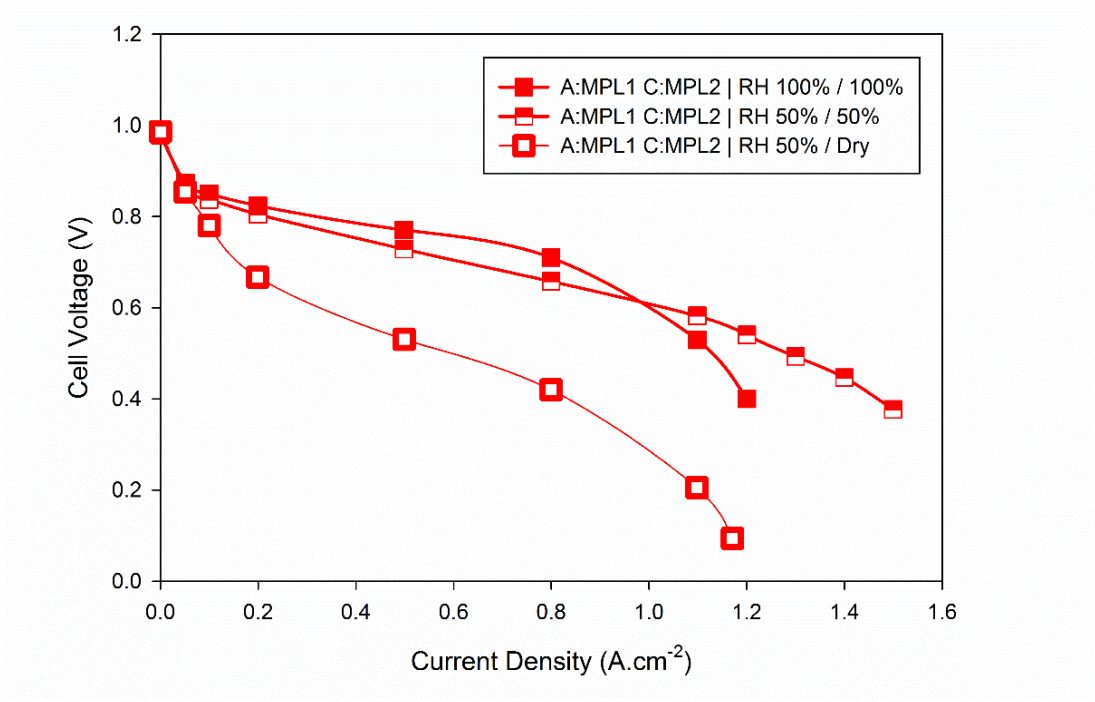


(b)

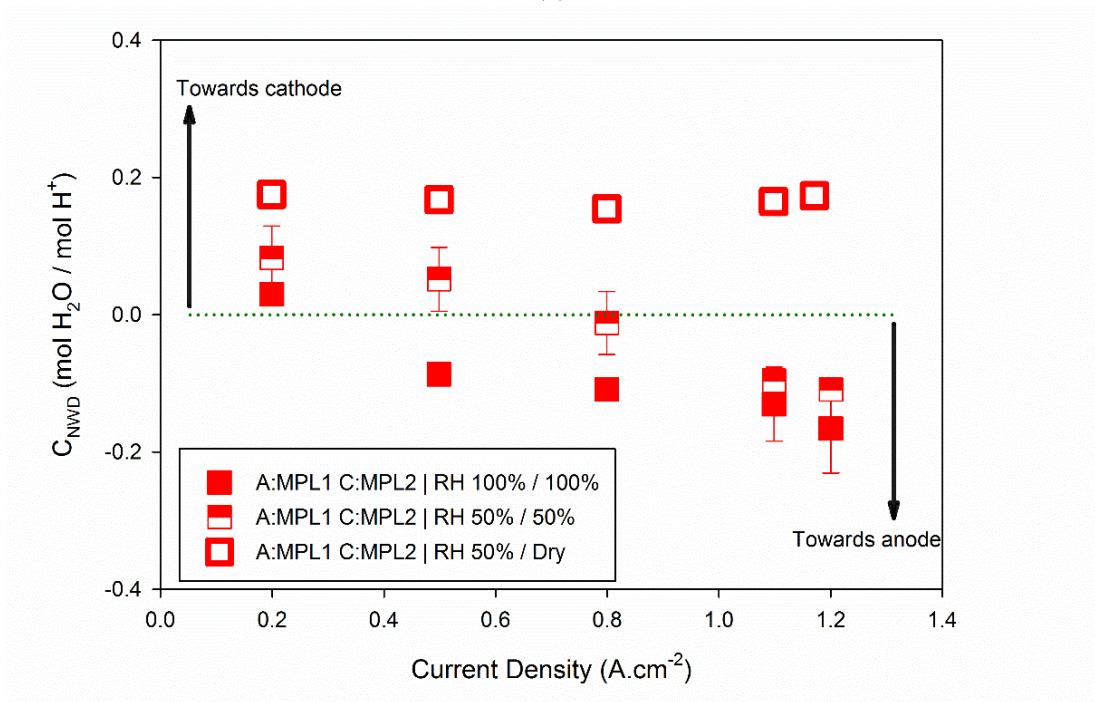
Figure 13-7: Material configuration 1 operating at different operating conditions (a) Performance curve (b) Net water drag coefficient.

For super dry operating conditions, the net water drag coefficient is relatively constant +0.1753 (molH₂O/molH⁺) at all current density tested. All the values of net water drag coefficient are positive for super dry operating conditions and therefore, for all the current densities tested, the flux of water is from anode to cathode side exhibiting the similar trend as symmetric material configuration. Figure 13-9 shows the performance curves and net water drag coefficients for material configuration 3 in which the thermal and mass transport resistance of cathode side is decreased. The dependency of polarization curves to operating conditions is similar to the behavior observed for material configuration 2 but with decreased mass transport overpotential at high current density regimes for wet conditions. In this case, for wet operating conditions, the inflection point is at the current density of 1.1 A.cm⁻² indicating improved mass transport properties.

Fig. 13-9(b) demonstrates the net water drag coefficient. For wet operating conditions, the net water drag coefficient is -0.0939 (molH₂O/molH⁺) at current density of 0.2 A.cm⁻² and increases to -0.0407 (molH₂O/molH⁺) at current density of 1.2 A.cm⁻². Therefore, increased current density decreases the water flux towards the anode side. For the range of current densities tested, however, the net water flux is still towards the anode side. For dry operating conditions, a similar trend to the material configuration 2 was observed. The direction of net water flux is towards cathode side at low current density regimes and the magnitude of the flux decreases via increased current density and the direction of water flux flips to anode side at current density of 0.44 A.cm⁻².



(a)



(b)

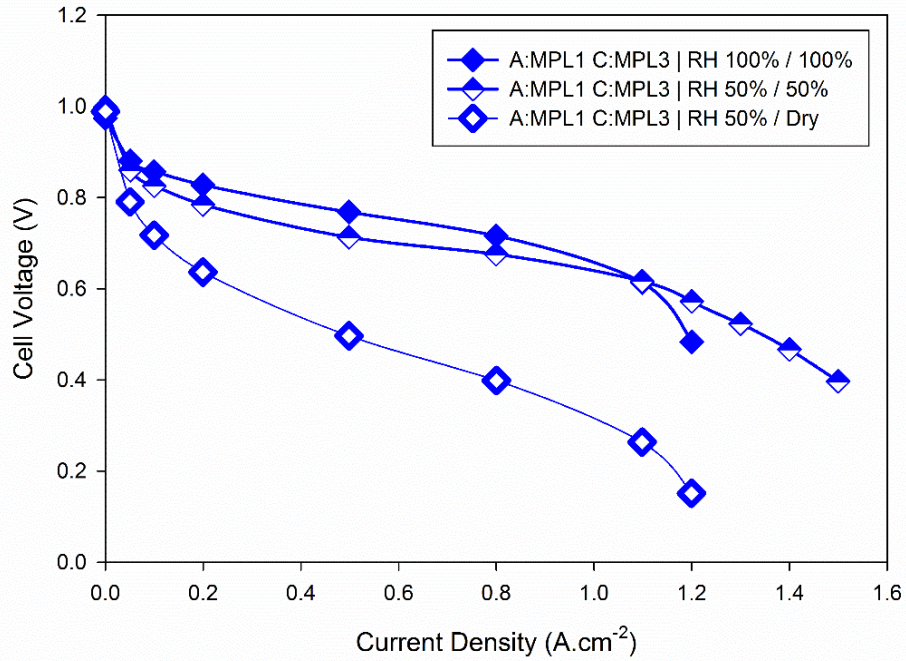
Figure 13-8: Material configuration 2 operating at different operating conditions
 (a) Performance curve (b) Net water drag coefficient.

For super dry operating condition, the net water drag coefficient is again relatively constant in the range of around +0.16 to +0.17. All the values of net water drag coefficient are positive for super dry operating conditions and therefore, for the range of current densities tested, the flux of water is from anode to cathode side exhibiting the similar trend observed at material configuration 1 and 2, reflecting the super dry conditions.

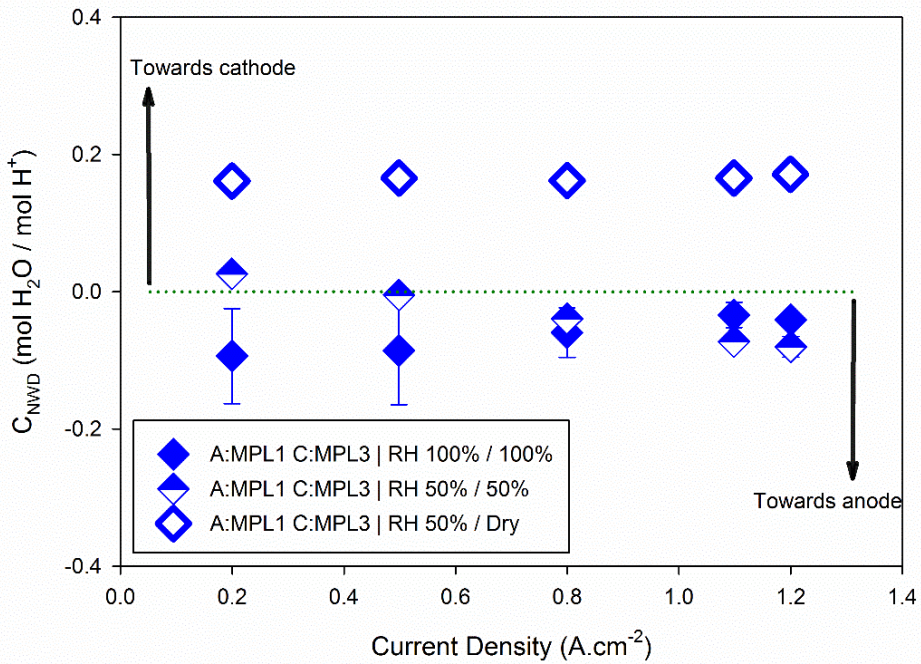
Figure 13-10(a) shows the comparison of performance curves for different material configurations operating at baseline conditions. The cell temperature is maintained at 80°C and the anode and cathode inlet gas streams are humidified to 100%. Both anode and cathode sides are pressurized to 150 kPa absolute at the outlet, so the pressure gradient across the membrane can be considered negligible.

The performance curves at low and medium current density are characterized with a kinetic drop at very low current densities and an ohmic region characterized by a constant slope at medium current density. The deviation from linear behavior at high current density regimes is the characteristic of dominant mass transport overpotential and at this regime, the mass transport of reactants to catalyst layers decreases the cell performance.

According to Fig. 13-10(a), the asymmetric material configuration decreases the mass transport overpotential (current densities above 0.8 A.cm⁻²) and specifically material configuration 3 with lower mass transport resistance, exhibits better mass transport behavior among other cases.



(a)

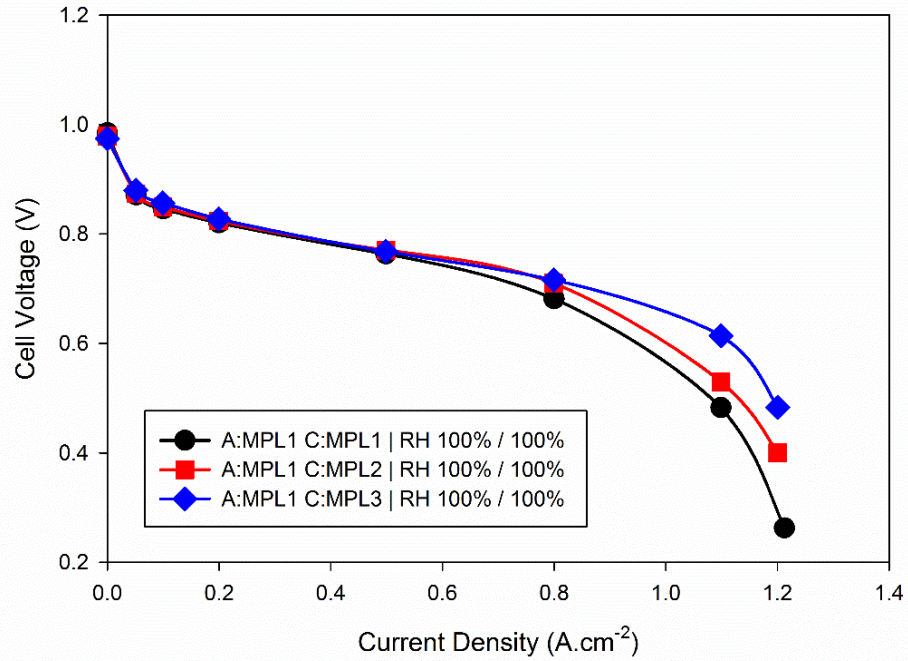


(b)

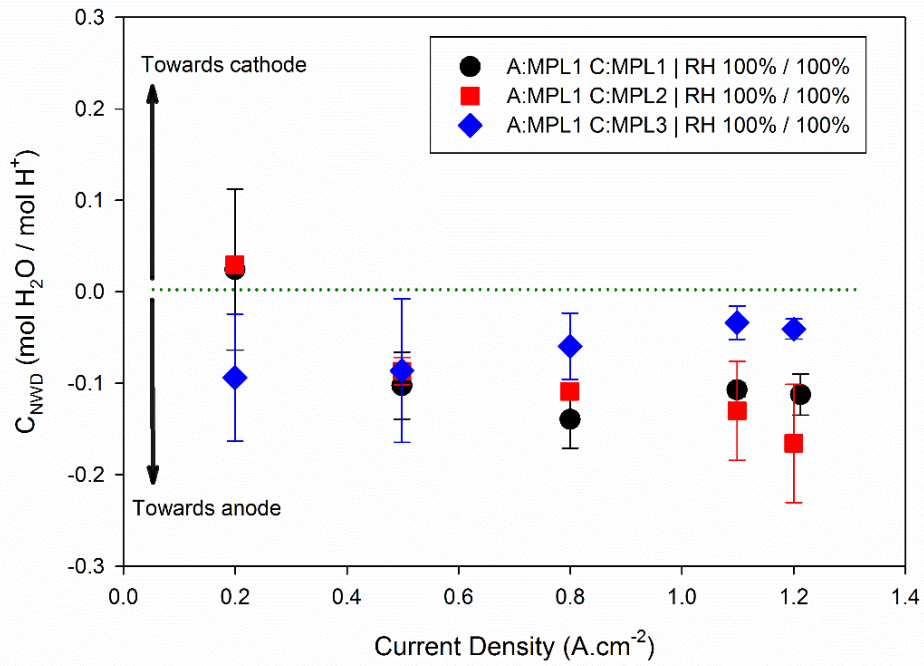
Figure 13-9: Material configuration 3 operating at different operating conditions
 (a) Performance curve (b) Net water drag coefficient.

Figure 13-10(b) shows the net water drag coefficients calculated for these baseline condition tests. For the symmetric case at baseline condition the net water drag coefficients starts from +0.0242 (molH₂O/molH⁺) at current density of 0.2 A.cm⁻² and decreases to -0.1125 (molH₂O/molH⁺) at current density of 1.2 A.cm⁻². Based on the results, the net flux of water is dominated by the back diffusion of water towards the anode side. A similar trend in net water drag coefficient is observed for asymmetric configuration 2 compared to the symmetric case, where the net water drag coefficient is +0.0297 (molH₂O/molH⁺) at current density of 0.2 A.cm⁻² and decreases to -0.1658 (molH₂O/molH⁺) at current density of 1.2 A.cm⁻². For this configuration as well, increasing the current density increases the back flux of water towards anode.

For a diffusive dominated system, changing the thermal resistance ratio across the cell does not change the trend of water flux. In contrast to latter cases, the net water drag coefficient exhibits a totally different trend for asymmetric configuration 3. The net water drag coefficient is -0.0939 (molH₂O/molH⁺) at current density of 0.2 A.cm⁻² and increases to -0.0407 (molH₂O/molH⁺) at current density of 1.2 A.cm⁻². Although the net water drag coefficients are still negative, the trend of the curve is clearly changed compared to the symmetric case. In this configuration, and under wet conditions, the mass transport properties of the MPL play a significant role in the overall water management. In this regime, the MPL works primarily as a barrier for the liquid water. As a result, decreased mass transport resistance in the cathode side decreases the back flux of water towards anode side.



(a)



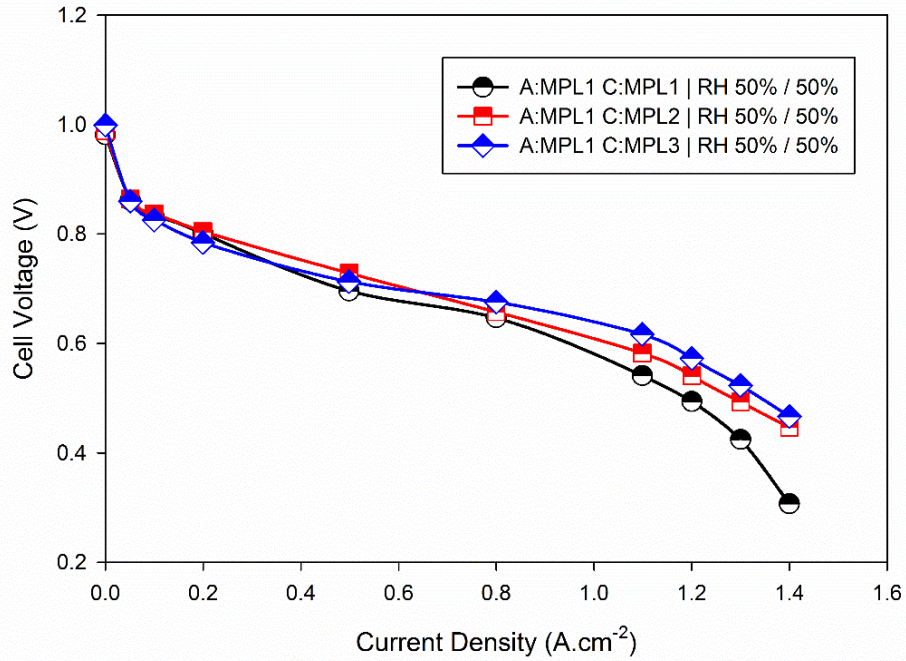
(b)

Figure 13-10: Comparison of various material configuration at baseline conditions
 (a) Performance curve (b) Net water drag coefficient.

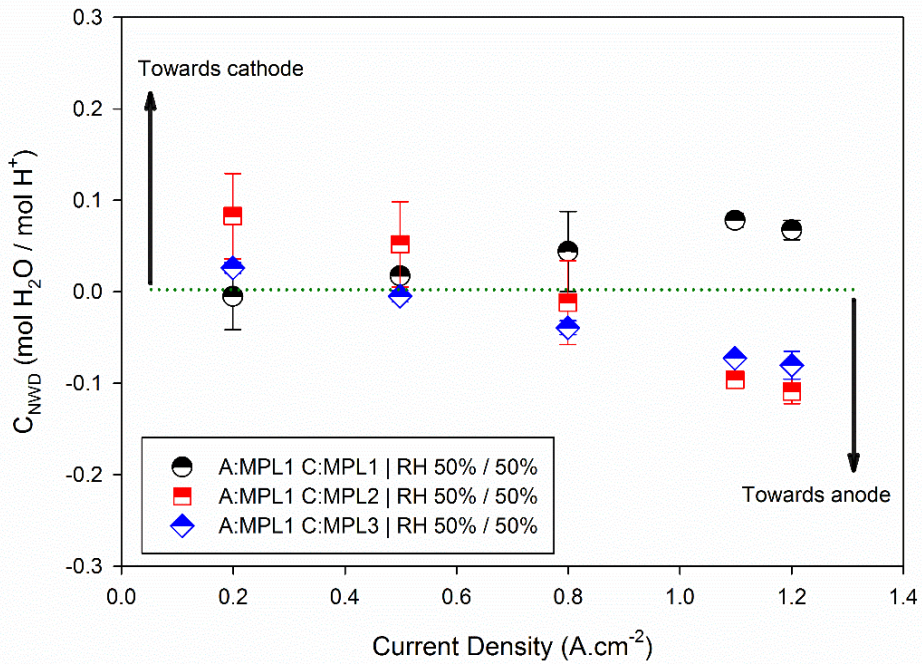
In summary, when the cell is operating at wet operating conditions, the mass transport resistance is a more significant factor in net water drag compared to thermal resistance. For wet operating conditions, the material configuration with decreased mass transport ratio of the cathode side is favored since configuration 3 allows for higher water flux removal from the cathode catalyst layer and a lower back flux of water towards the anode side. Figure 13-11(a) shows the comparison of polarization curves for different material configurations operating at relatively drier conditions. The cell temperature is maintained at 80°C and the anode and cathode inlet gas streams are humidified to 50%. Both anode and cathode sides were pressurized to 150 kPa absolute at the inlet. According to Fig. 11(a), the utilization of asymmetric material configuration with reduced thermal and mass transport resistance of the cathode side clearly decreases the mass transport losses at current densities greater than 0.8 A.cm⁻². Figure 13-11(b) shows the variation of net water drag coefficient for different material configurations operating at dry condition. According to Fig. 13-11(b), the net water drag coefficient for the symmetric configuration increases with increased current and goes from -0.005 (molH₂O/molH⁺) at 0.2 A.cm⁻² to +0.0676 (molH₂O/molH⁺) at 1.2 A.cm⁻².

This observation is consistent with previously observed behavior for symmetric cells operating at dry conditions, where the dominant water transport regime is electro-osmosis towards the cathode, evaporation and removal through the free stream ²¹. In comparison to the symmetric case, however, the asymmetric configuration 2 completely changes the trend of water transport. The net water drag is +0.0827 (molH₂O/molH⁺) at 0.2 A.cm⁻² and

decreases to -0.11 ($\text{molH}_2\text{O}/\text{molH}^+$) at $1.2 \text{ A}\cdot\text{cm}^{-2}$. A similar trend is observed for material configuration 3 where the net water drag is $+0.0262$ ($\text{molH}_2\text{O}/\text{molH}^+$) at $0.2 \text{ A}\cdot\text{cm}^{-2}$ and decreases to -0.08 ($\text{molH}_2\text{O}/\text{molH}^+$) at $1.2 \text{ A}\cdot\text{cm}^{-2}$. It is important to compare the net water drag coefficient behavior as a function of current density with the simulated temperature distribution data shown earlier (Fig. 13-6 and 13-7). The utilization of asymmetric configuration of cathode versus anode with decreased thermal resistance decreases the phase-changed induced flow (PCI) within the gas diffusion media of the cathode side at high current densities, when a significant through-plane temperature gradient is developed. The reason for decreased PCI flow is the decrease in temperature gradient across the diffusion media, since the magnitude of PCI flow is a function (Arrhenius behavior¹⁸) of temperature gradient across the diffusion media and the PCI flow is from cathode catalyst layer towards lands and water condensation appears underneath lands. Decreased PCI flow increases the back diffusion of water compared to electro-osmosis and results in increased net back flux of water towards anode. This behavior is clearly shown in Fig. 13-11(b), where the magnitude of net water flux becomes negative for high current densities regimes of configuration 2 and configuration 3. In summary, when the cell operating at relatively dry conditions, the thermal resistance is a more critical parameter compared to mass transport resistance, since the PCI flow plays an important role in the overall water management. The PCI flow out of the cathode decreases at high current density regimes for dry operating conditions if an MPL with lower thermal resistance is utilized in cathode side (configuration 2 and 3) and the decreased PCI flow increases the back flux of water towards the anode side.



(a)

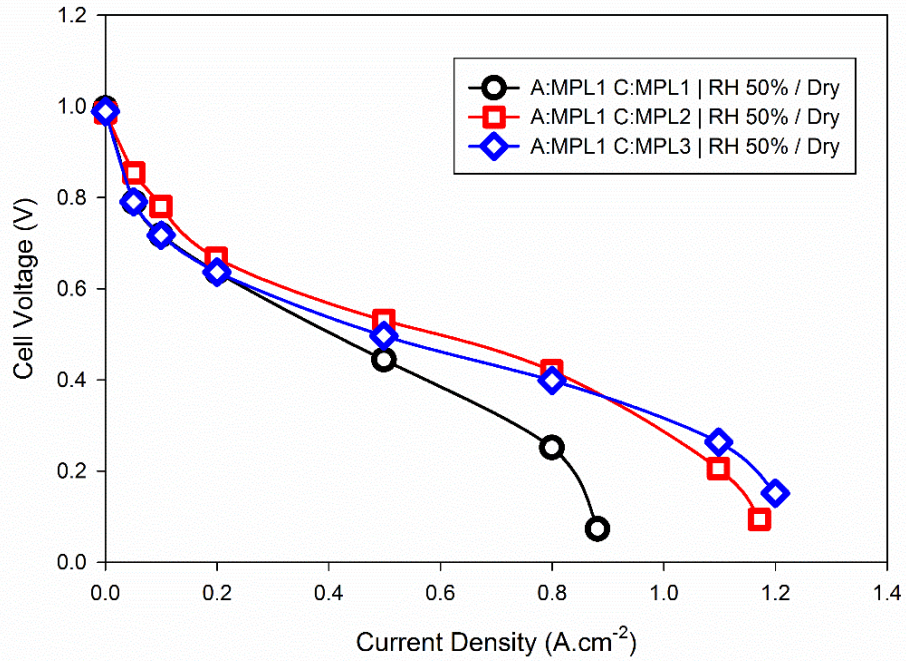


(b)

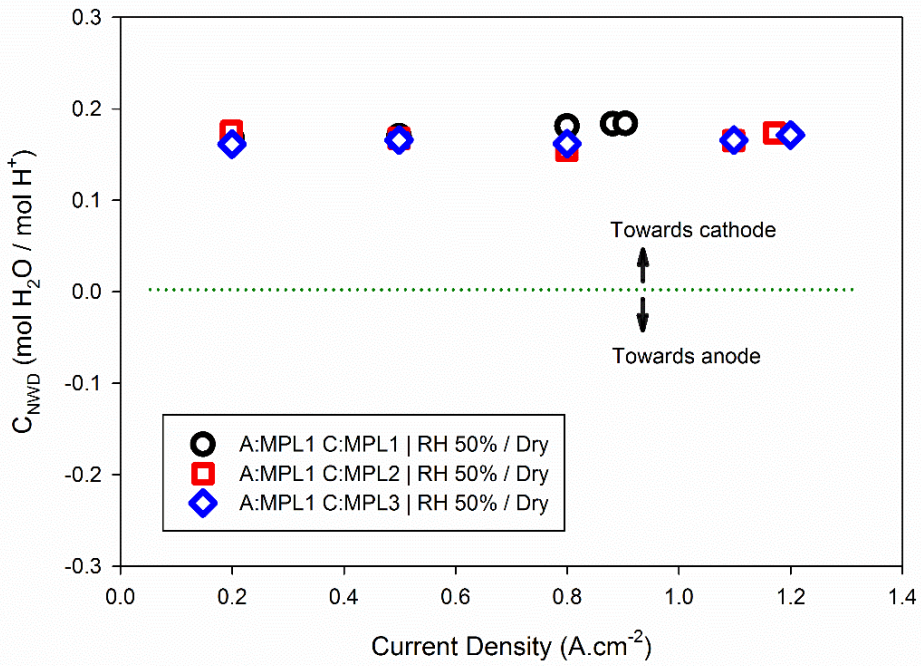
Figure 13-11: Comparison of various material configuration at dry operating conditions. (a) Performance curve (b) Net water drag coefficient

Figure 13-12(a) shows the comparison of performance curves for different material configurations operating at super dry conditions. The cell temperature is maintained at 80°C while the hydrogen gas is humidified to 50% and the cathode gas stream was not humidified. Both anode and cathode sides were pressurized to 150 kPa absolute at the inlet. In this operating condition, the ohmic losses associated with the dehydration of the membrane is the dominant losses. As it is shown, the utilization of asymmetric MPL configuration with the reduced thermal resistance of the anode side significantly reduces the ohmic overpotential and improves the cell performance. Figure 13-12(b) shows the net water drag coefficients for different material configurations at super dry operating conditions. In contrast to baseline and dry operating conditions, the water drag coefficients for all the cases are positive, confirming the dominant water flux from the anode to the cathode side via electro-osmosis drag. Overall, the asymmetric MPL configuration with different mass and thermal transport resistance of cathode versus anode can be utilized to engineer the water drag coefficient (and as a result the water transport behavior) at different operating conditions.

When the cell is operating in wet conditions, the utilization of an MPL with lower mass transport resistance of cathode versus anode side decreases the flooding, at high current density regimes. However, for dry and super dry operating conditions, the MPL with lower thermal resistance of cathode versus anode side is favored since it reduces the water removal via PCI flow increasing the back flux of water.



(a)



(b)

Figure 13-12: Comparison of various material configuration at super dry operating conditions (a) Performance curve (b) Net water drag coefficient.

13.5. Conclusions

In this chapter, net water drag coefficients in operating PEFCs were measured for different configurations of cell materials with varied thermal and mass transport resistance values in the microporous layer. The net water drag coefficient was measured in the range of -0.17 to +0.18 depending on the operating conditions and material configurations. For the material configurations tested, it was shown that for the systems operating at dry conditions, thermal properties of the MPL are more significant than the mass transport resistance in terms of engineering net water drag coefficient. However, for PEFCs operating under wet conditions, the mass transport properties are more significant. In addition, it was shown that the net water drag coefficients for symmetric anode and cathode MPLs are a strong function of operating conditions. Asymmetric configuration of MPLs can be used to improve the cell performance for high current. It was also shown that the material configuration with lower thermal resistance at the cathode side is capable of changing the overall net water drag coefficient trend with current for dry operating conditions at high current densities, which can be used to prevent dry-out at high current densities. In order to better understand the underlying reason for improved water balance management via using asymmetric material configuration, a mathematical model developed and the temperature distribution across the cell was simulated for different material configurations and operating conditions. According to the model prediction, the phase-change-induced flow dominates at dry operating conditions and therefore, reduced phase-change-induced flow via asymmetric material configuration increases the back flux of water and results in improved performance. Also, it was shown that for extremely dry

operating conditions the utilization of asymmetric material configuration is capable of decreasing the ohmic overpotential at high current density regimes but, does not affect the overall trend of net water drag coefficient. As a result, the net water drag coefficient remains relatively constant at super dry operating conditions independent of various material configurations. The results of this study can be used for engineering water balance in PEFCs as well as serve as bench mark data for computational validation studies.

13.6. Acknowledgments

Authors thank for the financial support for this work from the Department of Energy (DOE), project number: DE-FC36-086018052 "MANUFACTURING OF LOW-COST, DURABLE MEMBRANE ELECTRODE ASSEMBLIES ENGINEERED FOR RAPID CONDITIONING".

Yasser Ashraf Gandomi would also like to acknowledge University of Tennessee for providing Chancellors Graduate Fellowship support. The authors also thank W. L. Gore for providing the materials and Drs. A. K. Srouji and M. P. Manahan for their useful discussions.

13.7. Nomenclature

OC	Operating condition
MPL	Micro-Porous layer
DM	Diffusion media
k	Thermal conductivity ($\text{W} \cdot (\text{mK})^{-1}$)
T	Temperature (K)
l	Length (m)
i	Current density ($\text{A} \cdot \text{cm}^{-2}$)
A	Active area (cm^2)
P	Pressure (Pa)
<i>Greek letters</i>	
ε	Porosity (-)
ψ	Stoichiometric coefficient (-)
κ	Ionic conductivity ($\text{S} \cdot \text{m}^{-1}$)
σ	Electronic conductivity ($\text{S} \cdot \text{m}^{-1}$)
<i>Subscripts</i>	
sym	Symmetric material configuration
asym	Asymmetric material configuration
M	Mass transport
T	Thermal
NWD	Net water drag
dew	Dew point
sat	Saturation
<i>Superscript</i>	
in,anode	Anode inlet
out,anode	Anode outlet
in,cat	Cathode inlet
out,cat	Cathode outlet

CHAPTER FOURTEEN :
SUMMARY AND CONCLUSIONS

14.1. Summary and Motivations

Redox flow batteries (RFBs) are scalable energy storage devices with an open structure. Having open configuration enables decoupling energy storage capacity from power generating reactor. Therefore, reactor design along with electrolyte engineering are major areas of research in the field. Ultimately, reducing the installed cost of a RFB system below \$150 (target price determined by the Department of Energy (DOE)) is the main objective. Experimental diagnostics, material characterization techniques, and multiscale computational modeling are commonly employed to reach this target. A critical review discussing the experimental diagnostics and materials characterization techniques used on RFBs is available in a recent publication from Yasser Ashraf Gandomi et al ¹. An overview covering general aspects of design, material selection, characterization, and performance evaluation metrics for RFBs is also available in Chapter 1.

Different classes of materials including redox active colloids (RACs), redox active polymers (RAPs), redox active oligomers (RAOs), redox active organic molecules (ROMs), and redox active transition metal salts (RAMs) have been explored for RFBs. The readers can refer to Chapter 8 for a short review on these classes of electroactive materials. Along with redox active materials, different solvents (aqueous and non-aqueous) and supporting salts have also been investigated.

Commonly, a separator is used within RFBs structure. An ideal separator must be selective to charge-balancing ion and be impermeable to redox active materials. Having high

conductivity (for charge-balancing ion), superior stability (electromechanical and chemical), and long-term durability are other requirements for an ideal separator. Based on the size of electroactive materials, various separator configurations including porous separators (average pore size > 10 nm), polymers with intrinsic microporosity (PIMs, average pore size: ~1 nm), and ion-exchange membranes (IEMs, average pore size < 1 nm) are used. Ideally, it is desirable to design RFBs with a size-exclusive separator and not to rely on the charge-exclusion for mitigating the undesired transport of the electroactive species and the solvent through the membrane (i.e. crossover). However, in practical applications, the crossover is usually inevitable; thus, mitigating the crossover and/or recovering the capacity fade due to the crossover of electroactive species is necessary. A summary of different techniques used for capacity retention in RFBs along with various separator configurations is available in Chapter 8.

In this work, we have focused on the all-vanadium redox flow batteries (VRFBs). VRFBs utilize vanadium ions in both negative (V(II)/V(III)) and positive electrolytes (V(IV)/V(V)), a supporting electrolyte (e.g. sulfuric acid), and the water as the solvent. An ion-exchange membrane is commonly used for separating the negative and positive electrolytes. However, the crossover of vanadium ions and water is inevitable during cycling. Due to ionic and water crossover through the ion-exchange membrane, the capacity radically decreases during charge/discharge cycles. The lost capacity is recoverable since the side-reactions initiated due to crossover are reversible; however, the process of recovering the capacity is cumbersome and not well understood. Therefore, this

work has been dedicated for improving our understanding of ionic and water crossover during cycling of VRRBs and subsequently tackling this problem using novel experimental diagnostics and multiscale modeling for improved capacity retention. The major objectives and contributions to the field through this work are summarized in the following section.

14.2. Objectives and Contributions to the Field

14.2.1. Design and fabrication of a novel setup for real-time measurement of ionic crossover and in-situ potential distribution assessment within VRFB architecture

The concentration gradient along with electrostatic potential gradient are the major driving forces for the ionic crossover. The solvent transport through the membrane is induced by the gradient in the chemical potential of the solvent in conjunction with the electroosmotic drag.

The convective flux of the solute (vanadium ions) is subsequently induced by the solvent transport. Therefore, probing electric-field induced crossover is crucial since the electrostatic potential gradient as well as the electroosmotic drag are induced by the electric field. In this work, a novel setup (we named it: IonCrG: Ionic Crossover Gauge) including several electrochemical and flow cells were designed and fabricated. Schematic of the setup is shown Fig. (14-1). The IonCrG was equipped with UV/Vis spectroscopy apparatus, the electrochemical impedance spectroscopy (EIS) setup, multichannel potentiostat/galvanostat, and multichannel temperature control unit.

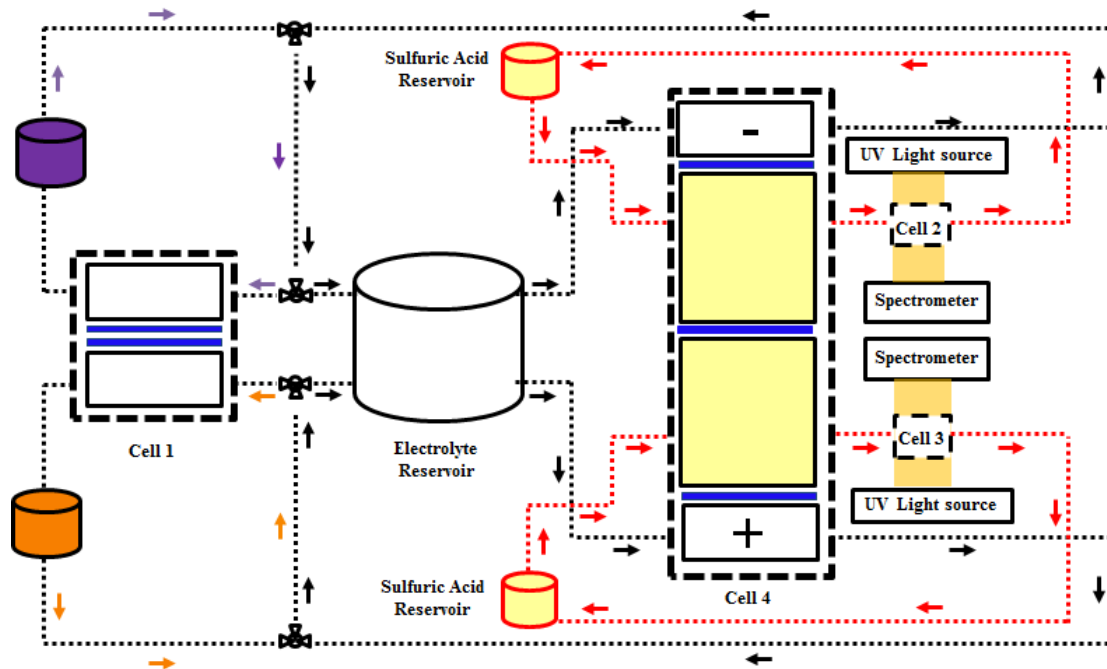


Figure 14-1: IonCrG: A novel set-up for real-time measurement of ionic crossover (The figure is adopted from Yasser Ashraf Gandomi et al. ²⁰²)

Different edge-type (e.g. silver chloride electrode) and sandwich-type (dynamic hydrogen electrode) reference electrodes were utilized within cell configurations shown in Fig. 14-1 for real-time assessment of potential distribution (across multilayers of the electrodes) as well as the half-cell potentials.

The IonCrG enabled a comprehensive characterization of the ionic crossover (with and without electric field effect), long term capacity decay, and performance metrics (voltaic and coulombic efficiency) for the VRFB configurations utilizing Nafion® membranes. A series of high-performance membranes (with various equivalent weights and degree of reinforcement) provided by W. L. Gore and Associates (Newark, DE) were also characterized using IonCrG. The IonCrG was also used to explore the influence of cell

design and electrolyte composition on the ionic crossover and subsequent capacity decay. Further details regarding the IonCrG are available in Chapter 4 and in a relevant publication ²⁰².

Utilizing IonCrG, an *in situ* potential distribution technique was developed to quantify the through-plane mass transport limitations formed during operation of VRFBs. Micro potential probes were installed within the layered porous carbon electrode at the positive side of the VRFB. It was shown that the reaction locations within the porous electrode shifted toward the flow plate side with increasing current density during discharge, revealing the electroactive species depletion mechanism in the through-plane direction within the electrodes. Further details regarding the potential distribution setup are available in Chapter 3 and in a relevant publication ¹²⁷.

14.2.2. Assessing the influence of electric-field and electrolyte composition on the ionic crossover

Differentiating the concentration gradient-induced crossover and electrostatic potential gradient-induced crossover through a perfluorosulphonic type (Nafion® 117) ion-exchange membrane was conducted for a wide range of operating conditions using the IonCrG. The permeability values for individual vanadium ions under concentration-gradient was measured. It was shown that the permeability of vanadium species through the ion-exchange membrane is state of charge (SoC) dependent and, therefore, the

interaction coefficients were introduced (for the first time) to account for coupled interactions.

The influence of the electric field on the ionic crossover was investigated using the multi-chamber cell shown in Fig. 14-1. It was also shown that the electric field has a significant effect on crossover and increases the rate of crossover for V(II)/V(III) and decreases the rate of crossover for V(IV)/V(V) during discharge; the opposite happens during charging conditions. The electric-field-induced transport coefficients were defined via fitting the experimental data. The electric-field-induced transport coefficients account for migration and convection transport modes due to the electric field.

It was also demonstrated that the effect of the electric field on the ionic crossover is asymmetric for charge and discharge processes for any vanadium species; this asymmetric trend was formulated via defining the dimensionless number γ to account for the relative importance of electric-field-induced crossover versus concentration gradient-induced crossover. Also, it was shown that the electric field effect is more significant on V(II)/V(III) than V(IV)/V(V) when the electric field is in the opposite direction of the concentration gradient-induced crossover.

Finally, the magnitude and the net direction of crossover current was measured for different operating conditions. Under symmetrical charge/discharge cycling, (i.e. utilizing similar charge/discharge current density) a net crossover current from negative to positive side was

quantified. Therefore, it was shown that during cycling of VRFBs, the accumulation of diffused vanadium ions in the positive electrolyte due to crossover decreases the capacity within the negative electrolyte. Subsequently, the state of charge and the state of discharge window decreases in the positive electrolyte (V(IV)/V(V)). Further details are available in Chapter 4 and in a relevant publication²⁰².

14.2.3. Investigating the influence of ion-exchange membrane's equivalent weight and reinforcement on ionic crossover

Among various components used within VRFB architecture, the ion-exchange membrane directly influences the rate of crossover. In addition, the membrane's cost is a major constituent of the overall cost. Therefore, designing inexpensive membranes with high selectivity, durability, and ionic conductivity is of great importance. Engineering the equivalent weight of the polymer chain along with reinforcement are key parameters towards reducing the cost and improving the selectivity and conductivity. In this work, the effects of equivalent weight and membrane reinforcement on capacity fade and crossover in a VRFB system were experimentally investigated. Three equivalent weights (800, 950 and 1100 g.mol⁻¹) were considered for non-reinforced and reinforced membranes. The non-reinforced and reinforced membranes were provided by W. L. Gore and Associates (Newark, DE). It is shown that vanadium crossover in VRFB systems can be mitigated either by increasing the ion-exchange membrane's equivalent weight or implementing reinforcement. However, there is a tradeoff between decreasing capacity decay and increasing area-specific resistance (ASR), though this tradeoff is strongly dependent on

equivalent weight. Also, it was shown that there exists a direct correlation between the discharge capacity decay over long-term cycling with V(IV) permeability values, confirming that the main contributor to capacity fade during cycling is due to vanadium crossover. Increased equivalent weight of the ion-exchange membrane decreases vanadium permeability, resulting in decreased the capacity fade over cycling. When the membranes are exposed to aqueous sulfuric acid and vanadium, they swell, but with different magnitudes. Increased equivalent weight increases the extent of swelling in both non-reinforced and reinforced membranes. As a result, the higher equivalent weight membranes impose extra resistance to vanadium crossover via increased diffusion path-length, ultimately reducing capacity fade. Comparing the non-reinforced and reinforced membranes, reinforcement decreases the degree of membrane swelling. However, the degree of vanadium crossover mitigation significantly increases as a function of reinforcement, as well. Since the impact of reinforcement on permeability is greater than that of through-plane swelling, reinforced ion-exchange membranes with higher equivalent weight best mitigate vanadium crossover. The readers can refer to Chapter 5 of this dissertation or a relevant publication (Yasser Ashraf Gandomi et al. ¹⁰²) for further details.

14.2.4. Probing real-time influence of ionic crossover on the redox flow battery performance using distributed, in-plane current distribution diagnostic

For VRFBs utilizing permeable membranes, the influence of ionic crossover on the real-time performance of the cell is expected. However, to the best of our knowledge, no

previous works have reported on this subject. Therefore, in this work, for the first time, the real-time influence of ionic crossover on the cell performance was explored.

The distributed current diagnostics has already been developed for VRFBs. This diagnostic provides in-plane resolution for the current distribution across the electrodes. In this work, the distributed current diagnostics, for the first time, was employed to investigate the real-time influence of ionic crossover on the cell performance. A series of membrane with varied equivalent weight and degree of reinforcement was characterized. The membranes were provided by W. L. Gore and Associates (Newark, DE).

Among them, two configurations with the highest and lowest ionic permeabilities (labeled as “Pure Cast Film EW800” and “GORE-SELECT® EW1100” respectively) selected and the real-time distributed current was implemented at various stoichiometric flows and with different flow plate designs.

The current distribution patterns measured for various flow plates configuration were further confirmed by the mathematical model simulations. It was shown that for the cells utilizing selective ion-exchange membrane, the distributed current across the electrode is dominated by the mass transport mechanism imposed by flow field design regardless of the flow condition. However, for the cell configurations with very permeable membrane, the distributed current is significantly altered by the ionic crossover through the membrane at low stoichiometric flow conditions. Increased flow stoichiometry, diminishes the dependency of distributed current on the ionic current even for highly permeable ion-

exchange membranes. Further details regarding the real-time assessment of the ionic crossover on the cell performance is available in Chapter 6. Details regarding the mathematical modeling details are provided in Chapter 3 and in a relevant publication (Yasser Ashraf Gandmi et al. ¹²⁷).

14.2.5. Exploring the influence of convective flux distribution on the ionic crossover

Among mass transport mechanisms through the electrodes (bulk diffusion, migration and convection), the convective flux can be engineered to substantially improve the performance of the cells. However, increased convection through the electrodes commonly increases the pressure drop for the system and subsequently decreases the system-level energy efficiency. The tradeoff between improved performance and increased pressure drop via increasing the convective flux within the electrodes is well -established in the field. In this work, we introduce another important criterion in engineering flow plate designs that substantially influences the capacity retention over long-term cycling for VRFBs. Based on the analysis provided in this work, it was shown that the distribution of the convective flux is the detrimental factor influencing the crossover and resulting capacity decay in an operating cell.

Several parameters can be tuned to alter the convective flux within the electrodes. Flow plates design is one of the major components that can be engineered for promoting the convection flux. Four different flow plates including serpentine, interdigitated, square flow-through, and rectangular flow-through designs were investigated. Long term cycling

experiments with aggressive voltage limits were considered to span a large state of charge and state of discharge window. In addition, UV/Vis spectroscopy was used to explore the concentration-gradient induced crossover for various flow plates.

It was shown that the serpentine flow plates exhibit higher sensitivity for the variations in convective flux. Increasing the convective flux within the electrodes substantially increases the rate of crossover for this design. However, the flow-through designs exhibit miniscule sensitivity to increased convective mass flux. Considering the mass transport mechanism within the electrodes, the through-plane component of the convective flux (through-plane average velocity component) was determined to be the key parameter directly affecting the rate of crossover. Therefore, future flow field designs must focus on optimizing the performance, reducing the pressure drop, and decreasing the ionic crossover via engineering the through-plane component of the convective flux.

To the best of our knowledge, no previous work has reported the influence of flow field design (i.e. convective flux) on the ionic crossover and subsequent capacity decay. Therefore, in this work, for the first time, we explored the effect of flow field design on the crossover. Further details are available in Chapter 7 of this dissertation.

14.2.6. Developing a macroscale, continuum mathematical model for simulating the performance of VRFBs

Several parameters contribute to the performance of VRFBs including operating conditions (e.g. volumetric flow rate, temperature), electrode and flow field design, electrolyte

composition (concentration of electroactive species, state of charge, concentration of supporting salt) and many others. Developing predictive mathematical models enables exploring the influence of operating conditions, cell component, and electrolyte composition on the performance of VRFBs. Therefore, in this work, a mathematical model was developed to quantify the species concentration distribution, multiple mass flux components, and solid-phase and electrolyte-phase potentials for an operando cell.

To verify the model predictions, a distributed potential distribution diagnostic was developed (further details on the potential distribution diagnostics are available in Chapter 3 and a related publication (Yasser Ashraf Gandomi et al. ¹²⁷)). The mathematical model agreed with the experimental data, with a maximum error of 9%. The lowest predicted and measured potential occurred close to the electrode/current-collector interface, indicating the dominant reaction location in the through plane direction. In addition, the model simulated the diffusive, convective and electrophoretic mass fluxes at different operating conditions. The model simulation showed that the convective mass transport flux is at least four orders of magnitude higher than the diffusive and electrophoretic fluxes at the corresponding cell location along the flow stream. The concentration gradient not only occurs along the flow direction, but also in the through-plane direction with the highest concentration gradient at the electrode/current-collector interface. If the cell is to be operated at high current density ($800 \text{ mA}\cdot\text{cm}^{-2}$ and higher), starvation of active species (V(II)/V(V)) needs to be prevented at the electrode/current-collector interface. This goal is achieved partially by increased convective mass flux (which was shown in this work). Mass

transport can further be increased by improved electrode design such that the mass transport resistance in the in-plane direction decreases along the flow direction. This would enable increased diffusion flux from the main stream of the flow towards the electrode/current-collector interface. Also, it was shown that when the cell is operating at high volumetric flow rate, a large concentration gradient of protons and bisulphate ions forms along the flow direction, resulting in varying conductivity values for the membrane along the flow direction. An improved design can eliminate this by providing more uniform distribution of the protons and bisulphate ions within the electrodes. The readers can refer to Chapter 3 or a relevant publication for further details (Yasser Ashraf Gandomi et al. ¹²⁷)

14.2.7. Multiscale modeling of the ion-exchange membranes

The ion-exchange membranes are commonly used within the configuration of redox flow batteries. Understanding the interactions of the membrane with the solvent and ion-balancing ion is of great importance. Developing rigorous multiscale mathematical models for simulating the transport of ionic species along with predicting the conductivity of the membrane swelled in different solvents (aqueous and non-aqueous) is crucial for engineering the electrolytes composition as well as the membrane morphology.

In the first phase, a macroscale continuum model is developed for simulating the multicomponent diffusion in the membrane (Nafion® with equivalent weight of 1100) of an all-vanadium redox flow battery based upon the Stefan-Maxwell multicomponent diffusion equation (concentrated solution theory). The multicomponent diffusion equation

results in the simulation of the species flux equations which are fully coupled. The transport of the species within the membrane with the high concentration (including protons (H^+), bisulfate (HSO_4^-), water (H_2O) and the sulfonate functional groups ($-\text{SO}_3^-$)) modeled and their interaction was simulated in a fully coupled framework. The driving force for species transport has been considered to be the gradient in electrochemical potential which can be decoupled in terms of the gradient of concentration and the gradient in electrostatic potential. The model successfully simulates the ionic transport numbers as well as water electro-osmosis drag coefficient for different acid concentrations. Further details are available in Chapter 11 and in a relevant publication (Yasser Ashraf Gandomi et al. ¹⁷⁹).

In the second phase, a molecular dynamic (MD) simulation was performed to simulate the conductivity of a lithiated ion-exchange membrane (Nafion® with equivalent weight of 1100) swelled in various non-aqueous solvents. The application of non-aqueous solvents along with redox active organic molecules (ROMs) is promising for designing next-generation RFBs since this combination of the solute/solvent can significantly reduce the cost and improve the performance.

The non-aqueous solvents are not limited by the voltage stability window of the aqueous solvents (i.e. ~ 1.23 V); thus, higher cell voltages can be sustained via non-aqueous solvents. The ROMs are significantly cheaper compared to redox active inorganic transition metal salts. Tunable characteristics of the ROMs enables engineering their structure for improved capacity, performance or durability.

In this work, two different non-aqueous solvents including dimethyl sulfoxide and acetonitrile were separately modeled using MD simulations. The MD simulations enabled predicting the diffusivity of the solvent, polymer chain, and lithium for different cases. Developing this modeling framework was substantial since it enables optimizing the solvents structure as well as the membrane morphology for improved performance and conductivity as well as reduced cost for RFB systems. Further details are available in Chapter 12.

14.2.8. Ion-exchange membrane stacking: an inexpensive approach for reducing the ionic crossover in RFBs

Implantation of multilayer stacking of ion-exchange membranes for reduced ionic crossover was investigated in this work. To the best of our knowledge, this approach has never been reported in the literature. Therefore, this work, is the first demonstration of this novel technique for reduced ionic crossover in RFBs. Ex-situ conductivity cells were designed, fabricated, and subsequently used to measure the in-plane conductivity of the membranes along with bathing solutions. The MacMullin number for Nafion membranes was calculated to correlate the ionic conductivity of the bathing solutions to the in-plane conductivity of the membranes.

The IonCrG was utilized to assess the ASR and real-time crossover of vanadium ions. The ASR associated with electrode-membrane interface was also deduced. Subsequently, a series of off-the-shelf ion-exchange membranes (i.e. NR211, NR212, N115, and N117)

were investigated in terms of ASR and vanadium crossover. Stacking multiple off-the-shelf membranes was explored as a promising yet inexpensive technique for tackling the rapid capacity decay issue associated with the operation of all-vanadium redox flow batteries. Design criteria for VRFBs utilizing stack of off-the-shelf membrane were introduced for high-performance, short-term, and extended (long-duration) cycling experiments. Further details are available in Chapter 10.

14.2.9. Developing a novel, inexpensive, and passive approach for capacity retention during long-term cycling for aqueous RFBs

In this work, a theoretical framework was developed for altering the chemical potential of the solvent across the ion-exchange membrane to reducing the ionic crossover. Three feasible strategies including imposing temperature gradient, hydraulic pressure gradient, and osmosis pressure gradient across the semi-permeable membrane were discussed. Considering the room-temperature operation of VRFBs and the vanadium precipitations issues associated with relatively high and low temperature operation, implementing temperature gradient across the semi-permeable membrane is not practical. Therefore, engineering hydraulic and osmotic pressure gradients across the membrane is of interest.

Two cases were explored to demonstrate the applicability of this approach in reducing the radical capacity decay during long-term cycling of VRFBs; imposing an asymmetric configuration of the cell architecture along with electrolyte composition. First, an asymmetric flow field configuration of the negative and positive sides was implemented

for a 9 cm² cell with serpentine flow field in the negative side (V(II)/V(III)) and flow-through flow field for the positive side (V(IV)/V(V)). It was shown that the asymmetric configuration of the flow field reduces the capacity decay by 33% (within 30 cycles) compared to symmetric flow field configuration. It was also demonstrated that the coulombic efficiency for the asymmetric flow field configuration remains unchanged compared to symmetric one (> 98%). The validity of asymmetric flow field configuring in reducing ionic crossover was further confirmed via conducting real-time concentration-gradient induced crossover experiments using UV/Vis spectroscopy apparatus within IonCrG.

Second, asymmetric acid configuration of the negative and positive electrolytes was implemented to impose osmotic pressure gradient across the ion-exchange membrane. Negative electrolyte with higher acidity (4M) compared to positive electrolyte (2M) was prepared. It was shown that implementing asymmetric acid configuration does not adversely alter the cell performance and performance metrics (i.e. voltaic efficiency). However, during long-term cycling (30 cycles at 100 mA.cm⁻², ~100 hours, wide state of charge and state of discharge window), asymmetric acid configuration reduces the capacity decay by 47% compared to symmetric acid configurations (for both 2M/2M and 4M/4M setups) at the end of cycling.

Although carbon paper electrodes were utilized for proof of concept in this work, the choice of carbon paper or carbon felt should make minor difference. The basic concept concerns

the use of an asymmetric cell (in which each side has a different flow field design) to inhibit the ionic crossover through the ion-exchange membrane. This novel approach can be optimized for any particular system (e.g., redox active chemistries, flow rates, electrolytes, etc.).

Imposition of asymmetric supporting electrolyte salt was demonstrated for VRFBs as a promising technique for reducing ionic crossover during cycling. This approach is easily applicable for other RFBs utilizing aqueous electrolytes along with semi-permeable membranes in their structure. Further details are available in Chapter 9.

14.3. Recommendations for Future Work

The crossover of electroactive species and the solvent through the membrane is a severe problem for widespread commercialization of redox flow batteries (RFBs). The ultimate goal in the field is to design and demonstrate long-term durability with reduced overall cost (below \$150, DOE target) for an installed RFB system. Therefore, engineering electrolyte composition (selecting electroactive species, supporting salt, and the solvent) along with designing the reactor must be tailored for fulfilling this objective.

Usually, the selection of electroactive species and the solvent dictates next steps in the design process. In this work, we focused on RFBs utilizing transition metal salts (vanadium) and the water within the electrolyte. Commonly, sulfuric acid is used as the supporting electrolyte for all-vanadium redox flow batteries. Therefore, the design of cell

reactor along with further engineering the electrolyte composition was tailored to overcome the issues associated with the crossover of vanadium ions during cycling of VRFBs since the crossover (vanadium ions and the solvent) through the membrane is inevitable based on the existing, commercially available ion-exchange membranes. Therefore, recommendations for the future work can be summarized in the form of following subcategories. First, it is necessary to develop highly selective membranes with superior conductivity. The next generation of membranes for VRFBs must be impermeable to vanadium ions and must have superior durability and stability (mechanical, chemical, and electrochemical).

Second, if the objective is to utilize the existing ion-exchange membranes for VRFBs, to demonstrate long-term durability, the crossover of ionic species along with the water through the membrane must be addressed appropriately. In Chapter 8 of this dissertation, recommendations were provided for mitigating the ionic crossover and/or recovering the lost capacity. The readers can refer to Chapter 8 for further details. In this work, for the first time, we demonstrated the influence of flow field design on the ionic crossover and subsequently introduced an asymmetric design criterion for mitigating the crossover. Therefore, future work can focus on designing VRFBs based on this asymmetric design criterion.

Third, the electrolyte composition can be engineered for improved vanadium solubility, durability and reduced ionic crossover. In this dissertation, we provided theoretical

framework explaining the tunable parameters for inducing the solvent transport through the membrane. One of our recommendations was to utilize asymmetric acid concentration for reduced capacity decay. Therefore, this design criterion can be further improved for utilizing mixed acid electrolytes for VRFBs.

Fourth, multiscale modeling provided invaluable insight to understanding the mechanism of crossover and ionic conductivity within the membrane. Therefore, the future work can further improve this modeling work. In particular, connecting the macroscale level insight to molecular level simulation is of great importance.

Fifth, the IonCrG (Ionic Crossover Gauge) was designed and fabricated in this work for comprehensive analysis of the ionic crossover and the water for VRFBs in real-time. The IonCrG enabled exploring the influence of electric field as well as the concentration-gradient on the ionic crossover for various ion-exchange membranes, cell architectures, and electrolyte compositions. The IonCrG can be applied to any RFB chemistry. Therefore, the experimental diagnostics for other RFB chemistries, in particular, the ones based on transition metal salts (e.g. all-iron and all-copper RFBs) can adopt the IonCrG for improving the design and durability.

REFERENCES

1. Y. A. Gandomi, D. Aaron, J. Houser, M. Daugherty, J. Clement, A. Pezeshki, T. Ertugrul, D. Moseley, and M. Mench, *Journal of The Electrochemical Society*, **165** (5), A970-A1010 (2018).
2. G. Huff, G. Huff, A. A. Akhil, A. A. Akhil, B. C. Kaun, B. C. Kaun, D. M. Rastler, D. M. Rastler, S. B. Chen, and S. B. Chen. Sandia National Laboratories (SNL-NM), Albuquerque, NM (United States), 2015.
3. F. Beck and P. Rüetschi, *Electrochimica Acta*, **45** (15), 2467-2482 (2000).
4. C. P. De Leon, A. Frias-Ferrer, J. González-García, D. Szánto, and F. C. Walsh, *Journal of Power Sources*, **160** (1), 716-732 (2006).
5. H. Ibrahim, A. Ilinca, and J. Perron, *Renewable and sustainable energy reviews*, **12** (5), 1221-1250 (2008).
6. G. L. Soloveichik, *Annual review of chemical and biomolecular engineering*, **2** 503-527 (2011).
7. A. Z. Weber, M. M. Mench, J. P. Meyers, P. N. Ross, J. T. Gostick, and Q. Liu, *Journal of Applied Electrochemistry*, **41** (10), 1137-1164 (2011).
8. M. L. Perry and A. Z. Weber, *Journal of The Electrochemical Society*, **163** (1), A5064-A5067 (2016).
9. *Grid Energy Storage*, U.S. Department of Energy, (2013).
10. *Grid-scale Rampable Intermittent Dispatchable Storage*, ARPA-E. U.S. Department of Energy (2015).
11. V. Viswanathan, A. Crawford, D. Stephenson, S. Kim, W. Wang, B. Li, G. Coffey, E. Thomsen, G. Graff, and P. Balducci, *Journal of Power Sources*, **247** 1040-1051 (2014).
12. A. Crawford, V. Viswanathan, D. Stephenson, W. Wang, E. Thomsen, D. Reed, B. Li, P. Balducci, M. Kintner-Meyer, and V. Sprenkle, *Journal of Power Sources*, **293** 388-399 (2015).
13. R. Dmello, J. D. Milshtein, F. R. Brushett, and K. C. Smith, *Journal of Power Sources*, **330** 261-272 (2016).
14. Z. Li, M. S. Pan, L. Su, P.-C. Tsai, A. F. Badel, J. M. Valle, S. L. Eiler, K. Xiang, F. R. Brushett, and Y.-M. Chiang, *Joule*, **1** (2), 306-327 (2017).
15. K. Gong, X. Ma, K. M. Conforti, K. J. Kuttler, J. B. Grunewald, K. L. Yeager, M. Z. Bazant, S. Gu, and Y. Yan, *Energy & Environmental Science*, **8** (10), 2941-2945 (2015).
16. M. Rychcik and M. Skyllas-Kazacos, *Journal of Power Sources*, **22** (1), 59-67 (1988).
17. E. Sum and M. Skyllas-Kazacos, *Journal of Power sources*, **15** (2-3), 179-190 (1985).
18. E. Sum, M. Rychcik, and M. Skyllas-Kazacos, *Journal of Power sources*, **16** (2), 85-95 (1985).
19. M. Skyllas-Kazacos, M. Rychick, and R. Robins. Google Patents, 1988.
20. L. H. Thaller. Google Patents, 1976.
21. L. H. Thaller. US-PATENT-3,996,064, 1976.
22. R. F. Gahn, N. H. Hagedorn, and J. A. Johnson. NASA-TM-87034, 1985.

23. M. Lopez-Atalaya, G. Codina, J. Perez, J. Vazquez, and A. Aldaz, *Journal of power sources*, **39** (2), 147-154 (1992).
24. M. Skyllas-Kazacos, *Journal of Power Sources*, **124** (1), 299-302 (2003).
25. M. Skyllas-Kazacos and Y. Limantari, *Journal of applied electrochemistry*, **34** (7), 681-685 (2004).
26. B. Huskinson, M. P. Marshak, C. Suh, S. Er, M. R. Gerhardt, C. J. Galvin, X. Chen, A. Aspuru-Guzik, R. G. Gordon, and M. J. Aziz, *Nature*, **505** (7482), 195-198 (2014).
27. B. Yang, L. Hooper-Burkhardt, F. Wang, G. S. Prakash, and S. Narayanan, *Journal of The Electrochemical Society*, **161** (9), A1371-A1380 (2014).
28. R. L. Clarke, B. Dougherty, S. Harrison, P. J. Millington, and S. Mohanta. Google Patents, 2009.
29. Y. Matsuda, K. Tanaka, M. Okada, Y. Takasu, M. Morita, and T. Matsumura-Inoue, *Journal of applied electrochemistry*, **18** (6), 909-914 (1988).
30. Q. Liu, A. E. Sleightholme, A. A. Shinkle, Y. Li, and L. T. Thompson, *Electrochemistry Communications*, **11** (12), 2312-2315 (2009).
31. Q. Liu, A. A. Shinkle, Y. Li, C. W. Monroe, L. T. Thompson, and A. E. Sleightholme, *Electrochemistry Communications*, **12** (11), 1634-1637 (2010).
32. A. E. Sleightholme, A. A. Shinkle, Q. Liu, Y. Li, C. W. Monroe, and L. T. Thompson, *Journal of Power Sources*, **196** (13), 5742-5745 (2011).
33. W. Wang, W. Xu, L. Cosimbescu, D. Choi, L. Li, and Z. Yang, *Chemical Communications*, **48** (53), 6669-6671 (2012).
34. R. V. Bugga, W. C. West, A. Kindler, and M. C. Smart. Google Patents, 2014.
35. A. N. Jansen, J. T. Vaughey, Z. Chen, L. Zhang, and F. R. Brushett. Google Patents, 2012.
36. W. Xu, L. Cosimbescu, X. Wei, W. Wang, and V. L. Sprenkle. Google Patents, 2013.
37. R. L. Clarke, B. Dougherty, S. Harrison, P. J. Millington, and S. Mohanta. Google Patents, 2007.
38. R. L. Clarke, B. Dougherty, S. Harrison, J. P. Millington, and S. Mohanta. Google Patents, 2009.
39. R. Zito. Google Patents, 1973.
40. L. Hruska and R. Savinell, *Journal of the Electrochemical Society*, **128** (1), 18-25 (1981).
41. A. Hazza, D. Pletcher, and R. Wills, *Physical Chemistry Chemical Physics*, **6** (8), 1773-1778 (2004).
42. D. Pletcher and R. Wills, *Physical Chemistry Chemical Physics*, **6** (8), 1779-1785 (2004).
43. D. Lloyd, T. Vainikka, and K. Kontturi, *Electrochimica Acta*, **100** 18-23 (2013).
44. M. Duduta, B. Ho, V. C. Wood, P. Limthongkul, V. E. Brunini, W. C. Carter, and Y. M. Chiang, *Advanced Energy Materials*, **1** (4), 511-516 (2011).
45. S. Kamasaki and H. Baba, *Mem. Fac. Technol., Tokyo Metrop. Univ*, **33** 3363-3370 (1983).

46. H. Kreutzer, V. Yarlagadda, and T. Van Nguyen, *Journal of The Electrochemical Society*, **159** (7), F331-F337 (2012).
47. H. Kaneko, A. Negishi, K. Nozaki, K. Sato, and M. Nakajima. Google Patents, 1994.
48. S. Hosseiny, M. Saakes, and M. Wessling, *Electrochemistry Communications*, **13** (8), 751-754 (2011).
49. C. Menictas and M. Skyllas-Kazacos, *Journal of Applied Electrochemistry*, **41** (10), 1223 (2011).
50. V. Yufit, B. Hale, M. Matian, P. Mazur, and N. Brandon, *Journal of The Electrochemical Society*, **160** (6), A856-A861 (2013).
51. R. P. Dowd, V. S. Lakhanpal, and T. Van Nguyen, *Journal of The Electrochemical Society*, **164** (6), F564-F567 (2017).
52. S. Siracusano, V. Baglio, N. Briguglio, G. Brunaccini, A. Di Blasi, A. Stassi, R. Ornelas, E. Trifoni, V. Antonucci, and A. Aricò, *International Journal of hydrogen energy*, **37** (2), 1939-1946 (2012).
53. R. M. Darling, K. G. Gallagher, J. A. Kowalski, S. Ha, and F. R. Brushett, *Energy & Environmental Science*, **7** (11), 3459-3477 (2014).
54. J. A. Kowalski, L. Su, J. D. Milshtein, and F. R. Brushett, *Current Opinion in Chemical Engineering*, **13** 45-52 (2016).
55. S. M. Laramie, J. D. Milshtein, T. M. Breault, F. R. Brushett, and L. T. Thompson, *Journal of Power Sources*, **327** 681-692 (2016).
56. J. D. Milshtein, J. L. Barton, T. J. Carney, J. A. Kowalski, R. M. Darling, and F. R. Brushett, *Journal of The Electrochemical Society*, **164** (12), A2487-A2499 (2017).
57. J. Huang, B. Pan, W. Duan, X. Wei, R. S. Assary, L. Su, F. R. Brushett, L. Cheng, C. Liao, and M. S. Ferrandon, *Scientific reports*, **6** 32102 (2016).
58. E. V. Carino, J. Staszak-Jirkovsky, R. S. Assary, L. A. Curtiss, N. M. Markovic, and F. R. Brushett, *Chem. Mater*, **28** (8), 2529-2539 (2016).
59. E. S. Beh, D. De Porcellinis, R. L. Gracia, K. T. Xia, R. G. Gordon, and M. J. Aziz, *ACS Energy Letters*, **2** (3), 639-644 (2017).
60. Q. Chen, L. Eisenach, and M. J. Aziz, *Journal of The Electrochemical Society*, **163** (1), A5057-A5063 (2016).
61. Q. Chen, M. R. Gerhardt, L. Hartle, and M. J. Aziz, *Journal of The Electrochemical Society*, **163** (1), A5010-A5013 (2016).
62. P. Leung, A. Shah, L. Sanz, C. Flox, J. Morante, Q. Xu, M. Mohamed, C. P. de León, and F. Walsh, *Journal of Power Sources*, **360** 243-283 (2017).
63. F. Y. Fan, W. H. Woodford, Z. Li, N. Baram, K. C. Smith, A. Helal, G. H. McKinley, W. C. Carter, and Y.-M. Chiang, *Nano letters*, **14** (4), 2210-2218 (2014).
64. D. Aaron, S. Yeom, K. D. Kihm, Y. A. Gandomi, T. Ertugrul, and M. M. Mench, *Journal of Power Sources*, **366** 241-248 (2017).
65. A. Parasuraman, T. M. Lim, C. Menictas, and M. Skyllas-Kazacos, *Electrochimica Acta*, **101** 27-40 (2013).

66. P. Alotto, M. Guarnieri, and F. Moro, *Renewable and Sustainable Energy Reviews*, **29** 325-335 (2014).
67. B. R. Chalamala, T. Soundappan, G. R. Fisher, M. R. Anstey, V. V. Viswanathan, and M. L. Perry, *Proceedings of the IEEE*, **102** (6), 976-999 (2014).
68. G. L. Soloveichik, *Chemical reviews*, **115** (20), 11533-11558 (2015).
69. L. Su, J. A. Kowalski, K. J. Carroll, and F. R. Brushett, in *Rechargeable Batteries*, p. 673-712, Springer, (2015).
70. M. Ulaganathan, V. Aravindan, Q. Yan, S. Madhavi, M. Skyllas-Kazacos, and T. M. Lim, *Advanced Materials Interfaces*, **3** (1), (2016).
71. M. Skyllas-Kazacos, G. Kazacos, G. Poon, and H. Verseema, *International Journal of Energy Research*, **34** (2), 182-189 (2010).
72. D. Aaron, Q. Liu, Z. Tang, G. Grim, A. Papandrew, A. Turhan, T. Zawodzinski, and M. Mench, *Journal of Power sources*, **206** 450-453 (2012).
73. L. Li, S. Kim, W. Wang, M. Vijayakumar, Z. Nie, B. Chen, J. Zhang, G. Xia, J. Hu, and G. Graff, *Advanced Energy Materials*, **1** (3), 394-400 (2011).
74. S. Roe, C. Menictas, and M. Skyllas-Kazacos, *Journal of The Electrochemical Society*, **163** (1), A5023-A5028 (2016).
75. V. Livshits, A. Ulus, and E. Peled, *Electrochemistry communications*, **8** (8), 1358-1362 (2006).
76. K. T. Cho, P. Ridgway, A. Z. Weber, S. Haussener, V. Battaglia, and V. Srinivasan, *Journal of The Electrochemical Society*, **159** (11), A1806-A1815 (2012).
77. K. T. Cho, P. Albertus, V. Battaglia, A. Kojic, V. Srinivasan, and A. Z. Weber, *Energy Technology*, **1** (10), 596-608 (2013).
78. R. M. Darling and M. L. Perry, *Journal of The Electrochemical Society*, **161** (9), A1381-A1387 (2014).
79. K. T. Cho, M. C. Tucker, M. Ding, P. Ridgway, V. S. Battaglia, V. Srinivasan, and A. Z. Weber, *ChemPlusChem*, **80** (2), 402-411 (2015).
80. G. Lin, P. Chong, V. Yarlagadda, T. Nguyen, R. Wycisk, P. Pintauro, M. Bates, S. Mukerjee, M. Tucker, and A. Weber, *Journal of The Electrochemical Society*, **163** (1), A5049-A5056 (2016).
81. M.-A. Goulet and E. Kjeang, *Journal of Power Sources*, **260** 186-196 (2014).
82. Y. Ashraf Gandomi, D. Aaron, J. Houser, M. Daugherty, J. Clement, A. Pezeshki, T. Ertugrul, D. Moseley, and M. Mench, *Journal of The Electrochemical Society*, **165** (5), A970-A1010 (2018).
83. K. A. Mauritz and R. B. Moore, *Chemical reviews*, **104** (10), 4535-4586 (2004).
84. B. Schwenzer, J. Zhang, S. Kim, L. Li, J. Liu, and Z. Yang, *ChemSusChem*, **4** (10), 1388-1406 (2011).
85. X. Li, H. Zhang, Z. Mai, H. Zhang, and I. Vankelecom, *Energy & Environmental Science*, **4** (4), 1147-1160 (2011).
86. S.-H. Shin, S.-H. Yun, and S.-H. Moon, *Rsc Advances*, **3** (24), 9095-9116 (2013).
87. M. Chakrabarti, N. Brandon, S. Hajimolana, F. Tariq, V. Yufit, M. Hashim, M. Hussain, C. Low, and P. Aravind, *Journal of Power Sources*, **253** 150-166 (2014).

88. M. Skyllas-Kazacos and F. Grossmith, *Journal of the Electrochemical Society*, **134** (12), 2950-2953 (1987).
89. X. Li and I. Sabir, *International Journal of Hydrogen Energy*, **30** (4), 359-371 (2005).
90. W. A. Braff, C. R. Buie, and M. Z. Bazant, *Journal of The Electrochemical Society*, **160** (11), A2056-A2063 (2013).
91. W. A. Braff, M. Z. Bazant, and C. R. Buie, *Journal of Fluid Mechanics*, **767** 85-94 (2015).
92. W. A. Braff, M. Z. Bazant, and C. R. Buie, *Nature communications*, **4** (2013).
93. R. Ferrigno, A. D. Stroock, T. D. Clark, M. Mayer, and G. M. Whitesides, *Journal of the American Chemical Society*, **124** (44), 12930-12931 (2002).
94. B.-Z. Magnes, I. B. David, E. Lancry, and M. Bergstein-Freiberg. Google Patents, 2013.
95. F. Cuevas-Muñiz, M. Guerra-Balcázar, F. Castaneda, J. Ledesma-García, and L. Arriaga, *Journal of Power Sources*, **196** (14), 5853-5857 (2011).
96. E. R. Choban, L. J. Markoski, A. Wieckowski, and P. J. Kenis, *Journal of Power Sources*, **128** (1), 54-60 (2004).
97. E. R. Choban, J. Spendelow, L. Gancs, A. Wieckowski, and P. Kenis, *Electrochimica Acta*, **50** (27), 5390-5398 (2005).
98. L. Cheng, R. S. Assary, X. Qu, A. Jain, S. P. Ong, N. N. Rajput, K. Persson, and L. A. Curtiss, *The journal of physical chemistry letters*, **6** (2), 283-291 (2015).
99. S. P. Ong, S. Cholia, A. Jain, M. Brafman, D. Gunter, G. Ceder, and K. A. Persson, *Computational Materials Science*, **97** 209-215 (2015).
100. X. Qu, A. Jain, N. N. Rajput, L. Cheng, Y. Zhang, S. P. Ong, M. Brafman, E. Maginn, L. A. Curtiss, and K. A. Persson, *Computational Materials Science*, **103** 56-67 (2015).
101. C. Choi, S. Kim, R. Kim, Y. Choi, S. Kim, H.-y. Jung, J. H. Yang, and H.-T. Kim, *Renewable and Sustainable Energy Reviews*, **69** 263-274 (2017).
102. Y. Ashraf Gandomi, D. S. Aaron, and M. M. Mench, *Membranes*, **7** (2), 29 (2017).
103. M. Skyllas-Kazacos and M. Kazacos, *Journal of Power Sources*, **196** (20), 8822-8827 (2011).
104. A. Price, S. Bartley, S. Male, and G. Cooley, *Power Engineering Journal*, **13** (3), 122-129 (1999).
105. K. Cathro, K. Cedzynska, and D. Constable, *Journal of power sources*, **19** (4), 337-356 (1987).
106. P. Leung, X. Li, C. P. De León, L. Berlouis, C. J. Low, and F. C. Walsh, *Rsc Advances*, **2** (27), 10125-10156 (2012).
107. M. Skyllas-Kazacos, M. Chakrabarti, S. Hajimolana, F. Mjalli, and M. Saleem, *Journal of the Electrochemical Society*, **158** (8), R55-R79 (2011).
108. C. Fabjan, J. Garche, B. Harrer, L. Jörissen, C. Kolbeck, F. Philippi, G. Tomazic, and F. Wagner, *Electrochimica Acta*, **47** (5), 825-831 (2001).
109. M. Gattrell, J. Qian, C. Stewart, P. Graham, and B. MacDougall, *Electrochimica acta*, **51** (3), 395-407 (2005).

110. M. Zhang, M. Moore, J. Watson, T. A. Zawodzinski, and R. M. Counce, *Journal of The Electrochemical Society*, **159** (8), A1183-A1188 (2012).
111. M. J. Watt-Smith, P. Ridley, R. Wills, A. Shah, and F. Walsh, *Journal of Chemical Technology and Biotechnology*, **88** (1), 126-138 (2013).
112. Y. A. Gandomi and M. M. Mench, *ECS Transactions*, **58** (1), 1375-1382 (2013).
113. Q. Liu, A. Turhan, T. A. Zawodzinski, and M. M. Mench, *Chem. Commun.*, **49** (56), 6292-6294 (2013).
114. P. Han, Y. Yue, Z. Liu, W. Xu, L. Zhang, H. Xu, S. Dong, and G. Cui, *Energy & Environmental Science*, **4** (11), 4710-4717 (2011).
115. S. Wang, X. Zhao, T. Cochell, and A. Manthiram, *The journal of physical chemistry letters*, **3** (16), 2164-2167 (2012).
116. K. JaeáKim and N. JináLee, *Chemical Communications*, **48** (44), 5455-5457 (2012).
117. C. P. De Leon, A. Frías-Ferrer, J. González-García, D. Szánto, and F. C. Walsh, *Journal of Power Sources*, **160** (1), 716-732 (2006).
118. S. Corcuera and M. Skyllas-Kazacos, *European Chemical Bulletin*, **1** (12), 511-519 (2012).
119. A. Shah, H. Al-Fetlawi, and F. Walsh, *Electrochimica Acta*, **55** (3), 1125-1139 (2010).
120. H. Al-Fetlawi, A. Shah, and F. Walsh, *Electrochimica Acta*, **55** (9), 3192-3205 (2010).
121. T. Mohammadi, S. Chieng, and M. Skyllas Kazacos, *Journal of membrane science*, **133** (2), 151-159 (1997).
122. E. Wiedemann, A. Heintz, and R. Lichtenthaler, *Journal of membrane science*, **141** (2), 207-213 (1998).
123. E. Wiedemann, A. Heintz, and R. Lichtenthaler, *Journal of membrane science*, **141** (2), 215-221 (1998).
124. A. Tang, J. Bao, and M. Skyllas-Kazacos, *Journal of Power Sources*, **196** (24), 10737-10747 (2011).
125. T. Sukkar and M. Skyllas-Kazacos, *Journal of Membrane Science*, **222** (1), 235-247 (2003).
126. M. Vijayakumar, L. Li, G. Graff, J. Liu, H. Zhang, Z. Yang, and J. Z. Hu, *Journal of Power Sources*, **196** (7), 3669-3672 (2011).
127. Y. A. Gandomi, D. Aaron, T. Zawodzinski, and M. Mench, *Journal of The Electrochemical Society*, **163** (1), A5188-A5201 (2016).
128. A. Heintz and C. Illenberger, *Berichte der Bunsengesellschaft für physikalische Chemie*, **102** (10), 1401-1409 (1998).
129. G. Oriji, Y. Katayama, and T. Miura, *Journal of Power Sources*, **139** (1), 321-324 (2005).
130. P. Blanc, C. Madic, and J. Launay, *Inorganic Chemistry*, **21** (8), 2923-2928 (1982).
131. Z. Tang, D. S. Aaron, A. B. Papandrew, and T. A. Zawodzinski, *ECS Transactions*, **41** (23), 1-9 (2012).

132. L. Liu, J. Xi, Z. Wu, W. Zhang, H. Zhou, W. Li, and X. Qiu, *Journal of Applied Electrochemistry*, **42** (12), 1025-1031 (2012).
133. D. N. Buckley, X. Gao, R. P. Lynch, N. Quill, and M. J. Leahy, *Journal of The Electrochemical Society*, **161** (4), A524-A534 (2014).
134. W. Zhang, L. Liu, and L. Liu, *RSC Advances*, (2015).
135. R. P. Brooker, C. J. Bell, L. J. Bonville, H. R. Kunz, and J. M. Fenton, *Journal of The Electrochemical Society*, **162** (4), A608-A613 (2015).
136. N. Roznyatovskaya, T. Herr, M. Küttinger, M. Fühl, J. Noack, K. Pinkwart, and J. Tübke, *Journal of Power Sources*, **302** 79-83 (2016).
137. C. Petchsingh, N. Quill, J. T. Joyce, D. N. Eidhin, D. Oboroceanu, C. Lenihan, X. Gao, R. P. Lynch, and D. N. Buckley, *Journal of The Electrochemical Society*, **163** (1), A5068-A5083 (2016).
138. W. Xie, R. M. Darling, and M. L. Perry, *Journal of The Electrochemical Society*, **163** (1), A5084-A5089 (2016).
139. R. Darling, K. Gallagher, W. Xie, L. Su, and F. Brushett, *Journal of The Electrochemical Society*, **163** (1), A5029-A5040 (2016).
140. C. Sun, J. Chen, H. Zhang, X. Han, and Q. Luo, *Journal of Power Sources*, **195** (3), 890-897 (2010).
141. X. Luo, Z. Lu, J. Xi, Z. Wu, W. Zhu, L. Chen, and X. Qiu, *The Journal of Physical Chemistry B*, **109** (43), 20310-20314 (2005).
142. S. Kim, J. Yan, B. Schwenzer, J. Zhang, L. Li, J. Liu, Z. G. Yang, and M. A. Hickner, *Electrochemistry Communications*, **12** (11), 1650-1653 (2010).
143. J. Xi, Z. Wu, X. Qiu, and L. Chen, *Journal of Power Sources*, **166** (2), 531-536 (2007).
144. Q. Luo, L. Li, Z. Nie, W. Wang, X. Wei, B. Li, B. Chen, and Z. Yang, *Journal of Power Sources*, **218** 15-20 (2012).
145. M. S. T. U. o. T. a. A. D. C. Sing, (2013).
146. J. S. Lawton, A. Jones, and T. Zawodzinski, *Journal of The Electrochemical Society*, **160** (4), A697-A702 (2013).
147. J. grosse Austing, C. N. Kirchner, L. Komsijska, and G. Wittstock, *Journal of Power Sources*, **306** 692-701 (2016).
148. L. Su, R. M. Darling, K. G. Gallagher, W. Xie, J. L. Thelen, A. F. Badel, J. L. Barton, K. J. Cheng, N. P. Balsara, and J. S. Moore, *Journal of The Electrochemical Society*, **163** (1), A5253-A5262 (2016).
149. Y. A. Gandomi and M. Mench, *under preparation* (2016).
150. J. Andre, N. Guillet, J.-P. Petit, and L. Antoni, *Journal of Fuel Cell Science and Technology*, **7** (4), 044501 (2010).
151. W. He and T. Van Nguyen, *Journal of The Electrochemical Society*, **151** (2), A185-A195 (2004).
152. E. Kjeang, R. Michel, D. A. Harrington, N. Djilali, and D. Sinton, *Journal of the American Chemical Society*, **130** (12), 4000-4006 (2008).
153. F. N. Büchi and G. G. Scherer, *Journal of the Electrochemical Society*, **148** (3), A183-A188 (2001).

154. M. Dollé, F. Orsini, A. S. Gozdz, and J.-M. Tarascon, *Journal of The Electrochemical Society*, **148** (8), A851-A857 (2001).
155. A. Küver, I. Vogel, and W. Vielstich, *Journal of power sources*, **52** (1), 77-80 (1994).
156. X. Ren, T. Springer, and S. Gottesfeld, *Journal of the Electrochemical Society*, **147** (1), 92-98 (2000).
157. G. Li and P. G. Pickup, *Electrochimica Acta*, **49** (24), 4119-4126 (2004).
158. T. Nann and G. A. Urban, *Sensors and Actuators B: Chemical*, **70** (1), 188-195 (2000).
159. S. Adler, B. Henderson, M. Wilson, D. Taylor, and R. Richards, *Solid State Ionics*, **134** (1), 35-42 (2000).
160. J. Winkler, P. Hendriksen, N. Bonanos, and M. Mogensen, *Journal of the Electrochemical Society*, **145** (4), 1184-1192 (1998).
161. Q. Liu, G. Grim, A. Papandrew, A. Turhan, T. A. Zawodzinski, and M. M. Mench, *Journal of The Electrochemical Society*, **159** (8), A1246-A1252 (2012).
162. D. S. Aaron, Z. Tang, J. S. Lawton, A. P. Papandrew, and T. A. Zawodzinski, *ECS Transactions*, **41** (23), 43-51 (2012).
163. I. Frateur, E. Bayet, M. Keddad, and B. Tribollet, *Electrochemistry communications*, **1** (8), 336-340 (1999).
164. Q. Liu, A. Turhan, T. A. Zawodzinski, and M. M. Mench, *Chemical Communications*, **49** (56), 6292-6294 (2013).
165. L. Minghua and T. Hikiyara, *IEICE transactions on fundamentals of electronics, communications and computer sciences*, **91** (7), 1741-1747 (2008).
166. A. Shah, M. Watt-Smith, and F. Walsh, *Electrochimica Acta*, **53** (27), 8087-8100 (2008).
167. M. Vynnycky, *Energy*, **36** (4), 2242-2256 (2011).
168. X. Ma, H. Zhang, and F. Xing, *Electrochimica Acta*, **58** 238-246 (2011).
169. Q. Xu, T. Zhao, and P. Leung, *Applied Energy*, **105** 47-56 (2013).
170. Q. Xu, T. Zhao, and C. Zhang, *Applied Energy*, **130** 139-147 (2014).
171. K. Oh, H. Yoo, J. Ko, S. Won, and H. Ju, *Energy*, (2014).
172. Y. Wang and S. C. Cho, *Journal of The Electrochemical Society*, **161** (9), A1200-A1212 (2014).
173. M. Skyllas-Kazacos and L. Goh, *Journal of Membrane Science*, **399** 43-48 (2012).
174. K. Knehr, E. Agar, C. Dennison, A. Kalidindi, and E. Kumbur, *Journal of The Electrochemical Society*, **159** (9), A1446-A1459 (2012).
175. X.-G. Yang, Q. Ye, P. Cheng, and T. S. Zhao, *Applied Energy*, **145** 306-319 (2015).
176. R. M. Darling, A. Z. Weber, M. C. Tucker, and M. L. Perry, *Journal of The Electrochemical Society*, **163** (1), A5014-A5022 (2016).
177. J. T. Gostick and A. Z. Weber, *Electrochimica Acta*, (2015).
178. T. F. Fuller, (1992).
179. Y. A. Gandomi, T. A. Zawodzinski, and M. M. Mench, *ECS Transactions*, **61** (13), 23-32 (2014).

180. A. Z. Weber and J. Newman, *Journal of the Electrochemical Society*, **151** (2), A311-A325 (2004).
181. Y. Ashraf Gandomi, in "228th ECS Meeting (October 11-15, 2015)". Ecs, 2015.
182. J. Newman and K. E. Thomas-Alyea, *Electrochemical systems*, John Wiley & Sons (2012).
183. P. Xu and B. Yu, *Advances in water resources*, **31** (1), 74-81 (2008).
184. D. M. Bernardi and M. W. Verbrugge, *AIChE journal*, **37** (8), 1151-1163 (1991).
185. J. L. Fales and N. Vandeborough, in "Electrochem. Soc. Proc", Vol. 86, p. 179-191, 1986.
186. M. W. Verbrugge and R. F. Hill, *Journal of the Electrochemical Society*, **137** (3), 886-893 (1990).
187. M. Gattrell, J. Park, B. MacDougall, J. Apte, S. McCarthy, and C. Wu, *Journal of the Electrochemical Society*, **151** (1), A123-A130 (2004).
188. A. Shah, R. Tangirala, R. Singh, R. Wills, and F. Walsh, *Journal of the Electrochemical society*, **158** (6), A671-A677 (2011).
189. T. Yamamura, N. Watanabe, T. Yano, and Y. Shiokawa, *Journal of The Electrochemical Society*, **152** (4), A830-A836 (2005).
190. C. Blanc. Ecole Polytechnique Fédérale de Lausanne, 2009.
191. G. Oriji, Y. Katayama, and T. Miura, *Electrochimica Acta*, **49** (19), 3091-3095 (2004).
192. D. Knopf, B. Luo, U. Krieger, and T. Koop, *The Journal of Physical Chemistry A*, **107** (21), 4322-4332 (2003).
193. C. L. Chen, H. K. Yeoh, and M. H. Chakrabarti, *Electrochimica Acta*, **120** 167-179 (2014).
194. K. Knehr and E. Kumbur, *Electrochemistry Communications*, **13** (4), 342-345 (2011).
195. A. J. Bard, L. R. Faulkner, J. Leddy, and C. G. Zoski, *Electrochemical methods: fundamentals and applications*, Wiley New York (1980).
196. D. You, H. Zhang, and J. Chen, *Electrochimica Acta*, **54** (27), 6827-6836 (2009).
197. D. Schmal, J. Van Erkel, and P. Van Duin, *Journal of applied electrochemistry*, **16** (3), 422-430 (1986).
198. M. W. Verbrugge and R. F. Hill, *The Journal of Physical Chemistry*, **92** (23), 6778-6783 (1988).
199. M. W. Verbrugge and R. F. Hill, *Journal of the Electrochemical Society*, **137** (4), 1131-1138 (1990).
200. Z. Tang, R. Svoboda, J. S. Lawton, D. S. Aaron, A. B. Papandrew, and T. A. Zawodzinski, *Journal of The Electrochemical Society*, **160** (9), F1040-F1047 (2013).
201. D. Aaron, C.-N. Sun, M. Bright, A. B. Papandrew, M. M. Mench, and T. A. Zawodzinski, *ECS Electrochemistry Letters*, **2** (3), A29-A31 (2013).
202. Y. A. Gandomi, D. Aaron, and M. Mench, *Electrochimica Acta*, **218** 174-190 (2016).
203. Y. Zhao, M. Li, Z. Yuan, X. Li, H. Zhang, and I. F. Vankelecom, *Advanced Functional Materials*, **26** (2), 210-218 (2016).

204. J. S. Lawton, A. M. Jones, Z. Tang, M. Lindsey, C. Fujimoto, and T. A. Zawodzinski, *Journal of The Electrochemical Society*, **163** (1), A5229-A5235 (2016).
205. S. Logette, C. Eysseric, G. Pourcelly, A. Lindheimer, and C. Gavach, *Journal of membrane science*, **144** (1), 259-274 (1998).
206. G. Pourcelly, P. Sistat, A. Chapotot, C. Gavach, and V. Nikonenko, *Journal of membrane science*, **110** (1), 69-78 (1996).
207. M. Vijayakumar, M. Bhuvaneshwari, P. Nachimuthu, B. Schwenzer, S. Kim, Z. Yang, J. Liu, G. L. Graff, S. Thevuthasan, and J. Hu, *Journal of Membrane Science*, **366** (1), 325-334 (2011).
208. R. Barklie, O. Girard, and O. Braddell, *The Journal of Physical Chemistry*, **92** (5), 1371-1377 (1988).
209. R. M. Darling and M. L. Perry, *ECS Transactions*, **53** (7), 31-38 (2013).
210. R. A. Potash, J. R. McKone, S. Conte, and H. D. Abruña, *Journal of The Electrochemical Society*, **163** (3), A338-A344 (2016).
211. S. Won, K. Oh, and H. Ju, *Electrochimica Acta*, (2015).
212. G. Qiu, A. S. Joshi, C. Dennison, K. Knehr, E. Kumbur, and Y. Sun, *Electrochimica Acta*, **64** 46-64 (2012).
213. P. A. Boettcher, E. Agar, C. Dennison, and E. C. Kumbur, *Journal of The Electrochemical Society*, **163** (1), A5244-A5252 (2016).
214. N. Berezina, S. Timofeev, and N. Kononenko, *Journal of membrane science*, **209** (2), 509-518 (2002).
215. J. E. Hensley, J. D. Way, S. F. Dec, and K. D. Abney, *Journal of membrane science*, **298** (1), 190-201 (2007).
216. W. Xie, G. M. Geise, B. D. Freeman, C. H. Lee, and J. E. McGrath, *Polymer*, **53** (7), 1581-1592 (2012).
217. Q. Luo, L. Li, W. Wang, Z. Nie, X. Wei, B. Li, B. Chen, Z. Yang, and V. Sprenkle, *ChemSusChem*, **6** (2), 268-274 (2013).
218. Y. A. Gandomi, M. Edmundson, F. Busby, and M. M. Mench, *Journal of The Electrochemical Society*, **163** (8), F933-F944 (2016).
219. J. Luo, O. Conrad, and I. F. Vankelecom, *Journal of Materials Chemistry A*, **1** (6), 2238-2247 (2013).
220. J. T. Clement, D. S. Aaron, and M. M. Mench, *Journal of The Electrochemical Society*, **163** (1), A5220-A5228 (2016).
221. J. T. Clement, (2016).
222. X. Ke, J. M. Prael, J. I. D. Alexander, and R. F. Savinell, *Journal of Power Sources*, **384** 295-302 (2018).
223. J. Houser, J. Clement, A. Pezeshki, and M. M. Mench, *Journal of Power Sources*, **302** 369-377 (2016).
224. C. Dennison, E. Agar, B. Akuzum, and E. Kumbur, *Journal of The Electrochemical Society*, **163** (1), A5163-A5169 (2016).
225. J. Houser, A. Pezeshki, J. T. Clement, D. Aaron, and M. M. Mench, *Journal of Power Sources*, **351** 96-105 (2017).

226. T. J. Latha and S. Jayanti, *Journal of Applied Electrochemistry*, **44** (9), 995-1006 (2014).
227. D. Reed, E. Thomsen, B. Li, W. Wang, Z. Nie, B. Koepfel, and V. Sprenkle, *Journal of Power Sources*, **306** 24-31 (2016).
228. Q. Xu, T. Zhao, and C. Zhang, *Electrochimica Acta*, **142** 61-67 (2014).
229. J. L. Barton, J. D. Milshtein, J. J. Hinricher, and F. R. Brushett, *Journal of Power Sources*, **399** 133-143 (2018).
230. E. C. Montoto, G. Nagarjuna, J. Hui, M. Burgess, N. M. Sekerak, K. Hernández-Burgos, T.-S. Wei, M. Kneer, J. Grolman, and K. J. Cheng, *Journal of the American Chemical Society*, **138** (40), 13230-13237 (2016).
231. M. Burgess, J. S. Moore, and J. Rodríguez-López, *Accounts of chemical research*, **49** (11), 2649-2657 (2016).
232. G. Nagarjuna, J. Hui, K. J. Cheng, T. Lichtenstein, M. Shen, J. S. Moore, and J. Rodríguez-López, *Journal of the American Chemical Society*, **136** (46), 16309-16316 (2014).
233. S. E. Doris, A. L. Ward, A. Baskin, P. D. Frischmann, N. Gavvalapalli, E. Chénard, C. S. Sevov, D. Prendergast, J. S. Moore, and B. A. Helms, *Angewandte Chemie*, **129** (6), 1617-1621 (2017).
234. F.R.Brushett, *TALENTED TWELVE*, (2017).
235. G.-J. Hwang and H. Ohya, *Journal of membrane Science*, **132** (1), 55-61 (1997).
236. H. Mögelin, G. Yao, H. Zhong, A. dos Santos, A. Barascu, R. Meyer, S. Krenkel, S. Wassersleben, T. Hickmann, and D. Enke, *Journal of Power Sources*, **377** 18-25 (2018).
237. J. Vrána, J. Charvát, P. Mazúr, P. Bělský, J. Dundálek, J. Pocič, and J. Kosek, *Journal of Membrane Science*, **552** 202-212 (2018).
238. K. Wang, L. Liu, J. Xi, Z. Wu, and X. Qiu, *Journal of Power Sources*, **338** 17-25 (2017).
239. J. H. Park, J. J. Park, O. O. Park, and J. H. Yang, *ChemSusChem*, **9** (22), 3181-3187 (2016).
240. D. Mu, Y. Zhao, L. Yu, L. Liu, and J. Xi, *Physical Chemistry Chemical Physics*, **19** (43), 29195-29203 (2017).
241. S. Burlatsky, R. M. Darling, D. Novikov, V. V. Atrazhev, V. I. Sultanov, T. Y. Astakhova, L. Su, and F. Brushett, *Journal of The Electrochemical Society*, **163** (10), A2232-A2239 (2016).
242. Z. Deng and K. A. Mauritz, *Macromolecules*, **25** (10), 2739-2745 (1992).
243. Z. Lu, M. Lanagan, E. Manias, and D. Macdonald, *ECS Transactions*, **28** (29), 95-105 (2010).
244. M. Fasano, T. Humplik, A. Bevilacqua, M. Tsapatsis, E. Chiavazzo, E. N. Wang, and P. Asinari, *Nature communications*, **7** 12762 (2016).
245. F. Rahman and M. Skyllas-Kazacos, *Journal of Power Sources*, **189** (2), 1212-1219 (2009).
246. T. A. Zawodzinski Jr, M. Neeman, L. O. Sillerud, and S. Gottesfeld, *The Journal of Physical Chemistry*, **95** (15), 6040-6044 (1991).

247. M. Doyle, M. E. Lewittes, M. G. Roelofs, and S. A. Perusich, *The Journal of Physical Chemistry B*, **105** (39), 9387-9394 (2001).
248. Y. Sone, P. Ekdunge, and D. Simonsson, *Journal of The Electrochemical Society*, **143** (4), 1254-1259 (1996).
249. J. Landesfeind, J. Hattendorff, A. Ehrl, W. A. Wall, and H. A. Gasteiger, *Journal of The Electrochemical Society*, **163** (7), A1373-A1387 (2016).
250. J. A. Kowalski, M. D. Casselman, A. P. Kaur, J. D. Milshtein, C. F. Elliott, S. Modekrutti, N. H. Attanayake, N. Zhang, S. R. Parkin, and C. Risko, *Journal of Materials Chemistry A*, **5** (46), 24371-24379 (2017).
251. S. A. Odom, A. P. Kaur, M. D. Casselman, N. H. Attanayake, J. Anthony, and F. R. Brushett, *ECS Transactions*, **77** (11), 145-151 (2017).
252. M. Doyle, M. E. Lewittes, M. G. Roelofs, S. A. Perusich, and R. E. Lowrey, *Journal of Membrane Science*, **184** (2), 257-273 (2001).
253. S. Sachan, C. A. Ray, and S. A. Perusich, *Polymer Engineering & Science*, **42** (7), 1469-1480 (2002).
254. R. J. Klein and J. Runt, *The Journal of Physical Chemistry B*, **111** (46), 13188-13193 (2007).
255. I. L. Escalante-García, J. S. Wainright, L. T. Thompson, and R. F. Savinell, *Journal of The Electrochemical Society*, **162** (3), A363-A372 (2015).
256. R. Semino, G. Zaldívar, E. J. Calvo, and D. Laria, *The Journal of chemical physics*, **141** (21), 214509 (2014).
257. X. Li, F. Li, Y. Shi, Q. Chen, and H. Sun, *Physical Chemistry Chemical Physics*, **12** (43), 14543-14552 (2010).
258. K. R. Hinkle, C. J. Jameson, and S. Murad, *The Journal of Physical Chemistry C*, **118** (41), 23803-23810 (2014).
259. J. Liu, N. Suraweera, D. J. Keffer, S. Cui, and S. J. Paddison, *The Journal of Physical Chemistry C*, **114** (25), 11279-11292 (2010).
260. C. R. Buie, J. D. Posner, T. Fabian, S.-W. Cha, D. Kim, F. B. Prinz, J. K. Eaton, and J. G. Santiago, *Journal of Power Sources*, **161** (1), 191-202 (2006).
261. S. Ge, X. Li, and I.-M. Hsing, *Electrochimica Acta*, **50** (9), 1909-1916 (2005).
262. S.-H. Ge, X.-G. Li, and I.-M. Hsing, *Journal of the Electrochemical Society*, **151** (9), B523-B528 (2004).
263. S. Litster, C. R. Buie, and J. G. Santiago, *Electrochimica Acta*, **54** (26), 6223-6233 (2009).
264. J. S. Yi, J. D. Yang, and C. King, *AIChE journal*, **50** (10), 2594-2603 (2004).
265. S. Litster, C. R. Buie, T. Fabian, J. K. Eaton, and J. G. Santiago, *Journal of The Electrochemical Society*, **154** (10), B1049-B1058 (2007).
266. A. Z. Weber, R. L. Borup, R. M. Darling, P. K. Das, T. J. Dursch, W. Gu, D. Harvey, A. Kusoglu, S. Litster, and M. M. Mench, *Journal of The Electrochemical Society*, **161** (12), F1254-F1299 (2014).
267. U. Pasaogullari and C.-Y. Wang, *Electrochimica Acta*, **49** (25), 4359-4369 (2004).
268. A. Z. Weber and J. Newman, *Journal of the Electrochemical Society*, **152** (4), A677-A688 (2005).

269. Q. Yan, H. Toghiani, and J. Wu, *Journal of Power Sources*, **158** (1), 316-325 (2006).
270. R. Zaffou, S. Y. Jung, H. R. Kunz, and J. M. Fenton, *Electrochemical and Solid-State Letters*, **9** (9), A418-A422 (2006).
271. H. K. Atiyeh, K. Karan, B. Peppley, A. Phoenix, E. Halliop, and J. Pharoah, *Journal of Power Sources*, **170** (1), 111-121 (2007).
272. D. Spornjak, A. K. Prasad, and S. G. Advani, *Journal of Power Sources*, **170** (2), 334-344 (2007).
273. A. Husar, A. Higier, and H. Liu, in "ASME 2007 International Mechanical Engineering Congress and Exposition", p. 1381-1389. American Society of Mechanical Engineers, 2007.
274. J. T. Gostick, M. A. Ioannidis, M. W. Fowler, and M. D. Pritzker, *Electrochemistry Communications*, **11** (3), 576-579 (2009).
275. J. M. LaManna, J. V. Bothe, F. Y. Zhang, and M. M. Mench, *Journal of Power Sources*, **271** 180-186 (2014).
276. S. Kim and M. Mench, *Journal of The Electrochemical Society*, **156** (3), B353-B362 (2009).
277. S. Kim and M. Mench, *Journal of Membrane Science*, **328** (1-2), 113-120 (2009).
278. D. Malevich, E. Halliop, B. A. Peppley, J. G. Pharoah, and K. Karan, *Journal of The Electrochemical Society*, **156** (2), B216-B224 (2009).
279. T. Kim, S. Lee, and H. Park, *international journal of hydrogen energy*, **35** (16), 8631-8643 (2010).
280. J. P. Owejan, J. E. Owejan, W. Gu, T. A. Trabold, T. W. Tighe, and M. F. Mathias, *Journal of The Electrochemical Society*, **157** (10), B1456-B1464 (2010).
281. R. Schweiss, *Fuel cells*, **16** (1), 100-106 (2016).
282. T. A. Zawodzinski, J. Davey, J. Valerio, and S. Gottesfeld, *Electrochimica Acta*, **40** (3), 297-302 (1995).
283. S. Motupally, A. J. Becker, and J. W. Weidner, *Journal of The Electrochemical Society*, **147** (9), 3171-3177 (2000).
284. M. D. Edmundson, T. Tomiie, and F. Busby, *ECS Transactions*, **33** (1), 1297-1307 (2010).
285. U. Beuscher, *Journal of The Electrochemical Society*, **153** (9), A1788-A1793 (2006).
286. M. Khandelwal and M. Mench, *Journal of Power Sources*, **161** (2), 1106-1115 (2006).
287. A. Srouji, L. Zheng, R. Dross, A. Turhan, and M. Mench, *Journal of Power Sources*, **239** 433-442 (2013).
288. E. W. Hooijschuur, C. E. Kientz, and A. Udo, *Journal of Chromatography A*, **982** (2), 177-200 (2002).
289. Y. Wang, Z. Yang, Z. Hou, D. Xu, L. Wei, E. S.-W. Kong, and Y. Zhang, *Sensors and Actuators B: Chemical*, **150** (2), 708-714 (2010).
290. Q. Zheng, Y.-c. Fu, and J.-q. Xu, *Procedia Engineering*, **7** 179-184 (2010).
291. T. J. Dale and J. Rebek Jr, *Angewandte Chemie*, **121** (42), 7990-7992 (2009).

292. X. Du, Z. Ying, Y. Jiang, Z. Liu, T. Yang, and G. Xie, *Sensors and Actuators B: Chemical*, **134** (2), 409-413 (2008).
293. C. Hartmann-Thompson, J. Hu, S. N. Kaganove, S. E. Keinath, D. L. Keeley, and P. R. Dvornic, *Chemistry of materials*, **16** (25), 5357-5364 (2004).
294. J. G. Hester, M. M. Tentzeris, and Y. Fang, in "Microwave Conference (EuMC), 2015 European", p. 857-860. IEEE, 2015.
295. X. Ji, J. Zheng, J. Xu, V. K. Rastogi, T.-C. Cheng, J. J. DeFrank, and R. M. Leblanc, *The Journal of Physical Chemistry B*, **109** (9), 3793-3799 (2005).
296. C. Karnati, H. Du, H.-F. Ji, X. Xu, Y. Lvov, A. Mulchandani, P. Mulchandani, and W. Chen, *Biosensors and Bioelectronics*, **22** (11), 2636-2642 (2007).
297. J. Liu and Y. Lu, *Sensors*, **14** (4), 6844-6853 (2014).
298. E. Snow, F. Perkins, E. Houser, S. Badescu, and T. Reinecke, *Science*, **307** (5717), 1942-1945 (2005).
299. F. Wang, H. Gu, and T. M. Swager, *Journal of the American Chemical Society*, **130** (16), 5392-5393 (2008).
300. J. S. Lee, O. S. Kwon, S. J. Park, E. Y. Park, S. A. You, H. Yoon, and J. Jang, *ACS Nano*, **5** (10), 7992-8001 (2011).
301. C. Zheng, A. Hu, K. D. Kihm, Q. Ma, R. Li, T. Chen, and W. Duley, *Small*, **11** (25), 3007-3016 (2015).
302. C. Cheng, S. Wang, J. Wu, Y. Yu, R. Li, S. Eda, J. Chen, G. Feng, B. Lawrie, and A. Hu, *ACS applied materials & interfaces*, **8** (28), 17784-17792 (2016).
303. G. Kosolapoff, p. 2964-2965. ROYAL SOC CHEMISTRY THOMAS GRAHAM HOUSE, SCIENCE PARK, MILTON RD, CAMBRIDGE CB4 0WF, CAMBS, ENGLAND, 1955.
304. F.-J. Ma, S.-X. Liu, C.-Y. Sun, D.-D. Liang, G.-J. Ren, F. Wei, Y.-G. Chen, and Z.-M. Su, *Journal of the American Chemical Society*, **133** (12), 4178-4181 (2011).

APPENDICES

Appendix A

Assessing the Limits of Water Management using Asymmetric Micro-Porous Layer Configurations

Yasser Ashraf Gandomi^a, Matthew M. Mench^{a, b}

^a The Electrochemical Energy Storage and Conversion Laboratory, Department of Mechanical, Aerospace and Biomedical Engineering, University of Tennessee, Knoxville, Tennessee 37996, USA

^b Energy and Transportation Science Division, Oak Ridge National Laboratory, Oak Ridge, Tennessee 37831, USA

Abstract

In high-power polymer electrolyte fuel cell systems, prevention of anode dry-out through enhanced back flux of water and restriction of evaporative losses is needed. One potential method to engineer the back flux of water to the anode is to utilize an asymmetric anode and cathode micro-porous layer configuration to independently tailor anode and cathode thermal and mass transport resistances. Extensive experimental tests have been performed to study the impact of asymmetric MPL configuration on the net water drag coefficient using sets of MPL with different thermal and mass transport resistances. It was observed that with asymmetric MPL alignment between the anode and cathode, the net water drag coefficient could be significantly altered, opening the door to enhanced high power performance at anode-dryout conditions.

Introduction

Water management remains an important topic in polymer electrolyte fuel cell (PEFC) systems. For polymer electrolyte fuel cells, proper water management is critical in order to keep the membrane hydrated enough to maintain ionic conductivity while ensuring liquid

removal to prevent flooding. Therefore, different water transport mechanisms within the PEFC should be well understood to optimize the performance. Water transport across the PEFC occurs by several driving modes including gradients in potential, concentration, temperature and pressure. These driving modes are shown schematically in Fig. A-1 and described in many publications. Recently, researchers working on high-power PEFC systems have recognized anode dry-out as a key limiting phenomenon ²⁸⁷. One potential method to engineer the back flux of water to the anode is to utilize an asymmetric anode and cathode micro-porous layer configuration. However, the relationship between mass and thermal resistances and overall water balance is complex and not completely understood, so that the impact of MPL configurations is not straightforward. The objective of this work is to understand the range of ability to engineer net water drag through asymmetric MPL configurations. Another objective is to reveal the interaction between thermal and mass transport resistance in water management and net water drag.

Experimental

Apparatus

The single cell used in this work has a single channel serpentine flow field and an active area of 5cm². All testing was conducted in galvanostatic mode. The membrane electrode assemblies (MEA) used had a catalyst loading of 0.3 mg Pt.cm⁻² for both anode and cathode sides. The macro diffusion media used on both electrodes was the same in all tests with a thickness of 165µm, but the micro-porous layers used were different for the anode and cathode electrodes, as summarized in Table A.1.

The fuel cell test station used was from Scribner Associates Inc. (Southern Pines, NC). For real time net water drag measurement, four calibrated dew point temperature sensors by Vaisala Inc. (Helsinki, Finland) were used to measure the dew point temperatures of the gases entering and exiting the anode and cathode of the PEFC, as shown in Fig. A-2.

Operating Conditions

Baseline operating conditions are summarized in Table A.2. The cell temperature for all the testing conditions was set to 80°C, with hydrogen (ultra-high purity) at the anode, and air (ultra-zero grade) at the cathode.

Constant anode and cathode stoichiometries of 4 were used for all the tests. The anode and cathode inlet relative humidities were both 100% at 80°C for the baseline conditions.

A back pressure of 50 kPa (gauge pressure) was applied to both anode and cathode for all the tests. Different operating conditions (OC) used for net water drag testing are listed in Table A.3. All operating parameters in these tests are identical to the baseline, with the exception of the relative humidity conditions shown.

Table A.1. Micro-Porous Layer (MPL) Properties.

GDL type	Thickness (μm)	Thermal Conductivity (W/(m.K))	Porosity (-)
MPL1	45	0.12	0.83
MPL2	70	0.13	0.83
MPL3	45	0.24	0.74

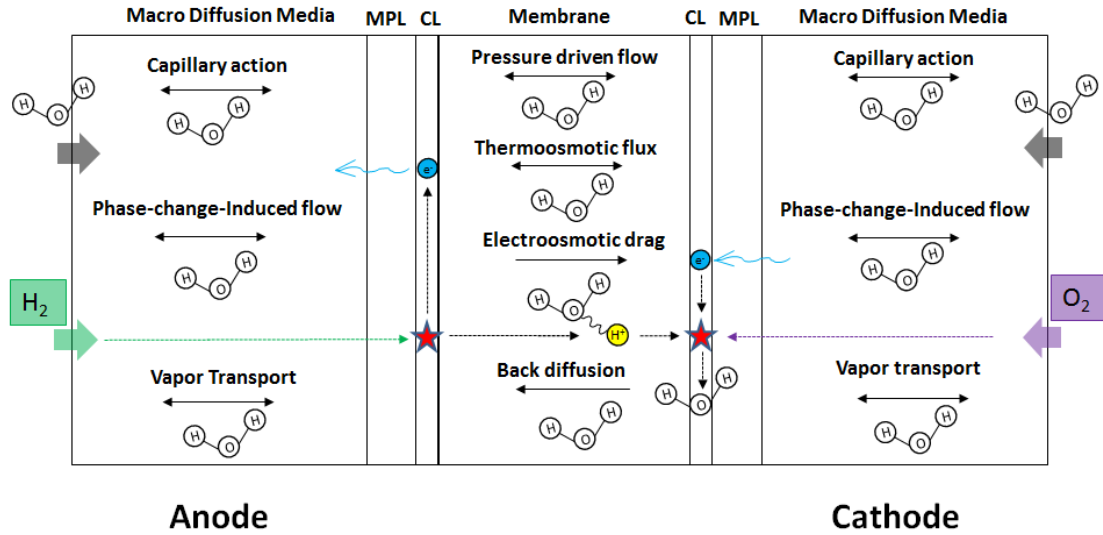


Figure A-2: Different modes of water transport in through-plane direction of a PEFC

PEFC Configurations

The different combinations of MPLs used to examine impact of the MPL on net water drag are listed in Table A.4.

Net Water Drag Calculations

The net water drag (NWD) is defined as the net water transferred across the membrane, and includes the combined effects of all modes of transport in the membrane. Accordingly, considering the conservation of mass on the water in the anode, the net water drag coefficient (C_{NWD}) is defined according to the following :

$$C_{NWD} = \frac{\dot{n}_{H_2O}^{in,an} - \dot{n}_{H_2O}^{out,an}}{\frac{iA}{F}} \quad [1]$$

According to Eq. (1), a positive net water drag coefficient implies an overall water transport from the anode to the cathode, and for a negative net water drag coefficient, there is a net transport from cathode to the anode.

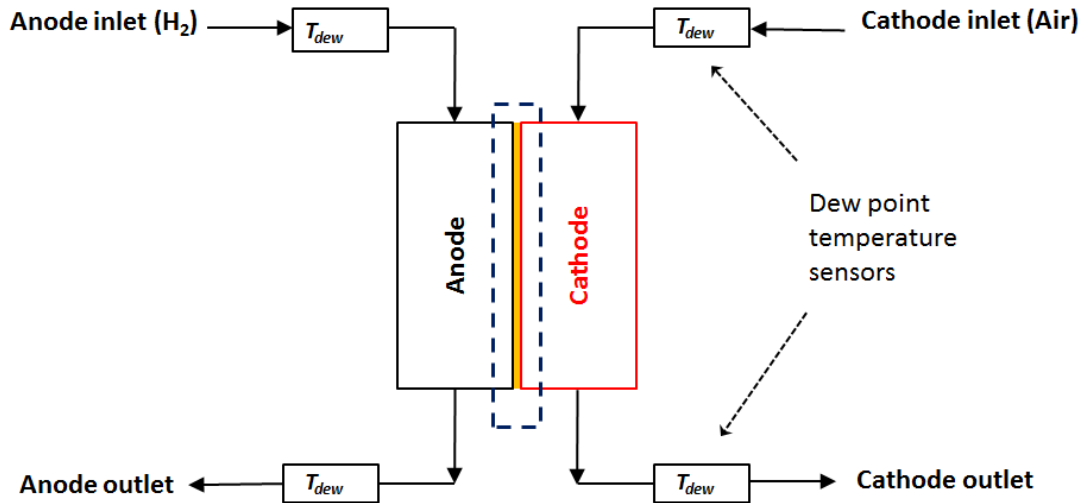


Figure A-3: Schematic representation of PEFC with in-line dew point temperature sensors

Careful heating of dew point sensors and exit lines is required to enable the dew point sensors to compute the net water drag coefficient in real-time. The dew point sensor at the anode inlet is used to determine the inlet water vapor flow rate based on the following (22).

$$\dot{n}_{H_2O}^{in,an} = \lambda_{H_2} \frac{iA}{2F} \frac{P_{sat}(T_{dew,an,in})}{[P - P_{sat}(T_{dew,an,in})]} \quad [2]$$

A similar approach is used to calculate the outlet water vapor flow rate at the anode. The dew point temperature sensors are also used in the reactant flow lines to calculate the water vapor flow rates in the inlet and outlet of cathode. A calculation at steady state following Equation 3 below is performed to verify that the total mass is conserved and the gauges are functioning properly.

$$\dot{n}_{H_2O}^{in,an} + \dot{n}_{H_2O}^{in,cat} + \dot{n}_{H_2O}^{gen} = \dot{n}_{H_2O}^{out,an} + \dot{n}_{H_2O}^{out,cat} \quad [3]$$

Table A.2. Baseline operating conditions

	Anode	Cathode
Gas stoichiometry	4	4
Relative humidity	100%	100%
Inlet pressure (kPa, absolute)	150	150

Table A.3. Operating conditions for net water drag calculations

	Relative Humidity (Anode/Cathode)
OC 1 (Baseline)	100% / 100%
OC 2 (Dry condition)	50% / 50%
OC 3 (Super Dry condition)	50% / Dry

Table A.4. PEFC configurations

	Anode	Cathode
Configuration 1 (symmetric)	MPL1	MPL1
Configuration 2 (asymmetric)	MPL1	MPL3
Configuration 3 (symmetric)	MPL2	MPL2
Configuration 4 (asymmetric)	MPL2	MPL1

Results and Discussion

Four different configurations of cells were built and tested, as described in Table A.4. Polarization curves and water drag coefficients were obtained for different configurations and operating conditions.

A comparison of polarization curves for “PEFC Configuration 1” and “PEFC Configuration 2” is shown in Fig. A-3. Configuration 1 was symmetric configuration and configuration 2 was asymmetric where the MPL thickness was the same but porosity and thermal conductivity was different. According to Fig. A-1, applying asymmetric MPL configuration increased the overall performance of the cell, especially in dryer conditions.

A comparison of “PEFC Configuration 3” versus “PEFC Configuration 4” is shown in Fig. A-4. The difference of configuration 3 and 4 is a thinner MPL in the cathode side for configuration 4 (asymmetric) compared to configuration 3 (symmetric).

As seen in Figure A-4, the asymmetric configuration improved the overall performance. Also, according to Fig. A-4, it is clear that the cell performance is affected by the flooding for the symmetric configuration when the cell is operating in wet conditions. A comparison of water drag coefficients is shown for “PEFC Configuration 1” versus “PEFC Configuration 2” in Fig. A-5.

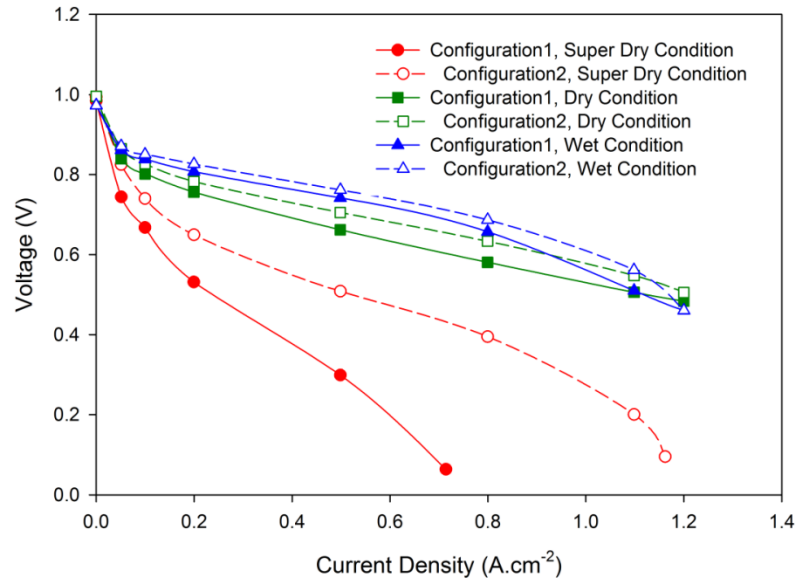


Figure A-4: Polarization curves for different operating conditions and MPL configuration

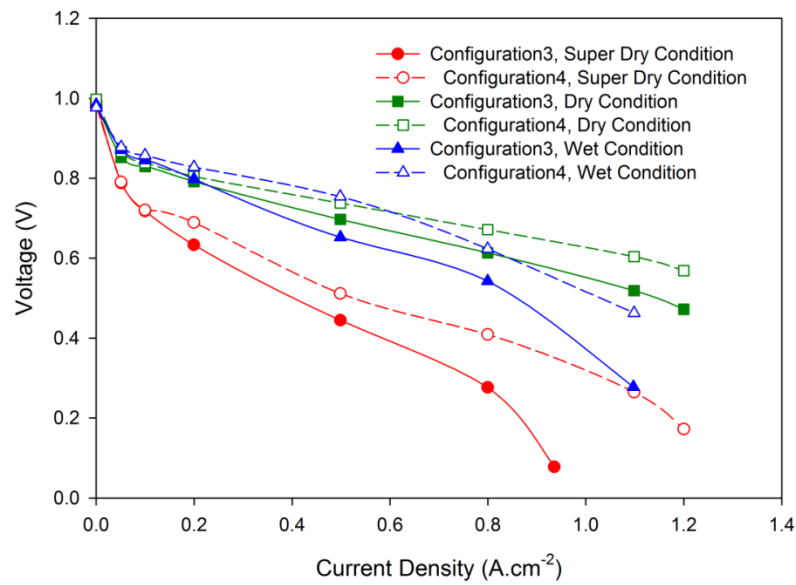


Figure A-5: Polarization curves for "PEFC configuration 3" versus "PEFC configuration 4" for different operating conditions and MPL configurations

Configuration 1 utilizes symmetric configuration while configuration 2 has asymmetric set. The thickness of the MPL is the same for two configurations but the thermal conductivity of the configuration 3 is higher, with lower porosity compared to configuration 1. For OC3, the net water drag coefficient is reduced when the asymmetric configuration was used. In other words, the net water towards the anode has increased.

In the porous electrode, MPL, and diffusion media, phase-change-induced (PCI) flow, gas-phase transport through diffusion or convection, and capillary action impact water transport and distribution. Therefore, alteration of either the thermal or mass transport resistance in the MPL is expected to impact the overall water balance, as shown here. More work is ongoing to more clearly separate the roles of the individual thermal or mass transport resistances on the net transport. The results shown here however, indicate that the net water drag can be engineered to some degree through MPL thermal or mass transport properties.

A comparison of calculated steady state water drag coefficients is shown in Fig. A-6. This figure compares the symmetric PEFC Configuration 3 to the asymmetric PEFC Configuration 4 which has a thinner, lower thermal conductivity cathode MPL compared to configuration 3. Similar to previous case, the asymmetric MPL configuration resulted in decreased water flux toward the cathode in dryer environments, although the trend was reversed in a wet environment.

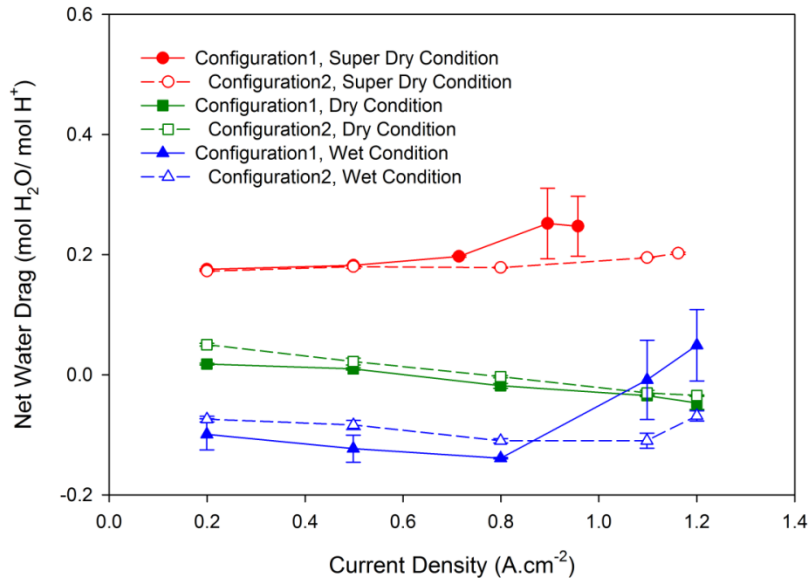


Figure A-6: Net water drag coefficients for “PEFC configuration 1” versus “PEFC configuration 2” for different operating conditions

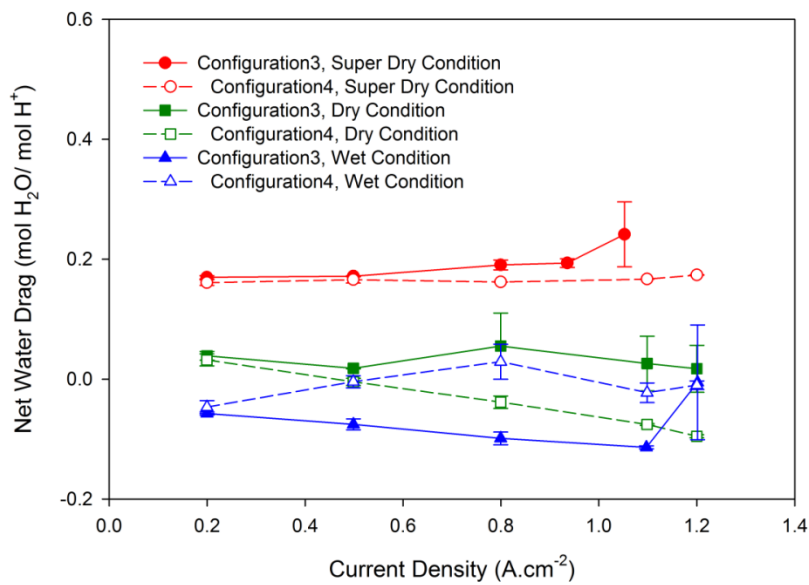


Figure A-7: Net water drag coefficients for “PEFC configuration 3” versus “PEFC configuration 4” for different operating conditions

For the wet operating condition, since the MPL used in the cathode side is thinner with the same porosity compared to the symmetric case, the water flux based on capillary action is higher from the cathode electrode towards the gas diffusion media resulting in a higher net water drag coefficient.

Conclusions

Four different configurations of PEFC were built and tested under dry and wet operating conditions with micro-porous layers engineered with varying thermal and mass transport properties to measure the impact of these transport resistances on net water transport across the membrane of an operating cell. The results clearly indicate that the MPL selection can influence the total water transport, and an asymmetric MPL configuration can be used to further adjust the net water drag to maximize performance. Additional work is ongoing to fully discern the impacts of the thermal and mass transport resistances and will be reported in a subsequent publication.

Appendix B

Fast Response Micro Scale Gas-Phase Toxin Sensor

Yasser Ashraf Gandomi¹, Shutong Wang^{2,3}, Vidyacharan Gopaluni Venkata⁴, Yongchao Yu³, Ruo-Zhou Li³, Subhadeep Chakraborty³, Doug S. Aaron^{1,3}, Anming Hu^{3,5}, and Matthew M. Mench^{1,6}

¹

Electrochemical Energy Storage and Conversion Laboratory, Department of Mechanical, Aerospace and Biomedical Engineering, University of Tennessee, Knoxville, Tennessee, USA; yashraf@utk.edu; daaron@utk.edu; mmench@utk.edu

² College of Electronics and Information Engineering, Sichuan University, Chengdu, China; swang66@utk.edu

³ Department of Mechanical, Aerospace and Biomedical Engineering, University of Tennessee, USA; swang66@utk.edu; yyu6@utk.edu; llrzz@163.com; schakrab@utk.edu; daaron@utk.edu

⁴ Department of Mechanical Engineering, University of Colorado, Boulder, Colorado, USA; vidyacharan.gopaluniVenkata@colorado.edu

⁵ Institute of Laser Engineering, Beijing University of Technology, Chaoyang District, Beijing, China; ahu3@utk.edu

⁶ Energy and Transportation Science Division, Oak Ridge National Laboratory, Oak Ridge, Tennessee, USA; mmench@utk.edu

Abstract

Developing highly sensitive portable sensors for fast detection of toxic gases is of great importance. In this work, two configurations of laser-induced and copper-coated carbon interdigitated microelectrode sensors were developed. Dimethyl methylphosphonate (DMMP) was used as the simulant representing sarin gas. The sensors were exposed to DMMP at ambient and elevated temperature (60°C) and were subjected to a pulsed voltage excitation protocol. It was shown that the copper-coated, interdigitated sensors are capable of detecting DMMP with very high sensitivity at room temperature. The carbon interdigitated sensors in comparison to copper-coated sensors showed lower sensitivity but superior stability. The sensitivity of the sensors increased significantly with increased temperature and overvoltage. The basic selectivity of the sensors was confirmed in dry air, nitrogen, and humid air environments.

Introduction

Extremely toxic gases such as sarin, tabun, and soman directly attack the nervous system and lead to serious injury and death. Being colorless and odorless, the early detection of these toxic, organo-phosphorous compounds is very challenging. Traditional methods of detecting toxic gases and vapors involve gas/liquid chromatography, spectroscopy, and capillary electrophoresis ²⁸⁸. These techniques require specialized apparatus and trained personnel, are time consuming, and usually impractical in emergent situations. Therefore, there is a significant need for developing sensitive, selective, robust, and portable devices for fast and early detection of toxic gases ²⁸⁹.

These extremely toxic gases disrupt the nerve system and, therefore, direct use of them is not feasible in the University lab environments. Nerve agent Sarin (2-(fluoro-methyl-phosphoryl) oxypropane) belongs to the organophosphorus compounds family, recognized as among the deadliest gases. Considering sarin's high toxicity, DMMP (dimethyl methalposphonate) is widely used as a laboratory simulant because of its similar chemical structure and much lower toxicity. A comparison has been provided regarding the molecule structure of sarin and DMMP. Also, the utilization of DMMP as a simulant for Sarin has been widely demonstrated in previous works ²⁹⁰. Several approaches have already been developed for the detection of nerve agents including surface acoustic wave (SAW) sensors, microcantilever and chemiresistive sensors, colorimetric and enzymatic assays, fluorometric analysis, molecular imprinting, inkjet-printed carbon nanomaterial based sensors, gas and mass spectroscopy, and photoacoustic spectroscopy ²⁹¹⁻²⁹⁹. The application

of thin film sensors made with single wall carbon nanotubes and carbon nanofibers has also been demonstrated³⁰⁰.

A sensing mechanism of DMMP utilizing ultra-fine carbon nanofibers (CNFs) based on faradaic charge transfer has been demonstrated²⁹⁹. DMMP is believed to be a strong electron donor; when DMMP vapor comes in contact with CNFs, it is adsorbed on the surface and provides a continuous pathway for the charge transfer of the electrons from DMMP to the CNFs²⁹⁹. Such a mechanism is illustrated in Fig. B-1 from Ref [299]. Chemiresistive sensors developed for the detection of DMMP operate based on the principle of varying impedance. Initially, there is an impedance associated with the sensor; after exposure to a simulant vapor, a change in the impedance magnitude is used as the sensing mechanism²⁹⁹.

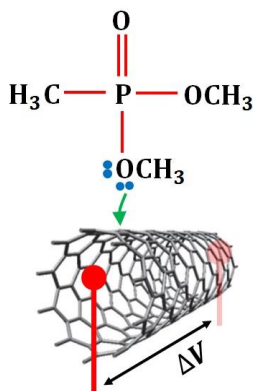


Figure B-1: Electrical conduction in carbon nanofiber exposed to DMMP vapor

299.

Although significant improvements have been made for the detection of DMMP using chemiresistive sensors, there exists a significant need for robust, highly sensitive, and more stable materials since these toxic gases are strongly corrosive and reactive. In this work, sensors consisting of pure carbon and copper-coated-on-carbon electrodes have been developed in the form of interdigitated electrodes on a polymer substrate, without any other functionalization or doping of the electrode material. Pure carbon sensors were chosen as the base material, and the copper-coated sensors were selected for high conductivity and low cost.

Experimental

Experimental set-up

Figure B-2 shows the experimental set-up: a sealed, air-tight reservoir contained in an environmental chamber (Thermal Product Solutions (TPS), Pennsylvania, USA) within which the sensor and DMMP were placed. To monitor the temperature of the DMMP solution in real time, a chemical-resistant thermocouple (OMEGA Engineering, INC., Connecticut, USA) was used.

A potentiostat (Bio-Logic, model SP240, France) was utilized to conduct the voltage-excitation experiments. DMMP was purchased from Alfa Aesar (97% concentration). To prepare for testing, dry nitrogen gas was purged through the reservoir.

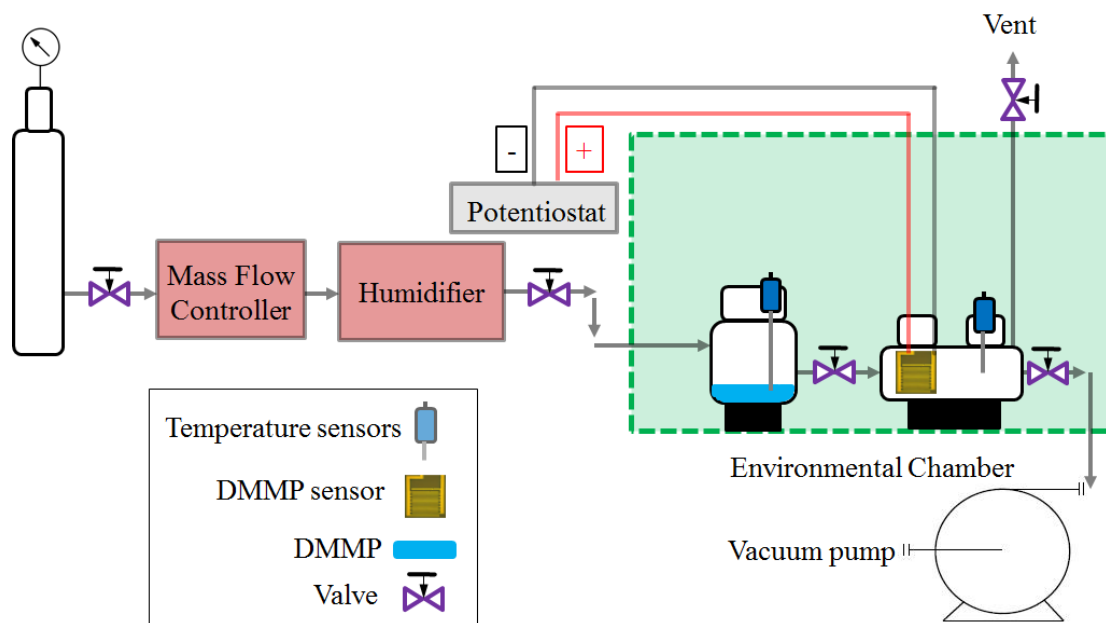


Figure B-2: Schematic of test setup.

Thereafter, liquid DMMP (10mL) was placed within a 250-mL reservoir while temperature and humidity were kept constant. The DMMP reservoir (250 mL) was thoroughly cleaned before and after each test to ensure that there was no residual DMMP in the system. As shown in Fig. B-2, all experiments were conducted using an environmental chamber in which the temperature was precisely controlled. Before exposing the sensors to DMMP gas vapor, sufficient time was given to achieve a stable temperature at 25 or 60°C. Prior to adopting the experimental set-up shown in Fig. B-2, other experimental set-ups equipped with mass flow controllers (MFCs) were also attempted. However, due to the severely corrosive nature of DMMP, all valves and other equipment in contact with DMMP vapor corroded during the experiment.

Fabrication and microstructure of sensors

A femtosecond laser (fs, Cazadero, Calmar Laser Inc.) was used to carbonize commercial flexible polyimide sheet (PI, Kapton, 100 μm thickness) to fabricate the gas sensors. The fs laser (1030 nm, 400 fs at a repetition rate of 120 kHz) was focused by a 20X microscope objective lens (NA=0.42) to irradiate PI sheet under ambient conditions, as shown in Fig. B-3(a). The fs laser power concentrated on the sample surface was 400 mW with an approximate spot size of 5 μm and 1 mm/s scanning speed. The PI sheet was mounted on a 2D-translation stage, which was controlled by a computer program. Before irradiation, the PI sheet was cleaned using ethanol and acetone.

Fig. B-3(b) illustrates the sensor patterned by the fs laser; the light orange region indicates pristine PI. Each laser induced sensor (LIS) was composed of 9 pairs of interdigitated microelectrodes with a size of 10 mm length, 100 μm width and 900 μm spacing between each electrode. Fig. B-3(d) is a SEM image of the porous flake morphology of irradiated regimes of LIS. Due to multi-photon absorption³⁰¹ and the thermal effect of high repetition rate fs laser, polyimide molecules initially dissociate and release gas molecules; then the carbonization process occurs, generating the porous flake surface morphology³⁰².

The copper-coated LIS sensor was prepared by electroplating Cu on the LIS surface. Fig. B-3(c) shows the two-electrode electroplating setup with a platinum wire as anode in 0.5 M CuSO₄ electroplating solution and the prepared LIS as the cathode. To ensure sufficient deposition of copper on the LIS surface, 30 mA/cm² constant current density was applied for 10 minutes. Then, deionized water was used to rinse off the residual plating solution

from the surface of LIS. Figure B-3(e) shows the SEM image of the LIS surface after copper plating. After plating, copper particles formed a dense film on the electrode's surface.

Test Protocol

To investigate the electrochemical performance of the interdigitated sensor configuration, it is necessary to distinguish the transient and steady -state current responses. Figure B-4 includes the response of an interdigitated sensor exposed to DMMP vapor and excited by a DC voltage step over multiple cycles. The current response of the cycle includes capacitive current followed by faradaic current.

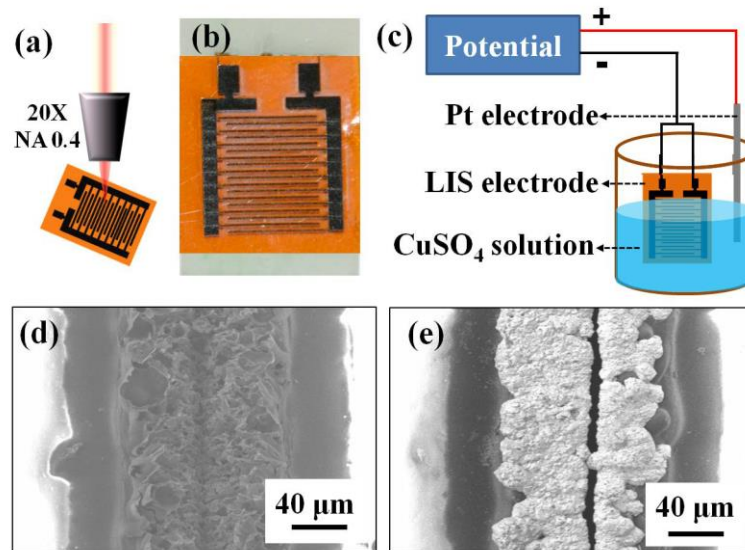


Figure B-3: Polarization curves (a) Schematic of the fs laser direct writing of sensor on a PI sheet, (b) a typical image of LIS, (c) Copper plating setup with two electrodes; (d) SEM images of the morphology of LIS before and (e) after copper coating.

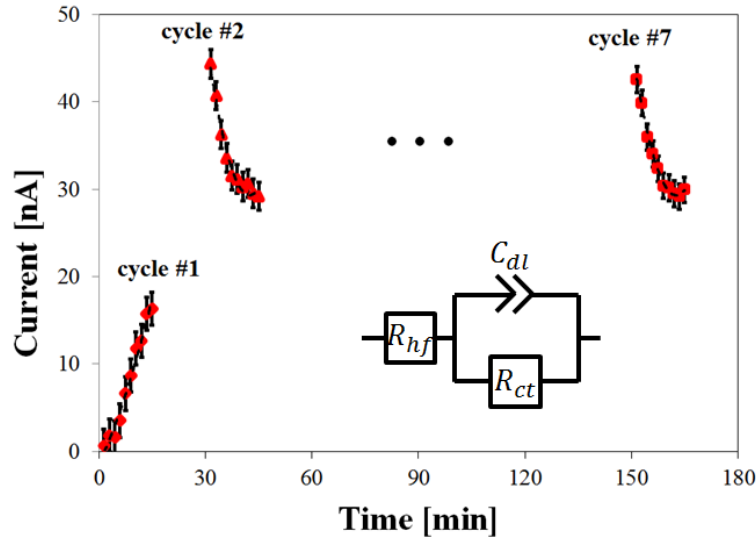


Figure B-4: A current response of the interdigitated sensor exposed to DMMP and excited by a DC voltage over multiple cycles and equivalent circuit model used to fit the data.

As shown in Fig. B-4, an equivalent circuit model can be used to fitting experimental data.

The equivalent circuit model includes high-frequency resistance (R_{hf}), charge transfer resistance (R_{ct}), and double layer capacitance (C_{dl}).

As shown in Fig. B-4, data acquisition begins as the sensor is exposed to DMMP stored within the reservoir. Initial contact with the DMMP vapor results in a rising current signal until a peak is reached. This is an indicator of homogeneous distribution of DMMP vapor which evolves within the reservoir during the first cycle. Therefore, the analysis here is focused on the signal response from 2nd and subsequent cycles only. Also, as shown in Fig. B-4, capacitive behavior is pronounced during the initial few seconds of the current response with an exponential damping followed by a steady state resistive response. In this work, we have focused on the resistive response.

In this work, a staircase pulsed voltage excitation protocol was applied to fully capture the voltage-dependence behavior (current-voltage (I-V) characteristics) of the sensor. As shown in Fig. B-5, the cycling was conducted by applying a DC voltage of 1, 3, 5, 7 and 9V for three minutes and resting for one minute at zero voltage.

Figure B-5 includes the staircase pulsed voltage excitation protocol used for investigating the current response of the interdigitated sensors exposed to DMMP vapor. The DC-voltage excitation protocol shown in Fig. B-5 was repeated for 7 cycles and the data analysis focused on the resistive response of cycle 2 through cycle 7. The output current was measured with the sampling rate of 10 Hz (with the resolution of 1 pA). This frequency measurement enables capturing the transient and steady-state behavior of the sensors.

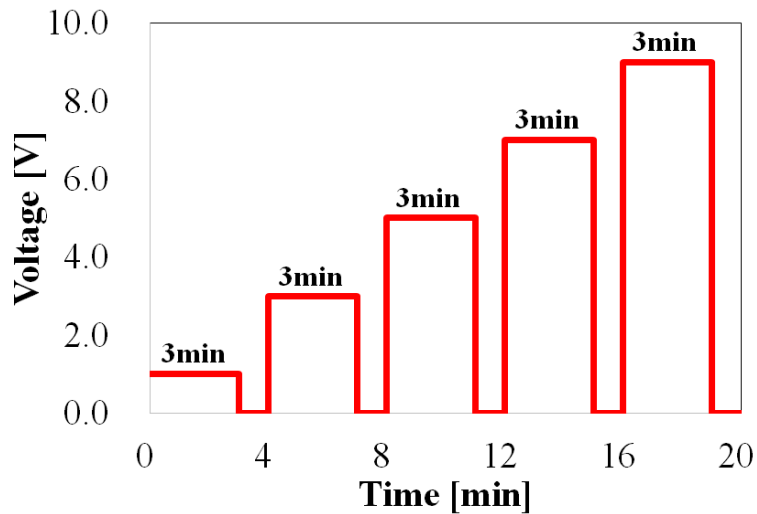


Figure B-5: Pulsed voltage excitation protocol.

Results

DMMP detection using carbon sensors

Figure B-6 exhibits the current response for the voltage excitations of the laser induced carbon sensors exposed to DMMP at two different temperatures. At steady-state, the volumetric concentration of DMMP was approximately 50 and 200 ppm for 25°C and 60°C, respectively, based on the difference between pre- and post-exposure mass. The saturated vapor pressure of DMMP can be obtained using the following equation developed by Kosolapoff³⁰³. This equation has also been verified and adopted by National Institute of Standards and Technology (NIST).

$$\log_{10}(P) = A - \left(\frac{B}{T + C}\right) \quad (1)$$

Where, P is the saturated vapor pressure of DMMP, T is the temperature and A , B and C are fitting parameters.

As shown in Fig. B-6, the current response of the carbon sensor has completely different trends as a function of temperature for the pulsed voltage excitation protocol. Here, the current response is solely due to the existence of DMMP as there are no other gases imposing a potential false-positive response; the selectivity of the sensor further was confirmed via exposure to basic gases at various operating conditions.

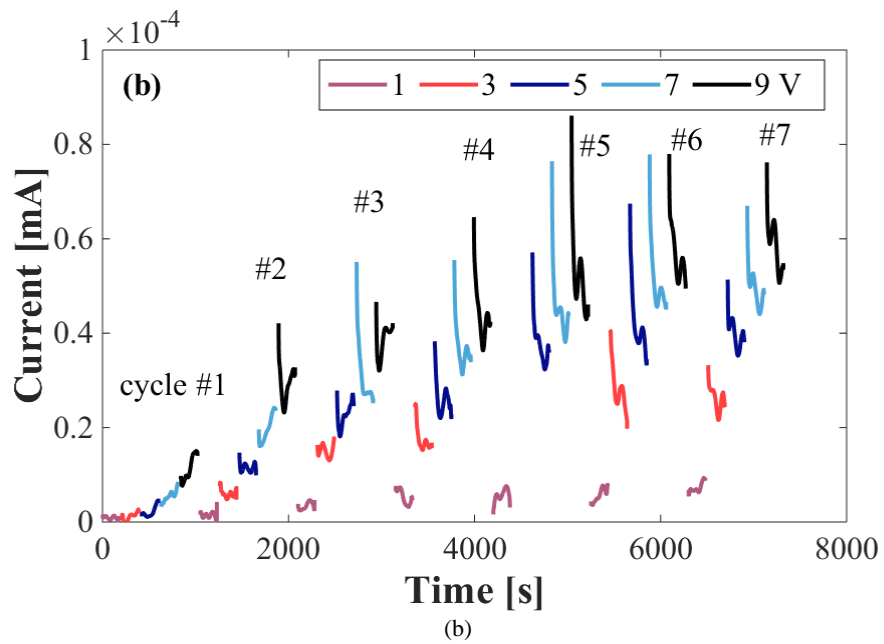
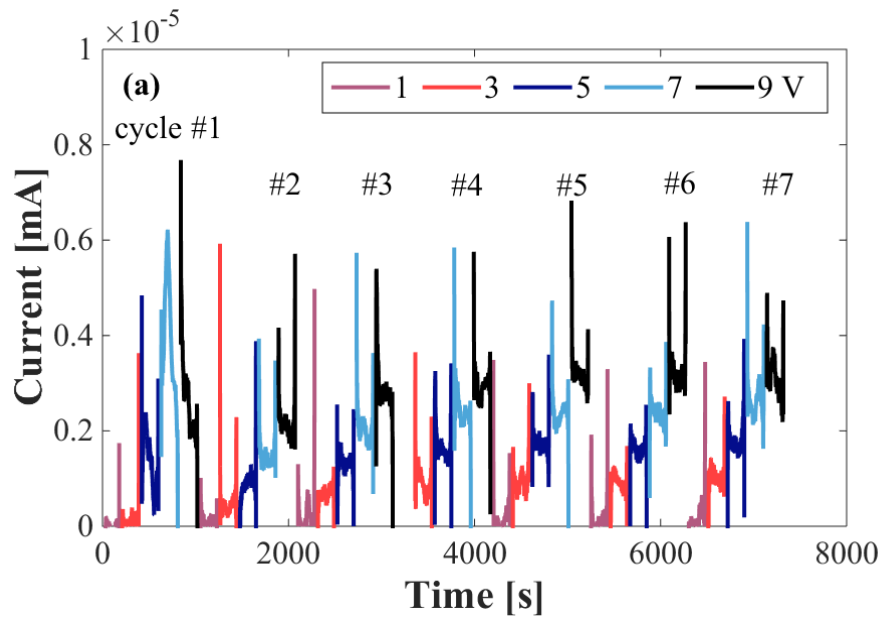


Figure B-6: DMMP detection using carbon sensor at two different temperatures (a) 25°C, (b) 60°C.

According to Fig. B-6(a), as the input voltage increases to 5 V, the output current rises to 2 nA. Further increasing the voltage to 7 V, the current increases to ~5 nA. Following this peak, the value of the output current decays (~3 nA); such behavior can be explained via the equivalent circuit model depicted in Fig. B-4. Although the peak current decreases to a relatively stable value, subsequent cycles do not result in a permanent reduction in the current. This decreased current does not permanently poison the sensor and the sensor is still capable of detecting DMMP. Further, the sensors clearly show a voltage dependency: at higher voltages, the output current is greater. For subsequent cycles, current at 7 V remains at 2 nA while it is steady at 3 nA for 9 V excitation.

Following DMMP sensing at 25°C, no further change was made to the setup. The reservoir containing DMMP was thoroughly cleaned and dried and 10 mL of new DMMP was added. The temperature of the chamber was set to 60°C. Figure B-6(b) includes the current response for the sensor exposed to DMMP at 60°C. As shown in Fig B-6(b), the value of the output current increases up to a peak value and then decays to a steady state value for the excitation of 1 V. However, for higher voltage excitations, the value of the current output increases with time. Also, as shown in Fig. B-6(b), no further decay in the magnitude of current is observed. Table B-1 includes numerical values for the comparison of current measurements using the carbon sensor at 60°C. As discussed, a comparison between cycle 2 and 7, skipping cycle 1, was assumed to provide sufficient time for full evaporation of DMMP within the reservoir. The primary reason for such an approach is to limit

degradation of the interdigitated sensors since the exposure to DMMP results in sensor degradation which is discussed in the following section.

To better illustrate the impedance behavior of the carbon sensor as a function of voltage excitation, current-voltage (I-V) relations have been established at two temperatures. For each class of sensor materials, two sets of tests were conducted, and error bars were calculated based on the deviation from the average data.

DMMP organic molecules adsorb on the PI sheet; such adsorption provides a conductive pathway for electronic current. To further elucidate the sensing mechanism, a modular configuration of the capacitive-electrolytic sensor with varying distance between the branches was designed, fabricated, and tested.

Table B.1. Micro-Porous Comparison of the increase in output current from the 2nd cycle to 7th cycle in a carbon sensor at 60°C.

Voltage [V]	Current in 2nd Cycle [nA]	Current in 7th Cycle [nA]	Current increase from 2nd to 7th Cycle [nA]
1.00	1.37	7.70	6.33
3.00	5.95	24.4	18.5
5.00	11.3	37.5	26.2
7.00	22.0	50.0	27.9
9.00	30.6	59.2	28.6

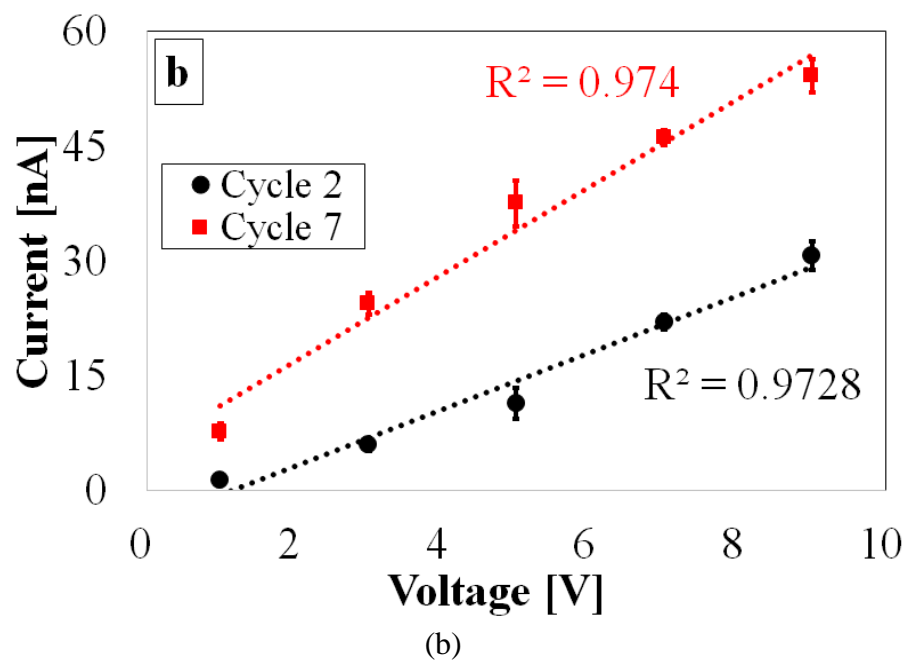
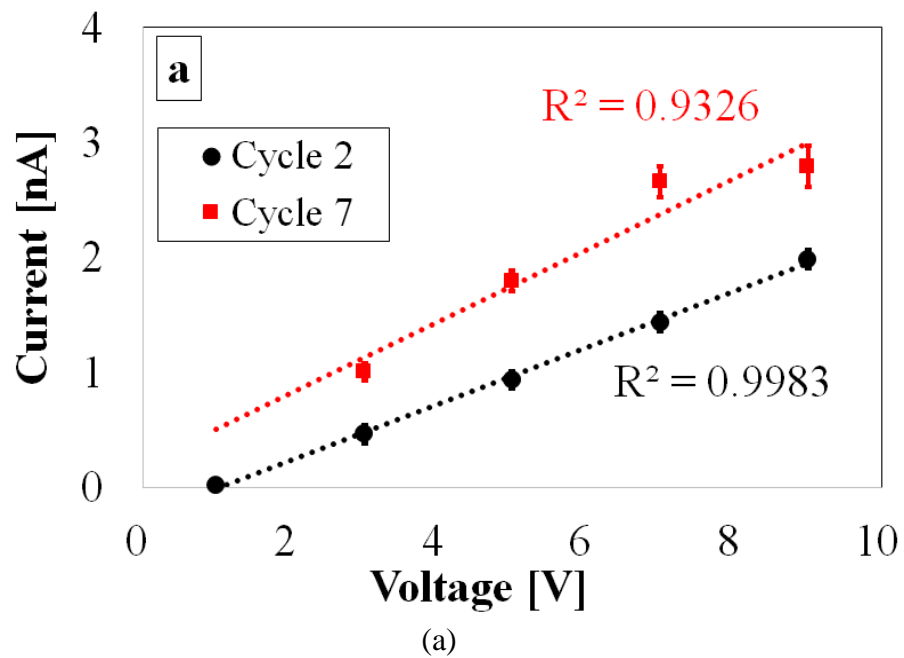


Figure B-7: Current-voltage response for DMMP detection using carbon sensor at two different temperatures, (a) 25°C, (b) 60°C.

The I-V graph for the carbon sensor at 25°C (Fig B-7 (a)) can be approximated by fitting a linear relationship between the voltage and current to simulate the resistive response of the sensor. The sensors developed in this work were capacitive-electrolytic sensor in which no faradaic current was measured during the experiments.

As shown in Fig. B-4, the charge transfer resistance and high frequency ohmic resistance can be approximated by resistors in order to simulate the sensor's behavior. It is important to note that, for an *in-situ* electrochemical sensor, there are three main sources of loss (generically called overpotential or overvoltage) including charge-transfer, ohmic, and mass transport overpotential. Charge transport overpotential is the driving force required to drive an electrochemical reaction in a particular direction. The charge transport overpotential is usually characterized by oxidation/reduction characteristics of DMMP which has been discussed elsewhere³⁰⁴.

Ohmic overpotential is the driving force for electronic and ionic current in conductive media. Mass transport overpotential is the excess voltage required to induce transport of reactive species from the bulk to the surface when the concentration difference of species (reactants and products) between the surface of the sensor and bulk becomes significant. In this work, early detection of DMMP at low concentration has been the major focus; thus; the mass transport overpotential is assumed to be negligible due to relatively low concentration of DMMP.

During the cycling experiments, the impedance of the carbon sensors (the reciprocal slope of the I-V graph in Fig. B-7) approaches a constant value, indicating steady state behavior. Figure B-7(b) is the I-V graph for the carbon sensor at 60°C. According to Fig. B-7, the slope of the I-V graphs decreases as a function of cycling, indicating a reduction of the sensor impedance for carbon sensors. Also, the carbon sensors exhibit very high response to increased temperature. For example, for the case of voltage excitation of the sensor at 9 V, increased temperature from 25 to 60°C increases the current by almost 20 times.

DMMP detection using copper-coated sensors

Figure B-8 includes the current response for the voltage excitations of the copper-coated sensors exposed to DMMP at two different temperatures. The voltage excitations protocol was applied according to Fig. B-5. The copper-coated sensors were exposed to DMMP maintained at two different constant temperatures of 25 and 60°C.

According to Fig. B-8(a), the current response of the copper-coated sensors declines over time, unlike the observed behavior of the carbon sensors. In this case, in the very first cycle, the output current at 9 V reaches a peak of 65-70 nA. Following this, the output decreases with every cycle; within the timeframe considered in this study, a clear steady state value is not reached. Also, as shown, increased excitation voltage results in an increase in the output current.

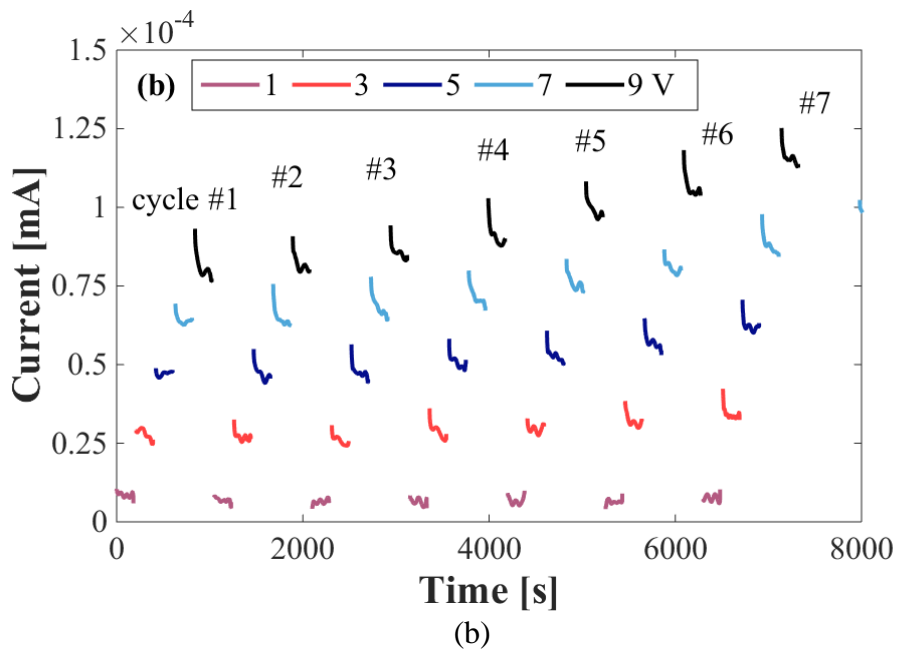
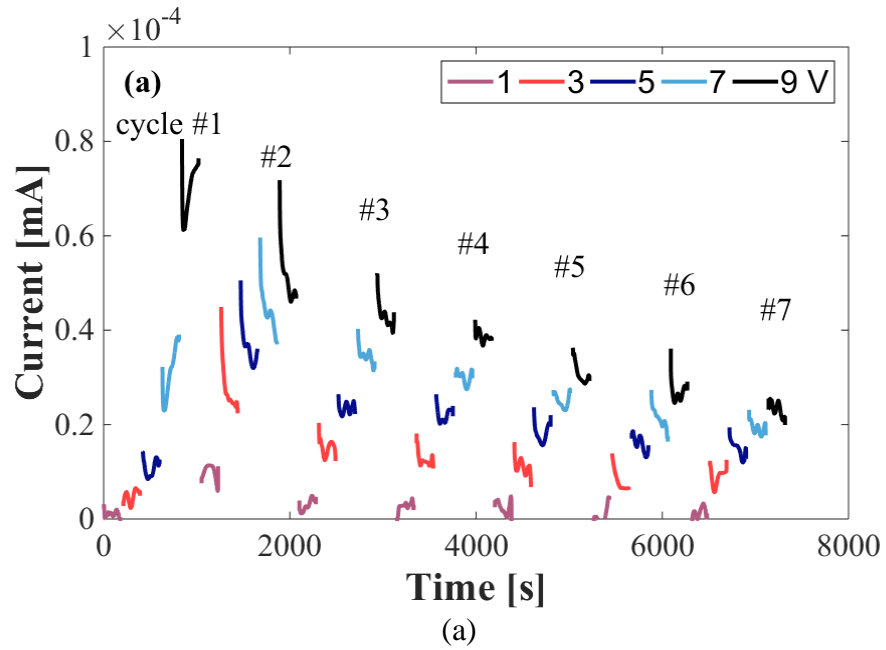


Figure B-8: DMMP detection using copper-coated sensor at two different temperatures.

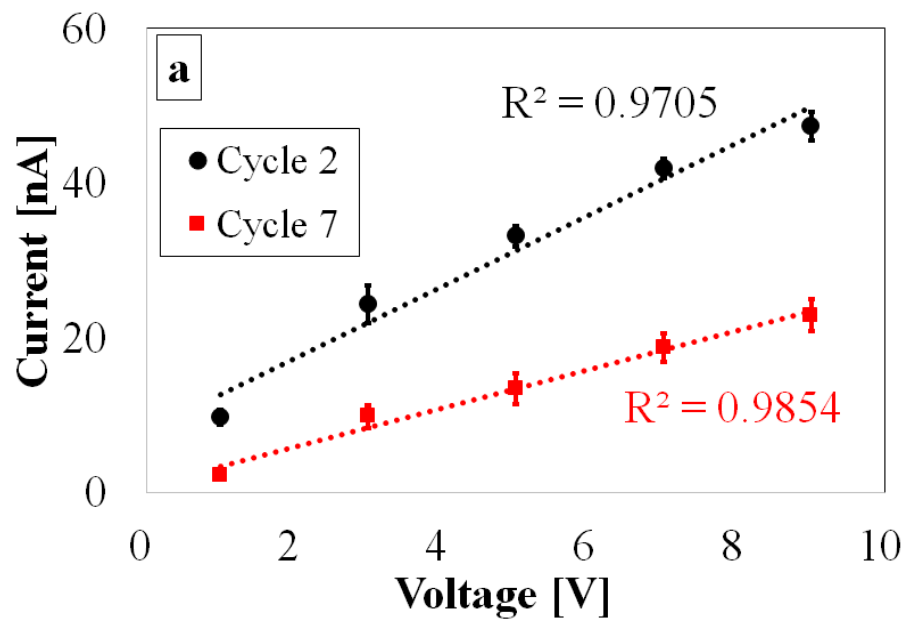
As shown in Fig. B-8(b), for the copper-coated sensors at 60°C, the output current as well as the rate of current increase constantly increases with time. At the lower voltages, such as 1, 3 and 5 V, the rate of increase is linear. However, for 7 V and 9 V, the graph has an exponential trend. In comparison with Fig. B-8(a) and (b), increased temperature not only increases the concentration of DMMP but also potentially affects the kinetic behavior of the reaction. The increase in output current during cycling is tabulated in Table B-2.

As presented in Table B-2, the rate of increase of current increases with the voltage. To better understand the impedance behavior of the copper-coated sensors as a function of voltage excitation, I-V relations were assessed at two temperatures and are shown in Fig. B-9.

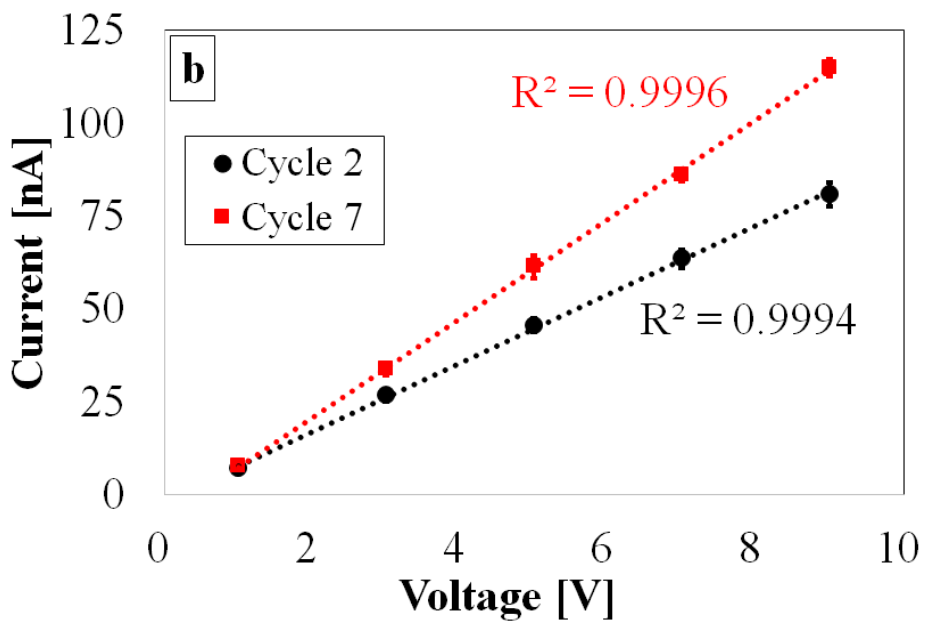
As shown in Fig. B-9(a), the behavior of copper-coated sensors is unlike that of the carbon sensors at 25°C.

Table B.2. Comparison of the increase in output current from the 2nd cycle to 7th cycle in a copper-coated sensor at 60°C.

Voltage [V]	Current in 2nd Cycle [nA]	Current in 7th Cycle [nA]	Current increase from 2nd to 7th Cycle [nA]
1.00	6.90	7.48	0.58
3.00	26.6	33.6	6.93
5.00	46.5	61.2	14.7
7.00	63.6	86.1	22.4
9.00	79.5	115	35.5



(a)



(b)

Figure B-9: Current-voltage response for DMMP detection using copper-coated sensor at two different temperatures (a) 25°C, (b) 60°C.

According to Fig. B-9 (a) the reciprocal slope of the I-V graphs increases over time indicating an increase in the sensor impedance, opposite of the trend observed for carbon sensors. This behavior indicates that the copper-coated sensors degrade after exposure to DMMP. Also, as shown in Fig. B-9(b) a linear relation is observed between voltage and current, indicating a resistive behavior for the sensor. However, the rate of increase is different. The reciprocal slope of the I-V graph decreases with time for the copper-coated sensor exposed to DMMP at 60°C, suggesting an increase in ohmic overpotential as a function of sensor poisoning. This behavior suggests that the rate of decrease in charge-transfer overpotential in addition to increased concentration of DMMP has a more significant effect in comparison to reduced current as a function of sensor degradation at 60°C for copper-coated sensors.

Comparison of carbon and copper-coated sensors

To compare the performance of carbon and copper-coated sensors, DMMP sensing is conducted at the same concentration, at 9 V, and at two different temperatures.

Figure B-10(a) shows the comparison between output currents at 9 V, 25°C for the carbon and the copper-coated sensors. It can be observed that, in the first cycle, the carbon sensor results in only 4 nA as a response to voltage excitation. However, the copper sensor provides 70 nA. With subsequent cycles, the value of copper sensor gradually decreases and reaches 22 nA by the 7th cycle.

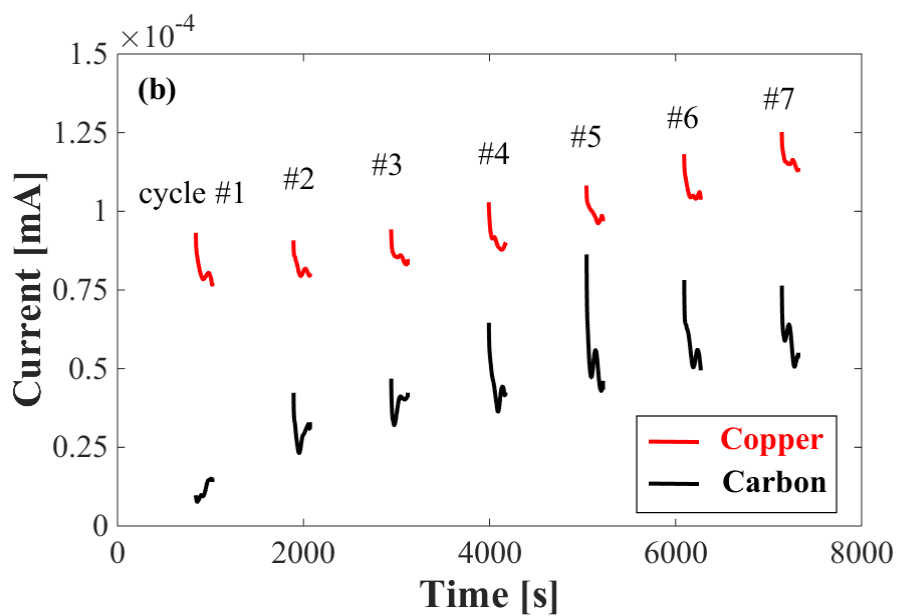
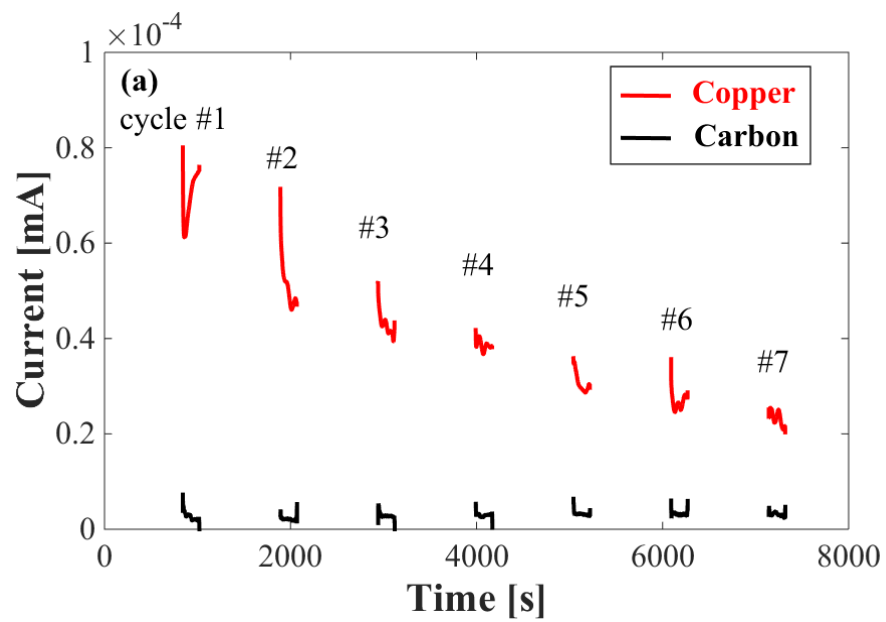


Figure B-10: DMMP detection using carbon and copper-coated sensors at two different temperatures for the voltage excitation of 9 V, (a) 25°C, (b) 60°C.

The carbon sensor, however, gives a steady output around 4 nA that does not decay. This observation indicates that the copper-coated sensors provide a higher current, thus higher sensitivity at the same concentration of DMMP, but suffer from more intense degradation. According to Fig. B-10(b), it can be observed that the copper-coated sensor gives a higher current value than the carbon sensor at 60°C. From the 2nd cycle, the change in response over time for both carbon and copper sensors is nearly linear. Comparing the two values, one can observe that the current response of carbon sensors is almost 62% to 49% lower than copper sensor. The values of both the copper and carbon sensors do not decrease with time.

Also, it is important to investigate the degradation behavior of carbon and copper-coated sensors exposed to DMMP. Degradation is defined based on the response signal of a sensor that had been previously exposed to DMMP at similar conditions. Figure B-11 includes the response of carbon and copper-coated sensors at 25°C for duplicated tests.

As shown in Fig. B-11, although the copper-coated sensors initially exhibit higher sensitivity, the degradation upon exposure and initial cycling has a significant effect on the sensitivity. The copper-coated sensor loses almost all sensitivity in the second usage, while the carbon sensors exhibit almost no degradation in sensitivity from exposure. Degradation behavior of carbon and copper-coated sensors exposed to DMMP at 60°C for the voltage excitation of 9 V is shown in Fig. B-12.

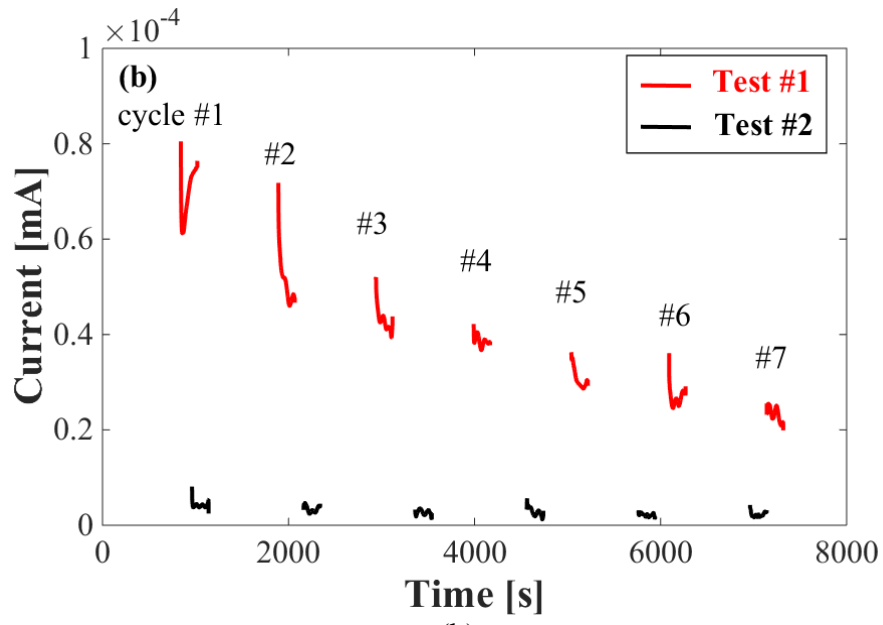
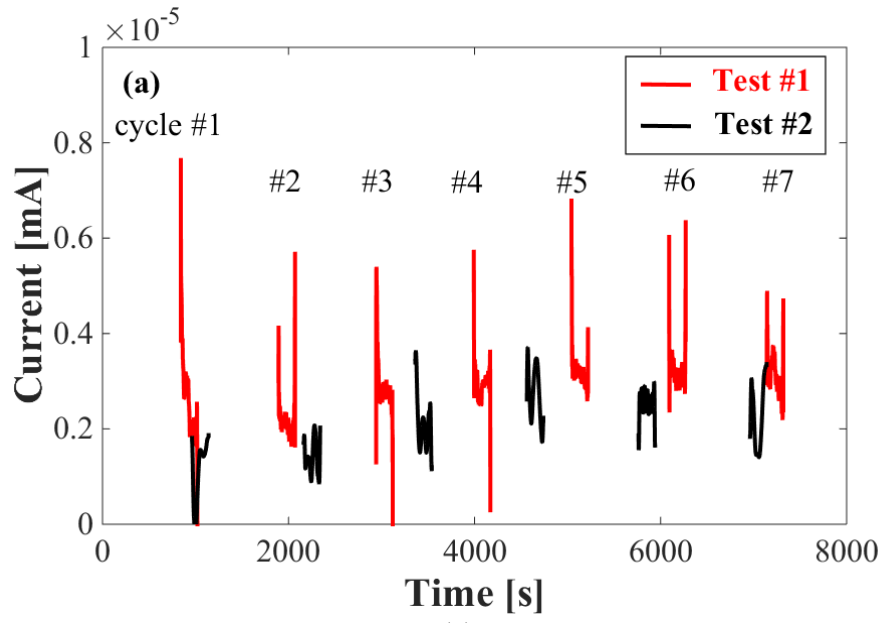


Figure B-11: DMMP detection for post-mode degradation using carbon and copper-coated sensors at 25°C for the voltage excitation of 9 V, (a) carbon, (b) copper-coated.

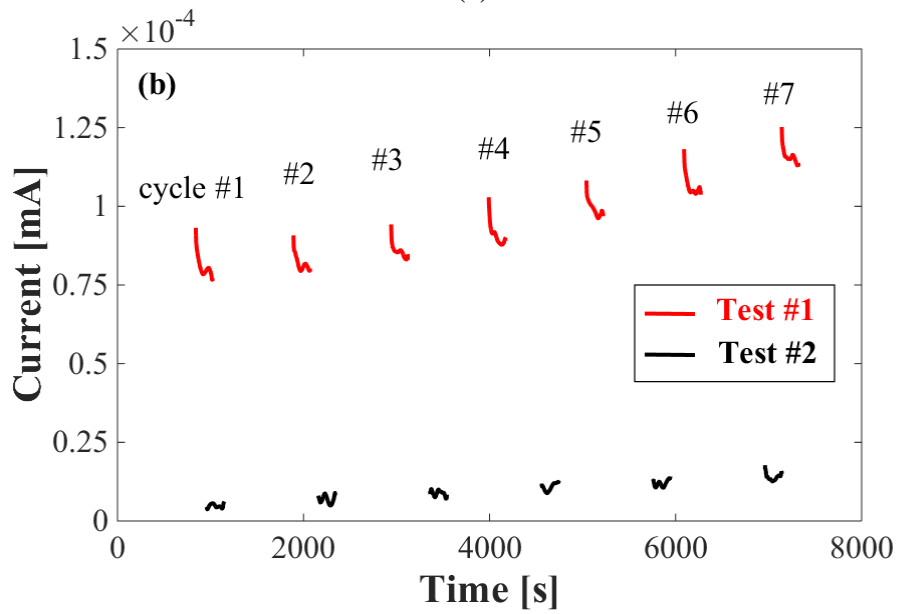
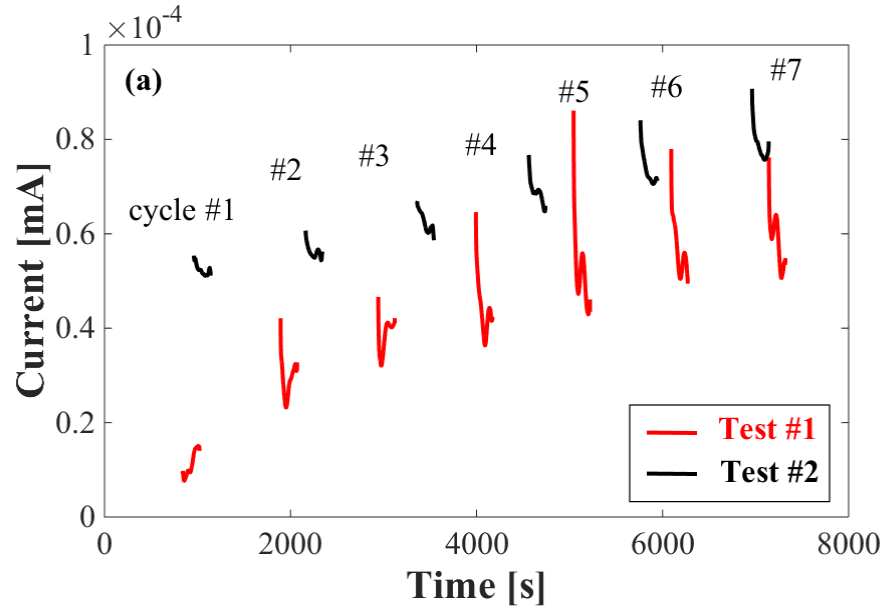


Figure B-12: DMMP detection for post-mode degradation using carbon and copper-coated sensors at 60°C for the voltage excitation of 9 V, (a) carbon, (b) copper-coated.

As shown in Fig. B-12, the carbon sensors not only show no appreciable degradation, the current response exhibits a slight increase. Such behavior suggests that the application of sensors at elevated temperature for the first time contributed to decreased charge-transfer overpotential in the second test. However, the copper-coated sensor lost almost all sensitivity for the second test.

Discussion

In this work, two sets of sensors were investigated, including carbon and copper-coated sensors, at 25°C and 60°C. Both the carbon and copper-coated sensors showed appreciable sensitivity for DMMP detection and were successful in detecting DMMP even at room temperatures. However, the copper-coated sensors showed very high sensitivity as a function of increased excitation voltage and increased temperature. It is important to note that the International Union of Pure and Applied Chemistry (IUPAC) defines the sensitivity as the slope of the calibration curve (sensor response versus concentration). The application of this definition has been adopted within the supplementary materials.

The carbon sensor additionally showed significantly lower degradation upon DMMP exposure. Also, the carbon sensor exhibited excellent stability compared to copper-coated sensors. It is possible that the primary reason for this behavior is the strength of bonding between DMMP molecules and carbon. As shown in Fig. B-1 the polar structure of DMMP has relatively light adhesion on non-polar carbon structures. The copper surface can, therefore, become essentially corroded and lose sensitivity after exposure to DMMP. Due

to severe degradation occurring in copper-coated sensors after exposure to DMMP vapor, the voltage excitation protocol with intervals of 3 min was adopted according to Fig. B-5; the main objective of such a voltage excitation was obtaining the maximum capacitive current at a short timeframe, avoiding degradation. However, exposing the carbon sensors to DMMP vapor for a longer time will eventually result in a stable, non-zero current. An example of such stable sensing current under longer time period for voltage excitation protocol between 0 and 9 V has been provided in supplementary data.

The increase in sensitivity of the sensors as a function of increased temperature is attributed to higher DMMP concentration and improved kinetics (the DMMP vapor pressure as a function of temperature is provided in the supplementary materials). This behavior is more pronounced for copper-coated sensors in comparison to carbon sensors. The higher voltage excitation results in higher sensor current response since the sensors behave as resistors. The sensors were exposed to dry nitrogen, dry air and humid air and excited via the application of constant voltage of 9 V; the interdigitated sensors exhibit no sensitivity for these gases. The data regarding the selectivity assessment of the interdigitated carbon and copper-coated sensors for basic gases have been provided in the supplementary materials.

Summary and Conclusions

In this work, laser induced interdigitated microelectrode sensors with two configurations of carbon and copper-coated developed for the detection of dimethyl methylphosphonate (DMMP) as a simulant of sarin gas. The sensors were exposed to DMMP at ambient and

elevated temperature (60°C) and a pulsed voltage excitation was applied to capture the capacitive and resistive behavior of the sensors. The copper-coated interdigitated sensors are capable of detecting DMMP with very high sensitivity; however, they rapidly degrade after exposure to DMMP. The carbon interdigitated sensors do not suffer from current degradation as a function of DMMP exposure and degradation of carbon sensors is significantly lower compared to copper sensors. The sensitivity of the sensors significantly increases with increased temperature due to an increase in simulant concentration and improved kinetics. The interdigitated sensor morphology exhibits a linear voltage-current response. The current results may pave the way to develop a simple, supersensitive sensor for fast in-situ detection of toxic gases.

Acknowledgments

This work is partially supported by Joint Directed Research and Development Project between University of Tennessee Knoxville and Oak Ridge National Lab for AH and Nature Science Foundation of China (51575016). This work is also supported in part (S. Wang) by the scholarship from China Scholarship Council (CSC) under the Grant CSC No.201506240097. Y.A.G. would like to acknowledge University of Tennessee for providing a Chancellors Graduate Fellowship.

Author Contributions

All authors contributed extensively to this work. Y.A.G. designed the interdigitated sensors, conceived of and executed the experimental studies. S.W., Y.Y., and R.L. built the sensors. V.G.V. conducted a significant portion of the experimental tests. Y.A.G.,

V.G.V. and D.S.A. wrote the paper. S.C., A.H. and M.M.M. supervised and guided the project.

Conflicts of Interest

The authors declare no conflict of interest.

VITA

Yasser Ashraf Gandomi was born in Tabriz. Prior to enrolling in the PhD program at University of Tennessee, he received a Master's as well as a Bachelor degree in Mechanical Engineering from the University of Tabriz. Yasser completed his second M.S. in 2014 and Ph.D. in 2018 under the supervision of Professor Matthew Mench at the University of Tennessee. Yasser will be a Postdoctoral Associate at the Massachusetts Institute of Technology (MIT) in December 2018.